

# **Complexes of Chiral Tridentate Ligands for Spin-Crossover and Catalysis**

Namrah Shahid

Submitted in accordance with the requirements for the degree of  
Doctor of Philosophy

The University of Leeds  
School of Chemistry

May 2021

The candidate confirms that the work submitted is her own and that appropriate credit has been given where reference has been made to the work of others. This copy has been supplied on the understanding that it is copyright material and that no quotation from the thesis may be published without proper acknowledgement.

The right of Namrah Shahid to be identified as Author of this work has been asserted by her in accordance with the Copyright, Designs and Patents Act 1988.

## Acknowledgements

بِسْمِ اللَّهِ الرَّحْمَنِ الرَّحِيمِ، الْحَمْدُ لِلَّهِ رَبِّ الْعَالَمِينَ.

Qu'ran [1:1-2]

In the name of Allah, the most compassionate, the most merciful.

All praises and thanks are for Allah, Lord of the worlds.

These pages represent my greatest academic achievement to date. What isn't shown is the whirlwind of emotions that came with it, but I know I always had Allah with me, listening to every prayer. It is only by His will that I have this PhD. Alhamdulillah.

This PhD has been bittersweet. Waking up in the middle of the night thinking about the endless to-do list I have to get through the next day, the constant worry of not having done enough and the constant doubt of not being smart enough. Countless hours spent in the lab, coming into the lab in the dark and going home in the dark, and not just in winter. It continually demanded from me. But strangely enough, it also became my solace. For the last four years, the lab became my place of refuge, my safe haven, my constant in an inconstant world.

Just as I entered my final year in March 2020, Covid-19 took my lab away from me for seven months. I never knew how much I'd miss lab 1.29 until that moment. While we were all struggling to adjust to the 'new normal', it was hard to not worry about how I would ever finish this PhD – I lost sight of the end just when it was coming into sight. Eventually, we returned to a new, one-way system-ed, decluttered, disinfected, socially-distanced, occupancy-limited, face-masked lab and it just wasn't quite the same. But by the grace and mercy of Allah, I had a rekindled motivation to plough through and do my utmost to finish this PhD, despite the circumstances.

In my eight years of university, I have encountered many people. There isn't one person on this journey that I haven't learnt something from and for that I owe a thank you to everyone who has been with me over the years. I would like to express my gratitude to a few particular people.

To my supervisor, Professor Malcolm Halcrow, I don't think I ever really thanked you for taking me under your wing and offering me this PhD position to start with, so I thank you now. I can only hope you haven't regretted it. For the last four years, you have been really patient with me and you have taught me a lot. I have done my best to hold on to every word of wisdom you have imparted. Every thesis probably has this same line about you, and whilst it sounds generic, there are no better words; thank you for being the best supervisor anyone could ask for, for your advice and guidance throughout. For being on the other side of a door-knock or the other end of an e-mail regardless of the day or time.

For sending me away from our monthly GRAD meetings motivated, for never underestimating me and mostly, for getting me to this point where I can say I have a PhD. Needless to say, it couldn't have been done without you. Thank you for this PhD. It's been an honour to work with you.

To my secondary supervisor, Professor Patrick McGowan, it was because of my master's project under your supervision that that I decided to embark upon this PhD, so thank you for that motivation. But also for your advice and guidance at each annual assessment stage and on the ruthenium work, the catalysis work and the anti-cancer pursuits. Thank you for your regular at-the-door one minute stories that always brought life to the office, for opening your home to me and hosting dinners.

To Dr Christopher Pask, there's a long list of all that I'm thankful for from you, a few lines can't possibly summarise it. Thank you for training me on the X-ray Diffractometer and the powder-XRD, for the work at the Diamond Synchrotron, for all the general lab advice, for help with all the lab admin work, for help with supervising the MChems, for all your continuous advice and feedback, chemistry-related and other. You are pivotal to the chemistry department at Leeds.

To the School of Physics for being so welcoming and friendly during my time working in the Condensed Matter Lab II. To Dr Oscar Cespedes for training me on the Superconducting Quantum Interference Device (SQUID) and for your advice during my time in Physics. To Dr Mark Howard, thank you for all the variable temperature Evan's  $^1\text{H}$  NMR Method experiments which have provided countless data for this thesis. Thank you for being so accommodating and efficient, it has been truly appreciated. Thank you to the staff at the Synchrotron at Diamond Light Source, for your hospitality, help and friendliness whilst I worked at the facilities. Thank you to the Elemental Analysis Service at the London Metropolitan University for the microanalysis and to Dr Rianne Lord at the University of East Anglia for the cell-line testing.

Finally, I would also like to thank the Engineering and Physical Sciences Research Council UK for funding this PhD and the University of the Leeds for providing me a scholarship to cover my tuition fees. There is not a chance I would have been able to do this PhD without this financial support. I owe an additional thank you to the EPSRC for granting me a funding extension due to the lab time lost over the Covid-19 pandemic. To the School of Chemistry and the University of Leeds, thank you for having me for the last eight years. Words cannot describe just how much I will miss this place.

At a more personal level, there have been a number of individuals and groups of individuals who have been so supportive of my endeavours and who have made my university years unforgettable. A massive thank you to my university family, the Leeds University Union's Islamic Society, for giving me a place of belonging, dozens of lifelong



friends, and some incredible memories. Never underestimate what you do for Muslim students on campus. Thank you to my fellow chemists next door in lab 1.32, just knowing you were all there with an open-door policy, always welcoming a chat and a hot drink meant a great deal to me. (Also, thank you for opening all the tightly screwed lids and canisters that my muscles have failed me on.) Thank you to my colleagues at Argos who were always cheering me on through my studies. I truly appreciated having this job on the weekends to block out all things PhD-related. To my fellow ambassadors at the Leeds Muslim Youth Forum, for your continued support, the endless opportunities and the platform to make a difference beyond the university bubble. To the girls at my running club, Hijabi Runners, I'm incredibly proud of all that you girls have achieved, you continually inspire me. Thank you for turning up to run sessions whatever the weather and for the all the chit chat whilst we ran. Never give up running.

Finally, Mum, thank you for your support over these years and for being my source of motivation. I know things haven't been easy, but things always worked out for the better in the end. Through thick and thin, Allah has always been with us. I hope you're proud!

There are *many* more people to thank and not enough pages left in this thesis to list them all, so personal acknowledgements have been sent to the rest.

## Abstract

This thesis delves into the breadths of chemistry, comprising the exploration of the organic synthesis of the underexplored, sulfur analogue of the ligand, 2,6-bis(oxazoline)pyridine (PyBOX), namely 2,6-bis(thiazolinyl)pyridine (thioPyBOX). A series of coordination complexes of iron(II), copper(I), copper(II) and ruthenium(II) featuring the PyBOX and thioPyBOX ligands, have been synthesised for a manifold of applications. These include molecular electronics, catalysis and metal-based anti-cancer medicines.

A continuous narrative throughout this work is the electronic and steric effects of swapping oxygen for sulfur in such coordination complexes and the impact of this on their chemistry in end applications. The exploration of chiral metal complexes, designed by the diastereomeric nature of substituted PyBOX and thioPyBOX ligands, forms a significant proportion of the work herein.

Substituted thioPyBOX ligands have been synthesised in two different enantiomeric forms, following which homochiral and heterochiral iron(II) thioPyBOX complexes were synthesised and studied. The concept of chiral discrimination of spin states was corroborated with a pair of enantiomers displaying a High Spin-Low Spin dichotomy at ambient conditions. Heteroleptic iron(II) (thio/)PyBOX complexes have also been synthesised of these ligands and with other classical N,N',N''-tridentate pincer ligands. The overall findings have demonstrated an increased stability of metal-thioPyBOX complexes compared to their PyBOX counterparts, this is attributed to the reduced electron-withdrawing nature of thiazoline compared to oxazoline.

Copper(I) and copper(II) (thio/)PyBOX complexes have been synthesised with a view to achieve an effective catalyst for the copper-catalysed azide-alkyne Click reaction and the copper-catalysed Ullman coupling reactions respectively. Furthering the catalysis aspect, ruthenium(II) (thio/)PyBOX complexes of mono- and bis- ligand coordination were synthesised for the catalysis of the asymmetric transfer hydrogenation reaction. Further afield, cell-line testing of one of these complexes was found to exhibit better cytotoxic activity than *cisplatin* against pancreatic cancer cells and human bone cancer cells which is also presented in this thesis.

## Table of Contents

<b>Acknowledgements</b> .....	<b>iii</b>
<b>Abstract</b> .....	<b>vi</b>
<b>Table of Contents</b> .....	<b>vii</b>
<b>List of Tables</b> .....	<b>xiii</b>
<b>List of Equations</b> .....	<b>xv</b>
<b>List of Figures</b> .....	<b>xvi</b>
<b>Abbreviations</b> .....	<b>xxx</b>
<b>Thesis Outline</b> .....	<b>1</b>
<b>Chapter 1 Introduction and Theory</b> .....	<b>3</b>
1.1 Coordination Complexes .....	3
1.1.1 Crystal Field Theory.....	4
1.1.2 Electron Configuration .....	5
1.1.3 Ligand Field Theory .....	6
1.1.4 Metal-Ligand $\pi$ - Bonding.....	7
1.2 The High-Spin - Low-Spin Dichotomy.....	9
1.2.1 Molecular Magnetism.....	10
1.3 The Jahn-Teller Effect.....	13
1.4. Spin Crossover.....	15
1.4.1. Applications of SCO materials .....	17
1.4.2 Origins of SCO .....	18
1.4.3 Metals that Exhibit SCO.....	19
1.4.4 The Fe(II)-N <sub>6</sub> System.....	20
1.4.5 The SCO transition point .....	21
1.4.6 Magnetic Bistability.....	24
1.4.7 Thermodynamics of SCO .....	26
1.4.8 External stimuli .....	27
1.4.9 Second Coordination Sphere effects .....	34
1.4.10 Measuring SCO.....	35
1.5 Computational methods .....	39
1.5.1 Density Functional Theory .....	41
<b>Thesis objectives and aims</b> .....	<b>43</b>
<b>Chapter 2 Synthesis and Characterisation of 2,6-Bis(thiazoliny)pyridine (ThioPyBOX) Ligands</b> .....	<b>44</b>
2.1 Introduction .....	44

2.1.1 N,N',N''- Ligands .....	44
2.1.1.1 Schiff-base ligands .....	44
2.1.1.2 N,N',N''-pincer ligands .....	46
2.1.1.3 2,2':6',2''- Terpyridine .....	47
2.1.1.4 2,6-Bis(pyrazolyl)pyridine.....	49
2.1.2 The PyBOX Ligand.....	51
2.1.3 The ThioPyBOX Ligand.....	54
2.2 Results & Discussion.....	60
2.2.1 Synthesis of 2,6-Bis(thiazolanyl)pyridines – A Two-Step Reaction .....	60
2.2.2 Heterocyclic formation and thiolation step.....	62
2.2.3 Analysis and characterisation .....	69
2.3 Conclusion .....	80
2.4 Experimental .....	80
2.4.1 Di(hydroxyl)pyridine-2,6-dicarboxamide.....	81
2.4.2 Macrocyclic, M1 .....	82
2.4.3 2,6-Bis(thiazolanyl)pyridine – ThioPyBOX.....	83
<b>Chapter 3 Spin-Crossover Complexes of Iron(II) ThioPyBOX .....</b>	<b>86</b>
3.1 Introduction .....	86
3.1.1 Chirality in Metal Complexes .....	86
3.1.1.1 “Chiral-at-Ligand” .....	88
3.1.2 Chirality in Spin-Crossover Complexes .....	89
3.1.2.1 Why are we interested? .....	90
3.1.2.2 Homochiral-SCO Compounds .....	91
3.1.3 Subtle Differences between SCO Complexes .....	93
3.1.3.1 Discrimination Between Polymorphs w.r.t SCO Activity .....	93
3.1.3.2 Switching Sulfur for Selenium .....	96
3.1.3.3 Switching Oxygen for Sulfur in Heterocyclic Ligand Frameworks.....	99
3.1.4 Chiral Discrimination of Spin States in Iron(II)PyBOX complexes .....	101
3.1.4.1 Solid State SCO results .....	102
3.1.4.2 Solution State SCO results .....	105
3.1.4.3 Racemisation studies.....	108
3.2 Results & Discussion.....	110
3.2.1 Iron(II)thioPyBOX <sup>R</sup> Complexes and Their Spin State Behaviour .....	110
3.2.1.1 Synthesis of Iron(II)-thioPyBOX Complexes .....	110
3.2.1.2 Complexes and Characterisation .....	111

3.2.1.3 Structural Characterisation by X-ray Diffraction .....	113
3.2.1.4 Solid State Magnetic Susceptibility .....	129
3.2.1.5 Solution State Magnetic Susceptibility .....	133
3.2.1.6 Van't Hoff Calculations .....	136
3.2.1.7 Racemisation Studies .....	137
3.3 Conclusion .....	144
3.4 Experimental .....	145
<b>Chapter 4 Heteroleptic Iron(II) PyBOX and thioPyBOX complexes for Spin-Crossover .....</b>	<b>149</b>
4.1 Introduction .....	149
4.1.1 Heteroleptic iron(II) SCO complexes .....	150
4.2 Results & Discussion.....	152
4.2.1 Iron(II) PyBOX <sup>Ph</sup> /thioPyBOX <sup>Ph</sup> complexes .....	152
4.2.1.1 Structural Characterisation by XRD .....	153
4.2.2 Spin-crossover Studies.....	159
4.2.2 Iron(II) PyBOX <sup>iPr</sup> /thioPyBOX <sup>iPr</sup> complexes .....	162
4.2.2.1 Structural Characterisation .....	162
4.2.2.2 Spin-crossover studies .....	167
4.2.3 An attempted iron(II)PyBOX/thioPyBOX <sup>iBu</sup> complex .....	169
4.2.4 Heteroleptic iron(II) (thio/)PyBOX complexes incorporating 2,6-bis(2-benzimidazolyl)pyridine (bzimpy).....	172
4.2.4.1 Iron(II) (thio/)PyBOX <sup>Ph</sup> complexes with bzimpy .....	174
4.2.4.2 Iron(II) (thio/)PyBOX <sup>iPr</sup> complexes with bzimpy .....	182
4.2.5 Iron(II) (thio/)PyBOX complexes incorporating 2,6-bis(pyrazol-1-yl)pyridine (1-bpp) .....	187
4.2.5.1 Structural characterisation .....	188
4.2.5.2 SCO studies .....	191
4.2.6 Iron(II) (thio/)PyBOX complexes incorporating 2,2':6',2''-terpyridine (terpy).....	193
4.3 Conclusion .....	197
4.4 Experimental .....	199
<b>Chapter 5 Copper (thio/)PyBOX Complexes for Catalysis .....</b>	<b>205</b>
5.1 Introduction .....	205
5.1.1 Base Metal Catalysis.....	206
5.1.1.1 Copper.....	206
5.1.2 Copper-PyBOX Catalysts .....	211
5.1.2.1 Self-assembled copper(I) PyBOX helicates .....	213

5.2 Results & Discussion.....	216
5.2.1 Copper complexes synthesised herein .....	216
5.2.1.1 Copper(II) complexes .....	216
5.2.1.2 Copper(I) complexes .....	222
5.2.2 Preliminary catalysis studies .....	228
5.2.2.1 Catalysis method .....	229
5.2.2.2 Test reaction.....	231
5.2.2.3 Preliminary Click Catalysis study .....	232
5.3 Conclusion .....	237
5.4 Experimental .....	238
<b>Chapter 6 Ruthenium PyBOX and thioPyBOX Complexes for Asymmetric Catalysis and Biological Activity .....</b>	<b>241</b>
6.1 Introduction .....	241
6.1.1 Asymmetric Catalysis .....	241
6.1.2 Pyridine bis(oxazoline) in Catalysis .....	242
6.1.3 Ruthenium-PyBOX Catalysts .....	242
6.1.4 Transfer Hydrogenation.....	244
6.1.4.1 Ruthenium-PyBOX catalysts for Transfer Hydrogenation.....	245
6.1.5 Ruthenium-PyBOX in Anti-cancer Studies.....	245
6.2 Results & Discussion.....	246
6.2.1 Ruthenium-N,N',N''- Complexes Synthesised.....	246
6.2.1.1 Ruthenium-terpyridine complexes.....	246
6.2.2 Ruthenium-PyBOX complexes .....	248
6.2.2.1 Ruthenium-PyBOX <i>trans</i> -iodide complexes .....	250
6.2.3 An unprecedented hemilabile Ru-thioPyBOX complex .....	252
6.2.4 Preliminary catalysis work .....	254
6.2.5 Biological Investigation.....	256
6.2.5.1 Cell-line testing .....	256
6.2.5.2 Results .....	257
6.3 Conclusion .....	258
6.4 Experimental .....	259
<b>Future Work Prospects .....</b>	<b>262</b>
<b>Overall Conclusions .....</b>	<b>263</b>
<b>Appendix X-ray Diffraction Crystallographic Data .....</b>	<b>265</b>
Chapter 2 XRD data.....	265
L4 C <sub>17</sub> H <sub>23</sub> N <sub>3</sub> S <sub>2</sub> (M =333.50 g mol <sup>-1</sup> ).....	265
L6 C <sub>19</sub> H <sub>27</sub> N <sub>3</sub> S <sub>2</sub> (M =361.55 g mol <sup>-1</sup> ).....	265

L5•L6 C <sub>19</sub> H <sub>27</sub> N <sub>3</sub> S <sub>2</sub> (M =361.55 g mol <sup>-1</sup> ):.....	265
M1•H <sub>2</sub> O C <sub>24</sub> H <sub>30</sub> N <sub>4</sub> O <sub>7</sub> (M =486.528 g mol <sup>-1</sup> ):.....	265
Chapter 3 XRD data.....	266
S-5 (BF <sub>4</sub> )•MeCN C <sub>48</sub> H <sub>38</sub> B <sub>2</sub> F <sub>8</sub> FeN <sub>7</sub> S <sub>4</sub> (M =1070.56 g mol <sup>-1</sup> ):.....	266
RS-5 (BF <sub>4</sub> )•1.5MeCN C <sub>49</sub> H <sub>42.5</sub> B <sub>2</sub> F <sub>8</sub> FeN <sub>7.5</sub> S <sub>4</sub> (M =1094.11 g mol <sup>-1</sup> ):.....	266
R-5 (ClO <sub>4</sub> )•MeCN C <sub>48</sub> H <sub>41</sub> CL <sub>2</sub> FeN <sub>7</sub> O <sub>8</sub> S <sub>4</sub> (M =1098.87 g mol <sup>-1</sup> ):.....	266
R-5•S-5 (ClO <sub>4</sub> )•3MeCN C <sub>91.5</sub> H <sub>77</sub> CL <sub>4</sub> Fe <sub>2</sub> N <sub>18.5</sub> O <sub>16</sub> S <sub>8</sub> (M =2201.69 g mol <sup>-1</sup> ):.....	266
RS-6•2MeCN C <sub>38</sub> H <sub>52</sub> CL <sub>2</sub> FeN <sub>8</sub> O <sub>7.835</sub> S <sub>4</sub> (M =979.86 g mol <sup>-1</sup> ):.....	266
S-7•(Me) <sub>2</sub> CO C <sub>41</sub> H <sub>55</sub> CL <sub>2</sub> FeN <sub>6</sub> O <sub>9.25</sub> S <sub>4</sub> (M =1034.90 g/mol):.....	267
S-7(i)•Et <sub>2</sub> O•MeCN C <sub>24.5</sub> H <sub>40.25</sub> N <sub>5.25</sub> O <sub>10.25</sub> CL <sub>2</sub> S <sub>2</sub> Fe (M =763.24 g mol <sup>-1</sup> ):	267
S-8•(Me) <sub>2</sub> CO C <sub>41</sub> H <sub>60</sub> CL <sub>2</sub> FeN <sub>6</sub> O <sub>13</sub> (M =971.70 g mol <sup>-1</sup> ) .....	267
Chapter 4 XRD data.....	267
S-9•MeCN C <sub>48</sub> H <sub>39</sub> CL <sub>2</sub> FeN <sub>7</sub> O <sub>10.76</sub> S <sub>1.24</sub> (M =1052.52 g mol <sup>-1</sup> ): .....	267
RS-9•MeCN C <sub>47</sub> H <sub>41</sub> CL <sub>2</sub> FeN <sub>7</sub> O <sub>12</sub> S <sub>2</sub> (M =1052.52 g mol <sup>-1</sup> ):.....	267
RS-10•MeCN C <sub>36</sub> H <sub>49</sub> CL <sub>2</sub> FeN <sub>7</sub> O <sub>9.875</sub> S <sub>2</sub> (M =928.69 g mol <sup>-1</sup> ):.....	268
S-11•(Me) <sub>2</sub> CO C <sub>41.01</sub> H <sub>56.02</sub> CL <sub>2</sub> FeN <sub>6</sub> O <sub>11.92</sub> S <sub>1.08</sub> (M =985.15 g mol <sup>-1</sup> ): ....	268
12•MeCN C <sub>44</sub> H <sub>35</sub> CL <sub>2</sub> FeN <sub>9</sub> O <sub>10</sub> (M =976.56 g mol <sup>-1</sup> ): .....	268
13 C <sub>42</sub> H <sub>32</sub> CL <sub>2</sub> FeN <sub>8</sub> O <sub>8</sub> S <sub>2</sub> (M =967.62 g mol <sup>-1</sup> ) .....	268
14 C <sub>36</sub> H <sub>35</sub> CL <sub>2</sub> FeN <sub>8</sub> O <sub>10</sub> (M =867.48 g mol <sup>-1</sup> ):.....	268
15•MeCN•Et <sub>2</sub> O C <sub>42</sub> H <sub>49</sub> CL <sub>2</sub> FeN <sub>9</sub> O <sub>9</sub> S <sub>2</sub> (M =1014.77 g mol <sup>-1</sup> ):.....	268
17•2MeCN C <sub>38</sub> H <sub>34</sub> CL <sub>2</sub> FeN <sub>10</sub> O <sub>8</sub> S <sub>2</sub> (M =949.62 g mol <sup>-1</sup> ):.....	269
Chapter 5 XRD data.....	269
22 C <sub>26.55</sub> H <sub>21.5</sub> CuF <sub>6</sub> N <sub>4</sub> O <sub>8</sub> S <sub>2</sub> (M =383.12 g mol <sup>-1</sup> ):.....	269
23 C <sub>27</sub> H <sub>23</sub> CuF <sub>6</sub> N <sub>4</sub> O <sub>6</sub> S <sub>4</sub> (M =805.27 g mol <sup>-1</sup> ):.....	269
24 C <sub>23</sub> H <sub>30</sub> CuF <sub>6</sub> N <sub>4</sub> O <sub>8</sub> S <sub>2</sub> (M =732.17 g mol <sup>-1</sup> ):.....	269
25•MeNO <sub>2</sub> C <sub>41</sub> H <sub>57</sub> CuF <sub>6</sub> N <sub>7</sub> O <sub>8</sub> S <sub>6</sub> (M =1145.83 g mol <sup>-1</sup> ): .....	269
26 C <sub>34</sub> H <sub>47</sub> Cu <sub>4</sub> l <sub>4</sub> N <sub>6</sub> O <sub>4</sub> (M =1397.06 g mol <sup>-1</sup> ): .....	269
27 C <sub>34</sub> H <sub>46</sub> Cu <sub>2</sub> F <sub>12</sub> N <sub>6</sub> O <sub>4</sub> P <sub>2</sub> (M =1019.79 g mol <sup>-1</sup> ): .....	270
28•2MeNO <sub>2</sub> C <sub>40</sub> H <sub>60</sub> B <sub>2</sub> Cu <sub>2</sub> F <sub>8</sub> N <sub>8</sub> O <sub>8</sub> (M =1021.43 g mol <sup>-1</sup> ): .....	270
29•MeNO <sub>2</sub> C <sub>47</sub> H <sub>41</sub> CuF <sub>12</sub> N <sub>7</sub> O <sub>6</sub> P <sub>2</sub> (M =1153.35 g mol <sup>-1</sup> ): .....	270
30 B <sub>2</sub> C <sub>69</sub> Cu <sub>3</sub> F <sub>9</sub> N <sub>9</sub> O <sub>6</sub> (M =1434.02 g mol <sup>-1</sup> ):.....	270
Chapter 6 XRD data.....	270
31 C <sub>18.25</sub> H <sub>16.25</sub> ClF <sub>7.625</sub> N <sub>5.5</sub> PRu (M =213.52 g mol <sup>-1</sup> ) .....	270
32 C <sub>31</sub> H <sub>24</sub> CL <sub>2</sub> F <sub>12</sub> N <sub>6</sub> P <sub>2</sub> Ru (M =942.47 g mol <sup>-1</sup> ) .....	271
33 C <sub>25</sub> H <sub>22</sub> CL <sub>2</sub> N <sub>4</sub> O <sub>2</sub> Ru (M =582.43 g mol <sup>-1</sup> ) .....	271
34 C <sub>46.75</sub> H <sub>42.2</sub> B <sub>2</sub> F <sub>8</sub> N <sub>6</sub> O <sub>5.35</sub> Ru (M =1048.394 g mol <sup>-1</sup> ) .....	271

35 $C_{25}I_2N_4O_2Ru$ ( $M=743.16 \text{ g mol}^{-1}$ ).....	271
36 $C_{19}H_{26}I_2N_4O_2Ru$ ( $M=697.31 \text{ g mol}^{-1}$ ).....	271
37 $C_{43}H_{37}I_4N_6RuS_4$ ( $M=1374.69 \text{ g mol}^{-1}$ ) .....	271
<b>List of References.....</b>	<b>272</b>



## List of Tables

Table 2.1. Summary of reported literature of the ThioPyBOX ligand synthesis. ....	57
Table 2.2. Selected bond lengths and angles for one of the unique molecules in L4 (Figure 2.47). ESDs shown in parentheses. ....	75
Table 2.3. Selected bond lengths and angles for the XRD structure of L6 (Figure 2.50). ESDs shown in parentheses. ....	77
Table 2.4. Selected bond lengths for the XRD structure of L5•L6 (Figure 2.52). ESDs shown in parentheses. ....	79
Table 2.5. Selected bond angles for the XRD structure of L5•L6 (Figure 2.52). ESDs shown in parentheses. ....	79
Table 3.1. Solid state magnetic susceptibility data of the iron(II)PyBOX <sup>R</sup> SQUID curves studied by Burrows et al. <sup>148</sup> .....	103
Table 3.2. Solution phase magnetic susceptibility data of the iron(II)PyBOX <sup>R</sup> data obtained by the Evan's method by Burrows <i>et al.</i> <sup>148</sup> .....	106
Table 3.3. Selected bond lengths and angles of the complexes <i>R</i> -5 (BF <sub>4</sub> ), <i>RS</i> -5 (BF <sub>4</sub> ), <i>R</i> -5 (ClO <sub>4</sub> ) and <i>RS</i> -5 (ClO <sub>4</sub> ).....	117
Table 3.4. Selected bond lengths and angles of the complex <i>RS</i> -6. ....	121
Table 3.5. Selected bond lengths and angles of the complex <i>S</i> -7. ....	124
Table 3.6. Selected bond lengths and angles for comparison of <i>S</i> -7 and <i>S</i> -8. ....	127
Table 3.7. Summarised SCO data from the SQUID graphs in Figure 3.49 of the phenyl- substituted complexes. ....	130
Table 3.8. Summarised SCO data from the SQUID graphs in Figure 3.50 of the isopropyl- substituted complexes. ....	131
Table 3.9. Summarised SCO data from the SQUID graphs in Figure 3.51 of the homochiral <i>tert</i> butyl- substituted complex. ....	133
Table 3.10. Solution state SCO parameters obtained for <i>S</i> -5 (BF <sub>4</sub> ), <i>R</i> -5 (ClO <sub>4</sub> ) and <i>R</i> -6.....	137
Table 4.1. Selected bond lengths and angles from the XRD structure solutions of <i>S</i> -9 and <i>RS</i> -9. ....	153
Table 4.2. Solution phase T <sub>1/2</sub> values and thermodynamic parameters obtained from van't Hoff calculations for <i>S</i> -9 and <i>RS</i> -9. Data for <i>S</i> -1, <i>RS</i> -1 <sup>148</sup> , <i>S</i> -5 and <i>RS</i> -5 are shown for comparison. ....	161
Table 4.3. Selected bond lengths and angles for the XRD structure of <i>RS</i> -10. Data for <i>RS</i> -2 and <i>RS</i> -6 are shown for comparison. ....	163
Table 4.4. T <sub>1/2</sub> values and thermodynamic parameters ΔH and ΔS of <i>S</i> -10 and <i>RS</i> -10. Data for <i>R</i> -6 is shown for comparison. ....	169
Table 4.5. Selected bond lengths and angles from the XRD structure of <i>S</i> -11. Data for <i>S</i> -7 and <i>S</i> -8 are shown for comparison. ....	170
Table 4.6. Selected bond lengths and angles for the XRD structures obtained of 12 and 13.....	174

Table 4.7. $T_{1/2}$ and thermodynamic parameters obtained for 12. *The $T_{1/2}$ for 13 was calculated based on the extrapolation of its solution state magnetic susceptibility data.....	181
Table 4.8. Selected bond lengths and angles from the XRD structure solutions of 14 and 15.....	182
Table 4.9. $T_{1/2}$ values and thermodynamic parameters calculated for 14 and 15. .	187
Table 4.10. Selected bond lengths and angles of the XRD structure of 17.....	188
Table 5.1. Selected XRD bond lengths and angles for 22 and 23. ....	217
Table 5.2. Selected XRD bond lengths and angles for complex 24. ....	219
Table 5.3. Selected XRD bond lengths and angles for complex 25. ....	221
Table 5.4. Selected bond lengths and angles from the XRD structure of 26.....	223
Table 5.5. Selected bond lengths and angles from the XRD structure of 27 and 28. ....	224
Table 5.6. Selected XRD bond lengths and angles of complex 29. *Both Cu-N <sub>ox</sub> bond lengths displayed are identical to the two not displayed. ....	226
Table 5.7. Selected bond lengths and angles from the XRD structure of 30.....	227
Table 6.1. Selected bond lengths and angles from the XRD structure solutions of 31 and 32.....	248
Table 6.2. Selected bond lengths and angles from the XRD structure solutions of 33 and 34.....	249
Table 6.3. Selected bond lengths and angles from the XRD structure solutions of 35 and 36.....	251
Table 6.4. Selected bond lengths and angles from the XRD structure solutions of 37. * The dihedral angle, $\theta$ , was measured between the planes of only the coordinated parts of the thioPyBOX ligands. ....	252

## List of Equations

Equation 1.1. The spin-only magnetic moment equation.....	11
Equation 1.2. The spin-only magnetic moment as a function of the number of unpaired electrons .....	11
Equation 1.3. The magnetic moment equation for the resultant angular momentum, $j$ .....	11
Equation 1.4. Magnetic moment equation when $\Delta E \ll k_B T$ .....	12
Equation 1.5. The relationship between $\mu_{\text{eff}}$ and $\chi_m$ . Where $N_A$ is Avogadro's constant and $\mu_0$ is the permeability of a vacuum. ....	12
Equation 1.6. The Curie law, where C is the Curie Constant.....	13
Equation 1.7. The Curie-Weiss law where $\Theta$ is the Weiss constant. ....	13
Equation 1.8. The Curie-Weiss law when $\theta = T_c$ . ....	13
Equation 1.9. The 2nd law of thermodynamics; Gibbs free energy equation. ....	26
Equation 1.10. The Boltzmann distribution equation which correlates $n_{\text{HS}}$ to $\Delta G$ . ....	27
Equation 1.11. The time-independent Schrödinger equation for a hydrogenic atom. ....	39
Equation 1.12. The Hamiltonian operator for a many-electron ( $n=2$ ) system, with approximations.....	40
Equation 1.13. The Hartree-Fock-Roothan equations. ....	40
Equation 1.14. The energy functional as a function of electron density. ....	41
Equation 3.15. The van't Hoff equation. ....	136

## List of Figures

Figure 1.1. Metal accepting lone-pair of electrons from Ligand in a Lewis Acid-Base model.....	3
Figure 1.2. The five d-orbitals along the Cartesian axes. ....	4
Figure 1.3. Crystal Field splitting of the <i>d</i> -orbitals in common coordination geometries. Figure adapted from Pearson. <sup>9</sup> .....	5
Figure 1.4. Construction of the MO diagram for [ML <sub>6</sub> ] <sup>n+</sup> , considering only M-L σ-bonding. Figure adapted from Yves. <sup>17</sup> .....	7
Figure 1.5. π-interactions between ligand and metal orbitals.....	7
Figure 1.6. The spectrochemical series of selected ligands in order of decreasing ligand-field strength. <sup>19,20</sup> .....	8
Figure 1.7. Expanded MO diagram for M-L bonding considering ligand π-orbital interactions, with the two scenarios of a.) where L is a π-donor ligand and b.) where L is a π-acceptor ligand. (a <sub>1g</sub> and t <sub>1u</sub> orbitals have been omitted for clarity). Scale is expanded from Figure 1.4. Figure reproduced from Housecroft and Sharpe. <sup>5</sup> .....	9
Figure 1.8. Low-spin (LS) and high-spin (HS) electronic configurations of a <i>d<sup>6</sup></i> metal ion in a ligand field. ....	10
Figure 1.9. A plot of χ <sub>m</sub> against T (left) and 1/χ <sub>m</sub> against T for a perfect paramagnet, which obeys the Curie law. <sup>5</sup> .....	13
Figure 1.10. <i>d</i> -orbital JT distortions of the e <sub>g</sub> orbitals in a HS <i>d<sup>4</sup></i> configuration (top), LS <i>d<sup>7</sup></i> configuration (middle) and <i>d<sup>9</sup></i> configuration (bottom). No distortion (left), JT elongation (centre) and JT compression (right). ....	14
Figure 1.11. Potential energy wells of an iron(II) SCO system, with respect to the Fe-N bond distance. The <sup>1</sup> A <sub>1g</sub> state is the LS state and the <sup>5</sup> T <sub>2g</sub> is the HS state. Figure reproduced from Gütllich <i>et al.</i> <sup>26</sup> .....	15
Figure 1.12. The SCO equilibrium.....	16
Figure 1.13. The general trends of magnetic susceptibility with increasing temperature for a.) an abrupt ST, b.) a gradual ST and c.) an incomplete ST. Figure adapted from Housecroft and Sharpe. <sup>5</sup> .....	16
Figure 1.14. Number of publications containing the phrase 'spin-crossover' or 'spin-equilibrium', per year. Figure (obtained from Web of Science) taken directly from publication. <sup>30</sup> .....	17
Figure 1.15. Structures of ferrohemoglobin (left), and with CO addition (carbonmonoxyhemoglobin) and O <sub>2</sub> addition (oxyhemoglobin) (right). ....	18
Figure 1.16. Structure of [Fe(phen) <sub>2</sub> X <sub>2</sub> ]. ....	19
Figure 1.17. The Fe <sup>II</sup> N <sub>6</sub> System.....	20
Figure 1.18. Pyridine-metal orbital interaction in π-back bonding. ....	21
Figure 1.19. UV-Vis spectrum of [Fe(ptz) <sub>6</sub> ](BF <sub>4</sub> ) <sub>2</sub> in the LS (left) and HS (right) spin states. Figure taken directly from publication. <sup>26</sup> .....	22
Figure 1.20. Orgel diagram for a <i>d<sup>1</sup></i> , <i>d<sup>4</sup></i> , <i>d<sup>6</sup></i> and <i>d<sup>9</sup></i> ion. Figure reproduced from Housecroft and Sharpe. <sup>5</sup> .....	22

Figure 1.21. Tanabe-Sugano diagram for the $d^6$ configuration in an octahedral ligand field. Figure taken directly from Hormann and Shaw III. <sup>73</sup> .....	23
Figure 1.22. Magnetic susceptibility vs. temperature displaying SCO with a thermal hysteresis loop. ....	24
Figure 1.23. Angular Jahn-Teller distortion in $[\text{Fe}(\text{1-bpp})_2]^{2+}$ where $\theta$ is the dihedral angle and $\varphi$ is the N(py)-Fe-N(py) trans angle. Figure taken from publication. <sup>77</sup> .....	25
Figure 1.24. The structure of 2,6-bis(pyrazol-1-yl)pyridine, $[\text{Fe}(\text{1-bpp})_2]^{2+}$ (left) and 2,2':6',2''-terpyridine, $[\text{Fe}(\text{terpy})_2]^{2+}$ (right). ....	26
Figure 1.25. Potential energy wells of an iron(II) SCO system, with respect to the Fe-N bond distance. The $^1A_{1g}$ state is the LS state and the $^5T_{2g}$ is the HS state. Figure reproduced from Gütlich <i>et al.</i> <sup>26</sup> .....	28
Figure 1.26. Magnetic moment of $[\text{Fe}(\text{S}_2\text{CNR}_2)_3]$ between 80-400 K with Van Vleck curves fitted to the data, for R= Py (pyrrolidyl), <i>n</i> -Bu ( <i>n</i> -butyl), Me (methyl) and <i>i</i> -Bu ( <i>i</i> -butyl). As reported by Ewald <i>et al.</i> , graph taken directly from publication. <sup>86</sup> .....	29
Figure 1.27. Magnetic susceptibility of $[\text{Fe}(\text{S}_2\text{CN}^n\text{Bu}_2)_3]$ between 0-3000 atm pressure applied. As reported by Ewald <i>et al.</i> , graph taken directly from publication. <sup>86</sup> .....	30
Figure 1.28. The change in potential energy of the $^5T_{2g}$ state at a higher pressure ( $P_2$ ), relative to the initial pressure ( $P_1$ ). Figure reproduced from Gütlich <i>et al.</i> <sup>92, 93</sup> .....	30
Figure 1.29. Graph of $X_m T$ vs. $T$ for $[\text{Fe}(\text{phen})_2(\text{SCN})_2]$ at pressures $10^5$ Pa, 0.17 Pa, 0.34 Pa and 0.57 Pa. Figure taken directly from Gütlich <i>et al.</i> <sup>93</sup> .....	31
Figure 1.30. Jablonski-style energy level diagram to show the transitions involved in the LIESST effect of an iron(II) SCO complex. Figure reproduced from Decurtins <i>et al.</i> <sup>97</sup> .....	32
Figure 1.31. Simplified graph of $\mu_{\text{eff}}$ vs. $T$ for a polycrystalline sample of $[\text{Fe}(\text{ptz})_6][\text{BF}_4]$ studied by Decurtins <i>et al.</i> Figure reproduced from publication. <sup>101</sup> .....	33
Figure 1.32. The Mössbauer spectra of $[\text{Fe}(\text{phen})_2(\text{NCS})_2]$ at 6 K, before light irradiation (A) and after light irradiation (B) for 1 hour. Figure taken directly from publication. <sup>97</sup> .....	34
Figure 1.33. Schematic diagram of the Gouy Balance. ....	36
Figure 1.34. The Meissner Effect (far right) in a superconducting material after applied field has been removed and $T < T_C$ . Figure reproduced from Fagaly. <sup>118</sup> .....	37
Figure 1.35. A SQUID loop with two Josephson junctions. Figure taken from publication. <sup>118</sup> .....	37
Figure 1.36. NMR tube with coaxial insert used for Evan's Method. Where TMS is the NMR reference sample, tetramethylsilane. ....	38
Figure 2.1. The copper-Schiff base complex studied by Noyori <i>et al.</i> <sup>160</sup> .....	45
Figure 2.2. Structure of 2,6-pyridindialdihydrazone. <sup>161</sup> .....	45

Figure 2.3. N,N',N''-Schiff base ligands employed in the study by Gehad. L1 = 2,6-pyridinedicarboxaldehydebis( <i>p</i> -hydroxyphenylimine) (left) and L2 = 2,6-pyridinedicarboxaldehydebis( <i>o</i> -hydroxyphenylimine) (right). <sup>163</sup> .....	45
Figure 2.4. Facial (left) and Meridonal (right) isomers of an [M(N,N',N''-tridentate) <sub>2</sub> ] complex. ....	46
Figure 2.5. Structure of a hydrotris(pyrazolyl)borate ('scorpionate') ligand. ....	46
Figure 2.6. Structures of 2,2'-bipyridine (left), 1,10-phenanthroline (middle) and 2,2':6'2'-terpyridine (right).....	47
Figure 2.7. Pyridine-metal orbital interaction in $\pi$ -back bonding. ....	48
Figure 2.8. The structures of a classical mono-terpy-metal complex (left) and a bis-terpy-metal complex (right) .....	48
Figure 2.9. The structure of 2,6-bis(N-pyrazol)pyridine (1-bpp).....	49
Figure 2.10. Different substituents and their positions studied in a structure-function relationship study of [Fe(bpp <sup>X,Y</sup> ) <sub>2</sub> ] <sup>2+</sup> . <sup>192</sup> .....	50
Figure 2.11. Factors governing steric and electronic control in pincer ligands. Figure adapted from Peris and Crabtree. <sup>175</sup> .....	50
Figure 2.12. The structures of bis(oxazoline), BOX (left) and 2,6-pyridine-bis(oxazoline), PyBOX (right).....	51
Figure 2.13. Rh-PyBOX catalyst studied by Nishiyama <i>et al.</i> <sup>198</sup> .....	52
Figure 2.14. PyBOX ligand with positions of substitution explored. X= 4- position of pyridine, Y= 4- position of oxazoline and Z= 5- position of oxazoline.....	52
Figure 2.15. Click-PyBOX unit for polymerisation. <sup>206</sup> .....	53
Figure 2.16. The possible isomers of the PyBOX ligand substituted on the oxazoline rings.....	53
Figure 2.17. The structures of pyridine-2,6-bis(imidazole), PyBIM (left) and pyridine-2,6-bis(thiazoline), thioPyBOX (right).....	54
Figure 2.18. Synthetic route to thioPyBOX by Abrunhosa <i>et al.</i> <sup>211,212</sup> and Le Maux <i>et al.</i> <sup>213</sup> .....	58
Figure 2.19. Synthetic route to thioPyBOX by Nishio <i>et al.</i> <sup>217</sup> .....	59
Figure 2.20. Synthetic route to thioPyBOX by Ackerman <i>et al.</i> <sup>218</sup> .....	59
Figure 2.21. Synthetic route to thioPyBOX by Nobbs <i>et al.</i> <sup>214</sup> .....	59
Figure 2.22. Synthetic route to thioPyBOX by Guo <i>et al.</i> <sup>215</sup> .....	60
Figure 2.23. Synthetic route to thioPyBOX by Pan <i>et al.</i> <sup>216</sup> .....	60
Figure 2.24. Synthesis of the hydroxy-pyridinecarboxamide by Kin Tse <i>et al.</i> <sup>223</sup> ..	61
Figure 2.25. Synthesis of the hydroxyamide adapted from Towers <i>et al.</i> <sup>224</sup> .....	62
Figure 2.26. Summary of the diamides synthesised by the method in Scheme 2.6, A1-A6. Yields in parentheses. ....	62
Figure 2.27. The structures of phosphorus pentasulfide (left) and the Lawesson's Reagent (right).....	63
Figure 2.28. Zwitterionic equilibrium of phosphorus(V)pentasulfide. ....	63

Figure 2.29. Zwitterionic equilibrium of Lawesson's Reagent. ....	63
Figure 2.30. The structure of the macrocycle formed. ....	64
Figure 2.31. Two possible reaction pathways to synthesise M1. ....	64
Figure 2.32. Synthesis of the macrocycle by Gao et al. <sup>229</sup> .....	65
Figure 2.33. <sup>1</sup> H NMR of the macrocycle. [CDCl <sub>3</sub> , 400 MHz]. ....	66
Figure 2.34. XRD structure of the macrocycle. Thermal ellipsoids are displayed at the 50% probability level. ....	66
Figure 2.35. Two molecules of M1 with hydrogen bonding shown (left) and a simplified packing diagram of M1 shown along the <i>a</i> -axis (right). ....	67
Figure 2.36. Column chromatography separation of thioPyBOX ligands with 1:9 DCM:MeCN. ....	68
Figure 2.37. Summary of the thioPyBOX ligands synthesised herein, L1-L6. Yields in parentheses. ....	69
Figure 2.38. <sup>1</sup> H NMR of ( <i>S,S</i> )-thioPyBOX <sup>Ph</sup> , L1. (400 MHz, CD <sub>3</sub> Cl).....	70
Figure 2.39. <sup>1</sup> H NMR of ( <i>S,S</i> )- thioPyBOX <sup>iPr</sup> , L4. (400 MHz, CD <sub>3</sub> Cl).....	70
Figure 2.40. <sup>1</sup> H NMR of ( <i>R,R</i> )- thioPyBOX <sup>tBu</sup> , L5. (400 MHz, CD <sub>3</sub> Cl).....	71
Figure 2.41. Δδ ppm between the two doublets of doublets arising from -S-CH <sub>2</sub> -CH- with different thiazoline R- substituents; <i>tert</i> butyl (top), <i>isopropyl</i> (middle) and phenyl (bottom). ....	72
Figure 2.42. <sup>1</sup> H NMR spectra of PyBOX <sup>Ph</sup> (top, red) and thioPyBOX <sup>Ph</sup> (bottom, black). ....	72
Figure 2.43. <sup>1</sup> H NMR spectra of PyBOX <sup>iPr</sup> (top, red) and thioPyBOX <sup>iPr</sup> (bottom, black). ....	73
Figure 2.44. <sup>1</sup> H NMR spectra of PyBOX <sup>tBu</sup> (top) and thioPyBOX <sup>tBu</sup> (bottom). ....	73
Figure 2.45. Comparison the -CH <sub>2</sub> -CH-R peak in the <sup>1</sup> H NMR spectra of the thioPyBOX ligands; thioPyBOX <sup>Ph</sup> (bottom), thioPyBOX <sup>iPr</sup> (middle) and thioPyBOX <sup>tBu</sup> (top).....	74
Figure 2.46. Comparison the -CH <sub>2</sub> -CH-R peak in the <sup>1</sup> H NMR spectra of the PyBOX ligands; PyBOX <sup>Ph</sup> (bottom), PyBOX <sup>iPr</sup> (middle) and PyBOX <sup>tBu</sup> (top) (highlighted in black for clarity). ....	74
Figure 2.47. XRD structure collected of one of the unique molecules in the structure of ( <i>S,S</i> )-thioPyBOX <sup>iPr</sup> , L4. Hydrogen atoms are omitted for clarity. Thermal ellipsoids are displayed at the 50% probability level. ....	75
Figure 2.48. XRD structure of two ligands, L4. ....	76
Figure 2.49. XRD packing diagram of L4, viewed along the <i>b</i> -axis. ....	76
Figure 2.50. XRD structure collected of ( <i>S,S</i> )-thioPyBOX <sup>tBu</sup> , L6. Hydrogen atoms are omitted for clarity. Thermal ellipsoids are displayed at the 50% probability level. ....	77
Figure 2.51. XRD structures of two ligands, L6 (left) and packing diagram of L6, viewed along the <i>b</i> -axis (right). ....	78
Figure 2.52. XRD structure of L5•L6. Hydrogen atoms are omitted for clarity. Thermal ellipsoids are displayed at the 50% probability level. ....	78

Figure 2.53. Overlay XRD structures of L4 and L6 .....	79
Figure 3.1. <i>Cis</i> - and <i>trans</i> - isomers of $[\text{Co}(\text{NH}_3)_4\text{Cl}_2]^+$ .....	86
Figure 3.2. An example of propeller-chirality in the structure of $[\text{Fe}(\text{bpy})_3]^{2+}$ .....	87
Figure 3.3. Stereogenic carbon and metal tetrahedral centres. ....	87
Figure 3.4. Arrows indicating the direction of substrate attack upon a $\text{C}_2$ -symmetric (left) and asymmetric (right) chiral metal-PyBOX complex. Arrows of the same colour leads to identical products. ....	88
Figure 3.5. A chiral Schiff-base copper(II) complex catalysing an enantioselective carbenoid reaction. <sup>260</sup> .....	89
Figure 3.6. XRD structure of (+)- $\text{Fe}_2[\text{Nb}(\text{CN})_8](4\text{-bromopyridine})_8 \cdot 2\text{H}_2\text{O}$ (a) and Fe and Nb coordination environments (b). (Red = Fe, blue = Nb, green = Br, yellow = C, light green = N). Figure taken directly from publication. <sup>279</sup> .....	90
Figure 3.7. Schematic representation of how MChD works on a chiral molecule. Figure adapted from publication. <sup>278</sup> .....	91
Figure 3.8. XRD structure of the heterometallic 1D polymer of cyanide-bridged $[\text{CoFe}]$ studied by Hoshino <i>et al.</i> (green = Fe, blue = Co, pink = B, grey = C, purple = N). Figure taken directly from publication. <sup>286</sup> .....	92
Figure 3.9. XRD structures of polymorph A (left) and polymorph B (right). Figures taken directly from publication. <sup>294</sup> .....	94
Figure 3.10. Chain of interactions in polymorph A (left) and polymorph B (right), between the thiazoline rings. A, B and C in the figures denotes the view along the <i>a</i> -axis, <i>b</i> -axis and <i>c</i> -axis respectively. Figures taken directly from publication. <sup>294</sup> .....	95
Figure 3.11. Structures of $[\text{Fe}(\text{PM-BiA})_2(\text{NCS})_2]$ (left) and $[\text{Fe}(\text{PM-PEA})_2(\text{NCS})_2]$ (right), studied by Létard <i>et al.</i> <sup>296</sup> .....	95
Figure 3.12. Comparison of $X_mT$ vs $T$ of single crystals of $[\text{Fe}(\text{PM-BiA})_2(\text{NCS})_2]$ (left) and of powder samples 1 and 2 (right). Figures taken directly from publication. <sup>296</sup> .....	96
Figure 3.13. Chemical structures of DPQ (left) and ABPT (right), studied by Moliner <i>et al.</i> <sup>298, 299</sup> .....	97
Figure 3.14. Iron(II) complex with thiocyanate ligands <i>cis</i> - to each other (left) and the selenocyanate analogue (right). ....	97
Figure 3.15. Structure of $[\text{Fe}(\text{bapbpy})(\text{NCS})_2]$ . ....	98
Figure 3.16. Iron(II) PyBOX complex (left) and iron(II) thioPyBOX complex (right). Figure reproduced from publication. <sup>216</sup> .....	100
Figure 3.17. Iron(II) PyBOX complexes studied by Burrows <i>et al.</i> , with the R groups = Ph, <i>i</i> Pr, Me and H. <sup>148</sup> .....	101
Figure 3.18. The relationship between an <i>R,R</i> - Homochiral iron-PyBOX complex (left) and an <i>R,S</i> - Heterochiral iron-PyBOX complex (right). ....	102
Figure 3.19. Solid state magnetic susceptibility measurements of the iron(II)PyBOX <sup>R</sup> complexes studied by Burrows <i>et al.</i> <sup>148</sup> .....	102
Figure 3.20. XRD structures of <i>RS</i> -2 (left) and <i>R</i> -2 (right) obtained by Burrows <i>et al.</i> .....	103



Figure 3.21. XRD structures of <i>RS-1</i> (left) and <i>R-1</i> (right) obtained by Burrows <i>et al.</i> .....	104
Figure 3.22. Solution phase magnetic susceptibility results of the iron(II)PyBOX <sup>R</sup> complexes studied by Burrows <i>et al.</i> <sup>148</sup> .....	106
Figure 3.23. Iron-PyBOX complexes studied by Kimura and Ishida with R-substituents on the 4-position of the pyridine ring. (R= H, Cl, Ph, OMe and SMe). <sup>317</sup> .....	107
Figure 3.24. Paramagnetic <sup>1</sup> H NMRs of [Fe(( <i>R</i> )-L <sup>Ph</sup> ) <sub>2</sub> ] <sup>2+</sup> (top, dark red), [Fe(( <i>R</i> )-L <sup>Ph</sup> )(( <i>S</i> )-L <sup>Ph</sup> ) <sub>2</sub> ] <sup>2+</sup> (middle, navy blue) and 1 : 1 : 1 of ( <i>R</i> )-L <sup>Ph</sup> : ( <i>S</i> )-L <sup>Ph</sup> : [Fe(ClO <sub>4</sub> ) <sub>2</sub> ] (bottom, green), in CD <sub>3</sub> CN. The feature at 50 ppm is a spectrometer artefact. ....	108
Figure 3.25. Paramagnetic <sup>1</sup> H NMRs of [Fe(( <i>R</i> )-L <sup>iPr</sup> ) <sub>2</sub> ] <sup>2+</sup> (top, dark red), [Fe(( <i>R</i> )-L <sup>iPr</sup> )(( <i>S</i> )-L <sup>iPr</sup> ) <sub>2</sub> ] <sup>2+</sup> (middle, navy blue) and 1 : 1 : 1 of ( <i>R</i> )-L <sup>iPr</sup> : ( <i>S</i> )-L <sup>iPr</sup> : [Fe(ClO <sub>4</sub> ) <sub>2</sub> ] (bottom, green), in (CD <sub>3</sub> ) <sub>2</sub> CO. ....	109
Figure 3.26. General metal complexation reaction scheme used for the synthesis of iron(II)thioPyBOX complexes. ....	111
Figure 3.27. Structures of the iron(II)thioPyBOX complexes, <i>S-5</i> (BF <sub>4</sub> ), <i>RS-5</i> (BF <sub>4</sub> ), <i>S-5</i> (ClO <sub>4</sub> ), <i>RS-5</i> (ClO <sub>4</sub> ), <i>S-6</i> , <i>RS-6</i> , <i>S-7</i> and <i>S-7</i> (i) and the iron(II)PyBOX <sup>tBu</sup> complex, <i>S-8</i> , synthesised herein. ....	112
Figure 3.28. XRD structures of <i>S-5</i> (BF <sub>4</sub> ) (left) and <i>RS-5</i> (BF <sub>4</sub> ) (right). Hydrogen atoms, counter-ions and solvents are omitted for clarity. Thermal ellipsoids are displayed at 50% probability level. ....	113
Figure 3.29. XRD structures of <i>R-5</i> (ClO <sub>4</sub> ). Hydrogen atoms, counter-ions and solvents are omitted for clarity. Thermal ellipsoids are displayed at 50% probability level. ....	114
Figure 3.30. Space-filling model of <i>RS-5</i> (BF <sub>4</sub> ). H atoms have been omitted for clarity. ....	115
Figure 3.31. Space-filling model of <i>S-5</i> (BF <sub>4</sub> ). H atoms have been omitted for clarity. ....	115
Figure 3.32. XRD structures of the homochiral phenyl- complex; <i>R-5</i> (left) and PyBOX analogue, <i>R-1</i> (right). <sup>148</sup> .....	116
Figure 3.33. XRD structures of the heterochiral phenyl- complex; <i>RS-5</i> (left) and the PyBOX analogue, <i>RS-1</i> (right). ....	116
Figure 3.34. Space-filling models of <i>R-5</i> (ClO <sub>4</sub> ) (left) and <i>R-1</i> (right). ....	117
Figure 3.35. XRD structures of <i>R-1</i> (left) and <i>R-5</i> (ClO <sub>4</sub> ) (right) highlighting the interatomic distances used for comparison. ....	118
Figure 3.36. Packing structures of <i>R-5</i> (ClO <sub>4</sub> ) (top) and <i>S-5</i> (BF <sub>4</sub> ) (bottom) with hydrogen bonding displayed, structures are both shown along the <i>b</i> -axis... ..	119
Figure 3.37. XRD structure of [Fe(( <i>R</i> )-L <sup>Ph</sup> ) <sub>2</sub> ][Fe(( <i>S</i> )-L <sup>Ph</sup> ) <sub>2</sub> ][ClO <sub>4</sub> ] <sub>4</sub> •2MeCN, <i>R-5</i> • <i>S-5</i> . Solvents, hydrogen atoms and counter-ions are omitted for clarity. Thermal ellipsoids are at the 50% probability level. ....	119
Figure 3.38. XRD structure of <i>RS-6</i> . Hydrogen atoms, counter-ions and solvents are omitted for clarity. Thermal ellipsoids are displayed at 50% probability level. ....	120

Figure 3.39. XRD structure of the heterochiral <i>isopropyl</i> - complex; <i>RS</i> -6 (left) and PyBOX analogue, <i>RS</i> -2 (right). <sup>148</sup> .....	121
Figure 3.40. Space-filling models of <i>RS</i> -6 (left) and <i>RS</i> -2 (right).....	122
Figure 3.41. Packing structures of <i>RS</i> -6 (left) and <i>RS</i> -2 (right) with hydrogen bonding displayed, only two complexes are shown for clarity. Structures are both shown along the <i>a</i> -axis.....	122
Figure 3.42. XRD structure of <i>S</i> -7. Hydrogen atoms, counter-ions and solvents are omitted for clarity. Thermal ellipsoids are displayed at 50% probability level.	123
Figure 3.43. The clamp angle $\phi$ plotted against average Fe-N bond distances in a series of $[\text{Fe}(\text{1-bpp})_2]^{2+}$ complexes. Upwards triangles are HS complexes, and downward triangles are LS. Figure taken from publication. <sup>329</sup> The added red triangle is approximately where the complex <i>S</i> -7 would fit this data. ....	124
Figure 3.44. XRD structure of <i>S</i> -7(i). Hydrogen atoms, counter-ions and solvents are omitted for clarity. Thermal ellipsoids are displayed at 50% probability level. ....	125
Figure 3.45. XRD structure of $[\text{Fe}((\text{S,S})\text{-tBu-PyBOX})_2][\text{ClO}_4]_2$ , <i>S</i> -8. ....	126
Figure 3.46. XRD structures of the homochiral <i>tert</i> butyl- complexes; <i>S</i> -7 (left) and its PyBOX analogue, <i>S</i> -8 (right). ....	127
Figure 3.47. Packing structures of <i>S</i> -7 (top) and <i>S</i> -8 (bottom) with hydrogen bonding displayed, only two complexes are shown for clarity. Structures are both shown along the <i>a</i> -axis.....	128
Figure 3.48. Space-filling models of <i>S</i> -7 (left) and <i>S</i> -8 (right).....	129
Figure 3.49. SQUID curves for <i>S</i> -5 ( $\text{BF}_4$ ) (red), <i>S</i> -5 ( $\text{ClO}_4$ ) (navy), <i>RS</i> -5 ( $\text{BF}_4$ ) (green) and <i>RS</i> -5 ( $\text{ClO}_4$ ) (yellow). N.B. 300→370K is the first heating upon which initial solvent is lost. ....	129
Figure 3.50. SQUID curves for <i>S</i> -6 (black) and <i>RS</i> -6 (blue). N.B. 300→370K is the first heating upon which initial solvent is lost. ....	131
Figure 3.51. SQUID curve for <i>S</i> -7. ....	132
Figure 3.52. VT Evan's Method curves for <i>RS</i> -5 ( $\text{BF}_4$ ) (green) and <i>S</i> -5 ( $\text{BF}_4$ ) (red) in $\text{CD}_3\text{CN}$ . ....	133
Figure 3.53. VT Evan's Method curves for <i>R</i> -6 (black) and <i>RS</i> -6 (blue) in $\text{CD}_3\text{CN}$ .	134
Figure 3.54. VT Evan's Method curves for <i>S</i> -7 (purple), <i>S</i> -8 (grey), a 1:1:1 solution of ( <i>R</i> )- $\text{L}^{\text{tBu}}$ :( <i>S</i> )- $\text{L}^{\text{tBu}}$ : $\text{Fe}^{2+}$ (pink) and a 2:1 solution of ( <i>S</i> )- $\text{L}^{\text{tBu}}$ : $\text{Fe}^{2+}$ (orange) in $\text{CD}_3\text{CN}$ . ....	135
Figure 3.55. Paramagnetic $^1\text{H}$ NMR of <i>RS</i> -5 ( $\text{BF}_4$ ) (bottom spectrum, green) and <i>S</i> -5 ( $\text{BF}_4$ ) (top spectrum, red). [ $\text{CD}_3\text{CN}$ , 600 MHz].....	138
Figure 3.56. Paramagnetic $^1\text{H}$ NMR spectra of <i>RS</i> -5 on day 1 (bottom), week 1 (middle) and week 2 (top). [ $\text{CD}_3\text{CN}$ , 600 MHz] .....	138
Figure 3.57. Paramagnetic $^1\text{H}$ NMR spectrum of the <i>in situ</i> 1:1:1 reaction mixture of ( <i>R</i> )- $\text{L}^{\text{Ph}}$ : ( <i>S</i> )- $\text{L}^{\text{Ph}}$ : $[\text{Fe}(\text{ClO}_4)_2]$ . ....	139
Figure 3.58. Paramagnetic $^1\text{H}$ NMR of a 1 : 1 : 1 solution of ( <i>R</i> )- $\text{L}^{\text{Ph}}$ : ( <i>S</i> )- $\text{L}^{\text{Ph}}$ : $[\text{Fe}(\text{ClO}_4)_2]$ on day 1 (bottom), week 1 (middle) and week 2 (top). [ $\text{CD}_3\text{CN}$ , 600 MHz] .....	140

Figure 3.59. Paramagnetic $^1\text{H}$ NMR of <i>RS</i> -6 (bottom spectrum, black) and <i>S</i> -6 (top spectrum, blue). [ $\text{CD}_3\text{CN}$ , 300 MHz].....	141
Figure 3.60. Paramagnetic $^1\text{H}$ NMR spectra of <i>RS</i> -6 on day 1 (bottom), week 1 (middle) and week 2 (top). [ $\text{CD}_3\text{CN}$ , 300 MHz].....	141
Figure 3.61. Paramagnetic $^1\text{H}$ NMR spectrum of the in situ 1:1:1 reaction mixture of (R)-L <sup>iPr</sup> : (S)-L <sup>iPr</sup> : $[\text{Fe}(\text{ClO}_4)_2]$ .....	142
Figure 3.62. Paramagnetic $^1\text{H}$ NMR of <i>S</i> -7, with peak expansions in the diamagnetic region. Expanded part is overlaid with the $^1\text{H}$ NMR spectrum of thioPyBOX <sup>tBu</sup> . [ $\text{CD}_3\text{CN}$ , 300 MHz] .....	143
Figure 3.63. Paramagnetic $^1\text{H}$ NMR of <i>S</i> -8, with peak expansions in the diamagnetic region. [ $\text{CD}_3\text{CN}$ , 300 MHz] .....	143
Figure 4.1. The structures of 2,6-bis(2-benzimidazolyl)pyridine, bzimpy (left), 2,6-bis(pyrazol-1-yl)pyridine, 1-bpp (middle) and 2,2':6',2''-terpyridine, terpy (right). .....	149
Figure 4.2. 3-Bpp derivatives employed in the study by Barrios <i>et al.</i> H <sub>4</sub> L1, 2,6-bis(5-(2-hydroxyphenyl)pyrazol-3-yl)pyridine and H <sub>2</sub> L3, 2,6-bis(5-naphthylpyrazol-3-yl)pyridine. <sup>340</sup> .....	150
Figure 4.3. The structure of H <sub>2</sub> L4, 2,6-bis(5-([1,1'-biphenyl]-4-yl)-1 <i>H</i> -pyrazol-3-yl)pyridine, employed in the work by García-López <i>et al.</i> <sup>338</sup> .....	151
Figure 4.4. Solution state SCO activity for $[\text{Fe}((\text{R},\text{S})\text{-PyBOX}^{\text{Ph}})_2][\text{ClO}_4]_2$ (1( $\text{ClO}_4$ ), $[\text{Fe}((\text{S},\text{S})\text{-PyBOX}^{\text{Ph}})_2][\text{ClO}_4]_2$ (2( $\text{ClO}_4$ ) and $[\text{Fe}((\text{R},\text{R})\text{-PyBOX}^{\text{Ph}})((\text{S},\text{S})\text{-PyBOX}^{\text{Ph}})][\text{ClO}_4]_2$ (3( $\text{ClO}_4$ )). Figure taken from publication. <sup>208</sup> .....	151
Figure 4.5. Structures of the heteroleptic iron(II)PyBOX/thioPyBOX complexes synthesised herein. <i>S</i> -9, <i>RS</i> -9, <i>S</i> -10 and <i>RS</i> -10. ....	152
Figure 4.6. XRD structure solutions obtained for <i>S</i> -9 (left) and <i>RS</i> -9 (right). .....	153
Figure 4.7. Space-filling models of <i>RS</i> -9 (front and back views). .....	154
Figure 4.8. Space-filling models of <i>RS</i> -1 (left) and <i>RS</i> -5 (right).....	155
Figure 4.9. Powder-XRD data obtained for <i>S</i> -9 (left) and <i>RS</i> -9 (right). Experimentally obtained patterns are in black and simulated patterns from the single crystal XRD solution is in blue.....	155
Figure 4.10. Paramagnetic $^1\text{H}$ NMR spectra of <i>RS</i> -9 (top, blue) and <i>S</i> -9 (bottom, red). [ $\text{CD}_3\text{CN}$ , 300 MHz].....	156
Figure 4.11. Paramagnetic $^1\text{H}$ NMR spectra of <i>S</i> -9. Red dots indicate the homoleptic $[\text{Fe}(\text{PyBOX}^{\text{Ph}})_2]^{2+}$ complex, <i>S</i> -1 and yellow dots indicate the homoleptic $[\text{Fe}(\text{thioPyBOX}^{\text{Ph}})_2]^{2+}$ , <i>S</i> -5. [ $\text{CD}_3\text{CN}$ , 300 MHz]. .....	157
Figure 4.12. Paramagnetic $^1\text{H}$ NMRs of a 1:1:1 solution of (S,S)-PyBOX <sup>Ph</sup> : (R,R)-thioPyBOX <sup>Ph</sup> : $\text{Fe}(\text{ClO}_4)_2 \cdot 6\text{H}_2\text{O}$ over a 35 day period. Red dots indicate the homoleptic $[\text{Fe}(\text{PyBOX}^{\text{Ph}})_2]^{2+}$ complex and yellow dots indicate the homoleptic $[\text{Fe}(\text{thioPyBOX}^{\text{Ph}})_2]^{2+}$ . [ $\text{CD}_3\text{CN}$ , 300 MHz].....	158
Figure 4.13. Variable temperature magnetic susceptibility curves in the solid phase using the SQUID for <i>RS</i> -9 (blue curve) and <i>S</i> -9 (red curve). N.B. 300→370K is the first heating cycle, upon which initial solvent is lost.....	159

Figure 4.14. Variable temperature magnetic susceptibility curves in the solution phase using the VT Evan's method for <i>RS-9</i> (blue curve) and <i>S-9</i> (red curve). .....	160
Figure 4.15. XRD structure of <i>RS-10</i> . Solvents, counter-ions and hydrogen atoms are omitted for clarity. Thermal ellipsoids are at the 50% probability level. ...	163
Figure 4.16. XRD structure of <i>RS-10</i> with intermolecular interactions displayed. .	164
Figure 4.17. <sup>1</sup> H NMR spectra of <i>S-10</i> (bottom, purple) and <i>RS-10</i> (top, green)....	165
Figure 4.18. Paramagnetic <sup>1</sup> H NMR of <i>S-10</i> . Red dots indicate the homoleptic [Fe(PyBOX <sup>iPr</sup> ) <sub>2</sub> ] <sup>2+</sup> complex ( <i>S-2</i> ) and yellow dots indicate the homoleptic [Fe(thioPyBOX <sup>iPr</sup> ) <sub>2</sub> ] <sup>2+</sup> ( <i>S-6</i> ). [CD <sub>3</sub> CN, 300 MHz]. .....	165
Figure 4.19. Paramagnetic <sup>1</sup> H NMR of <i>S-10</i> over a three month period. Red dots indicate the homoleptic [Fe(PyBOX <sup>Ph</sup> ) <sub>2</sub> ] <sup>2+</sup> complex, <i>S-2</i> , and yellow dots indicate the homoleptic [Fe(thioPyBOX <sup>Ph</sup> ) <sub>2</sub> ] <sup>2+</sup> . [CD <sub>3</sub> CN, 300 MHz].....	166
Figure 4.20. Experimentally obtained pXRD analysis of <i>S-10</i> (purple). The simulated pXRD pattern of <i>RS-10</i> from the single crystal XRD structure is also shown for comparison (black). .....	166
Figure 4.21. Variable temperature magnetic susceptibility measurements in the solid state for <i>S-10</i> (purple) and <i>RS-10</i> (green) using SQUID. N.B. 300→370K is the first heating cycle, upon which initial solvent is lost. ....	167
Figure 4.22. Variable temperature magnetic susceptibility measurements in the solution phase for <i>S-10</i> (purple) and <i>RS-10</i> (green). [CD <sub>3</sub> CN, 500 MHz]. ...	167
Figure 4.23. VT magnetic susceptibility in solution of <i>RS-2</i> (blue), <i>RS-10</i> (green) and <i>RS-6</i> (black). .....	168
Figure 4.24. XRD structure obtained of <i>S-11</i> . Hydrogen atoms, counter-ions and solvents are omitted for clarity. Thermal ellipsoids are at the 50% probability level. ....	170
Figure 4.25. Paramagnetic <sup>1</sup> H NMR of <i>S-11</i> . Spectra of <i>S-7</i> and <i>S-8</i> are also shown for comparison. Yellow dots indicate peaks belonging to [Fe(thioPyBOX <sup>tBu</sup> ) <sub>2</sub> ] <sup>2+</sup> , <i>S-7</i> and red dots indicate [Fe(PyBOX <sup>tBu</sup> ) <sub>2</sub> ] <sup>2+</sup> , <i>S-8</i> . [CD <sub>3</sub> CN, 300 MHz]. .....	171
Figure 4.26. Variable temperature magnetic susceptibility data for <i>S-11</i> in the solid state using the SQUID (black line) and in the solution state using the VT Evan's method (pink line). .....	172
Figure 4.27. Structures of the complexes; [Fe(( <i>R</i> )-PyBOX <sup>Ph</sup> )(bzimpy)][ClO <sub>4</sub> ] <sub>2</sub> , 12; [Fe(( <i>R</i> )-thioPyBOX <sup>Ph</sup> )(bzimpy)][ClO <sub>4</sub> ] <sub>2</sub> , 13; [Fe(( <i>S</i> )-PyBOX <sup>iPr</sup> )(bzimpy)][ClO <sub>4</sub> ] <sub>2</sub> , 14 and [Fe(( <i>S</i> )-thioPyBOX <sup>iPr</sup> )(bzimpy)][ClO <sub>4</sub> ] <sub>2</sub> , 15.....	173
Figure 4.28. XRD structure of [Fe(( <i>R</i> )-PyBOX <sup>Ph</sup> )(bzimpy)][ClO <sub>4</sub> ] <sub>2</sub> , 12 and [Fe(( <i>R</i> )-thioPyBOX <sup>Ph</sup> )(bzimpy)][ClO <sub>4</sub> ] <sub>2</sub> , 13. Counter-ions and hydrogen atoms are omitted for clarity. Thermal ellipsoids are at the 50% probability level. ....	174
Figure 4.29. Space-filling XRD models of 12 (left) and 13 (right).....	175
Figure 4.30. XRD packing structure of 12 shown along the <i>a</i> -axis. ....	175
Figure 4.31. XRD packing structure of 13 shown along the <i>b</i> -axis. ....	176

Figure 4.32. XRD packing of 12 displaying hydrogen bond interactions with the perchlorate ion. Solvent omitted for clarity.....	177
Figure 4.33. XRD packing of 13 displaying hydrogen bond interactions with the perchlorate ion. ....	177
Figure 4.34. Paramagnetic <sup>1</sup> H NMR of 12 (top) and 13 (bottom). [CD <sub>3</sub> CN, 300 MHz]. ....	178
Figure 4.35. Paramagnetic <sup>1</sup> H NMR spectrum of [Fe(bzimpy) <sub>2</sub> ] <sup>2+</sup> . [CD <sub>3</sub> CN, 300 MHz]. ....	179
Figure 4.36. pXRD pattern of 12 (left) and 13 (right). Experimentally obtained patterns are in black and simulated pXRD from the single crystal XRD solutions are in blue. ....	179
Figure 4.37. Variable temperature solid state magnetic susceptibility of 12 (red) and 13 (black) using the SQUID magnetometer. N.B. 300→370K is the first heating cycle, upon which initial solvent is lost. ....	180
Figure 4.38. Variable temperature solution state magnetic susceptibility of 12 (red) and 13 (black) using the Evan's <sup>1</sup> H NMR method. ....	181
Figure 4.39. XRD structures of 14 (left) and 15 (right). Counter-ions, hydrogen atoms and solvents are omitted for clarity. Thermal ellipsoids are at the 50% probability level. ....	182
Figure 4.40. The clamp angle, φ compared to the average Fe-N bond distance in [Fe(1-bpp) <sub>2</sub> ] <sup>2+</sup> complexes reported by Kershaw Cook <i>et al.</i> <sup>329</sup> Upwards triangles are HS complexes and downwards triangles are LS. Red triangles are approximately where complexes 14 and 15 (labelled) fit on the graph. Figure adapted from publication. ....	183
Figure 4.41. pXRD analysis of complex 14 (left) and 15 (right). Experimentally obtained is in black and pXRD pattern simulated from the single crystal XRD structure is in blue. ....	184
Figure 4.42. Paramagnetic <sup>1</sup> H NMR spectra of 14 (bottom) and 15 (top). [CD <sub>3</sub> CN, 300 MHz]. ....	184
Figure 4.43. Paramagnetic <sup>1</sup> H NMR spectrum of 14 with red dots highlighting the peaks corresponding to [Fe(PyBOX <sup>Pr</sup> ) <sub>2</sub> ] <sup>2+</sup> . [CD <sub>3</sub> CN, 300 MHz]. ....	185
Figure 4.44. Variable temperature solid state magnetic susceptibility of 14 (green) and 15 (gold) using the SQUID magnetometer. ....	185
Figure 4.45. Variable temperature solution phase magnetic susceptibility of 14 (green) and 15 (gold) using the Evan's <sup>1</sup> H NMR method. ....	186
Figure 4.46. Structures of complexes 16-19. ....	187
Figure 4.47. XRD structure of [Fe(1-bpp)(( <i>R</i> )-thioPyBOX <sup>Ph</sup> )] [ClO <sub>4</sub> ] <sub>2</sub> , 17. Hydrogen atoms, counter-ions and solvents are omitted for clarity. Thermal ellipsoids are at the 50% probability level. ....	188
Figure 4.48. Paramagnetic <sup>1</sup> H NMRs of 16 (bottom) and 17 (top) with peaks identified as green circles (16), orange circles (17) and blue circles ([Fe(1-bpp) <sub>2</sub> ] <sup>2+</sup> ). [300 MHz, CD <sub>3</sub> CN]. ....	189

- Figure 4.49. Paramagnetic  $^1\text{H}$  NMRs of 18 (bottom) and 19 (top) with peaks identified as 18 (blue circles), 19 (red circles) or possibly  $[\text{Fe}(\text{1-bbp})_2]^{2+}$  (navy circles). [300 MHz,  $\text{CD}_3\text{CN}$ ]. .....190
- Figure 4.50. Magnetic susceptibility data in the solid state at various temperatures, obtained using the SQUID magnetometer of 16 (green), 17 (orange), 18 (blue) and 19 (red). N.B. 300 $\rightarrow$ 370K is the first heating cycle, upon which initial solvent is lost. ....191
- Figure 4.51. Magnetic susceptibility data in the solution state at various temperatures, obtained using the Evans'  $^1\text{H}$  NMR method of 16 (green), 17 (orange), 18 (blue) and 19 (red). ....191
- Figure 4.52. Structures of 20 (left) and 21 (right).....193
- Figure 4.53. Paramagnetic  $^1\text{H}$  NMR spectra of  $[\text{Fe}((R)\text{-PyBOX}^{\text{Ph}})(\text{terpy})]^{2+}$ , 20 (bottom) and  $[\text{Fe}((S)\text{-PyBOX}^{\text{iPr}})(\text{terpy})]^{2+}$ , 21 (top). [300 MHz,  $\text{CD}_3\text{CN}$ ]. .....194
- Figure 4.54. Paramagnetic  $^1\text{H}$  NMR spectrum of complex 20 with expansion of the diamagnetic region. [300 MHz,  $\text{CD}_3\text{CN}$ ]. ....194
- Figure 4.55. Experimentally obtained pXRD analysis of 20 (navy blue, middle) and 21 (top, dark red), shown with the pXRD pattern simulated from the single crystal XRD structure of  $[\text{Fe}(\text{terpy})_2][\text{ClO}_4]_2$  (bottom, black). .....195
- Figure 4.56. Magnetic susceptibility data of complexes 20 (blue) and 21 (red) in the solid state (squares) and solution state (triangles) at varying temperatures using the SQUID magnetometer at 0.5T for the solid state and using the Evans  $^1\text{H}$  NMR method in (500 MHz,  $\text{CD}_3\text{CN}$ ) for the solution state. ....196
- Figure 5.1. A. Wilkinson's catalyst, B. an example of Noyori's catalysts, C. the first generation Grubbs' catalyst and D. an example of the  $\text{Pd}^0$  catalyst employed by Heck, Negishi and Suzuki.....205
- Figure 5.2. Cu(II)-catalysed *meta*-arylation of acetanilidine reported by Phipps and Gaunt and the complementary Pd(II)-catalysed *ortho*-selective reaction also shown. Figure adapted from publication. <sup>395</sup> .....207
- Figure 5.3. Reaction schemes for the Cu-catalysed *N*-amidation of aryl iodides (top) and *N*-arylation of heterocycles (bottom) studied by Klapars *et al.* Figure reproduced from publication. <sup>390</sup> .....208
- Figure 5.4. Ullman coupling of an aniline with an aryl halide (top reaction) and of phenol with an aryl halide (bottom reaction). <sup>399, 400</sup> Figure adapted from Sambigiio *et al.* <sup>393</sup> .....208
- Figure 5.5. Reaction cycle for the copper catalysed Ullman coupling of an aryl halide with and aryl amine.....209
- Figure 5.6. The two most active copper(II) iminopyridine catalysts reported by Ouali *et al.* <sup>408</sup> .....209
- Figure 5.7. Reaction scheme of the 1,3-dipolar cycloaddition reported by Huisgen <sup>410, 411</sup> (top) and the copper-catalysed version reported by Meldal <sup>409</sup> and Sharpless <sup>389</sup> (bottom). Figure adapted from publication. <sup>412, 413</sup> .....210
- Figure 5.8. Initial catalytic cycle of the CuAAC proposed by Sharpless and Fokin (left) and more recent mechanism of the CuAAC proposed by Fokin (right). Figure adapted from El Ayouchia *et al.* <sup>420</sup> .....211

Figure 5.9. Diels-Alder reaction of cyclopentadiene with acrylamide derivatives catalysed by $[\text{Cu}((S)\text{-BOX}^{\text{tBu}})]_2[\text{SbF}_6]_2$ reported by Evans <i>et al.</i> <sup>421, 422</sup> .....	211
Figure 5.10. The Mukaiyama aldol reaction of benzyloxyacetaldehyde with a tBu-thioacetate silyl ketene acetal, catalysed by $[\text{Cu}((S)\text{-PyBOX}^{\text{R}})]_2[\text{SbF}_6]_2$ where R = Ph, iPr, Bn, tBu, reported by Evans <i>et al.</i> <sup>423</sup> .....	212
Figure 5.11. The reaction scheme of phenylacetylene with <i>N</i> -benzylideneaniline catalysed by $\text{PyBOX}^{\text{Ph}}\text{-CuOTf}$ , reported by Wei and Li. <sup>424, 425</sup> .....	212
Figure 5.12. The CuAAC reaction of phenethyl azide with phenyl acetylene catalysed by copper(I) iodide with PyBOX derivative, L studied by Meng <i>et al.</i> <sup>430</sup> .....	213
Figure 5.13. The structure of the mononuclear copper(I) $\text{PyBOX}^{\text{R}}$ complexes reported by Panera <i>et al.</i> <sup>442, 443</sup> .....	214
Figure 5.14. The structures of the dinuclear copper(I) $\text{PyBOX}^{\text{R}}$ complexes reported by Panera <i>et al.</i> <sup>442, 443</sup> Bottom structure is the $\mu$ -chloro bridged analogue...215	215
Figure 5.15. The structure of the tetranuclear copper(I) $\text{PyBOX}^{\text{R}}$ complexes reported by Panera <i>et al.</i> <sup>442, 443</sup> .....	215
Figure 5.16. XRD structures obtained of complex 22 (left) and 23 (right). Ball and stick models are shown for clarity. Hydrogen atoms omitted for clarity. ....	217
Figure 5.17. Simplified packing structures of 22 (left) and 23 (right) with hydrogen contacts displayed. ....	218
Figure 5.18. XRD structure solution obtained of complex 24 (left). Intermolecular interactions are also shown in a simplified packing diagram (right). Structure is shown as a ball and stick model for clarity. Hydrogen atoms omitted in the left image for clarity. ....	219
Figure 5.19. XRD structure solution obtained of $[\text{Cu}((S)\text{-thioPyBOX}^{\text{tBu}})_2][\text{OTf}]_2$ , complex 25. Hydrogen atoms, counter-ions and solvents are omitted for clarity. Thermal ellipsoids are at the 50% probability level. ....	220
Figure 5.20. XRD structure and relevant data of the dicationic $[\text{Cu}(\text{bpp})_2][\text{BF}_4]_2$ complex reported by Solanki <i>et al.</i> <sup>446, 447</sup> Figure taken from publication. <sup>445</sup> 222	222
Figure 5.21. XRD structure solution obtained for $[\text{Cu}_4\text{I}_4((R)\text{-PyBOX}^{\text{iPr}})_2]$ , 26. Hydrogen atoms are omitted for clarity. Ball and stick model shown for clarity. ....	222
Figure 5.22. XRD structure solutions of $[\text{Cu}_2((S)\text{-PyBOX}^{\text{iPr}})_2][\text{PF}_6]_2$ , 27 (left) and $[\text{Cu}_2((S)\text{-PyBOX}^{\text{tBu}})_2][\text{BF}_4]_2$ , 28 (right). Hydrogen atoms, solvent and counter-ions are omitted for clarity. Thermal ellipsoids are at the 50% probability level. ....	223
Figure 5.23. XRD structures of 27 (left) and 28 (right) looking down the central pyridine ring. Hydrogen atoms, counter-ions and solvent are omitted for clarity. Thermal ellipsoids are at the 50% probability level. ....	225
Figure 5.24. XRD structure of $[\text{Cu}((R)\text{-PyBOX}^{\text{Ph}})_2][\text{PF}_6]$ , 29. Hydrogen atoms, solvents and counter-ions are omitted for clarity. Thermal ellipsoids are at the 50% probability level. ....	226
Figure 5.25. XRD structure of $[\text{FCu}_3((R)\text{-PyBOX}^{\text{Ph}})_3][\text{BF}_4]_2$ , complex 30. Hydrogen atoms and solvent are omitted for clarity. Ball and stick model shown for clarity. ....	227

- Figure 5.26. XRD packing structure of 30 shown along the *c*-axis. Hydrogen atoms are omitted for clarity. Ball and stick model shown for clarity.....228
- Figure 5.27. Reaction scheme for the synthesis of benzyl azide from benzyl bromide.....229
- Figure 5.28. Reaction scheme for the click reaction employed herein to study the copper catalysts. ....229
- Figure 5.29. Copper catalysts, 26, 27 and 28 tested herein on the CuAAC reaction in Figure 5.28. ....229
- Figure 5.30. Overlaid <sup>1</sup>H NMR spectra of benzyl azide (black), phenyl acetylene (red) and 1-benzyl-4-phenyl-1,2,3-triazole (blue). CD<sub>3</sub>Cl, 400 MHz. ....230
- Figure 5.31. The test reaction progression of the synthesis of 1-benzyl-4-phenyl-1,2,3-triazole, monitored by the growth of the <sup>1</sup>H NMR peak corresponding to the CH<sub>2</sub> group in the triazole, with catalysts 26 (pink), 27 (blue), 28 (orange) and Cu<sub>2</sub>O (green). The black line at 1440 mins corresponds to T = 24 hrs.....232
- Figure 5.32. Carousel round 1 (top) and round 2 (bottom). The reaction progression of the synthesis of 1-benzyl-4-phenyl-1,2,3-triazole, monitored by the growth of the <sup>1</sup>H NMR peak corresponding to the CH<sub>2</sub> group in the triazole, with catalysts 26 (pink), 27 (blue), 28 (orange), Cu<sub>2</sub>O (green) and an uncatalysed reaction (grey). The black line at 1440 mins corresponds to T = 24 hrs.....234
- Figure 6.1. Epoxidation of *trans*-stilbene studied by Nishiyama *et al.* catalysed by ruthenium(II) PyBOX complexes; [Ru(PyBOX<sup>R</sup>)(PyDIC)] and [Ru(terpy)(PyDIC)], to give the *trans*-epoxide product. <sup>480</sup> .....242
- Figure 6.2. The cyclopropanation of styrene with menthyl diazoacetate catalysed by [Ru(*hm*-PyBOX)Cl<sub>2</sub>] studied by Iwasa *et al.* <sup>472</sup> .....243
- Figure 6.3. C-H amination reaction studied by Milczek *et al.* using ruthenium(II) PyBOX catalysts. <sup>474</sup> .....244
- Figure 6.4. The transfer hydrogenation reaction of a ketone to a secondary alcohol. <sup>484</sup> .....244
- Figure 6.5. One of the C<sub>2</sub>-symmetric ruthenium(II) catalysts studied by Noyori and Hashiguchi. <sup>470</sup> .....245
- Figure 6.6. Schematic diagram of how the Ru-PyBOX catalyst behaves enantioselectively in the asymmetric transfer hydrogenation reaction of an aromatic ketone. Figure taken from publication. <sup>475</sup> .....245
- Figure 6.7. Structures of [Ru(terpy)(MeCN)<sub>2</sub>Cl][PF<sub>6</sub>], 31 (left) and [Ru(terpy)<sub>2</sub>][(PF<sub>6</sub>)<sub>2</sub>], 32 (right). ....247
- Figure 6.8. XRD structures obtained of 31 (left) and 32 (right). Hydrogen atoms, counter-ions and solvents are omitted for clarity. Structures are shown as a ball and stick model for clarity. ....247
- Figure 6.9. XRD structures of [Ru((*R*)-PyBOX<sup>Ph</sup>)Cl<sub>2</sub>MeCN], 33 (left) and [Ru((*R*)-PyBOX<sup>Ph</sup>)<sub>2</sub>][BF<sub>4</sub>]<sub>2</sub>, 34 (right). Hydrogen atoms, solvents and counter-ions are omitted for clarity. Thermal ellipsoids are at the 50% probability level. ....249
- Figure 6.10. XRD structures of [Ru((*S*)-PyBOX<sup>Ph</sup>)I<sub>2</sub>MeCN], 35 (left) and [Ru((*R*)-PyBOX<sup>Pr</sup>)I<sub>2</sub>MeCN], 36 (right). Hydrogen atoms, solvents and counter-ions are omitted for clarity. Thermal ellipsoids are at the 50% probability level. ...251



- Figure 6.11. XRD structure solution of  $[\text{Ru}((R)\text{-thioPyBOX}^{\text{Ph}})_2\text{I}][\text{I}_3]$ , 37 (left). Hydrogen atoms and counter-ions are omitted for clarity. Ball and Stick model is shown for clarity.....252
- Figure 6.12. XRD structure 37 highlighting the bent conformation of two of the thiazoline rings.....253
- Figure 6.13. The transfer hydrogenation of acetophenone.  $[\text{Ru}]$  is the ruthenium(II) catalyst employed,  $^t\text{BuOK}$  is the base, potassium tertbutoxide. The reaction was carried out in isopropanol.....254
- Figure 6.14. Preliminary catalysis examination of complexes 35 and 36. An uncatalysed reaction and two standard reactions catalysed by  $[\text{Ru}(p\text{-cymene})\text{Cl}_2]_2$  and  $[\text{Ru}(p\text{-cymene})\text{I}_2]_2$  were simultaneously performed for comparison. ....255
- Figure 6.15. The  $\text{IC}_{50}$  values obtained of complexes 35, 36 cisplatin (CDDP) and carboplatin (CARB) against the pancreatic cancer cell line (MIA PaCa-2) (48 h – green\*, 96 h - orange) and the osteosarcoma cell line (143B) (48 h – purple). \* $\text{IC}_{50}$  values for cisplatin and carboplatin are pending. Results are obtained from duplicate of triplicate repeats. ....257

## Abbreviations

(TI)SE -	(Time-Independent) Schrodinger Equation
143B -	human bone cancer cell line
1-bpp -	2,6-bis(pyrazol-1-yl)pyridine
2-pic -	2-aminomethylpyridine
AAC -	Azide-Alkyne Cycloaddition
bpy -	2,2'-bipyridine
CARB -	cis-diammine(1,1-cyclobutanedicarboxylato)platinum(II) (carboplatin)
CCSD -	Cambridge Crystallographic Structural Database
CDDP -	cis-diamminedichloroplatinum(II) (cisplatin)
CFSE -	Crystal Field Stabilisation Energy
CFT -	Crystal Field Theory
DCM -	Dichloromethane
DMF -	N,N'-dimethylformamide
DFT -	Density Functional Theory
DMSO -	dimethyl sulfoxide
DSC -	Differential Scanning Calorimetry
EPR -	Electron Paramagnetic Resonance
HFR -	Hartree-Fock-Roothan
HS -	High Spin
IC50 -	the half maximal inhibitory concentration
IRPD -	Infrared Photodissociation
ISC -	Intersystem Crossing
JT -	Jahn-Teller
LCAO -	Linear Combination of Atomic Orbitals
LFT -	Ligand Field Theory
LIESST -	Light Induced Excited Spin State Trapping
LS -	Low Spin

MAO -	methylaluminoxane
MIA PaCa-2 -	Pancreatic cancer cell line
MLCT -	Metal-to-Ligand Charge Transfer
MO -	Molecular Orbital
NMR -	Nuclear Magnetic Resonance
OAM -	Orbital Angular Momentum
PGM -	Platinum-Group Metals
phen -	1,10-phenanthroline
ptz -	1-propyltetrazole
pXRD -	Powder X-ray Diffraction
PyDIC -	pyridine-2,6-dicarboxylate
RB -	Round-Bottom
SCF -	Self-Consistent Field
SCO -	Spin Crossover
SD -	Standard Deviation
SET -	Single Electron Transfer
SQUID -	Superconducting Quantum Interference Device
ST -	Spin Transition
terpy -	2,2':6',2''-terpyridine
$T_{1/2}$ -	Temperature at which half the molecules occupy the HS state
$T_{\text{LIESST}}$ -	Temperature at which molecules fully occupy the HS state (in LIESST studies)
TMB -	1,3,5-trimethoxybenzene
T-S -	Tanabe-Sugano
UV/vis -	Ultraviolet/visible
VT -	Variable Temperature
XRD -	X-ray Diffraction
$\Delta_{\text{oct}}$ -	Octahedral crystal field splitting parameter

## Thesis Outline

Chapter 1 covers the fundamentals of inorganic and coordination chemistry that form the foundations of this thesis. These include the developments from Crystal Field Theory (CFT) to Ligand Field Theory (LFT),  $\pi$ -bonding and the Spectrochemical series. The High Spin (HS)-Low Spin (LS) dichotomy of spin states is introduced, linking into the phenomenon of Spin-Crossover (SCO), which is core to this thesis. SCO is discussed in great depth along with literature examples, starting from its origins, covering some more recent SCO studies and methods of perturbing and measuring SCO. Its rich contribution to research and potential applications in the field of molecular electronics is also discussed, along with how computational methods can be employed in SCO research.

Chapter 2 focuses on the ligand system employed throughout this thesis; 2,6-bis(thiazolinyl)pyridine (thioPyBOX). Initially a discussion on the N,N',N''-tridentate ligand system with a focus of some common ligands such as, Schiff-base ligands, 2,2':6'2''-terpyridine (terpy) and 2,6-bis(pyrazolyl)pyridine (bpp). Focus is drawn on the 2,6-pyridine(bisoxazoline) ligand (PyBOX) which introduces thioPyBOX - the key ligand framework in this thesis. A detailed discussion of the eight pieces of literature that synthesise thioPyBOX is presented, followed by synthetic strategies employed, reaction optimisation and purification work. A macrocyclic product formed in attempted thioPyBOX synthesis is also presented.

Chapter 3 introduces the concept of chirality in metal complexes and its applications in functional materials, catalysis and molecular electronics. This is followed by some examples of differences in SCO activity between isostructural complexes. The previously reported chiral discrimination between the spin states of iron(II) PyBOX<sup>R</sup> complexes is discussed. This introduces the study of the spin state behaviour of homochiral and heterochiral iron(II) thioPyBOX<sup>R</sup> complexes in the solid and solution states. Chiral discrimination of these complexes is explored along with solution stability studies of the heterochiral complexes. This research is compared against that previously observed for the PyBOX complexes.

Chapter 4 builds on the work presented in Chapter 3 by exploring heteroleptic iron(II) complexes featuring the PyBOX and thioPyBOX ligands, as a means to optimise SCO activity. Homochiral and heterochiral mixed PyBOX and thioPyBOX iron(II) complexes are synthesised and magnetic susceptibility behaviour is studied in the solid and solution states, along with ligand redistribution studies. Adding to this, heteroleptic complexes of iron(II) (thio-/)PyBOX with other N,N',N''-pincer ligands, such as 2,6-bis(2-benzimidazolyl) (bzimpy), 2,6-bis(pyrazol-1-yl)pyridine (1-bpp) and 2,2':6',2''-terpyridine (terpy), are presented along with their spin state behaviour.

Chapter 5 visits the primary application that metal-PyBOX complexes were first known for, which is catalysis. This chapter discusses the efforts made to replace the successful platinum-group metals (PGMs) with cheaper and more earth-abundant base metals such as iron and copper, for catalysis. A series of copper(II) PyBOX and thioPyBOX complexes are presented, with an aim to achieve an effective catalyst for reactions such as the Ullman Coupling. Copper(I) PyBOX complexes have also been synthesised in this chapter; these form dinuclear and tetranuclear helicate structures. An unprecedented trinuclear copper(I)-PyBOX helicate has also been synthesised. An initial catalysis study of the copper(I) helicates is presented on an azide-alkyne cycloaddition reaction, with some interesting results.

Chapter 6 adds to the catalysis theme of Chapter 5 with a small series of ruthenium(II) PyBOX complexes, primarily for the catalysis of asymmetric transfer hydrogenation reactions. Mono- and bis- coordinated ruthenium-terpy and ruthenium-PyBOX complexes are presented, which demonstrate how these two coordination modes can be achieved through experimental design. Ruthenium(II) mono-PyBOX complexes have been synthesised featuring *trans*-chloride and *trans*-iodide motifs to gain an insight on the halide effect in their catalysis. An attempt at incorporating the thioPyBOX ligand resulted in a bis-thioPyBOX ruthenium complex with a hemilabile coordination of one of the ligands. Finally, biological investigation on the cytotoxic activity of two of these complexes against pancreatic cancer cells, MIA-PaCa-2 and human bone cancer cells, 143B, is presented, with some promising results!

# Chapter 1

## Introduction and Theory

### 1.1 Coordination Complexes

The concept of transition metal coordination chemistry was founded by Alfred Werner, who received the Nobel Prize in 1913 for his theory of coordination. <sup>1</sup> In his teachings, the concept of ligands being in a spatial arrangement around a metal nucleus was established, in addition to the concepts of coordination number and coordination geometry and proving the two are connected.

In the theory of coordination, empty or partially-filled metal valence orbitals accept one or more lone-pairs of electrons from a ligand, in a dative-covalent or coordinate bond. <sup>2</sup> The  $\sigma$ -bond formed renders the metal ion and ligand, a Lewis acid-Lewis base pair respectively, <sup>3</sup> which is the simplest explanation of coordination compounds (Figure 1.1). It is therefore befitting to first examine the more multifaceted, and further developed, theories on transition metal coordination complexes that will form the foundations of this thesis.

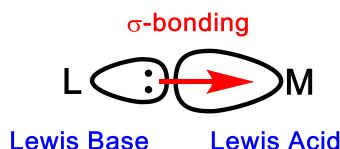


**Figure 1.1. Metal accepting lone-pair of electrons from Ligand in a Lewis Acid-Base model.**

There are five  $d$ -orbitals in each electron shell with  $n \geq 3$  electrons (Figure 1.2) which depict the five solutions to the Schrödinger equation. Three of these  $d$ -orbitals, labelled  $d_{xy}$ ,  $d_{xz}$ , and  $d_{yz}$ , have lobes pointing between the Cartesian axes and according to group theory, together they come under the  $t_{2g}$  symmetry term. <sup>4</sup> There are then another three orbitals aligned with the Cartesian axes;  $d_{x^2-y^2}$ ,  $d_{z^2-y^2}$  and  $d_{z^2-x^2}$ , where a linear combination of the latter two is taken to give only  $d_{x^2-y^2}$  and  $d_{z^2}$ , which come under the  $e_g$  symmetry term. <sup>4,5</sup>

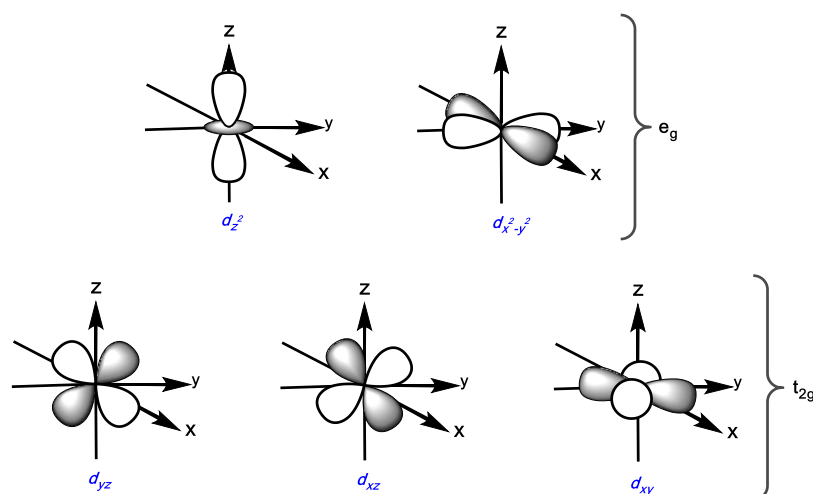


**Figure 1.2. The five d-orbitals along the Cartesian axes.**

### 1.1.1 Crystal Field Theory

Though the five *d*-orbitals are degenerate in energy in free metal ions, Crystal Field Theory (CFT) more usefully describes how the interaction of ligands with a free metal ion, i.e. in a coordination complex, distorts this *d*-orbital degeneracy.<sup>6, 7</sup>

In CFT, the *d*-electron distribution of the metal ion becomes anisotropic owing to the electrostatic repulsion arising from ligands in the coordination sphere of the metal. It should be noted that in this theory, ligands are treated as negative point charges, hence this model is often referred to as an electrostatic model.<sup>8</sup> The electrons therefore favourably occupy the *d*-orbitals as to minimise repulsion from the coordinated ligands. This in turn results in an increased stabilisation of the orbitals that are not directly aligned with the ligand point charges, disrupting the degeneracy of the five orbitals. This moderates the metal complex to a more stabilised energy, by an amount known as the Crystal Field Stabilisation Energy (CFSE).<sup>9, 10</sup>

The CFSE depends on various factors, one of which is the geometry of the coordination complex. This will result in different alignments of metal *d*-orbitals with the ligands, stabilising different *d*-orbitals as a result, shown in Figure 1.3. The energy separation between the *d*-orbitals is denoted as ' $\Delta_{\text{oct}}$ ' which equals  $10Dq$ , though both units are found in the literature, the former unit is used herein.  $\Delta_{\text{oct}}$  can be experimentally determined by UV/vis spectroscopy, and therefore serves as a measure of the strength of the crystal field, where a small  $\Delta_{\text{oct}}$  represents weak field *d*-orbital splitting and a large  $\Delta_{\text{oct}}$  is indicative of strong field splitting.<sup>5</sup>

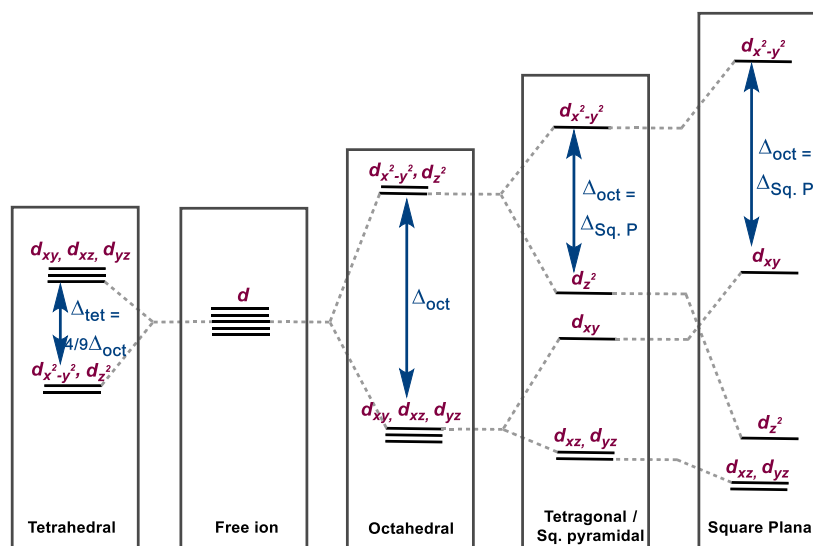


Figure 1.3. Crystal Field splitting of the  $d$ -orbitals in common coordination geometries. Figure adapted from Pearson.<sup>9</sup>

### 1.1.2 Electron Configuration

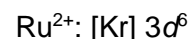
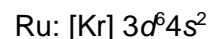
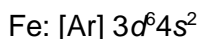
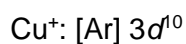
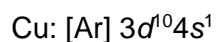
Contributing factors to the CFSE optimisation include three laws of electronic configuration arrangement and orbital occupancy, which is described by *Pauli's exclusion principle*, the *Aufbau principle* and *Hund's rule*.

Pauli's exclusion principle states that no two fermions can have the same set of four quantum numbers,  $n$ ,  $l$ ,  $m_s$  and  $m_l$ . Knowing that a maximum of two electrons can occupy the same orbital, it was conceived that those electrons must have opposite spin for this to hold true, giving  $m_s \pm 1/2$ .<sup>11, 12</sup>

The Aufbau principle is the concept of filling orbitals that are lowest in energy first, then working in order to higher energy orbitals, which was first speculated by Niels Bohr.<sup>13</sup> It was later established by Erwin Madelung who reported this as a rule for neutral atoms, which stated that the order of electrons filling shells is of  $(n+l)$  quantum number sum. His rule supports the filling of the  $4s$  orbital before the  $3d$  in transition metals and justifies that  $4f$  electrons do not appear before  $Z=56$  for metal atoms in the gaseous phase.<sup>14</sup> Though a useful first approximation, there are flaws in this theory, demonstrated with the example of scandium. Scandium has experimentally shown that the electrons are filled into the  $3d$  orbital before the  $4s$ , and not as the Aufbau principle suggests and therefore, in the first ionisation, the electron is removed from the  $4s$  orbital.<sup>13</sup> In any molecules where the metal forms covalent bonds, the orbitals also abide by the ordering of  $3d < 4s$ .

This trend is consistent across the transition metals, lanthanides and actinides. Herein, the metals, iron, ruthenium and copper are discussed in their ionised forms and their electronic configurations follow the example set by scandium, rather than by the Aufbau principle, outlined below.





The third law, is that described by *Hund's rule*, which states that electrons first singularly occupy degenerate orbitals before spin pairing occurs. This can also be understood as, the lowest energy state, is that where the multiplicity is maximised in the electronic configuration. <sup>15</sup> As with the Aufbau principle, limitations exist to the rule. Deviations from the rule are commonly found in experimental data and the rule is mostly reliable for the ground state configuration, as the model is centred around interelectron repulsion, failing to account for nuclear attraction. <sup>16</sup>

Additionally, Hund's rule fails in the case of strong-field ligands, which forms the basis of the High-Spin (HS) and Low-Spin (LS) dichotomy. HS and LS electronic configurations arise in certain metal complexes as a result from competition between the Aufbau principle and Hund's rule. This forms the foundation of the phenomenon of Spin-Crossover (SCO) which is of key focus in this thesis (see later in Sections 1.2 and 1.4).

### 1.1.3 Ligand Field Theory

Ligand Field Theory (LFT) is an application of Molecular Orbital Theory to transition metals, and further rationalises the interaction of ligands with a metal ion. This theory however, unlike CFT, adopts a covalent approach by considering the overlap of symmetrical ligand and metal orbitals to produce bonding and anti-bonding molecular orbitals. The resulting bonding orbitals are more stable in energy than either the metal or ligand orbitals alone, and the resulting anti-bonding orbitals are less stable, which is considered a driving force for this interaction. <sup>8</sup>

Though approximations are used in LFT, the model still provides useful insight for understanding metal-ligand interactions in coordination complexes. As the scenario of an  $[\text{ML}_6]^{n+}$  with an octahedral geometry (point group  $O_h$ ), is of most relevance here, the construction of its Molecular Orbital (MO) diagram is outlined below (Figure 1.4). It should be noted that the metal  $t_{2g}$  orbitals have no symmetry alignment with the ligand orbitals and therefore are classed as non-bonding as they do not contribute to the MO bonding interactions.

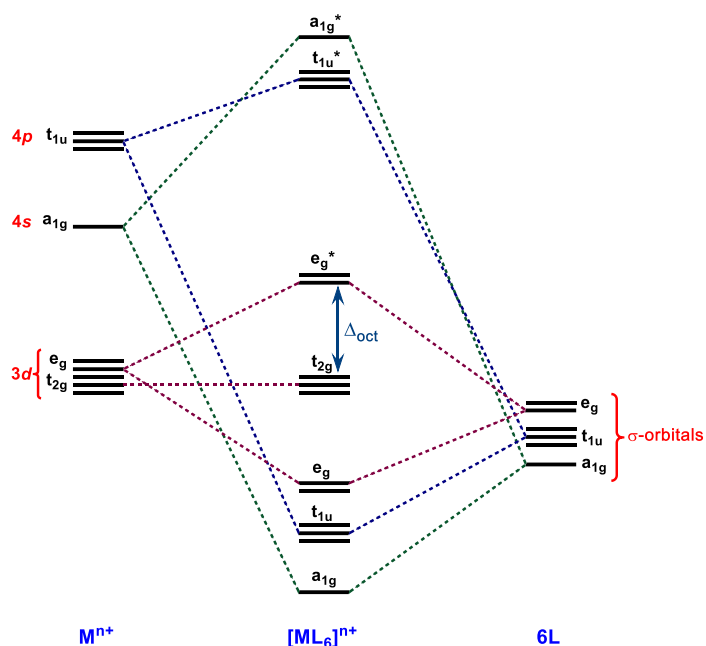


Figure 1.4. Construction of the MO diagram for  $[ML_6]^{n+}$ , considering only M-L  $\sigma$ -bonding. Figure adapted from Yves.<sup>17</sup>

### 1.1.4 Metal-Ligand $\pi$ - Bonding

It is important to note that in the above figure, only M-L bonding from  $\sigma$ -interactions are accounted for. Ligands with available  $p$ -orbitals have the appropriate orbital symmetry to interact with the  $d_{xy}$ ,  $d_{xz}$  and  $d_{yz}$  orbitals, thus M-L  $\pi$ -interactions can additionally occur.<sup>5</sup> There are two categories of this;  $\pi$ -donor ligands, where electrons are donated from a filled ligand  $p$ -orbital to an empty metal orbital, and  $\pi$ -acceptor ligands, where electrons are additionally accepted from filled metal  $t_{2g}$  orbitals to an empty ligand  $p$ -orbital. When the latter occurs, particularly with strongly  $\pi$ -accepting ligands, this is known as  $\pi$ -back-bonding (Figure 1.5).<sup>18</sup>

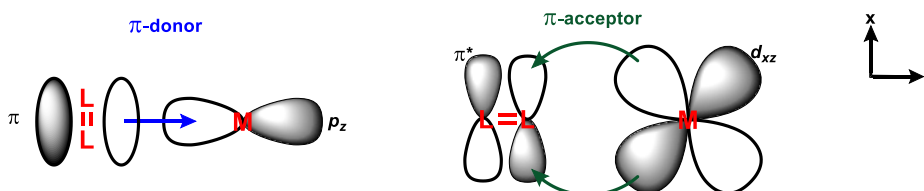


Figure 1.5.  $\pi$ -interactions between ligand and metal orbitals.

Ligands can therefore be classified as, pure  $\sigma$ -donors,  $\pi$ -donors or  $\pi$ -acceptors. These form an order of increasing strength of ligand field, respective to the type(s) of bonding interactions involved. This is known as the spectrochemical series.

The series considers all ligands, irrespective of charges, and orders them according to their effect on the energy of the first band of the UV-Vis spectra of their cobalt(III) complexes. From the series of spectra obtained, hypsochromic and bathochromic shifts were observed when different ligands were substituted for one another, confirming the order for the spectrochemical series, outlined below (Figure 1.6).<sup>19, 20</sup>

**CO, CN<sup>-</sup>, PMe<sub>3</sub>, NO<sub>2</sub><sup>-</sup>, PPh<sub>3</sub>, bpy, phen, NH<sub>3</sub>, py, ONO<sup>-</sup>, O<sub>2</sub><sup>2-</sup>, acac<sup>-</sup>,**

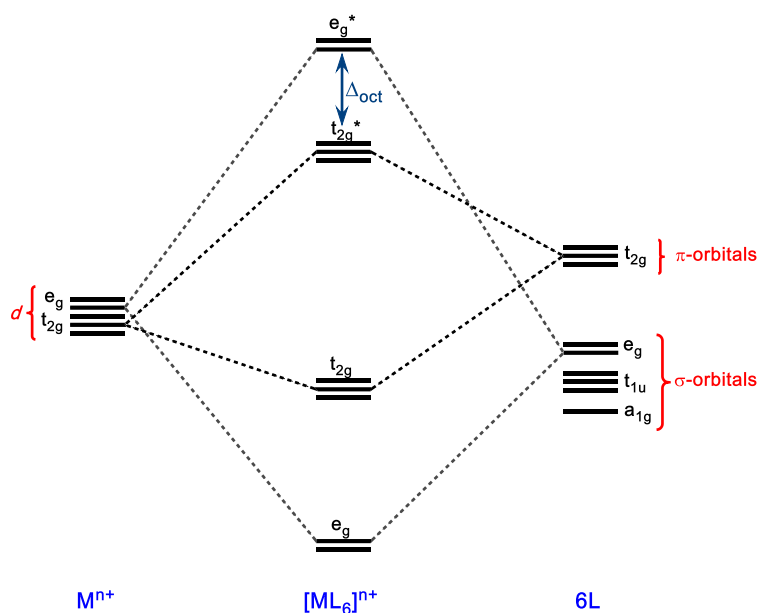
**Strong-field ligand** —————→

**H<sub>2</sub>O, NCS<sup>-</sup>, O<sub>2</sub><sup>-</sup>, OH<sup>-</sup>, NO<sub>3</sub><sup>-</sup>, F<sup>-</sup>, N<sub>3</sub><sup>-</sup>, SCN<sup>-</sup>, Cl<sup>-</sup>, Br<sup>-</sup>, CrO<sub>4</sub><sup>2-</sup>, I<sup>-</sup>**

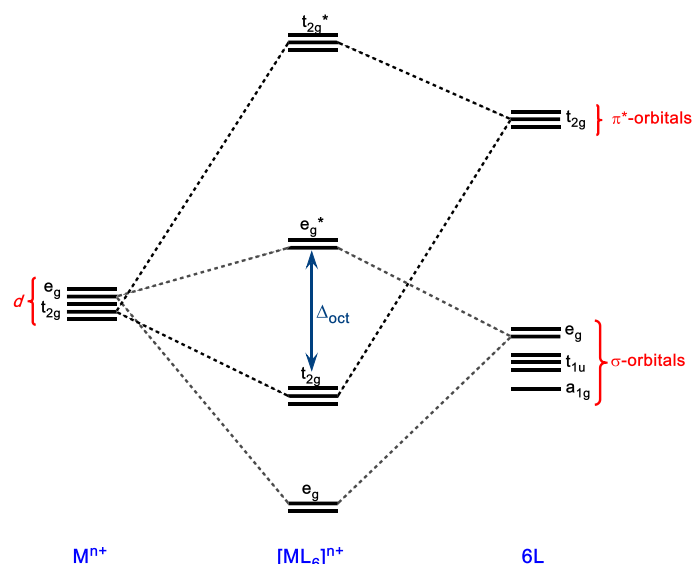
—————→ **Weak-field ligand**

**Figure 1.6. The spectrochemical series of selected ligands in order of decreasing ligand-field strength.**<sup>19, 20</sup>

Strong-field ligands in the spectrochemical series are generally good  $\pi$ -acceptors and therefore undergo  $\pi$ -back-bonding with metal complexes, while weak-field ligands are usually just  $\pi$ - or  $\sigma$ -donors. The addition of  $\pi$ -interactions modifies the MO diagram, as metal  $t_{2g}$  orbitals now form bonding (and anti-bonding) M-L orbital combinations, whose energies differ, relative to the  $e_g$  orbitals, depending on whether the ligands are  $\pi$ -acceptors or  $\pi$ -donors (Figure 1.7).



a.) where L is a  $\pi$ -donor ligand



b.) where L is a  $\pi$ -acceptor ligand

**Figure 1.7. Expanded MO diagram for M-L bonding considering ligand  $\pi$ -orbital interactions, with the two scenarios of a.) where L is a  $\pi$ -donor ligand and b.) where L is a  $\pi$ -acceptor ligand. ( $a_{1g}$  and  $t_{1u}$  orbitals have been omitted for clarity). Scale is expanded from Figure 1.4. Figure reproduced from Housecroft and Sharpe. <sup>5</sup>**

From the MO diagram in Figure 1.4 and the two MO diagrams in Figure 1.7, it is clear that the type of ligand affects the energies of the resulting M-L bonding interactions and therefore the all-important  $\Delta_{oct}$  values. The value of  $\Delta_{oct}$  is largest when  $\pi$ -accepting ligands are bonded to the metal and is smallest when  $\pi$ -donor ligands are complexed, due to the stabilisation and destabilisation of the  $t_{2g}$  bonding and anti-bonding orbitals.

In addition to the metal complex geometry and the strength of the ligand field, the metal ion itself can also dictate the size of  $\Delta_{oct}$ . Metal ions with larger atomic radii and more diffuse  $d$ -orbitals increase  $\Delta_{oct}$ , as the increased orbital overlap with the ligand results in a greater energy separation of the  $t_{2g}$  and  $e_g$  orbitals. Therefore the pairing energy,  $P$ , becomes less than  $\Delta_{oct}$ . This is further supported by the reduced repulsion between paired electrons in larger orbitals. Furthermore, where different oxidation states of the same metal are concerned, a higher oxidation state, which has a higher charge density, will increase  $\Delta_{oct}$  due to the increased metal-ligand repulsion.

## 1.2 The High-Spin - Low-Spin Dichotomy

The HS-LS dichotomy arises as a result of the factors that affect the crystal field splitting ( $\Delta_{oct}$ ) and therefore the CFSE. First row transition metal ions with  $d^4$ - $d^7$  electrons can adopt one of two possible configurations across the  $d$ -orbital splitting. In one of these the energy of spin pairing,  $P$ , exceeds the energy of accessing a higher energy vacant  $d$ -orbital, giving rise to the HS state, and the other, where the energy required to access

a higher energy orbital exceeds P gives the LS state. Figure 1.8 demonstrates the two states with an iron(II) complex ( $3d^6$ ). Second and third row  $d^4$ - $d^7$  transition metals generally have a  $\Delta_{\text{oct}}$  too large to allow the HS state and so only adopt the LS configuration. As the size of  $\Delta_{\text{oct}}$  governs the spin-state, the aforementioned factors that affect  $\Delta_{\text{oct}}$  equally dictate whether a complex adopts the HS or LS configuration.

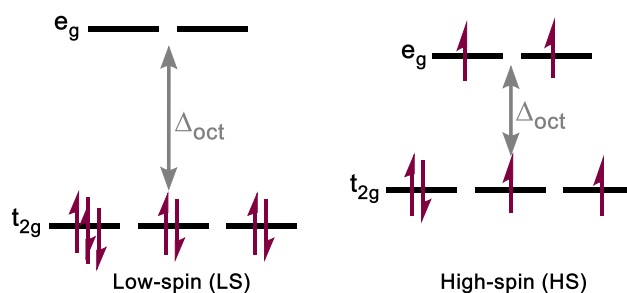


**Figure 1.8. Low-spin (LS) and high-spin (HS) electronic configurations of a  $d^6$  metal ion in a ligand field.**

Any factor that increases  $\Delta_{\text{oct}}$ , such as a square planar geometry, a strong-field ligand on the spectrochemical series or a larger metal ion, results in a preference for the LS state. Therefore, factors that decrease  $\Delta_{\text{oct}}$  will result in a preference for the HS state. It's also worth noting that in the case of the HS state, as there is now electron occupancy in the antibonding orbitals, the length of the metal-ligand bond ( $r_{\text{(M-L)}}$ ) will be increased, compared to its respective LS state. This is a particularly useful diagnostic tool for distinguishing between the HS/LS states which will be later elaborated on. From this knowledge, one can design metal complexes as to give rise to a particular spin-state.

### 1.2.1 Molecular Magnetism

For the octahedral geometry shown above for iron(II), there are two possible spin states which can be distinguished by measuring the magnetic moment. This is because the LS state has no unpaired electrons ( $t_{2g}^6 e_g^0$ ) and so the metal is in the diamagnetic singlet state ( $S=0$ ) and the HS form has 4 unpaired electrons ( $t_{2g}^4 e_g^2$ ), and so is in the paramagnetic pentet state ( $S=2$ ).

Where there is only a diamagnetic effect in an ion or complex, there is no resultant spin ( $s$ ) or orbital angular momentum ( $l$ ), and such compounds repel an applied magnetic field. However, in the case of paramagnetism, there is a net spin to account for as there are unpaired electrons. When a magnetic field is applied, these spins are weakly attracted and generate their own internal field. That is, the material has a positive magnetic susceptibility.

Assuming a zero orbital angular momentum in a paramagnet, the magnetic moment,  $\mu$ , is given by Equation 1.1. As this equation considers the spin only, the spin-only magnetic moment is denoted as  $\mu_{so}$ , and has units of Bohr Magnetons (BM).<sup>21</sup> Substituting  $S = \frac{1}{2}n$  where  $n$  is the number of unpaired electrons, Equation 1.1 can also be written as below in Equation 1.2.

$$\mu_{so} = (4S(S + 1)) BM$$
$$\text{where } BM = \frac{he}{4\pi mc}$$

**Equation 1.1. The spin-only magnetic moment equation.**

$$\mu_{so} = \sqrt{n(n + 2)} BM$$

**Equation 1.2. The spin-only magnetic moment as a function of the number of unpaired electrons**

From this, a HS iron(II) complex with 4 unpaired electrons, has a  $\mu_{so} = 4.90$  BM whereas for a LS iron(II) complex with 0 unpaired electrons, has  $\mu_{so} = 0$  BM.

An electron has orbital angular momentum (OAM), in cubic coordination geometries such as a tetrahedron or octahedron, if an unpaired electron is able to move between vacant or half-filled orbitals that are degenerate in energy but not of the same spin (Pauli's principle). This is permitted as long as there is a rotation axis between degenerate orbitals to enable this, i.e. the  $d_{xy}$  and  $d_{xz}$  orbitals are related by a  $90^\circ$  rotation.<sup>5</sup>

Considering the addition of OAM on the magnetic moment, i.e.  $\neq 0$ , the effect of spin-orbit coupling is now incorporated to give Equation 1.3. Where the resultant of spin and orbit moments is denoted by the quantum number  $j$ , termed by the Russell-Saunders approximation, and  $g$  is the Landé splitting factor. As the OAM is now factored in, the moment is now considered to be the effective magnetic moment,  $\mu_{eff}$ .

$$\mu_{eff} = g\sqrt{j(j + 1)} BM$$

**Equation 1.3. The magnetic moment equation for the resultant angular momentum,  $j$ .**

Equation 1.3 holds true where the separation of the ground state energy levels exceeds the average thermal energy,  $K_B T$ . However, when  $\Delta E \ll K_B T$ , the moments are now individually quantised so are treated distinctly to give Equation 1.4.<sup>21</sup>

$$\mu_{eff} = \sqrt{4S(S + 1) + l(l + 1)} BM$$

**Equation 1.4. Magnetic moment equation when  $\Delta E \ll K_B T$ .**

However, since an anisotropic field generated by a crystal field of point charges splits the degeneracy of the ground state (CFT), the coordination of a ligand restricts the rotation axes which, either partially or fully, quenches the OAM of the *d*-orbitals.<sup>22</sup> This effect is most pronounced with the 3*d* orbitals, than complexes with 4*d* and 5*d* orbitals, as the crystal field effect dominates over smaller spin-orbit coupling in the 3*d* case. Therefore differences between  $\mu_{so}$  and  $\mu_{eff}$  are most distinct in 2<sup>nd</sup> and 3<sup>rd</sup> row *d*-block metals.

Hund's third law states that for a half-filled subshell or less,  $j=|l-s|$ , and for a more than half-filled subshell,  $j=(l+s)$ , therefore when the OAM is quenched ( $l=0$ )  $j=s$  and the  $\mu_{so}$  equation provides a good enough approximation for the magnetic moment. Experimental values of the magnetic moment will however always be slightly higher than  $\mu_{so}$  as there is always some weak magnitude of spin-orbit coupling even when angular momentum is quenched.

The molar magnetic susceptibility,  $\chi_m$ , is correlated to the magnetic moment,  $\mu$  by Equation 1.5. The advantage of measuring  $\chi_m$  is that it can account for the presence of an applied magnetic field and temperature-dependency, so can determine how much of a sample is para- or dia- magnetic at a given temperature. It can be said that  $\chi_m = \chi_{para} + \chi_{dia}$  and the effect of paramagnetism is stronger than diamagnetism such that  $\chi_{para} > |\chi_{dia}|$ . If  $\chi_m > 0$  the sample is paramagnetic and if  $\chi_m \leq 0$  the sample is diamagnetic.<sup>23</sup>

$$\mu_{eff} (BM) = \sqrt{\frac{3K_b T \chi_m}{N_A \mu_0}}$$

**Equation 1.5. The relationship between  $\mu_{eff}$  and  $\chi_m$ . Where  $N_A$  is Avogadro's constant and  $\mu_0$  is the permeability of a vacuum.**

**1.2.1.1 The Curie Law**

The Curie law (Equation 1.6) demonstrates the temperature-dependence of a paramagnetic material, and although rare, perfect paramagnets obey the Curie law. This can be shown by a graphical plot of  $1/\chi_m$  against  $T$ , which shows a directly proportional straight line centred at the origin (Figure 1.9). Where the magnitude of spin-orbit coupling is more prominent, the temperature dependency of  $\mu_{eff}$  is increased. The Curie law highlights the importance of stating the magnetic susceptibility at specific temperatures.

$$\chi_m = \frac{C}{T}$$

$$\text{Where } C = S(S + 1) \left( \frac{N_A g^2 B^2}{3K_b} \right)$$

**Equation 1.6. The Curie law, where C is the Curie Constant.**

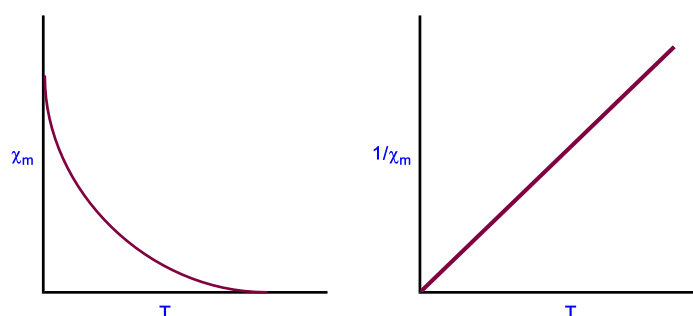


**Figure 1.9. A plot of  $\chi_m$  against T (left) and  $1/\chi_m$  against T for a perfect paramagnet, which obeys the Curie law. <sup>5</sup>**

Where the paramagnetism of individual metal centres is carried throughout a material (ferromagnetism, antiferromagnetism or ferrimagnetism), the Weiss constant can be additionally added to the Curie equation (Equation 1.7). This now accounts for the temperature at which a paramagnetic material goes from spontaneous magnetisation to an ordered magnetisation, known as the Curie Temperature,  $T_c$ . This forms the Curie-Weiss law (Equation 1.8). When the Weiss constant,  $\Theta$  is equal to zero, Curie behaviour is observed and the sample is a simple paramagnet.

$$\chi_m = \frac{C}{(T - \Theta)}$$

**Equation 1.7. The Curie-Weiss law where  $\Theta$  is the Weiss constant.**

$$\chi_m = \frac{C}{(T - T_c)}$$

**Equation 1.8. The Curie-Weiss law when  $\Theta = T_c$ .**

### 1.3 The Jahn-Teller Effect

The Jahn-Teller (JT) theory, furthers the understanding of electronic configuration beyond that described in CFT and LFT. The JT theory, is a distortion effect that arises where there are degenerate orbitals within an incomplete shell. <sup>24</sup> This allows for electrons to 'hop' into a vacant degenerate orbital which results in further splitting of the  $d$ -orbitals. The driving force for this is an overall increased stabilisation of the complex. Where spin-orbit coupling has been extinguished in a metal complex, JT effects are more pronounced, and therefore this is most notable in first row transition metals. <sup>22</sup> The



number of  $d$ -electrons, complex geometry and whether a complex adopts a HS or LS configuration, affects the degree of JT distortion. Characteristics of JT distorted ions include magnetic anisotropy, lattice distortions, phase transitions, reduced lattice symmetry and temperature-dependent exchange interactions.<sup>25</sup>

Considering an octahedral geometry, a weak JT distortion is observed for complexes with 1 or 2  $d$ -electrons and HS complexes with 6 or 7  $d$ -electrons. The effect is even stronger for HS  $d^4$ , and  $d^9$  complexes as shown in Figure 1.10. LS octahedral complexes with 4 or 5  $d$ -electrons are weakly distorted, whilst a pronounced effect is expected for LS  $d^7$ , and  $d^9$  configurations.<sup>22</sup>

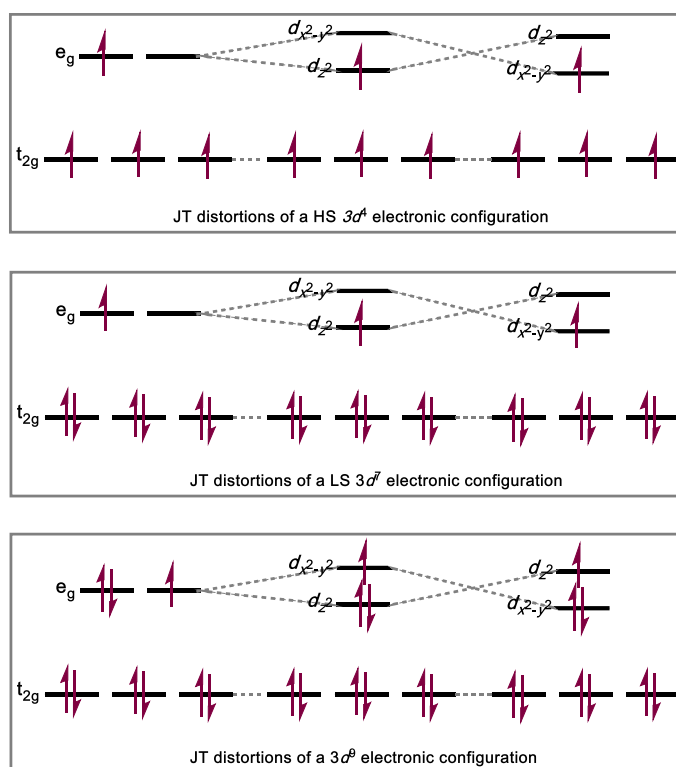


**Figure 1.10.  $d$ -orbital JT distortions of the  $e_g$  orbitals in a HS  $d^4$  configuration (top), LS  $d^7$  configuration (middle) and  $d^9$  configuration (bottom). No distortion (left), JT elongation (centre) and JT compression (right).**

The distortion of the crystal lattice can be observed in X-ray crystallographic structures by observing contraction or elongation of bonds along certain axes or general deviations from the expected classical geometry. Electron Paramagnetic Resonance (EPR) spectroscopy is another way to measure JT distortions, an example of this is with  $\text{Cu}^{2+}$  ions ( $d^9$ ) which show deviations from the typical  $g_{\text{para}}$  and  $g_{\text{perp}}$  values due to the anisotropy. A cooperative JT effect is one where a significant number of individual metal centres are JT-distorted across the bulk material, and this may give rise to a specific magnetic behaviour, a dynamic JT effect results in a crystal system transition to a lower symmetry, demonstrating the prominence of the effect.<sup>25</sup>

## 1.4. Spin Crossover

Figure 1.11 shows the harmonic oscillator model of the LS and HS states as their potential energy wells as a function of the increasing metal-ligand bond length for an iron(II)-nitrogen bond. If the energy difference between the lowest lying vibronic energy level of the  $^1A_{1g}$  and  $^5T_{2g}$  states is sufficiently small and approximates to the average thermal energy ( $\Delta E_{HL} \approx k_b T$ ), then a small external perturbation to the system can induce a spin-transition (ST) from the LS to the HS state,<sup>26</sup> where the quintet spin state becomes the ground state over the singlet term. As this involves a change of spin states, this can be considered as a non-radiative Intersystem Crossing (ISC) process.<sup>27</sup> This overall phenomenon is known as spin-crossover (SCO).

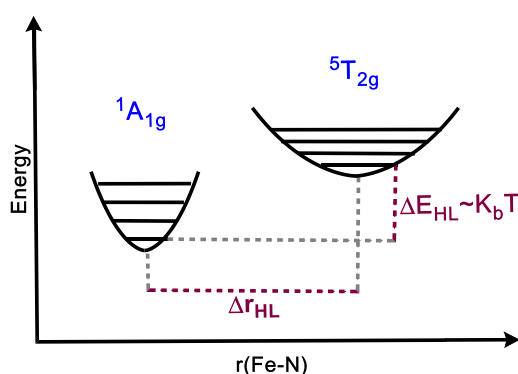


**Figure 1.11. Potential energy wells of an iron(II) SCO system, with respect to the Fe-N bond distance. The  $^1A_{1g}$  state is the LS state and the  $^5T_{2g}$  is the HS state.**

**Figure reproduced from Gütlich *et al.*<sup>26</sup>**

The energy levels in the harmonic oscillator model in Figure 1.11 each have an energy corresponding to  $E = 1/2fr^2$  where  $f$  is the bond force constant and  $r$  is the M-L bond length. The displacement along the x-axis between the two wells is roughly  $\Delta r_{HL} = 0.2 \text{ \AA}$  and the displacement along the y-axis shows the greater stability (lower energy) of the LS state for an isolated iron(II) SCO complex at a given temperature.<sup>28</sup>

SCO can also be understood as an equilibrium between the HS and LS spin states (Figure 1.12) as the switching can potentially work in either direction and be reversed in some cases, though the term equilibrium is most appropriate for solution state SCO.<sup>29</sup> Common external stimuli in SCO are temperature, pressure or light irradiation.

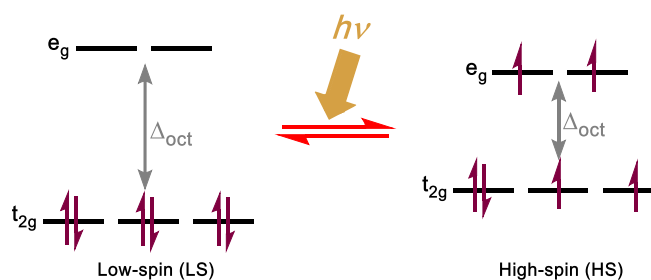


**Figure 1.12. The SCO equilibrium.**

There are different degrees to which a SCO transition can occur and the most distinct of these are depicted in Figure 1.13. A sharp SCO transition, (a) in Figure 1.13 is indicative of a highly cooperative SCO system, which is where the switch in spin states is efficiently propagated throughout the bulk material (see Section 1.4.6 for a discussion on cooperativity). A gradual SCO system (b) has a much less abrupt ST, and often does not reach complete transition, due to poor cooperative effects. (c) is an incomplete system with very slow propagation of spins, in most of these cases, only the start of a ST is apparent.

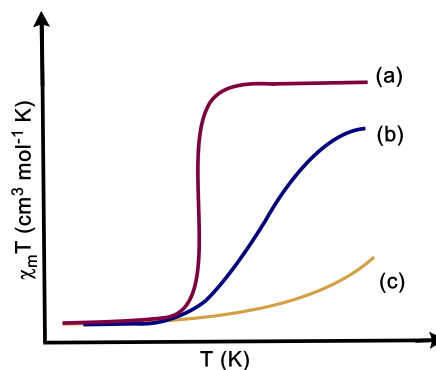


**Figure 1.13. The general trends of magnetic susceptibility with increasing temperature for a.) an abrupt ST, b.) a gradual ST and c.) an incomplete ST. Figure adapted from Housecroft and Sharpe. <sup>5</sup>**

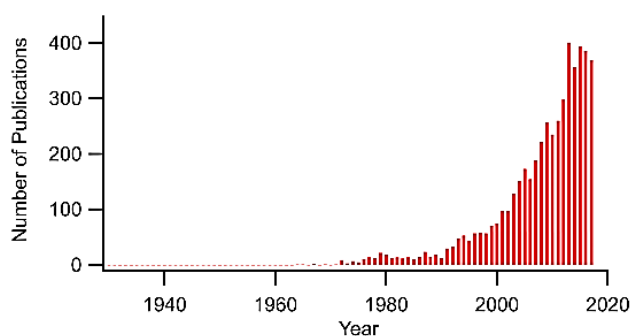


**Figure 1.14. Number of publications containing the phrase 'spin-crossover' or 'spin-equilibrium', per year. Figure (obtained from Web of Science) taken directly from publication.** <sup>30</sup>

An important measurement in SCO systems is the temperature at which the ST occurs. This is universally taken to be the temperature at which half the molecules in a system are in the HS state and half are in the LS state. This is known as the transition temperature and is denoted as  $T_{1/2}$ .

In the last couple of decades there has been significant expansion on the studies of SCO. Takahashi reports the number of publications containing the phrase 'spin-crossover' (or equivalent) in the title or keywords as of 2018, presented in the graph shown in Figure 1.14. <sup>30</sup> This highlights the rapidly growing interest in the field.

#### 1.4.1. Applications of SCO materials

The desire for miniaturised technology components for today's vastly expanding industry of electronic communication devices, is ever-increasing. The field of molecular electronics has particularly flourished over the last decade, with an example being the transition of the inorganic LED to organic-LEDs (OLEDs) in smart-screens, which offer greater colour variations and improved speed of response. <sup>31</sup> However, challenges in the field of molecular electronics include replicating electronic components, such as modulators, switches, resistors, and rectifiers <sup>32</sup> at the molecular level. A current difficulty in their design is connecting the molecular components such that they achieve complete circuits that can carry out the functions required for computation. <sup>33</sup>

SCO is an example of a molecular switching system, which can be controlled by physical and external stimulation. Further applications of SCO systems include memory devices, data storage and sensors, owing to the structural and chemical changes, namely the magnetic response, that SCO systems typically undergo upon a ST. <sup>34</sup>

Advantages of using molecular-based electronic materials are a.) being able to achieve components that undergo ST on the nanoscale, b.) transitions centred around room temperature can be achieved, c.) transition metals offer versatility in the design of new materials and d.) hysteresis can be achieved around room temperature - ideal for

memory applications in particular (Section 1.4.6).<sup>34</sup> These are the target characteristics in the design of SCO molecules.

For application purposes, the most ideal ST is the case of an abrupt transition. This forms the basis of a molecular magnetic switching system, as this is most analogous to an on/off switch, which mimics a binary [0,1] system at the molecular level. Such molecular systems are highly desirable in the fields of sensory and memory devices, molecular electronics, switching devices and sensors.<sup>34</sup>

### 1.4.2 Origins of SCO

In 1936, Pauling and Coryell observed differences in the magnetic susceptibilities of ferrohemoalbumin, which was reported as 5.46 BM per iron site, with oxyhemoalbumin and carbonmonoxyhemoalbumin which showed no magnetic susceptibility (0 BM) at the iron sites, which was attributed to different degrees of covalent and ionic bonding.<sup>35</sup> The former complex corresponds to 4 unpaired electrons, as is with the HS configuration of  $\text{Fe}^{2+}$ , and the latter complexes, the LS configuration of  $\text{Fe}^{2+}$  which has 0 unpaired electrons. Switching between these two states was obtained by simply binding the oxygen or carbon monoxide molecule at the 6<sup>th</sup> axial position of ferrohemoalbumin (Figure 1.15). Cambi and Szegö also observed SCO in a series of iron(III) dithiocarbamate complexes around the same time, however with a focus of temperature-dependency.<sup>36-38</sup> Together, these are believed to be the first findings that have alluded to the concept of SCO.<sup>39</sup>

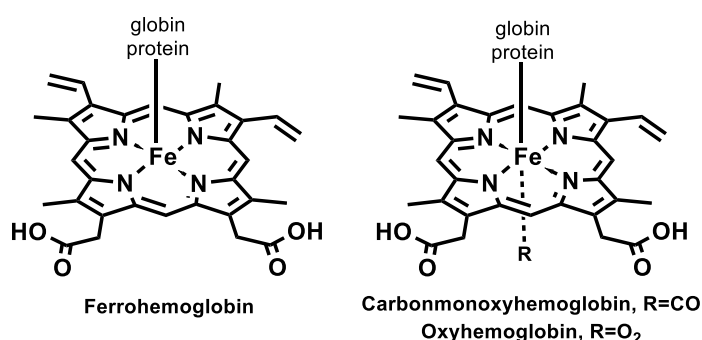


**Figure 1.15. Structures of ferrohemoalbumin (left), and with CO addition (carbonmonoxyhemoalbumin) and O<sub>2</sub> addition (oxyhemoalbumin) (right).**

König and Madeja set out to define a SCO point using a systematic approach with varying anions.<sup>40</sup> In their work, they corroborated findings from Schilt who observed diamagnetism in an iron(II) complex of 1,10-phenanthroline (phen) ligand with cyanide ions,  $[\text{Fe}(\text{phen})_2(\text{CN})_2]$ ,<sup>41</sup> with findings from Basolo and Dwyer who reported a paramagnetic response for an analogous complex, in which the X-ligands were chloride

ions, to give  $[\text{Fe}(\text{phen})_2(\text{Cl})_2]$ .<sup>42</sup> König and Madeja observed the magnetic susceptibility for a series of  $[\text{Fe}(\text{phen})_2\text{X}_2]$  (Figure 1.16) complexes with  $\text{X} = \text{Br}^-$ ,  $\text{Cl}^-$ ,  $\text{SCN}^-$ ,  $\text{N}_3^-$ ,  $\text{OCN}^-$ ,  $\text{HCOO}^-$  and  $\text{CN}^-$ , and of these, only found diamagnetism in  $[\text{Fe}(\text{phen})_2(\text{CN})_2]$ .<sup>40</sup> These findings are in agreement with the reported ordering of ligand-field strength.

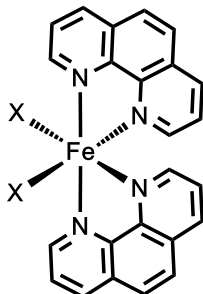


Figure 1.16. Structure of  $[\text{Fe}(\text{phen})_2\text{X}_2]$ .

The bis-bromide and thiocyanate findings were supported by Baker Jr. and Bobonich,<sup>43</sup> who also extended this work to  $[\text{Fe}(\text{phen})_2(\text{SeCN})_2]$  and  $[\text{Fe}(\text{bpy})_2(\text{SCN})_2]$ , which showed an abrupt ST from  $\sim 5$  BM to  $\sim 1.5$  BM upon a decrease in temperature from  $\sim 300$  K to  $\sim 110$  K, over a narrow temperature range.<sup>44</sup>

### 1.4.3 Metals that Exhibit SCO

Though SCO examples of iron(II) and iron(III) complexes dominate the field, there are also some, albeit fewer, examples involving cobalt(II) that have been studied over the years.<sup>45-50</sup> Cobalt(III) in an octahedral geometry is known to almost always adopt the LS configuration owing to its exceptional stability of the  $d^6$  configuration. However, though rare, paramagnetism in the cobalt(III) ion has been demonstrated<sup>51</sup> and there are a few examples recorded of HS cobalt(III) complexes such as  $[\text{Co}(\text{F}_6)]^{3-}$  and  $[\text{Co}(\text{H}_2\text{O})_3(\text{F})_3]$ .<sup>52</sup>

In contrast to this, manganese(III) is known to almost always adopt the HS configuration, owing to the stability of the  $d^4$  HS configuration. There have been very few examples of Mn(III) complexes that undergo SCO, the first of which was reported by Sim and Sinn in 1980, of the complex  $[\text{Mn}(\text{trp})]$  (trp= tris[1-(2-azoly)-2-azabuten-4-yl]amine).<sup>53</sup> There has since been more examples of SCO Mn(III) complexes, such as those researched by Morgan *et al.*<sup>54</sup> and collaborators.<sup>55, 56</sup> A known LS example is the complex  $[\text{Mn}(\text{CN})_6]^{3-}$ .<sup>53, 57</sup> Analogous to the aforementioned hexafluoride cobalt(III) complex, is  $[\text{NiF}_6]^{3-}$  which is the only known example of a HS nickel(III) complex.<sup>29</sup> This is consistent with the spectrochemical series of ligand-field strength, where fluoride is weak-field and cyanide is a strong-field ligand.

Further advances include dinuclear and polynuclear SCO complexes, where SCO-active metal centres are covalently linked within discrete molecules, in an effort to enhance SCO properties.<sup>58-60</sup> Such structures include coordination polymers,<sup>61</sup> helicates,<sup>62</sup> cages,<sup>63</sup> and supramolecules<sup>64</sup> that can undergo host-guest chemistry.

#### 1.4.4 The Fe(II)-N<sub>6</sub> System

The FeN<sub>6</sub> chromophore dominates the literature in the field of SCO. The most well-researched metal-ligand combination is that of iron(II) with tridentate chelating N-donor ligands (Figure 1.17), particularly with N-heterocycles or N-pseudohalides as the ligand-field produced by these is most fitting for the CFSE to allow SCO.<sup>29, 65</sup> Of this class of compounds, the octahedral geometry forms the most prominent framework.

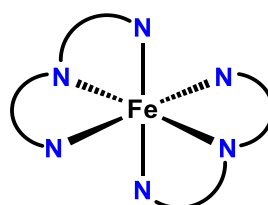


Figure 1.17. The Fe<sup>II</sup>N<sub>6</sub> System.

There are a multitude of reasons for the dominance of Fe<sup>II</sup>N<sub>6</sub> SCO complexes which are summarised as follows (however are further elaborated on in Section 1.4.10):

- There is a dramatic change in the magnetic response between the LS and HS states of iron(II), which makes monitoring its spin state by means of magnetometry (SQUID and Evans) and paramagnetic <sup>1</sup>H NMR, more straightforward.
- Differences between the LS and HS can be observed structurally using X-ray crystallography as there is a 10% difference in the Fe-N bond lengths in the two states.
- Mössbauer spectroscopy can be used on iron, as differences in the quadrupolar splitting and isomer shifts are evident between the two states.
- The two spin states have distinct colours, where the LS state is usually strongly coloured (purple-red hues) while the HS state is weakly coloured (white-yellow hues). This allows qualitative observations simply by eye.<sup>66</sup>

Between the high- and low- spin states of iron(II) nitrogen-donor complexes, there are significant structural differences<sup>67</sup> resulting in cooperative STs that are associated with these differences,<sup>68</sup> and are therefore notably distinguishable between the two states.

#### 1.4.4.1 The Ligand System

Adding to the vast library of  $\text{Fe}^{\text{II}}\text{N}_6$  SCO complexes, pyridine-containing ligands will form the framework of iron(II) SCO complexes studied herein. This metal-ligand combination is supported by a favourable Lewis Acid-Lewis Base binding in accordance with the Hard-Soft Acid-Base theory. As pyridine is a relatively strong-field ligand in the spectrochemical series, the synergistic  $\pi$ -back-bonding interactions contributes to the stability of resulting metal complexes (Figure 1.18).

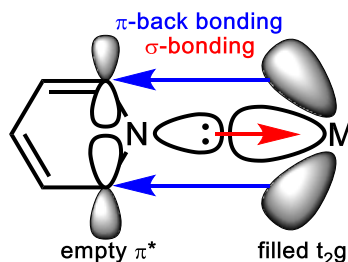


Figure 1.18. Pyridine-metal orbital interaction in  $\pi$ -back bonding.

The ligand framework employed herein is elaborated on in Chapter 2.

#### 1.4.5 The SCO transition point

With the exception of a  $d^6$  HS complex (which has an isotropic electron distribution), the CFT of octahedral complexes predicts only a single absorption band in its electronic UV-Vis spectrum, corresponding to the energy of the crystal field splitting parameter,  $\Delta_{\text{Oct}}$ . However, experimentally obtained absorption spectra of HS octahedral complexes, often show 2 or 3 peaks, known as ' $d-d$ ' bands, which indicate additional electron-electron interactions.<sup>69</sup> An example of the difference in number of  $d-d$  bands evident in a UV-Vis spectrum, between the LS and HS states, is shown in Figure 1.19 of the complex  $[\text{Fe}(\text{ptz})_6](\text{BF}_4)_2$  (where ptz = 1-propyltetrazole) discussed by Gütlich *et al.*<sup>26</sup>



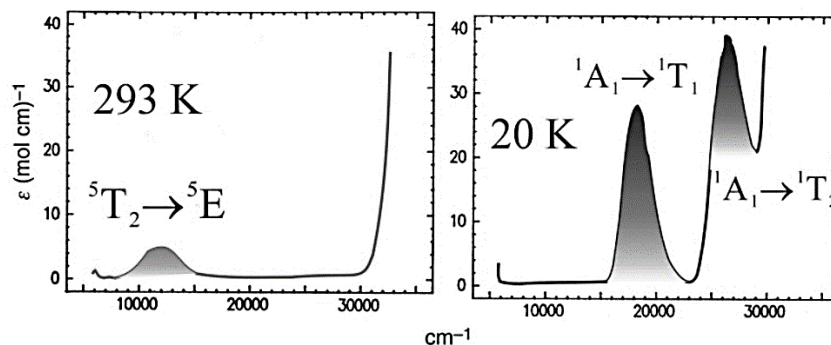


Figure 1.19. UV-Vis spectrum of  $[\text{Fe}(\text{ptz})_6](\text{BF}_4)_2$  in the LS (left) and HS (right) spin states. Figure taken directly from publication.<sup>26</sup>

These ‘ $d-d$ ’ bands can be spin-forbidden, which give rise to very weak peaks in the absorption spectrum -though these are not very commonly observed, one known example of this is  $[\text{Mn}(\text{H}_2\text{O})_6]^{2+}$  (HS  $d^5$ ).<sup>5</sup> More commonly, ‘ $d-d$ ’ bands are Laporte-forbidden and therefore spin-allowed, which are the most typically observed.

An Orgel diagram shows the energy transition between an octahedral and tetrahedral ligand field, however is a qualitative representation and it cannot be quantitatively used to determine the energy of such ‘ $d-d$ ’ transitions. The diagram shows only spin-allowed transitions and is only valid in the case of HS ions, where the electron-electron repulsion is more significant than the CFSE effect. Orgel diagrams consider only the highest spin multiplicity term of a metal ion in correlation to its ligand field. There are only two Orgel diagrams known, Figure 1.20 shows the one for octahedral/tetrahedral metal ions with  $d^1$ ,  $d^4$ ,  $d^6$  and  $d^9$  electrons.

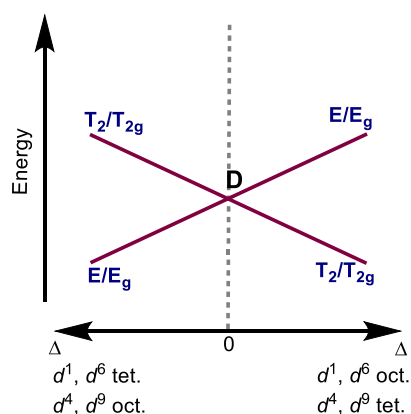
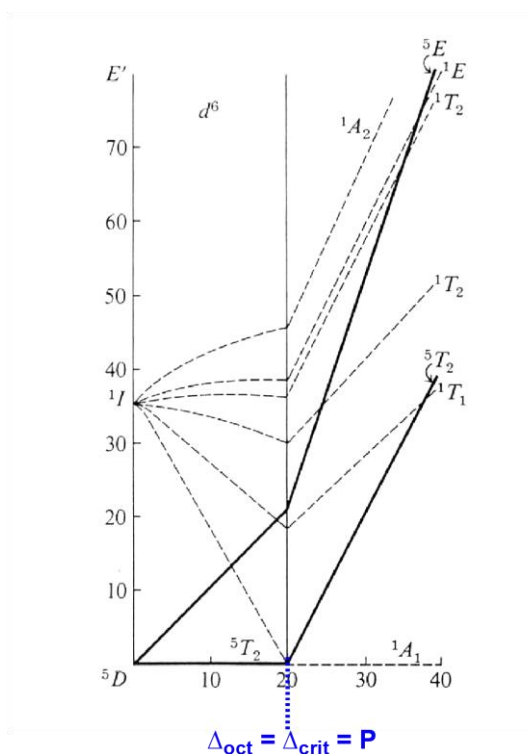


Figure 1.20. Orgel diagram for a  $d^1$ ,  $d^4$ ,  $d^6$  and  $d^9$  ion. Figure reproduced from Housecroft and Sharpe.<sup>5</sup>

The interelectron repulsion is denoted by the Racah parameters B and C, which allows for comparison of the energies of different term states. If the energies are experimentally obtained, then the Racah parameters can be calculated from this.

More advanced than the Orgel diagram, is the Tanabe-Sugano (T-S) diagram in which both high and low spin complexes are now accounted for. Tanabe and Sugano developed the idea from CFT, using the Racah parameter to quantitatively describe the absorption spectra of octahedral complex ions.<sup>70</sup> They approximated values of the Racah parameters for each *d*-electron configuration and drew up calculated energies for each electronic state forming the T-S diagram.<sup>71, 72</sup> Using such diagram, the energy required for the HS-LS transition ( $P=\Delta_{\text{oct}}$ ) can be determined.



**Figure 1.21. Tanabe-Sugano diagram for the  $d^6$  configuration in and octahedral ligand field. Figure taken directly from Hormann and Shaw III.<sup>73</sup>**

The crossover point between the HS and LS states occurs at crystal field energy ' $\Delta_{\text{crit}}$ ', which equals P. In Figure 1.21, the T-S diagram is of a  $3d^6$  ion in the  $O_h$  point group, such as  $\text{Fe}^{2+}$  and  $\text{Co}^{3+}$ . The HS state occurs when  $\Delta < \Delta_{\text{crit}}$  and the lowest energy term is  $^5T_{2g}$ , and the LS state occurs when  $\Delta > \Delta_{\text{crit}}$  and the lowest energy term becomes the  $^1A_{1g}$ . A thermal equilibrium between both the LS and HS states may occur if the energy difference between  $\Delta_{\text{oct}}$  and P, is of the same order of magnitude to the average thermal energy,  $K_bT$ , and therefore both spin states may be populated.<sup>74</sup>

Though the Tanabe-Sugano diagrams depict the electronic energies of the LS and HS states relative to the ligand-field strength, the potential energy surfaces relative to the M-L bond distance must be considered to explain the SCO region.<sup>75</sup>

### 1.4.6 Magnetic Bistability

Cooperativity is the transmission of a spin state change through a solid lattice. This is governed by the ability of an individual molecule, that undergoes structural or electronic alterations, to stimulate neighbouring metal centres to undergo conforming changes.<sup>26</sup> Highly cooperative systems can be identified by an abrupt ST over a narrow temperature range of just a few Kelvin.

Thermal hysteresis is a result of cooperativity effects. It is where there is a delay in the magnetic susceptibility response recorded against increasing and decreasing temperature. The heating and cooling cycle(s) of a sample do not go back on themselves in a sample that observes thermal hysteresis. The spin state is held for longer when the loop region is entered from that spin state. In a hysteretic system there are two values of  $T_{1/2}$ , one from the cooling transition and one from the heating transition,  $T_{1/2 \downarrow}$  and  $T_{1/2 \uparrow}$  respectively (Figure 1.22), and the width of the hysteresis loop is expressed as the difference between these two temperatures,  $\Delta T_{1/2}$ .<sup>66</sup>

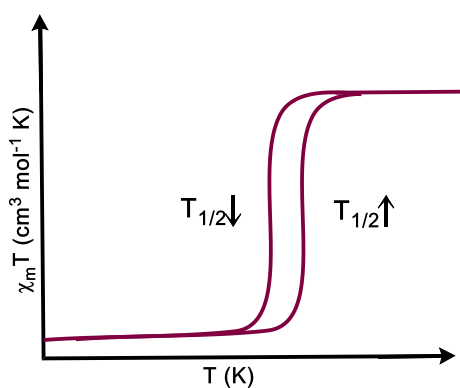


**Figure 1.22. Magnetic susceptibility vs. temperature displaying SCO with a thermal hysteresis loop.**

A molecule that observes hysteretic behaviour is said to have magnetic bistability as it is able to attain two spin states inside the hysteresis loop with an associated memory effect. The system is said to mimic a binary system at the molecular level which make such molecules highly desirable in memory devices.

Intermolecular bonding throughout a crystal lattice, such as hydrogen bonds, contribute strongly to the cooperativity effects of the spin state conversion throughout a lattice.<sup>76</sup>

Additional factors that will affect cooperativity and therefore the likelihood of hysteresis are counter-ions, lattice solvates and crystal packing effects (or the lack of).

It should be noted that where angular JT distortions inhibit SCO in the solid state of certain HS iron(II) complexes, this is not a translatable effect to the solution state.

#### 1.4.6.1 JT Effect in HS Iron(II) complexes

Aside from JT effects resulting in bond elongations or contractions, a structural angular distortion from a perfect coordination geometry is another form of JT distortion effects. This is oftentimes evident in certain HS iron(II) complexes with meridional tridentate nitrogen-donor ligands, that are conformationally rigid owing to their tight 'bite' angle in an octahedral complex. Such JT effects results in a reduced symmetry of the complex.

The unoccupied  $e_g^*$  orbitals in the LS state render its octahedral coordination sphere more robust than for HS complexes. JT-distorted HS complexes show distortion in the coordination geometry or ligand conformation and this can significantly impact the spin state behaviour of such complexes. Solid state HS structures that differ too greatly from their respective LS structures may not undergo SCO if the associated structural change for the ST requires a too costly conformational rearrangement. As cooperativity is crucial for a successful ST, propagation of a spin conversion would hinder all individual SCO centres in a molecule. Therefore, such HS complexes remain 'trapped' in this spin state.<sup>39, 68</sup> The magnitude of this distortion can be quantified by the deviation of bond angles from perfect octahedral geometry as depicted in Figure 1.23.

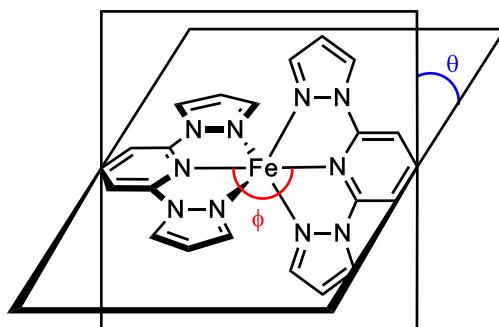


**Figure 1.23. Angular Jahn-Teller distortion in  $[Fe(1-bpp)_2]^{2+}$  where  $\theta$  is the dihedral angle and  $\phi$  is the N(py)-Fe-N(py) trans angle. Figure taken from publication.<sup>77</sup>**

The dihedral angle,  $\theta$ , quantifies the angular twist between the least-squares planes of the two ligands, and the second angular component,  $\phi$ , quantifies the trans N-Fe-N angle which depicts the degree of rotation between the two ligands across the iron centre. The

degree of distortion can be expressed by these parameters where  $\theta \leq 90^\circ$  and  $\varphi \leq 180^\circ$  ( $\theta = 90^\circ$  and  $\varphi = 180^\circ$  for a perfect octahedron).<sup>77</sup>

A few well-known examples of such 'trapped' HS molecules include, iron(II) complexes of 2,6-bis(pyrazol-1-yl)pyridine (1-bpp)  $[\text{Fe}(1\text{-bpp})_2](\text{X}_2)$  where  $\text{X} = \text{BF}_4^-$ ,  $\text{PF}_6^-$ ,  $\text{ClO}_4^-$ ,  $\text{SbF}_6^-$ ,  $\text{I}_3^-$ ,<sup>77-79</sup> and iron(II) complexes of 6,6''-substituted terpyridine (terpy) ligands (Figure 1.24),  $[\text{Fe}(\text{L})_2](\text{X}_2)$  where  $\text{X} = \text{PF}_6^-$  or  $\text{ClO}_4^-$ . The perchlorate salts of the latter demonstrated a particularly high degree of JT distortions, such that coordination number of the centre was closer to 4 than 6.<sup>80</sup> Iron(II) complexes with 'scorpionate' ligands such as tris(pyrazolyl)borate ligand have also demonstrated a 'trapped' HS state associated with significant JT distortion, independent of temperature.<sup>81</sup>

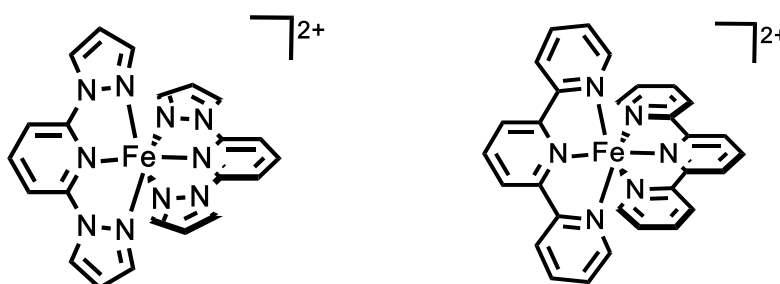


**Figure 1.24. The structure of 2,6-bis(pyrazol-1-yl)pyridine,  $[\text{Fe}(1\text{-bpp})_2]^{2+}$  (left) and 2,2':6',2''-terpyridine,  $[\text{Fe}(\text{terpy})_2]^{2+}$  (right).**

The most prevalent class of angular JT-distorted iron(II) complexes is of the HS  $[\text{Fe}(1\text{-bpp})_2]^{2+}$  series<sup>82</sup> which have a 'bite' angle of around  $73^\circ$ .<sup>78</sup> The most distorted complex is that reported by Kilner and Halcrow in 2006, which is  $[\text{Fe}(1\text{-bpp})_2](\text{SbF}_6)_2$  which recorded  $\theta = 59.84(3)^\circ$  and  $\varphi = 154.52(14)^\circ$ .<sup>83</sup>

#### 1.4.7 Thermodynamics of SCO

The process of SCO can be considered to be governed by thermodynamics, as the feasibility of the ST is dependent on Gibb's free energy,  $\Delta G$ , of the transition (Equation 1.9). Here  $\Delta G$  is defined as the free energy difference between the HS and LS states ( $\Delta G = G^{\text{HS}} - G^{\text{LS}}$ ).

$$\Delta G = \Delta H - T\Delta S$$

**Equation 1.9. The 2nd law of thermodynamics; Gibbs free energy equation.**

The number of molecules in the HS state is denoted as  $n_{HS}$ , which is a fraction between 0 and 1 which denotes the population distribution amongst the two states. This term can be related to the  $\Delta G$  through the Boltzmann equation, Equation 1.10. <sup>84</sup>

$$n_{HS}(T) = \left( 1 + e^{\left(\frac{\Delta G}{k_b T}\right)} \right)^{-1}$$

**Equation 1.10. The Boltzmann distribution equation which correlates  $n_{HS}$  to  $\Delta G$ .**

Due to stronger bonding character and therefore larger CFSE, the LS state is enthalpically favoured, so it is stable at low temperatures, whilst the HS state is dependent on the electronic and vibrational entropy contributions and so is stable at high temperatures. <sup>66, 85</sup>

#### **1.4.8 External stimuli**

We have seen how chemical modifications both to the ligand, and to the metal, <sup>40</sup> can control the spin-state through tuning of electron-donating and electron-withdrawing environments. We have also seen how the binding of an additional ligand, which through alteration of both the complex's geometry and electronics, can affect the spin state of the resulting complex. <sup>35</sup> However, more fitting for the aforementioned applications is the control of spin state by an external and physical stimulus.

##### **1.4.8.1 Temperature**

Considering the potential energy wells of the LS and HS states for iron(II) (Figure 1.11 - reproduced below as Figure 1.25), as the temperature of the system is increased, the complex takes this added thermal energy and converts it into vibrational energy in an adiabatic process. This allows for the population of the excited vibrational energy levels up to the 'crossing point' of the LS and HS energy wells. According to the Franck-Condon principle, this is where the LS/HS ST occurs. <sup>28</sup>

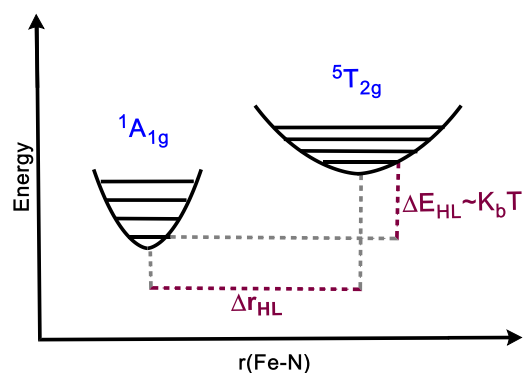


**Figure 1.25. Potential energy wells of an iron(II) SCO system, with respect to the Fe-N bond distance. The  $^1A_{1g}$  state is the LS state and the  $^5T_{2g}$  is the HS state. Figure reproduced from Gütlich *et al.* <sup>26</sup>**

The introduction of a temperature-dependence on the SCO activity was first reported by Cambi and Szegö with iron(III) dithiocarbamates. <sup>36</sup> Upon finding distinct magnetic moments at room temperature amongst a series of iron(III) (N,N)-dialkyldithiocarbamates, Cambi and Szegö explored this further by recording magnetic measurements of the series at the temperatures 84 K, 194 K, 291 K and 350 K and then connecting these points to show a general trend. <sup>37, 38</sup>

This work inspired Ewald *et al.* to further explore the temperature-dependency of iron(III) dithiocarbamate complexes, taking more measurements at smaller temperature intervals. <sup>86</sup> In their work they varied the alkyl group, R, in  $[Fe(S_2CNR_2)_3]$ , to be methyl, *i*-butyl, *n*-butyl and pyrrolidyl. In this work,  $\mu$  (BM) was recorded between 80-400 K and curves were fitted to the plots using Van Vleck's equation. Upon changing the R group of the ligating system, significant differences were observed in the SCO behaviour with increasing temperature; the pyrrolidyl- substituted complex remained high-spin, while the *n*-butyl- substituted complex showed some form of a SCO transition and the *i*-butyl- and me- substituted complexes showed weak, more low-spin-like, behaviour (Figure 1.26). <sup>86</sup>

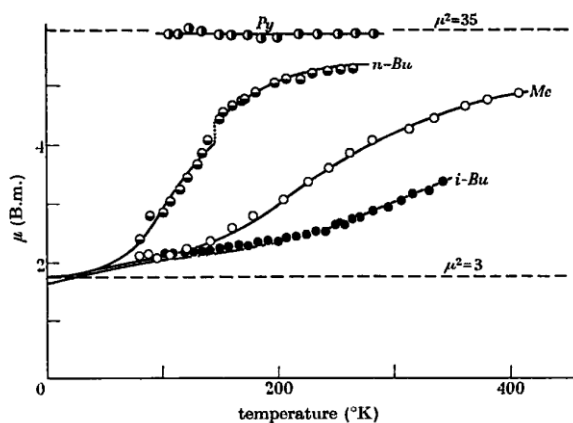


**Figure 1.26. Magnetic moment of  $[\text{Fe}(\text{S}_2\text{CNR}_2)_3]$  between 80-400 K with Van Vleck curves fitted to the data, for R= Py (pyrrolidyl), *n*-Bu (*n*-butyl), Me (methyl) and *i*-Bu (*i*-butyl). As reported by Ewald *et al.*, graph taken directly from publication. <sup>86</sup>**

SCO in chromium(II) complexes induced by temperature was first reported by Halepoto *et al.* in 1989, who explored a series of phosphine-based bidentate ligands with  $\text{Cr}^{2+}$  ( $d^4$ ).<sup>87</sup> The complex  $[\text{CrI}_2(\text{depe})_2]$  (depe=1,2-bis-(diethylphosphino)ethane) showed an abrupt ST in the temperature range 165-175 K, with a  $T_{1/2}$  calculated at 171 K. This complex was compared to analogues  $[\text{CrI}_2(\text{dmpe})_2]$  and  $[\text{CrCL2}(\text{dmpe})_2]$  (dmpe = 1,2-bis(dimethylphosphino)ethane) which both showed LS character. X-ray Diffraction (XRD) analysis indicated an elongation of the Cr-P bond lengths in  $[\text{CrI}_2(\text{depe})_2]$ , compared to  $[\text{CrCL2}(\text{dmpe})_2]$ ,<sup>88</sup> by about 0.15 Å -analogous to the elongation of Fe-N bonds upon SCO in iron(II) complexes. Furthermore, the Cr-I bond distances did not show any significant deviations from the values found for  $[\text{CsCrI}_3]$ <sup>89</sup> and  $[\text{CrI}_2]$ .<sup>90</sup> Thus differences in the magnetic susceptibility was attributed solely to modifications of the phosphine ligand,<sup>87</sup> highlighting the influence of ligand modification in designing SCO complexes.

#### 1.4.8.2 Pressure

A pressure-induced SCO is useful for applications of such materials in pressure sensors. Ewald *et al.* furthered their work by considering the pressure-dependency on the magnetic susceptibility, in which they focussed on the iron(III)  $N,N'$ -*n*Bu-dithiocarbamate complex as this gave a clear ST with varying temperatures. Their findings showed that magnetic susceptibility of  $[\text{Fe}(\text{S}_2\text{CN}^n\text{Bu}_2)_3]$  in chloroform decreased as the pressure applied was increased from 0 to 3000 atm (Figure 1.27).<sup>86</sup> This is known to be the first example of SCO stimulated by pressure.



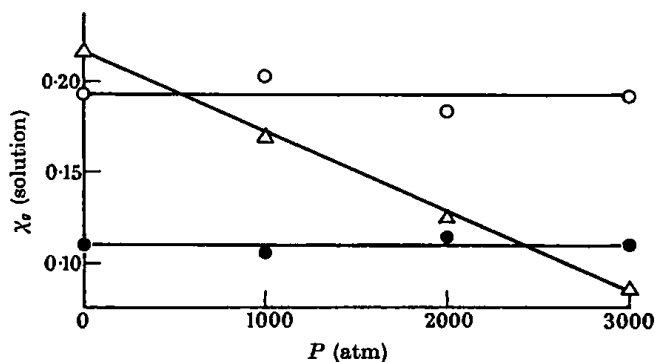


**Figure 1.27. Magnetic susceptibility of  $[\text{Fe}(\text{S}_2\text{CN}^m\text{Bu}_2)_3]$  between 0-3000 atm pressure applied. As reported by Ewald *et al.*, graph taken directly from publication.<sup>86</sup>**

This pressure-dependency of iron(III) dicarbamates in solution was corroborated in further studies, where it was found that increasing pressure favoured the  ${}^2\text{T}_2$  state (LS), over the  ${}^6\text{A}_1$  state (HS), as it has a smaller molecular volume.<sup>91</sup>

A ST is driven by thermodynamics as there is a change in entropy due to the difference in metal-ligand bond length between the two spin states. The M-L distance,  $r$ , between the two states is approximately  $\Delta r_{\text{HS/LS}} \approx 0.1 \text{ \AA}$  for iron(III) and  $0.2 \text{ \AA}$  for iron(II), which is significant considering this is approximately a 10% change in bond length. As the potential energy wells depicted earlier in Figure 1.11 shows the vibronic energy levels as a function of  $r_{(\text{M-L})}$  for the two spin states,  $\Delta r_{\text{HS/LS}}$  can be used to rationalise the pressure influence (Figure 1.28).<sup>92</sup>

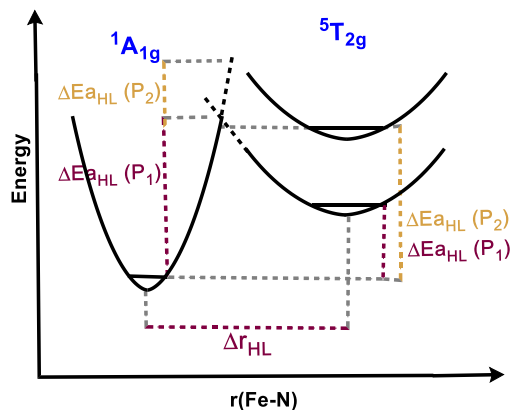


**Figure 1.28. The change in potential energy of the  ${}^5\text{T}_{2g}$  state at a higher pressure ( $P_2$ ), relative to the initial pressure ( $P_1$ ). Figure reproduced from Gütlich *et al.*<sup>92, 93</sup>**

The simplified schematic in Figure 1.28 shows how an increased pressure displaces the potential energy well for a  $3d^6$  ion. The LS state is favoured upon applied pressure and

the  $T_{1/2}$  becomes shifted to a higher temperature. This is due to the change in zero-point energy between the LS and HS states,  $\Delta E_{HL}$ , which is greater at a higher pressure,  $P_2$ . Furthermore, the activation energy  $\Delta E_{aHL}$  is increased at  $P_2$  which favours the LS state.<sup>28, 92</sup>

One of the most well studied systems for SCO is  $[\text{Fe}(\text{phen})_2(\text{NCS})_2]$ ,<sup>43</sup> which shows an abrupt ST at  $10^5$  Pa with increasing temperature, but a complete loss of ST (effectively just LS) at 0.57 GPa over the same temperature range (Figure 1.29).<sup>93</sup>

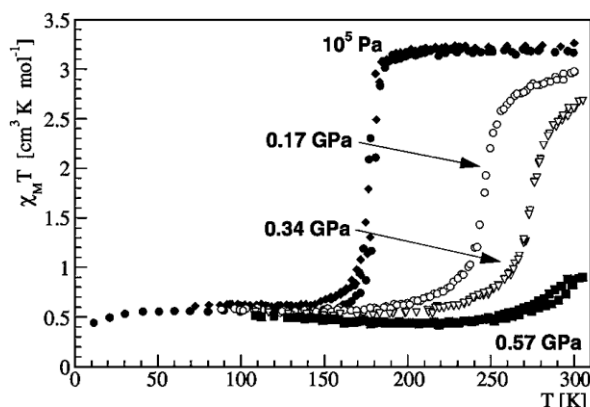


**Figure 1.29. Graph of  $X_M T$  vs.  $T$  for  $[\text{Fe}(\text{phen})_2(\text{SCN})_2]$  at pressures  $10^5$  Pa, 0.17 Pa, 0.34 Pa and 0.57 Pa. Figure taken directly from Gütlich *et al.*<sup>93</sup>**

Increasing the pressure at a constant temperature on the solid iron(III) complexes studied by Ewald *et al.* was found to induce phase changes,<sup>91</sup> though interestingly it was noted that cobalt(III) dithiocarbamates which are isomorphous to these complexes, did not show any phase changes under the same experimental conditions.

#### 1.4.8.3 Light Irradiation -The LIESST Effect

SCO can be induced by light irradiation in a process known as the Light-Induced Excited Spin-State Trapping (LIESST) effect. Materials that undergo the LIESST effect, are particularly of interest for application in optical switches, information sensors and displays.<sup>94</sup> The process involves irradiation of the LS sample into spin-allowed  $d-d$  bands or Metal-to-Ligand Charge Transfer bands (MLCT) using green light ( $\lambda \approx 530$  nm), giving a metastable HS state.<sup>75</sup> Considering the energy diagram in Figure 1.30, relaxation of this  $^5T_2$  state to the  $^1A_1$  state can occur if there is sufficient thermal energy *via* intersystem crossing to the  $^3T_1$  and  $^3T_2$  states, or by quantum mechanical tunnelling. If the sample temperature is low enough, this relaxation cannot occur and the material can become 'trapped' in the metastable HS state ( $^5T_2$ ). A reversal of the system back to

the LS state can sometimes be induced under these conditions by irradiating a low-energy  $^5T_2$  *d-d* band using red light ( $\lambda \approx 850$  nm).<sup>95</sup>

The critical temperature,  $T_{\text{LIESST}}$ , is the temperature at which the molecules fully occupying the HS state, have sufficient thermal energy to relax from the HS to the LS state (Figure 1.31).  $T_{\text{LIESST}}$  is found by measuring the temperature, starting from 10 K at increments of  $0.3 \text{ K min}^{-1}$ , at which there is no longer a photomagnetic effect from a material.<sup>94</sup>

The relaxation time,  $\tau$ , from this metastable state to the LS state is measured and the temperature of this thermal relaxation,  $T_{\text{LIESST}}$  can be obtained<sup>77, 96</sup> as a quantitative measure of the SCO behaviour. As there is no relaxation pathway from  $^5T_2$  to  $^1A_1$ , the iron(II) system is trapped in the HS state, if  $T_{\text{LIESST}}$  has not been exceeded.<sup>97</sup>

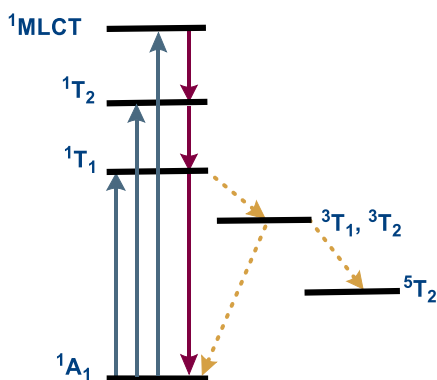


**Figure 1.30. Jablonski-style energy level diagram to show the transitions involved in the LIESST effect of an iron(II) SCO complex. Figure reproduced from Decurtins *et al.*<sup>97</sup>**

The LIESST effect is a solid state phenomenon owing to the rigid lattice at low temperatures, which inhibits thermal relaxation processes and is able to trap the HS state. However, initial studies to understand the mechanistic pathways of green light irradiation at low temperatures ( $\leq 50$  K) were first reported by McGarvey and Lawthers in iron(II) and iron(III) complexes in the solution state.<sup>98-100</sup> The complexes  $[\text{Fe}(\text{HPyBIM})_3]^{2+}$  and  $[\text{Fe}(\text{HPyIM})_3]^{2+}$  (where HPyIM = 2-(2-pyridyl)imidazole and HPyBIM = 2-(2-pyridyl)benzimidazole) were investigated in three solvents, acetonitrile (MeCN), acetone ( $\text{Me}_2\text{CO}$ ) and a methanol/acetonitrile mixture (MeOH-20% MeCN). The  $^1A \approx ^5T$  equilibrium was perturbed by light at  $\lambda=530$  nm, and the relaxation time was measured. This value was then be used in the calculation of the activation volumes for the  $^1A$ - $^5T$  transition ( $\Delta V_{15}$ ) and the  $^5T$ - $^1A$  transition ( $\Delta V_{51}$ ), and their respective activation entropies,  $\Delta S_{15}/\Delta S_{51}$ . Their findings exhibited differences in  $\Delta V_{15}$  and  $\Delta V_{51}$ , as the former showed a solvent-dependency, with MeCN giving the most distinct and favourable results, while

the latter showed unfavourable activation volumes and activation entropies with no solvent-dependence.<sup>99</sup> This solvent dependency was also highlighted with the iron(III) complexes studied,  $[\text{Fe}(\text{XSaL2trien})]\text{Y}$  where  $\text{X} = \text{H}$  or  $\text{OMe}$ , and  $\text{Y} = \text{PF}_6^-$  or  $\text{NO}_3^-$ . Distinct differences in the activation enthalpy and entropy parameters were observed for the obtained relaxation times in  $\text{MeOH}$  and  $\text{Me}_2\text{CO}$ , attributed to potential Hydrogen-bonding interactions with the N-H functionality of  $\text{SaL2trien}$ .<sup>100</sup>

This work was extended to the solid state by Decurtins *et al.* on the complex  $[\text{Fe}(\text{ptz})_6][\text{BF}_4]_2$  (where  $\text{ptz} = 1\text{-propyltetrazole}$ ), in which Mössbauer spectroscopy and single crystal absorption measurements were used to monitor the iron species. It was reported that upon light irradiation, the HS state became long-lived, at temperatures below 50 K ( $T_{\text{LIESST}} \approx 50$  K).<sup>101</sup> By raising the temperature, to 97 K, the additional thermal energy provided caused all the molecules previously trapped in the HS state to be relaxed down to the LS state. Further increase in temperature to 148 K, i.e. exceeding the  $T_{1/2\uparrow}$  of 135 K,<sup>102</sup> resulted in thermally-induced SCO again from the LS to HS states (Figure 1.31).

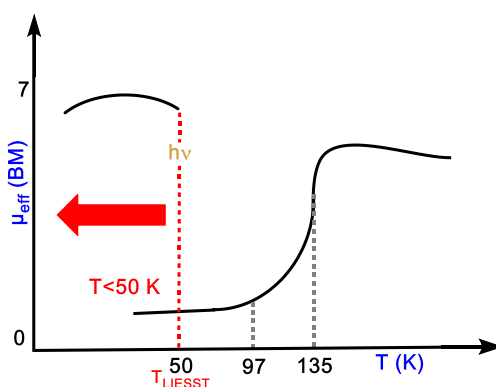


**Figure 1.31. Simplified graph of  $\mu_{\text{eff}}$  vs.  $T$  for a polycrystalline sample of  $[\text{Fe}(\text{ptz})_6][\text{BF}_4]$  studied by Decurtins *et al.* Figure reproduced from publication.<sup>101</sup>**

Decurtins *et al.* added to their preliminary findings with studies on the SCO-famous  $[\text{Fe}(\text{phen})_2(\text{NCS})_2]$ <sup>97</sup> and  $[\text{Fe}(\text{2-pic})_3]\text{CL2.EtOH}$ <sup>103</sup> complexes (where  $\text{phen} = 1,10\text{-phenanthroline}$  and  $\text{2-pic} = 2\text{-aminomethylpyridine}$ ). Both these complexes are deeply coloured in the LS state and so Mössbauer characterisation proved useful in these experiments for characterising the light-induced HS state (Figure 1.32).  $[\text{Fe}(\text{2-pic})_3]\text{CL2.EtOH}$  showed a colour change from red to yellow ( ${}^1\text{A}_{1g}$  to  ${}^5\text{T}_{2g}$ ) when illuminated with light below its  $T_c$  of 25K, and  $[\text{Fe}(\text{phen})_2(\text{NCS})_2]$  underwent bleaching from dark blue-violet to white below its  $T_c$  of 55K, indicating the occurrence of the LIESST effect. Key differences of  $[\text{Fe}(\text{2-pic})_3]\text{CL2.EtOH}$  compared to  $[\text{Fe}(\text{ptz})_6][\text{BF}_4]$ , were that a.) the volume change accompanied by the irradiation at  $\approx 25$  K caused the crystals to

shatter and b.) when the temperature was raised between  $25 < T < 30$  K, relaxation from the HS state was observed within just 60 minutes. <sup>103</sup>

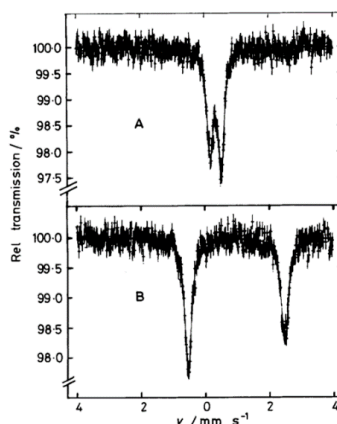


**Figure 1.32. The Mössbauer spectra of  $[\text{Fe}(\text{phen})_2(\text{NCS})_2]$  at 6 K, before light irradiation (A) and after light irradiation (B) for 1 hour. Figure taken directly from publication. <sup>97</sup>**

There is a vast amount of research on the perturbations of SCO and a selected sample of its early origins has been discussed herein. These have included chemical stimuli by ligand design or ligand substitution, and physical stimuli such as temperature, pressure and light irradiation. Although omitted here, an additional physical stimulus includes the use of high magnetic fields to induce a spin transition. <sup>104, 105</sup>

#### 1.4.9 Second Coordination Sphere effects

Intermolecular interactions, such as hydrogen bonding, non-coordinating anions and lattice solvent come under the 'second coordination sphere' in a crystal lattice. These entities can influence the magnetic behaviour by a.) its effect on the packing of the crystal lattice, b.) mediating interactions between iron centres and c.) by electronic interplay with the ligands. <sup>59</sup> This in turn affects the SCO behaviour of complexes featuring such characteristics.

Nanoporous materials that can adsorb and desorb gases and solvents through 'host-guest' chemistry can exploit this feature, to achieve the desirable magnetic bistability centred around room temperature, with memory effects that are guest-dependent. <sup>106</sup> Many other studies have been undertaken to understand the extent to which second coordination sphere effects can impact a ST and how such effects can be controlled.

A study of iron(III)  $\text{FeN}_4\text{O}_2$  complexes showed distinct magnetic susceptibility measurements as the counter-ion was changed. The complex  $[\text{Fe}(\text{salen})(\text{Him})_2](\text{X})$  (where Him= imidazole) was studied by Nihei *et al.* <sup>107</sup> with  $\text{X}=\text{PF}_6^-$ ,  $\text{BPh}_4^-$ ,  $\text{ClO}_4^-$  or  $\text{BF}_4^-$ .

It was found that complexes with the former two counter-ions produced purely HS complexes, while complexes with the latter two counter-ions demonstrated gradual SCO. Of the perchlorate complex, XRD structures were obtained in the HS and LS states (at 295 K and 120 K respectively) which showed distinct Fe-N bond length changes of 0.154 Å for both Fe-N bond types, whilst the Fe-O bond length change was negligible (0.002 Å) between the two spin states. The differences were attributed to a change in the configurations about the coordination sphere, as the chelating salen ligand adopted an envelope configuration when the counter-ion was  $\text{ClO}_4^-$  or  $\text{BF}_4^-$  but adopted a *meso* configuration when the counter-ion was  $\text{PF}_6^-$ .<sup>107</sup> This evidences the magnitude to which the counter-ion affects the ST.

A study of anions and solvate effects was carried out by Judge and Baker.<sup>45</sup> In this work the effective magnetic moment was measured for a series of cobalt(II) bis-terpyridine complexes with varying counter-ions and degree of hydration between 15 and 400 K in order to study their temperature-dependences. It was shown that  $[\text{Co}(\text{terpy})_2](\text{F}_2) \cdot 3.5\text{H}_2\text{O}$  recorded a  $\mu_{\text{eff}} \approx 2.0$  BM (LS  $\mu_{\text{so}}=1.73$  BM) between 20-300 K while  $[\text{Co}(\text{terpy})_2](\text{F}_2) \cdot 4.5\text{H}_2\text{O}$  recorded a  $\mu_{\text{eff}} \approx 4.0$  BM (HS  $\mu_{\text{so}}=3.87$  BM) showing that just 1 molecule of water distinguished the LS and HS states.

Furthermore, it was shown that this trend was not consistent across the halogen counter-ions, as when the anion was a chloride or iodide, their hydrated analogues, though only slightly, showed lower magnetic moments than their dehydrated counterparts.<sup>45</sup> There have been many more, and more recent, studies of lattice solvent effects on iron(II) SCO complexes.<sup>29, 39</sup> This has included studies of different solvates influencing structural phase transitions,<sup>108</sup> observations on solvates stabilising one spin state over the other,<sup>109</sup> the reversibility of the dehydration-hydration process,<sup>110, 111</sup> and studies of solvate-loss on more versatile structures such as 1D coordination polymers.<sup>61</sup>

#### 1.4.10 Measuring SCO

Studies reported within this thesis use temperature to probe SCO behaviour. Methods of measuring this perturbation discussed below is limited to methods and facilities that are capable of variable temperature (VT) measurements.

In the solid state, there are lattice effects which can affect the population of the  $e_g$  and  $t_{2g}$  levels, through two dominant mechanisms, (a) by an inflicted distortion from the octahedral geometry, relative to the unbound molecule and (b) by atoms from neighbouring molecules in the lattice affecting the ligand-field.<sup>91</sup> These effects are not present in solution, therefore there are discrepancies between studies in the solid and solution states, and methods of measuring SCO can be split accordingly.

#### 1.4.10.1 Solid state SCO

The previously discussed, Mössbauer spectroscopy<sup>97, 101, 103</sup> affords information on the spin state, spin transition, magnetic susceptibility, iron concentration and structural distortions on iron(II) SCO complexes.<sup>112</sup> However, additional solid state techniques to measure SCO include the Gouy method, the Faraday method, and, the more modern-day technique, the Superconducting Quantum Interference Device (SQUID) magnetometer, which can record measurements down to liquid helium temperatures.

The Gouy method<sup>113</sup> involves suspending a sample from a balance in the presence of a magnetic field generated by electromagnets (Figure 1.33). The difference in the weight with and without the magnet of the sample is recorded, and the difference will be positive or negative depending on whether the same is paramagnetic or diamagnetic respectively.<sup>114</sup> As this is a bench-top method, the simple addition of a thermostat can allow for temperature-dependent measurements, and changing the strength of the magnet used can also determine sample dependency on the field strength.<sup>115</sup> Mathematical calculations can also be applied to determine the volume susceptibility.<sup>116</sup>

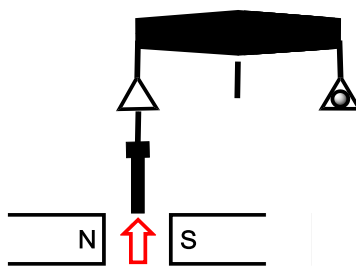


**Figure 1.33. Schematic diagram of the Gouy Balance.**

The modern-day SQUID magnetometer<sup>117</sup> was evolved from the Gouy method. It involves a superconducting loop with Josephson junctions. The uniqueness of the SQUID is the use of a superconducting material, and in the presence of an applied magnetic field, the magnetic flux lines cannot penetrate the superconducting region. Instead it expels it to the extent that it circulates the superconducting ring in a phenomenon known as the Meissner effect (Figure 1.34). Since a superconductor has zero electrical resistance at  $T < T_c$ , when the field is turned off below  $T_c$ , the current remains in circulation around the ring rather than decaying as a non-superconducting material would.<sup>118</sup>

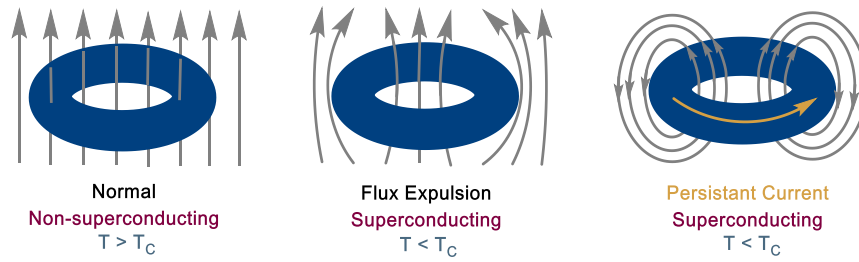


**Figure 1.34. The Meissner Effect (far right) in a superconducting material after applied field has been removed and  $T < T_c$ . Figure reproduced from Fagaly. <sup>118</sup>**

Josephson junctions are resistive barriers which are known as weak bridge points across the superconducting ring, these Josephson loops are inductively coupled to the superconducting input coil (Figure 1.35). The SQUID magnetometer incorporates these to measure very small variations in the magnetic flux by measuring changes in the voltage drop across the Josephson junction. <sup>118</sup> The SQUID is significantly sensitive to the extent that it can even detect very weak signals such as ones originating from the brain! <sup>5</sup> Magnetoencephalography in biological studies is an application that exploits this extremely high sensitivity. <sup>119</sup>

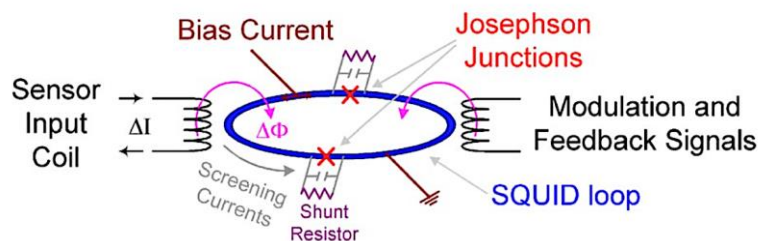


**Figure 1.35. A SQUID loop with two Josephson junctions. Figure taken from publication. <sup>118</sup>**

The lack of resistance at  $T < T_c$  in the SQUID allows for high magnetic fields to be achieved. The SQUID has been reported to achieve a field resolution down to  $10^{-17}$  T, <sup>118</sup> and the SQUID instrument used in this thesis can achieve a magnetic field of up to 9T and reach temperatures as low as 5 K with liquid helium as the active cryogen. This allows for accurate VT studies of SCO complexes with as little as 5 mg of sample from 5-375 K. A SQUID instrument coupled to an optical source through optical fibre has even been used to measure the LIESST effect and photomagnetism <sup>94</sup>

Furthermore, other solid-state techniques such as single crystal X-ray Diffraction (XRD) and powder-XRD (pXRD) can offer structural information between structures in the LS and HS states. In addition to bond lengths and bond angles, the coordination volume



( $V_{\text{Oh}}$ ) can be obtained by XRD and is distinct between the LS and HS states. For example, complexes of  $[\text{Fe}(\text{bpp})_2]^{2+}$  have been reported to have  $V_{\text{Oh}} = 9.6 \pm 0.2 \text{ \AA}^3$  for LS state, and their HS equivalents have  $V_{\text{Oh}} = 12.6 \pm 0.2 \text{ \AA}^3$ .<sup>120</sup>

Thermodynamic parameters such as enthalpy and entropy of the SCO<sup>112</sup> process can be calculated from calorimetric methods such as, Differential Scanning Calorimetry (DSC). Combined use of all these analytical techniques provides researchers as close to as full a picture as is currently achievable in SCO research.

#### 1.4.10.2 Solution state SCO

The Evan's Method, founded in 1959,<sup>121</sup> crucially supplements solid state magnetic measurements with solution state VT studies. This involves the use of  $^1\text{H}$  NMR, where a paramagnetic  $^1\text{H}$  NMR is recorded of a sample with a reference containing just the solvent and no paramagnetic species, is inserted coaxially (Figure 1.36). The chemical shift difference,  $\Delta\delta$  ppm, between the peaks from the solvent in the presence and in the absence of the paramagnetic sample, is obtained and used in subsequent calculations to obtain values of the magnetic molar susceptibility,  $\chi_m$ . These spectra can be recorded at various temperatures (solvent permitting) in order to determine SCO behaviour.

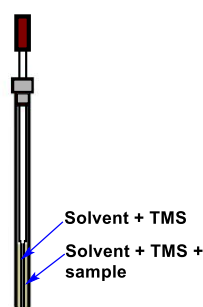


**Figure 1.36. NMR tube with coaxial insert used for Evan's Method. Where TMS is the NMR reference sample, tetramethylsilane.**

The calculations involve a series of corrections as proposed by the following. In 1970, Live and Chan reported that a diamagnetic correction<sup>122</sup> should be applied for the differences in bulk and reference magnetic susceptibility,<sup>123</sup> two years later, Ostfeld and Cohen noted that the density of the solvent used also needs to be corrected for at the different temperatures.<sup>124</sup> This is imperative in VT studies as this would affect the concentration of the paramagnetic solute, and therefore the values of  $\mu_{\text{eff}}$  and any correlating thermodynamic parameters. It was later noted by Piguet that this solvent correction is only applicable for small paramagnetic molecules and can be neglected for large molecules.<sup>125</sup> Finally, in 1992 Shubert reported the need for corrections for spectra

recorded on modern day NMR instruments which use a superconducting magnet, and therefore run at higher fields. <sup>126</sup>

Overall, the combined efforts <sup>121-126</sup> have resulted in today's VT Evan's <sup>1</sup>H NMR method, with decent accuracy. While it should be noted that the method has been reported to have a high error of 5-10%, <sup>127</sup> is highly concentration dependent and impurities can significantly impede results, <sup>128</sup> it has been sufficiently accurate for use herein for solution state SCO studies of iron(II) complexes.

Other solution state techniques include, the more simple paramagnetic <sup>1</sup>H NMR, which is sufficient for quick inspection of the degree to which a sample is in the HS or LS state, at room temperature. Furthermore, particularly useful in photophysical studies, is the use of UV-Vis optical spectroscopy, as SCO is often accompanied by a colour change. From this, *d-d* absorption bands can be identified and used to track the ST. <sup>112</sup> In Chapter 3, we see how even High Resolution Mass Spectrometry (HRMS) can be used for quick inspection of spin-state at instrument-operating temperatures.

## 1.5 Computational methods

The Time-Independent Schrödinger Equation ((TI)SE) for a one electron system is shown in Equation 1.11 where *H* is the Hamiltonian operator of the wavefunction (*Ψ*) and *E* is the eigenvalue operator. The Hamiltonian operator is a summation of the kinetic energy and potential energy components of the electron. <sup>129</sup>

$$H\Psi(r) = E\Psi(r)$$
$$\text{Where } H = \left[ -\frac{\nabla^2}{2m} - \left( \frac{1}{4\pi\epsilon_0} \right) \frac{Z}{r} \right]$$

### Equation 1.11. The time-independent Schrödinger equation for a hydrogenic atom.

Though it is impossible to solve the SE for a many-electron ( $n \geq 2$ ) system, which involves additional electron-electron interactions, such as Coulombic repulsions, approximations can be taken for these systems and the ultimate goal is to achieve the best approximation to the real wavefunction.

In the many-electron system, the *Born-Oppenheimer* approximation <sup>130</sup> to the Hamiltonian is taken, which considers the electronic motion of an electron separately to the vibrational motion. This can be assumed as the motion of a nucleus is effectively frozen compared to the fast motion of the, much lighter, electron. However, this

approximation alone is insufficient for solving the (TI)SE, and further advances have been developed to solve the many-electron system.

The Hamiltonian operator is as shown in Equation 1.12 for a two electron system, where there are distinct kinetic energies for the two electrons (1 and 2), and separated potential energy components for the electrons and protons (A and B). The coulombic attractive terms are  $-\frac{1}{r_{1A}}, -\frac{1}{r_{1B}}, -\frac{1}{r_{2A}}$  and  $-\frac{1}{r_{2B}}$  and the terms  $+\frac{1}{r_{12}}$  and  $+\frac{1}{R}$  are the inter-electron and inter-proton repulsions respectively.

$$H = -\frac{1}{2}(\nabla_1^2 + \nabla_2^2) - \frac{1}{r_{1A}} - \frac{1}{r_{1B}} - \frac{1}{r_{2A}} - \frac{1}{r_{2B}} + \frac{1}{r_{12}} + \frac{1}{R}$$

**Equation 1.12. The Hamiltonian operator for a many-electron (n=2) system, with approximations.**

As the number of electrons in a system increases, so does the number of variables to add to the (TI)SE. This is known as the 'many-body' problem. This can be approximated best by taking a Linear Combination of Atomic Orbitals (LCAO) for each MO.

The *Variational theory* states that any ground state energy achieved for a trial solution of the SE will always be greater than the true ground state obtained from the exact wavefunction. This theory is applied with normalised MOs to obtain the set of Hartree-Fock-Roothan (HFR) equations, which contain the Fock integral and the Overlap integral (Equation 1.13).<sup>131-133</sup> The Self-Consistent Field (SCF) method is then applied.<sup>134</sup> This is an iterative energy optimisation method of each one electron MO, used to obtain the best set of coefficients for each MO, which is then used in subsequent calculations until self-consistency (minimised energy) is achieved of all the orbitals.

$$\sum_j^N C_{ij}(F_{ij} - E_i S_{ij}) = 0$$

**Equation 1.13. The Hartree-Fock-Roothan equations.**

The SCF method replaces real electron-electron interactions with an average interaction. Therefore the HFR is missing this important contribution to the energy, the *Correlation energy*, which is the difference between the real and missing energies.

The HFR method is based on a single Slater Determinant,<sup>135</sup> which overestimates the ionic contribution to the wavefunction, relative to the covalent contribution, particularly at long bond-lengths. Therefore an improvement to the wavefunction would be the use of multiple Slater Determinants, in what is known as multiconfigurational methods.

Examples of these post-SCF methods include, the *Configuration Interaction* method,<sup>136</sup> the *Møller-Plesset Perturbation theory*,<sup>137</sup> and *Density Functional Theory (DFT)*.<sup>138</sup>

### 1.5.1 Density Functional Theory

In DFT, functionals (functions of functions) of electron density are applied to the many-body system. The ground state energy of N electrons in 3N spatial coordinates of electron density is determined. This can be divided into the terms shown in Equation 1.14. The energy functional as a function of electron density,  $E_{DFT}(\rho)$ , was achieved as a result of the combined efforts from Thomas,<sup>139</sup> Fermi<sup>124</sup> and Dirac,<sup>140, 141</sup> Kohn and Hohenberg<sup>142</sup> and Kohn and Sham.<sup>143</sup> The overall functional is a summation of the orbital kinetic energy term, ( $T_s(\rho)$ ), nuclear energy term ( $E_{ne}(\rho)$ ), the coulomb term ( $J(\rho)$ ) and finally, the exchange correlation term,  $E_{xc}(\rho)$ , the latter of which was proposed by Kohn and Sham.<sup>143</sup>

$$E_{DFT}(\rho) = T_s(\rho) + E_{ne}(\rho) + J(\rho) + E_{xc}(\rho)$$

**Equation 1.14. The energy functional as a function of electron density.**

DFT has demonstrated great use in the study of iron(II) SCO complexes, and generally of transition-metal complexes, with moderate computational cost. It can handle calculations of large molecules i.e. of 100 atoms, with fairly accurate results.<sup>144</sup>

It was first used in SCO by Paulsen *et al.*<sup>84</sup> who carried out a full geometry optimisation on the HS and LS states of the complex  $[\text{Fe}(\text{tpen})]^{2+}$  (where tpen = tetrakis(2-pyridylmethyl)ethylenediamine) and several other iron(II) complexes including the SCO-famous  $[\text{Fe}(\text{phen})_2(\text{NCS})_2]$ ,  $[\text{Fe}(\text{phen})_2(\text{NCSe})_2]$  and  $[\text{Fe}(\text{bpp})_2]^{2+}$  complexes. DFT calculations were performed on these models, using experimentally obtained  $T_{1/2}$  values, to compute values for  $E_{\text{el}}(0)$ ,  $\Delta E_{\text{vib}}(T_{1/2})$ ,  $\Delta S(T_{1/2})$  and  $\Delta G(T_{1/2})$  in order to predict  $n_{\text{HS}}(T)$ .<sup>84</sup>

The study employed Becke's three-parameter exchange functional, as a hybrid method with the correlation functional from Lee, Yang and Parr,<sup>145</sup> giving the B3LYP method<sup>146</sup> - a popular functional used in chemistry.<sup>147</sup> This was performed with different basis sets, which demonstrated an influence on the value obtained for  $\Delta E_{\text{el}}(0)$ . Though DFT is a useful theoretical tool, some contrasts still remain between theory and experiment, therefore, improvements to the method employed should be explored as a means to reduce these disparities.<sup>84</sup>

In addition to the electronic and thermodynamic parameters, electronic structure calculations from DFT allow for quantitative understanding of the theoretically most stable configuration, isomer or molecular geometry of a given molecule at specified

temperatures. With metal complexes, oxidation states and charge on the metal ion can also be accounted for in calculations. Furthermore, such calculations can be used to design future iron(II) SCO complexes with given properties,<sup>144</sup> demonstrating how powerful this computation tool can be.

## **Thesis objectives and aims**

Following recent findings within the Halcrow group that concluded a distinction in SCO behaviour through chiral discrimination of metal-PyBOX complexes, this thesis sets out to further investigate this chiral discrimination in SCO complexes, endeavouring to explore if it can be further enhanced.

A core objective of this thesis is to build an understanding on the effect of swapping oxygen for sulfur in the PyBOX ligand, giving thioPyBOX, on the SCO activity of analogous complexes. Since there is little literature concerning the thioPyBOX ligand, this thesis aims to add to the literature regarding the synthesis of the thioPyBOX ligand and its derivatives, whilst adding further characterisation and data that has not previously been reported in the chemical catalogue.

Catalytic activity of metal-PyBOX complexes are of particular interest as the PyBOX ligand is renowned for its contribution to successful metal catalysts. The work herein aims to build on this research with further demonstrations of metal-PyBOX catalysis.

## Chapter 2

### Synthesis and Characterisation of 2,6-Bis(thiazoliny)pyridine (ThioPyBOX) Ligands

#### 2.1 Introduction

The unique design of ligands and their intricacies is what allows chemists to control the function and output of coordination complexes.<sup>148</sup> Even small electronic and steric alterations in metal complexes can be influenced by the ligand. Thus, it is important to discuss and understand the design, development, and synthetic strategies employed in the synthesis of the ligands within this thesis.

##### 2.1.1 N,N',N''- Ligands

N,N',N''-ligands are intrinsic to the world of coordination chemistry, forming the structural basis for a vast library of nitrogen-donating ligands. A countless number of N,N',N''-ligands can be achieved through featuring various nitrogen-based functional groups from amines, amides and imines to heterocycles such as pyridines, pyrazines, pyrazoles and pyrroles.<sup>149</sup>

##### 2.1.1.1 Schiff-base ligands

A well-established class of N-donor ligands are based on the Schiff-bases, established by Hugo Schiff in the 19<sup>th</sup> century.<sup>150, 151</sup> Schiff's discovery of this reactive class of imines has resulted in huge victories in the world of science such as the synthesis of  $\beta$ -lactams for antibiotics.<sup>152</sup> Other biological activities against *Escherichia coli*, *Staphylococcus aureus* and *Bacillus subtilis* have also been demonstrated by metal complexes of tridentate Schiff-bases,<sup>153</sup> as well as anti-urease activity,<sup>154</sup> and anti-inflammatory activities.<sup>155</sup>

In coordination chemistry, metal complexes of Schiff-bases, bearing N and O donor sites, have been widely employed as catalysts in polymerisations, oxidations and reductions of organic compounds.<sup>155</sup> The Schiff-bases are used as molecular scaffolds to design and fine-tune metal complexes of its derivatives to diversify its applications.<sup>156</sup> They are selectively used owing to their facile synthesis,<sup>157</sup> thermal-, air- and moisture- stabilities and high product selectivity if the Schiff-base is chiral.<sup>155</sup> Schiff bases can also give rise to other desirable properties in coordination complexes such as spin-crossover and magnetic coupling.<sup>48, 49, 158</sup> One of the first examples of a chiral metal-Schiff base complex was demonstrated by Noyori *et al.* in 1968 using copper (Figure 2.1),<sup>159</sup> which contributed to his award of the Nobel Prize in Chemistry in 2001.

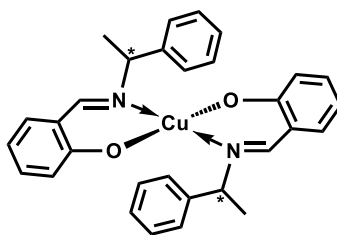


Figure 2.1. The copper-Schiff base complex studied by Noyori *et al.* <sup>159</sup>

With an interest in exploring the  $\pi$ -bonding nature of unsaturated N-donor atoms, N,N',N'' Schiff-base ligands were pioneered by Stoufer and Busch using pyridinaldehyde scaffolds (Figure 2.2). <sup>160</sup> These systems have since been further developed using this N,N',N'' Schiff-base architecture, creating pincer-ligands featuring N-heterocyclic systems. These systems are fundamental in organic synthesis and natural product chemistry, <sup>161</sup> as well as medicinal chemistry as demonstrated by Gehad with the metal complexes  $[MX_2(L1 \text{ or } L2)] \cdot nH_2O$  where M = Fe(II), Co(II), Ni(II), Cu(II) and Zn(II), X = Cl, **L1** = 2,6-pyridinedicarboxaldehydebis(*p*-hydroxyphenylimine) and **L2** = 2,6-pyridinedicarboxaldehydebis(*o*-hydroxyphenylimine) (Figure 2.3). Their studies showed the metal complexes of these ligands to be more potent against the bacteria *E. coli*, *P. aeruginosa*, *S. aureus* and *Fungi*, than the uncomplexed ligand alone. <sup>162</sup>

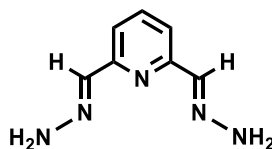


Figure 2.2. Structure of 2,6-pyridindialdihydrazone. <sup>160</sup>

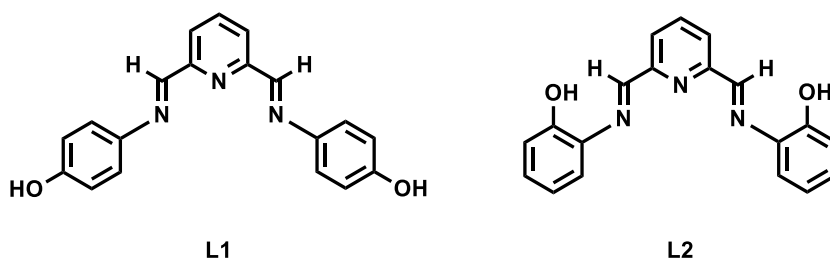
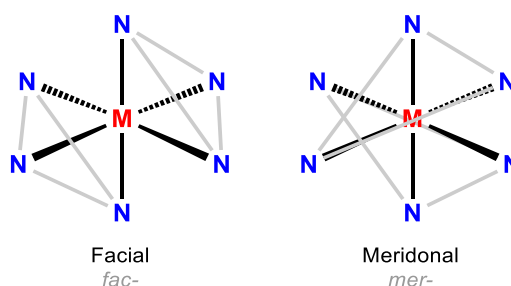


Figure 2.3. N,N',N''-Schiff base ligands employed in the study by Gehad. **L1** = 2,6-pyridinedicarboxaldehydebis(*p*-hydroxyphenylimine) (left) and **L2** = 2,6-pyridinedicarboxaldehydebis(*o*-hydroxyphenylimine) (right). <sup>162</sup>



### 2.1.1.2 N,N',N''-pincer ligands

N,N',N''-pincer ligands in general are particularly ubiquitous in coordination chemistry due to their favourable binding through chelation, which thermodynamically favours the metal complexation and renders ligand dissociation undesirable.<sup>163</sup> In the case of  $[M(N,N',N'')_2]$  complexes, where the ligand is tridentate, there are two geometric isomers; facial (*fac*-) and meridonal (*mer*-),<sup>164</sup> which are shown in Figure 2.4.



**Figure 2.4. Facial (left) and Meridonal (right) isomers of an  $[M(N,N',N''\text{-tridentate})_2]$  complex.**

A model class of *fac*-tridentate ligands are the 'scorpionate' ligands, and the most well-known of examples of these are hydrotris(pyrazolyl)borates (Tp)<sup>165, 166</sup> (Figure 2.5), which can coordinate to a metal from each N-donor site on the pyrazole groups.<sup>167</sup> Derivatives of these can be synthesised by substitution at the pyrazole 3-, 4- and 5-positions, to design and control the sterics and electronics of the resulting ligand. Though Tp ligands are most widely used to add stability to a coordination system, they have been employed as a model system for three histidine ligands in metalloenzyme active sites,<sup>168</sup> in catalytic systems for polymerisation studies<sup>169</sup>, C-C coupling<sup>170</sup> and more generally used as a stabilising group to 'cap' the corner of a metal's coordination sphere.<sup>171</sup> A 1:1 metal:Tp ratio affords a half-sandwich or 'piano-stool' complex, while a 1:2 ratio affords the *fac*- structure shown in Figure 2.4, provided the size of the metal ion can accommodate this. Furthermore, scorpionate ligands have attracted attention from their similarity to the well-respected, cyclopentadienyl ligand (Cp). Similarities include their anionic binding, the geometries of their complexes and both being  $6e^-$  donor systems.<sup>171</sup>

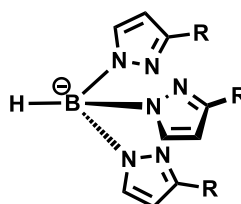


**Figure 2.5. Structure of a hydrotris(pyrazolyl)borate ('scorpionate') ligand.**

The diversity of the Tp ligand is demonstrated in its ability to switch between tridentate and bidentate coordination modes, with non-innocent interactions. Additionally, the angle of the pincer 'bite' to the metal can be controlled by the length and conformational flexibility of a tether incorporated at the R positions of each pyrazole. Tethered Tp ligands have shown to encourage the formation of a cationic octahedral  $[M(Tp^R)_2]^{n+}$  sandwich complex,<sup>172</sup> while less restrictive tethers tend to favour a piano-stool geometry.<sup>173</sup>

While complexes of monodentate N-donor ligands dictate geometry through sterics, electronics and CFSE, complexes of N,N',N''-tridentate analogues featuring N-heterocycles have extensive  $\pi$ -conjugation, and so are more sterically demanding as these favour planarity. These N,N',N''-pincer type ligands often result in constrained conformations about a metal centre, which can dictate metal complex geometry based on accommodation of the pincer ligand(s). This reaches an extent where a compromise is needed between the metal and ligand geometries, which often leads to geometric distortions (angular JT distortion effects), and in extreme cases, can result in only partial-binding of a multidentate ligand to a metal. This hemilability of pincer ligands has proven advantageous in applications such as catalysis.<sup>174</sup>

### 2.1.1.3 2,2':6',2''- Terpyridine

Prompted by earlier studies of classic N,N'-bidentate ligands such as 2,2'-bipyridine (bpy) and 1,10-phenanthroline (phen), 2,2':6',2''- terpyridine (terpy) and its derivatives were introduced (Figure 2.6). These are typical pincer ligands used in the design of transition-metal catalysts and in the structural architecture of supramolecules, as stable linkers.<sup>175</sup> Terpy has been extensively studied and has been shown to chelate to a multitude of metal ions such as copper,<sup>176</sup> cobalt, iron,<sup>177</sup> zinc,<sup>178</sup> ruthenium, osmium,<sup>179</sup> and palladium.<sup>180</sup> It has also shown the ability to stabilise low-valent metals such as nickel.<sup>181</sup>

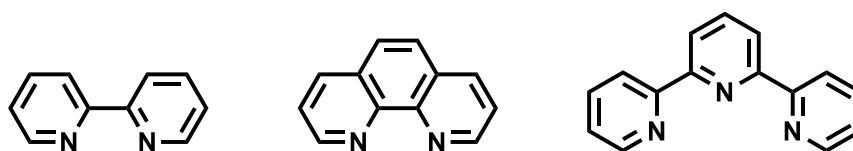


**Figure 2.6. Structures of 2,2'-bipyridine (left), 1,10-phenanthroline (middle) and 2,2':6',2''-terpyridine (right).**

The high affinity of terpy towards metal ions, is due to the  $\pi$ -accepting nature of the three bonded pyridine rings over which its electron density is delocalised. Whilst terpy provides a strong  $\sigma$ -donation of electron density to the metal centre, synergistically, the electron

deficiency of the pyridine rings renders terpy a good receptor of  $\pi$ -electrons from the metal into its LUMOs, rendering it a strongly  $\pi$ -back-bonding ligand (Figure 2.7). This, coupled with a strong chelate effect, entropically drives its complexation with metals.

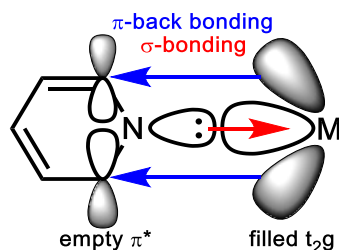


**Figure 2.7. Pyridine-metal orbital interaction in  $\pi$ -back bonding.**

Terpy adopts a quasi-planar geometry when there is one unit complexed to a metal, but in a bis-terpy metal complex, the two planar terpy ligands adopt a perpendicular conformation to each other to give a *mer*-octahedral geometry (Figure 2.8).

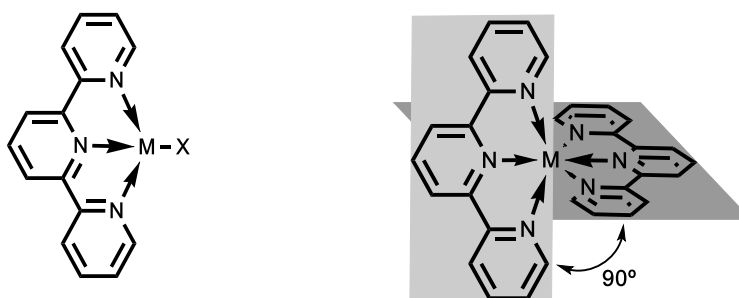


**Figure 2.8. The structures of a classical mono-terpy-metal complex (left) and a bis-terpy-metal complex (right)**

Vast research into transition-metal-terpyridine complexes have shown applications of functionalised terpy ligands in the architecture of coordination polymers principally using iron(II) and ruthenium(II)<sup>182</sup> as well as, catalysing essential C-C cross coupling reactions,<sup>183</sup> dye degradation<sup>184</sup> and artificial photosynthesis.<sup>185</sup> This provides confidence in this N,N',N''- heterocyclic system as a ligand for catalytic coordination compounds.

Owing to its inexpensiveness and commercial availability, the terpy ligand is used as an initial model system for the design of some of the metal complexes in this thesis. The ligand also provides a route to understanding and predicting the chemical behaviour and properties of the ligand system employed herein.

#### 2.1.1.4 2,6-Bis(pyrazolyl)pyridine

Elaborating on N,N',N''-heterocyclic ligands is the ligand system 2,6-bis(N-pyrazolyl)pyridine (bpp) (Figure 2.9) along with its library of functionalised derivatives.<sup>186</sup> This ligand system is particularly well-known in the field of Spin-Crossover (SCO), due to its flexible synthetic routes which result in a vast library of functionalised bpp derivatives. These derivatives are fine-tuned in its steric and electronic properties to induce a desirable SCO behaviour, most notably in its iron(II) complexes.<sup>77</sup> Although bpp features a central pyridine ring like terpy and the N,N',N''-Schiff base ligands, the other two heterocycles bound at the 2- and 6- positions of pyridine are now pyrazoles, which are five membered rings, with two carbon atoms substituted for nitrogens. As with terpy, its C<sub>2</sub>-symmetric structure simplifies its synthesis and the resulting configuration of subsequent products formed. Despite appearing similar to the terpy ligand at first glance, it in fact holds very different chemical properties such as different routes to synthesis, kinetic lability,  $\pi$ -orbital energies and differing electron-richness of the resulting metal-bpp complexes,<sup>186</sup> rendering bpp a class of its own.

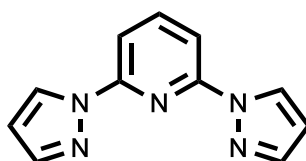


**Figure 2.9. The structure of 2,6-bis(N-pyrazolyl)pyridine (1-bpp).**

Iron(II) and iron(III) complexes with the bpp ligand, and its derivatives, have been explored in the context of SCO compounds, which are of interest in the application of molecular switches, as they can mimic a [1,0] binary system at the molecular level.<sup>187</sup> For application as a molecular switch in memory and storage devices, optical displays and sensors,<sup>188</sup> the complexes ideally need to be designed to produce an abrupt spin-transition and a hysteretic response centred around room temperature, 300 K.<sup>189</sup> Successful molecules can then be tethered to the components in these devices. Many derivatives of the bpp ligand have been achieved, an example of such are di- and tri-(pyrazolyl)azines which have been studied within the research group to produce coordination polymers and helicate structures.<sup>190</sup>

Furthermore, a substantial amount of work, particularly within the Halcrow group, has been undertaken to explore how functionalisation of the bpp ligand affects the SCO behaviour of its iron complexes.<sup>191, 192</sup> Both the identity of the ligand substituents and their position on the bpp ligand framework have been explored (Figure 2.10). This provides researchers a more in-depth understanding of the structure-function relationship in SCO compounds. This highlights just how much control one can have by

fine-tuning the ligand design to produce specific chemical and physical behaviours of metal complexes of these ligands.

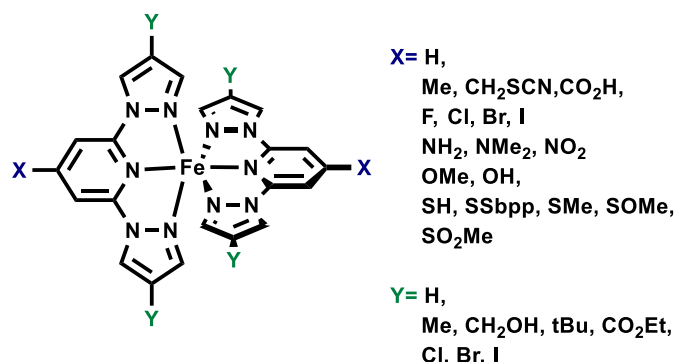


**Figure 2.10. Different substituents and their positions studied in a structure-function relationship study of  $[\text{Fe}(\text{bpp}^{\text{X,Y}})_2]^{2+}$ .** <sup>191</sup>

It should be noted that though ligand design is a crucial way of designing SCO-active compounds, it is not the sole way. Other factors such as lattice solvent in the solid material, counter-ions and ultimately crystal packing effects, <sup>29, 193</sup> can significantly affect the SCO behaviour of such metal complexes. This will be elaborated on in Chapter 3.

Across all the pincer ligands discussed so far, there are key steric and electronic factors that can dictate the chemistry of resulting metal complexes. These are summarised in Figure 2.11.

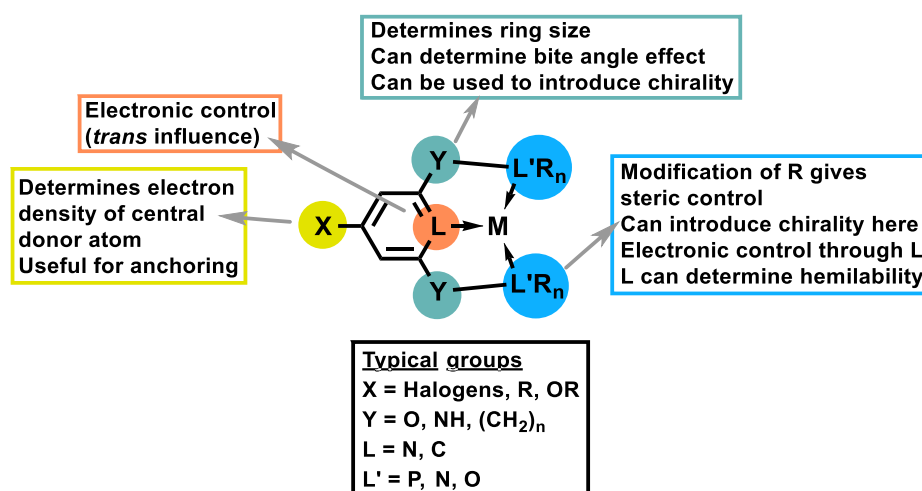


**Figure 2.11. Factors governing steric and electronic control in pincer ligands. Figure adapted from Peris and Crabtree.** <sup>174</sup>

### 2.1.2 The PyBOX Ligand

Further functionalisation of the N,N',N''- ligand system can involve altering the atomic makeup of the heterocyclic rings. The ligand, pyridine-2,6-bis(oxazoline), abbreviated to PyBOX, is the tridentate counterpart of the bis(oxazoline) ligand family (BOX) (Figure 2.12).<sup>194</sup> Mutual to terpy and bpp, PyBOX is also a C<sub>2</sub>-symmetric molecule and features a central pyridine ring and, similarly to bpp, has two 5-membered heterocyclic rings at the 2- and 6- positions of the pyridine. The key difference between bpp and PyBOX is the more electronegative oxygen atom within the 5-membered heterocycles. Furthermore, the 2- and 6- positions of the pyridine ring are now bound to these heterocycles by a stronger C-C bond rather than a weaker C-N bond (bond energies: 346 kJ mol<sup>-1</sup> and 305 kJ mol<sup>-1</sup> respectively<sup>195</sup>). Since its emergence into the chemical catalogue, the PyBOX ligand and its derivatives have been most commonly employed in the field of catalysis.<sup>196</sup>

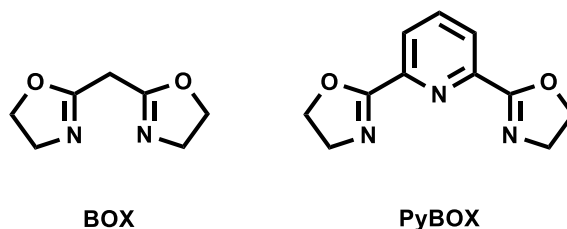


**Figure 2.12. The structures of bis(oxazoline), BOX (left) and 2,6-pyridine-bis(oxazoline), PyBOX (right).**

Substituted PyBOX ligands, with the R- groups *isopropyl*-, *tertbutyl*- and *secbutyl*-, were first synthesised by Nishiyama *et al.* in 1989. These were complexed with rhodium(III) chloride to produce a series of successful chiral catalysts for the enantioselective hydrosilylation of ketones (Figure 2.13).<sup>197, 198</sup> Similarly efficient catalysis was also found using rhodium(I)/PyBOX catalyst precursors.<sup>199</sup> Since then, the synthesis of the PyBOX ligand has been further established by the development of alternative preparative routes. An example of this is demonstrated by Cornejo *et al.*, where a one-pot synthesis of the ligand was achieved that required fewer purification steps with little compromise of the yields.<sup>200</sup>

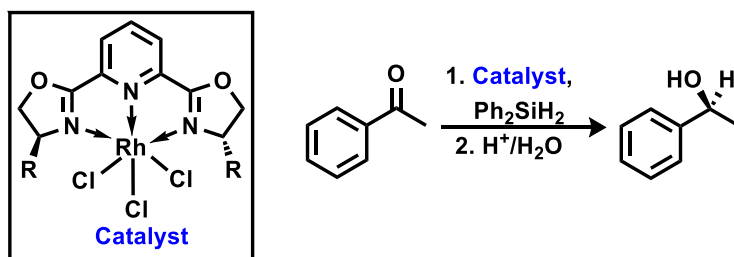


Figure 2.13. Rh-PyBOX catalyst studied by Nishiyama *et al.*<sup>197</sup>

Furthermore, functionalisation of the PyBOX ligand has included modifications at the 4- position on the pyridine ring, and at the 4- position of the oxazoline rings (X and Y respectively in Figure 2.14), to explore electronic effects on their corresponding metal complexes. Nishiyama *et al.* followed up their preliminary findings with the 4-chloro-, 4-methoxy- and 4-(N,N-dimethylamino)-PyBOX derivatives and their rhodium(III) complexes.<sup>201</sup> Later on, Desimoni *et al.* revealed the importance of substituting the 5- position of the oxazoline rings (position Z in Figure 2.14). It was found that when there is a phenyl substituent in this position, its complexes of  $\text{Ln}(\text{Otf})_3$  were particularly well-suited to catalysing the Mukaiyama-Michael reaction<sup>202</sup> and the enantioselective Diels-Alder reaction.<sup>203</sup>

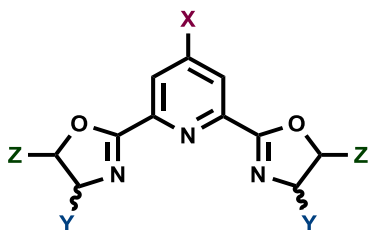


Figure 2.14. PyBOX ligand with positions of substitution explored. X= 4- position of pyridine, Y= 4- position of oxazoline and Z= 5- position of oxazoline.

Further afield from this, the PyBOX ligand has been bound to polymer beads as a route to providing recyclable polymer-supported catalysts.<sup>204</sup> An example of how this has been explored includes functionalising the PyBOX ligand, at the 4- position of the pyridine ring, to be able to undergo *Click Chemistry* to produce a polystyrene-supported PyBOX (Figure 2.15).<sup>205</sup> The PyBOX-polymer ligand can then coordinate to a metal such as ruthenium for the catalysis of, in one example, a cyclopropanation reaction.<sup>204</sup> Copper has also been reported in the same context using a polymer-functionalised BOX ligand.<sup>206</sup>

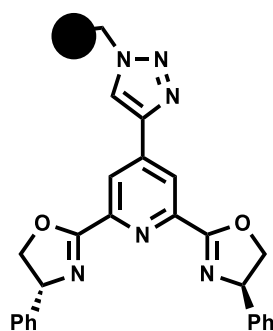


Figure 2.15. Click-PyBOX unit for polymerisation. <sup>205</sup>

The work herein will focus solely on the substitution of the 4- position of the oxazoline and thiazoline heterocycles of PyBOX and thioPyBOX (see later) respectively. Substitution at this position induces chirality in the ligand, which when coordinated to a metal centre can result in chiral metal complexes, which is befitting of their dominance in the field of asymmetric catalysis. Since the molecule is  $C_2$ -symmetric, using stoichiometric quantities of reagent, will result in substitution of the 4-position of both oxazoline rings producing what is strictly speaking, a diastereomer. The isomeric relationship is explained below in Figure 2.16. Since the relationship between the diastereomeric pairs is not addressed in this work, the (*R,R*)- and (*S,S*)- substituted ligands will be referred to hereon as enantiomers of one another.

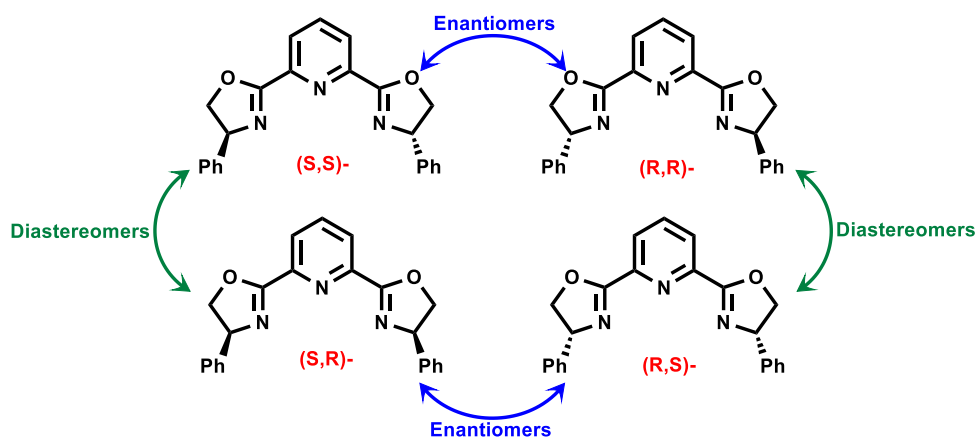


Figure 2.16. The possible isomers of the PyBOX ligand substituted on the oxazoline rings.

Very recently, Wang *et al.* successfully synthesised the first *meso*-(*R,S*)-PyBOX diastereomer, which they complexed to iron(II) to study the effect of ligand symmetry on the SCO behaviour of  $[\text{Fe}(\text{PyBOX})_2]^{2+}$  complexes. <sup>207</sup>

An elaborate number of PyBOX derivatives can be found in the literature. Yu *et al.* made use of 15 variations of the PyBOX ligand for the optimisation of their nickel catalyst for



C-C cross coupling.<sup>208</sup> This consisted of substitutions at either the 4-position of the pyridine ring or the 5-position of the oxazoline ring, or both. The best catalytic results were found when (S)-PyBOX<sup>sBu</sup> and (4-Cl)-PyBOX<sup>H</sup> were used, where yields up to 92% were achieved.<sup>208</sup>

Replacing the oxygen atoms of the PyBOX ligand with nitrogen was pioneered by Bhor *et al.* who were the first to synthesise the pyridine-2,6-bis(imidazoline) (PyBIM) ligand (Figure 2.17, left).<sup>209</sup> The purpose of this was to create a PyBOX-derivative that can undergo N-group functionalisations such as an N-alkylation reaction, to tune the selectivity of the ligand. Considering this concept of tuning the electronics of a ligand by means of changing the atomic make-up of the structure, it is fitting to introduce the ligand family of focus in this thesis; 2,6-bis(thiazoline)pyridine, thioPyBOX (Figure 2.17, right).

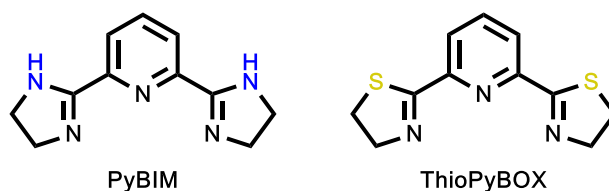


**Figure 2.17. The structures of pyridine-2,6-bis(imidazole), PyBIM (left) and pyridine-2,6-bis(thiazoline), thioPyBOX (right).**

Previous work reported in the Halcrow group considered iron(II) complexes of various PyBOX ligands in the context of SCO, rather than catalysis.<sup>210</sup> This work has built the foundations for investigating this ligand system, with a motive of investigating the electronic and steric influence of the thioPyBOX ligand on its iron(II) complexes with regards to SCO activity (*vide infra* in Chapter 3).

### 2.1.3 The ThioPyBOX Ligand

Unlike its PyBOX counterpart, the thioPyBOX ligand is not commercially available, and as far as is understood, there are only seven reported papers,<sup>211-217</sup> and one patent,<sup>218</sup> in the literature that synthesise the ligand. It has been speculated that the limited research carried out on sulfur-containing oxazolines is due to the thiol-based starting materials, such as the 2-aminothiols, being less commercially available compared to their alcohol counterparts.<sup>211</sup> In addition to this, the synthesis can involve lengthy reaction times of up to 4 days for just the thiolating step, followed by a work-up and then more often than not, purification by column chromatography (Table 2.1). Since the final yields are often modest – for example, the phenyl-substituted thioPyBOX has been synthesised in no more than a 31% yield – it becomes clear why there is so little research concerning the thioPyBOX ligand.

Nevertheless, the hypothesis that changing oxygen to sulfur, with its lower electronegativity and larger atomic radius, will interestingly affect both the electronics and sterics of the resulting metal complexes, particularly with regards to SCO behaviour, offsets the cumbersome synthetic routes involved.

Table 2.1 summarises the reported the synthetic approaches employed in the 8 pieces of literature on the thioPyBOX ligand.

Publication	Starting Material	Intermediate	Reaction Time	Reaction Conditions	Purification	Product & Yield
Abrunhosa <i>et al.</i> 2001 <sup>211</sup>	Dithioester, aminoalcohol	Dithioamide	Up to 4 days (Unspecified)	Room temp., base (Et <sub>3</sub> N),	Silica Column Chromatography	diPh: 69 %, (S,S)-tBu: 70%
Abrunhosa <i>et al.</i> 2004 <sup>212</sup>	As reported in <sup>211</sup>	As reported in <sup>211</sup>	As reported in <sup>211</sup>	As reported in <sup>211</sup>	As reported in <sup>211</sup>	(S,S)-iPr: 61 %
Le Maux <i>et al.</i> 2004 <sup>213</sup>	As reported in <sup>211</sup>	As reported in <sup>211</sup>	As reported in <sup>211</sup>	As reported in <sup>211</sup>	As reported in <sup>211</sup>	(R,R)-Et: 75%, (S,S)-iPr: 70 %, (R,R)-Bn: 67 %
Nishio <i>et al.</i> 2005 <sup>217</sup>	Bis-( <i>N</i> -acylamino alcohols)	N/A	N/A	Lawesson's Reagent (LR), Reflux	N/A	Ph-Bn-iPr (yields N/A)
Ackerman <i>et al.</i> 2008 <sup>218</sup>	Diamide, aminoalcohol	Hydroxy-pyridine-carboxamide	40 hours	Reflux, P <sub>2</sub> S <sub>5</sub>	Silica gel Biotage	(S,S)-Ph: 31%

Nobbs <i>et al.</i> 2012 <sup>214</sup>	2,6- pyridinedicarbonyl dichloride, aminoalcohol	Hydroxy-pyridine- carboxamide	3 hours	Reflux, P <sub>2</sub> S <sub>5</sub> , base (Et <sub>3</sub> N)	Recrystallised from methanol	(R,R)-Ph: 30 %, (S,S)-tBu: 45 %, (S,S)-iPr: 22%, diPh: 53 %
Guo <i>et al.</i> 2015 <sup>215</sup>	Pyridine-2,6- dicarboxylic acid, aminoalcohol	Chloro-pyridine carboxamide	4 hours	Reflux, P <sub>2</sub> S <sub>5</sub> , base (Et <sub>3</sub> N), thionyl chloride	Recrystallised from methanol	(R,R)-iPr: 32%
Pan <i>et al.</i> 2020 <sup>216</sup>	Pyridine-2,6- dicarboxylic acid	a. Dimethyl pyridine-2,6- dicarboxylate b. Hydroxy- pyridine- carboxamide	30 hours	Reflux, P <sub>2</sub> S <sub>5</sub> , base (Et <sub>3</sub> N)	Silica Column Chromatography or Recrystallisation from Ethanol	DiMe: 67 %, H: 45 %

**Table 2.1. Summary of reported literature of the ThioPyBOX ligand synthesis.**

Abrunhosa *et al.* reported the synthesis of thioBOX, thioPyBOX and some of its derivatives, using dithioesters as the source of sulfur (Figure 2.18).<sup>211</sup> With this, they published preliminary findings from palladium catalysis of an allylic substitution reaction, with one of their thioBOX ligands. Using this ligand, a high enantiomeric excess (87%) was achieved, showing promise of the ligand and its derivatives in asymmetric catalysis.<sup>211</sup> However, similar enantiomeric excesses and yields were found in a rhodium(I) catalysis study, between BOX and thioBOX ligands for the hydrosilylation of acetophenone.<sup>219</sup>

This work was then followed up with further studies of palladium-based thioBOX vs BOX catalysts for the same reaction. The preliminary findings were supported when it was found that the palladium-bis(thiazolines) were significantly better catalysts than their oxygen counterparts. However, when the pyridine ring was incorporated and the thioPyBOX vs. PyBOX ligands were studied, the trend did not follow through and the Pd-PyBOX complexes were found to be the more active catalysts.<sup>212</sup>

Following this, Le Maux *et al.* employed the thioPyBOX ligands with R- substituents, (*R,R*)-ethyl-, (*S,S*)-isopropyl-, (*S,S*)-benzyl- and (*R,R*)-phenyl- to make chiral ruthenium catalysts for the cyclopropanation of styrenes.<sup>213</sup> They compared their catalytic results with previous findings by Nishiyama *et al.* with their Ru-PyBOX analogues,<sup>220</sup> and found comparable results with small differences in enantiomeric excess. The synthetic approach Le Maux *et al.* took to in synthesising their thioPyBOX ligands, was as reported by Abrunhosa *et al.*<sup>213</sup> Le Maux's publication concluded with words of encouragement for the further exploration of the chiral bis(thiazoline) ligand.

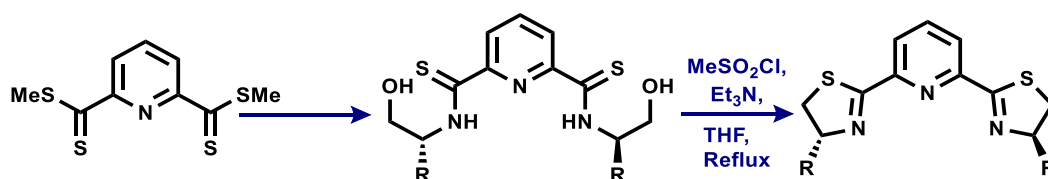


**Figure 2.18. Synthetic route to thioPyBOX by Abrunhosa *et al.*<sup>211, 212</sup> and Le Maux *et al.*<sup>213</sup>**

A publication by Nishio *et al.* in 2005, outlines the synthesis of a small library of chiral bis-thiazolines.<sup>217</sup> While little information is available concerning the synthetic procedures and ligands formed, it is notable that this is the only piece of literature that employs the Lawesson's Reagent (LR) in the synthesis of the thioPyBOX ligand, also in the absence of a base (Figure 2.19).



Figure 2.19. Synthetic route to thioPyBOX by Nishio *et al.* <sup>217</sup>

A patent was published by Ackerman *et al.* in 2008, which introduces using the diacyl chloride species as the starting material, to produce the dihydroxypyridinedicarboxamide intermediate. This was followed by use of the thiolating reagent, phosphorus pentasulfide ( $P_2S_5$ ) in dichloromethane for the second step of the procedure (Figure 2.20), <sup>218</sup> which later methodologies seem to have adopted.

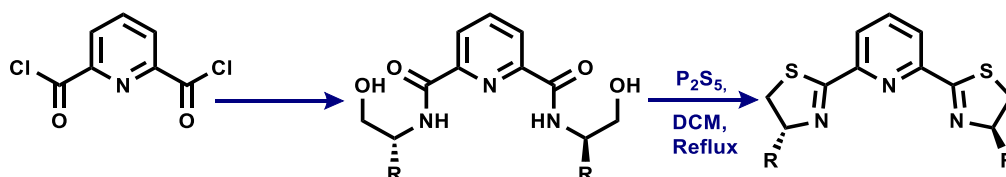


Figure 2.20. Synthetic route to thioPyBOX by Ackerman *et al.* <sup>218</sup>

Nobbs *et al.* published an alternative method to thioPyBOX synthesis to that described by Abrunhosa and Le Maux *et al.* This procedure followed closely to that explored by Ackerman *et al.* as it involved thiolation and cyclisation of substituted bis(N-acylamino alcohols) (Figure 2.21). <sup>214</sup> This method also uses the reagent phosphorus pentasulfide, however in the presence of a base, which is a previously reported method for the cyclisation of sulfur-containing heterocycles. <sup>218, 221</sup> The synthesis is an adaption of a method that employs 2,4-bis(p-methoxyphenyl)-1,3,2,4-dithiaphosphetane-2,4-disulfide (Lawesson's Reagent) in lieu of phosphorus pentasulfide. <sup>217, 222</sup> It is also worth noting that this procedure was carried out in toluene rather than dichloromethane.

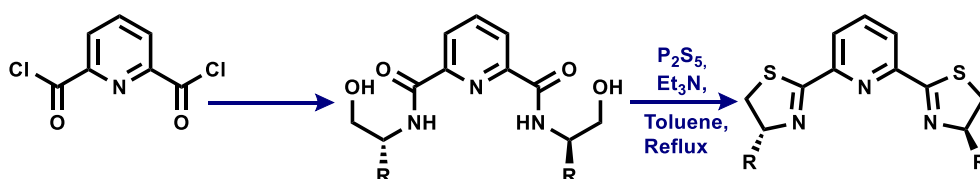


Figure 2.21. Synthetic route to thioPyBOX by Nobbs *et al.* <sup>214</sup>

Guo *et al.* also synthesised the (R,R)-thioPyBOX<sup>iPr</sup> ligand <sup>215</sup> using the same method, with slight modification, employed by Nobbs *et al.* <sup>214</sup> The modifications included a different intermediate species to the bis(N-acylamino alcohol), in their reaction, in which the hydroxy- group is substituted for a chlorine (Figure 2.22).

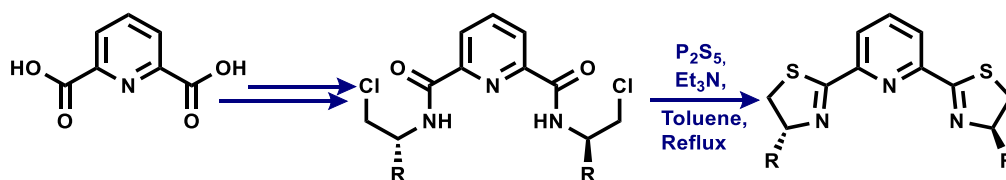


Figure 2.22. Synthetic route to thioPyBOX by Guo *et al.* <sup>215</sup>

Similar to Guo *et al.*, Pan *et al.* also synthesised their thioPyBOX ligands starting with pyridine-2,6-carboxylic acid. <sup>216</sup> They however, took a multistep approach in which the methyl ester was first synthesised and isolated before reacting this with the aminoalcohol to afford the dihydroxypyridinedicarboxamide. This was then treated with phosphorus pentasulfide and triethylamine under anhydrous conditions in toluene to give the thioPyBOX ligand (Figure 2.23). The dimethyl-substituted thioPyBOX was purified by column chromatography (1:1 dichloromethane/ethyl acetate) achieving a 67 % yield, whilst the achiral derivative was recrystallised from methanol achieving a 45 % yield.

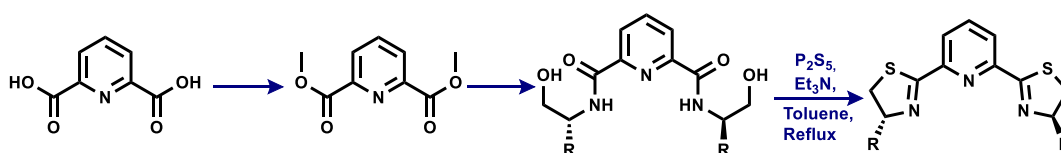


Figure 2.23. Synthetic route to thioPyBOX by Pan *et al.* <sup>216</sup>

The only X-ray diffraction data for a thioPyBOX variant reported in the literature to date, is for phenyl-thioPyBOX. <sup>214</sup> XRD structures of the *isopropyl*- and *tertbutyl*-thioPyBOX ligands, as well as a co-crystallised (R,R)-*tertbutyl*- and (S,S)-*tertbutyl*-structure, are reported herein.

## 2.2 Results & Discussion

### 2.2.1 Synthesis of 2,6-Bis(thiazoliny)pyridines – A Two-Step Reaction

After experimenting with the previously discussed methods of thioPyBOX synthesis from the literature, an alternative synthetic protocol was developed that also follows

a two-step reaction procedure. First is the synthesis of the di(2-hydroxyethylamide) intermediate, followed by the thiolating and cyclisation step. The second step is performed using Lawesson's Reagent, as employed by Nishio *et al.* for the conversion of the chiral bis-(*N*-acylamino alcohols) into chiral bis-(thiazolines) for application in the enantioselective Diels-Alder reaction.<sup>217</sup>

### 2.2.1.1 Synthesis of the Dihydroxy pyridine Dicarboxamide

The synthesis of the diamide intermediate was first attempted following the procedure reported by Kin Tse *et al.*<sup>223</sup> where pyridine dicarbonyl dichloride is reacted with the aminoalcohol in chloroform at room temperature, in the presence of triethylamine (Figure 2.24). This method encountered difficulties in dissolving the pyridine reagent in chloroform. Even after heat was applied, this still only achieved partial dissolution. After following the experimental through regardless, crude analysis confirmed the diamide had formed but in poor purity, low yield and with remnant triethylamine. Therefore alternative routes to diamide synthesis were investigated.

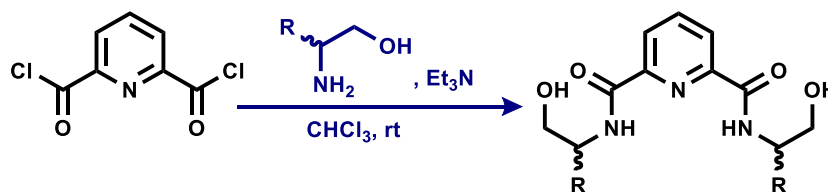


**Figure 2.24. Synthesis of the hydroxy-pyridinecarboxamide by Kin Tse *et al.*<sup>223</sup>**

Alternative methods included that which was employed by Burrows *et al.*, which is the same as that in<sup>223</sup>, however, with the substitution of dichloromethane for chloroform.<sup>210</sup> The issues faced with this method were akin to that when the reaction proceeded in chloroform. Research into alternative methods was undertaken until a satisfactory synthetic route was found, which would produce the amide in yields appropriate to explore the second step of the ligand synthesis.

The synthetic approach adopted for the diamide synthesis is an adaptation of the protocol reported by Towers *et al.*<sup>224</sup> which proceeds as a multiphasic reaction (Figure 2.25). The method involves the mild base, potassium hydrogen carbonate, being added to the amino alcohol in ethyl acetate, followed by the dropwise addition of pyridine dicarbonyl dichloride in chloroform at 70 °C. The mixture was stirred at reflux, and then at room temperature overnight. It is important to note that the reaction



proceeds with no inversion of stereochemistry, and so the stereochemistry of the starting aminoalcohol is retained through to the thioPyBOX ligand.

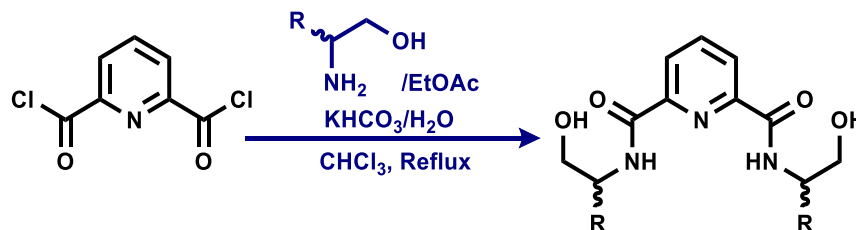


Figure 2.25. Synthesis of the hydroxyamide adapted from Towers *et al.* <sup>224</sup>

Though a slightly lengthier procedure, this method produced the diamide cleanly in most cases, without need of further purification and in moderate yields, averaging 56%. Both the (*R,R*)- and (*S,S*)- enantiomers of the diamides with phenyl, *isopropyl*, and *tert*butyl substituents were successfully isolated (Figure 2.26) and these were characterised by <sup>1</sup>H NMR, <sup>13</sup>C{<sup>1</sup>H} NMR and HRMS.

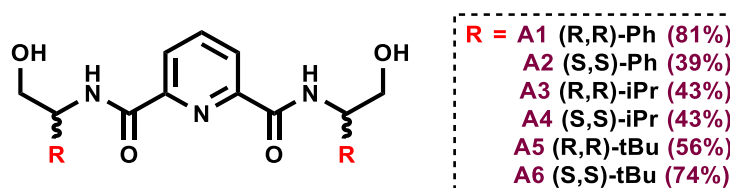
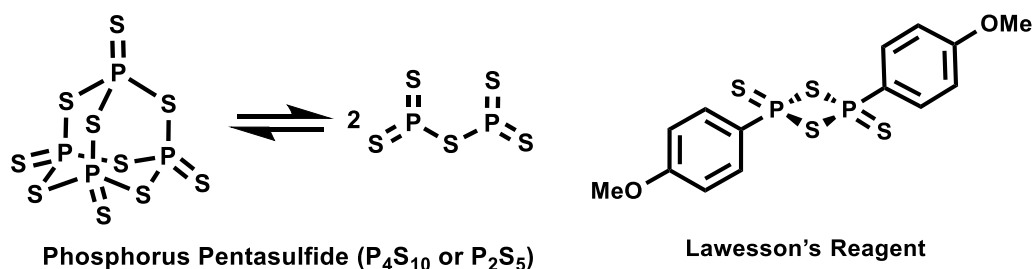


Figure 2.26. Summary of the diamides synthesised by the method in Scheme 2.6, A1-A6. Yields in parentheses.

### 2.2.2 Heterocyclic formation and thiolation step

Since the diamides had been successfully synthesised, the thiolating and cyclisation step was then explored. This initially followed the aforementioned procedure by Nobbs *et al.*, <sup>214</sup> however using Lawesson's Reagent (LR) in place of P<sub>2</sub>S<sub>5</sub> (Figure 2.27). Upon failure this was then repeated but using a greater excess of LR. Crude analysis confirmed the product had still not formed. Alternative routes to general thiazoline synthesis were studied. Two other procedures, one from Bengtsson *et al.* <sup>225</sup> which employed LR, and another from Aitken *et al.* <sup>226</sup> which employed P<sub>2</sub>S<sub>5</sub> with sodium hydroxide, were trialled, again with little success.



**Figure 2.27. The structures of phosphorus pentasulfide (left) and the Lawesson's Reagent (right).**

Comparative studies on Lawesson's Reagent versus phosphorus pentasulfide have been widely discussed in synthetic organic and organometallic chemistry for the thiolation of carbonyl-containing compounds.<sup>227</sup> The mechanism by which these reagents are activated is analogous to the Wittig reaction in which the P-S-P bonds cleave to give two monomeric species which exists in equilibrium with their reactive zwitterionic states (Figure 2.28-Figure 2.29). The formation of the energetically favourable P=O bond is the driving force behind their reactivity. Though LR has several advantages over P<sub>2</sub>S<sub>5</sub>, such as shorter reaction times and lower quantities needed, it cannot be generally concluded which is the better thiolating agent, and so it is worth trialling both reagents for specific reactions.<sup>227</sup>

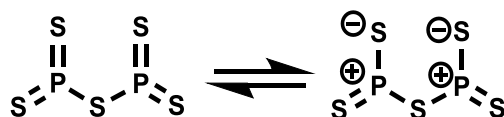


**Figure 2.28. Zwitterionic equilibrium of phosphorus(V)pentasulfide.**

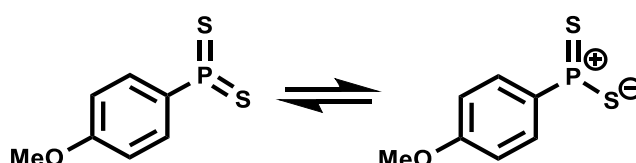


**Figure 2.29. Zwitterionic equilibrium of Lawesson's Reagent.**

Eventually, success was achieved in synthesising thioPyBOX ligands by following the protocol used by Nishio *et al*, which was the reaction of the hydroxy- amide and LR at reflux in toluene, under inert conditions, and importantly, in the absence of a base.<sup>217</sup> Furthermore, the importance of using at least an equimolar amount of LR to hydroxy-amide was highlighted, as given the hydroxy group is more reactive than the

amide. A substoichiometric quantity of LR would favour the thioamide product, and the cyclisation step would not proceed to the thiazoline.<sup>228</sup>

### 2.2.2.1 A Macrocyclic Product

In a repeated attempt of the adapted method employed in<sup>214</sup>, an unexpected product formed. Rather than the desired thioPyBOX ligand, a non-sulfur containing macrocycle was isolated (Figure 2.30). Only just enough of the material for <sup>1</sup>H NMR, HRMS and XRD analysis was crystallised.

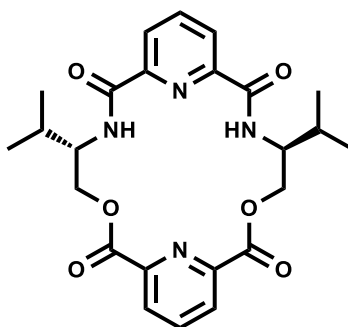


Figure 2.30. The structure of the macrocycle formed.

Considering the structure of the macrocycle (**M1**) as an extension of the amide, it is clear it had formed from the amide intermediate, which could have either reacted with itself, or with pyridine dicarbonyl dichloride (Figure 2.31). The latter option (reaction ii. In Figure 2.31) seems the most feasible, considering the acyl chloride has a more nucleophilic carbonyl group, and the chlorides are a better leaving-group, compared to the hydroxyamide. This macrocycle formation reaction has been previously reported in the literature. For example Gao *et al.*<sup>229</sup> used the nucleophilic catalyst 4-dimethylamino pyridine (DMAP) in the synthesis (Figure 2.32).

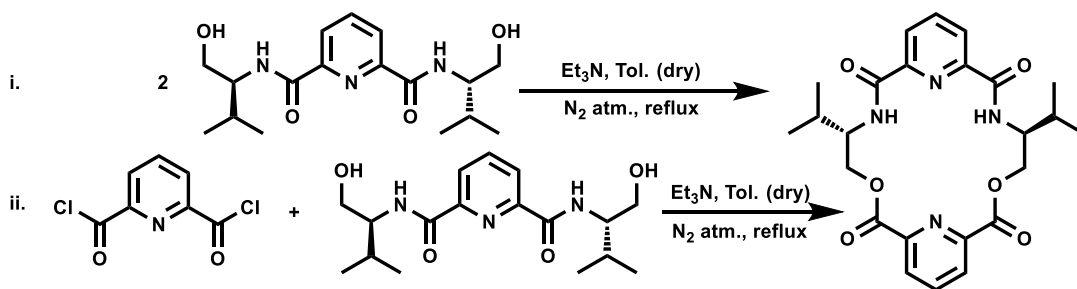


Figure 2.31. Two possible reaction pathways to synthesise M1.

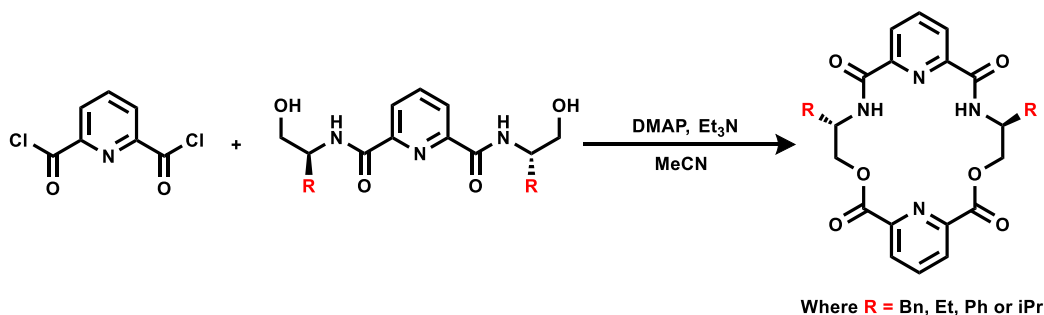
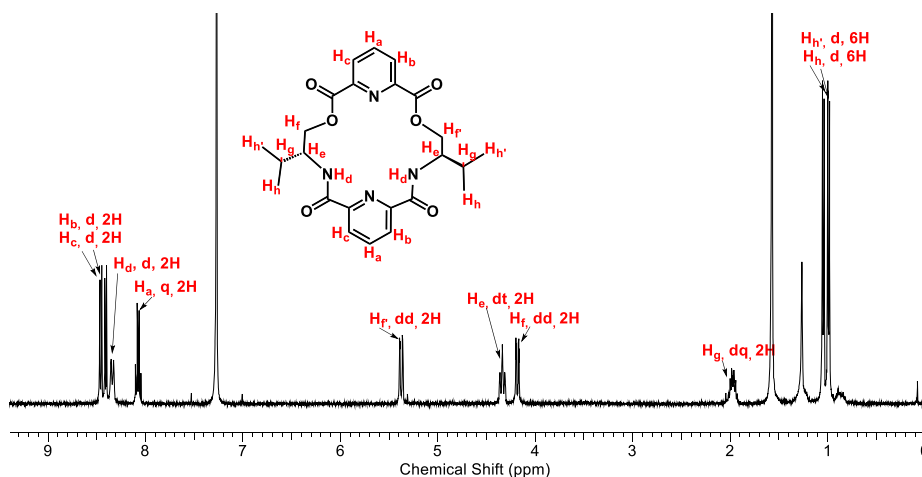


Figure 2.32. Synthesis of the macrocycle by Gao et al.<sup>229</sup>

Lawesson's Reagent was present in this reaction, as this was initially an attempt to synthesise thioPyBOX in toluene. However, it was noted that the thermocouple used in the experimental set up had failed to hold the reaction at the reflux temperature of 130 °C. Instead, the reaction did not exceed 108 °C over the 16 hours. Given LR is unstable above 110 °C,<sup>230</sup> it is clear the thiolating agent remained deactivated during this reaction and was simply a spectator, enabling the macrocycle formation. Additionally the formation of the macrocycle can be reasoned by the presence of triethylamine in the reaction. The triethylammonium cation has a pKa ≈ 10 for the dissociation of its proton to give triethylamine,<sup>231</sup> and so would readily deprotonate a carboxylic acid (pKa ≈ 5) driving the nucleophilic attack at the acyl chloride carbon, where there is no competing reaction.

Although not an objective in this thesis, **M1** is still a particularly interesting molecule as the tridentate nitrogen-structure could coordinate a base metal such as copper, as shown for other N<sub>3</sub>O<sub>2</sub><sup>-</sup> macrocyclic systems<sup>232</sup>. Such metal-macrocycle complex could prove beneficial in catalysis considering the larger structure could act as a host in host-guest chemistry.

The <sup>1</sup>H NMR spectrum of **M1** is shown below in Figure 2.33, confirming the structure in the solution state.



**Figure 2.33.**  $^1\text{H}$  NMR of the macrocycle.  $[\text{CDCl}_3, 400 \text{ MHz}]$ .

A single crystal suitable for X-ray Diffraction was grown by vapour diffusion of pentane into a concentrated sample of the macrocycle in dichloromethane. The molecular structure obtained from XRD collection is shown in Figure 2.34.

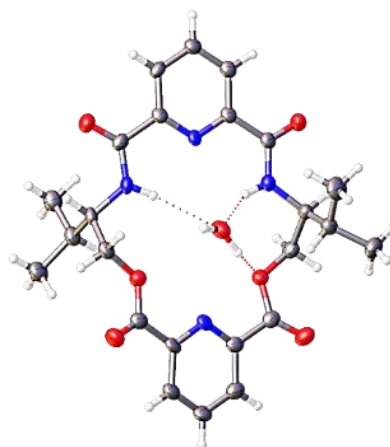


**Figure 2.34.** XRD structure of the macrocycle. Thermal ellipsoids are displayed at the 50% probability level.

The macrocycle was crystallised in a triclinic crystal system and was solved in the space group  $P1$  with two molecules in the unit cell. From the XRD structure, it is notable that a molecule of water sits in the cavity of the macrocycle, and is held by hydrogen bonds between the  $\text{N-H}\dots\text{O-H}$  and  $\text{O-H}\dots\text{O-C}$  groups. An XRD diagram of two macrocycles together show that there are intermolecular hydrogen bonds in the bulk crystalline material (Figure 2.35, left). The packing structure generated (Figure 2.35, right) further support this and shows favourable intermolecular interactions

between the isopropyl groups owing to van der Waals' forces of attraction between the macrocycle units. It is also clear that from the packing diagrams, particularly along the *b*- and *c*- axis that there is favourable offset  $\pi$ - $\pi$  stacking between the pyridine rings of each unit.

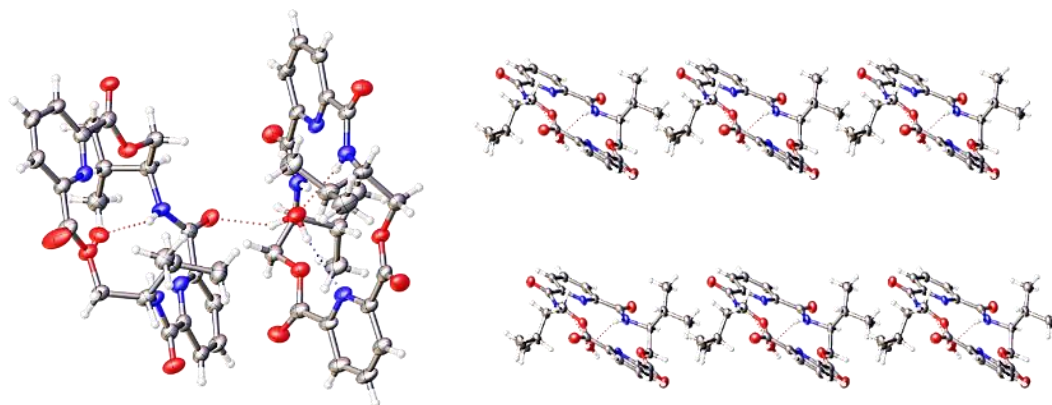


**Figure 2.35. Two molecules of M1 with hydrogen bonding shown (left) and a simplified packing diagram of M1 shown along the *a*-axis (right).**

#### 2.2.2.2 Reaction optimisation work

Since the thioPyBOX ligand was successfully synthesised, work towards reaction optimisation was carried out in order to achieve an optimal yield of ligand for ensuing metal complexation reactions.

Purification of the ligand was initially carried out by silica gel column chromatography as has been previously reported<sup>211-213</sup>, but employing a different mobile phase. TLC analysis showed that a good product separation was achieved when the eluent system was 10% dichloromethane and 90% acetonitrile. This gave clear separate bands on the column, a blue coloured one for the remnant phosphorus reagent and a yellow band, which elutes first, for the thioPyBOX ligand (Figure 2.36). The separation varied for the different analogues of the thioPyBOX ligand, with the phenyl- and *tert*butyl-thioPyBOX ligands giving modest separation, while the *isopropyl*-thioPyBOX ligand gave poor separation with the bands appearing more closely spaced.

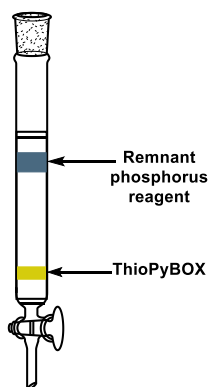


**Figure 2.36. Column chromatography separation of thioPyBOX ligands with 1:9 DCM:MeCN.**

Though a very useful and widely used method of purification, column chromatography is tedious and time-consuming, using large quantities of silica gel and solvents, while its efficacy is highly dependent on structural differences between the components of the mixture.

In attempts to find alternative methods of purifying the thioPyBOX ligands, it was found that for the phenyl-analogue, treatment of the crude product with an excess of acetone induced precipitation of the product from solution as a pale yellow powder, which could be cleanly collected by vacuum filtration. Excess acetone was also tested with the *tert*butyl- and *isopropyl*- analogues but did not yield the same results. Considering that alkyl groups tend to be more soluble in organic solvents compared to their aromatic counterparts, other solvents were trialed. From this test, it was found that the *tert*butyl- thioPyBOX ligand cleanly precipitates from an excess of acetonitrile. The *t*Bu- ligand isolates as a clean white precipitate, which is contrary to the literature which reports the ligand as a yellow solid.<sup>211, 214</sup>

Excess acetonitrile was tested with the *isopropyl*- ligand, considering its structural similarity to the *t*Bu- analogue. However, this was not successful and purification of the *isopropyl*- ligand still remains a challenge. Smaller quantities of the ligand, i.e. on the milligram scale, can be obtained by dissolution into pentane. However this was found to not work on a large scale.

The ligands were initially synthesised using no more than 100 mg of amide at a time, until a robust method of synthesis was achieved. On this scale the ligands formed in yields of 10-20%. Upon scaling up the reaction, such that the initial diamide quantity was in the range of 1-5 g, the yields generally improved up to around 40%.

An *in situ* method was also tested, where the diamide intermediate was not isolated after synthesis. Instead, the crude diamide was reacted directly with LR to give the corresponding (phenyl- substituted in this case) thioPyBOX ligand. In this

experiment, 12.25 g of (S,S)-phenylglycinol gave 7.25 g of (S,S)-thioPyBOX<sup>Ph</sup>. Assuming the average amide yield of 56%, this renders the theoretical mass of the ligand to be 10.1 g, which means the ligand was produced in a remarkable 72% yield. However, this of course cannot be taken to be the absolute value. Optimistically assuming the amide was produced *in situ* in a 100% yield, equalling to 18.1 g of amide, the yield of the ligand still reaches 40%. It is therefore more accurate to say the yield of the (S,S)-thioPyBOX<sup>Ph</sup> ligand from this experiment was no less than 40% and is most likely to be in the range of 40-72%, if not better. This exceeds the current record of 31% yield reported for the phenyl-thioPyBOX ligand.<sup>214, 218</sup>

### 2.2.3 Analysis and characterisation

The six thioPyBOX ligands synthesised are summarised in Figure 2.37. The identity of the compounds was confirmed by <sup>1</sup>H NMR, <sup>13</sup>C{<sup>1</sup>H} NMR, and HRMS. Additionally, XRD structures were obtained for the *isopropyl*- and *tert*butyl- thioPyBOX ligands which have not previously been reported. As all analysis is identical for each enantiomer of the same ligand, only one set of data per substituent is discussed below. The full analysis for all six ligands can be found in Section 2.4.

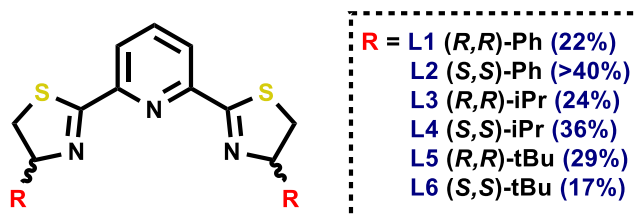


**Figure 2.37. Summary of the thioPyBOX ligands synthesised herein, L1-L6. Yields in parentheses.**

#### 2.2.3.1 NMR

The <sup>1</sup>H NMR spectra are shown in Figure 2.38- Figure 2.40.



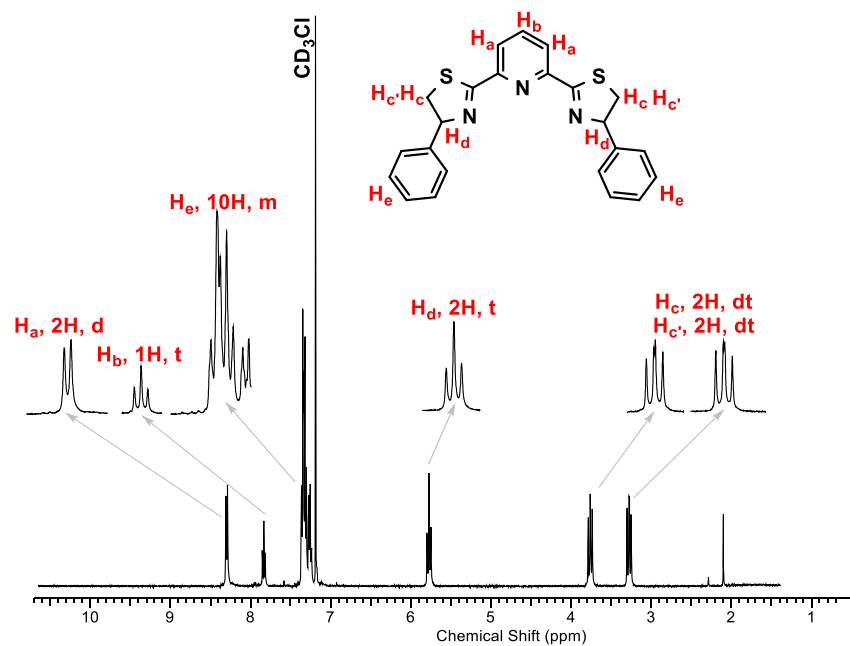


Figure 2.38. <sup>1</sup>H NMR of (S,S)-thioPyBOX<sup>Ph</sup>, L1. (400 MHz, CD<sub>3</sub>Cl)

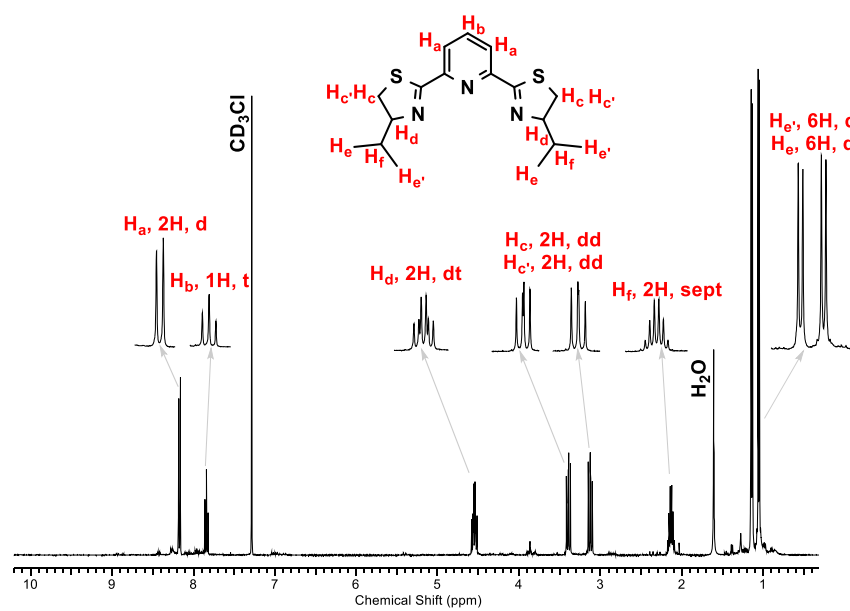


Figure 2.39. <sup>1</sup>H NMR of (S,S)-thioPyBOX<sup>iPr</sup>, L4. (400 MHz, CD<sub>3</sub>Cl)

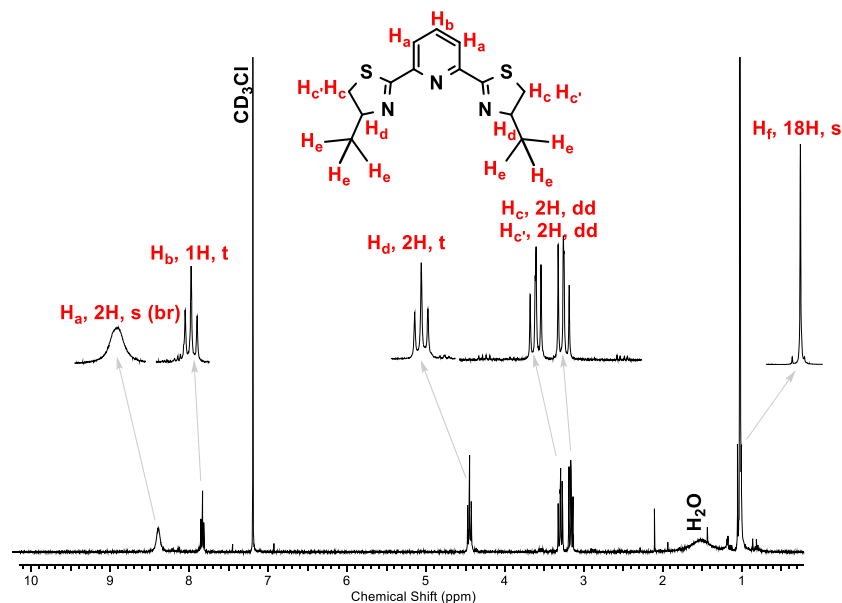
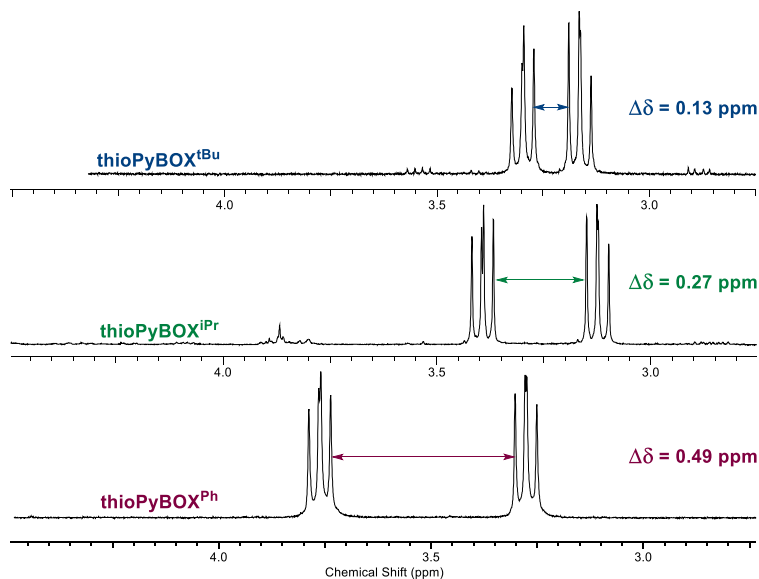


Figure 2.40. <sup>1</sup>H NMR of (R,R)- thioPyBOX<sup>tBu</sup>, L5. (400 MHz, CD<sub>3</sub>Cl)

The C<sub>2</sub>-symmetry of the thioPyBOX ligand reduces complexity in the NMR spectra. For example, though there are 19 protons in thioPyBOX<sup>Ph</sup> there are only 8 unique proton environments in the spectrum including the distinct *ortho*, *meta*, and *para* proton environments on the phenyl substituents. Equally, the thioPyBOX<sup>iPr</sup> spectra has 21 protons in 8 unique environments and thioPyBOX<sup>tBu</sup> has 27 protons in 6 environments. Each of the ligands shows a similar pattern of peaks with the three protons arising from the pyridine ring, appearing as a doublet with an integration of 2H and a triplet with an integration of 1H in the chemical shift range of 7.5-8.5 ppm, depending on the R- substituent. This is analogous to the PyBOX equivalent.<sup>233</sup> The two protons on the carbon adjacent to the sulfur atom (S-CH<sub>2</sub>-) are diastereotopically inequivalent owing to the adjacent stereogenic centre. This results in two separate peaks with geminal coupling constants in the range of 10-12 Hz, indicative of their proximity in the molecule. In thioPyBOX<sup>iPr</sup> the methyl substituents of the *isopropyl* group are also diastereotopically inequivalent, which is why these proton environments appears as two doublets with an integration of 6H each, rather than one doublet with an integration of 12H.

It is also worth noting there is a chemical shift difference,  $\Delta\delta$  ppm, between the diastereotopic S-CH<sub>2</sub>-C(H)R peaks across the three thioPyBOX derivatives, summarised in Figure 2.41. As the R- substituent changes from phenyl to *isopropyl* to *tert*butyl,  $\Delta\delta$  decreases which is consistent with the increased electron-donating effect of the substituents on the ligand. That is, in the order *tert*butyl > *isopropyl* > phenyl, where *tert*butyl is the most electron-donating/has the greatest positive inductive effect.



**Figure 2.41.**  $\Delta\delta$  ppm between the two doublets of doublets arising from  $-S-CH_2-CH-$  with different thiazoline R- substituents; *tert*butyl (top), *isopropyl* (middle) and phenyl (bottom).

Though the same number of peaks are evident in the  $^1H$  NMR spectrum of the  $PyBOX^{Ph}$  ligand compared the  $thioPyBOX$  equivalent, it is noteworthy that the three peaks upfield of the aromatic region appear at different chemical shifts to the  $thioPyBOX$  analogue as shown by the stacked spectra in Figure 2.42. There is greater disparity in chemical shifts between the  $=N-CH-Ph-$  and  $-S-CH_2-CH-$  protons, of  $thioPyBOX^{Ph}$  than with  $PyBOX^{Ph}$ , evidencing the strong influence on the electronic properties of the azoline ring system when switching oxygen for sulfur.

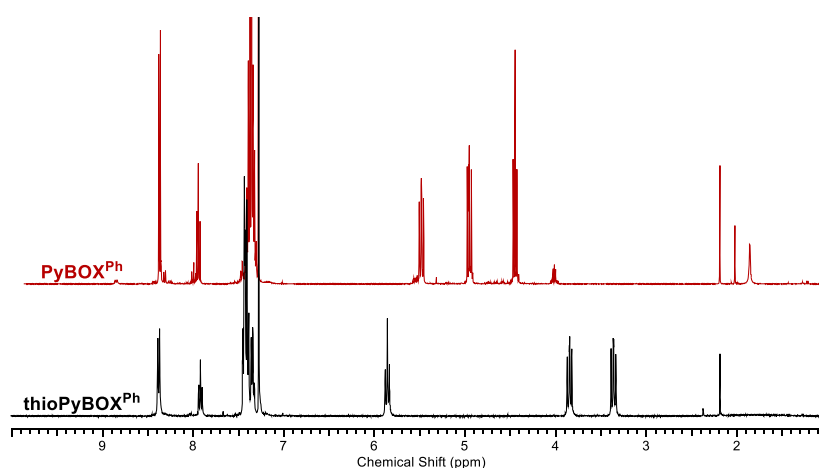


**Figure 2.42.**  $^1H$  NMR spectra of  $PyBOX^{Ph}$  (top, red) and  $thioPyBOX^{Ph}$  (bottom, black).

The same trend is observed for the PyBOX<sup>iPr</sup>/thioPyBOX<sup>iPr</sup> (Figure 2.43) and PyBOX<sup>tBu</sup>/thioPyBOX<sup>tBu</sup> (Figure 2.44) <sup>1</sup>H NMR spectra when compared.

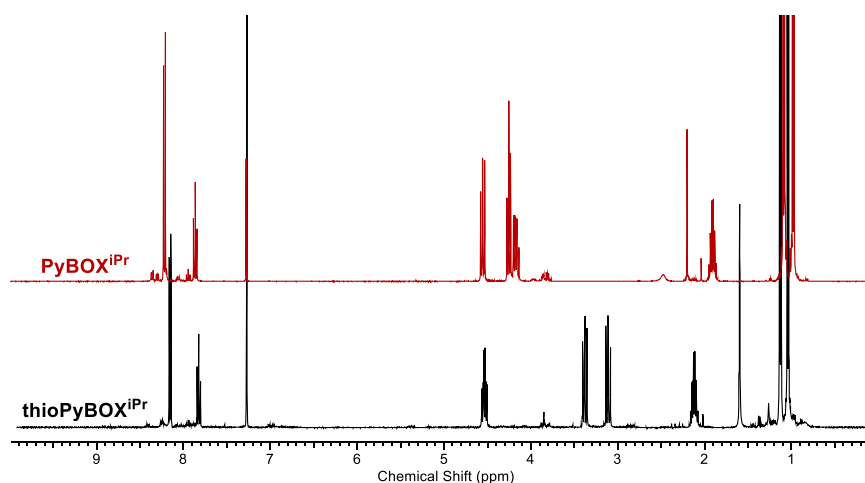


Figure 2.43. <sup>1</sup>H NMR spectra of PyBOX<sup>iPr</sup> (top, red) and thioPyBOX<sup>iPr</sup> (bottom, black).

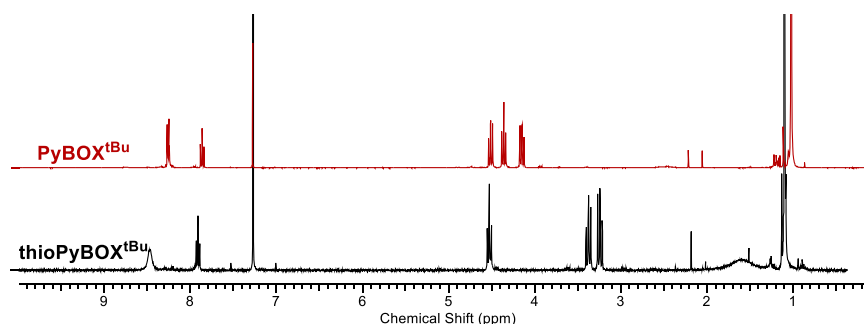
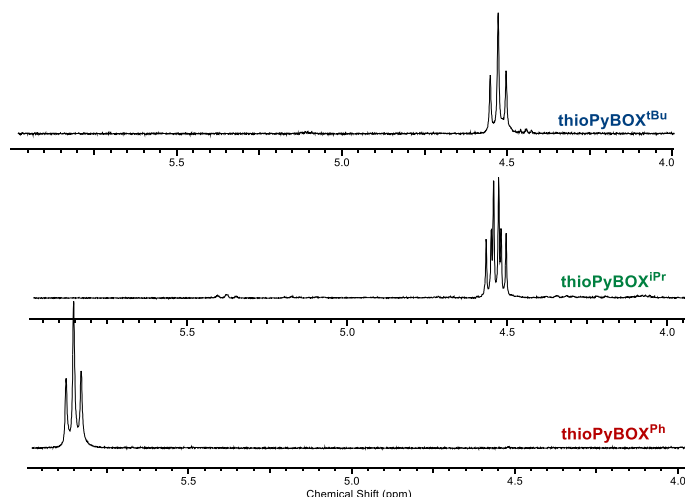


Figure 2.44. <sup>1</sup>H NMR spectra of PyBOX<sup>tBu</sup> (top) and thioPyBOX<sup>tBu</sup> (bottom).

Another interesting point of comparison from the <sup>1</sup>H NMR spectra of the three thioPyBOX ligands is the peak that arises from the proton on the chiral carbon centre of the thiazoline, -CH<sub>2</sub>-CH-R. The splitting of this proton for both the *tert*butyl- and phenyl- derivatives appears as a triplet due to the adjacent -CH<sub>2</sub> protons with no other protons within a <sup>3</sup>J coupling distance, which can be clearly seen in the spectra. However for the *isopropyl*- thioPyBOX, this splitting is now a doublet of triplets due to additionally splitting of the -CH(CH<sub>3</sub>)<sub>2</sub> proton (Figure 2.45). This proton on the phenyl- analogue is also significantly de-shielded due to the electron-withdrawing effect of the phenyl rings, which shifts this peak downfield by >1 ppm as can be seen in Figure 2.45.



**Figure 2.45. Comparison the  $-\text{CH}_2-\underline{\text{CH}}-\text{R}$  peak in the  $^1\text{H}$  NMR spectra of the thioPyBOX ligands; thioPyBOX<sup>Ph</sup> (bottom), thioPyBOX<sup>iPr</sup> (middle) and thioPyBOX<sup>tBu</sup> (top).**

The same comparison can be made between the analogous PyBOX ligands, which shows the same proton as a triplet in the tBu- and Ph- ligands, but also is now a triplet in the iPr- ligand too (Figure 2.46). The exchanged positions of the proton environments  $-\text{CH}_2-\underline{\text{CH}}-\text{R}$  and  $-\text{CH}_2-\underline{\text{CH}}-\text{R}$  in PyBOX compared to thioPyBOX can be understood by the proximity to the much more electronegative oxygen atom in the oxazoline ring which greatly deshields neighbouring protons, more than sulphur would do in thiazoline. It can be reasoned that the greater polarity difference across the  $-\text{O}-\text{CH}_2-\underline{\text{CH}}-\text{R}$  chain means that the splitting of the  $\underline{\text{CH}}$  by the more polarised  $\text{CH}_2$  group dominates over any secondary splitting effect from the  $-\underline{\text{CH}}(\text{CH}_3)_2$  proton in the PyBOX<sup>iPr</sup> ligand.

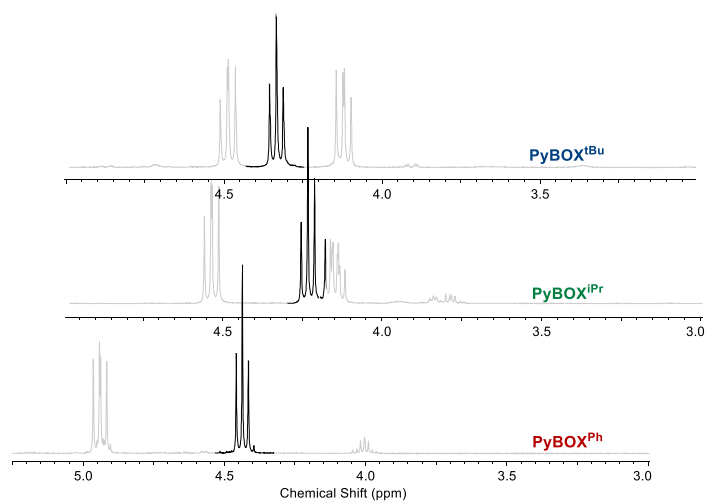


**Figure 2.46. Comparison the  $-\text{CH}_2-\underline{\text{CH}}-\text{R}$  peak in the  $^1\text{H}$  NMR spectra of the PyBOX ligands; PyBOX<sup>Ph</sup> (bottom), PyBOX<sup>iPr</sup> (middle) and PyBOX<sup>tBu</sup> (top) (highlighted in black for clarity).**

### 2.2.3.2 XRD

Yellow, needle-like, crystals, of (*S,S*)-thioPyBOX<sup>iPr</sup>, **L4**, suitable for XRD, were obtained by vapour diffusion of diethyl ether into a concentrated solution of the ligand in acetonitrile. **L4** was crystallised in a monoclinic crystal system and was solved in the space group *P2*<sub>1</sub>, with 4 ligands in the unit cell. The structure obtained is shown in Figure 2.47 and selected bond lengths and angles are tabulated below in Table 2.2.

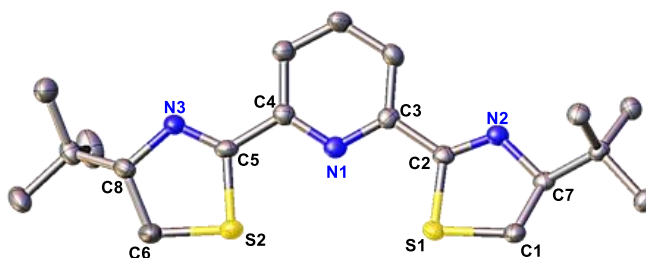


**Figure 2.47.** XRD structure collected of one of the unique molecules in the structure of (*S,S*)-thioPyBOX<sup>iPr</sup>, **L4**. Hydrogen atoms are omitted for clarity. Thermal ellipsoids are displayed at the 50% probability level.

Bond	Bond length (Å)	Angle	Bond Angle (°)
<b>N2-C3</b>	1.334(18)	<b>S1-C2-N1</b>	119.8(12)
<b>N2-C4</b>	1.346(19)	<b>S2-C5-N3</b>	118.8(10)
<b>N1-C2</b>	1.256(17)	<b>C1-S1-C2</b>	90.3(7)
<b>N3-C5</b>	1.275(16)	<b>C6-S2-C5</b>	89.4(8)
<b>S1-C1</b>	1.827(15)	<b>C3-N2-C4</b>	119.2(14)
<b>S1-C2</b>	1.756(16)	<b>C7-C1-S1</b>	104.5(9)
<b>S2-C6</b>	1.813(15)	<b>C8-C6-S2</b>	108.2(11)
<b>S2-C5</b>	1.735(16)		

**Table 2.2.** Selected bond lengths and angles for one of the unique molecules in **L4** (Figure 2.47). ESDs shown in parentheses.

Aside from the *isopropyl* substituents, the ligand is mostly planar, which is ideal for metal coordination. The C-S bonds are 1.7-1.8 Å, which is significantly longer than both species of C-N bonds owing to the larger atomic radius of the sulfur atom. The presence of the C=N bond is confirmed by the shorter bond length of 1.26-1.27 Å compared to 1.33-1.35 Å for the single C-N bond. The bond angles of S1-C2-N1 and S2-C5-N3 are 120 ° as expected for an *sp*<sup>2</sup> hybridised carbon with a trigonal planar geometry, whereas, the C7-C1-S1 and C8-C6-S2 angles are more fitting to an *sp*<sup>3</sup>

hybridised carbon atom. The geometry about the sulfur atoms are  $90^\circ$  which reflects the influence of the larger lone pairs on the geometry of an S atom.<sup>234</sup>

Though one molecule is shown in Figure 2.47 for clarity, there are actually two molecules in the asymmetric unit cell, which sit offset and upside-down from one another (Figure 2.48). Furthermore, considering the packing structure, it is clear that this positioning facilitates optimal  $\pi$ - $\pi$  stacking, in addition to the *isopropyl* interactions, across the bulk sample (Figure 2.49).

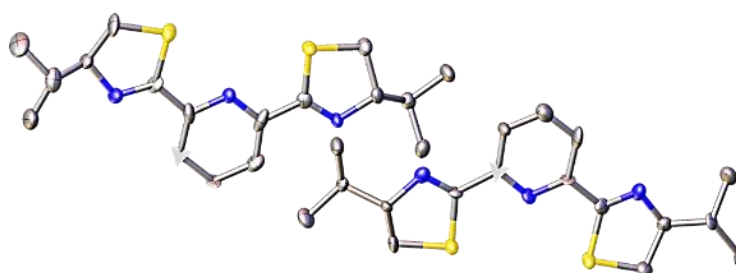


**Figure 2.48. XRD structure of two ligands, L4.**

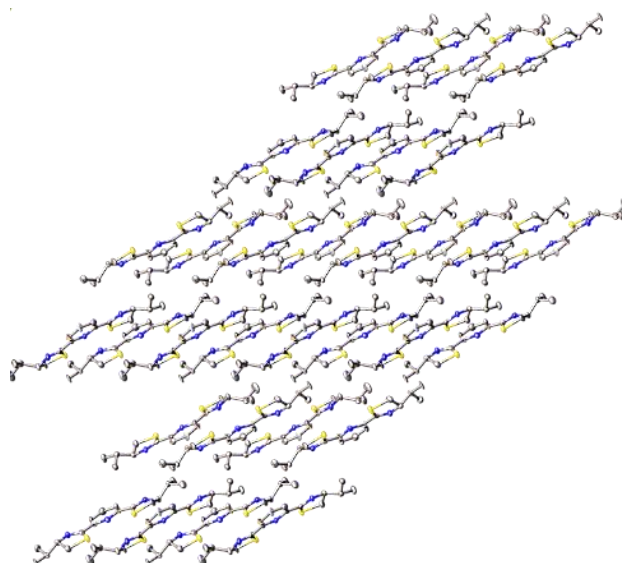


**Figure 2.49. XRD packing diagram of L4, viewed along the *b*-axis.**

This structure can be compared to that obtained of the (*S,S*)-thioPyBOX<sup>tBu</sup>, **L6** (Figure 2.50), which, unsurprisingly, looks analogous to its *isopropyl* counterpart. Though it was crystallised in an orthorhombic crystal system and was solved in the space group  $P2_12_12_1$ , there are also 4 ligands in the unit cell and the bond lengths and angles (Table 2.3) are akin to that for **L4**.

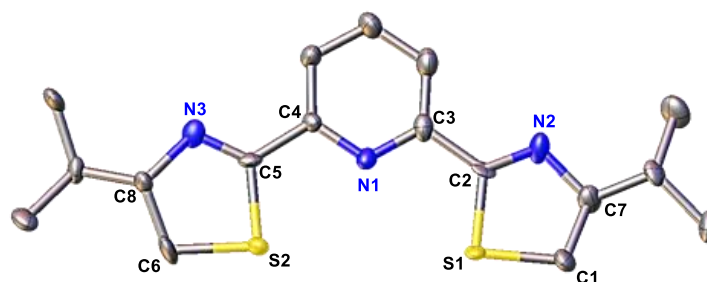


Figure 2.50. XRD structure collected of (S,S)-thioPyBOX<sup>tBu</sup>, L6. Hydrogen atoms are omitted for clarity. Thermal ellipsoids are displayed at the 50% probability level.

Bond	Bond length (Å)	Angle	Bond Angle (°)
N1-C3	1.339(4)	S1-C2-N2	118.5(2)
N1-C4	1.340(4)	S2-C5-N3	118.4(2)
N2-C2	1.266(4)	C1-S1-C2	88.51(16)
N3-C5	1.266(4)	C6-S2-C5	88.60(14)
S1-C1	1.807(4)	C3-N1-C4	117.7(3)
S1-C2	1.778(3)	C7-C1-S1	107.0(2)
S2-C6	1.818(3)	C8-C6-S2	106.3(2)
S2-C5	1.780(3)		

Table 2.3. Selected bond lengths and angles for the XRD structure of L6 (Figure 2.50). ESDs shown in parentheses.

The crystallographic data obtained are consistent with those previously discussed for **L4** and show almost identical values for the bond lengths and angles. However the difference in packing of the structure of **L6** (Figure 2.51) arises from the different unit cell systems. Although both crystals show the same alkyl group intermolecular interactions, there are less  $\pi$ - $\pi$  interactions in **L6** indicating that the *tert*butyl Van der Waals interactions dominate the crystal packing. Two molecules of **L6** and the packing diagram are observed in Figure 2.51, unlike with **L4** in Figure 2.48, where the ligands are both facing in the same direction. These differences can be attributed to the added steric bulk from the *tert*butyl substituents, which is evident from the more spaced out packing diagram.



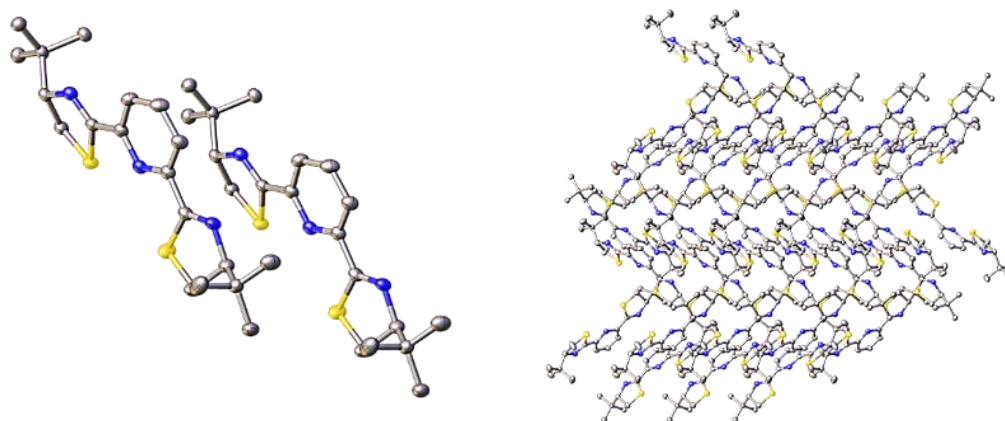


**Figure 2.51.** XRD structures of two ligands, L6 (left) and packing diagram of L6, viewed along the *b*-axis (right).

A co-crystallised structure of (*S,S*)-thioPyBOX<sup>tBu</sup>•(*R,R*)-thioPyBOX<sup>tBu</sup> (**L5•L6**) was obtained from a reaction attempt of the heterochiral iron complex [Fe(**L5**)(**L6**)]([ClO<sub>4</sub>])<sub>2</sub>. The XRD structure is shown in Figure 2.52 with selected bond lengths and bond angles tabulated in Table 2.4 and Table 2.5.

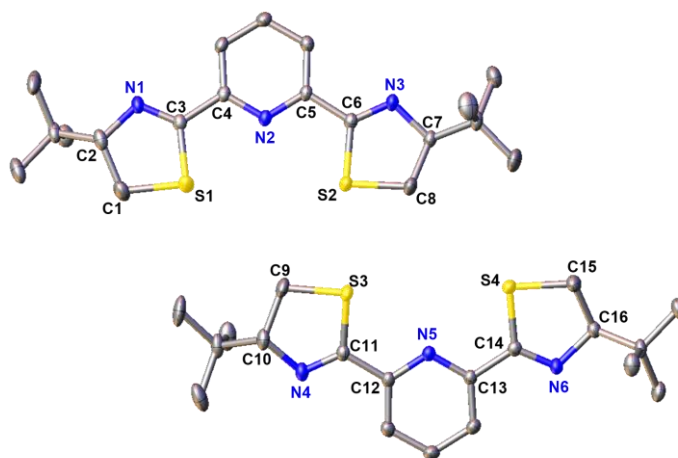


**Figure 2.52.** XRD structure of L5•L6. Hydrogen atoms are omitted for clarity. Thermal ellipsoids are displayed at the 50% probability level.

Enantiomer 1		Enantiomer 2	
Bond	Bond length (Å)	Bond	Bond length (Å)
N2-C5	1.3443(19)	N5-C12	1.3471(19)
N2-C4	1.3394(19)	N5-C13	1.3427(19)
N3-C6	1.271(2)	N6-C14	1.271(2)
N1-C3	1.272(2)	N4-C11	1.274(2)
S1-C3	1.7658(16)	S3-C11	1.7647(16)
S1-C1	1.8169(17)	S3-C9	1.8158(16)
S2-C6	1.7629(16)	S4-C14	1.7662(15)
S2-C8	1.8183(16)	S4-C15	1.8171(16)

Table 2.4. Selected bond lengths for the XRD structure of L5•L6 (Figure 2.52). ESDs shown in parentheses.

Enantiomer 1		Enantiomer 2	
Angle	Bond Angle (°)	Angle	Bond Angle (°)
S1-C3-N1	118.92(12)	S3-C11-N4	119.23(12)
S2-C6-N3	119.08(12)	S4-C14-N6	118.73(12)
C1-S1-C3	88.91(8)	C9-S3-C11	88.68(8)
C8-S2-C6	88.67(7)	C15-S4-C14	89.15(7)
C4-N5-C5	117.25(13)	C12-N5-C13	116.75(13)
C7-C8-S2	105.83(11)	C10-C9-S3	105.90(11)
C2-C1-S1	106.04(11)	C16-C15-S4	105.95(11)

Table 2.5. Selected bond angles for the XRD structure of L5•L6 (Figure 2.52). ESDs shown in parentheses.

As a final study, the XRD structures of L4 and L6 were overlaid for comparison (Figure 2.53). As expected, only minimal differences are evident in their structure solutions, and these are at the substituents and the thiazoline ring where there is an increased steric bulk in L6.

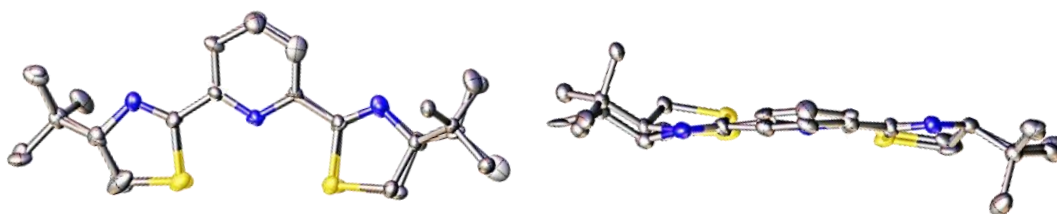


Figure 2.53. Overlay XRD structures of L4 and L6 .

## 2.3 Conclusion

A comparative study on PyBOX versus its sulfur analogue, thioPyBOX has been discussed and the design and development of the thioPyBOX ligand family is the core of this chapter. The eight pieces of existing literature on synthetic routes to the thioPyBOX ligand has been discussed in this chapter and the method of synthesis employed herein follows that first demonstrated by Nishio *et al.* using Lawesson's Reagent.<sup>217</sup> Although the majority of the yields reported are lower or on par with the literature, the phenyl derivative was synthesised in a yield higher than has yet been reported. Furthermore, a facile method of purification has been established for the phenyl- and *tert*butyl- derivatives that removes the need of column chromatography. Six thioPyBOX ligands have been synthesised bearing three different substituents, each in two enantiomeric forms. These have been fully characterised by <sup>1</sup>H NMR, <sup>13</sup>C NMR, HRMS and elemental analysis. In addition, three XRD structures contributing to the thioPyBOX library have been reported, (S,S)-thioPyBOX<sup>iPr</sup> (**L4**), (S,S)-thioPyBOX<sup>tBu</sup> (**L6**) and a co-crystallised structure of (S,S)-thioPyBOX<sup>tBu</sup>•(R,R)-thioPyBOX<sup>tBu</sup>. In exploration of synthetic routes to thioPyBOX synthesis, a macrocycle has been isolated and characterised by the standard methods including X-ray crystallography.

## 2.4 Experimental

All reactions in this thesis were performed either under ambient conditions, or under inert conditions using a standard Schlenk and inert atmosphere techniques. All commercially available reagents were used without further purification. Dry solvents were obtained from the University of Leeds Solvent Purification System. <sup>1</sup>H and <sup>13</sup>C NMR experiments in this chapter were conducted on a two-channel Bruker AV3HD NMR spectrometer operating at 9.4 T (400 MHz <sup>1</sup>H, 100 MHz <sup>13</sup>C) and equipped with a 5 mm Broad Band Probe.

Elemental microanalysis was performed by Stephen Boyer at London Metropolitan University. Mass spectrometry was performed using a Bruker Daltonics (micro T.O.F) instrument operating in the positive ion electrospray mode and the spectra were acquired over the m/z range of 50 - 4000. All spectra were recorded using methanol or acetonitrile as the eluent and a sodium formate solution to calibrate the system. Experimental details of X-ray Diffraction are outlined in the Appendix.

### 2.4.1 Di(hydroxyl)pyridine-2,6-dicarboxamide

Adapted from Towers *et al.* <sup>224</sup>

#### A1. **N,N'-bis[(1R)-2-hydroxy-1-phenylethyl]-pyridine-2,6-dicarboxamide.**

Potassium hydrogen carbonate (5.15g, 0.051 mols, 1.6 eq.) was dissolved in water (20 mL) with stirring. Separately, (R)-2-phenylglycinol (5 g, 0.036 mols, 1.1 eq.) was dissolved in ethyl acetate (60 mL) at room temperature. The base solution was then added to the phenylglycinol and gently heated to 55 °C. Separately, 2,6-pyridinedicarbonyl dichloride (6.54 g, 0.032 mols, 1 eq.) was dissolved in chloroform (30 mL) to give a cloudy solution which was heated to 70 °C to aid dissolution. This solution was added to the deprotonated aminoalcohol dropwise over a period of 10 minutes. Once all the white fumes of hydrogen chloride were no longer visible, the reaction mixture was heated under reflux overnight (16 hrs, 85 °C). The reaction was then left to cool to room temperature before being left to stir overnight (16 hrs, 20 °C), producing a clear pale yellow solution. The sample was then extracted from ethyl acetate (2x30 mL) and the aqueous layer was treated with excess dilute hydrochloric acid which was then re-extracted with ethyl acetate. The organic layers were combined, dried by addition of excess anhydrous magnesium sulphate, filtered by gravity filtration and the solvent was removed by rotary evaporation to give an off-white residue. Diethyl ether was added to the residue and was stirred, producing a white precipitate which was collected by vacuum filtration. Yield = 5.98g (81%). **<sup>1</sup>H NMR (400 MHz, CDCl<sub>3</sub>)** δ 8.26 (d, J = 8 Hz, 2H), 7.96 (t, J = 8 Hz, 1H), 7.34-7.23 (m, 10H), 5.18 (dt, J = 8, 12 Hz, 2H), 3.93 (dd, J = 4, 8 Hz, 4H). Full characterisation has been previously reported by Hermange *et al.* <sup>235</sup>

#### A2. **N,N'-Bis[(1S)-2-hydroxy-1-phenylethyl]-pyridine-2,6-dicarboxamide.**

Prepared according to the procedure for A1 using 2,6-pyridinedicarbonyl dichloride (3.77 g, 18.5 mmols, 1eq.) in chloroform (20 mL), (S)-2-phenylglycinol (5 g, 36.4 mmols, 1.97 eq.) in ethyl acetate (50 mL) and potassium hydrogen carbonate (3.92 g, 39.2 mmols, 2.1 eq.) in water (20 mL). Yield = 2.94g (39%). **<sup>1</sup>H NMR (400 MHz, CDCl<sub>3</sub>)** δ 8.36 (d, J = 8 Hz, 2H), 8.06 (t, J = 8 Hz, 1H), 7.42-7.32 (m, 10H), 5.27 (dt, J = 2, 5 Hz, 2H), 4.04 (d, J = 5 Hz, 4H).

#### A3. **N,N'-Bis[(1R)-1-(hydroxymethyl)-2-methylpropyl]-pyridine-2,6-dicarboxamide.**

Prepared according to the procedure for A1 using 2,6-pyridinedicarbonyl dichloride (3 g, 14.7 mmols, 1eq.) in chloroform (15 mL), (D)-valinol (3.2 mL, 29.0 mmols, 1.97 eq.) in ethyl acetate (30 mL) and potassium hydrogen carbonate (3.09 g, 30.9 mmols, 2.1 eq.) in water (15 mL). Yield = 2.14g (43%). **<sup>1</sup>H NMR (400 MHz, CDCl<sub>3</sub>)** δ 8.35 (d, J = 8 Hz, 2H), 8.06 (q, J = 8 Hz, 1H), 3.95 (dt, J = 4, 12 Hz, 2H), 3.85 (dt, J = 4, 12 Hz, 4H), 2.34 (s (br), 4H), 2.09 (sept, J = 7 Hz, 2H), 1.04 (dd, J = 2, 9 Hz, 12H).

**A4. N,N'-Bis[(1S)-1-(hydroxymethyl)-2-methylpropyl]-pyridine-2,6-dicarboxamide.** Prepared according to the procedure for A1 using 2,6-pyridinedicarbonyl dichloride (0.75 g, 3.7 mmols, 1eq.) in chloroform (5 mL), (L)-valinol (0.8 mL, 7.3 mmols, 1.97 eq.) in ethyl acetate (25 mL) and potassium hydrogen carbonate (0.79 g, 7.8 mmols, 2.1 eq.) in water (5 mL). Yield = 0.70 g (56%). <sup>1</sup>H NMR (400 MHz, CDCl<sub>3</sub>) δ 8.33 (d, J = 7.5 Hz, 2H), 8.05 (q, J = 7.5 Hz, 1H), 3.95 (dt, J = 3, 8 Hz, 2H), 3.84 (dt, J = 4, 11 Hz, 4H), 2.61 (s (br), 2H), 2.09 (sept, J = 7 Hz, 2H), 1.04 (dd, J = 1, 7 Hz, 12H).

**A5. N,N'-Bis[(1R)-1-(hydroxymethyl)-2,2-dimethylpropyl]-pyridine-2,6-dicarboxamide.** Prepared according to the procedure for A1 using 2,6-pyridinedicarbonyl dichloride (0.88g, 4.3 mmols, 1eq.) in chloroform (5 mL), (D)-tert-leucinol (0.99 g, 8.4 mmols, 1.96 eq.) in ethyl acetate (25 mL) and potassium hydrogen carbonate (0.95 g, 9.5 mmols, 2.2 eq.) in water (5.4 mL). Yield = 1.01 g (64%). <sup>1</sup>H NMR (400 MHz, CDCl<sub>3</sub>) δ 8.02 (d, J = 8 Hz, 2H), 7.85 (t, J = 8 Hz, 1H), 4.94 (s, br, 2H), 3.87 (d, J = 12 Hz, 4H), 3.65 (t, J = 8, 12 Hz, 2H), 0.94 (s, 18H).

**A6. N,N'-Bis[(1S)-1-(hydroxymethyl)-2,2-dimethylpropyl]-pyridine-2,6-dicarboxamide.** Prepared according to the procedure for A1 using 2,6-pyridinedicarbonyl dichloride (0.88g, 4.3 mmols, 1eq.) in chloroform (5.4 mL), (L)-tert-leucinol (1.01 g, 8.6 mmols, 2 eq.) in ethyl acetate (25 mL) and potassium hydrogen carbonate (0.93 g, 9.3 mmols, 2.2 eq.) in water (5.4 mL). Yield = 1.17 g (74%). <sup>1</sup>H NMR (400 MHz, CDCl<sub>3</sub>) δ 8.00 (d, J = 8 Hz, 2H), 7.91 (t, J = 8 Hz, 1H), 3.89 (d, J = 12 Hz, 4H), 3.67 (t, J = 8, 12 Hz, 2H), 0.97 (s, 18H).

#### 2.4.2 Macrocyclic, M1

**M1.** The following procedure was carried out under N<sub>2</sub> atmosphere. N,N'-bis[(1R)-2-hydroxy-1-phenylethyl]-pyridine-2,6-dicarboxamide, A1, (83.2 mg, 0.25 mmol) was added to the Lawesson's reagent (100mg, 0.25 mmol) with triethylamine (1 mL, 13.5 mmol) in toluene (dry) (25 mL) and was heated overnight with stirring (108 °C, 17 hrs). Upon which the initially yellow solution had turned dark brown. The reaction mixture was left to cool to room temperature, by which point a solid had formed at the bottom of the reaction flask whilst the solvent floated above. The solvent was decanted, rotary evaporated to dryness and the remaining oily residue purified by column chromatography; stationary phase: silica gel and mobile phase: 10 % dichloromethane and 90 % acetonitrile. The fractions containing the compound were collected and combined and crystallised by vapour diffusion of pentane into dichloromethane. <sup>1</sup>H NMR (400 MHz, CDCl<sub>3</sub>) δ 8.46 (d, J = 8 Hz, 2H), 8.41 (d, J = 8 Hz, 2H), 8.34 (d (broad), J = 8 Hz, 2H), 8.07 (q, J = 4, 8 Hz, 2H), 7.27 (CDCl<sub>3</sub>), 5.37

(dd, J = 12 Hz, 2H), 4.34 (tt (broad), J = 8, 12 Hz, 2H), 4.18 (dd, J = 4, 12 Hz, 2H), 1.97 (m, 2H), 1.57 (H<sub>2</sub>O), 1.26 (s, 3H), 1.05 (d, J = 4 Hz, 6H), 0.99 (d, J = 8 Hz, 6H). **HRMS [ES]<sup>+</sup> [M+H]<sup>+</sup> Predicted: 469.2042 Found: 469.2086.**

### 2.4.3 2,6-Bis(thiazoliny)pyridine – ThioPyBOX

**L1. 2,6-Bis[(4R)-4-phenyl-4,5-dihydro-1,3-thiazol-2-yl]-pyridine.** The following procedure was carried out under anhydrous conditions. N,N'-bis[(1R)-2-hydroxy-1-phenylethyl]pyridine-2,6-dicarboxamide, A1 (4.0 g, 9.83 mmol, 1 eq.) was combined with the Lawesson's reagent (4.9 g, 12.0 mmol, 1.2 eq.) and was flushed with nitrogen before the addition of dry toluene (70 mL). The reaction was heated under reflux (24 hrs, 130 °C) and then left to stir at room temperature (24 hrs, 20 °C) producing a clear bright yellow solution. The solution was washed with water (2x20 mL), the toluene layer collected and the remnant yellow product from the water layer was extracted with dichloromethane (10 mL) and combined with the toluene layer. The organic layers were dried with magnesium sulphate, filtered by gravity and the solvent was removed by rotary evaporation producing a yellow-brown residue. Excess acetone was added to the residue and was allowed to sit in the fridge for 1 hour, before being filtered under vacuum to give a pale yellow precipitate. Yield = 0.85 g (22 %). **<sup>1</sup>H NMR (400 MHz, CDCl<sub>3</sub>)** δ 8.28 (d, J = 8 Hz, 2H), 7.87 (t, J = 8 Hz, 1H), 7.44-7.31 (m, 10H), 5.83 (t, J = 9 Hz, 2H), 3.82 (dd, J = 2, 11 Hz, 2H), 3.33 (dd, J = 2, 11 Hz, 2H). **<sup>13</sup>C NMR (100 MHz, CDCl<sub>3</sub>)** δ 170.9, 150.5, 141.9, 137.1, 128.7, 127.7, 126.6, 123.3, 81.4, 39.8. **HRMS [ES]<sup>+</sup> [M+H]<sup>+</sup> Predicted: 402.1054 Found: 402.1108. Elemental analysis calculated (%) C 68.80, H 4.77, N 10.46; found C 68.67, H 4.84, N 10.36.**

**L2. 2,6-Bis[(4S)-4-phenyl-4,5-dihydro-1,3-thiazol-2-yl]-pyridine.** Prepared according to the procedure for L1 using N,N'-bis[(1S)-2-hydroxy-1-phenylethyl]pyridine-2,6-dicarboxamide, A2 (10.2 g, 0.025 mol, 1 eq.), Lawesson's reagent (18 g, 0.045 mol, 1.8 eq.) and dry toluene (90 mL). Yield = 7.3 g (40-72 %). **<sup>1</sup>H NMR (400 MHz, CDCl<sub>3</sub>)** δ 8.38 (d, J = 8 Hz, 2H), 7.92 (t, J = 8 Hz, 1H), 7.45-7.32 (m, 10H), 5.86 (t, J = 9 Hz, 2H), 3.85 (dd, J = 2, 11 Hz, 2H), 3.36 (dd, J = 2, 11 Hz, 2H). **<sup>13</sup>C NMR (100 MHz, CDCl<sub>3</sub>)** δ 171.9, 150.1, 141.5, 137.5, 128.9, 128.0, 126.7, 124.0, 80.8, 39.6. **HRMS [ES]<sup>+</sup> [M+H]<sup>+</sup> Predicted: 402.1054 Found: 402.1105. Elemental analysis calculated (%) C 68.80, H 4.77, N 10.46; found C 68.67, H 4.67, N 10.35.**

**L3. 2,6-Bis[(4R)-4-iso-propyl-4,5-dihydro-1,3-thiazol-2-yl]-pyridine.** The following procedure was carried out under anhydrous conditions. N,N'-Bis[(1R)-1-(hydroxymethyl)-2-methylpropyl]-pyridine-2,6-dicarboxamide, A3 (0.52 g, 1.54 mmol, 1 eq.) was combined with the Lawesson's reagent (0.85 g, 2.10 mmol, 1.4 eq.) and

was flushed with nitrogen before the addition of dry toluene (40 mL). The reaction was heated under reflux (24 hrs, 130 °C) and then left to stir at room temperature (8 hrs, 20 °C) producing a clear bright yellow solution. The solution was washed with water (2x20 mL), the toluene layer collected and the remnant yellow product from the water layer was extracted with dichloromethane (10 mL) and combined with the toluene layer. The organic layers were dried with magnesium sulphate, filtered by gravity and the solvent was removed by rotary evaporation producing a yellow residue. The product was purified by column chromatography on silica, with a 1:9 dichloromethane:acetonitrile eluent. The solvent was removed from the collected fractions yielding a yellow powder. Yield = 0.13g (24%). **<sup>1</sup>H NMR (400 MHz, CDCl<sub>3</sub>)** δ 8.14 (d, J = 8 Hz, 2H), 7.81 (t, J = 8 Hz, 1H), 4.52 (dt, J = 8, 12 Hz, 2H), 3.36 (dd, J = 8, 12 Hz, 2H), 3.09 (dd, J = 8, 12 Hz, 2H), 2.10 (sept, J = 4, 8 Hz, 2H), 1.10 (d, J = 8 Hz, 6H) 1.02 (d, J = 8 Hz, 6H). **<sup>13</sup>C NMR (100 MHz, CDCl<sub>3</sub>)** δ 169.0, 150.5, 137.0, 123.0, 84.5, 34.0, 33.4, 19.7, 18.9. **HRMS [ES] + [M+H] +** Predicted: 334.1367 Found: 334.1445. **Elemental analysis** calculated (%) C 61.22, H 6.95, N 12.60; found C 61.04, H 6.82, N 12.46.

**L4. 2,6-Bis[(4S)-4-iso-propyl-4,5-dihydro-1,3-thiazol-2-yl]-pyridine.** The following procedure was carried out under anhydrous conditions. N,N'-Bis[(1S)-1-(hydroxymethyl)-2-methylpropyl]-pyridine-2,6-dicarboxamide, A4 (0.6 g, 1.78 mmol, 1 eq.) was combined with the Lawesson's reagent (0.81 g, 2.0 mmol, 1.1 eq.) and was flushed with nitrogen before the addition of dry toluene (30 mL). The reaction was heated under reflux (24 hrs, 130 °C) and then left to stir at room temperature (8 hrs, 20 °C) producing a clear bright yellow solution. The solution was washed with water (2x20 mL), the toluene layer collected and the remnant yellow product from the water layer was extracted with dichloromethane (10 mL) and combined with the toluene layer. The organic layers were dried with magnesium sulphate, filtered by gravity and the solvent was removed by rotary evaporation producing a yellow-green residue. Excess pentane was added and mixture was filtered by vacuum filtration. The filtrate was collected and the pentane was removed by rotary evaporation to give a pale green precipitate. Yield = 0.21g (36%). **<sup>1</sup>H NMR (400 MHz, CDCl<sub>3</sub>)** δ 8.40 (s,br, 2H), 7.91 (t, J = 8 Hz, 1H), 4.62 (dt, J = 6, 15 Hz, 2H), 3.43 (dd, J = 10 Hz, 2H), 3.17 (dd, J = 10 Hz, 2H), 2.23 (sept, br, 2H), 1.13 (d, J = 7 Hz, 6H) 1.06 (d, J = 7 Hz, 6H). **<sup>13</sup>C NMR (100 MHz, CDCl<sub>3</sub>)** δ 169.0, 150.5, 137.0, 123.0, 84.5, 34.0, 33.4, 19.7, 19.0. **HRMS [ES] + [M+H] +** Predicted: 334.1367 Found: 334.1411. **Elemental analysis** unobtainable for **L4**, however has been obtained for **[Fe(L4)<sub>2</sub>][ClO<sub>4</sub>]<sub>2</sub>**: calculated (%) C 44.30, H 5.03, N 9.12; found (%) C 44.14, H 4.98, N 8.73.

**L5. 2,6-Bis[(4R)-4-tert-butyl-4,5-dihydro-1,3-thiazol-2-yl]-pyridine.** The following procedure was carried out under anhydrous conditions. N,N'-Bis[(1R)-1-

(hydroxymethyl)-2,2-dimethylpropyl]-pyridine-2,6-dicarboxamide, A5 (1.0 g, 2.74 mmol, 1 eq.) was combined with the Lawesson's reagent (1.34 g, 3.3 mmol, 1.2 eq.) and was flushed with nitrogen before the addition of dry toluene (30 mL). The reaction was heated under reflux (24 hrs, 130 °C) and then left to stir at room temperature overnight (16hrs, 20 °C) producing a light brown solution. The solution was washed with water (2x20 mL), the toluene layer collected and the remnant brown product from the water layer was extracted with dichloromethane (10 mL) and combined with the toluene layer. The organic layers were dried with magnesium sulphate, filtered by gravity and the solvent was removed by rotary evaporation producing a yellow-brown residue. Excess acetonitrile was added and mixture was filtered by vacuum filtration to give a white precipitate. Yield = 0.29g (29%). **<sup>1</sup>H NMR (400 MHz, CDCl<sub>3</sub>)** δ 8.17 (d, J = 8 Hz, 2H), 7.82 (t, J = 8 Hz, 1H), 4.46 (t, J = 10 Hz, 2H), 3.31 (t, J = 10 Hz, 2H), 3.19 (t, J = 10 Hz, 2H), 1.06 (s, 18H). **<sup>13</sup>C NMR (100 MHz, CDCl<sub>3</sub>)** δ 167.9, 150.4, 136.4, 122.4, 88.2, 35.1, 32.4, 26.5. **HRMS [ES] + [M+H] + Predicted:** 362.1680 Found: 362.1852. **Elemental analysis** calculated (%) C 63.12, H 7.53, N 11.62; found C 63.00, H 7.58, N 11.24.

**L6. 2,6-Bis[(4S)-4-tert-butyl-4,5-dihydro-1,3-thiazol-2-yl]-pyridine.** Prepared according to the procedure for **L5** using N,N'-Bis[(1S)-1-(hydroxymethyl)-2,2-dimethylpropyl]-pyridine-2,6-dicarboxamide, A6 (6.3 g, 0.017 mol, 1 eq.), Lawesson's Reagent (11.7 g, 0.029 mol, 1.7 eq.) and dry toluene (75 mL). Yield = 1.04 g (17 %). **<sup>1</sup>H NMR (400 MHz, CDCl<sub>3</sub>)** δ 8.47 (s, br, 2H), 7.91 (t, J = 8 Hz, 1H), 4.53 (t, J = 10 Hz, 2H), 3.31 (t, J = 10 Hz, 2H), 3.19 (t, J = 10 Hz, 2H), 1.06 (s, 18H). **<sup>13</sup>C NMR (100 MHz, CDCl<sub>3</sub>)** δ 168.2, 150.7, 136.8, 122.8, 88.5, 35.5, 32.8, 26.9. **HRMS [ES] + [M+H] + Predicted:** 362.1680 Found: 362.1735. **Elemental analysis** calculated (%) C 63.12, H 7.53, N 11.62; found C 63.05, H 7.20, N 11.28.



## Chapter 3

### Spin-Crossover Complexes of Iron(II) ThioPyBOX

#### 3.1 Introduction

##### 3.1.1 Chirality in Metal Complexes

Alongside the many other concepts theorised by Werner that form the foundations of coordination chemistry today, he found that metal complexes can in fact exhibit chirality.<sup>236</sup> Rivalled at the time by Jørgensen who rejected Werner's theory on metal complex stereoisomerism, convinced of only structural isomerism,<sup>237</sup> Werner finally concreted his theory with the demonstration of *cis*- and *trans*- isomers of the trivalent cobalt complex,  $[\text{Co}(\text{NH}_3)_4\text{Cl}_2]\text{Cl}$  (Figure 3.1).<sup>238-240</sup>

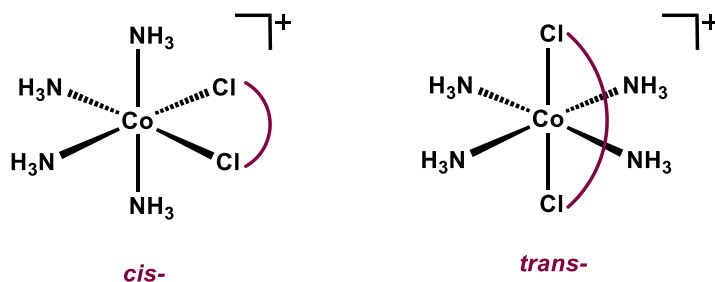
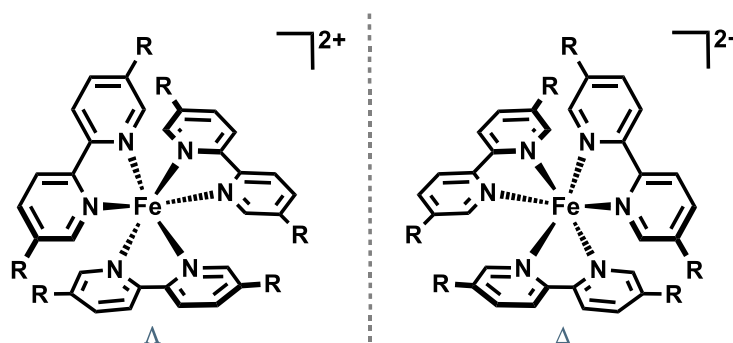


Figure 3.1. *Cis*- and *trans*- isomers of  $[\text{Co}(\text{NH}_3)_4\text{Cl}_2]^+$ .

In addition to *cis*- and *trans*-, and *fac*- and *mer*- isomerism, octahedral metal complexes can also exhibit 'propeller' or helical chirality<sup>241</sup> in which two or three bidentate ligands can coordinate in multiple ways that results in non-superimposable mirrored structures termed  $\Lambda$  or  $\Delta$ , an example of this is shown in Figure 3.2.<sup>242</sup> Such chirality has been applied in the design of chiral tetrahedral cages, which can separate racemic mixtures of alcohols using host-guest chemistry.<sup>243</sup>



**Figure 3.2.** An example of propeller-chirality in the structure of  $[\text{Fe}(\text{bpy})_3]^{2+}$ .

Chirality in metal complexes can be likened to that studied in organic chemistry. Tetrahedral metal complexes can exhibit chirality, if four different monodentate ligands are coordinated, resulting in optical isomers analogous to an  $sp^3$  stereogenic carbon centre (Figure 3.3).<sup>244</sup>

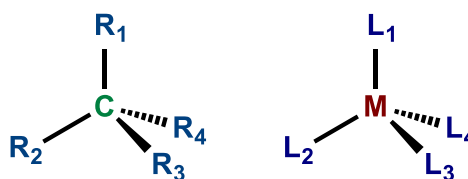


**Figure 3.3.** Stereogenic carbon and metal tetrahedral centres.

Having said this, tetrahedral metal complexes tend to be less configurationally stable in comparison to their octahedral counterparts,<sup>245</sup> but particularly in comparison to their organic analogues. In chiral organic moieties, carbon tends to form strong covalent bonds, unlike metal-ligand bonding which involves weaker, dative-covalent bonds. A continuous challenge faced by chemists in the synthesis and study of chiral metal complexes is a consequence of this weaker bonding, that is - the possibility of racemisation, of an otherwise enantiopure sample in solution, over time. This coupled with labile ligands, can result in facile M-L bond-cleavage and re-formation, enabling the racemisation to take place.<sup>244</sup> It is because of this that the applications and significance of such complexes are underexplored compared to their organic equivalents.<sup>246</sup>

In the above-mentioned types of chirality, the metal ion is considered the stereocentre, and these types of chirality are known as “chiral-at-metal”.

In the case of octahedral “chiral-at-metal” compounds, there is a stereochemical richness and complexity that arises from the possibility of 30 stereoisomers from just one octahedral stereocentre with six monodentate ligands. This has proven

convenient for a manifold of uses, such as multifunctional catalysis<sup>247</sup> and deserves to be further exploited. Furthermore, chiral octahedral complexes can offer unique chemistry, such as greater rigidity, by using conformationally-restricting chelating ligands. This has allowed such complexes to be employed in biological studies for binding to DNA and to proteins.<sup>248</sup> Their larger size (compared to organic equivalents) renders them a better pocket-filling fit in studies of protein sites and other enzymes, where complementarity can only be achieved with a specific complex configuration.<sup>249</sup>

### 3.1.1.1 “Chiral-at-Ligand”

The other class of chirality in metal complexes, is that of “chiral-at-ligand”, in which there is at least one stereogenic centre in the ligand. This ligand then coordinated to a metal, imparts chirality to the overall molecule, giving a chiral metal complex. This can be employed as a chiral catalyst in asymmetric reactions, where a particular enantiomer is the solely desired reaction product.<sup>250</sup> Furthermore, chiral metal complexes are important for catalysing the production of enantiopure materials for the pharmaceutical industry<sup>251, 252</sup> and in agriculture.<sup>253</sup>

Chiral  $C_2$ -symmetric ligands are ideal for catalysis, as they act as stereochemical directors to control the stereochemistry of involved transition states and therefore respective products.<sup>254</sup> This results in enantioselectivity of the reaction pathway with a minimal number of possible transition states, as depicted in Figure 3.4. This highlights the importance of symmetry in the ligand.

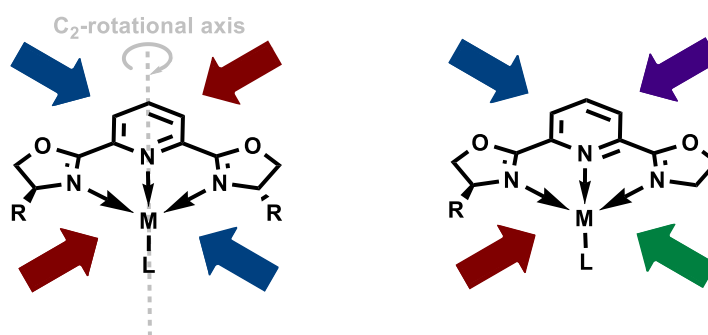


**Figure 3.4. Arrows indicating the direction of substrate attack upon a  $C_2$ -symmetric (left) and asymmetric (right) chiral metal-PyBOX complex. Arrows of the same colour leads to identical products.**

Other strategies to induce chirality in a metal complex include: the attachment of chiral auxiliary groups to a coordinated ligand that can control the reaction pathway before then being cleaved off at the end; the use of chiral counterions<sup>255</sup> or co-

crystallisation with a chiral anion;<sup>256</sup> and a temporary coordination of a chiral ligand directly to the metal.<sup>257, 258</sup>

Asymmetric catalysis is where complexes with chiral ligands were first and foremost employed. The use of such catalysts allows for an absolute control of stereochemical outcome by distinguishing between diastereomeric transition states with as little as 10 kJ mol<sup>-1</sup> accuracy.<sup>259</sup> The first homogeneous chiral metal catalyst employed in asymmetric catalysis was a chiral Schiff-base copper(II) complex in the reaction of styrene with ethyl diazoacetate. This gave *cis*- and *trans*- products (Figure 3.5) in a less than 10% enantiomeric excess (ee).<sup>260</sup>

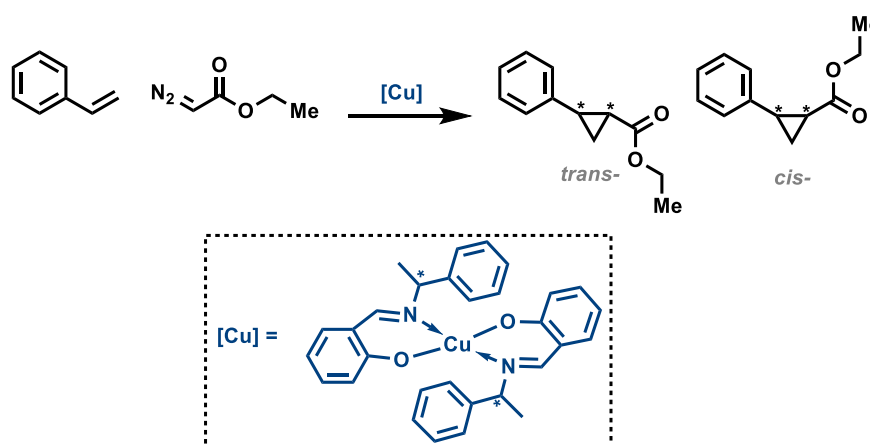


**Figure 3.5. A chiral Schiff-base copper(II) complex catalysing an enantioselective carbenoid reaction.**<sup>260</sup>

This thesis intends to further explore the concept of chirality in metal complexes.

### 3.1.2 Chirality in Spin-Crossover Complexes

There has been a growing interest in developing functional materials that are SCO-active, coupled with other chemical and physical functionalities such as liquid crystallinity,<sup>261-263</sup> electrical conductivity,<sup>264, 265</sup> fluorescence,<sup>266</sup> chirality<sup>267</sup> and ferroelectricity,<sup>268, 269</sup> to improve use in end applications.<sup>270, 271</sup> Herein we will focus on the interplay between SCO and chirality.

The combination of chirality, magnetism and light in a complex, dates back to 1811 where Arago discovered natural optical activity (NOA) in chiral quartz crystals.<sup>272, 273</sup> This work was followed by Faraday in 1846, who discovered optical activity which was magnetically-induced (MOA) in lead borate glass -resulting in the Faraday Effect.<sup>274, 275</sup> Then in 1848, Pasteur successfully separated the two enantiomers of sodium ammonium tartrate crystals manually,<sup>276</sup> but was unsuccessful when he tried to isolate an isomer of tartaric acid crystals in the presence of a magnetic field.<sup>277</sup> It

is only in the recent years that the interplay between chirality and magnetism has been brought back into light.<sup>278</sup>

### 3.1.2.1 Why are we interested?

Combining chirality with SCO complexes can afford fascinating results that can be applied in functional materials. For example, chirality in a ferromagnetic material can affect magnetic, optical and electric properties, by interference effects which arise from the loss of inversion and mirror symmetry elements.<sup>279</sup> Therefore, such materials can be used to tune these properties. Furthermore, introducing an element of chirality to SCO complexes has been proposed as a method to facilitate retaining stored data in molecular electronics. The optical rotation of chiral molecules allows for detection at lower-energy/longer wavelength irradiation, compared to their achiral counterparts.<sup>280</sup> This is less likely to damage stored data information during the read-out process (non-destructive readout), improving their application as magneto-chiral switches in SCO-memory devices.<sup>280, 281</sup>

An application of light-induced reversible SCO in chiral molecular magnets is presented in the field of non-linear optics (NLOs), which could prove useful in developing optoelectronics with the emergent miniaturisation of technological devices.<sup>282, 283</sup> Ohkoshi *et al.* demonstrated an example of this with the 3D bimetallic structure of (+)-Fe<sub>2</sub>[Nb(CN)<sub>8</sub>](4-bromopyridine)<sub>8</sub>·2H<sub>2</sub>O (Figure 3.6) in which they tested its NLO behaviour.<sup>279</sup>

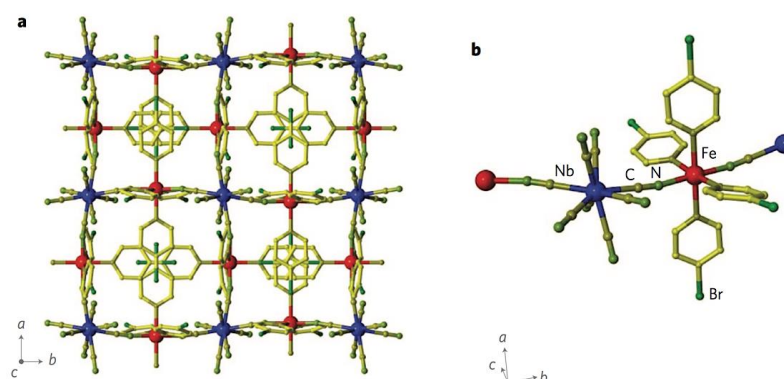


**Figure 3.6. XRD structure of (+)-Fe<sub>2</sub>[Nb(CN)<sub>8</sub>](4-bromopyridine)<sub>8</sub>·2H<sub>2</sub>O (a) and Fe and Nb coordination environments (b). (Red = Fe, blue = Nb, green = Br, yellow = C, light green = N). Figure taken directly from publication.<sup>279</sup>**

Magneto-Chiral Dichroism (MChD)<sup>284</sup> is another application of chiral magnetic systems, which particularly depends on light-matter interaction. Chiral systems that can be magnetised, either spontaneously or under a stimulus, can absorb or emit unpolarised light depending on the light propagation vector and configuration of the system. The strength of absorption depends on the chirality of the metal complex. A schematic of this is shown in Figure 3.7.<sup>278</sup>

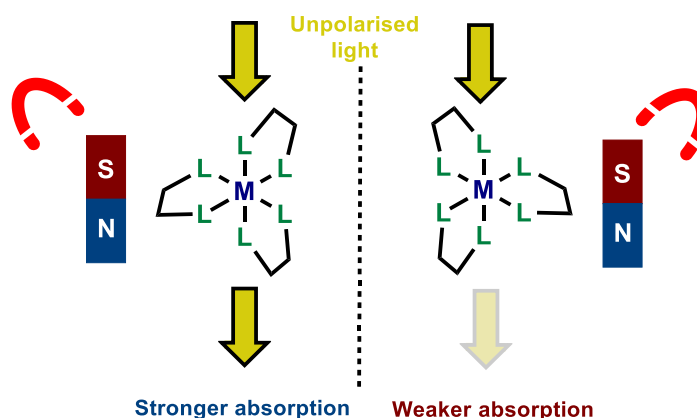


**Figure 3.7. Schematic representation of how MChD works on a chiral molecule. Figure adapted from publication.**<sup>278</sup>

### 3.1.2.2 Homochiral-SCO Compounds

The iron-octacyanonitrate complex by Ohkoshi *et al.*<sup>279</sup> crystallises in a chiral space group, and shows a temperature-dependent, and hysteretic, SCO transition at  $T_{1/2\downarrow} = 112$  K and  $T_{1/2\uparrow} = 124$  K. Reversible photo-switching between two phases with long-range magnetic ordering,  $P1-1$  and  $P1-2$ , was also demonstrated by light irradiation at 473 nm and 785 nm at 10 K. The team also investigated the effect of optical switching on Magnetisation-Induced Second-Harmonic Generation (MSHG), where a polarised plane of SH light is switched perpendicularly by light irradiation. The 90° rotation was achieved by adding a chiral functionality to the complex.<sup>279</sup> This breakthrough by Ohkoshi *et al.* was the first of its kind that demonstrated the interplay between SCO and chirality.<sup>285</sup>

Examples of chiral-SCO compounds include homochiral 1D-coordination polymers, where the iron(II) centres along the chain are the same  $\Lambda$  or  $\Delta$  chirality.<sup>285</sup> Heterometallic chiral 1D-coordination polymers have also been reported, such as the cyanide-bridged [CoFe] structure reported by Hoshino *et al.* (Figure 3.8).<sup>286</sup> The iron component is  $[\text{Fe}^{\text{II}}(\text{tp})(\text{CN})_3](\text{BF}_4) \cdot \text{MeOH} \cdot 2\text{H}_2\text{O}$  (tp = hydrotris(pyrazol-1-yl)borate) and the cobalt component is  $[\text{Co}^{\text{II}}((R)\text{-pabn})]$  ( $(R)\text{-pabn} = (R)\text{-N}(2),\text{N}(2')\text{-bis}(\text{pyridin-2-ylmethyl})\text{-1,1'-binaphthyl-2,2'-diamine}$ ). The chirality arises from the tetradentate ligand coordinated to cobalt, which gives a  $\Lambda$ -metal centre and this chirality is imparted to the rest of the molecule. The structure is both magnetically and

electrically bistable over the same temperatures. The use of (*S*)-pabn formed the analogous homochiral (*S*)-complex, while a racemic mixture of (*R*)-pabn and (*S*)-pabn formed an achiral nonanuclear complex instead;  $[\text{Fe}^{\text{III}}_4\text{Co}^{\text{III}}_4\text{Co}^{\text{II}}(\text{CN})_{12}(\text{tp})_4((\text{R})\text{-pabn})_2((\text{S})\text{-pabn})_2](\text{BF}_4)_{10}\cdot 12\text{H}_2\text{O}\cdot 40\text{CH}_3\text{OH}$ .<sup>286</sup>

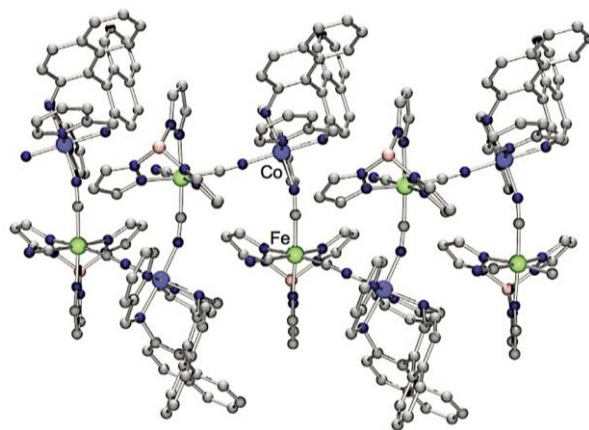


**Figure 3.8. XRD structure of the heterometallic 1D polymer of cyanide-bridged [CoFe] studied by Hoshino *et al.* (green = Fe, blue = Co, pink = B, grey = C, purple = N). Figure taken directly from publication.<sup>286</sup>**

Where there are extended homochiral intermolecular interactions between individual chiral units, a higher dimensionality from self-organisation may be achieved, resulting in a 2- or 3-D chiral conglomerate that can be crystallised.<sup>287</sup> There are mixed-valence examples of this, such as the homochiral species,  $[\text{Fe}^{\text{II}}\text{H}_3\text{L}][\text{Fe}^{\text{III}}\text{L}](\text{NO}_3)_2$  (where  $\text{H}_3\text{L}$  = tris((2-((imidazole-4-yl)methylidene)amino)ethyl)amine), which was synthesised from achiral components.<sup>280</sup> The iron(II) and iron(III) centres form  $\text{FeN}_6$  octahedral coordination environments with propeller-chirality and this 2D conglomerate supramolecular structure can undergo SCO with cooperative effects from the mixed valency across the assembly.<sup>280</sup> The cobalt analogue,  $[\text{Co}^{\text{II}}(\text{H}_3\text{L})][\text{Co}^{\text{III}}(\text{L})]\text{CL3}\cdot 8\text{H}_2\text{O}$  has also been reported to crystallise as a chiral conglomerate.<sup>288-290</sup> Following this, Sunatsuki *et al.* exploited host-guest chemistry using chiral recognition of the iron conglomerate with a  $[\text{Cr}(\text{ox})_3]^{3-}$  guest and along with the SCO behaviour of the  $[\text{Fe}^{\text{III}}(\text{H}_3\text{L})]^{3+}$  species.<sup>287</sup>

Hashibe *et al.* synthesised and isolated *fac*- $\Lambda$ - $[\text{Fe}^{\text{II}}(\text{HL}^{\text{R}})_3](\text{ClO}_4)_2\cdot \text{EtOH}$  where  $\text{HL}^{\text{R}}$  is the bidentate ligand, 2-methylimidazol-4-yl-methylideneamino-R-(+)-1-methylphenyl.<sup>291</sup> The complex preferentially adopts the *fac*- $\Lambda$ - isomer over the possible *mer*- and/or  $\Delta$ - conformations, due to the steric hindrance provided by the methyl substituents on the ligand. However interestingly, XRD analysis of  $[\text{Fe}^{\text{II}}(\text{HL}^{\text{S}})_3](\text{ClO}_4)_2\cdot \text{EtOH}$ , where  $\text{HL}^{\text{S}}$  is the *S*-enantiomer of the ligand, showed that the *fac*- $\Delta$ - iron complex formed preferentially - rationalised by steric effects. Their

findings showed that the  $\Lambda$ - complex underwent a steep SCO transition at  $T_{1/2} = 195$  K, owing to cooperative effects from the chain-like packing, directed by hydrogen bonds from the counter-ion and solvent.<sup>291</sup> This highlights the significance of chirality from 'chiral-at-ligand' complexes.

Other SCO structures incorporating chirality include that reported by Lui *et al.* on the 3-dimensional Metal-Organic Framework (MOF)  $[\text{Fe}^{\text{II}}(\text{mptpy})_2]\text{EtOH}\cdot 0.2\text{DMF}$  (where  $\text{Hmptpy} = 3\text{-methyl-2-(5-(4-(\text{pyridin-4-yl})\text{phenyl})-4\text{H-1,2,4-triazol-3-yl})-pyridine}$ ), which was found to be particularly stable and exhibit two spin transitions either side of  $T = 300$  K.<sup>270</sup> Homochiral tetrahedral iron(II) cages that undergo spin transitions close to room temperature have also been published in the recent years.<sup>271</sup>

The above discussed examples of chirality in SCO complexes consider only homochiral species. Mixed-chiralities have also been reported, for example in the 2D network material  $[\text{Fe}^{\text{III}}(5\text{-NO}_2\text{saL2-trien})]-[\text{Mn}^{\text{II}}\text{Cr}^{\text{III}}(\text{ox})_3](\text{CH}_3\text{NO}_2)0.5(\text{H}_2\text{O})$  discussed by Clemente-León *et al.*<sup>292</sup> The different chiral configurations arise from the different metal centres, the  $\text{Cr}^{3+}$  ions taking the  $\Delta$ - configuration, while the  $\text{Mn}^{2+}$  adopts the  $\Lambda$ - isomer, resulting in a  $\dots\Lambda\Delta\Lambda\Delta\dots$  pattern. The complex undergoes ferromagnetic-ordering at long-range around  $T = 5$  K. However, the study attributed changes in the spin state of the overall complex to the electron- donating or withdrawing character of the substituent bound to saL2-trien, rather than to the doping of the achiral-SCO species into the chiral framework.<sup>292</sup>

### 3.1.3 Subtle Differences between SCO Complexes

While multidimensional SCO-species offer optimal cooperativity through their highly-connected systems, mononuclear species such as the  $\text{FeN}_6$  chromophore, discussed in Chapter 1, can also provide strong cooperative effects.<sup>293</sup> From here on,  $\text{FeN}_6$  systems will be the focus.

#### 3.1.3.1 Discrimination Between Polymorphs w.r.t SCO Activity

There are mononuclear SCO materials that can exist and crystallise out as polymorphs. Studies of these polymorphs have shown that they can present distinct SCO behaviours from one another, which is vital to furthering our understanding of other ways to attain control in SCO systems.

Ozowski *et al.* isolated two polymorphs of the iron(II) complex  $\text{cis-}[\text{Fe}(\text{bt})_2(\text{NCS})_2]$  (where  $\text{bt} = 2,2'$ -bithiazoline).<sup>294</sup> Though both polymorphs (**A** and **B**) crystallised in the same crystal system and space group (triclinic,  $P\bar{1}$ ), and both had the thiocyanate



ligands in a *cis*- conformation to each other, more subtle structural differences were evident from XRD analysis (Figure 3.9).<sup>294</sup>

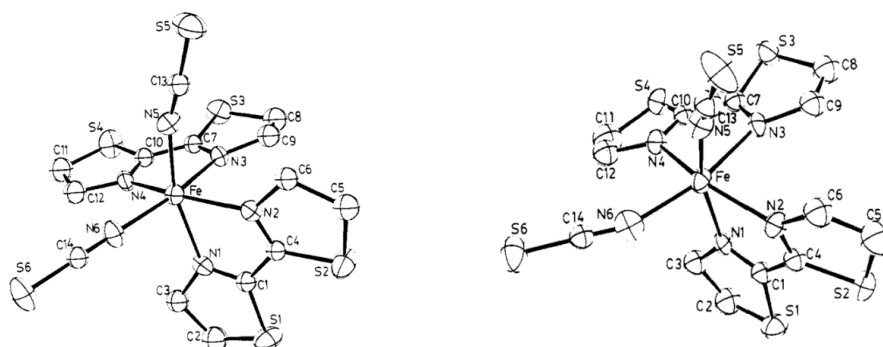


**Figure 3.9. XRD structures of polymorph A (left) and polymorph B (right). Figures taken directly from publication.**<sup>294</sup>

XRD analysis showed differences in the bond angles Fe-N-C and N-C-S of the thiocyanate ligands. Polymorph **A** had one thiocyanate near the expected 180 °, but had the other display a distinct Fe-N-C angle close to 160 ° instead, while Polymorph **B** showed both Fe-N-C angles close to 180 °. Furthermore, it was noted that the bond lengths, N-C and C-S, in polymorph **B** are longer compared to **A**. SCO studies of the two polymorphs rather interestingly revealed that polymorph **A** underwent a hysteretic Spin Transition (ST) around ~170-180 K, while polymorph **B** remained in the HS state across 77-300 K.

This was rationalised by the differences in the packing structures of the polymorphs (Figure 3.10), with **A** presenting more effective intermolecular interactions owing to slightly shorter intermolecular S...S distances, affecting the geometry of the iron(II) coordination sphere, and therefore its ability to undergo a cooperative ST.<sup>293, 294</sup>

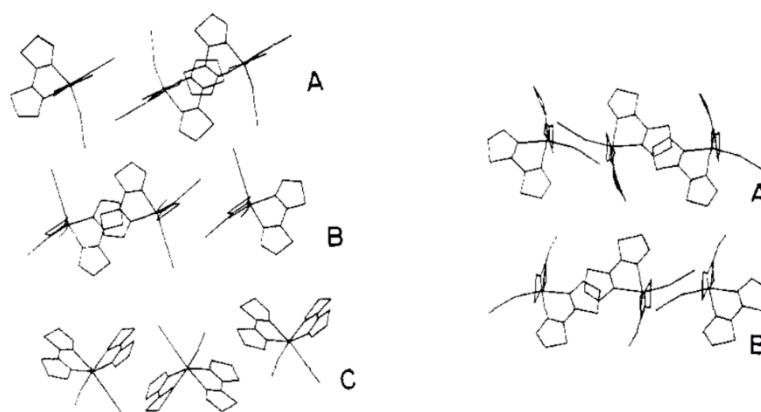


**Figure 3.10. Chain of interactions in polymorph A (left) and polymorph B (right), between the thiazoline rings. A, B and C in the figures denotes the view along the *a*-axis, *b*-axis and *c*-axis respectively. Figures taken directly from publication. <sup>294</sup>**

In contrast to the bipyridine analogue  $[\text{Fe}(\text{bpy})_2(\text{NCS})_2]$  studied by König and Madeja <sup>295</sup> in which all three polymorphs exhibit SCO-activity, this study is the first that discriminates between polymorphs with regards to their SCO-behaviour.

Derivatives of SCO complexes have been developed to achieve optimum cooperative SCO activity. This involves exploiting both steric and electronic effects at an individual molecular level, in order to improve the overall cooperativity across the bulk sample through these structural variations. Létard *et al.* studied *cis*-complexes of iron(II) bis-thiocyanate species  $[\text{Fe}(\text{PM-BiA})_2(\text{NCS})_2]$  and  $[\text{Fe}(\text{PM-PEA})_2(\text{NCS})_2]$  (where PM-BiA = N-(2-pyridylmethylene)aminobiphenyl and PM-PEA = N-(2'-pyridylmethylene)-4-(phenylethynyl)anilino) (Figure 3.11) <sup>296, 297</sup> to investigate the effect of additional intermolecular  $\pi$ -interactions on the cooperativity of the ST.

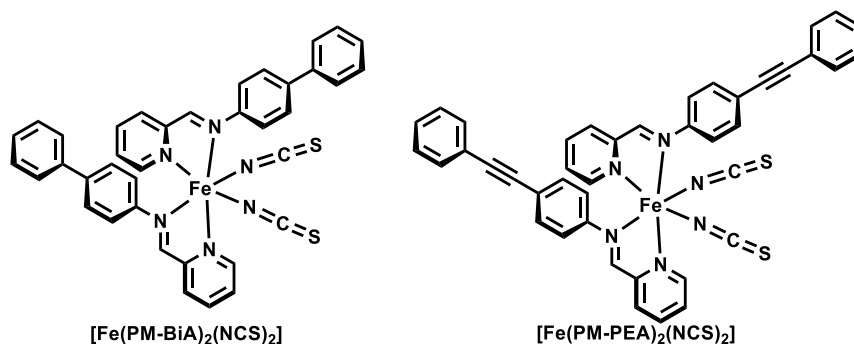


**Figure 3.11. Structures of  $[\text{Fe}(\text{PM-BiA})_2(\text{NCS})_2]$  (left) and  $[\text{Fe}(\text{PM-PEA})_2(\text{NCS})_2]$  (right), studied by Létard *et al.* <sup>296</sup>**

Within this work, it was found that single crystals of  $[\text{Fe}(\text{PM-BiA})_2(\text{NCS})_2]$  underwent an abrupt thermal ST with a 5 K hysteresis loop and a powder sample (1) matching

the diffraction pattern of the single crystal agreed perfectly with this (Figure 3.12). However, a powdered sample produced from a different synthetic approach (2), that involved an excess of ligand, showed a more gradual ST with significantly higher  $T_{1/2}$  values (Figure 3.12, right).

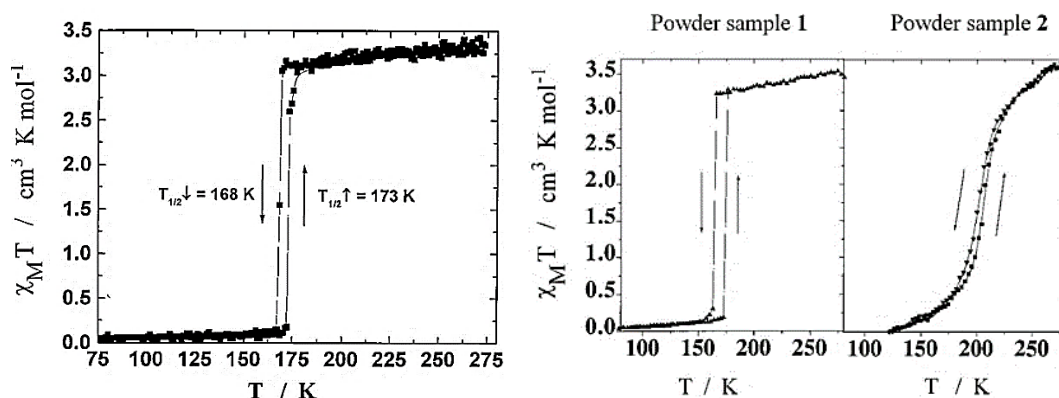


**Figure 3.12. Comparison of  $\chi_M T$  vs  $T$  of single crystals of  $[\text{Fe}(\text{PM-BiA})_2(\text{NCS})_2]$  (left) and of powder samples 1 and 2 (right). Figures taken directly from publication.<sup>296</sup>**

The two powder samples were identified as polymorphs of one another, which explains their differences in SCO behaviours.<sup>297</sup> These differences highlight not only how powder and single crystal samples can be used synergistically to support one another, but also how differences in magnetic measurement data can become apparent from polymorphs of the same sample. Such polymorphs can be produced simply from following different synthetic procedures.

### 3.1.3.2 Switching Sulfur for Selenium

Other examples of discrimination based on SCO activity, includes that between structurally analogous complexes, which differ by a single atom. Despite slight chemical differences in their atomic makeup, these structures are said to be isostructural, and these can present interesting differences with regards to SCO activity.

The complexes  $[\text{Fe}(\text{DPQ})_2(\text{NCS})_2]$  and  $[\text{Fe}(\text{ABPT})_2(\text{NCX})_2]$  (where DPQ = 2,3-bis-(2'-pyridyl)-quinoxaline, ABPT = 4-amino-3,5-bis(pyridin-2-yl)-1,2,4-triazole and X = S, Se (Figure 3.13)) were studied by Moliner *et al.*<sup>298, 299</sup> This study compares the effect of swapping sulfur for selenium in the thiocyanate ligand in a mononuclear iron(II) complexes (Figure 3.14) and observing how the SCO behaviour differs between the two analogues. It should be noted that the complexes have a pseudo-octahedral

geometry and the thiocyanate or selenocyanate groups are *trans*- to each other. In such  $\alpha$ -diimine complexes, pseudo-halide groups would more commonly adopt *cis*- conformations to each other, rendering this the first example of a *trans*- oriented thiocyanate  $\alpha$ -diimine complex.<sup>299</sup>

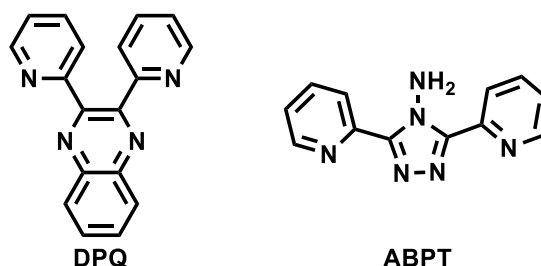


Figure 3.13. Chemical structures of DPQ (left) and ABPT (right), studied by Moliner *et al.*<sup>298, 299</sup>

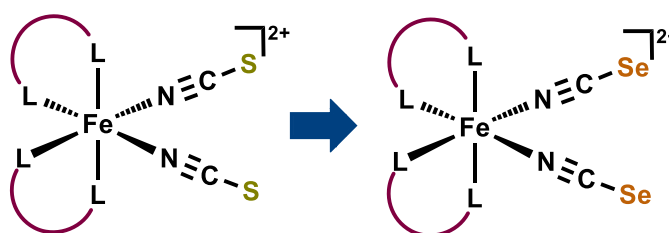


Figure 3.14. Iron(II) complex with thiocyanate ligands *cis*- to each other (left) and the selenocyanate analogue (right).

Solid state variable temperature magnetic measurements gave a  $T_{1/2}$  value = 180 K for  $[\text{Fe}(\text{ABPT})_2(\text{NCS})_2]$  and  $T_{1/2} = 240$  K for  $[\text{Fe}(\text{ABPT})_2(\text{NCSe})_2]$ . Furthermore, Differential Scanning Calorimetry (DSC) measurements showed the thiocyanate complex to be enthalpically more favourable than the selenocyanate analogue, and the selenocyanate to be more entropically favourable.<sup>299</sup> For comparison, the magnetic susceptibility of the complex  $[\text{Fe}(\text{DPQ})_2(\text{NCS})_2] \cdot \text{CO}(\text{CH}_3)_2$  was measured, and was found to remain in the HS spin state between 4.2-290 K. This was rationalised by exceedingly long Fe-N (iron-quinoxaline) bonds and considerably shorter Fe-N (iron-thiocyanate) bonds,<sup>298</sup> compared to other  $[\text{Fe}(\text{L})_2(\text{NCS})_2]$  analogues that undergo SCO.<sup>294, 300-303</sup>

Across the series of complexes *trans*- $[\text{Fe}(\text{R}_2\text{bapbpy})(\text{NCX})_2]$  (where bapbpy = N6,N6'-bis(pyridin-2-yl)-2,2'-bipyridine-6,6'-diamine and X= S or Se) (Figure 3.15), it was found that substitution of sulfur with selenium resulted in reduced cooperative effects in the material, due to the lower electronegativity of selenium compared to

sulfur. The cooperativity is said to arise from N-H...S interactions, therefore, if the R group is bulky and positioned close to the N-H bridge, it will sterically hinder the interaction with the sulfur atom. It was also noted that higher transition temperatures were also generally observed with the thiocyanate complexes.

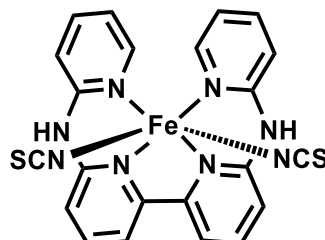


Figure 3.15. Structure of [Fe(bapbpy)(NCS)<sub>2</sub>].

An exception to this trend was found with an isoquinolin-3-yl analogue of bapbpy, as this complex showed a more cooperative ST effect with selenocyanate.<sup>304, 305</sup> The different SCO behaviours, attributed to the change between NCS<sup>-</sup> and NCS<sup>Se-</sup>, were corroborated by earlier findings from Bréfuel *et al.*<sup>306</sup> Their research showed that an iron(II) complex containing the selenocyanate anion was found to produce a one-step and steeper ST, compared to its thiocyanate analogue, which produced a two-step ST with small hysteresis.<sup>306</sup>

The intersection between polymorphs and isostructural SCO complexes was studied in polymorphs of *cis*-[Fe(bqen)(NCX)<sub>2</sub>], where bqen is the tetradentate ligand, N,N'-bis(8-quinolyl)ethane-1,2-diamine and X = S or Se.<sup>293</sup> It was found that swapping thiocyanate for selenocyanate in these complexes affected the ST by as much as  $\Delta T_{1/2} = 100$  K (where  $\Delta T_{1/2} = T_{1/2}(\text{NCSe}) - T_{1/2}(\text{NCS})$ ), with the selenocyanate complex affording the higher  $T_{1/2}$  value. This  $\Delta T_{1/2}$  is larger than the  $\Delta T_{1/2}$  values that have been obtained for other iron(II) thio-/selenocyanates with  $\alpha$ -diimines. For [Fe(phen)<sub>2</sub>(NCX)<sub>2</sub>],  $\Delta T_{1/2} = 55$  K<sup>307</sup> and for [Fe(PM-PEA)<sub>2</sub>(NCX)<sub>2</sub>]  $\Delta T_{1/2\downarrow} = 62$  K and  $\Delta T_{1/2\uparrow} = 75$  K.<sup>308</sup>

However, there have been findings of distinct ST temperatures between polymorphs of a complex, with  $\Delta T_{1/2}'$  values (where  $\Delta T_{1/2}' = |T_{1/2}(\text{polymorph I}) - T_{1/2}(\text{polymorph II})|$ ) that are similar to the  $\Delta T_{1/2} = 100$  K obtained by Bartual-Murgui *et al.*<sup>293</sup> A polymorph (I) of the complex *trans*-[Fe(tzpy)<sub>2</sub>(NSC)<sub>2</sub>] where tzpy = 3-(2-pyridyl)[1,2,3]-triazolo[1,5-a]pyridine, exhibits a gradual ST with a  $T_{1/2}$  between 120 and 200 K, whilst polymorph II of the complex exhibits an abrupt ST at  $T_{1/2} = 102$  K.<sup>309</sup> This demonstrates how not only the exchange of S for Se can affect the SCO activity, but also the polymorph.

The differences in SCO activity of the iron(II) centre between the thiocyanate and selenocyanate analogues can be attributed to two rationales, based on electronic and steric arguments:

- **Electronegativity difference.** As sulfur is more electronegative than selenium, it has a greater electron-withdrawing effect from the nitrogen atom of the coordinated thiocyanate ligand. This in turn reduces the effect of the ligand field around the iron centre, lowering the crystal field splitting energy between the  $t_{2g}$  -  $e_g^*$  orbitals, which stabilises the HS state and makes it more accessible.<sup>293</sup> Therefore the expected trend of sulfur analogues is to be more 'HS-like' in character compared to selenium equivalents.
- **Geometric distortion.** Angular distortion parameters of  $\theta < 90^\circ$  and  $\phi < 180^\circ$ , show deviations from a perfect octahedron ( $\theta = 90^\circ$  and  $\phi = 180^\circ$ ),<sup>77</sup> and these deviations can influence the  $T_{1/2}$  value. It has been found that substitution of  $\text{NCS}^-$  for  $\text{NCSe}^-$  can result in greater distortion parameters.<sup>293</sup> This can be understood by the increased atomic radius of Se versus S. The larger Se atom increases steric strain in the ligands, which can force more obtrusive geometries about the iron centre in order to accommodate. It is more useful to understand the difference in these distortion parameters between the HS and LS states of a complex, to appreciate why a ST may be hindered.

### 3.1.3.3 Switching Oxygen for Sulfur in Heterocyclic Ligand Frameworks

The same rationale can be applied to the exchange of oxygen for its third row counterpart, sulfur. With sulfur being a less electronegative atom than oxygen and larger in atomic radius ( $r_S = 1.07 \text{ \AA}$  and  $r_O = 0.63 \text{ \AA}$ <sup>310</sup>), oxygen analogues would be expected to demonstrate a SCO behaviour more 'HS-like' in character compared to its sulfur equivalents, and sulfur analogues more 'LS-like' in SCO activity.

Similar steric and electronic arguments as discussed for sulfur vs. selenium in  $\text{NCS}^-$  and  $\text{NCSe}^-$  complexes, can be likened to comparison of oxygen vs. sulfur in heterocyclic ligands. The lower electronegativity of sulfur compared to oxygen in a nitrogen-containing heterocycle promotes a greater ligand field splitting in its complexes. The increased size of the sulfur atom can afford better conformational flexibility of the  $\text{N,N',N''}$ -tridentate heterocyclic ligand about the iron coordination sphere, provided the denticity and ring-size of the ligand permit so. This higher flexibility of thiazoline compared to oxazoline in the ligand is said to have less of an energy cost associated with its conformational rearrangement upon a ST.<sup>216, 311-313</sup>

Not only has it been theorised that swapping oxygen for sulfur in this system can improve the completeness of the ST, but also, it may tune the  $T_{1/2}$  temperature of the spin transition to higher, more ambient, temperatures.<sup>216</sup> These improved results may be more suitable for application-purposes in molecular electronics, which demonstrates why the effect of swapping oxygen for sulfur is of interest herein.

Preliminary investigations into this hypothesis were supported by Pan *et al.* in one of their recent publications,<sup>216</sup> in which they studied the SCO activity in achiral  $[\text{Fe}(\text{thioPyBOX}^{\text{R}})_2]^{2+}$  complexes where  $\text{R} = \text{H}$  or  $\text{Me}_2$  (Figure 3.16).

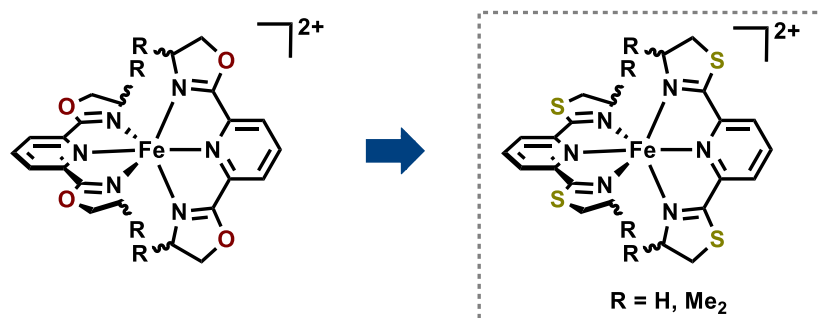


**Figure 3.16. Iron(II) PyBOX complex (left) and iron(II) thioPyBOX complex (right). Figure reproduced from publication.<sup>216</sup>**

In their work they found the complex  $[\text{Fe}(\text{thioPyBOX}^{\text{Me}_2})_2][\text{ClO}_4]_2$  underwent a gradual SCO in the solid state and upon multiple heating/cooling cycles observed a hysteretic effect with a  $T_{1/2\downarrow} = 319 \text{ K}$  and  $T_{1/2\uparrow} = 349 \text{ K}$  giving the hysteresis loop  $\Delta T = 30 \text{ K}$ . A study of the LIESST effect on the same species, showed an excitation of 16 % of iron(II) centres from the LS state to the HS state upon application of the laser. This was corroborated by a solution state SCO study of the same complex which was shown to exhibit a ST with a  $T_{1/2} = 240 \text{ K}$ . Complete HS character is attained across the bulk sample at  $283 \text{ K}$  with  $X_{\text{mT}} = 3.81 \text{ cm}^3 \text{ K mol}^{-1}$ . However, with the complex  $[\text{Fe}(\text{thioPyBOX}^{\text{H}})_2][\text{ClO}_4]_2$  both solid and solution state studies showed the LS state was maintained across all temperatures. That reflects the increased steric effect of the methyl substituents in  $[\text{Fe}(\text{thioPyBOX}^{\text{Me}_2})_2][\text{ClO}_4]_2$ , which weakens its ligand field.<sup>216</sup>

While their work addresses the comparisons between complexes of iron(II) -PyBOX and -thioPyBOX ligands, their SCO activity using multiple diagnostic tools in both solid and solution states and the effect of changing counter-ions, the work only explores the unsubstituted thioPyBOX ligand and one substituted ligand, which has an electron-donating nature. Furthermore, both ligands are achiral which leaves

studies of chiral discrimination in iron(II)thioPyBOX<sup>R</sup> complexes and other substituent (R ≠ H/Me<sub>2</sub>) effects, an uncharted field of research.

### 3.1.4 Chiral Discrimination of Spin States in Iron(II)PyBOX complexes

The first demonstration of chiral discrimination between spin states in an iron(II) complex, was demonstrated with a series of homochiral and heterochiral iron(II) PyBOX complexes. This was studied within the Halcrow group by Burrows *et al.* in 2017.<sup>210</sup> This was the first known study of chiral discrimination in SCO complexes that also investigated solution state SCO behaviour in comparison to the solid state.

The R- substituent on the 4-position of the PyBOX ligand was varied in their research to be phenyl (Ph), isopropyl (iPr), methyl (Me) and an achiral analogue (H), and complexes of these were studied (Figure 3.17). The counter-ion used throughout their work was the perchlorate anion.

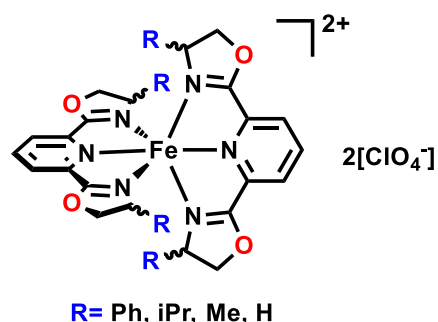


**Figure 3.17. Iron(II) PyBOX complexes studied by Burrows *et al.*, with the R groups = Ph, iPr, Me and H.<sup>210</sup>**

Though their work consisted of four ligand variants, the study of chiral discrimination between homochiral and heterochiral iron(II) PyBOX complexes was carried out with only PyBOX ligands bearing the R- substituents phenyl and *isopropyl* (L<sup>Ph</sup> and L<sup>iPr</sup> respectively). This afforded the homochiral complexes [Fe((R)-L<sup>Ph</sup>)<sub>2</sub>][ClO<sub>4</sub>]<sub>2</sub>, **R-1** and Fe((R)-L<sup>iPr</sup>)<sub>2</sub>][ClO<sub>4</sub>]<sub>2</sub>, **R-2**, where the R- denotes an *R,R*-chirality of the ligand. The heterochiral analogues of these complexes studied were [Fe((R)-L<sup>Ph</sup>)((S)-L<sup>Ph</sup>)] [ClO<sub>4</sub>]<sub>2</sub>, **RS-1** and [Fe((R)-L<sup>iPr</sup>)((S)-L<sup>iPr</sup>)] [ClO<sub>4</sub>]<sub>2</sub>, **RS-2** where one ligand is the *R,R*-diastereomer and the other is its *S,S*-enantiomer.

Figure 3.18 depicts how these homochiral and heterochiral complexes are related. This is the only type of chirality that will be discussed hereon.



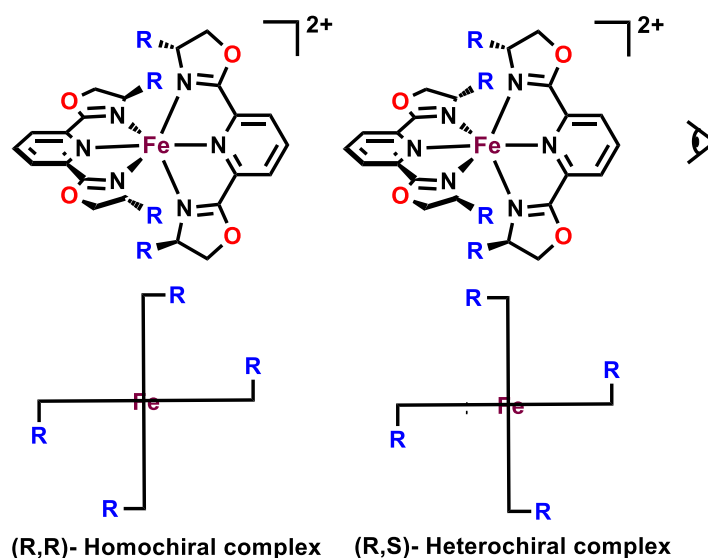


Figure 3.18. The relationship between an *R,R*- Homochiral iron-PyBOX complex (left) and an *R,S*- Heterochiral iron-PyBOX complex (right).

### 3.1.4.1 Solid State SCO results

In the solid state, the magnetic moment was measured between 5-350 K, using the Superconducting Quantum Interference Device (SQUID) magnetometer, at 0.5 T and with a scan rate of 5 K min<sup>-1</sup>, of the various iron-PyBOX complexes. The solid state magnetic susceptibility results are shown in Figure 3.19 and the accompanying data is tabulated beneath in Table 3.1.

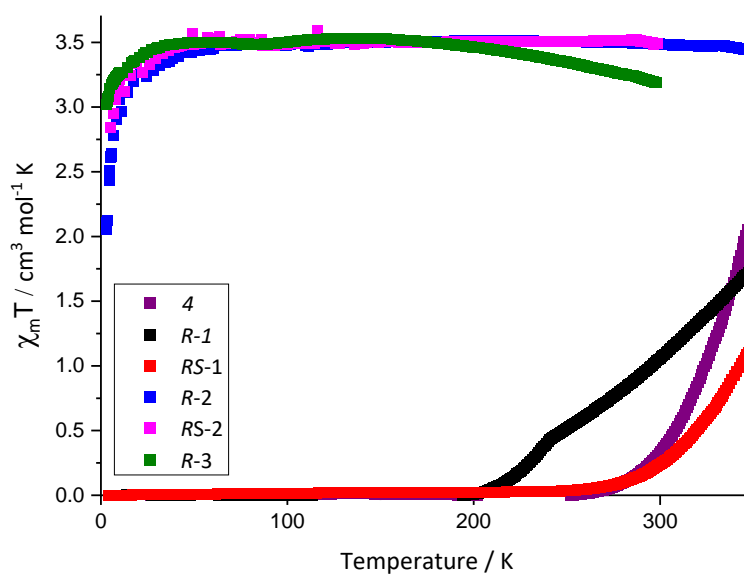
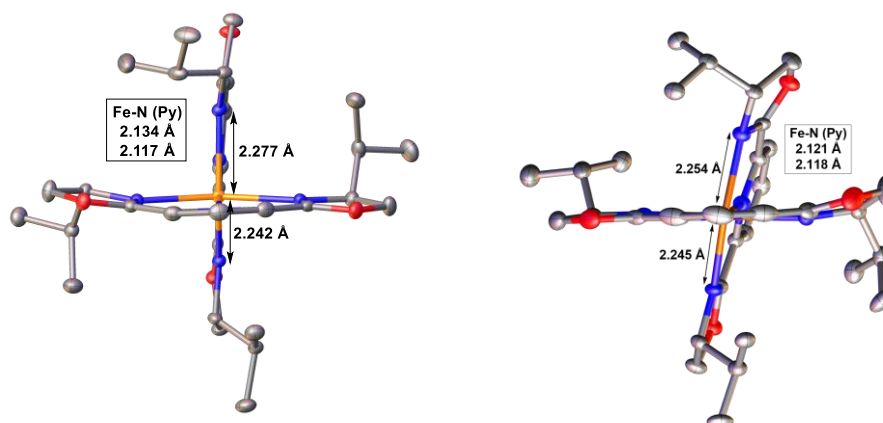


Figure 3.19. Solid state magnetic susceptibility measurements of the iron(II)PyBOX<sup>R</sup> complexes studied by Burrows *et al.*<sup>210</sup>

	Complex	R- substituent	T <sub>1/2</sub> (K)
<b>R-1</b>	[Fe((R)-L <sup>Ph</sup> ) <sub>2</sub> ][ClO <sub>4</sub> ] <sub>2</sub>	Ph	≈ 350
<b>RS-1</b>	[Fe((R)-L <sup>Ph</sup> )(S)-L <sup>Ph</sup> )]][ClO <sub>4</sub> ] <sub>2</sub>	Ph	> 400
<b>R-2</b>	[Fe((R)-L <sup>iPr</sup> ) <sub>2</sub> ][ClO <sub>4</sub> ] <sub>2</sub>	iPr	HS
<b>RS-2</b>	[Fe((R)-L <sup>iPr</sup> )(S)-L <sup>iPr</sup> )]][ClO <sub>4</sub> ] <sub>2</sub>	iPr	HS
<b>R-3</b>	[Fe((R)-L <sup>Me</sup> ) <sub>2</sub> ][ClO <sub>4</sub> ] <sub>2</sub>	Me	HS
<b>4</b>	[Fe(L <sup>H</sup> ) <sub>2</sub> ][ClO <sub>4</sub> ] <sub>2</sub>	H	≈ 340

**Table 3.1. Solid state magnetic susceptibility data of the iron(II)PyBOX<sup>R</sup> SQUID curves studied by Burrows et al.<sup>210</sup>**

Both the homochiral and heterochiral iron-PyBOX<sup>iPr</sup> complexes, **R-2** (blue line) and **RS-2** (pink line) show virtually the same results as each other, which is a completely high spin bulk sample ( $X_m T = 3.5 \text{ cm}^3 \text{ K mol}^{-1}$ ) across all temperatures. This can be attributed to the steric bulk from the *isopropyl* groups which significantly distorts the complex away from the classical octahedral geometry. This high degree of distortion can be seen in the XRD structure solutions obtained for **R-2** and **RS-2** (Figure 3.20).



**Figure 3.20. XRD structures of RS-2 (left) and R-2 (right) obtained by Burrows et al.**

From inspection of these structures, it is clear the ligands are very strained upon coordinating to the iron centre. The elongated Fe-N bonds are also fitting with the expected range for a HS structure (2.0-2.2 Å).<sup>66</sup> From the XRD data, the angular Jahn-Teller distortion parameters (Section 1.4.6.1)<sup>77</sup> were obtained, which were found to be  $70.03(3) \leq \theta \leq 70.32(3)^\circ$  for **R-2** and  $\theta = 89.23(1)^\circ$  in **RS-2**. Both complexes were said to be so distorted that the conformational rearrangement

required to switch between LS and HS states is energetically unfavourable. Therefore, the complex does not undergo the transition and effectively remains 'trapped' in the HS state at all temperatures. The inhibition of vibrational motions between molecules can also add to the hindrance of a ST in the solid state.<sup>314</sup>

From the SQUID data obtained on the iron(II)PyBOX series (Figure 3.19, Table 3.1), a particularly interesting result was observed with the homochiral and heterochiral Ph- complexes, **R-1** (black line) and **RS-1** (red line) respectively. While both species start in the LS state, as the temperature is increased from 5 K upwards, the homochiral species begins to undergo a very gradual ST just after 200 K. It is not until an approximate 50 K later, i.e. above 250 K, its heterochiral analogue begins to undergo a ST. The  $T_{1/2}$  values are estimated to be  $\approx 350$  K for **R-1** and  $> 400$  K for **RS-1**, from taking its  $X_m T \approx 1.75 \text{ cm}^3 \text{ mol}^{-1} \text{ K}$ .<sup>210</sup> This finding demonstrates a clear distinction in the SCO behaviour between these two isomers in the solid state. The XRD structures for **R-1** and **RS-1** are shown in Figure 3.21.

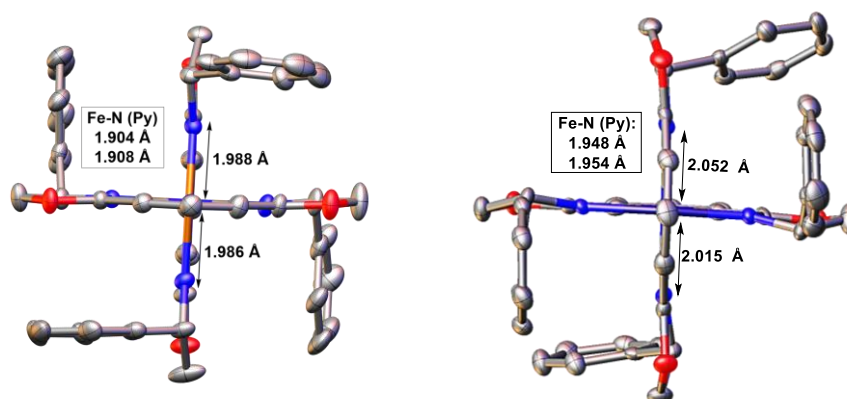


**Figure 3.21.** XRD structures of **RS-1** (left) and **R-1** (right) obtained by Burrows *et al.*

The distortion parameters obtained are  $82.45(2) \leq \theta \leq 86.00(2)^\circ$  (across both phases) for **R-1** and  $88.94(2) \leq \theta \leq 89.14(4)^\circ$  for **RS-1**.<sup>210</sup> Additionally, the Fe-N bond lengths, though both in accordance with that of a LS Fe-N bond ( $1.8\text{-}2.0 \text{ \AA}$ )<sup>66</sup>, still have some disparities between the chiralities, with the homochiral isomer showing slightly longer bond lengths accompanying the slightly more distorted geometry. This reflects the steric clash observed between the phenyl substituents occupying the same quadrant. As the R- substituents point towards each other in the homochiral complexes, the geometry of the ligands is forced to twist a little more, destabilising this isomer. Since the substituents point away from each other in the heterochiral analogues, this twisting has a less-pronounced effect. The geometric distortion in the homochiral

complexes reduces the stability of this isomer, which rationalises the earlier onset of a ST in **R-1** compared to **RS-1**. Considering that single crystal XRD data are typically collected at 100-120 K, the geometry of the phenyl- complexes are supported by the  $X_mT$  values in this temperature region in the SQUID curves which confirms the LS features.

**R-1** and **RS-1** undergo a more gradual spin transition in the SQUID than its achiral counterpart (**4**). However, in the plot of **R-1** a blip is noticeable in the curve around 240 K, which must be attributed to the phenyl substituent, as this is the only difference between the two complexes. The discontinuity of the SQUID curve was probed in the solvated complex **R-1**•MeNO<sub>2</sub>, by collecting x-ray diffraction patterns at 10 K temperature intervals between 125-275 K using the same crystal. From this work it was found that a crystallographic phase change was observed at  $170 \pm 5$  K. However, being 70 K below the blip in the curve, this could not be the sole contribution to the discontinuity. Refinement models of the structures incorporating disorder at the phenyl- substituents on the ligand between 170-235 K seemed to rationalise the blip better.<sup>210</sup>

#### 3.1.4.2 Solution State SCO results

In solution, variable temperature (VT) Evan's <sup>1</sup>H NMR method<sup>121</sup> was used to determine solution state SCO activity of the [Fe(PyBOX<sup>R</sup>)]<sup>2+</sup> series. The solution phase magnetic susceptibility data obtained by Burrows *et al.* (Figure 3.22 and Table 3.2) showed some considerable differences to the findings in the solid state. This is due to the removal of intermolecular forces embedded in the packing of the crystal lattice, such as hydrogen bonding or  $\pi$ - $\pi$  interactions between individual complexes, anions or solvents. These effects affect the cooperativity of the ST across the bulk material. However, in solution individual complexes exist freely as cations, so these secondary effects become irrelevant. There is also now a dilution factor to consider in the solution state and solvent interactions with the NMR solvent and this has been shown to generally lower the  $T_{1/2}$  in the solution state compared to the solid state.<sup>216</sup>

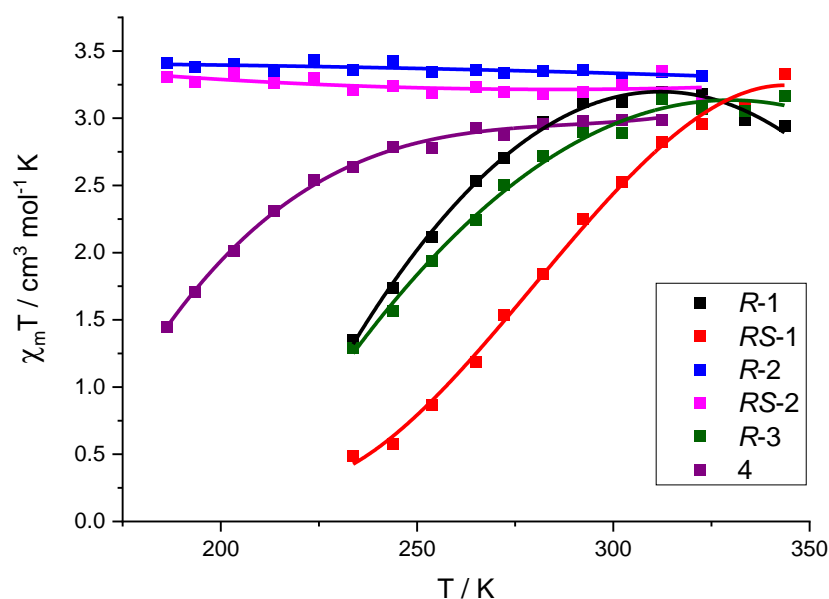


Figure 3.22. Solution phase magnetic susceptibility results of the iron(II)PyBOX<sup>R</sup> complexes studied by Burrows *et al.*<sup>210</sup>

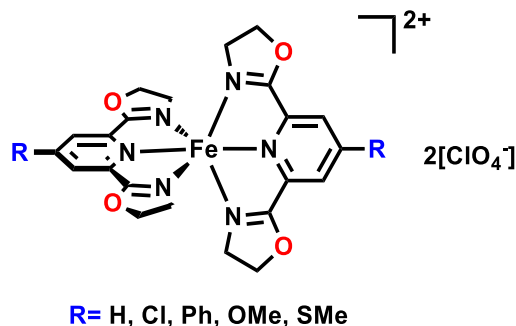
	Complex	R- substituent	T <sub>1/2</sub> (K)
<b>R-1</b>	[Fe((R)-L <sup>Ph</sup> ) <sub>2</sub> ][ClO <sub>4</sub> ] <sub>2</sub>	Ph	244
<b>RS-1</b>	[Fe((R)-L <sup>Ph</sup> )(S)-L <sup>Ph</sup> ][ClO <sub>4</sub> ] <sub>2</sub>	Ph	278
<b>R-2</b>	[Fe((R)-L <sup>iPr</sup> ) <sub>2</sub> ][ClO <sub>4</sub> ] <sub>2</sub>	iPr	HS
<b>RS-2</b>	[Fe((R)-L <sup>iPr</sup> )(S)-L <sup>iPr</sup> ][ClO <sub>4</sub> ] <sub>2</sub>	iPr	HS
<b>R-3</b>	[Fe((R)-L <sup>Me</sup> ) <sub>2</sub> ][ClO <sub>4</sub> ] <sub>2</sub>	Me	192
<b>4</b>	[Fe(L <sup>H</sup> ) <sub>2</sub> ][ClO <sub>4</sub> ] <sub>2</sub>	H	245

Table 3.2. Solution phase magnetic susceptibility data of the iron(II)PyBOX<sup>R</sup> data obtained by the Evan's method by Burrows *et al.*<sup>210</sup>

Upon comparison of the VT measurements in the solution state (Figure 3.22) with the solid state (Figure 3.19), it is clear there is a distinction between the two phases. For example, the complex [Fe((R)-L<sup>Me</sup>)<sub>2</sub>]<sup>2+</sup>, **R-3** (green line in Figure 3.22) showed a spin transition in the solution phase, whereas in the solid state, the perchlorate salt of the complex showed a HS only complex from 5-350 K. These differences highlight the importance of studying VT magnetic susceptibility in both phases of matter. It is notable that more recent SCO studies are now incorporating Evans' VT <sup>1</sup>H NMR method.<sup>216, 315, 316</sup>

Kimura and Ishida also investigated a series of iron(II)-PyBOX complexes but with changing the substituent on the 4-position of the pyridine ring as to explore the electronic effect of having the substituents: H, Cl, Ph, OMe and SMe *trans* to the

ligating N-donor atom of the pyridine ring (Figure 3.23).<sup>317</sup> Inspired by Burrows *et al.*, they also explored the trends in magnetic susceptibility across a temperature range in both the solid and solution states.



**Figure 3.23. Iron-PyBOX complexes studied by Kimura and Ishida with R-substituents on the 4-position of the pyridine ring. (R= H, Cl, Ph, OMe and SMe).**<sup>317</sup>

A remarkable difference was noted when the substituent on the pyridine ring was a methoxy- group (OMe), which was HS at all temperatures in the solid state, but underwent a ST with a  $T_{1/2} = 170$  K in solution,<sup>317</sup> corroborating the different behaviours found by Burrows *et al.*<sup>210</sup> between the two phases. Furthermore, XRD analysis of a single crystal of the methoxy- complex showed a high degree of distortion. Their results are fitting with the electronic behaviours of the R substituents; OMe is the most electron-donating substituent in their study, therefore OMe enhances the  $\pi$ -donor character of the pyridine ring, overpowering its  $\pi$ -accepting ability from the iron centre, which lowers  $\Delta_{\text{oct}}$ , favouring the HS state.

The solution state results by Burrows *et al.* reaffirms the HS character of the homochiral and heterochiral *isopropyl*- complexes (**R-2** and **RS-2** – blue and pink lines respectively). Even with the removal of the secondary coordination sphere effects in the solution state, these complexes seem to remain ‘trapped’ in their HS states at all temperatures between ~200 K to ~300 K.

As observed in the SQUID data, the homochiral and heterochiral phenyl- complexes (**R-1** and **RS-1** – black and red lines respectively) undergo SCO in solution and still observe distinct temperatures at which the spin transitions occur. The  $T_{1/2}$  for **R-1** = 244 K while the  $T_{1/2}$  for **RS-1** = 278 K, which gives a temperature difference,  $\Delta T = 34$  K in solution. That supports the destabilised nature of the homochiral isomer.

### 3.1.4.3 Racemisation studies

In order to further understand the stability of the heterochiral complexes **RS-1** and **RS-2** in solution, a study on the racemisation effects was carried out. This involved monitoring the  $^1\text{H}$  paramagnetic NMRs of these complexes, to observe whether  $^1\text{H}$  NMR peaks corresponding to the homochiral species were present in the heterochiral solution. The  $^1\text{H}$  paramagnetic NMR of the homochiral complexes show distinct peaks from the heterochiral isomer as the proton environments depend on their through-bond Fermi contact shifts and through-space Dipolar pseudocontact interactions with the paramagnetic iron(II) centre.<sup>318</sup> In the heterochiral isomer **RS-1**, there are reduced contact shifts as the substituents each occupy their own molecular quadrant. This results in a reduced magnetic moment at room temperature (Figure 3.24), so the NMR of **RS-1** appears more diamagnetic in character compared to the spectrum of its homochiral isomer. The contact shifts of **R-2** and **RS-2** are more similar to each other, since both complexes are fully high-spin at room temperature (Figure 3.25)

The  $^1\text{H}$  NMR of the heterochiral complex **RS-1** is shown in Figure 3.24 (middle NMR, navy blue) below. For comparison, stacked above and below this NMR in the figure are the homochiral analogue **R-1** (top, dark red) and a 1:1:1 mixture of (*R*)-L<sup>Ph</sup> : (*S*)-L<sup>Ph</sup> : [Fe(ClO<sub>4</sub>)<sub>2</sub>] (bottom, green).

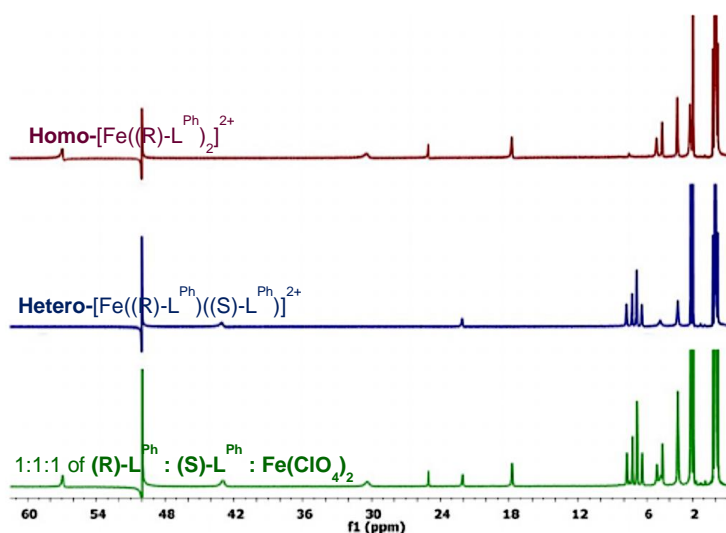


**Figure 3.24.** Paramagnetic  $^1\text{H}$  NMRs of  $[\text{Fe}((R)\text{-L}^{\text{Ph}})_2]^{2+}$  (top, dark red),  $[\text{Fe}((R)\text{-L}^{\text{Ph}})((S)\text{-L}^{\text{Ph}})]^{2+}$  (middle, navy blue) and 1 : 1 : 1 of (*R*)-L<sup>Ph</sup> : (*S*)-L<sup>Ph</sup> : [Fe(ClO<sub>4</sub>)<sub>2</sub>] (bottom, green), in CD<sub>3</sub>CN. The feature at 50 ppm is a spectrometer artefact.

From inspection of the **RS-1** NMR spectrum, it is clear that there are no peaks corresponding to the homochiral species in this spectrum and therefore no evidence

of attempted ligand redistribution to the homochiral **R**- and **S**- complexes, over a 24 hour period.<sup>319</sup>

Ligand redistribution in a solution of a heterochiral complex would occur where the heterochiral complex is less stable than its homochiral counterpart. The weakly-bound ligands would dissociate from the heterochiral complex and then preferentially re-distribute in solution to the homochiral structures. This would produce a solution of equal quantities of homochiral **R**- and **S**- complexes, instead of the heterochiral **RS**-form. It is worth mentioning that the homochiral **R**- and **S**- complexes exhibit identical NMR spectra.

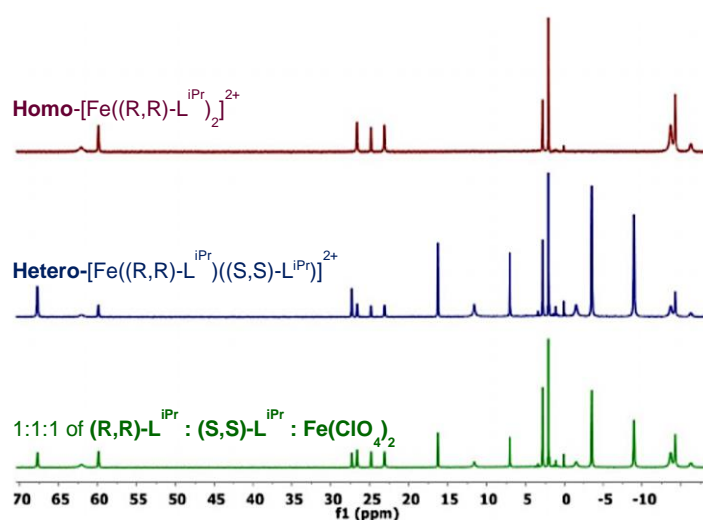


**Figure 3.25.** Paramagnetic  $^1\text{H}$  NMRs of  $[\text{Fe}((R)\text{-L}^{\text{iPr}})_2]^{2+}$  (top, dark red),  $[\text{Fe}((R)\text{-L}^{\text{iPr}})((S)\text{-L}^{\text{iPr}})]^{2+}$  (middle, navy blue) and 1 : 1 : 1 of  $(R)\text{-L}^{\text{iPr}}$  :  $(S)\text{-L}^{\text{iPr}}$  :  $[\text{Fe}(\text{ClO}_4)_2]$  (bottom, green), in  $(\text{CD}_3)_2\text{CO}$ .

In the ligand redistribution study of **RS-2** (Figure 3.25), the paramagnetic  $^1\text{H}$  NMR spectrum of **RS-2** (middle NMR, navy blue), shows peaks corresponding to the homochiral species, **R-2**, in solution. This demonstrates a reduced stability of the heterochiral isomer, in contrast to what was observed with **RS-1**. Upon leaving to stand, the ligand redistribution, was found to present a close to 1 : 1 statistical mixture of **R-2/S-2** : **RS-2** in solution (the initially formed statistical distribution was between 1:5 and 1:3).<sup>210, 319</sup>

In both cases, the *in situ* solution mixtures of 1:1:1 of  $(R)\text{-L} : (S)\text{-L} : \text{Fe}(\text{ClO}_4)_2$  were found to demonstrate paramagnetic  $^1\text{H}$  NMRs with a roughly equal proportion of homochiral and heterochiral species. Hence, in both cases, neither chirality dominates in solution. However, in the case of the 1 : 1 : 1 solution with the phenyl ligands, a preferential crystallisation of the heterochiral complex is clear. However,



once these crystals are re-dissolved, the homochiral species is no longer apparent in the solution.

## 3.2 Results & Discussion

### 3.2.1 Iron(II)thioPyBOX<sup>R</sup> Complexes and Their Spin State Behaviour

The aim of the research in this chapter is a follow-on from the findings by Burrows *et al.* The main objective is to determine whether the chiral discrimination between spin states of an iron(II) complex can be further distinguished beyond what has been reported by Burrows *et al.* for a pair of homochiral and heterochiral iron(II)/PyBOX complexes. This can be accurately studied by measuring the  $\Delta T_{1/2}$  between diastereomers and comparing this to results found with the iron-PyBOX series. The study of the thioPyBOX equivalents will enable parallels and differences to be drawn between these analogous complexes.

Fine-tuning spin state behaviour by using isostructural complexes in the PyBOX/ThioPyBOX system has been demonstrated by Pan *et al.*<sup>216</sup> While they have verified the increased stabilisation of the LS state with the oxygen-replaced sulfur azoline heterocycle of two achiral iron(II)thioPyBOX complexes, chiral discrimination in these compounds is yet to be addressed.

Inspired by the results of Burrows *et al.* along with promising theoretical calculations obtained by Density Functional Theory (DFT),<sup>320</sup> a series of iron(II)thioPyBOX<sup>R</sup> complexes were synthesised and studied using the thioPyBOX<sup>R</sup> ligands discussed in chapter 2.

#### 3.2.1.1 Synthesis of Iron(II)-thioPyBOX Complexes

After long-awaited success in the arduous attempts to synthesise the thioPyBOX ligand, a series of iron-thioPyBOX complexes were prepared by simple metal complexation reactions at room temperature in either acetonitrile or nitromethane. Details of the experimental procedure can be found in Section 3.4.

A 2 : 1 ratio of (*R*)-L<sup>R</sup> or (*S*)-L<sup>R</sup> : [Fe(ClO<sub>4</sub>)<sub>2</sub>]•6H<sub>2</sub>O was used to produce the homoleptic, homochiral iron-thioPyBOX complexes, while a 1 : 1 : 1 ratio of (*R*)-L<sup>R</sup> : (*S*)-L<sup>R</sup> : [Fe(ClO<sub>4</sub>)<sub>2</sub>]•6H<sub>2</sub>O was used to produce the heterochiral complexes (Figure 3.26).

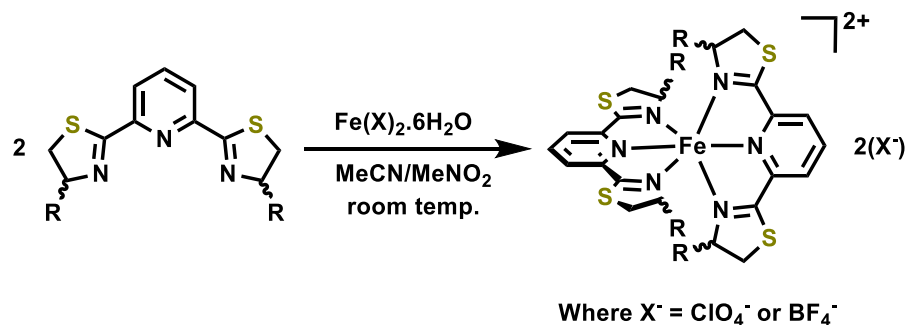


**Figure 3.26. General metal complexation reaction scheme used for the synthesis of iron(II)thioPyBOX complexes.**

The final products were isolated by crystallisation, using the vapour diffusion method. Diffusion of diethyl ether into a concentrated solution of the product in acetonitrile, nitromethane or acetone afforded the complexes in good purity.

### 3.2.1.2 Complexes and Characterisation

The complexes obtained are shown in Figure 3.27. The same notation format has been used as with the iron-PyBOX series, where an **S,S**-complex is a homochiral **S,S**-complex, **R,R**- denotes an **(R,R)**- homochiral complex and **RS**- denotes an **(R,R),(S,S)**-heterochiral complex.

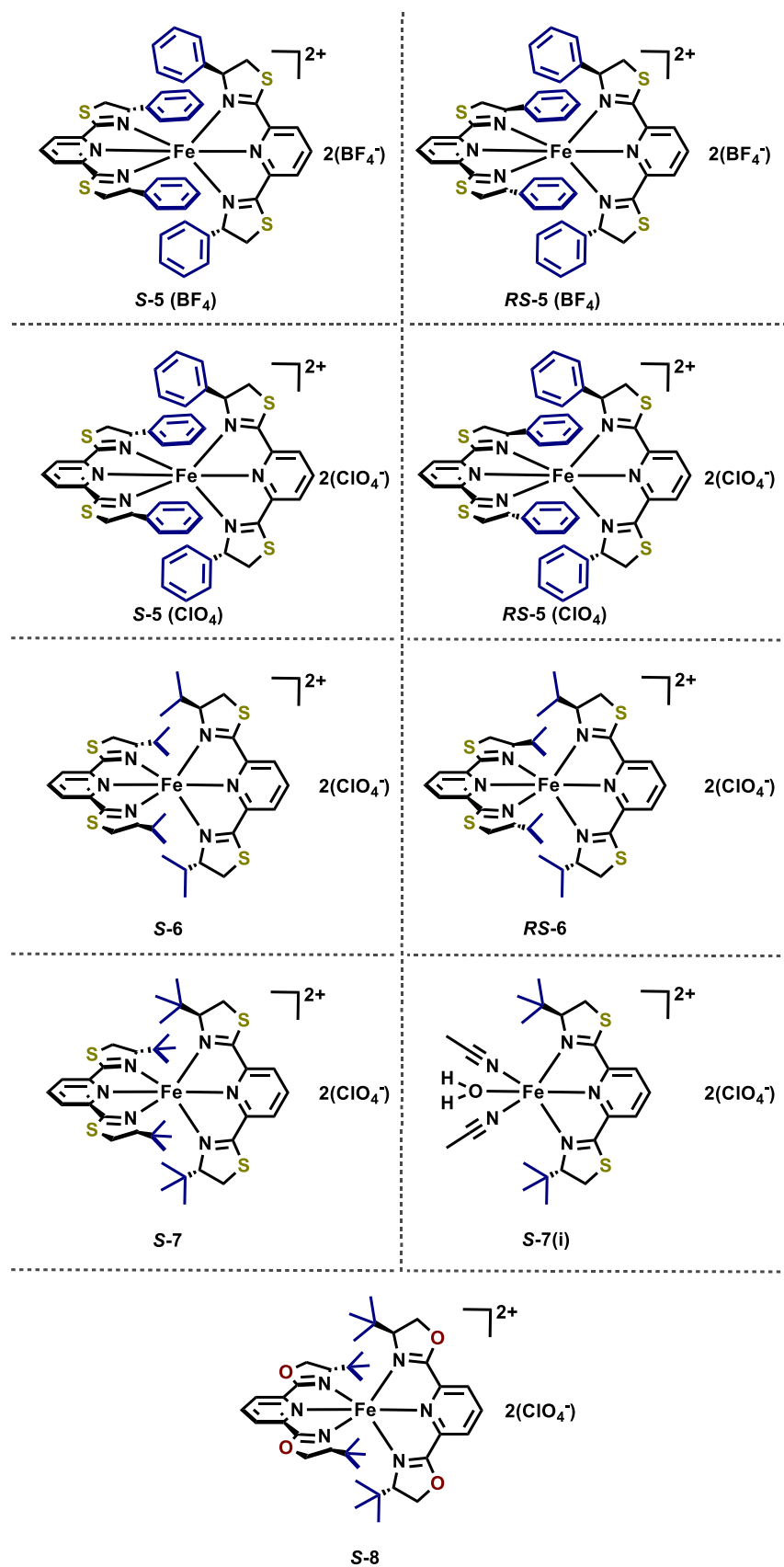


Figure 3.27. Structures of the iron(II)thioPyBOX complexes, S-5 (BF<sub>4</sub>), RS-5 (BF<sub>4</sub>), S-5 (ClO<sub>4</sub>), RS-5 (ClO<sub>4</sub>), S-6, RS-6, S-7 and S-7(i) and the iron(II)PyBOX<sup>tBu</sup> complex, S-8, synthesised herein.

N.B. Although Figure 3.27 displays only the *S*-chirality of the homochiral Ph- and *i*Pr-complexes (**S-5** ( $\text{ClO}_4$ ), **S-5** ( $\text{BF}_4$ ) and **S-6**), their *R*-diastereomers have also been synthesised, giving **R-5** ( $\text{ClO}_4$ ), **R-5** ( $\text{BF}_4$ ) and **R-6** which may also be referred to in this work.

Each complex obtained has been fully characterised by paramagnetic  $^1\text{H}$  NMR, High Resolution Mass Spectrometry (HRMS), single crystal XRD and Elemental Analysis. Magnetic susceptibility measurements have been obtained in the solid state using the SQUID magnetometer, and in the solution state using the VT Evans'  $^1\text{H}$  NMR method – as was performed with the PyBOX analogues (Section 3.1.4).

### 3.2.1.3 Structural Characterisation by X-ray Diffraction

#### 3.2.1.3.1 Iron(II) thioPyBOX<sup>Ph</sup> Structures

The structure solutions obtained using XRD are shown in Figure 3.28-Figure 3.42.

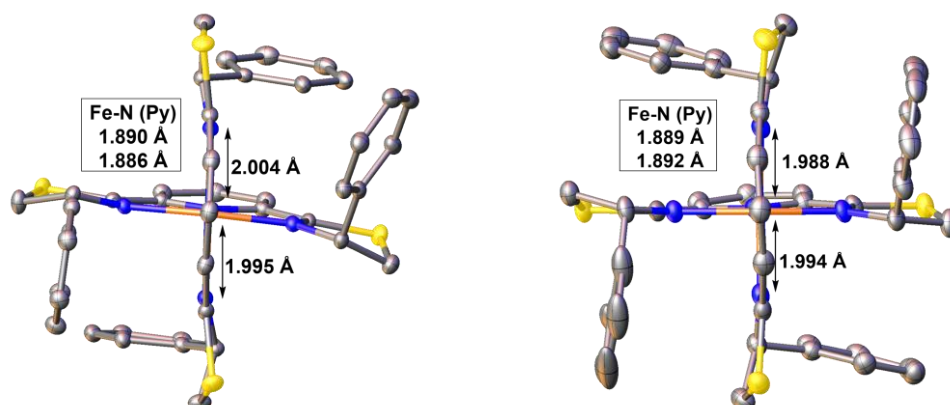


**Figure 3.28.** XRD structures of **S-5** ( $\text{BF}_4$ ) (left) and **RS-5** ( $\text{BF}_4$ ) (right). Hydrogen atoms, counter-ions and solvents are omitted for clarity. Thermal ellipsoids are displayed at 50% probability level.

The XRD structures of **S-5** ( $\text{BF}_4$ ) and **RS-5** ( $\text{BF}_4$ ) were collected at 100 K using the synchrotron at Diamond Light Source. These structures both show bond lengths and angles similar to each other fitting within the LS range of an Fe-N bond. At first glance, there does not seem to be a huge degree of distortion in the geometries, except for the homochiral complex **S-5** ( $\text{BF}_4$ ) which has a slight twist in its coordination owing to the phenyl substituents which are canted to minimise a steric clash within their shared space. This is the only notable difference between these two chiralities and is akin to that seen with the PyBOX equivalents. This is supported by their JT angular distortion parameters,  $\theta$  of  $81.63(10)^\circ$  for **S-5** ( $\text{BF}_4$ ) and  $88.09(12)^\circ$  for **RS-5** ( $\text{BF}_4$ )

(Section 1.4.6.1). The value of  $\theta$  for **S-5 (BF<sub>4</sub>)** is ca. 10 ° greater than found in **R-2** ( $70.03(3) \leq \theta \leq 70.32(3)$ )<sup>210</sup> which shows that the larger S atom in thioPyBOX<sup>Ph</sup> alleviates some of the steric strain in the coordination sphere. This difference is however most notable in the homochiral complexes, as the  $\Delta\theta$  for the heterochiral analogues is only approximately 3 ° with  $\theta_{RS-5(BF_4)} > \theta_{RS-2}$ .

The equivalent XRD structure was collected for the complex of the perchlorate counter-ion **R-5 (ClO<sub>4</sub>)** however at 120 K using Cu source x-ray beam (Figure 3.29). This structure shows remarkable similarity to the tetrafluoroborate equivalent and is therefore also indicative of LS state. The homochiral tetrafluoroborate and perchlorate complex salts are isostructural with one another and their complexes are confidently reproducible as they are phase pure, which was confirmed by powder-XRD (pXRD) analysis.

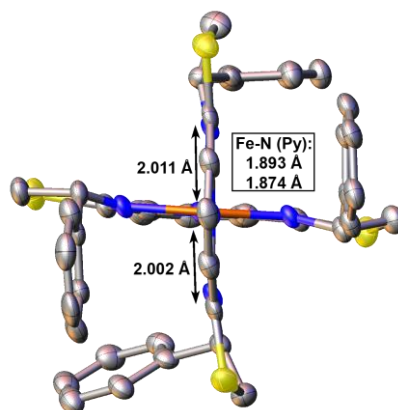


**Figure 3.29.** XRD structures of **R-5 (ClO<sub>4</sub>)**. Hydrogen atoms, counter-ions and solvents are omitted for clarity. Thermal ellipsoids are displayed at 50% probability level.

The heterochiral species **RS-5**, shows a similar degree of phenyl group canting to the homochiral species despite the substituents no longer pointing towards one another. This twist in the R- group in this diastereomer can be attributed to the intramolecular interaction between the sulfur atom of the thiazoline ring and the phenyl groups. The S...Ph interaction in **RS-5 (BF<sub>4</sub>)** is evident in the space-filling model of the XRD structure which shows the thiazoline ring and phenyl substituent are in close contact (Figure 3.30), which is otherwise unapparent in its homochiral analogue (Figure 3.31).

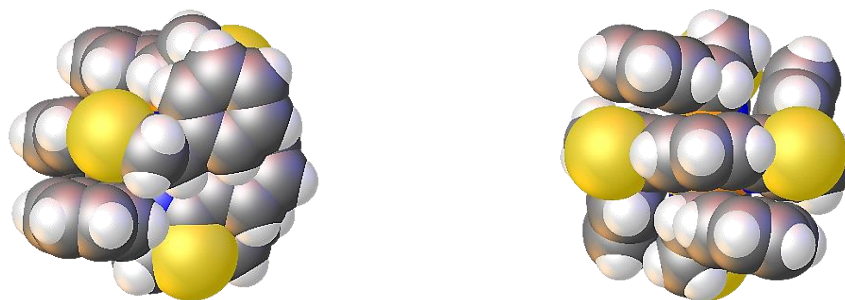


**Figure 3.30. Space-filling model of *RS-5* ( $\text{BF}_4$ ). H atoms have been omitted for clarity.**

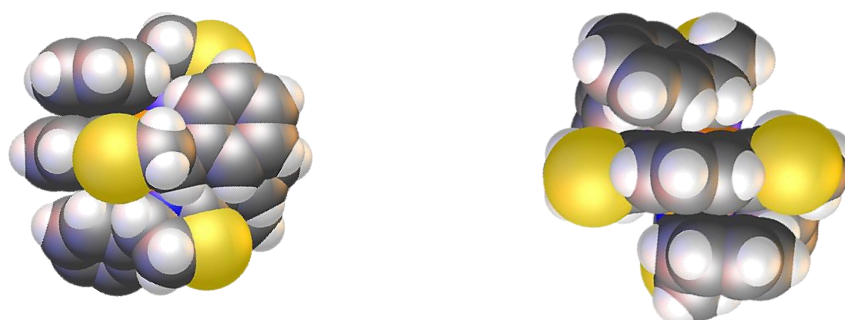


**Figure 3.31. Space-filling model of *S-5* ( $\text{BF}_4$ ). H atoms have been omitted for clarity.**

Space-filling models of the PyBOX analogues demonstrates the stability of the heterochiral PyBOX<sup>Ph</sup> complexes, *meso*-[M((*R*)-L<sup>Ph</sup>)((*S*)-L<sup>Ph</sup>)]<sup>2+</sup> (where M= Fe, Co, Zn) with the interactions between the phenyl substituents in each quadrant, which display offset  $\pi$ - $\pi$  interactions with the pyridine ring of the co-ligand in the molecule.<sup>210, 319</sup> This three-layer offset  $\pi$ - $\pi$  interaction can also be seen in the thioPyBOX isostructure in Figure 3.30. Furthermore, a clash between the C-H group of the substituent phenyl ring with the pyridine ring in the co-ligand can be observed in the homochiral complex, which also contributes to the destabilisation of this isomer. This effect was also observed by Burrows *et al.*<sup>210</sup>

Considering that the spin state of both the PyBOX<sup>Ph</sup> and thioPyBOX<sup>Ph</sup> complexes, ***R-1*** and ***R-5* ( $\text{ClO}_4$ )** respectively, and ***RS-1*** and ***RS-5* ( $\text{BF}_4$ )** respectively, are the same at 120 K, the XRD structure of the two analogues can be compared (Figure 3.32 and Figure 3.33).

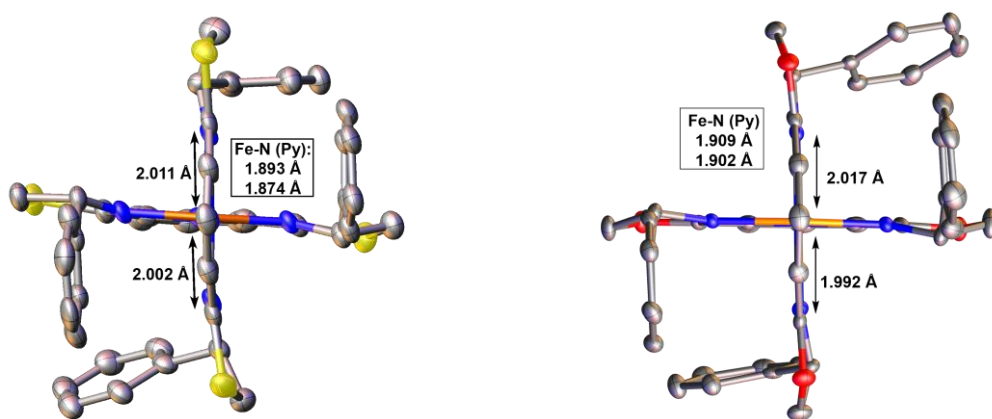


Figure 3.32. XRD structures of the homochiral phenyl- complex; *R-5* (left) and PyBOX analogue, *R-1* (right).<sup>210</sup>

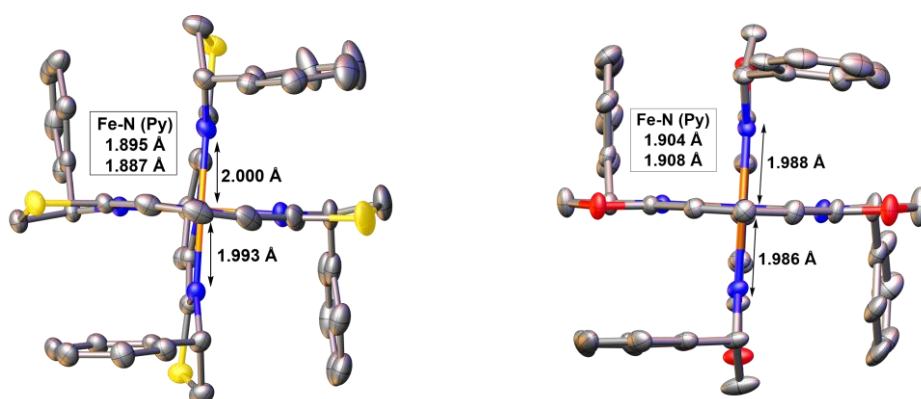


Figure 3.33. XRD structures of the heterochiral phenyl- complex; *RS-5* (left) and the PyBOX analogue, *RS-1* (right).

Considering the homoleptic complexes in Figure 3.32, their structures show minimal differences between them. The Fe-N bond lengths are slightly shorter in the thioPyBOX complex which is as anticipated from the reduced electron-withdrawing effect from the thiazoline ring to the iron centre, compared to oxazoline. The oblique phenyl substituents twist in both cases, however the space-filling models shows this occurs to a greater extent in the PyBOX complex, which is reasonable considering its more constricted coordination sphere and therefore experiences a greater degree of inter-ligand repulsion (Figure 3.34). An XRD structure obtained within this work of the tetrachloroiron(III) salt of *R-5*,  $R-5[Fe^{III}Cl_4]_2$ , showed almost no canting on the phenyl- substituents of the ligand, which suggests the canting arises due to crystal packing of *R-1* and *R-5* with the similar sized anions  $ClO_4^-$  and  $BF_4^-$ .

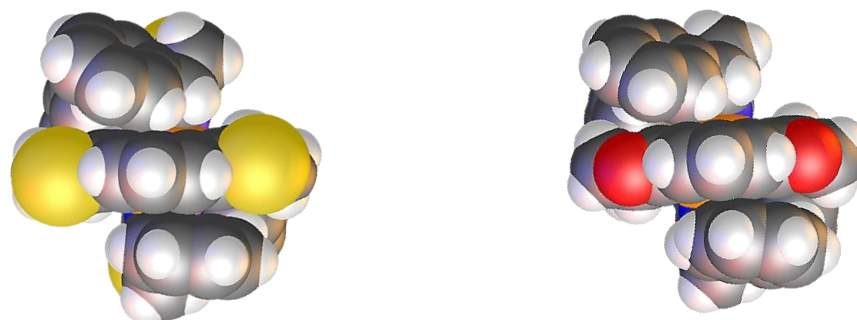


Figure 3.34. Space-filling models of *R*-5 ( $\text{ClO}_4$ ) (left) and *R*-1 (right).

Though some degree of canting of the phenyl- substituents is evident in *RS*-5, this is still more of a twist than is observed in other reported heterochiral metal-PyBOX complexes,  $[\text{M}((R)\text{-L}^{\text{PyBOX}})((S)\text{-L}^{\text{PyBOX}})]^{2+}$  <sup>319, 321</sup> ( $\text{M} = \text{Fe}$ , <sup>210</sup>  $\text{Cu}$ , <sup>322</sup>  $\text{Zn}$ , <sup>323</sup>  $\text{Co}$ , <sup>324</sup>).

Comparison of the *meso*-heterochiral complexes in Figure 3.33 shows a degree of twisting in the backbone of the thioPyBOX complex *RS*-5 ( $\text{BF}_4$ ), which is not observed in the PyBOX analogue. This strain across the ligand framework is a consequence of the ring strain in the thiazoline ring, which puckers due to the larger size of the sulfur atom. This sulfur atom is in direct contact with the phenyl- groups and so the structure twists to accommodate this repulsion. The two thiazoline rings on the same ligand twist in opposite directions, i.e. *transoid* to each other, as to minimise steric clash. That results in a slight twist across the pyridine ring. The *trans*- $\text{N}_{\text{Py}}\text{-Fe-N}_{\text{Py}}$  angles ( $\phi$ ) <sup>78</sup> across both isomers show a slightly smaller  $\phi$  than their PyBOX counterparts (ca. 176-177 ° vs. 178-179 °; Section 1.4.6.1), <sup>210</sup> supporting this observation (Table 3.3). A point of further comparison is the *trans* angles across the same ligands from one nitrogen of the thiazoline/oxazoline ring, across the Fe centre, to the nitrogen of the other thiazoline/oxazoline ring,  $\text{N}_{\text{Ox}}\text{-Fe-N}_{\text{Ox}}$  ( $\varphi$  in Table 3.3) which are in the same range as its PyBOX counterparts for both isomers. This is fitting with the distortion observed in the pyridine rings in the iron-thioPyBOX complexes.

Complex	<i>S</i> -5 ( $\text{BF}_4$ )	<i>RS</i> -5 ( $\text{BF}_4$ )	<i>R</i> -5 ( $\text{ClO}_4$ )
$\text{Fe-N}_{\text{Py}}$ (Å)	1.889(2) 1.887(2)	1.889(2) 1.895(2)	1.893(6) 1.874(7)
$\text{Fe-N}_{\text{Ox}}$ (Å)	1.995(2)-2.005(2)	1.957(2)- 2.000(3)	2.002(8)- 2.016(7)
$\theta$ (°)	81.632	91.906	81.728
$\phi$ (°)	176.46(10)	176.86(11)	176.56(3)
$\varphi$ (°)	159.61(10) 159.93(10)	159.45(10) 159.28(10)	159.64(3) 159.94(3)

Table 3.3. Selected bond lengths and angles of the complexes *R*-5 ( $\text{BF}_4$ ), *RS*-5 ( $\text{BF}_4$ ), *R*-5 ( $\text{ClO}_4$ ) and *RS*-5 ( $\text{ClO}_4$ ).



While a degree of canting of the phenyl substituents is evident in both homochiral complexes, the increased spatial conformation of the thioPyBOX ligand in iron's coordination sphere, compared to the PyBOX ligand, reduces the steric clash between the phenyl substituents in **R-5**. The interatomic distances between the two closest carbon atoms on each pair of phenyl rings can be compared. These are the *ortho* carbon atoms on each phenyl substituent, that is closest to the *ortho* carbon on the other phenyl ring in its same quadrant (Figure 3.35). The greater spatial arrangement between the phenyl substituents in **R-5 (ClO<sub>4</sub>)** further evidences that this isostructure is more stabilised.

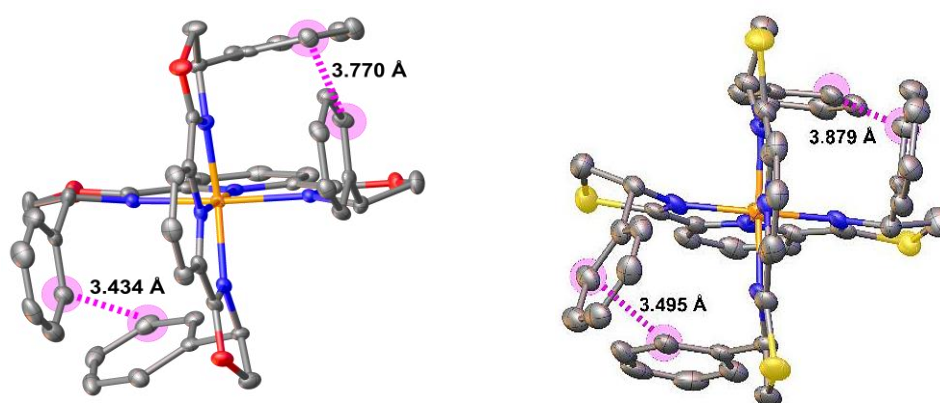


**Figure 3.35. XRD structures of R-1 (left) and R-5 (ClO<sub>4</sub>) (right) highlighting the interatomic distances used for comparison.**

The observations comparing **R-5 (ClO<sub>4</sub>)** and **S-5 (BF<sub>4</sub>)** are rather consistent with each other throughout this work, displaying minimal differences in their solid state analysis. Their packing structures (Figure 3.36) both show a strong network of C-H...X contacts between the anions and the phenyl C-H groups most appropriately aligned for the interaction. In **R-5 (ClO<sub>4</sub>)** the ClO<sub>3</sub>O<sup>-</sup>...H-Ph contact has an average interatomic distance of 2.45 Å while in **S-5 (BF<sub>4</sub>)** the <sup>-</sup>BF<sub>3</sub>F...H-Ph contact has an average distance of 2.38 Å, plus an additional contact interaction with one hydrogen from the CH<sub>2</sub> group of the thiazoline ring. This contact has a distance of 2.41 Å. These distances are all 0.1-0.2 Å shorter than the sum of the van der Waals radii of an H and an F/O atom.<sup>325</sup>

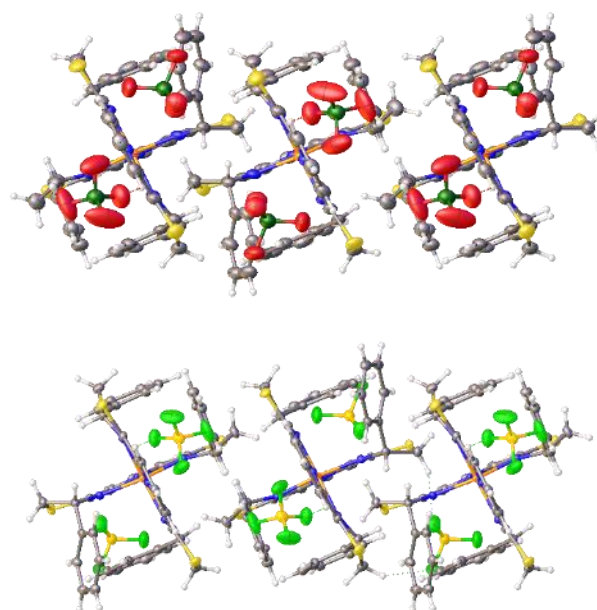


**Figure 3.36. Packing structures of *R*-5 ( $\text{ClO}_4$ ) (top) and *S*-5 ( $\text{BF}_4$ ) (bottom) with hydrogen bonding displayed, structures are both shown along the *b*-axis.**

In one of the attempts to synthesise the heterochiral complex ***RS*-5**, a racemic conglomerate, ***[R-5•S-5][ClO<sub>4</sub>]<sub>4</sub>•2MeCN*** was discovered in addition to the *meso*-heterochiral complex ***RS*-5[ClO<sub>4</sub>]<sub>2</sub>•2MeCN**. This was formed by the slow evaporation method and was confirmed by single crystal XRD analysis (Figure 3.37). The *meso*-heterochiral isomer is the one that preferentially crystallises owing to its greater thermodynamic stability.

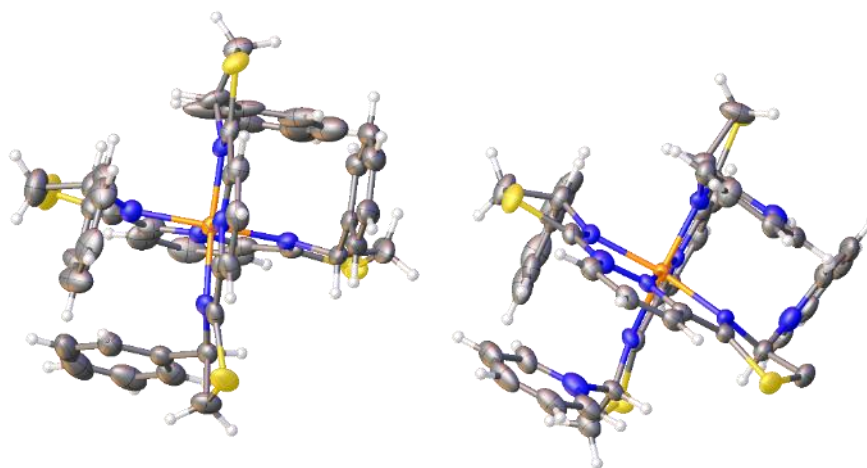


**Figure 3.37. XRD structure of  $[\text{Fe}((R)\text{-L}^{\text{Ph}})_2][\text{Fe}((S)\text{-L}^{\text{Ph}})_2][\text{ClO}_4]_4\cdot 2\text{MeCN}$ , *R*-5•*S*-5. Solvents, hydrogen atoms and counter-ions are omitted for clarity. Thermal ellipsoids are at the 50% probability level.**

### 3.2.1.3.2 Iron(II) thioPyBOX<sup>iPr</sup> Structures

The XRD structure of the perchlorate salt of the heterochiral *isopropyl* complex, **RS-6** is shown in Figure 3.38.

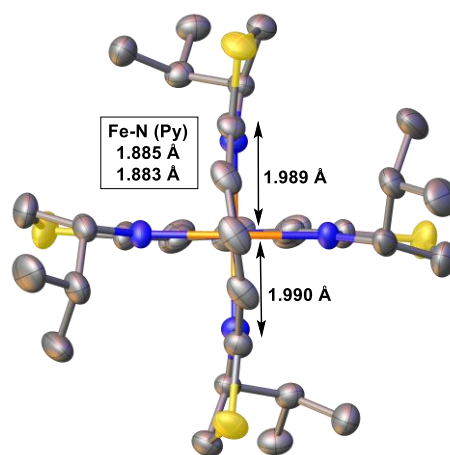


**Figure 3.38.** XRD structure of **RS-6**. Hydrogen atoms, counter-ions and solvents are omitted for clarity. Thermal ellipsoids are displayed at 50% probability level.

The XRD structure of **RS-6**, collected at 120 K, shows bond lengths and angles akin to the phenyl- complexes, and so also indicate a LS structure. From the XRD structure, it is notable that bulky *isopropyl* groups are oriented as to have the CH<sub>3</sub> groups pointing externally to the coordination sphere as to minimise steric clash. This leaves the much smaller hydrogen atom  $\text{HC}(\text{CH}_3)_2$  oriented towards the pyridyl ring of the co-ligand.

In comparison to **RS-5**, **RS-6** demonstrates a slightly greater twist about the ligand conformation, giving the structure a small degree of helicity. This is due to the greater steric influence of the *isopropyl*- substituents on the backbone of the complex framework, as was observed in the PyBOX analogues.

Considering the HS nature of **RS-2** and the LS nature of **RS-6**, a direct comparison of the two structures cannot be made due to their different spin states at the temperature of measurement. The distinctions between the two XRD structures obtained are highlighted in Figure 3.39 below.

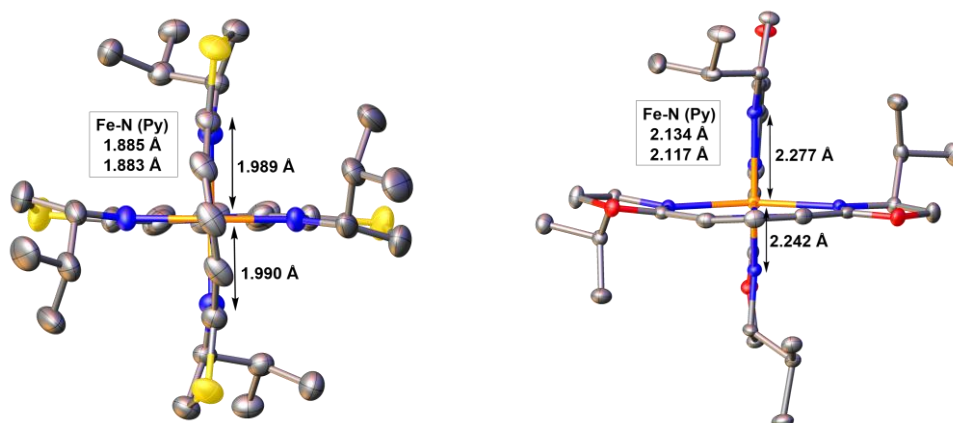


**Figure 3.39. XRD structure of the heterochiral *isopropyl*- complex; *RS-6* (left) and PyBOX analogue, *RS-2* (right).<sup>210</sup>**

Though the two complexes in Figure 3.39, only differ in the sulfur/oxygen atom in the ligand, these complexes have distinct geometrical differences between them correlated to their differences in spin state behaviour.

The  $[\text{Fe}((R)\text{-PyBOX}^{iPr})((S)\text{-PyBOX}^{iPr})][\text{ClO}_4]_2$  complex, ***RS-2***, has a more JT-distorted structure than the thioPyBOX analogue, ***RS-6***. This is particularly evident from its elongated bonds and higher degree of angular distortions between the two planes of the ligands showing a clear deviation from an octahedral geometry, which is indicative of the HS state. This is contrasting with the thioPyBOX equivalent which displays much more LS-like features (Table 3.4). The XRD structure of ***RS-6*** highlights the reduced steric strain provided by the sulfur atom about the iron coordination sphere.

Complex	<i>RS-6</i>
Fe-N <sub>Py</sub> (Å)	1.885(4) 1.883(4)
Fe-N <sub>Ox</sub> (Å)	1.989(4)-1.994(3)
$\theta$ (°)	89.749
$\phi$ (°)	179.71(14)
$\varphi$ (°)	158.73(17) 161.01(17)

**Table 3.4. Selected bond lengths and angles of the complex *RS-6*.**

The data from the XRD solution for the complex ***RS-2*** reported by Burrows *et al.* show bond lengths in the HS range of 2.1170(14) – 2.2771(15) Å, and the dihedral angle between the least squares planes of the two ligands to be 89.23 °.<sup>210</sup> The JT distortion in the structure is evident from the *trans* N<sub>Py</sub>-Fe-N<sub>Py</sub> angle  $\phi = 163.62$  °

which is apparent in the XRD structure which shows the pyridine ring backbone of one of the ligands to be bent out of plane (Figure 3.39).

While all four of the *isopropyl* substituents orient themselves in the same way in **RS-6**, and three out of the four substituents in **RS-2** agree with this, the fourth one, which is in the bottom centre in **RS-2** in Figure 3.39 has a different orientation where it points downwards. The space-filling diagrams highlights this difference (Figure 3.40).

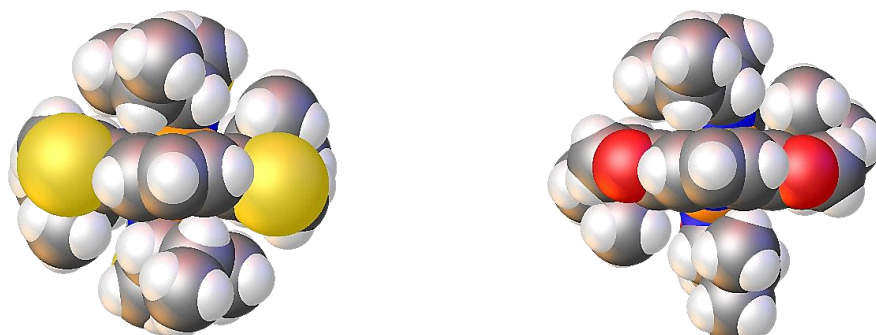


**Figure 3.40. Space-filling models of *RS-6* (left) and *RS-2* (right)**

Consideration of the packing diagram with the intermolecular interactions displayed, helps to understand the incentive for this preferential configuration for **RS-2** (Figure 3.41).

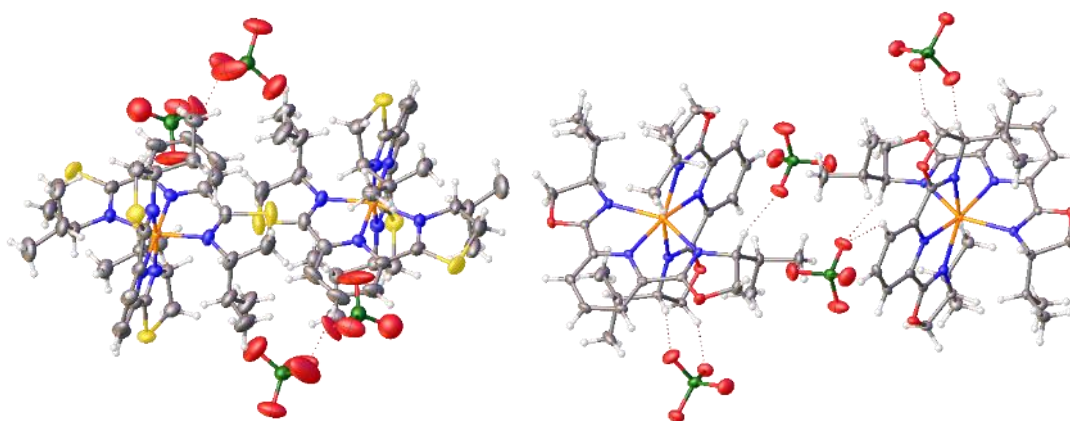


**Figure 3.41. Packing structures of *RS-6* (left) and *RS-2* (right) with hydrogen bonding displayed, only two complexes are shown for clarity. Structures are both shown along the *a*-axis.**

A network of C-H...O contacts is observed in **RS-2** between the  $\text{ClO}_4^-$  ion and a hydrogen atom from one of the *isopropyl* groups on each ligand, plus a second

contact is evident from the same oxygen atom to either the  $\underline{\text{H}}\text{C}(\text{CH}_3)_2$  or the  $-\underline{\text{H}}\text{C}-$  at the 3- or 5- position of the pyridine ring. Interestingly, while there are still hydrogen contacts and bifurcated hydrogen contacts in **RS-6**, none of them involve an *isopropyl* group. Rather these contacts occur between the  $\text{ClO}_4^-$  anion and the *trans*  $-\underline{\text{H}}\text{C}-$  of pyridine ring (i.e. at the 4- position). The contacts in **RS-6** are slightly stronger than those in **RS-2** as the average hydrogen contacts distances are 2.34 Å and 2.43 Å respectively. The contacts in **RS-6** demonstrates the *trans* influence of the shorter and stronger Fe-N<sub>Py</sub> bonds on the C-H bond *para* to it in the complex.

### 3.2.1.3.3 Iron(II) thioPyBOX<sup>tBu</sup> Structures

The formation of the complex  $[\text{Fe}((\text{S})\text{-thioPyBOX}^{\text{tBu}})_2][\text{ClO}_4]_2$  was expected to be highly unlikely considering the increased steric bulk from the *tert*butyl- substituents, which would result in unfavourable steric clash in the homochiral isomer.

Many crystallisation attempts using vapour diffusion and slow diffusion methods were carried out to obtain a single crystal of the homochiral *tert*butyl- complex, **S-7**, for XRD analysis. A multitude of different approaches including varying solvent combinations and synthesising the complex with different counter-ions such as tetrafluoroborate and triflate, proved unsuccessful. The increased difficulties with isolating this complex can be attributed to the hydrophobic nature of the *tert*butyl substituents which solubilise the complex.

Eventually it was found that vapour diffusion of diethyl ether into a solution of the perchlorate salt of the complex in acetone grew suitable single crystals. This gave **S-7** which was collected at 100 K using a synchrotron source (Figure 3.42).

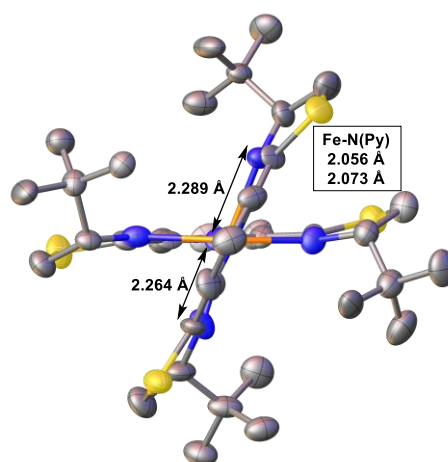


**Figure 3.42.** XRD structure of **S-7**. Hydrogen atoms, counter-ions and solvents are omitted for clarity. Thermal ellipsoids are displayed at 50% probability level.

The HS structure of **S-7** has a highly twisted geometry, to accommodate the steric clash between the *tert*butyl groups. The energetic cost of the structural rearrangement to its LS structure is too large and therefore the complex remains trapped in the HS state, particularly in the solid state as seen in some of the PyBOX derivatives.<sup>210, 326-328</sup> The bond lengths and angles are shown in Table 3.5.

Complex	S-7
Fe-N <sub>Py</sub> (Å)	2.056(9), 2.073(9)
Fe-N <sub>Ox</sub> (Å)	2.264(11)-2.292(10)
$\theta$ (°)	57.164
$\phi$ (°)	178.1(4)
$\varphi$ (°)	150.1(3) 148.5(4)

**Table 3.5. Selected bond lengths and angles of the complex S-7.**

While the *trans* N<sub>Py</sub>-Fe-N<sub>Py</sub> angle, ( $\phi$ ) minimally deviates from the perfect octahedral value of  $\phi = 180^\circ$ , the ligand bite angle  $\varphi$  is among the lower values observed for such meridonal N,N',N'' tridentate ligands, and fits the HS data in the graph of clamp angle ( $\varphi$ ) vs. Fe-N bond length (Å) for [Fe(1-bpp)<sub>2</sub>]<sup>2+</sup> complexes discussed by Kershaw Cook *et al.* (Figure 3.43).<sup>329</sup>

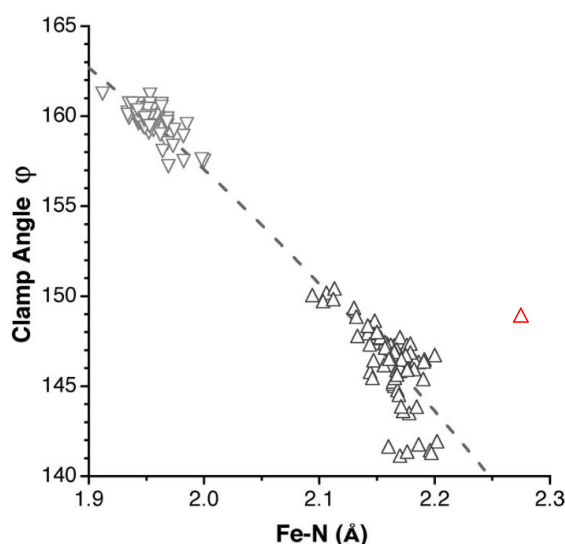


**Figure 3.43. The clamp angle  $\varphi$  plotted against average Fe-N bond distances in a series of [Fe(1-bpp)<sub>2</sub>]<sup>2+</sup> complexes. Upwards triangles are HS complexes, and downward triangles are LS. Figure taken from publication.<sup>329</sup> The added red triangle is approximately where the complex S-7 would fit this data.**



The JT angle between the two least squares planes of the thioPyBOX<sup>tBu</sup> ligands in **S-7** is 57.16(4) °. This shows an even greater JT angular distortion than the current record holder of [Fe(bppyz)<sub>2</sub>][SbF<sub>6</sub>]<sub>2</sub> where bppyz = 2,6-di(pyrazolyl)pyrazine, which has been reported to have a dihedral angle of 59.84(3) °.<sup>83</sup> This high degree of angular distortion has also been previously reported in other tris-heterocyclic HS iron(II) complexes.<sup>329</sup>

While the bond lengths are clearly indicative of a HS structure at the XRD temperature, some Fe-N bond lengths even exceed the typical 2.0-2.2 Å range for a HS structure.<sup>66</sup> The large steric influence of the bulky *tert*butyl- substituents disfavours short Fe-N bond lengths which are otherwise associated with the LS state.<sup>67, 330</sup> **S-7** is among the most distorted HS iron(II) complexes that have been reported to date. Sections 3.2.1.5-3.2.1.6 will show how this high degree of distortion hinders accessing the LS state at low temperatures by thermally-stimulated SCO.<sup>78, 331</sup>

Many attempts were made, to synthesise and isolate the heterochiral *tert*butyl-complex, as was done with the phenyl- and *isopropyl*- analogues. However, this proved unsuccessful. One attempt gave a co-crystallised unit of both diastereomers of the tBu-ligand, in the absence of any metal; (R)-L<sup>tBu</sup>•(S)-L<sup>tBu</sup>, which is described in chapter 2. Another single crystal, from the same reaction attempt, instead gave a mono-thioPyBOX<sup>tBu</sup> complex, [Fe((S)-L<sup>tBu</sup>)(NCMe)<sub>2</sub>(OH<sub>2</sub>)][ClO<sub>4</sub>]<sub>2</sub> **S-7(i)**, of which a structure solution was obtained using XRD (Figure 3.44).

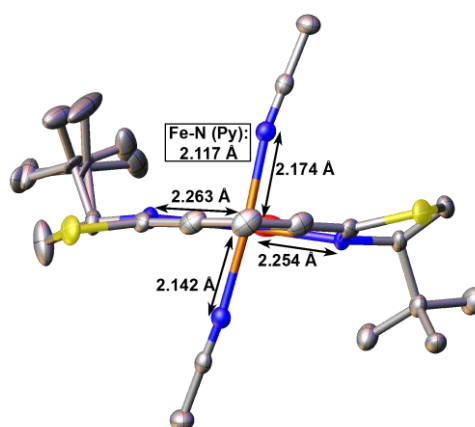


**Figure 3.44.** XRD structure of **S-7(i)**. Hydrogen atoms, counter-ions and solvents are omitted for clarity. Thermal ellipsoids are displayed at 50% probability level.

This complex was crystallised by vapour diffusion of diethyl ether into a concentrated solution of the complex in acetonitrile. Considering the twist in the ligand backbone



observed with the heterochiral *isopropyl* complex **RS-6**, it can be thought that this distortion would only be more pronounced in the heterochiral *tert*butyl analogue, hindering its formation. While the homochiral isomer can accommodate a distortion, the stoichiometric quantity in the reaction mixture made this unfavourable and so this structure is observed, which preferentially binds just one thioPyBOX<sup>tBu</sup> ligand. Acetonitrile molecules occupy two of the remaining coordination sites, *trans* to each other, and a water molecule occupies the sixth equatorial position. As expected of such mono- complex, the reduced  $\pi$ -back bonding effects results in a completely high spin structure.

As was speculated with **S-7**, it was expected that formation of the equivalent PyBOX<sup>tBu</sup> complex would be even more unlikely. However, following the successful isolation of **S-7**, several attempts were then made at the synthesis of the PyBOX<sup>tBu</sup> equivalent. Using the same crystallisation method and solvents as was used for the thioPyBOX analogue, a single crystal suitable for XRD was obtained confirming the structure, which has not yet been reported in the literature (Figure 3.45).

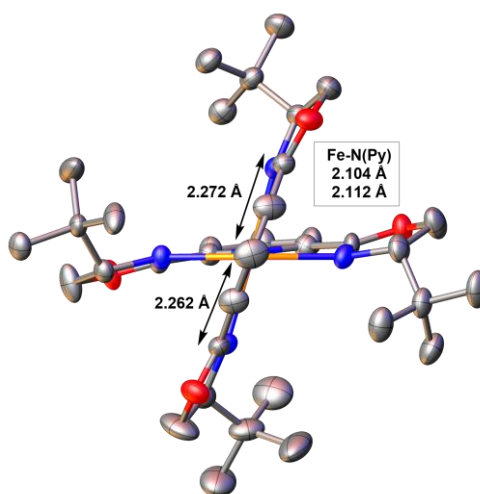


**Figure 3.45.** XRD structure of  $[\text{Fe}((\text{S,S})\text{-tBu-PyBOX})_2][\text{ClO}_4]_2$ , **S-8**.

The homoleptic iron(II) *tert*butyl- complexes can be directly compared since they both display the same spin state behaviour at 120 K, that is, HS in both the solid and solution states at all temperatures. Figure 3.46 shows the comparison of both these XRD images.

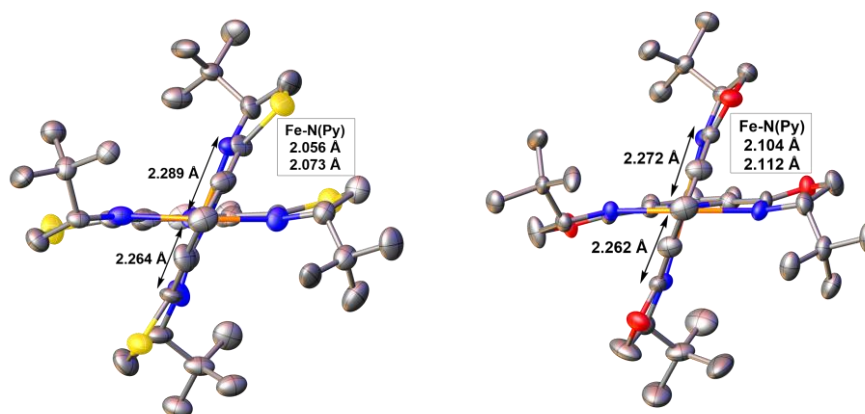


**Figure 3.46. XRD structures of the homochiral *tert*butyl- complexes; **S-7** (left) and its PyBOX analogue, **S-8** (right).**

The bond lengths and JT distortion angles of these isostructural compounds are tabulated in Table 3.6.

Complex	<b>S-7</b>	<b>S-8</b>
<b>Fe-N<sub>Py</sub> (Å)</b>	2.056(9), 2.073(9)	2.104(5), 2.112(5)
<b>Fe-N<sub>Ox</sub> (Å)</b>	2.264(11)-2.292(10)	2.262(5)- 2.272(5)
$\theta$ (°)	57.164	61.859
$\phi$ (°)	178.1(4)	175.12(19)
$\varphi$ (°)	150.1(3)	148.63(18)
	148.5(4)	148.28(18)

**Table 3.6. Selected bond lengths and angles for comparison of **S-7** and **S-8**.**

While the Fe-N<sub>Ox</sub> bond lengths and ligand bite angle N<sub>Ox</sub>-Fe-N<sub>Ox</sub>,  $\phi$  are within error of one another for **S-7** and **S-8**, the differences between the two structures seem to be where the N<sub>Py</sub>-Fe bonds are involved. The N<sub>Py</sub>-Fe-N<sub>Py</sub> bond angle is slightly smaller by 3 ° and the Fe-N<sub>Py</sub> bond lengths are elongated by ca. 0.4 Å in **S-8** compared to **S-7**. Figure 3.47 shows their packing structures with their hydrogen bonding networks.

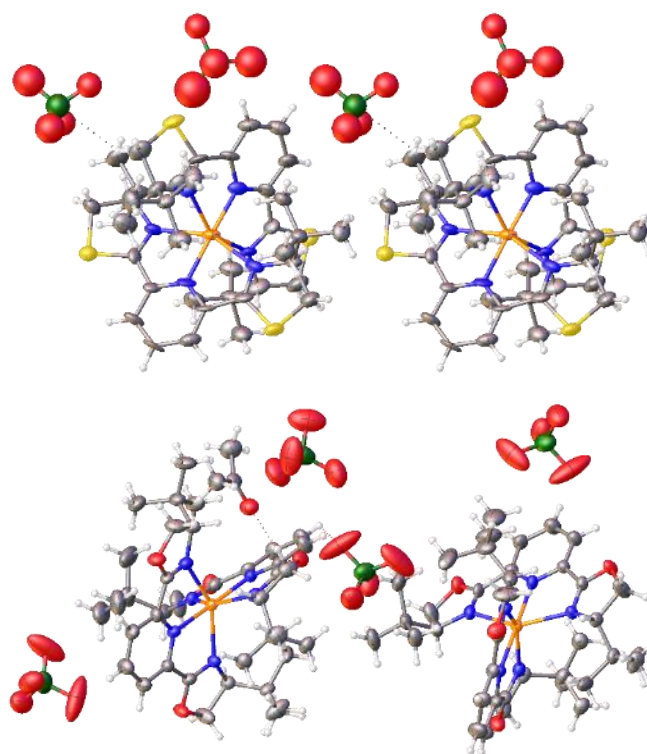


**Figure 3.47. Packing structures of S-7 (top) and S-8 (bottom) with hydrogen bonding displayed, only two complexes are shown for clarity. Structures are both shown along the *a*-axis.**

As with other iron PyBOX and thioPyBOX complexes, the network of C-H...X contacts also differs between **S-7** and **S-8**. This can be understood by their different electronic effects. While the oxygen atom of the oxazoline ring is more electronegative than the sulfur of the thiazoline ring, this results in a greater polarity difference between oxygen and its neighbouring CH<sub>2</sub> group. This increased polarity of the CH<sub>2</sub> group renders those hydrogen atoms more susceptible to hydrogen bonding. The electronegative oxygen atoms of the perchlorate counter-ions further facilitates this interaction which can be observed in Figure 3.47. This hydrogen atom also forms C-H...O contacts with the acetone solvent, which is uninvolved in H-bonding in the thioPyBOX analogue. In **S-7**, the less electronegative sulfur atom does not polarise the thiazoline CH<sub>2</sub> group as much and there is now no attractive interaction between these hydrogens and the O atom of the perchlorate anion.

Aside from the different heteroatoms, the space-filling models of **S-7** and **S-8** appear almost identical (Figure 3.48).

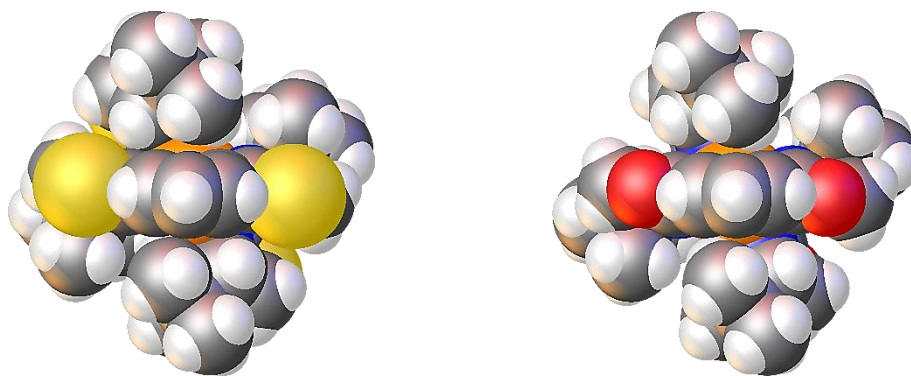


Figure 3.48. Space-filling models of S-7 (left) and S-8 (right).

### 3.2.1.4 Solid State Magnetic Susceptibility

The magnetic susceptibility of the complexes in the solid state was measured using the SQUID magnetometer from 5 -370 K at a scan rate of 5 K min<sup>-1</sup> in an applied magnetic field of 0.5 T. The raw SQUID data were processed to account for the magnetic field, the magnetic moment of the sample holder, the molecular weight and mass of the sample.

Figure 3.49 displays the SQUID curves for the [Fe(thioPyBOX<sup>Ph</sup>)<sub>2</sub>][X]<sub>2</sub> series; **S-5 (ClO<sub>4</sub>)**, **S-5 (BF<sub>4</sub>)**, **RS-5 (ClO<sub>4</sub>)** and **RS-5 (BF<sub>4</sub>)**. The SCO behaviour including the T<sub>1/2</sub> values where applicable are tabulated in Table 3.7.

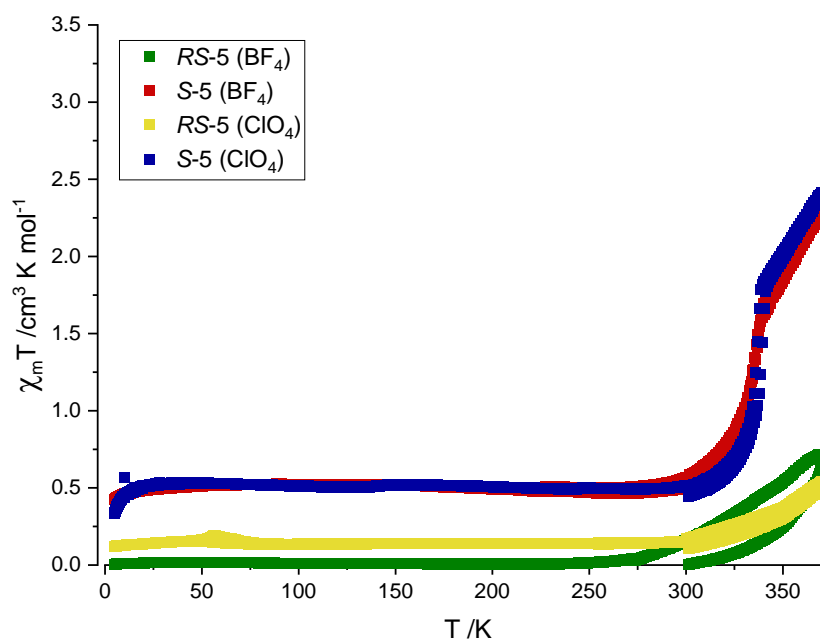


Figure 3.49. SQUID curves for S-5 (BF<sub>4</sub>) (red), S-5 (ClO<sub>4</sub>) (navy), RS-5 (BF<sub>4</sub>) (green) and RS-5 (ClO<sub>4</sub>) (yellow). N.B. 300→370K is the first heating upon which initial solvent is lost.

Complex		SCO behaviour
<b>S-5 (ClO<sub>4</sub>)</b>	[Fe((S)-L <sup>Ph</sup> ) <sub>2</sub> ][ClO <sub>4</sub> ] <sub>2</sub>	SCO at 330 K
<b>S-5 (BF<sub>4</sub>)</b>	[Fe((S)-L <sup>Ph</sup> ) <sub>2</sub> ][BF <sub>4</sub> ] <sub>2</sub>	SCO at 330 K
<b>RS-5 (ClO<sub>4</sub>)</b>	[Fe((R)-L <sup>Ph</sup> )((S)-L <sup>Ph</sup> )]ClO <sub>4</sub> ] <sub>2</sub>	LS < 300 K, SCO > 350 K
<b>RS-5 (BF<sub>4</sub>)</b>	[Fe((R)-L <sup>Ph</sup> )((S)-L <sup>Ph</sup> )]BF <sub>4</sub> ] <sub>2</sub>	LS < 300 K, SCO > 350 K

**Table 3.7. Summarised SCO data from the SQUID graphs in Figure 3.49 of the phenyl- substituted complexes.**

The SQUID curves of the phenyl- complexes **S-5 (BF<sub>4</sub>)** (red), **S-5 (ClO<sub>4</sub>)** (navy), **RS-5 (BF<sub>4</sub>)** (green) and **RS-5 (ClO<sub>4</sub>)** (yellow) (Figure 3.49), show distinct SCO behaviours between the diastereomers irrelevant of counter-ion differences. The de-solvated homochiral complexes adopt the LS state from 5-300 K, although some fraction of the sample (10-15%) is in the HS state from 5-300 K and retains this HS character, as is expected, upon heating above room temperature, where any lattice solvent would be lost. This fraction of HS sample suggests a secondary crystal phase in the bulk sample which, if significant enough, may be apparent in powder X-ray diffraction analysis (pXRD).

Approximately half of the sample which is LS at 300 K, undergoes an initial abrupt ST at  $T_{1/2} = 330 \text{ K} (\pm 2 \text{ K})$ . Considering this ST from  $X_{\text{mT}} \approx 0.5 \text{ cm}^3 \text{ mol}^{-1} \text{ K}$  to  $X_{\text{mT}} \approx 2.0 \text{ cm}^3 \text{ mol}^{-1} \text{ K}$ , this only accounts for 40-45% of the sample having undergone a transition. Therefore, there is a remaining percentage of sample that has not yet undergone a thermal ST by 330 K, which is accounted for in a second transition phase from  $T_{1/2} \geq 370 \text{ K}$ . Due to operating limitations, this temperature could not be exceeded and therefore this transition is incomplete in the measurement. It should be noted that these STs are not solvent-dependent as the SQUID curves produced upon re-heating and re-cooling cycles are identical and reproducible.

Of a phase pure batch of the heterochiral complexes, **RS-5 (ClO<sub>4</sub>)** and **RS-5 (BF<sub>4</sub>)**, almost 100% of the samples remains LS across the examined temperature range 5-350 K, but then shows the onset of a gradual ST just as the temperature approaches 350 K. This corroborates the destabilisation of the LS state of the homochiral complexes compared to their heterochiral counterparts, as discussed earlier.

For comparison of the solid state SCO behaviour of the previously reported iron(II)PyBOX<sup>Ph</sup> analogues, the ST of the **S-5 (ClO<sub>4</sub>)** and **RS-5 (ClO<sub>4</sub>)** complexes are considered. In the PyBOX analogues, **R-1** and **RS-1**, the SCO transitions occur at lower temperatures compared to their sulfur analogues, backing the results found by Pan *et al.*<sup>216</sup>

The magnetic susceptibility of **S-6** and **RS-6** across the same temperature span in the solid state is shown in the SQUID curves in Figure 3.50.

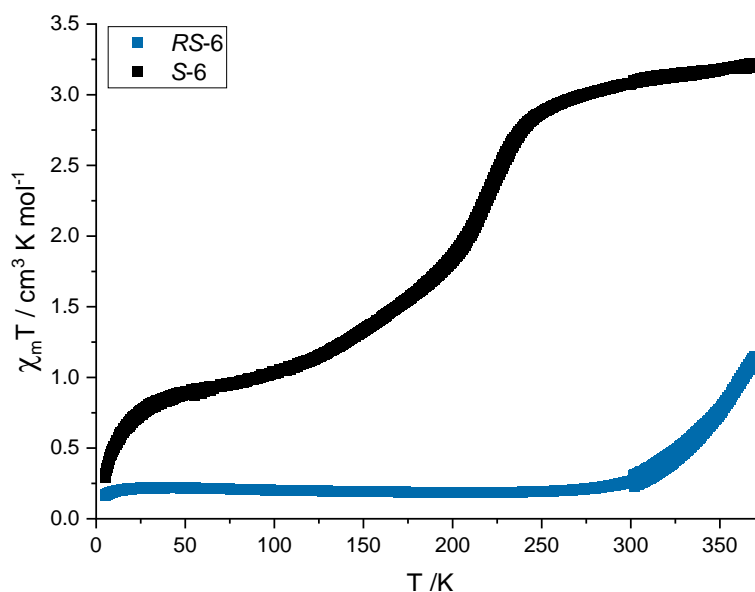


**Figure 3.50. SQUID curves for S-6 (black) and RS-6 (blue). N.B. 300→370K is the first heating upon which initial solvent is lost.**

Complex		SCO behaviour
<b>S-6</b>	$[\text{Fe}((\text{S})\text{-L}^{\text{iPr}})_2][\text{ClO}_4]_2$	SCO at 200 K
<b>RS-6</b>	$[\text{Fe}((\text{R})\text{-L}^{\text{iPr}})((\text{S})\text{-L}^{\text{iPr}})][\text{ClO}_4]_2$	SCO > 350 K

**Table 3.8. Summarised SCO data from the SQUID graphs in Figure 3.50 of the isopropyl- substituted complexes.**

Considering the SQUID curves for the homochiral and heterochiral isopropyl iron thioPyBOX complexes, **S-6** and **RS-6** respectively (Figure 3.50), (Table 3.8) there is a clear distinction between the two chiralities.

Not all the iron centres in **S-6** are in the LS state in the low temperature region ( $T < 150$  K), as approximately 25-30 % of these centres are already in the HS state at this point. However the remainder of the bulk sample does undergo some extent of a spin transition just above 200 K, resulting in a fully HS sample above 250 K. This is unlike its heterochiral counterpart which shows a completely LS structure at all temperatures in the range 5-300 K, where only above 300 K does the onset of a ST become apparent.

Furthermore, this is fitting with the XRD structure of **RS-6**, which shows LS characteristics at 120 K. This SQUID data allows a more informed prediction of the XRD structure of **S-6**, which can be expected to show some JT-angular distortion, with elongated bond lengths around 2.0 Å on the border of the HS-LS distinction – a geometry in between that observed for [Fe((S)-PyBOX<sup>iPr</sup>)<sub>2</sub>][ClO<sub>4</sub>]<sub>2</sub> and [Fe((S)-thioPyBOX<sup>iPr</sup>)((R)-thioPyBOX<sup>iPr</sup>)] [ClO<sub>4</sub>]<sub>2</sub>.

If we study the target temperature region (300 K) for SCO activity, on the SQUID curves of **S-6** and **RS-6**, it is clear that the homochiral complex is completely HS, whilst the heterochiral complex is almost fully LS. Therefore a complete HS-LS distinction has been achieved for this pair of diastereomers in the solid state. This proves that by simply switching the chirality, one can achieve good control over the spin state behaviour. This a huge advance compared to what was discovered for the PyBOX complexes where the spin state behaviour was the same for a pair of diastereomers, however only with a temperature distinction.

Finally, considering the solid state SCO behaviour for the last of the series, the *tert*butyl iron thioPyBOX and thioPyBOX complexes, **S-7** and **S-8** respectively. The SQUID curve, shown in Figure 3.51 from 5-300 K, shows a flat line at  $\chi_m T = 3.5 \text{ cm}^3 \text{ mol}^{-1} \text{ K}$  for both species, correlating to 4 unpaired electrons, which demonstrates a completely HS structure (Table 3.9) as was expected from their highly distorted XRD structures.

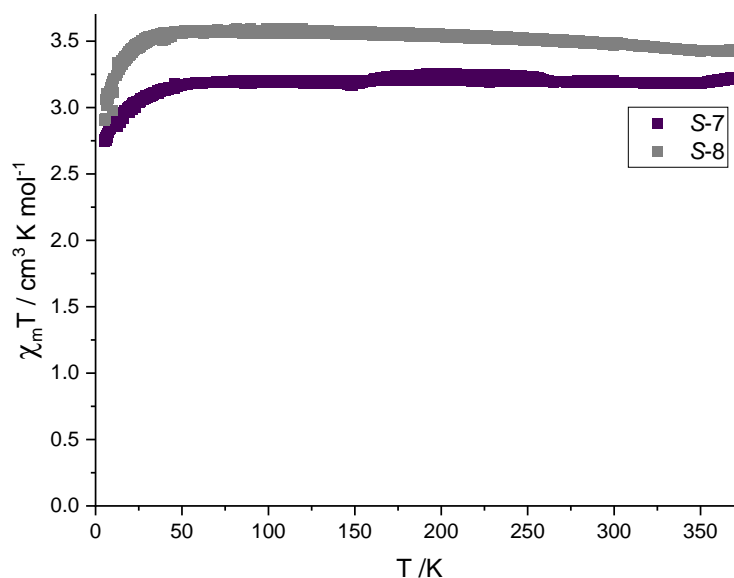


Figure 3.51. SQUID curve for S-7.

Complex		SCO behaviour
<b>S-7</b>	[Fe((S)-thioPyBOX <sup>tBu</sup> ) <sub>2</sub> ][ClO <sub>4</sub> ] <sub>2</sub>	HS
<b>S-8</b>	[Fe((S)-PyBOX <sup>tBu</sup> ) <sub>2</sub> ][ClO <sub>4</sub> ] <sub>2</sub>	HS

**Table 3.9. Summarised SCO data from the SQUID graphs in Figure 3.51 of the homochiral *tert*butyl- substituted complexes, S-7 and S-8.**

### 3.2.1.5 Solution State Magnetic Susceptibility

The solution state SCO activity of these complexes was observed using the VT Evans' <sup>1</sup>H NMR method. This was done in deuterated acetonitrile with tetramethylsilane (TMS) as the internal standard. The temperature range examined was -35 °C to +55 °C, on either a 500 MHz or 600 MHz NMR spectrometer. The raw data obtained from the <sup>1</sup>H NMRs was corrected for the solvent at each temperature, the concentration of the sample in the solution and the operating frequency of the NMR machine.

The curves produced from the Evan's Method analysis are obtained by applying a best fit through the data points. The **R-5 (BF<sub>4</sub>)** and **RS-5 (BF<sub>4</sub>)** complexes are shown in Figure 3.52.

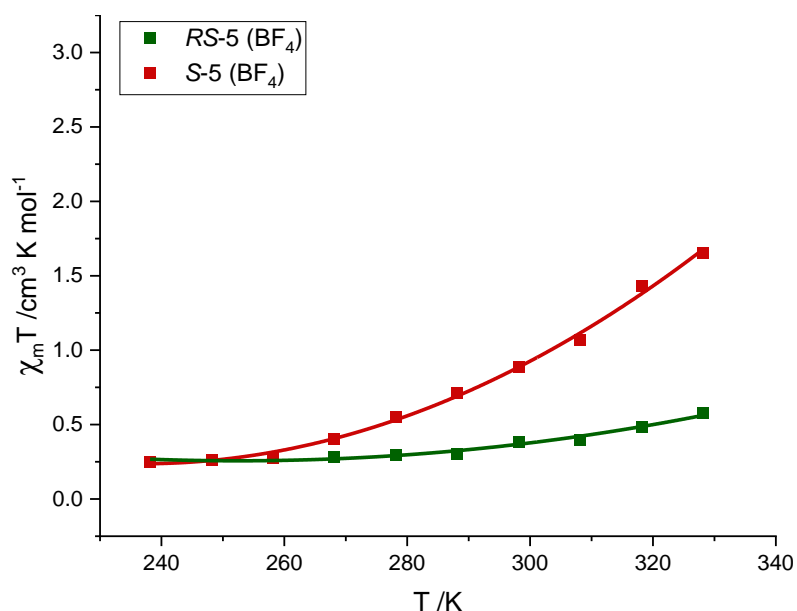


**Figure 3.52. VT Evan's Method curves for RS-5 (BF<sub>4</sub>) (green) and S-5 (BF<sub>4</sub>) (red) in CD<sub>3</sub>CN.**

The solution magnetic susceptibility data for the phenyl- complexes, **RS-5 (BF<sub>4</sub>)** and **S-5 (BF<sub>4</sub>)**, (Figure 3.52) generally show similar trends to what was observed in the



solid state data (Figure 3.49). Both heterochiral species show more LS behaviour compared to their homochiral counterparts and then show a gradual onset of a ST above 300 K. While the homochiral species show SCO behaviour in solution, this is now not as abrupt as was observed in the SQUID data. This is a common observation with solution state studies, due to the greater dilution factor in solution.

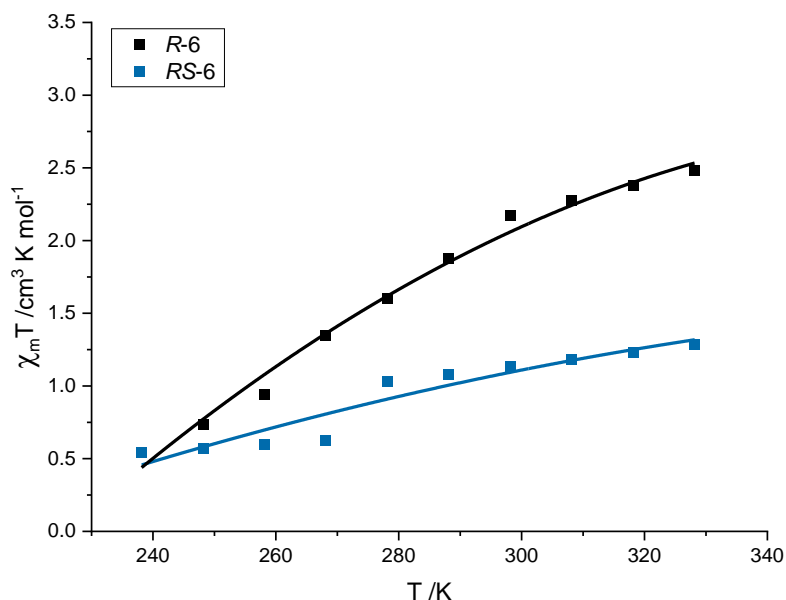


**Figure 3.53. VT Evan's Method curves for R-6 (black) and RS-6 (blue) in CD<sub>3</sub>CN.**

The *isopropyl* complexes, **R-6** and **RS-6** show some interesting differences in their magnetic susceptibility from 240 – 330 K in solution (Figure 3.53). While the homochiral isomer shows a clear ST in solution similar to the solid state, the heterochiral complex now shows some HS character from the low temperature measurement at 240 K. A very gradual ST is observed in solution, which was not evident below 300 K in the SQUID data. The LS *meso*-heterochiral *isopropyl* complex is now destabilised in solution due to the loss of crystal packing effects.

Consistent with Burrows *et al.*,  $T_{1/2}$  of the homochiral species is consistently lower than the  $T_{1/2}$  of their heterochiral counterparts for the phenyl- complexes in both the solid and solutions states, but with different origins of explanations.<sup>210</sup> This theory can be translated across to this series where the  $T_{1/2}$  for the homochiral phenyl-complexes occurs at a higher temperature than the  $T_{1/2}$  observed for **S-6**. This demonstrates a destabilisation of the LS state when the ligand features *isopropyl*-substituents rather than phenyl- substituents. Since the phenyl groups in the homochiral isomer experience steric clashes, while the *isopropyl* groups do not (they do not in the PyBOX analogue so it is reasonable to assume this for the thioPyBOX

equivalent), the electron-donating nature of the *isopropyl* group can justify its destabilisation.

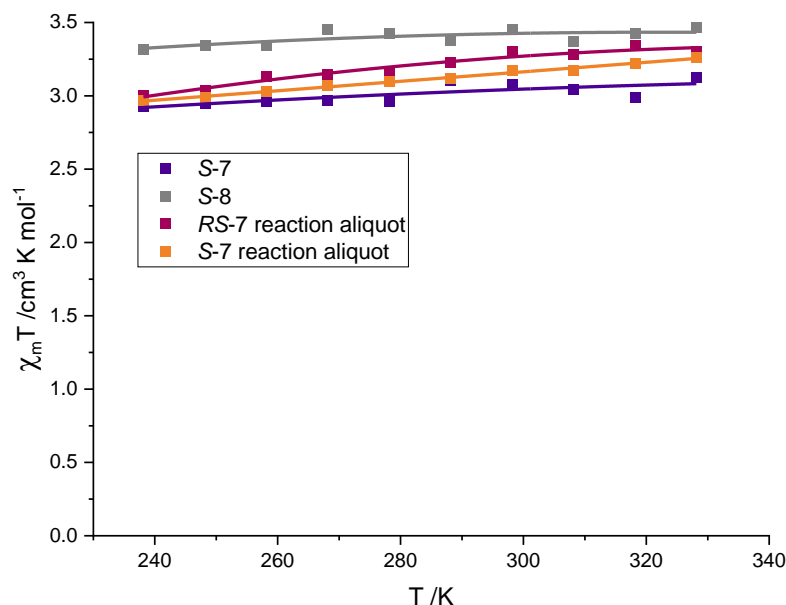


**Figure 3.54.** VT Evan's Method curves for **S-7** (purple), **S-8** (grey), a 1:1:1 solution of (*R*)-L<sup>tBu</sup>:(*S*)-L<sup>tBu</sup>:Fe<sup>2+</sup> (pink) and a 2:1 solution of (*S*)-L<sup>tBu</sup>:Fe<sup>2+</sup> (orange) in CD<sub>3</sub>CN.

The solution state magnetic susceptibility for the *tert*butyl- complexes, **S-7** and **S-8** are shown in Figure 3.54, as well as a 1:1:1 solution of (*R*)-L<sup>tBu</sup>:(*S*)-L<sup>tBu</sup>:Fe<sup>2+</sup> and a 2:1 solution of (*S*)-L<sup>tBu</sup>:Fe<sup>2+</sup>. The 1:1:1 solution mixture was studied as a means to identify whether any heterochiral species forms *in situ*, which would be understood from some difference in the SCO trend. However this data fits exactly (allowing for any concentration errors) with the data for both the homochiral complexes PyBOX and thioPyBOX *tert*butyl complexes. The additional *in situ* study of the 2:1 mixture of (*S*)-L<sup>tBu</sup>:Fe<sup>2+</sup> was studied simultaneously to the 1:1:1 reaction mixture for direct comparison. This study alludes to the possibility that the heterochiral species does not form altogether and rather preferentially forms a solution of statistically distribution of **S-7** and **R-7** complexes.

All the data in Figure 3.54 supports a fully HS complex at all temperatures with the *tert*butyl ligands. This shows that even in the solution state, where the likelihood of a ST would be greater, the twisted HS geometry is retained and the complex is far too distorted and trapped in this form to allow a ST to occur. The highly electron-donating *tert*butyl groups would also favour the HS state through its strongly  $\pi$ -donating character. **S-7** and **S-8** are the only PyBOX/thioPyBOX pair of complexes that show identical spin state behaviour across all temperatures in solid and solution states.

Since the *in situ* analysis of the 1:1:1 reaction aliquot was performed in (deuterated) acetonitrile, it is also possible that the complex **S-7(i)** could have formed. Since this is only a mono-substituted ligand, the **ML6** ligand field around the Fe<sup>2+</sup> centre would not allow for the possibility of a HS-LS dichotomy. Such a structure would only adopt the HS electronic configuration, which is supported by the XRD structure and data obtained for **S-7(i)**.

### 3.2.1.6 Van't Hoff Calculations

A van't Hoff analysis<sup>332</sup> can be studied on the solution state SCO systems as the HS-LS dichotomy of this diluted system is in a thermal equilibrium, governed by the Boltzmann distribution. Such calculations cannot be applied to solid state SCO as this is not a state of equilibrium but is a system governed by cooperativity. The HS-LS equilibrium has an equilibrium constant, K, which is calculated using the fraction of molecules in the HS out of the fraction of molecules in the LS state. If lnK is plotted against 1/T and observes a straight line, then the van't Hoff analysis can be applied to this SCO system.<sup>333</sup> This has been demonstrated with iron(II) 2,6-di(pyrazol-1-yl)pyridine systems,<sup>78</sup> and the iron(II) PyBOX series.<sup>210</sup>

The least-squares fitting of lnK vs. 1/T can produce the thermodynamic parameters; the Gibb's energy between the spin states, ΔG; the enthalpy of the system, ΔH and the entropy of the system, ΔS, using the following equation (Equation 3.15). These values can then be used to obtain the excess heat capacity of the system, ΔC<sub>p</sub>.<sup>333</sup>

$$\ln K = -\frac{\Delta G}{RT} = -\frac{\Delta H}{RT} + \frac{\Delta S}{R}$$

**Equation 3.15. The van't Hoff equation.**

Substituting K = 1 i.e. when 50% of the molecules are in the HS state and 50 % of the molecules are in the LS state, using these thermodynamic parameters, will give a calculated value for T<sub>1/2</sub>, which can be done using Equation 3.15. These values are tabulated along with the thermodynamic parameters for **S-5 (BF<sub>4</sub>)** and **R-6** in Table 3.10. Note that plots of lnK vs 1/T obtained for **R-5 (ClO<sub>4</sub>)** showed curvature and so the line of best fit produced cannot be taken with confidence for use in the subsequent van't Hoff calculations. The heterochiral complexes, **RS-5 (BF<sub>4</sub>)**, **RS-5 (ClO<sub>4</sub>)** and **RS-6** do not display a ST, as these are mostly LS and so van't Hoff calculations cannot be applied here.

Complex	T <sub>1/2</sub> /K	ΔH /kJ mol <sup>-1</sup>	ΔS /J K <sup>-1</sup> mol <sup>-1</sup>
<b>S-5 (BF<sub>4</sub>)</b>	327	18.9	55
<b>R-6</b>	286	19.6	69

**Table 3.10. Solution state SCO parameters obtained for S-5 (BF<sub>4</sub>), R-5 (ClO<sub>4</sub>) and R-6.**

The only comparison that can be made from these results is that obtained for the homochiral phenyl-substituted complex. While the [Fe((*R*)-PyBOX<sup>Ph</sup>)<sub>2</sub>]<sup>2+</sup> complex has a solution state ST of 244 K, which is significantly lower than its observed solid state ST of ≈ 350 K, the cationic thioPyBOX analogue **S-5**, shows a T<sub>1/2</sub> of 327 K in solution and similarly, 330 K in the solid state. This highlights a reduced impact of the intermolecular interactions in the thioPyBOX complexes.

The ST enthalpy difference of **S-5** is notably lower than the PyBOX complex, by ~ 6 kJ mol<sup>-1</sup>, which suggests a less unfavourable change in the bond energies involved upon ST in the thioPyBOX complex. This is understandable from the reduced electron-withdrawing effects of the thiazolanyl S atoms which lead to overall stronger M-L bonding in the thioPyBOX complex. The entropic differences show that the PyBOX analogue is much more entropically inclined to a LS→HS ST, by almost double that observed in the thioPyBOX analogue (102 J K<sup>-1</sup> mol<sup>-1</sup> vs. 55 J K<sup>-1</sup> mol<sup>-1</sup> respectively).

### 3.2.1.7 Racemisation Studies

The stability of the heterochiral complexes, **RS-5** and **RS-6** can be understood from their solution state behaviour. Ligand redistribution in these heterochiral complexes, and then re-coordination to form a 1:1 mixture of the **R**- : **S**- homochiral complexes, would show a lower stability of the heterochiral isomer over the homochiral. This racemisation behaviour can be observed using <sup>1</sup>H paramagnetic NMR in which peaks corresponding to proton environments in the heterochiral and homochiral diastereomers are unique to the diastereomers, as was shown in the iron(II)PyBOX series.

#### 3.2.1.7.1 [Fe((*R*)-L<sup>Ph</sup>)((*S*)-L<sup>Ph</sup>)]<sup>2+</sup>

The paramagnetic <sup>1</sup>H NMR of dissolved crystals of the complex **RS-5 (BF<sub>4</sub>)** in CD<sub>3</sub>CN (Figure 3.55, bottom spectrum, green), shows a LS complex at the NMR operating conditions (ambient temperature), as all the peaks fall within the diamagnetic region. This is distinguishable from the paramagnetic <sup>1</sup>H NMR of dissolved crystals of **S-5**

(**BF<sub>4</sub>**) (Figure 3.55, top spectrum, red) in which some proton environments are influenced by the paramagnetism of the iron(II) centre, leading to a broadening in the peaks at 10.8 ppm and 14.2 ppm.

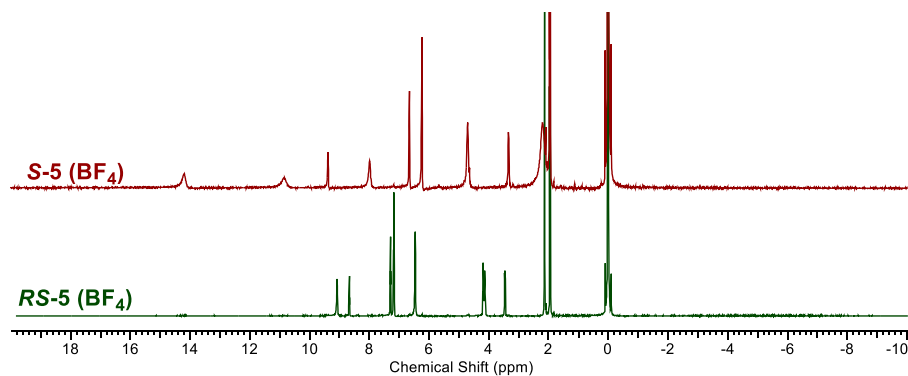


**Figure 3.55. Paramagnetic <sup>1</sup>H NMR of *RS-5* (BF<sub>4</sub>) (bottom spectrum, green) and *S-5* (BF<sub>4</sub>) (top spectrum, red). [CD<sub>3</sub>CN, 600 MHz]**

Upon leaving ***RS-5*** (BF<sub>4</sub>) standing for approximately two weeks, no changes were observed in its NMR spectra, which remained identical to the initial spectrum of the freshly prepared NMR sample (Figure 3.56).

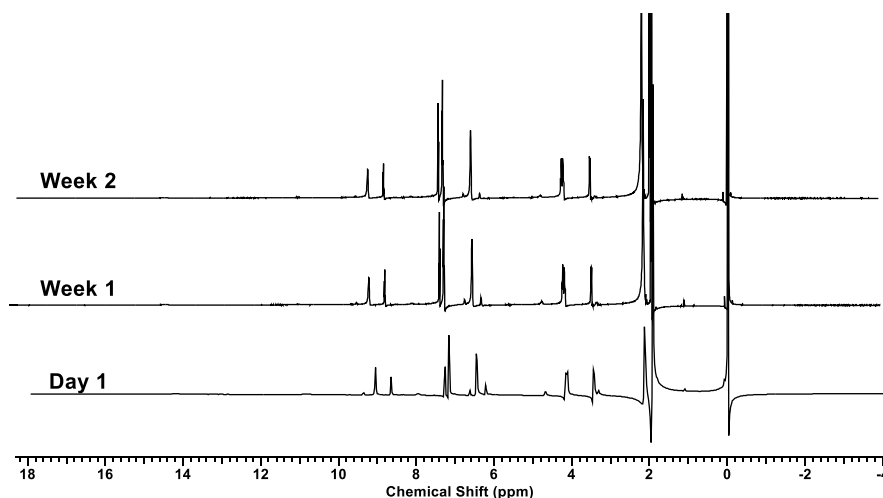


**Figure 3.56. Paramagnetic <sup>1</sup>H NMR spectra of *RS-5* on day 1 (bottom), week 1 (middle) and week 2 (top). [CD<sub>3</sub>CN, 600 MHz]**

These spectra reaffirm the stability of the ***RS-5*** complexes, which akin to the PyBOX equivalent, shows no ligand redistribution in an attempt to racemise to its homochiral isomers. This is consistent with the VT Evan's method data (Figure 3.52) which suggests a mostly LS spin state of ***RS-5*** around 300 K.

The racemic mixture of the crystals  $[\text{Fe}((R)\text{-thioPyBOX}^{\text{Ph}})_2][\text{Fe}((S)\text{-thioPyBOX}^{\text{Ph}})_2][(\text{ClO}_4)_4] \cdot 2\text{MeCN}$  which formed from an attempted isolation of **RS-5**, led to speculations over the thermodynamic favourability of the crystallisation of the homochiral complex over the heterochiral analogue. To gain further insight, the paramagnetic  $^1\text{H}$  NMR spectrum was also recorded of a 1 : 1 : 1 *in situ* mixture of  $(R)\text{-L}^{\text{Ph}} : (S)\text{-L}^{\text{Ph}} : [\text{Fe}(\text{ClO}_4)_2]$  (Figure 3.57).

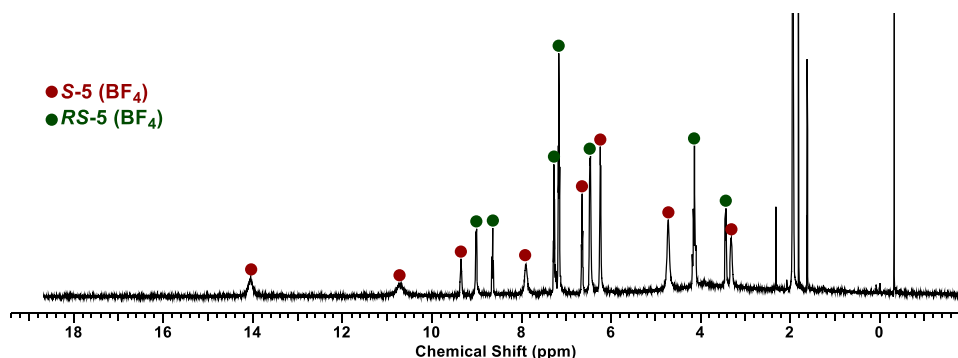


**Figure 3.57.** Paramagnetic  $^1\text{H}$  NMR spectrum of the *in situ* 1:1:1 reaction mixture of  $(R)\text{-L}^{\text{Ph}} : (S)\text{-L}^{\text{Ph}} : [\text{Fe}(\text{ClO}_4)_2]$ .

The spectrum of this freshly prepared sample shows peaks corresponding to proton environments that indicates the presence of both homochiral and heterochiral complexes. Integrations of these peaks show an approximately 1:1 ratio of both diastereomers in solution, which shows that *in situ* neither species dominates and rather they both coexist. This NMR sample was also left to stand over two weeks in order to determine the thermodynamic product between the possible species (Figure 3.58).

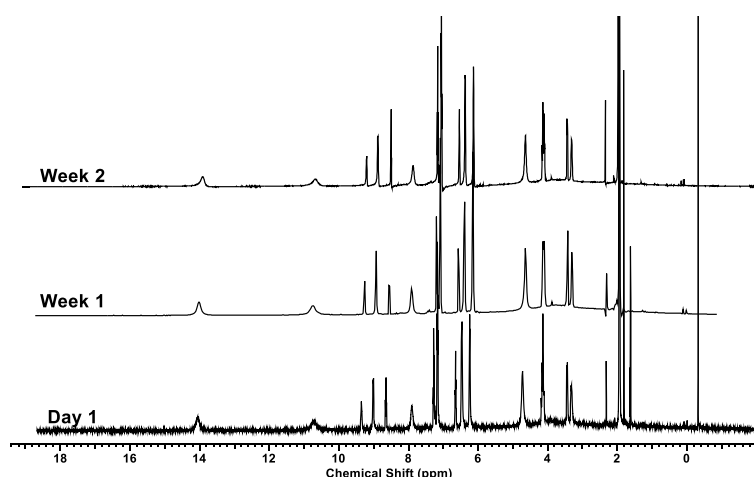


**Figure 3.58. Paramagnetic  $^1\text{H}$  NMR of a 1 : 1 : 1 solution of  $(R)\text{-L}^{\text{Ph}}$  :  $(S)\text{-L}^{\text{Ph}}$  :  $[\text{Fe}(\text{ClO}_4)_2]$  on day 1 (bottom), week 1 (middle) and week 2 (top).  $[\text{CD}_3\text{CN}$ , 600 MHz]**

The spectra show that over this period of time, there appears to be no change in dominance between the diastereomers, showing that *in situ* both chiralities are stable and co-exist, which is the same as was observed for the PyBOX analogues. Upon crystallisation of the 1:1:1 solution, it is the *meso*-heterochiral complex that preferentially crystallises, however re-dissolution of these crystals renders the heterochiral species perfectly stable in solution, as there is no evidence of racemisation. This demonstrates that once this species is formed, it is inert to ligand substitution.

The enhanced stability in the homochiral and heterochiral iron(II)thioPyBOX<sup>Ph</sup> complexes is supported by High Resolution Mass Spectrometry (HRMS) analysis. This shows **RS-5 (BF<sub>4</sub>)**, **RS-5 (ClO<sub>4</sub>)**, **R-5 (ClO<sub>4</sub>)** (and **S-5 (ClO<sub>4</sub>)**) as the dicationic iron complex,  $[\text{ML}_2]^{2+}$  with a  $m/z = 429.0719$  corresponding to  $[\text{Fe}(\text{thioPyBOX}^{\text{Ph}})_2]^{2+}$  ( $= 858.14 \text{ g mol}^{-1}$ ). In the PyBOX equivalents, the HRMS data only showed the  $m/z$  peak corresponding to the dissociated ligand as  $[\text{L}+\text{H}]^+$ . This nicely demonstrates the greater stability and inertness to ligand dissociation of the thioPyBOX<sup>Ph</sup> series. Interestingly the homochiral tetrafluoroborate complexes **R-5 (BF<sub>4</sub>)** and **S-5 (BF<sub>4</sub>)**, also only shows the  $[\text{L}+\text{H}]^+$  peak at  $m/z = 402.1091$  ( $\text{thioPyBOX}^{\text{Ph}} = 401.55 \text{ g mol}^{-1}$ ) (3.4 Experimental).

### 3.2.1.7.2 $[\text{Fe}((R)\text{-L}^{\text{iPr}})((S)\text{-L}^{\text{iPr}})]^{2+}$

Now considering the heterochiral *isopropyl*- complex, **RS-6**, the paramagnetic  $^1\text{H}$  NMR of its dissolved crystals was studied and compared with the spectrum of dissolved crystals of the **S-6** complex (Figure 3.59).

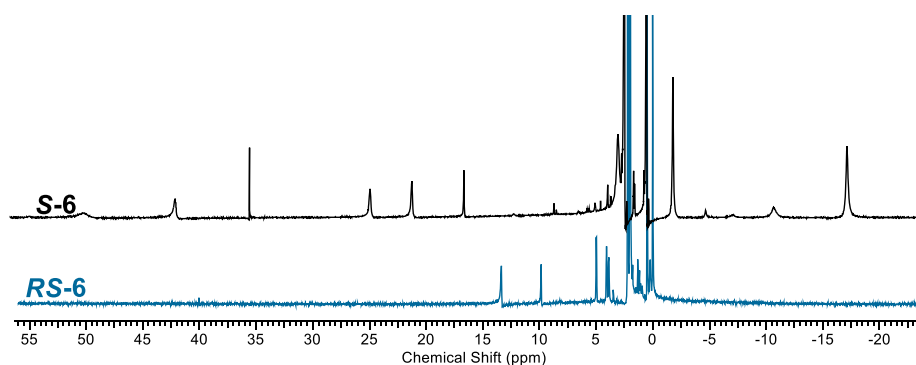


Figure 3.59. Paramagnetic  $^1\text{H}$  NMR of *RS-6* (bottom spectrum, black) and *S-6* (top spectrum, blue). [ $\text{CD}_3\text{CN}$ , 300 MHz]

The freshly prepared NMR sample of *RS-6* was also studied over a two week period to determine the stability of this complex (Figure 3.60).

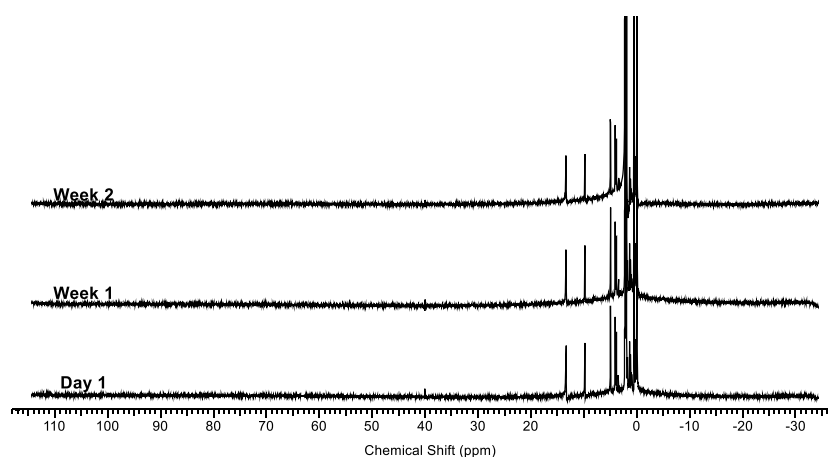
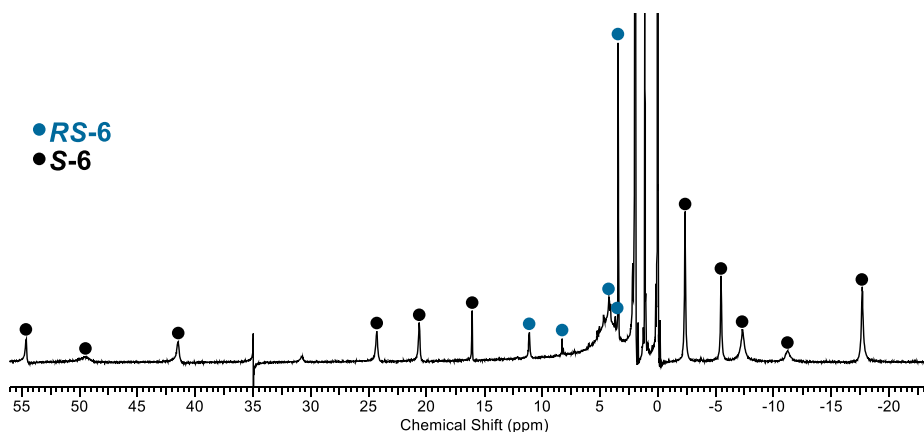


Figure 3.60. Paramagnetic  $^1\text{H}$  NMR spectra of *RS-6* on day 1 (bottom), week 1 (middle) and week 2 (top). [ $\text{CD}_3\text{CN}$ , 300 MHz]

The NMR spectra remain purely heterochiral over the observed time period, with no evidence of the homochiral species present. The complex *RS-6* is significantly more stable than its PyBOX counterpart, which immediately underwent ligand redistribution in solution.<sup>210</sup>

To determine whether racemisation occurs *in situ*, the paramagnetic  $^1\text{H}$  NMR of a 1 : 1 : 1 reaction mixture of (*R*)- $\text{L}^{\text{iPr}}$  : (*S*)- $\text{L}^{\text{iPr}}$  :  $[\text{Fe}(\text{ClO}_4)_2]$  was compared (Figure 3.61).





**Figure 3.61. Paramagnetic  $^1\text{H}$  NMR spectrum of the in situ 1:1:1 reaction mixture of  $(R)\text{-L}^{\text{iPr}} : (S)\text{-L}^{\text{iPr}} : [\text{Fe}(\text{ClO}_4)_2]$ .**

The NMR spectrum shows that the 1 : 1 : 1 solution of  $(R)\text{-L}^{\text{iPr}} : (S)\text{-L}^{\text{iPr}} : [\text{Fe}(\text{ClO}_4)_2]$  behaves exactly as was observed with the phenyl- analogue, with both diastereomers co-existing in solution. An approximately even statistical distribution of both isomers are present and neither chirality seems to dominate *in situ*. However, when this solution is crystallised, the stable LS **RS-6** complex preferentially crystallises, with no traces of the homochiral complex present. The stabilities of **RS-5** and **RS-6** in solution are therefore very similar to each other and the stability of **RS-6** is significantly different to its PyBOX congener.

### 3.2.1.7.3 $[\text{Fe}((S)\text{-L}^{\text{tBu}})_2]^{2+}$

While the complexes **S-7** and **S-8** do not have a heterochiral counterpart and so cannot be studied with regards to racemisation, they are still considerably unstable structures given their highly JT-distorted geometries. Their stabilities in solution can still be studied by paramagnetic  $^1\text{H}$  NMR by observing if the complex dissociates. The NMR spectrum for **S-7** shows a high degree of complex dissociation, which is evident from the peaks in the diamagnetic region which dominate the paramagnetic peaks in intensity. These peaks match the NMR spectrum of the uncoordinated ligand as shown in Figure 3.62, showing the preferential dissociation of **S-7** into its free ligand, confirming its poor stability.

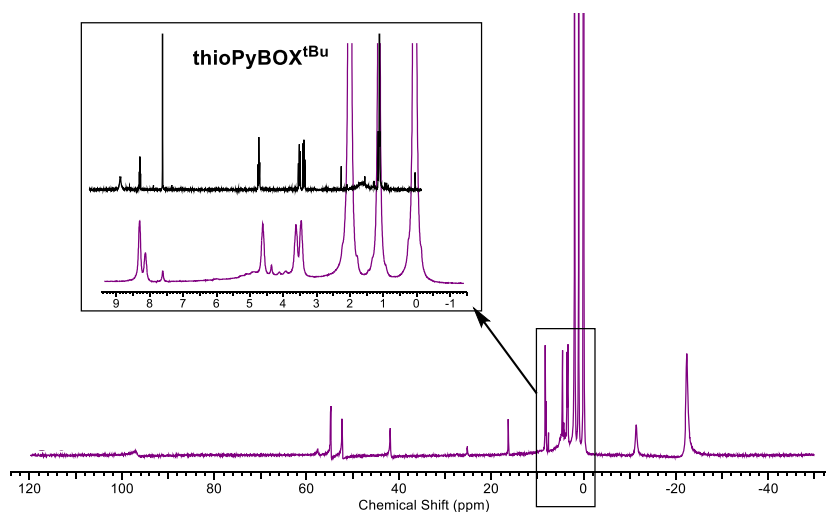


**Figure 3.62. Paramagnetic <sup>1</sup>H NMR of **S-7**, with peak expansions in the diamagnetic region. Expanded part is overlaid with the <sup>1</sup>H NMR spectrum of thioPyBOX<sup>t</sup>Bu. [CD<sub>3</sub>CN, 300 MHz]**

Analysis of the integrations of the peaks in the NMR spectrum in Figure 3.62 gives a ratio of 1 : 2.4 of **S-7** : thioPyBOX<sup>t</sup>Bu.

The equivalent NMR spectrum for the PyBOX analogue, **S-8** is shown in Figure 3.63, along with an expansion in the diamagnetic region again.

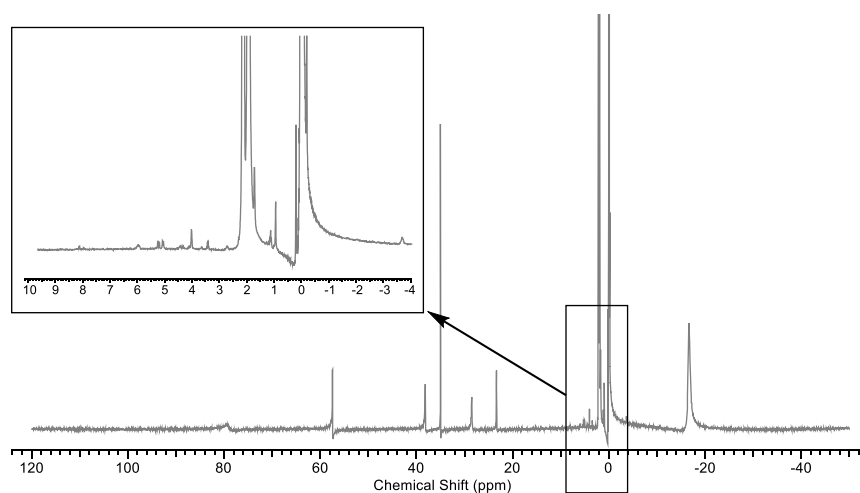


**Figure 3.63. Paramagnetic <sup>1</sup>H NMR of **S-8**, with peak expansions in the diamagnetic region. [CD<sub>3</sub>CN, 300 MHz]**

The spectrum for **S-8** now shows a greater stability of the complex compared to **S-7**. Significantly less complex dissociation occurs, evidenced by the reduced intensity in peaks of free ligand in the diamagnetic region. Comparing integrations of the ligand

peaks with the complex peaks gave a ratio of 1 : 0.17 of **S-8** : PyBOX<sup>tBu</sup>, showing the quantity of dissociated ligand is negligible in this case.

### 3.3 Conclusion

In this chapter a library of chiral iron(II)thioPyBOX complexes was synthesised; **R-5 (BF<sub>4</sub>)**, **RS-5 (BF<sub>4</sub>)**, **R-5 (ClO<sub>4</sub>)**, **RS-5 (ClO<sub>4</sub>)**, **S-6**, **RS-6**, **S-7**, **S-7(i)** and **S-8**. XRD structure solutions have been obtained for all of these complexes with the exception of homochiral **S-6/R-6**. An in depth analysis of these structure solutions has been discussed, including their Fe-N bond angles and lengths, intermolecular interactions, packing structures and space-filling models where applicable. A comparative study throughout has been core to this chapter in which the focus has been to further studies on previous work in the Halcrow group on the iron(II)PyBOX series.<sup>210</sup>

A core aim of this work was to achieve an enhanced chiral discrimination between a pair of diastereomers. This was the rationale behind employing thioPyBOX over the PyBOX ligand for iron(II) SCO studies. A combination of electronic and steric effects was found to influence the SCO behaviour depending on the R- substituent at the 4-position of the thioPyBOX thiazolanyl rings. These steric and electronic influences are akin to what was observed with the substituted iron(II)PyBOX series, where the phenyl- substituents in its homochiral complex experience steric clash, destabilising this isomer over its *meso*-heterochiral analogue. While the *isopropyl* substituents do not clash, they rather twist the ligand backbone, distorting its structure.

The *tert*butyl complexes are new to both ligand families. Their homochiral complexes surprisingly formed but unsurprisingly displayed highly JT-distorted structures, which remain trapped in the HS state at all temperatures in both the solid and solution states.

Chiral discrimination of spin state was observed for the phenyl and *isopropyl* complexes. In the solid state an abrupt ST for the phenyl complexes at  $T_{1/2} = 330\text{K}$  was observed, whilst the heterochiral analogues were LS and only showed the onset of a ST at  $T_{1/2} > 350\text{K}$ . The SCO behaviour in the solid state was identical for the perchlorate and tetrafluoroborate complexes. The solution state SCO behaviour of these isomers also displayed a chiral distinction, with a  $\Delta T \approx 30\text{K}$ , which is similar to what was observed for the PyBOX analogues.

At 300 K, the homochiral *isopropyl* complex is fully HS, whilst its heterochiral analogue is LS – this has achieved a fully HS-LS distinction between these diastereomers. This distinction is also observed in the solution state for these complexes.

Where racemisation was observed in the heterochiral PyBOX<sup>iPr</sup> complex, this did not occur in the thioPyBOX equivalent, nor in any other heterochiral iron thioPyBOX complex. That should be reflect their predominantly low-spin nature, which is much more inert to ligand redistribution reactions.

In all cases, where a ST was observed, the  $T_{1/2}$  values are higher than for its PyBOX equivalent, which corroborates the recent work by Pan *et al.*<sup>216</sup> Overall, the reduced electron-withdrawing strength of the thioPyBOX ligand compared to the PyBOX ligand was found to strengthen the FeN<sub>6</sub> ligand field, resulting in more stabilised LS states and generally more 'LS-like' behaviour in their iron(II) complexes.

### 3.4 Experimental

In addition to the general experimental methods and techniques highlighted in Section 2.4, Evans' Method variable temperature solution based paramagnetic susceptibility measurements were performed by Dr. Mark Howard on a four-channel Bruker AV-NEO NMR spectrometer operating at 11.7 T (500 MHz <sup>1</sup>H) and equipped with 5mm TBO (<sup>1</sup>H/<sup>19</sup>F/BB) and TXI (<sup>1</sup>H/<sup>13</sup>C/<sup>15</sup>N) probes. All Evans' VT datasets were acquired from 238 K – 328 K at 10 K intervals, using acetonitrile-d<sub>3</sub> as the solvent and trimethylsilane (TMS) as the reference. Paramagnetic <sup>1</sup>H NMR were collected by the author on Solid state Magnetic susceptibility measurements were collected by the author on a two-channel Bruker AV3 NMR spectrometer operating at 7.05 T (300 MHz <sup>1</sup>H) and equipped with a 5 mm BBO probe.

Quantum Design SQUID-VSM magnetometer, in an applied field of 5000 Oe in the Condensed Matter Lab II in the School of Physics, University of Leeds. The sample preparation, data processing and analysis for the Evans' and SQUID data was performed by the author.

Where applicable, X-ray powder diffraction data were obtained by the author or Dr. Christopher Pask using a Bruker D2 Phaser machine. The simulated powder patterns were obtained using Mercury<sup>334, 335</sup> and were based on the crystal structures discussed above. Powder diffraction experiments were performed on samples of fresh material.

No problems have been experienced during the synthesis of complexes discussed in this thesis, however metal-organic perchlorates used in this chapter and Chapter 4 are potentially explosive and should be handled carefully and in small quantities.

**R-5 (ClO<sub>4</sub>).** [Fe((R)-thioPyBOX<sup>Ph</sup>)<sub>2</sub>][ClO<sub>4</sub>]<sub>2</sub>. Addition of solid Fe[ClO<sub>4</sub>]<sub>2</sub>·6H<sub>2</sub>O (35.1 mg, 0.10 mmols, 1.4 eq.) to a solution of (R)-thioPyBOX<sup>Ph</sup>, **L1** (50.8 mg, 0.13 mmols, 2 eq.) in acetonitrile (15 mL) afforded a violet solution, which was stirred at room

temperature until all the solid had dissolved (16hrs, 20 °C). The solution was concentrated, and slow diffusion of diethyl ether vapour into the concentrate produced violet crystals of the complex suitable for X-ray diffraction. Yield= 47.2 mg (71%). **Paramagnetic <sup>1</sup>H NMR (300 MHz, CD<sub>3</sub>CN)** δ 13.91 (4H), 10.55 (4H), 9.33 (2H), 7.81 (4H), 6.68 (4H), 6.27 (8H), 4.77 (8H), 3.33 (4H). **HRMS [ES]<sup>+</sup> [M-2(ClO<sub>4</sub>)]<sup>2+</sup>** Predicted: 429.0695 Found: 429.0719. **Elemental analysis calculated (%)** C 52.23, H 3.62, N 7.94; found C 52.34, H 3.70, N 8.03.

**S-5 (ClO<sub>4</sub>). [Fe((S)-thioPyBOX<sup>Ph</sup>)<sub>2</sub>][ClO<sub>4</sub>]<sub>2</sub>.** Method as for **R-5 (ClO<sub>4</sub>)**, but using (S)-thioPyBOX<sup>Ph</sup>, **L2** (49.9 mg, 0.12 mmols, 2 eq.) and Fe[ClO<sub>4</sub>]<sub>2</sub>·6H<sub>2</sub>O (33.4 mg, 0.09 mmols, 1.4 eq.) in acetonitrile (15 mL). The crude product was recrystallized from acetonitrile/diethyl ether by the vapour diffusion method which afforded violet crystals suitable for X-ray diffraction. Yield= 54.5 mg (83%). **Paramagnetic <sup>1</sup>H NMR (300 MHz, CD<sub>3</sub>CN)** δ 13.98 (4H), 10.63 (4H), 9.34 (2H), 7.86 (4H), 6.66 (4H), 6.26 (8H), 4.76 (8H), 3.33 (4H). **HRMS [ES]<sup>+</sup> [M-2(ClO<sub>4</sub>)]<sup>2+</sup>** Predicted: 429.0695 Found: 429.0586. **Elemental analysis calculated (%)** C 52.23, H 3.62, N 7.94; found C 52.06, H 3.71, N 8.02.

**RS-5 (ClO<sub>4</sub>). [Fe((S)-thioPyBOX<sup>Ph</sup>)((R)-thioPyBOX<sup>Ph</sup>)] [ClO<sub>4</sub>]<sub>2</sub>.** Method as for **R-5 (ClO<sub>4</sub>)**, but using (R)-thioPyBOX<sup>Ph</sup>, **L1** (49.9 mg, 0.12 mmols, 1 eq.), (S)-thioPyBOX<sup>Ph</sup>, **L2** (49.9 mg, 0.12 mmols, 1 eq.) and Fe[ClO<sub>4</sub>]<sub>2</sub>·6H<sub>2</sub>O (62.2 mg, 0.17 mmols, 1.4 eq.) in acetonitrile (15 mL). The crude product was recrystallized from acetonitrile/diethyl ether by the vapour diffusion method which afforded violet crystals suitable for X-ray diffraction. Yield= 110 mg (61%). **Paramagnetic <sup>1</sup>H NMR (600 MHz, CD<sub>3</sub>CN)** δ 9.07 (s (br), 4H), 8.67 (t, 2H), 7.29 (t, 4H), 7.18 (t (br), 8H), 6.47 (s(br), 8H), 4.16 (dt (br), 8H), 3.46 (d, 4H). **HRMS [ES]<sup>+</sup> [M-2(ClO<sub>4</sub>)]<sup>2+</sup>** Predicted: 429.0695 Found: 429.0584. **Elemental analysis calculated (%)** C 52.23, H 3.62, N 7.94; found C 52.29, H 3.71, N 7.99.

**R-5 (BF<sub>4</sub>). [Fe((S)-thioPyBOX<sup>Ph</sup>)<sub>2</sub>][BF<sub>4</sub>]<sub>2</sub>.** Method as for **R-5 (ClO<sub>4</sub>)**, but using (R)-thioPyBOX<sup>Ph</sup>, **L1** (25.8 mg, 0.09 mmols, 2 eq.) and Fe[BF<sub>4</sub>]<sub>2</sub>·6H<sub>2</sub>O (14.9 mg, 0.04 mmols, 1.4 eq.) in acetonitrile (15 mL). The crude product was recrystallized from acetonitrile/diethyl ether by the vapour diffusion method which afforded violet crystals suitable for X-ray diffraction. Yield = 26 mg (84%). **Paramagnetic <sup>1</sup>H NMR (300 MHz, CD<sub>3</sub>CN)** δ 14.00 (4H), 10.65 (4H), 9.34 (2H), 7.87 (4H), 6.67 (4H), 6.26 (8H), 4.75 (8H), 3.33 (4H). **HRMS [ES]<sup>+</sup> [L+H]<sup>+</sup>** Predicted: 402.1054 Found: 402.1091. **Elemental analysis calculated (%)** C 53.51, H 3.71, N 8.14; found C 53.41, H 3.68, N 8.18.

**S-5 (BF<sub>4</sub>). [Fe((S)-thioPyBOX<sup>Ph</sup>)<sub>2</sub>][BF<sub>4</sub>]<sub>2</sub>.** Method as for **R-5 (ClO<sub>4</sub>)**, but using (S)-thioPyBOX<sup>Ph</sup>, **L2** (60.2 mg, 0.15 mmols, 2 eq.) and Fe[BF<sub>4</sub>]<sub>2</sub>·6H<sub>2</sub>O (35.3 mg, 0.10 mmols, 1.4 eq.) in acetonitrile (15 mL). The crude product was recrystallized from

acetonitrile/diethyl ether by the vapour diffusion method which afforded violet crystals suitable for X-ray diffraction. Yield= 63.4 mg (82%). **Paramagnetic  $^1\text{H NMR}$  (600 MHz,  $\text{CD}_3\text{CN}$ )**  $\delta$  14.17 (4H), 10.82 (4H), 9.37 (2H), 7.98 (4H), 6.65 (4H), 6.22 (8H), 4.69 (8H), 3.32 (4H). **HRMS [ES] $^+$  [L+H] $^+$**  Predicted: 402.1054 Found: 402.1094. **Elemental analysis calculated (%)** C 53.51, H 3.71, N 8.14; found C 53.36, H 3.78, N 8.25.

**RS-5 ( $\text{BF}_4$ ).** **[Fe((S)-thioPyBOX $^{\text{Ph}}$ )((R)-thioPyBOX $^{\text{Ph}}$ )] $[\text{BF}_4]_2$ .** Method as for **R-5 ( $\text{ClO}_4$ )**, but using (R)-thioPyBOX $^{\text{Ph}}$ , **L1** (50.2 mg, 0.13 mmols, 1 eq.), (S)-thioPyBOX $^{\text{Ph}}$ , **L2** (49.6 mg, 0.12 mmols, 1 eq.) and Fe $[\text{BF}_4]_2 \cdot 6\text{H}_2\text{O}$  (58.4 mg, 0.17 mmols, 1.4 eq.) in acetonitrile (20 mL). The crude product was recrystallized from acetonitrile/diethyl ether by the vapour diffusion method which afforded violet crystals suitable for X-ray diffraction. Yield= 111.5 mg (87%). **Paramagnetic  $^1\text{H NMR}$  (600 MHz,  $\text{CD}_3\text{CN}$ )**  $\delta$  9.07 (s, br, 4H), 8.67 (t, 2H), 7.30 (t, 4H), 7.19 (t, 8H), 6.46 (s, br, 8H), 4.17 (t, 4H), 4.12 (t, 4H), 3.46 (dd, 4H). **HRMS [ES] $^+$  [M-2( $\text{ClO}_4$ )] $^{2+}$**  Predicted: 429.0695 Found: 429.0705. **Elemental analysis calculated (%)** C 53.51, H 3.71, N 8.14; found C 49.06, H 3.50, N 8.09.

**R-6.** **[Fe((R)-thioPyBOX $^{\text{iPr}}$ ) $_2$ ] $[\text{ClO}_4]_2$ .** Method as for **R-5 ( $\text{ClO}_4$ )**, but using (R)-thioPyBOX $^{\text{iPr}}$ , **L3** (10.0 mg, 0.03 mmols, 2 eq.) and Fe $[\text{ClO}_4]_2 \cdot 6\text{H}_2\text{O}$  (5.6 mg, 0.015 mmols, 1 eq.) in acetonitrile (10 mL). The crude product was recrystallized from acetonitrile/diethyl ether by the vapour diffusion method which afforded violet crystals suitable for X-ray diffraction. Yield= 8.6 mg (62%). **Paramagnetic  $^1\text{H NMR}$  (300 MHz,  $\text{CD}_3\text{CN}$ )**  $\delta$  49.6 (2H), 41.5 (4H), 24.5 (4H), 20.60 (4H), 16.2 (4H), -2.40 (12H), -11.3 (4H), -17.6 (12H). **HRMS [ES] $^+$  [L+H] $^+$**  Predicted: 334.1367 Found: 334.1421. **Elemental analysis calculated (%)** C 44.30, H 5.03, N 9.12; found C 44.14, H 4.98, N 8.73.

**S-6.** **[Fe((S)-thioPyBOX $^{\text{iPr}}$ ) $_2$ ] $[\text{ClO}_4]_2$ .** Method as for **R-5 ( $\text{ClO}_4$ )**, but using (S)-thioPyBOX $^{\text{iPr}}$ , **L4** (31.1 mg, 0.09 mmols, 2 eq.) and Fe $[\text{ClO}_4]_2 \cdot 6\text{H}_2\text{O}$  (23.8 mg, 0.07 mmols, 1.4 eq.) in acetonitrile (15 mL). The crude product was recrystallized from acetonitrile/diethyl ether by the vapour diffusion method which afforded dark plum coloured crystals. Yield= 34.4 mg (80%). **Paramagnetic  $^1\text{H NMR}$  (300 MHz,  $\text{CD}_3\text{CN}$ )**  $\delta$  49.58 (2H), 41.38 (4H), 24.23 (4H), 20.57 (4H), 16.02 (4H), -2.34 (12H), -11.34 (4H), -17.72 (12H). **HRMS [ES] $^+$  [L+H] $^+$**  Predicted: 334.1367 Found: 334.1418. **Elemental analysis calculated (%)** C 44.30, H 5.03, N 9.12; found C 44.11, H 5.00, N 8.79.

**RS-6.** **[Fe((S)-thioPyBOX $^{\text{iPr}}$ )((R)-thioPyBOX $^{\text{iPr}}$ )] $[\text{ClO}_4]_2$ .** Method as for **R-5 ( $\text{ClO}_4$ )**, but using (R)-thioPyBOX $^{\text{iPr}}$ , **L3** (25.0 mg, 0.08 mmols, 1.3 eq.), (S)-thioPyBOX $^{\text{iPr}}$ , **L4** (24 mg, 0.07 mmols 1.2 eq.) and Fe $[\text{ClO}_4]_2 \cdot 6\text{H}_2\text{O}$  (20.9 mg, 0.06 mmols, 1 eq.) in acetonitrile (10 mL). The crude product was recrystallized from acetonitrile/diethyl

ether by the vapour diffusion method which afforded violet crystals suitable for X-ray diffraction. Yield= 32.8 mg (49%). **Paramagnetic  $^1\text{H NMR}$  (300 MHz,  $\text{CD}_3\text{CN}$ )**  $\delta$  13.32 (4H), 9.79 (2H), 4.93 (4H), 4.04 (4H), 3.82 (4H), 0.45 (12H), 0.17 (4H), -0.05 (12H). **HRMS [ES] $^+$  [L+H] $^+$**  Predicted: 334.1367 Found: 334.1403. **Elemental analysis calculated (%)** C 44.30, H 5.03, N 9.12; found C 43.15, H 5.23, N 9.41.

**S-7.  $[\text{Fe}((\text{S})\text{-thioPyBOX}^{\text{tBu}})_2][\text{ClO}_4]_2$ .** Method as for **R-5 ( $\text{ClO}_4$ )**, but using (S)-thioPyBOX<sup>tBu</sup>, **L6** (70.8 mg, 0.20 mmols, 2 eq.) and  $\text{Fe}[\text{ClO}_4]_2 \cdot 6\text{H}_2\text{O}$  (35 mg, 0.10 mmols, 2 eq.) in acetonitrile (20 mL). The crude product was recrystallized from acetone/diethyl ether by the vapour diffusion method which afforded red crystals suitable for X-ray diffraction. Yield= 85.5 mg (89%). **Paramagnetic  $^1\text{H NMR}$  (300 MHz,  $\text{CD}_3\text{CN}$ )**  $\delta$  97.00 (2H), 54.74 (2H), 52.38 (4H), 41.77 (2H), 25.12 (2H), 16.33 (2H), -11.47 (6H) -22.34 (30H). **HRMS [ES] $^+$  [L+H] $^+$**  Predicted: 362.1680 Found: 362.1721. **Elemental analysis calculated (%)** C 46.67, H 5.57, N 8.59; found C 45.25, H 5.30, N 8.14.

**S-7(i).  $[\text{Fe}((\text{S})\text{-thioPyBOX}^{\text{tBu}})(\text{MeCN})_2\text{H}_2\text{O}][\text{ClO}_4]_2$ .** Method as for **R-5 ( $\text{ClO}_4$ )**, but using (R)-thioPyBOX<sup>tBu</sup>, **L5** (9.5 mg, 0.03 mmols, 1 eq.), (S)-thioPyBOX<sup>tBu</sup>, **L6** (9.5 mg, 0.03 mmols, 1 eq.) and  $\text{Fe}[\text{ClO}_4]_2 \cdot 6\text{H}_2\text{O}$  (9.9 mg, 0.03 mmols, 1 eq.) in acetonitrile (15 mL). The crude product was recrystallized from acetone/diethyl ether by the vapour diffusion method which afforded some red powder, which when agitated and then left to sit for 48hrs afforded a single dark red block of crystals suitable for X-ray diffraction. Yield unobtained due to insufficient quantity. **Paramagnetic  $^1\text{H NMR}$  (300 MHz,  $\text{CD}_3\text{CN}$ )** 97.07, 57.34, 54.76, 52.33, 41.87, 27.72, 25.22, 16.30, -11.47, -22.38. Integrations cannot be accurately obtained due to ligand dissociation and contamination of **S-7**. Insufficient quantity produced for further analysis.

**S-8.  $[\text{Fe}((\text{S})\text{-PyBOX}^{\text{tBu}})_2][\text{ClO}_4]_2$ .** Method as for **R-5 ( $\text{ClO}_4$ )**, but using commercially available (S)-PyBOX<sup>tBu</sup> (40.7 mg, 0.12 mmols, 2 eq.) and  $\text{Fe}[\text{ClO}_4]_2 \cdot 6\text{H}_2\text{O}$  (21.3 mg, 0.06 mmols, 1 eq.) in acetonitrile (10 mL). The crude product was recrystallized from acetone/diethyl ether by the vapour diffusion method which afforded red crystals suitable for X-ray diffraction. Yield= 35.0 mg (65%). **Paramagnetic  $^1\text{H NMR}$  (300 MHz,  $\text{CD}_3\text{CN}$ )**  $\delta$  79.24 (2H), 57.43 (4H), 38.18 (4H), 28.48 (4H), 23.32 (2H), -16.68 (36H). **HRMS [ES] $^+$  [L+H] $^+$**  Predicted: 330.2137 Found: 330.2203. **Elemental analysis calculated (%)** C 49.96, H 5.96, N 9.2; found C 49.87, H 6.14, N 9.04.

## Chapter 4

### Heteroleptic Iron(II) PyBOX and thioPyBOX complexes for Spin-Crossover

#### 4.1 Introduction

The comparative study of iron(II)- PyBOX and thioPyBOX SCO complexes in Chapter 3 prompted an interest in studying the SCO behaviour of an iron complex containing both the PyBOX and thioPyBOX ligand families. Considering the derivatives of the PyBOX and thioPyBOX ligands available, there are many heteroleptic iron(II) complexes that can be formed. Combinations of complexes can arise from having different substituents on each ligand and then also from having different chiralities of these ligands. From this an  $n^{\text{th}}$  number of complexes can be formed building this vast library.

This chapter focusses on two types of heteroleptic complexes: examples containing PyBOX<sup>R</sup> and ThioPyBOX<sup>R</sup> ligands in the same molecule; and, compounds combining these with other N,N',N''-tridentate ligands. Heteroleptic [Fe(PyBOX<sup>R</sup>)(thioPyBOX<sup>R</sup>)]<sup>2+</sup> complexes using the aforementioned ligands from chapter 2 bearing R- substituents phenyl, isopropyl and *tert*butyl at the 4- position of the thiazoline/oxazoline rings are first discussed, including their homochiral and heterochiral isomers. Following this, heteroleptic complexes of iron PyBOX/thioPyBOX with either 2,6-bis(2-benzimidazolyl)pyridine (bzimpy), 2,6-bis(pyrazol-1-yl)pyridine (1-bpp) or 2,2':6',2''-terpyridine (terpy) (Figure 4.1), are also discussed. It was hoped steric protection from the PyBOX/ThioPyBOX Ph- or *i*Pr- substituents might lead to selective formation of heteroleptic complex products.

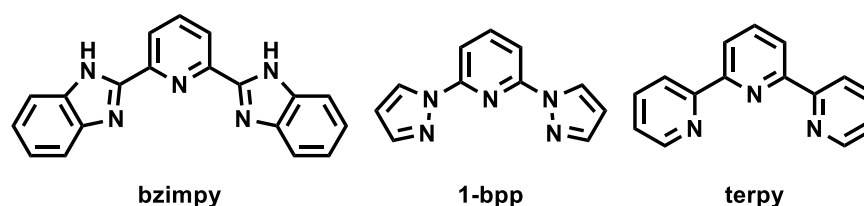


**Figure 4.1. The structures of 2,6-bis(2-benzimidazolyl)pyridine, bzimpy (left), 2,6-bis(pyrazol-1-yl)pyridine, 1-bpp (middle) and 2,2':6',2''-terpyridine, terpy (right).**

Since there are no stereogenic centres in bzimpy, bpp or terpy, the complexes of those ligands do not form homochiral or heterochiral diastereomers.



### 4.1.1 Heteroleptic iron(II) SCO complexes

A key challenge in exploring the field of heteroleptic complexes using two N,N',N''-heterocyclic-based tridentate ligands comes from the stoichiometric formation of each homoleptic complex as an alternative to the desired heteroleptic product. This is particularly common where one of the homoleptic products is low-spin, which makes it a thermodynamic sink in the reaction mixture.<sup>315, 316, 336</sup> Studies of such mixed ligand complexes, involving bis(pyrazolyl)pyridine (bpp) and terpyridine (terpy) (Sections 2.1.1.3-2.1.1.4) derivatives, have however shown that a quantitative crystallisation of the heteroleptic species can be carefully designed and achieved.<sup>337-339</sup>

Barrios *et al.* studied heteroleptic  $[\text{Fe}(\text{L})(\text{L}')][\text{ClO}_4]_2$  complexes with  $\text{L}/\text{L}' = 1\text{-bpp}, 2\text{-bzimpy}, \text{terpy}$ ,<sup>340</sup> as a means to enhance the SCO behaviour, building on their previous work of homoleptic complexes using 3-bpp ligand derivatives.<sup>337, 339</sup> Their results showed remarkable differences in the spin state behaviours of three complexes  $[\text{Fe}(\text{H}_4\text{L1})(\text{Cl-terpy})][\text{ClO}_4]_2 \cdot \text{C}_3\text{H}_6\text{O}$  (1),  $[\text{Fe}(\text{H}_2\text{L3})(\text{Me-3-bpp})][\text{ClO}_4]_2 \cdot \text{C}_3\text{H}_6\text{O}$  (2),  $[\text{Fe}(\text{H}_4\text{L1})(2\text{-bzimpy})][\text{ClO}_4]_2 \cdot 3\text{C}_3\text{H}_6\text{O}$  (3) (where  $\text{H}_4\text{L1}$  and  $\text{H}_2\text{L3}$  are 3-bpp derivatives (Figure 4.2)). Complex (1) is LS, (2) is HS and (3) is initially HS but loses three molecules of acetone in its crystal structure when exposed to the atmosphere, which in turn converts it to the LS state.<sup>340</sup>

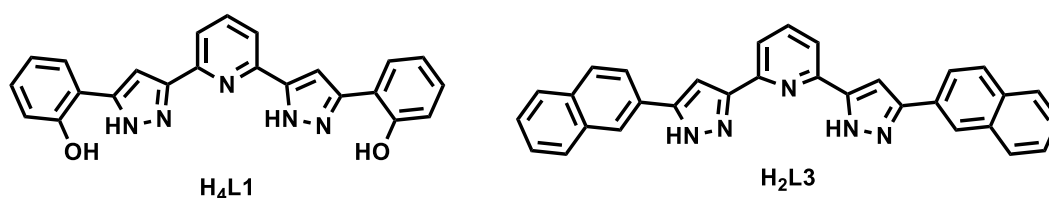


**Figure 4.2.** 3-Bpp derivatives employed in the study by Barrios *et al.*  $\text{H}_4\text{L1}$ , 2,6-bis(5-(2-hydroxyphenyl)pyrazol-3-yl)pyridine and  $\text{H}_2\text{L3}$ , 2,6-bis(5-naphthylpyrazol-3-yl)pyridine.<sup>340</sup>

García-Lopez *et al.* were able to shift the  $T_{1/2}$  of the previously reported homoleptic iron(II)1-bpp derivative,  $[\text{Fe}(\text{1-bppCOOH})_2][\text{ClO}_4]_2$ , towards room temperature and with a hysteresis loop of 13 K, by employing this ligand in a heteroleptic complex with a 3-bpp derivative,  $\text{H}_2\text{L4}$  (2,6-bis(5-([1,1'-biphenyl]-4-yl)-1H-pyrazol-3-yl)pyridine, Figure 4.3), to form a solvated complex,  $[\text{Fe}(\text{1-bppCOOH})(\text{H}_2\text{L4})][\text{ClO}_4]_2$ .<sup>338</sup>  $\text{H}_2\text{L4}$  was purposely employed to achieve this target, due to its extensive  $\pi$ -system, which will favour  $\pi$ - $\pi$  stacking and C-H... $\pi$  intermolecular interactions that would enhance the cooperativity of the system in the solid state. Their work also reported the first heteroleptic compound containing two 1-bpp tridentate ligands,  $[\text{Fe}(\text{1-bppCOOH})(\text{1-}$

bppCOOEt)][ClO<sub>4</sub>]<sub>2</sub>•0.5Me<sub>2</sub>CO which was found to undergo a ST above room temperature.<sup>338</sup> The latter result resembles its homoleptic counterparts [Fe(1-bppCOOH)<sub>2</sub>][ClO<sub>4</sub>]<sub>2</sub> (T<sub>1/2</sub> = 380 K)<sup>341</sup> and [Fe(1-bppCOOEt)<sub>2</sub>][ClO<sub>4</sub>]<sub>2</sub> (T<sub>1/2</sub> = 330 K).<sup>342</sup>

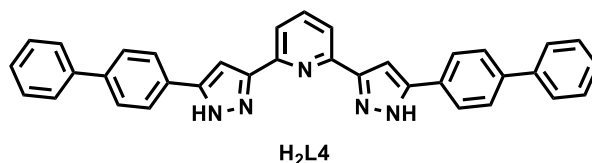


**Figure 4.3.** The structure of H<sub>2</sub>L4, 2,6-bis(5-([1,1'-biphenyl]-4-yl)-1H-pyrazol-3-yl)pyridine, employed in the work by García-López *et al.*<sup>338</sup>

While the chemistry of two different ligand families have been studied as a means to achieve optimal SCO activity in such heteroleptic complexes, fine-tuning the complexes using ligand chirality was another way of optimising SCO activity. Chapter 3 discussed the chiral discrimination achieved between pairs of diastereomeric iron(II) SCO complexes, which recent work by Wang *et al.* has extended to the *meso*-homochiral iron complex, produced by the *meso*-(R,S)-PyBOX<sup>Ph</sup> ligand, L<sup>meso</sup>. Their results found a clear distinction in the T<sub>1/2</sub> values for the solution state STs for the three diastereomers of [Fe(PyBOX<sup>Ph</sup>)<sub>2</sub>]<sup>2+</sup> (Figure 4.4).<sup>207</sup>

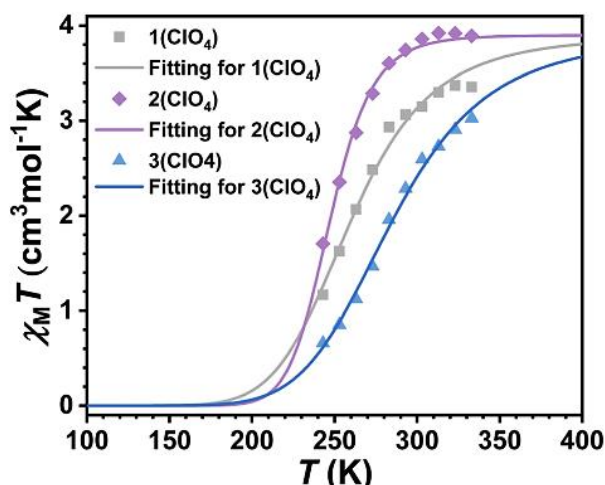


**Figure 4.4.** Solution state SCO activity for [Fe((R,S)-PyBOX<sup>Ph</sup>)<sub>2</sub>][ClO<sub>4</sub>]<sub>2</sub> (1(ClO<sub>4</sub>)), [Fe((S,S)-PyBOX<sup>Ph</sup>)<sub>2</sub>][ClO<sub>4</sub>]<sub>2</sub> (2(ClO<sub>4</sub>)) and [Fe((R,R)-PyBOX<sup>Ph</sup>)(S,S)-PyBOX<sup>Ph</sup>][ClO<sub>4</sub>]<sub>2</sub> (3(ClO<sub>4</sub>)). Figure taken from publication.<sup>207</sup>

## 4.2 Results & Discussion

### 4.2.1 Iron(II) PyBOX<sup>Ph</sup>/thioPyBOX<sup>Ph</sup> complexes

A series of heteroleptic iron(II)PyBOX/thioPyBOX complexes has been synthesised herein:  $[\text{Fe}((\text{S,S})\text{-PyBOX}^{\text{Ph}})((\text{S,S})\text{-thioPyBOX}^{\text{Ph}})](\text{ClO}_4)_2$ , **S-9**,  $[\text{Fe}((\text{S,S})\text{-PyBOX}^{\text{Ph}})((\text{R,R})\text{-thioPyBOX}^{\text{Ph}})](\text{ClO}_4)_2$ , **RS-9**,  $[\text{Fe}((\text{S,S})\text{-PyBOX}^{\text{iPr}})((\text{S,S})\text{-thioPyBOX}^{\text{iPr}})](\text{ClO}_4)_2$ , **S-10** and  $[\text{Fe}((\text{R,R})\text{-PyBOX}^{\text{iPr}})((\text{S,S})\text{-thioPyBOX}^{\text{iPr}})](\text{ClO}_4)_2$ , **RS-10** (Figure 4.5). These complexes have been structurally characterised by XRD where possible, by HRMS and paramagnetic <sup>1</sup>H NMR. SCO studies have been carried out in the solid state using the SQUID and in solution using the VT Evans <sup>1</sup>H NMR method, as was employed in Chapter 3. In this chapter only the perchlorate salts of the complexes are discussed, unless otherwise stated.

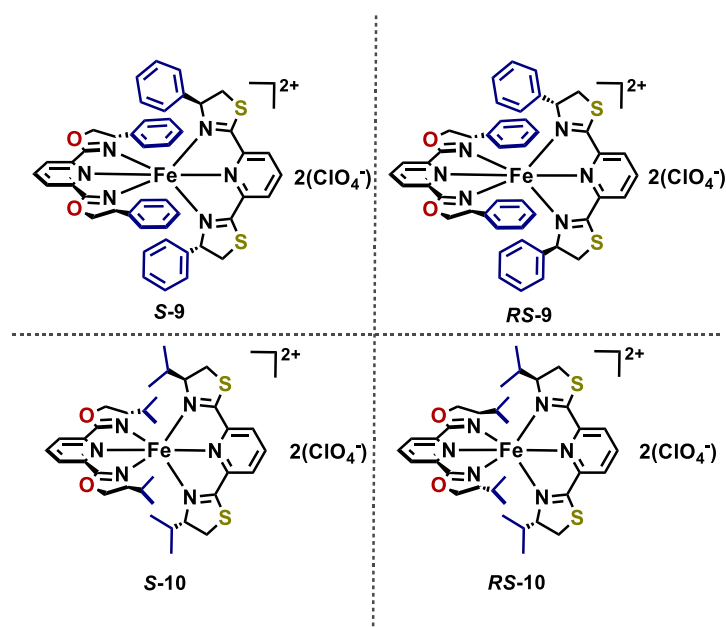


**Figure 4.5. Structures of the heteroleptic iron(II)PyBOX/thioPyBOX complexes synthesised herein. S-9, RS-9, S-10 and RS-10.**

All complexes were synthesised by a 1:1:1 reaction of PyBOX<sup>R</sup> : thioPyBOX<sup>R</sup> : Fe[ClO<sub>4</sub>]<sub>2</sub>•6H<sub>2</sub>O in acetonitrile. Crystals were grown by slow diffusion of diethyl ether or diisopropyl ether into a concentrated sample of the reaction mixture in either acetonitrile, nitromethane or acetone. Details of this are outlined in Section 4.4.

#### 4.2.1.1 Structural Characterisation by XRD

The XRD structure solutions obtained for **S-9** and **RS-9** are shown in Figure 4.6 and the relevant bond lengths and angles are tabulated below (Table 4.1).

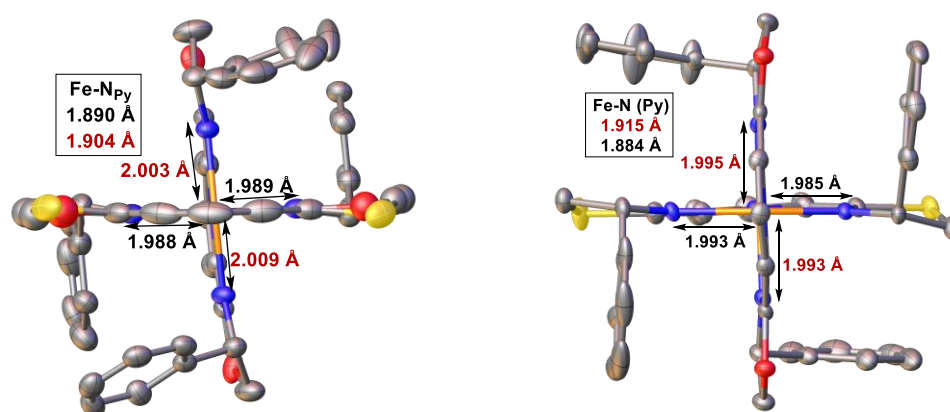


Figure 4.6. XRD structure solutions obtained for **S-9** (left) and **RS-9** (right).

Complex	<b>S-9</b>	<b>RS-9</b>
<b>Fe-N<sub>Py</sub> (PyBOX) (Å)</b>	1.904(4)	1.915(3)
<b>Fe-N<sub>Py</sub> (thioPyBOX) (Å)</b>	1.890(4)	1.884(3)
<b>Fe-N<sub>oxazoline</sub> (Å)</b>	2.009(4)	1.993(3)
	2.003(4)	1.995(3)
<b>Fe-N<sub>thiazoline</sub> (Å)</b>	1.990(4)	1.985(3)
	1.988(4)	1.993(3)
$\theta$ (°)	83.183	88.559
$\phi$ (°)	178.10(18)	179.45(14)
$\varphi$ (°) oxazoline	159.14(16)	158.69(12)
$\varphi$ (°) thiazoline	156.78(18)	159.44(12)

Table 4.1. Selected bond lengths and angles from the XRD structure solutions of **S-9** and **RS-9**.

The XRD structure solution of **S-9** shows that this reaction does not cleanly crystallise as a 1:1:1 structure of PyBOX<sup>Ph</sup> : thioPyBOX<sup>Ph</sup> : Fe. Rather the structure of **S-9** is a mixture of **S-9** and **S-1**, with **S-9** being the major component. While one ligand structurally fits the PyBOX<sup>Ph</sup> ligand exactly, the other ligand site is a PyBOX<sup>Ph</sup>/thioPyBOX<sup>Ph</sup> mixture, which is modelled in Figure 4.6. The disorder was indicated by the –C-O/S-CH<sub>2</sub>- bond angle of the oxazoline/thiazoline ring which is typically ~90 ° in the thiazoline ring and ~105 ° in the oxazoline ring, but fell in between these values in **S-9** prior to modelling the disorder. No such disorder is apparent in crystals of **RS-9**, which has crystallised cleanly from the reaction mixture.

The Fe-N<sub>Py</sub> bond lengths seem to have retained the nature of the ligand they belong to in the heteroleptic complex, **RS-9**. The Fe-N<sub>Py</sub> (PyBOX) bonds fit perfectly with the equivalent bond lengths in **RS-1**<sup>210</sup>, whilst the Fe-N<sub>Py</sub> (thioPyBOX) distances are more fitting with the equivalent bond lengths in **RS-5** (Section 3.2.1.3.1). However considering the Fe-N<sub>ox./thiox.</sub> bonds, these appear more averaged between the equivalent bond lengths observed for the **RS-1** and **RS-5**. This evidences that even in this mixed ligand complex, the different electron-withdrawing natures of the two ligands are still distinct but most notably along the axial coordination sites where the pyridyl groups are bound.

The dihedral angle,  $\theta$ , between the least squares planes of the two ligands in **S-9** is 83.18 ° and in **RS-9** is 88.56 °. This agrees with the differences observed between the chiral pairs **R-1** and **RS-1** and **S-5** and **RS-5**, where the homochiral complexes displayed a greater distortion from the ideal geometry, owing to the clash of the phenyl substituents. **RS-9** shows minimal deviation from the perfect octahedral value of 90 °,<sup>329</sup> which is more similar to **RS-1** than to **RS-5**, as **RS-5** shows a relatively higher degree of angular distortion in  $\theta$ . Though independent of the dihedral angle,<sup>77</sup> the N<sub>Py</sub>-Fe-N<sub>Py</sub> *trans* angle,  $\phi$ , also shows negligible deviation from its ideal geometry of 180 ° in both isomers. This angle is most similar to that in **S-1** and **RS-1**, which is consistent with greater contribution of the PyBOX<sup>Ph</sup> ligand to the composition of the heteroleptic crystal of **S-9**.

The space-filling models of **RS-9** are shown in Figure 4.7 and for comparison, the space-filling models of the **RS-1** and **RS-5** equivalents are also shown (Figure 4.8).

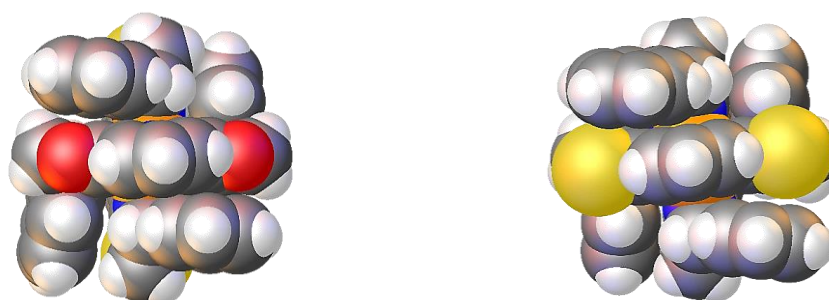


**Figure 4.7. Space-filling models of *RS-9* (front and back views).**

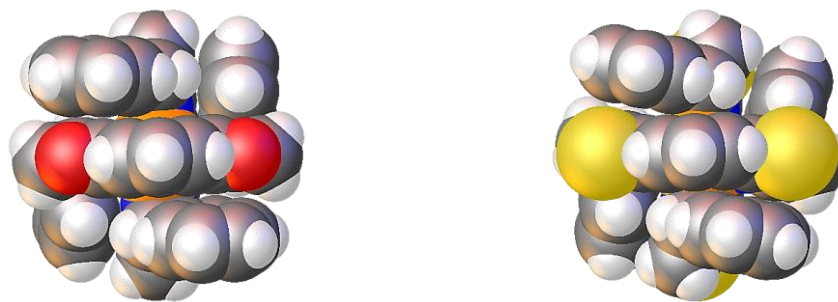


**Figure 4.8. Space-filling models of *RS-1* (left) and *RS-5* (right).**

The space-filling model of ***RS-9*** (Figure 4.7) shows a similar degree of canting of the phenyl rings as is observed in the homoleptic species in Figure 4.8. The slightly shorter PyBOX ligand experiences a greater steric clash from the bulkier thiazoline ring and so the phenyl rings of this ligand pushes outwards to accommodate this, which is evident in the space-filling model in Figure 4.7.

To confirm that these single crystal XRD structures are representative of the bulk sample in the solid state, powder-XRD (pXRD) data was collected on a sample of ***S-9*** and ***RS-9*** (Figure 4.9). The data in both cases, shows the exact same trend of key peaks when compared against the pXRD pattern simulated from the single crystal XRD structure. This confirms that the bulk samples in the solid state are phase pure and is solely the complexes ***S-9*** and ***RS-9***.

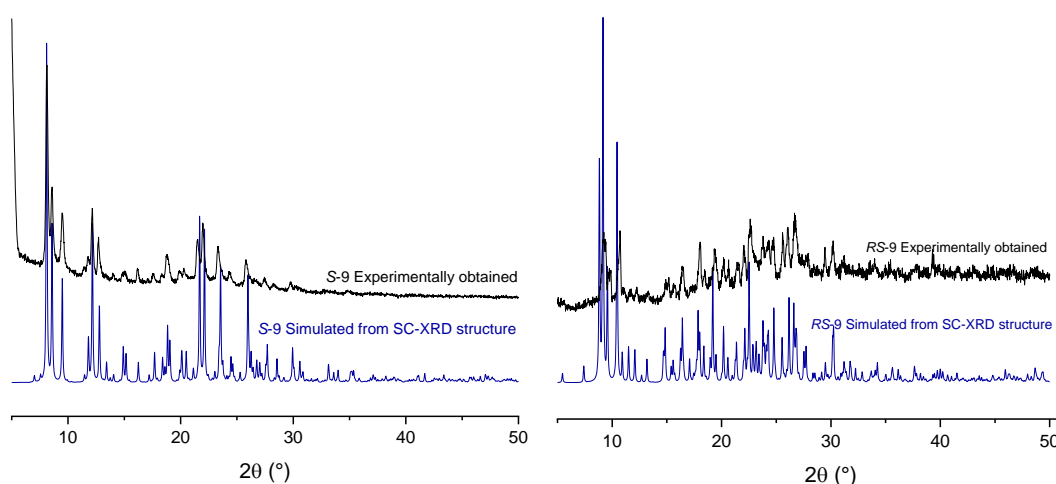


**Figure 4.9. Powder-XRD data obtained for *S-9* (left) and *RS-9* (right). Experimentally obtained patterns are in black and simulated patterns from the single crystal XRD solution is in blue.**

The purity of the bulk sample observed from the pXRD pattern was further confirmed by elemental analysis, which showed no contamination of the bulk sample in the solid state (Section 4.4).

The paramagnetic  $^1\text{H}$  NMR spectrum of the homochiral analogue, **S-9** is shown in comparison to **RS-9** in Figure 4.10.

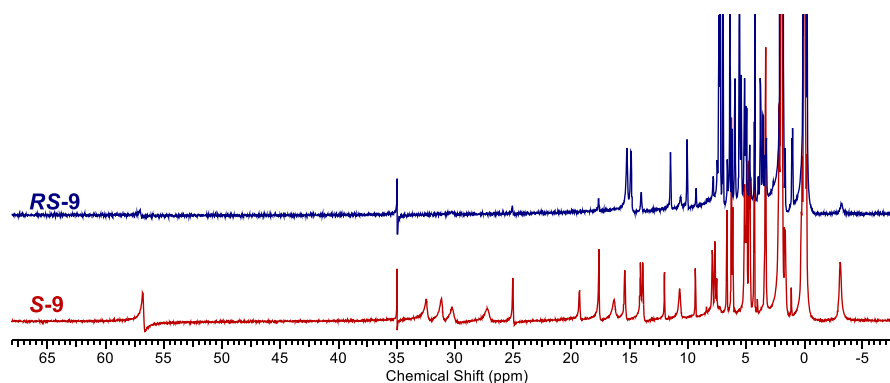


**Figure 4.10. Paramagnetic  $^1\text{H}$  NMR spectra of **RS-9** (top, blue) and **S-9** (bottom, red). [ $\text{CD}_3\text{CN}$ , 300 MHz].**

The  $^1\text{H}$  NMR for **RS-9** (blue spectrum in Figure 4.10) shows 16 paramagnetically shifted  $^1\text{H}$  environments which corresponds to the 8 unique heterocyclic proton environments per ligand. The different electronic character of the PyBOX vs thioPyBOX ligand results in distinct  $^1\text{H}$  peaks for each ligand as was shown in Chapter 2. This distinction is retained even in their heteroleptic iron complexes.

The spectrum of **S-9** (red spectrum in Figure 4.10) shows 24 distinct paramagnetic proton environments, eight of which match with the  $^1\text{H}$  NMR spectrum of **S-1** and another eight match the spectrum of **S-5** (Figure 4.11). This shows that the three complexes **S-1**, **S-5** and **S-9** are all present in this solution.

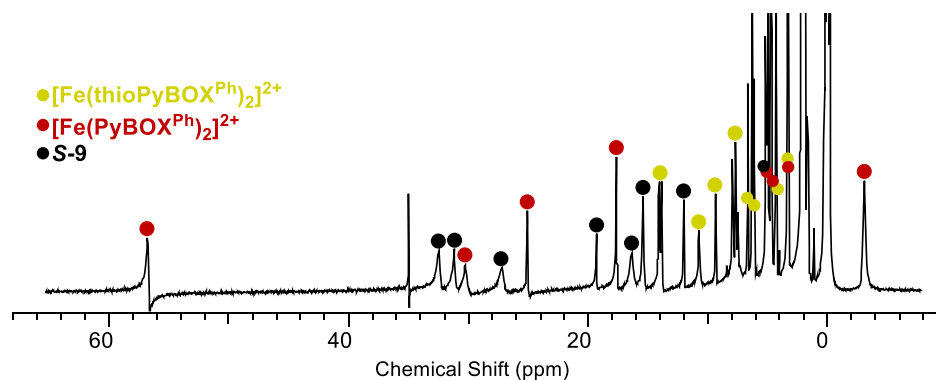


**Figure 4.11. Paramagnetic  $^1\text{H}$  NMR spectra of **S-9**. Red dots indicate the homoleptic  $[\text{Fe}(\text{PyBOX}^{\text{Ph}})_2]^{2+}$  complex, **S-1** and yellow dots indicate the homoleptic  $[\text{Fe}(\text{thioPyBOX}^{\text{Ph}})_2]^{2+}$ , **S-5**.  $[\text{CD}_3\text{CN}$ , 300 MHz].**

Analysis of the integrations shows an approximately 1:1:1 ratio of these three species. This suggests that all three cations are stable in solution, and the homoleptic complexes are slightly more stable than the heteroleptic product (since a purely statistical mixture of the three species would have a 1:2:1 distribution). The presence of the homochiral complex **S-5** is further supported by HRMS analysis which shows a cationic peak corresponding to the stable species  $[\text{Fe}(\text{thioPyBOX}^{\text{Ph}})_2]^{2+}$ . This supports the disordered XRD structure obtained for **S-9**.

An *in situ* study of **RS-9** involved running the paramagnetic  $^1\text{H}$  NMR spectra of a 1 : 1 : 1 reaction mixture of (R)-thioPyBOX<sup>Ph</sup> : (S)-PyBOX<sup>Ph</sup> :  $[\text{Fe}(\text{ClO}_4)_2] \cdot 6\text{H}_2\text{O}$  at regular intervals over a 35 day period. This was to gain an understanding of the relative stabilities of the possible complexes in solution, observing the thermodynamic and kinetic species (Figure 4.12). The equivalent study of **S-9** was not carried out due to time constraints.



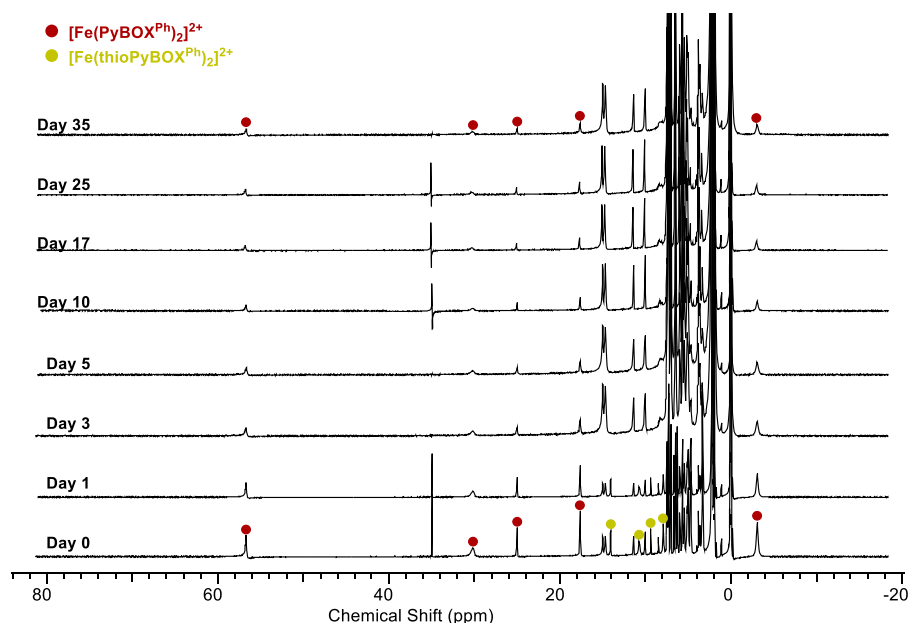


**Figure 4.12. Paramagnetic  $^1\text{H}$  NMRs of a 1:1:1 solution of (S,S)-PyBOX<sup>Ph</sup> : (R,R)-thioPyBOX<sup>Ph</sup> :  $\text{Fe}(\text{ClO}_4)_2 \cdot 6\text{H}_2\text{O}$  over a 35 day period. Red dots indicate the homoleptic  $[\text{Fe}(\text{PyBOX}^{\text{Ph}})_2]^{2+}$  complex and yellow dots indicate the homoleptic  $[\text{Fe}(\text{thioPyBOX}^{\text{Ph}})_2]^{2+}$ . [ $\text{CD}_3\text{CN}$ , 300 MHz].**

The 35-day study of the *in situ* mixture shows that initially (day 0) both the homoleptic complexes form in addition to **RS-9**. Analysis of the integrations of the peaks revealed an approximately 1 : 1 : 1 ratio of the three species. After 3 days, the peaks corresponding to **R-5** disappears, which shows it was a kinetic product that was able to quickly form but ultimately proved to be the least stable of the three species. Over the 35-day period, the solution equilibrates to give **RS-9** as the major species in solution, rendering **RS-9** the thermodynamically favoured complex. Interestingly the homoleptic complex  $[\text{Fe}(\text{PyBOX}^{\text{Ph}})_2]^{2+}$  remains in solution even when the equilibrium is established, as can be seen by the red dots highlighted on the day 35 spectrum in Figure 4.12. The integrations of these peaks shows a significantly reduced amount of this species at this time period, that is, only 10% of the solution is the homoleptic iron(II)PyBOX<sup>Ph</sup> complex and 90% is **RS-9**. Re-dissolved crystals of **RS-9** also showed this same 10% contamination of the homoleptic complex, which is apparently too small to detect crystallographically.

The stability of **RS-9** is further confirmed by the High Resolution Mass Spectrometry (HRMS) analysis which shows a dicationic peak at  $m/z = 413.0939$  which corresponds to the pure **RS-9**. The HRMS of **S-9** shows a dicationic peak at  $m/z = 429.0706$  corresponding to **S-5** (Section 4.4), highlighting the lower stability of **S-9**.

#### 4.2.2 Spin-crossover Studies

The solid and solution state magnetic susceptibilities were measured using SQUID and Evan's method  $^1\text{H}$  NMR respectively at varying temperatures, as was employed in previous studies. The solid state magnetic susceptibility is shown in Figure 4.13.

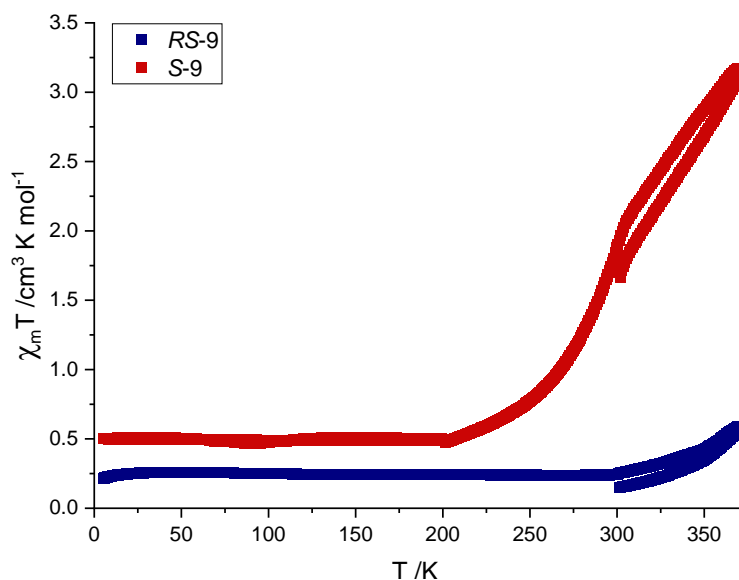


**Figure 4.13. Variable temperature magnetic susceptibility curves in the solid phase using the SQUID for *RS-9* (blue curve) and *S-9* (red curve). N.B. 300→370K is the first heating cycle, upon which initial solvent is lost.**

The solid state plot of the magnetic susceptibility of ***RS-9*** (blue curve in Figure 4.13) shows the complex is completely LS from 5 – 300 K, but begins to show the onset of a ST above 300 K. This is almost exactly the same as was observed in the SQUID curves for the heterochiral thioPyBOX<sup>Ph</sup> complexes ***RS-5* (ClO<sub>4</sub>)** and ***RS-5* (BF<sub>4</sub>)**. This is also fitting with the heterochiral PyBOX<sup>Ph</sup> complex, ***RS-1*** which only showed the start of a ST above 280 K and has a  $T_{1/2}$  estimated to occur above 400 K. Since the ST of ***RS-5*** occurs at a similar temperature (Section 3.2.1.4), the solid state  $T_{1/2}$  of ***RS-9*** would most likely be close to this value.

On the contrary, the SQUID curve for the homochiral complex ***S-9*** (red curve in Figure 4.13) shows a much steeper ST starting with ~15% of the sample in the HS state from 5-200 K and then undergoing a ST, with almost all of the sample in the HS state at 370 K. The  $T_{1/2}$ , obtained from taking  $X_mT = 1.75 \text{ cm}^3 \text{ mol}^{-1} \text{ K}$  in the graph for ***S-9***, is approximately 300 K, which is lower than both the  $T_{1/2}$  values for ***S-1*** and ***S-5*** (350 K and 330 K respectively). The temperature of the ST for ***S-9*** is however much more ideal, as it falls at an ambient temperature which is most suitable for application purposes.

The solution state magnetic susceptibility is a more accurate depiction of the variable temperature spin state behaviour of a complex due the absence of intermolecular interactions that arise from the crystal packing. As only the cationic species is considered in solution, this is the best data set to use in drawing comparisons between the spin state behaviour of complexes provided the analysis is performed using the same NMR solvent and reference. The solution phase magnetic susceptibility obtained by the VT Evans method is shown in Figure 4.14 for **RS-9** (blue curve) and **S-9** (red curve).

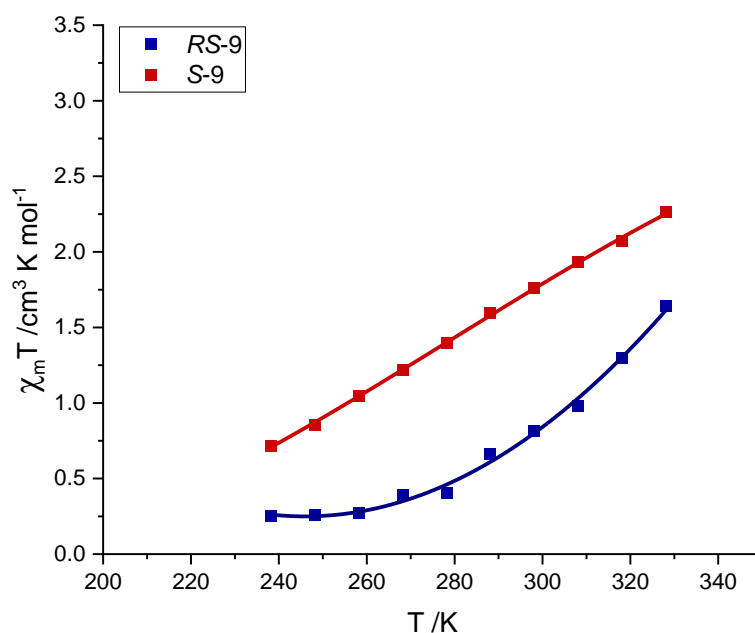


**Figure 4.14. Variable temperature magnetic susceptibility curves in the solution phase using the VT Evan's method for **RS-9** (blue curve) and **S-9** (red curve).**

The solution state data obtained for **RS-9** shows a much steeper ST occurring in solution compared to that observed in the solid state. The ST for **RS-9** becomes apparent from as early as 250 K. While the data obtained is restricted to the temperature range 235 - 330 K due to the liquid range of the solvent, it is clear that around 250 K the complex is almost completely in the LS state, but then reaches a close to 50 % conversion to the HS state at 330 K. The curve for **S-9** however, does not show a ST with the typical curvature usually observed in SCO compounds. A straight line is observed for **S-9**, which is more gradual in gradient compared to the thermal equilibrium observed for **RS-9**. This is due to the ligand redistribution observed in the solution studies of **S-9** which shows a clear 1:1:1 mixture of three different species, each of which will respond differently and individually to the applied

heat stimulus. **RS-9** is a ~90% pure compound in solution so displays a more typical ST curve.

Since the **S-9** mixture contains ~ 33% **S-1** which has  $X_mT \approx 1.60 \text{ cm}^3 \text{ mol}^{-1} \text{ K}$  at 240 K and undergoes a ST with a  $T_{1/2} \approx 244 \text{ K}$  (Section 3.1.4.2) and ~ 33% **S-5**, which has  $X_mT = 0.25 \text{ cm}^3 \text{ mol}^{-1} \text{ K}$  at 240 K (Section 3.2.1.5). Accounting for these values of the homoleptic complexes, the  $X_mT = 0.75 \text{ cm}^3 \text{ mol}^{-1} \text{ K}$  at 240 K of the **S-9** mixture means that, the fraction of the sample that is purely the heteroleptic **S-9** complex (~ 33%) has a  $X_mT \approx 0.35 \text{ cm}^3 \text{ mol}^{-1} \text{ K}$  at 240 K. Using the same calculations, it is found that the purely **S-9** fraction of the sample reaches  $X_mT = 1.95 \text{ cm}^3 \text{ mol}^{-1} \text{ K}$  at ~330 K. This means that of the pure heteroleptic **S-9**, ~45% of the sample undergoes a spin conversion to the HS state. This is fitting with the observed percentages of 40-45% undergoing a ST in **S-1** and **S-5**, demonstrating a similar SCO ability of the pure **S-9** sample.

Van't Hoff calculations were used to calculate the anticipated  $T_{1/2}$  along with the thermodynamic parameters  $\Delta H$  and  $\Delta S$ , which can be compared to the equivalent data for the PyBOX<sup>Ph</sup> and thioPyBOX<sup>Ph</sup> complexes (Table 4.2).

Complex	$T_{1/2} / \text{K}$	$\Delta H / \text{kJ mol}^{-1}$	$\Delta S / \text{J K}^{-1} \text{ mol}^{-1}$
<b>RS-9</b>	331	18.1	51
<b>RS-1</b>	278	26.2	94
<b>RS-5</b>	362	14.3	37
<b>S-9</b>	298	14.1	47
<b>R-1</b>	244	25.0	102
<b>S-5</b>	327	18.9	55

**Table 4.2. Solution phase  $T_{1/2}$  values and thermodynamic parameters obtained from van't Hoff calculations for **S-9** and **RS-9**. Data for **S-1**, **RS-1**<sup>210</sup>, **S-5** and **RS-5** are shown for comparison.**

The data in Table 4.2 shows the  $T_{1/2}$ ,  $\Delta H$  and  $\Delta S$  values for **RS-9** falls in-between the equivalent data obtained for the heterochiral PyBOX and thioPyBOX complexes. The entropic contribution to the feasibility of a ST in **RS-9** is much less than was observed in **RS-1** but is enthalpically more favourable, as was the case for **RS-5** compared to **RS-1**, but to a lesser extent. While the thermodynamic parameters for **S-9** are presented in Table 4.2, these were calculated using the impure variable temperature solution state data containing the multiple species. Therefore the values for the  $T_{1/2}$ ,  $\Delta H$  and  $\Delta S$  displayed are weighted averages including these values for **S-1** and **S-5** as well as the pure **S-9**. Subtracting out the values from these different species leaves

the pure **S-9** fraction with a  $T_{1/2} = 323$  K which is reasonable. The short temperature range of the measurements used in these van't Hoff calculations can lead to unreliable data. This is most likely the case when calculating  $\Delta H$  and  $\Delta S$  from the averages, as the averaged values are lower. Calculating the values this way also assumes an exactly equal proportion of the three species in solution, which was only approximated from the integrations of the NMR spectra.

The thermodynamic parameters for **RS-9** and **S-9** are most similar to that observed for the thioPyBOX complexes, which suggests the contribution of the thioPyBOX<sup>Ph</sup> ligand in these heteroleptic complexes dominates over the PyBOX<sup>Ph</sup> ligand. While the  $T_{1/2}$  of **RS-9** is closer to ambient temperatures than was calculated for **RS-5**, it is still too high for application purposes.

#### 4.2.2 Iron(II) PyBOX<sup>iPr</sup>/thioPyBOX<sup>iPr</sup> complexes

While both the homochiral and heterochiral Iron(II)PyBOX<sup>Ph</sup> and iron(II)thioPyBOX<sup>Ph</sup> complexes showed some degree of a ST or the onset of a ST, it was reasonable to expect some SCO behaviour in the mixed complexes **S-9** and **RS-9**. With the *isopropyl* complexes thus far (**R-2**, **RS-2**, **R-6** and **RS-6**), a clear distinction was observed in the SCO activity between the PyBOX<sup>iPr</sup> and thioPyBOX<sup>iPr</sup> complexes. The PyBOX<sup>iPr</sup> complexes displayed purely HS character at all temperatures in both solid and solution phases (Section 3.1.4.1-3.1.4.2), whilst the thioPyBOX<sup>iPr</sup> analogues showed a ST in the case of **S-6** and the onset of a ST at high temperatures in the case of **RS-6** (Section 3.2.1.4-3.2.1.5). This leaves the mixed iron(II)PyBOX<sup>iPr</sup>/thioPyBOX<sup>iPr</sup> complexes particularly intriguing to study.

Two heteroleptic iron(II) PyBOX<sup>iPr</sup>/thioPyBOX<sup>iPr</sup> complexes were synthesised; a homochiral complex [Fe((S)-PyBOX<sup>iPr</sup>)((S)-thioPyBOX<sup>iPr</sup>)] [ClO<sub>4</sub>]<sub>2</sub> and its heterochiral counterpart [Fe((R)-PyBOX<sup>iPr</sup>)((S)-thioPyBOX<sup>iPr</sup>)] [ClO<sub>4</sub>]<sub>2</sub>. These will be referred to as **S-10** and **RS-10** respectively (Figure 4.5).

##### 4.2.2.1 Structural Characterisation

Dark purple-pink crystals suitable for XRD were obtained for **RS-10**. This structure solution is shown in Figure 4.15 and relevant data is tabulated below (Table 4.3).

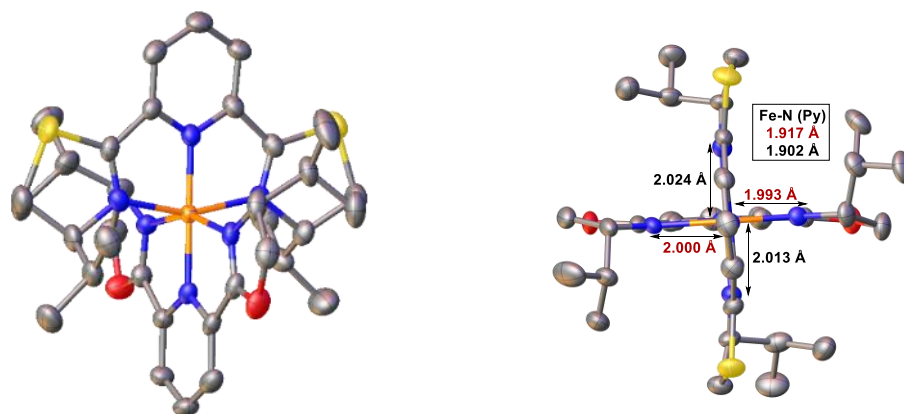


Figure 4.15. XRD structure of **RS-10**. Solvents, counter-ions and hydrogen atoms are omitted for clarity. Thermal ellipsoids are at the 50% probability level.

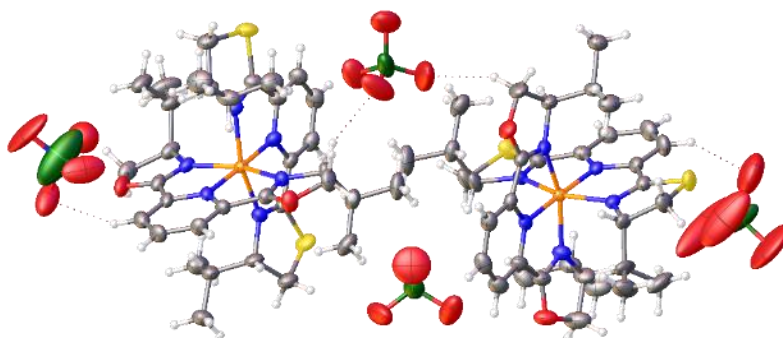
Complex	<b>RS-10</b>	<b>RS-2</b> <sup>210</sup>	<b>RS-6</b>
<b>Fe-N<sub>Py</sub> (PyBOX) (Å)</b>	1.917(5)	2.1170(14),	1.885(4)
<b>Fe-N<sub>Py</sub> (thioPyBOX) (Å)</b>	1.902(5)	2.1343(14)	1.883(4)
<b>Fe-N<sub>oxazoline</sub> (Å)</b>	1.993(5)	2.2009(14)–	1.989(4)–
<b>Fe-N<sub>thiazoline</sub> (Å)</b>	2.000(5)	2.2771(15)	1.994(3)
	2.024(5)		
	2.013(5)		
$\theta$ (°)	90.332	89.23(1)	89.749
$\phi$ (°)	178.4(2)	163.62(6)	179.71(14)
$\varphi$ (°) oxazoline	158.3(2)	148.11(5)	158.73(17)
$\varphi$ (°) thiazoline	159.0(2)	148.57(6)	161.01(17)

Table 4.3. Selected bond lengths and angles for the XRD structure of **RS-10**. Data for **RS-2** and **RS-6** are shown for comparison.

While the Fe-N bonds fall within the LS range of 1.8-2.0 Å for **RS-6** and lie within the HS range of 2.1-2.3 Å for **RS-2**, the equivalent bonds in **RS-10** sit close to ~ 2.0 Å which is also closer to the LS range. Considering the XRD was collected at 130 K, this suggests a ST might occur in the solid state above this temperature. A recollection of the XRD data at a higher temperature i.e. 250 – 300 K could show a structure solution with bond lengths and angles more similar to that observed in **RS-2**.

The N<sub>Py</sub>-Fe-N<sub>Py</sub> bond angle in **RS-10** comes close to the ideal value of  $\phi = 180^\circ$  which is most similar to that observed in **RS-6**. This is least like the structure for **RS-2** which shows a large JT distortion across this angle. The clamp angles ( $\varphi$ ), of **RS-10** further support the greater resemblance of this structure to **RS-6** than of **RS-2**, which

suggests that **RS-10** is not in the HS state at 120 K as was observed with **RS-2** (Section 3.1.4). Furthermore, all four *isopropyl* substituents point in the same direction in **RS-10**, unlike that observed in **RS-2** where one substituent was observed to be more pendant-like to accommodate intermolecular interactions with a CH<sub>3</sub> group.<sup>210</sup> These structural differences show that the mixed ligand complex **RS-10** adopts more of the thioPyBOX<sup>iPr</sup> geometry found in **RS-6**. A network of intermolecular interactions is evident in the crystal packing of the structure (Figure 4.16).



**Figure 4.16.** XRD structure of **RS-10** with intermolecular interactions displayed.

The dominant interactions are ClO<sub>4</sub><sup>-</sup>...H<sub>2</sub>C-, where the CH<sub>2</sub> group belongs to the oxazoline ring of the PyBOX ligand. This shows the greater polarisation of the CH<sub>2</sub> unit in the oxazoline ring than in the thiazoline ring, as the latter does not form any C-H...O contacts with the perchlorate anion. Neither pyridine rings form any hydrogen bond-type interactions at the *para* 4- position as was observed in **RS-6**. This shows a reduced *trans* effect which is fitting with the weakened Fe-N<sub>Py</sub> bonds in **RS-10** compared to in **RS-6**.

The paramagnetic <sup>1</sup>H NMR spectra for **S-10** and **RS-10** are shown in Figure 4.17.

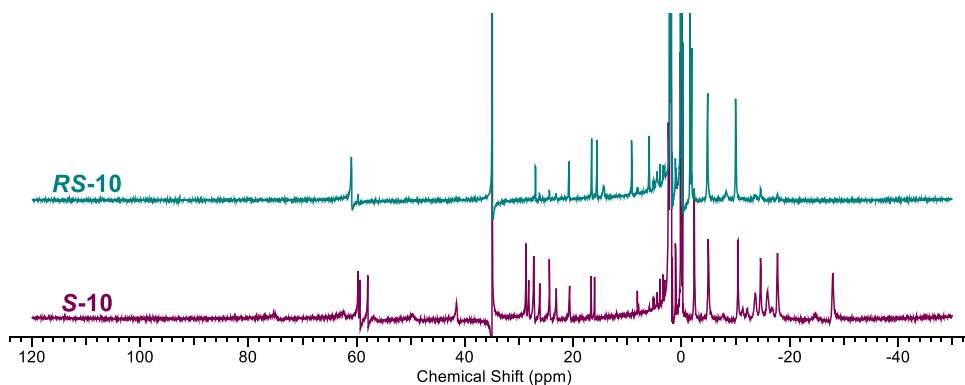


**Figure 4.17.**  $^1\text{H}$  NMR spectra of **S-10** (bottom, purple) and **RS-10** (top, green).

The  $^1\text{H}$  NMR spectrum of **S-10** shows 24 peaks which is almost three times as many as observed in **RS-10**. This suggests there are three complexes in the solution of **S-10** which must arise from ligand redistribution to form the homoleptic complexes **S-2** and **S-6**. This seems to be a recurring observation with the homochiral isomers of this heteroleptic complex series.

Comparison of the peaks in the spectrum of **S-10** against the  $^1\text{H}$  NMR spectra obtained for **S-2** and **S-6** confirmed the presence of both species in addition to **S-10** (Figure 4.18). Further analysis of the NMR spectrum shows an approximate 1:1:1 statistical distribution of the three complexes, which remained unchanged after three months (Figure 4.19).

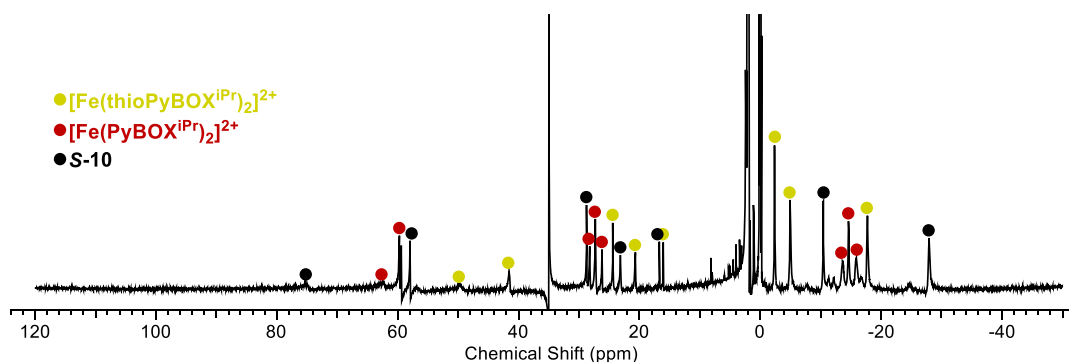


**Figure 4.18.** Paramagnetic  $^1\text{H}$  NMR of **S-10**. Red dots indicate the homoleptic  $[\text{Fe}(\text{PyBOX}^{\text{iPr}})_2]^{2+}$  complex (**S-2**) and yellow dots indicate the homoleptic  $[\text{Fe}(\text{thioPyBOX}^{\text{iPr}})_2]^{2+}$  (**S-6**).  $[\text{CD}_3\text{CN}, 300 \text{ MHz}]$ .



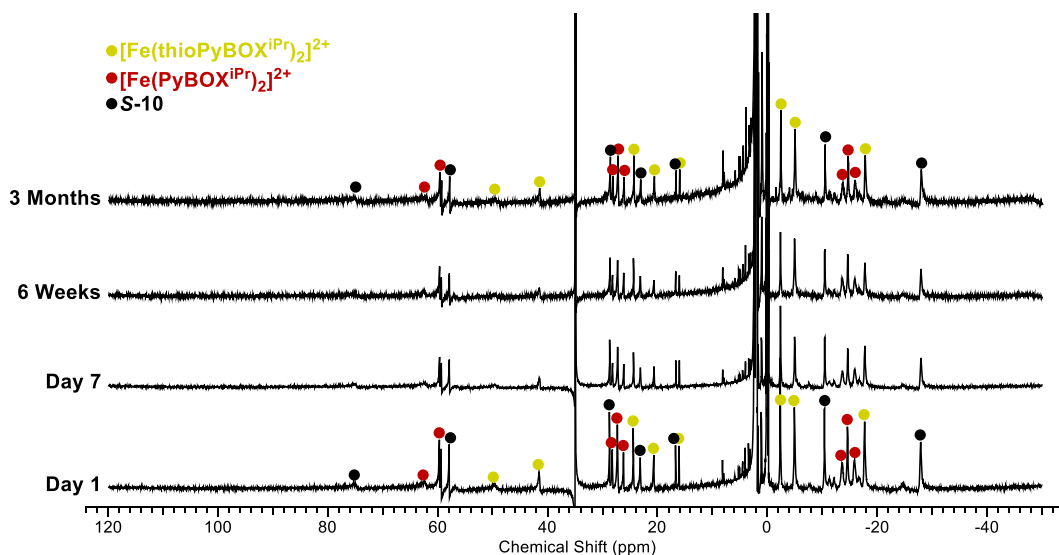


**Figure 4.19. Paramagnetic  $^1\text{H}$  NMR of **S-10** over a three month period. Red dots indicate the homoleptic  $[\text{Fe}(\text{PyBOX}^{\text{Ph}})_2]^{2+}$  complex, **S-2**, and yellow dots indicate the homoleptic  $[\text{Fe}(\text{thioPyBOX}^{\text{Ph}})_2]^{2+}$ . [ $\text{CD}_3\text{CN}$ , 300 MHz]**

The study of the  $^1\text{H}$  NMR spectrum over the three month period shows a degree of stability of the homoleptic complexes in addition to the heteroleptic species. This is fitting with the racemisation studies by Burrows *et al.* which showed a preference for the heterochiral complex **RS-2** to undergo ligand redistribution in solution to form **S-2**.<sup>210</sup>

Upon crystallisation, only the heteroleptic complexes **S-10** and **RS-10** crystallise from their respective solutions. This purity was confirmed by elemental analysis which shows samples of both batches of **S-10** and **RS-10** to be pure (Section 4.4). The pXRD analysis of the bulk samples (Figure 4.20) confirms the purity of **S-10**, insufficient quantity was obtained of **RS-10** for pXRD analysis so this dataset is pending.

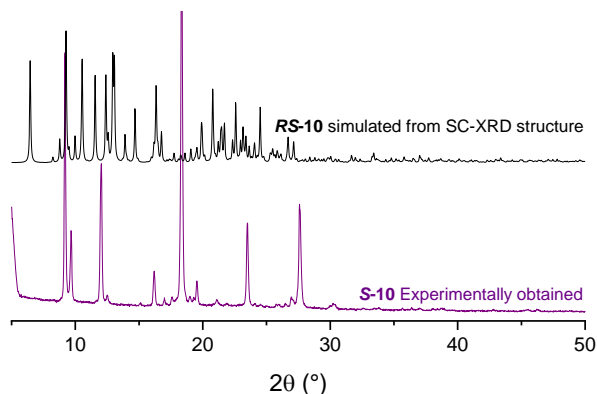


**Figure 4.20. Experimentally obtained pXRD analysis of **S-10** (purple). The simulated pXRD pattern of **RS-10** from the single crystal XRD structure is also shown for comparison (black).**

#### 4.2.2.2 Spin-crossover studies

The magnetic susceptibility data obtained for **S-10** and **RS-10** are shown in Figure 4.21 and Figure 4.22 for the solid state and solution states respectively.

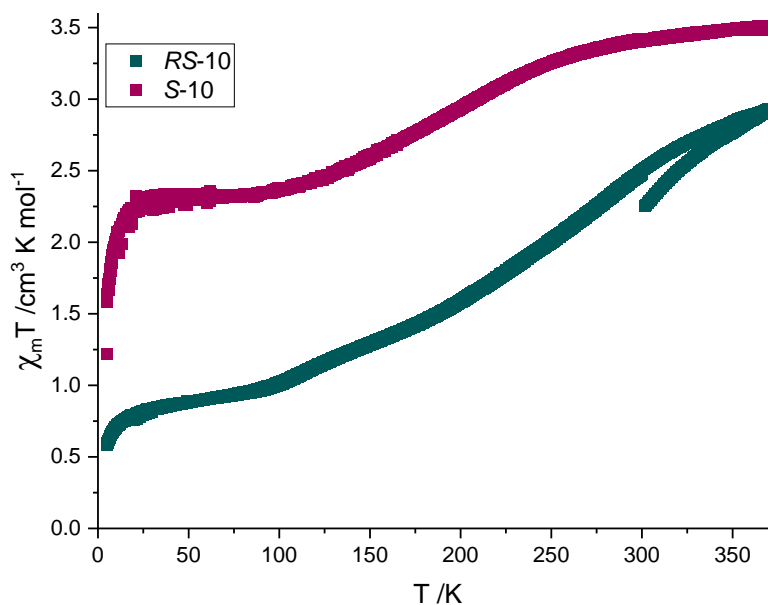


**Figure 4.21.** Variable temperature magnetic susceptibility measurements in the solid state for **S-10** (purple) and **RS-10** (green) using SQUID. N.B. 300→370K is the first heating cycle, upon which initial solvent is lost.

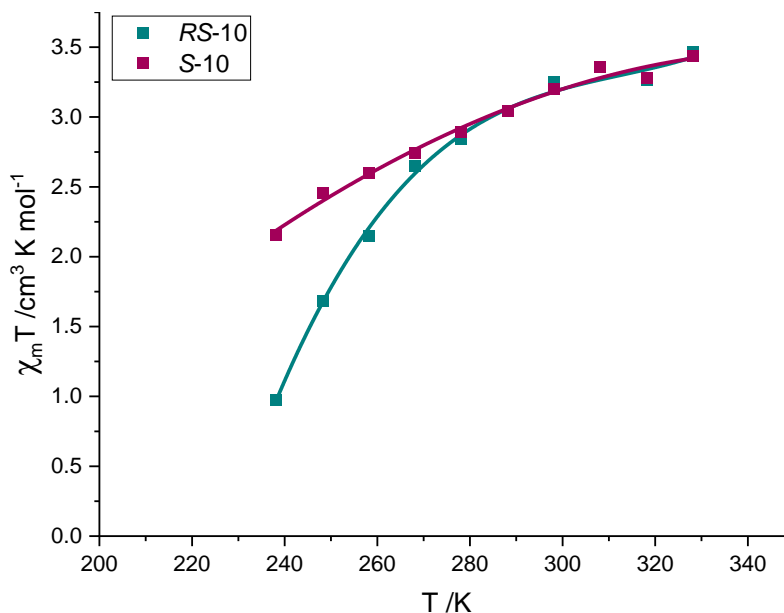


**Figure 4.22.** Variable temperature magnetic susceptibility measurements in the solution phase for **S-10** (purple) and **RS-10** (green). [ $\text{CD}_3\text{CN}$ , 500 MHz].

The solution phase data shows that at 240 K the majority of **S-10** is already in the HS state. This is reasonable considering that in solution **S-2** is also present which is fully HS at all temperatures and **S-6** is present which has ~30% of the sample in the HS state at the low T measurements. If an approximate two-thirds of the **S-10** sample are the homoleptic complexes, then this would mean about 40-45% of the whole sample can be expected to be in the HS state already. The Evans curve for **S-10** shows just over 60% of the sample in the HS state at 240 K, which leaves 15-20% of the HS fraction attributable to pure **S-10**.

**RS-10** shows an abrupt ST (relative to **S-10**), with approximately 70-75% of the sample undergoing a LS→HS conversion between 240 and 300 K. This is exactly an ‘in-between’ behaviour of **RS-2**, which is fully HS, and **RS-6** which is mostly LS, with the onset of a very gradual ST above 280 K. This comparison is shown in Figure 4.23.

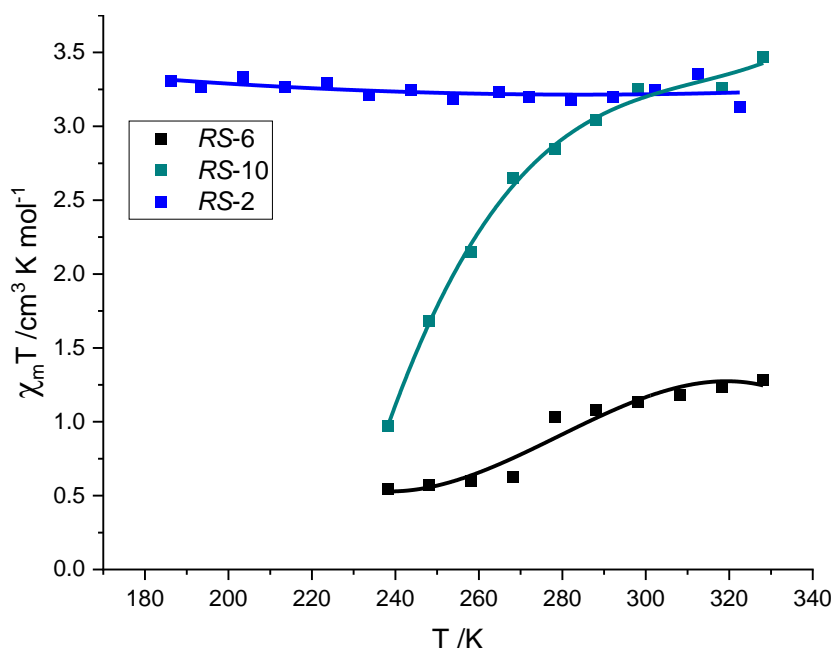


**Figure 4.23.** VT magnetic susceptibility in solution of **RS-2** (blue), **RS-10** (green) and **RS-6** (black).

In the solution state, the magnetic susceptibility for **S-10** and **RS-10** (Figure 4.22) at 280 K displays both sets of data merging into one; following the same curvature and trend reaching a fully HS state between 300-330 K. The  $T_{1/2}$  values and thermodynamic parameters are shown in Table 4.4.

Complex	T <sub>1/2</sub> /K	ΔH /kJ mol <sup>-1</sup>	ΔS /J K <sup>-1</sup> mol <sup>-1</sup>
<b>RS-10</b>	251	34.2	136
<b>RS-2</b>	HS	-	-
<b>RS-6</b>	LS	-	-
<b>S-10</b>	234	23.0	98
<b>R-2</b>	HS	-	-
<b>R-6</b>	286	19.6	69

**Table 4.4.** T<sub>1/2</sub> values and thermodynamic parameters ΔH and ΔS of **S-10** and **RS-10**. Data for **R-6** is shown for comparison.

While the LS→HS conversion for **RS-10** is enthalpically the most unfavourable out of all the complexes thus far, it is entropically the most favourable. The favourable entropic contribution to the thermodynamic probability of a ST in **RS-10** seems to dominate. The Gibbs free energy, ΔG, confirms this as it shows that at ambient temperature (298 K), ΔG = -6.3 kJ mol<sup>-1</sup> which means a ST is very feasible. Similarly to that observed with **S-9**, the thermodynamic parameters obtained from the van't Hoff calculations contain contributions from the homoleptic complexes **S-2** and **S-6**. The obtained values of the T<sub>1/2</sub>, ΔH and ΔS can be assumed to be averages over the three species in solution. Considering that there is not a thermal equilibrium in **S-2** and therefore the van't Hoff calculation cannot be applied to this complex, the contribution from this complex in the mixed solution will impede the accuracy of the data calculated for pure **S-10**.

#### 4.2.3 An attempted iron(II)PyBOX/thioPyBOX<sup>tBu</sup> complex

In an attempt to synthesise and isolate the heteroleptic complex [Fe((S)-PyBOX<sup>tBu</sup>)((S)-thioPyBOX<sup>tBu</sup>)] [ClO<sub>4</sub>]<sub>2</sub> a 1:1:1 reaction of (S)-PyBOX<sup>tBu</sup> : (S)-thioPyBOX<sup>tBu</sup> : Fe(ClO<sub>4</sub>)<sub>2</sub>•6H<sub>2</sub>O was carried out which gave bright red crystals upon slow diffusion of diethyl ether into the concentrated sample in acetone. A suitable crystal was analysed by XRD which gave the structure, **S-11**, shown in Figure 4.24.

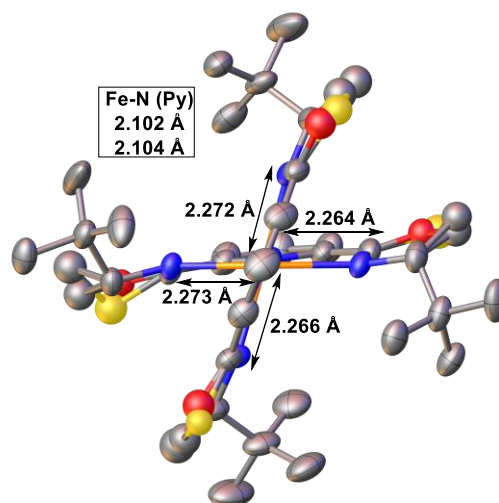


**Figure 4.24.** XRD structure obtained of **S-11**. Hydrogen atoms, counter-ions and solvents are omitted for clarity. Thermal ellipsoids are at the 50% probability level.

This structure solution obtained for **S-11** is a disordered solid solution of PyBOX<sup>tBu</sup> and thioPyBOX<sup>tBu</sup> homochiral complexes. This was particularly notable from the four -C-O/S-CH<sub>2</sub>- bond angles prior to modelling the structure over the two homochiral complexes. The -C-O/S-CH<sub>2</sub>- angles were 93.7(5) °, 97.3(6) °, 100.3(7) ° and 103.9(7) ° which falls in between that expected for oxazoline and thiazoline rings. Upon modelling the structure solution obtained across both **S-7** and **S-8** structures, these angles were resolved as best as possible for the separate thiazoline and oxazoline rings. These angles along with other selected XRD data are tabulated below in Table 4.5.

Complex	<b>S-11</b>	<b>S-7</b>	<b>S-8</b>
<b>Fe-N<sub>Py</sub> (Å)</b>	2.104(5) 2.102(5)	2.056(9) 2.073(9)	2.104(5), 2.112(5)
<b>Fe-N<sub>ox.thiox.</sub> (Å)</b>	2.273(5)- 2.264(5)	2.264(11)- 2.292(10)	2.262(5)- 2.272(5)
$\theta$ (°)	58.671	57.164	61.859
$\phi$ (°)	174.5(19)	178.1(4)	175.12(19)
$\varphi_{\text{ox./thiox.}}$ (°)	148.7(19) 148.5(19)	150.1(3) 148.5(4)	148.63(18) 148.28(18)
<b>-C-O/S-CH<sub>2</sub>- (°)</b>	96.9(6)-105.1(7), 84.2(15)-99.5(4)	89.5(6), 89.9(7), 89.1(6), 88.8(6)	105.5(4), 104.2(5), 105.2(5), 103.8(5)

**Table 4.5.** Selected bond lengths and angles from the XRD structure of **S-11**. Data for **S-7** and **S-8** are shown for comparison.

Most of the data for **S-11**, specifically the Fe-N<sub>Py</sub> bond lengths, the dihedral angle, the *trans* N<sub>Py</sub>-Fe-N<sub>Py</sub> angle and the clamp angles, resembles the data obtained for **S-8**. In comparison, **S-7** has a greater JT-distortion about the dihedral angle and a *trans* N<sub>Py</sub>-Fe-N<sub>Py</sub> angle closer to the ideal 180°. This suggests the structure solution contains more **S-8** character than **S-7**. The structure has been modelled with an O:S ratio of 2.92:1.08 which reflects the greater contribution of **S-8**.

The solution state character of **S-11** can be understood from its paramagnetic <sup>1</sup>H NMR shown in Figure 4.25.

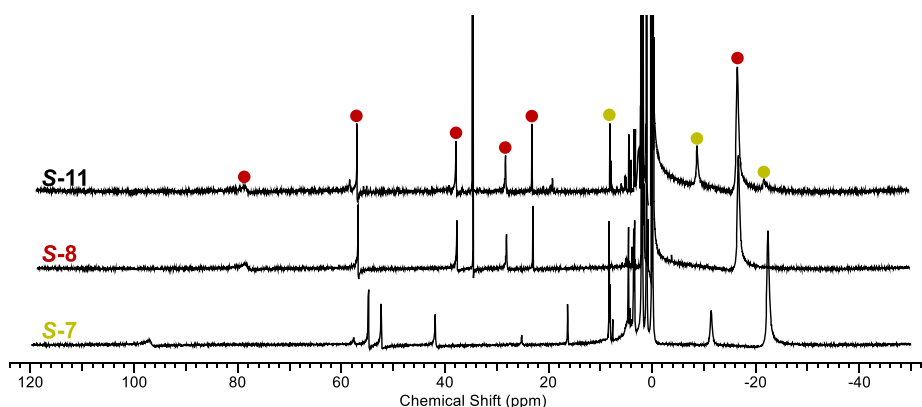


**Figure 4.25. Paramagnetic <sup>1</sup>H NMR of S-11. Spectra of S-7 and S-8 are also shown for comparison. Yellow dots indicate peaks belonging to [Fe(thioPyBOX<sup>tBu</sup>)<sub>2</sub>]<sup>2+</sup>, S-7 and red dots indicate [Fe(PyBOX<sup>tBu</sup>)<sub>2</sub>]<sup>2+</sup>, S-8. [CD<sub>3</sub>CN, 300 MHz].**

Most notable from the spectra shown in Figure 4.25 is that the spectrum of **S-11** is almost identical to that of **S-8**. Which shows that a heteroleptic mixed-ligand complex of **S-11** does not exist in solution, but rather **S-8** is the dominant species present. This shows a strong degree of **S-8** character in **S-11** compared to **S-7** in solution, which agrees with the data observed in the solid state. The lower stability of **S-7** is highlighted in these spectra as instead of observing complex peaks corresponding to **S-7**, the thioPyBOX<sup>tBu</sup> is present as uncoordinated ligand. This is the same ligand dissociation in solution that was observed for **S-7** (Section 3.2.1.7.3).

The magnetic susceptibility data for **S-11** in the solid and solution phases are plotted together in Figure 4.26 below. As expected, both sets of data agree with each other and show a completely HS structure at all temperatures in both phases.

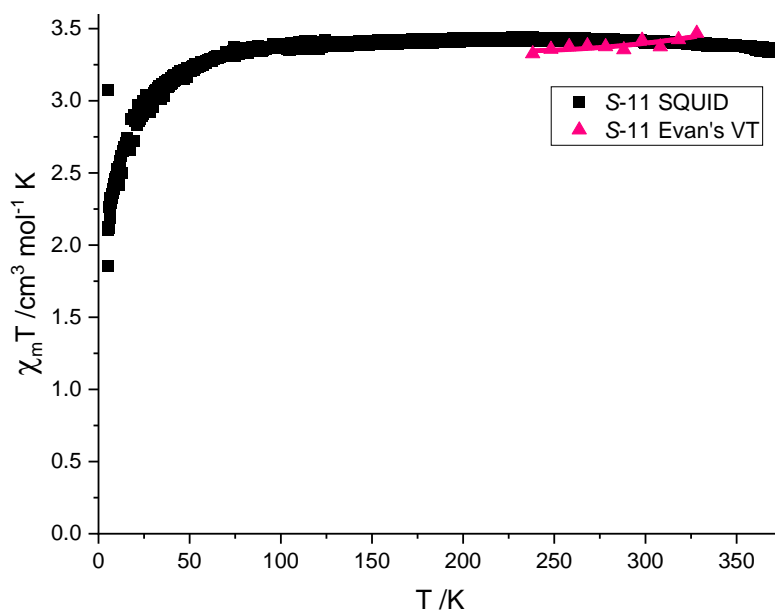


**Figure 4.26. Variable temperature magnetic susceptibility data for S-11 in the solid state using the SQUID (black line) and in the solution state using the VT Evan's method (pink line).**

#### 4.2.4 Heteroleptic iron(II) (thio)PyBOX complexes incorporating 2,6-bis(2-benzimidazolyl)pyridine (bzimpy)

Bzimpy has been widely employed as a fluorescence sensor,<sup>343</sup> chemosensor,<sup>344</sup> a receptor for urea recognition,<sup>345</sup> and as a DNA/protein binder for cytotoxic activity.<sup>346-348</sup> Its diversity of applications comes from its ability to partake in host-guest chemistry owing to its internal cavity, being a thermodynamically stable molecule with a simple route to synthesis from commercially available starting materials, and having a simple  $C_2$ -symmetric structure.<sup>343, 344</sup>

The ligand family has also been studied with regards to its iron complexes for SCO activity.<sup>349</sup> For example, the homoleptic complex  $[\text{Fe}(\text{bzimpy})_2][\text{ClO}_4]_2 \cdot 0.25\text{H}_2\text{O}$  is dominantly LS at 200 K but then shows an increasing magnetic susceptibility above 220 K, which continues even above room temperature to give a  $T_{1/2} = 403$  K with a hysteresis of  $\Delta T = 12$  K.<sup>350</sup> This work was followed up with different salts and varying number of molecules of water of crystallisation of  $[\text{Fe}(\text{bzimpy})_2][\text{X}]_2 \cdot n\text{H}_2\text{O}$ , which showed that when  $\text{X} = \text{SO}_4^-$  or  $\text{BPh}_4^-$  and  $n = 4$ , SCO was observed. Whereas when  $n = 0$  or  $2$  for the tetraphenylborate salt, the complex was only in the HS state. Furthermore, the differences in the abruptness of the STs was highlighted, which showed that the perchlorate and sulfate salts underwent much more gradual and incomplete STs compared to that observed in the tetraphenylborate salt.<sup>351</sup>

What makes bzimpy a particularly good candidate for SCO complexes is its highly conjugated aromatic system, which results in a high degree of cooperativity across the solid state system due to the  $\pi$ - $\pi$  stacking feature of the aromatic rings between different SCO sites.<sup>352</sup> This cooperativity contributes strongly in achieving abrupt STs with thermal hysteresis (Section 1.4.6),<sup>296</sup> as was demonstrated by Boča *et al.* with  $[\text{Fe}(\text{bzimpy})_2][\text{BPh}_4]_2 \cdot 4\text{H}_2\text{O}$ .<sup>351, 352</sup> These findings have inspired the use of the bzimpy ligand in this work.

A series of heteroleptic complexes were synthesised and isolated herein. These were structurally characterised and their SCO behaviour was studied in the solid and solution states. All complexes are perchlorate salts and the chirality of the relevant PyBOX and thioPyBOX ligands is not regarded. The complexes discussed in this part of the heteroleptic SCO complexes study are  $[\text{Fe}((R)\text{-PyBOX}^{\text{Ph}})(\text{bzimpy})][\text{ClO}_4]_2$ , **12**, its thioPyBOX equivalent;  $[\text{Fe}((R)\text{-thioPyBOX}^{\text{Ph}})(\text{bzimpy})][\text{ClO}_4]_2$ , **13**; the *isopropyl* analogue,  $[\text{Fe}((S)\text{-PyBOX}^{\text{iPr}})(\text{bzimpy})][\text{ClO}_4]_2$ , **14**, and its thioPyBOX counterpart;  $[\text{Fe}((S)\text{-thioPyBOX}^{\text{iPr}})(\text{bzimpy})][\text{ClO}_4]_2$ , **15**. Owing to time constraints the *tert*butyl-substituted analogues of these complexes were not studied. The structures of the complexes **12-15** are shown in Figure 4.27.

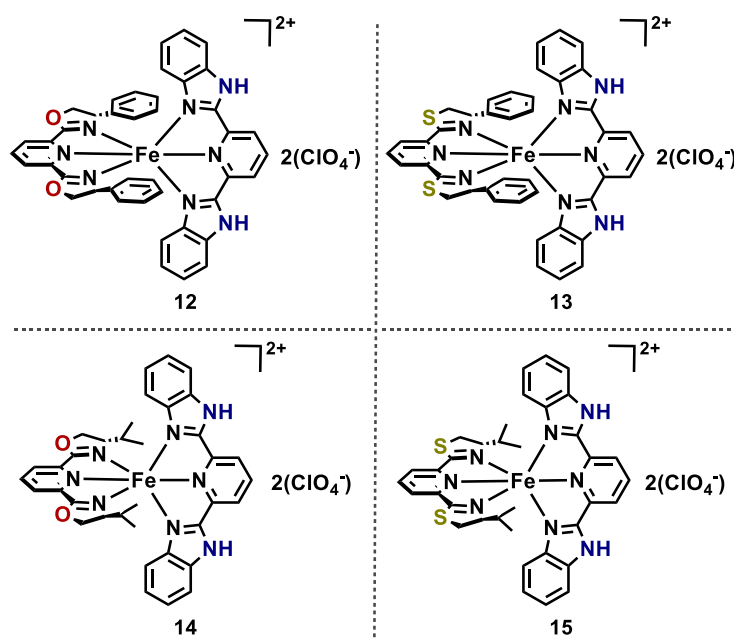


**Figure 4.27.** Structures of the complexes;  $[\text{Fe}((R)\text{-PyBOX}^{\text{Ph}})(\text{bzimpy})][\text{ClO}_4]_2$ , **12**;  $[\text{Fe}((R)\text{-thioPyBOX}^{\text{Ph}})(\text{bzimpy})][\text{ClO}_4]_2$ , **13**;  $[\text{Fe}((S)\text{-PyBOX}^{\text{iPr}})(\text{bzimpy})][\text{ClO}_4]_2$ , **14** and  $[\text{Fe}((S)\text{-thioPyBOX}^{\text{iPr}})(\text{bzimpy})][\text{ClO}_4]_2$ , **15**.



#### 4.2.4.1 Iron(II) (thio)PyBOX<sup>Ph</sup> complexes with bzimpy

##### 4.2.4.1.1 Structural characterisation of [Fe(PyBOX<sup>Ph</sup>)(bzimpy)][ClO<sub>4</sub>]<sub>2</sub> (**12**) and [Fe(thioPyBOX<sup>Ph</sup>)(bzimpy)][ClO<sub>4</sub>]<sub>2</sub> (**13**).

Single crystals of complexes **12** and **13** were grown by slow diffusion of diethyl ether into a concentrated solution of the complexes. These afforded dark purple/violet crystals that were suitable for XRD analysis. The structure solution obtained of **12** and **13** are shown in Figure 4.28 and selected XRD data for these is shown below in Table 4.6.

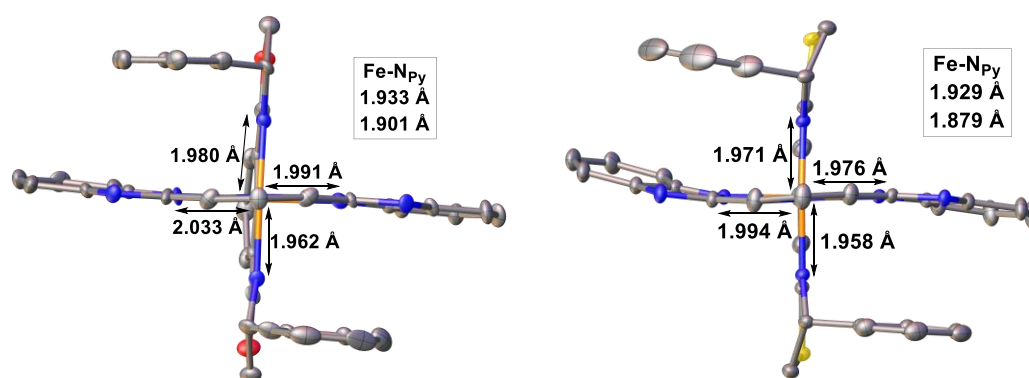
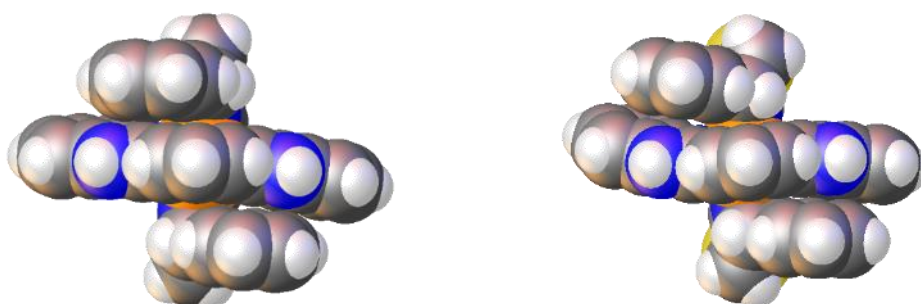


Figure 4.28. XRD structure of [Fe(*R*-PyBOX<sup>Ph</sup>)(bzimpy)][ClO<sub>4</sub>]<sub>2</sub>, **12** and [Fe(*R*-thioPyBOX<sup>Ph</sup>)(bzimpy)][ClO<sub>4</sub>]<sub>2</sub>, **13**. Counter-ions and hydrogen atoms are omitted for clarity. Thermal ellipsoids are at the 50% probability level.

Complex	<b>12</b>	<b>13</b>
Fe-N <sub>Py</sub> (Å)	1.933(7) 1.900(8)	1.929(6) 1.879(6)
Fe-N <sub>ox/thiox.</sub> (Å)	1.979(7) 1.963(7)	1.958(5) 1.971(5)
Fe-N <sub>bzimpy</sub> (Å)	1.992(8) 2.033(7)	1.976(6) 1.994(6)
$\theta$ (°)	88.801	91.291
$\phi$ (°)	177.9(4)	179.8(2)
$\varphi_{\text{ox/thiox.}}$ (°)	159.5(3)	159.2(2)
$\varphi_{\text{bzimpy}}$ (°)	159.5(3)	159.3(2)

Table 4.6. Selected bond lengths and angles for the XRD structures obtained of **12** and **13**.

The XRD structure solutions obtained of **12** and **13** show very similar bond lengths and angles to each other. The noticeable difference is along the  $N_{Py}-Fe-N_{Py}$  bonds angle which is  $2^\circ$  smaller in **12** than in **13**. This is evident in the XRD structure images which shows a slight bending of the pyridine ring of the PyBOX<sup>Ph</sup> ligand out of the axial plane, which is not the case in thioPyBOX<sup>Ph</sup> in **13**. Furthermore, a greater degree of bending of the bzimpy ligand is observed in **13**, which results in a larger deviation of the bzimpy ligand from planarity. This is confirmed by the angle between the centroids of the phenyl rings, which is  $6.025^\circ$  in **12** but is  $14.992^\circ$  in **13**. This can be understood from the space-filling models of **12** and **13** (Figure 4.29).



**Figure 4.29.** Space-filling XRD models of **12** (left) and **13** (right).

The space-filling models shows that the phenyl rings of thioPyBOX in **13** are more bent out of plane due to the steric bulk of the thiazoline rings. This more oblique positioning results in the slanting of the bzimpy ligand, in order to maintain the offset  $\pi-\pi$  interaction.

The crystal packing structures of **12** and **13** are shown in Figure 4.30 -Figure 4.31.

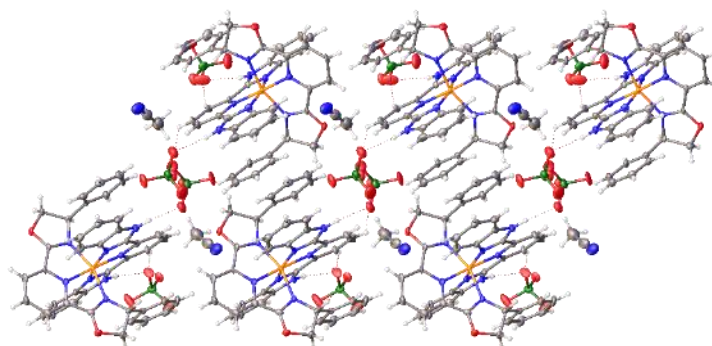


**Figure 4.30.** XRD packing structure of **12** shown along the *a*-axis.

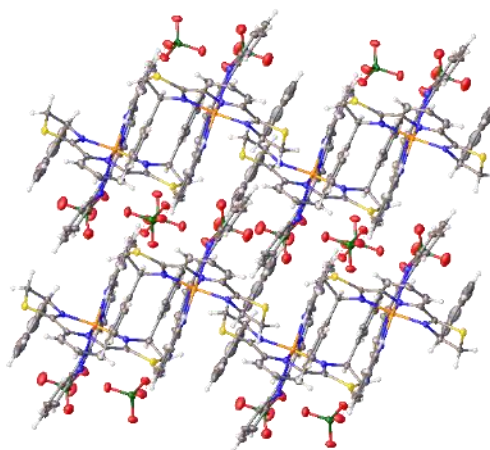


**Figure 4.31. XRD packing structure of **13** shown along the *b*-axis.**

Both crystal packing structures of **12** and **13** show an extensive offset  $\pi$ - $\pi$  stacking system between the benzimidazole rings of the bzimpy ligands and the phenyl substituent of the (thio-)PyBOX<sup>Ph</sup> ligand. This interaction is less compact in **12** than in **13**, which can be understood by the added solvent moiety in the packing structure. This is evidenced by the distances between the centroids of the phenyl rings; **13** has an average distance of 4.3 Å for the intramolecular  $\pi$ - $\pi$  contacts and 4.9 Å for the intermolecular contacts, whereas **12** shows the equivalent distances as 4.7 Å and 5.4 Å respectively. Though these values are reasonable for a typical offset  $\pi$ - $\pi$  interaction ( $> 3.8$  Å<sup>353</sup>), neither are as compact as was observed in the complex [Fe(bzimpy)<sub>2</sub>][ClO<sub>4</sub>]<sub>2</sub>•0.25H<sub>2</sub>O, in which the perfect intermolecular  $\pi$ - $\pi$  stacking between the benzimidazole rings was found to be as short 3.6 Å and no longer than 3.99 Å.<sup>352</sup>

While the  $\pi$ - $\pi$  interactions position the molecules uniformly across the crystal packing structure, the perchlorate anions quite notably sit evenly spaced apart on the periphery of each benzimidazole. This is because each ClO<sub>4</sub><sup>-</sup> ion forms a hydrogen bond with each of the N-H bonds of the bzimpy ligand, which can be seen in Figure 4.32 and Figure 4.33.

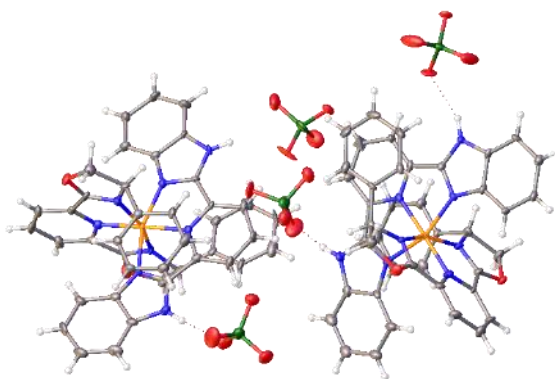


**Figure 4.32. XRD packing of 12 displaying hydrogen bond interactions with the perchlorate ion. Solvent omitted for clarity.**

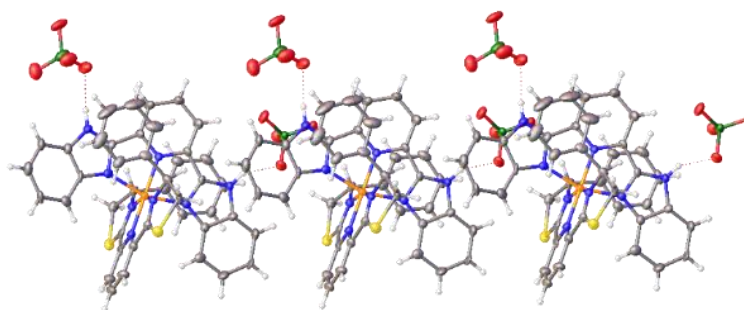


**Figure 4.33. XRD packing of 13 displaying hydrogen bond interactions with the perchlorate ion.**

The hydrogen bonds in **13** are particularly strong with N-H... $\text{OCIO}_3$  distances between 1.96 and 2.05 Å, which is significantly shorter than the sum of the Van der Waals radii of a H and O atom.<sup>325</sup> The two N-H...O bond angles in each molecule are 173.2 ° and 146.0 ° which also evidences hydrogen bonding, with the angle closest to 180 ° being a stronger bond.<sup>354</sup> The hydrogen bonds in **12** are slightly weaker than in **13** with N-H... $\text{OCIO}_3$  distances between 2.03 and 2.12 Å and bond angles of 168.8 ° and 156.7 °. The acetonitrile solvent in **12** is not involved in any hydrogen bonding.

The presence of these highly directional hydrogen bonds strongly influences the crystal packing. This, coupled with the intermolecular and intramolecular  $\pi$ - $\pi$  interactions, suggests a high degree of cooperativity across this crystal packing structure which could lead to a more abrupt ST in the solid state. The stronger network of hydrogen bonds in **13** and the more compact  $\pi$ - $\pi$  interactions suggest the cooperativity of **13** may be stronger than in **12**, however the electronic differences between PyBOX and thioPyBOX are significant enough (discussed in Chapter 3) to offset this.

Considering the solution state, the paramagnetic  $^1\text{H}$  NMR spectra can be studied (Figure 4.34)

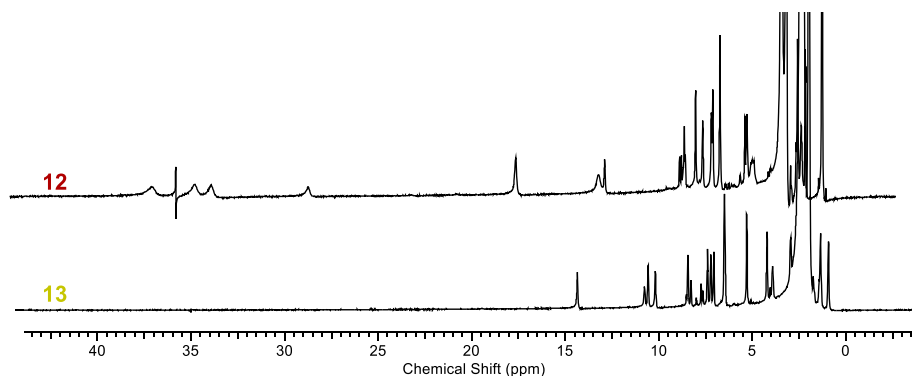


**Figure 4.34. Paramagnetic  $^1\text{H}$  NMR of **12** (top) and **13** (bottom). [ $\text{CD}_3\text{CN}$ , 300 MHz].**

The paramagnetic  $^1\text{H}$  NMR spectrum of **12** shows more paramagnetic character than is observed in **13**, with broad peaks at high chemical shifts (above 25 ppm) indicating some paramagnetic iron(II) centres in the samples. While there are still a number of diamagnetic peaks (below 15 ppm), it seems some spin transition may be occurring around the NMR operating temperature of 298 K. This is unlike the spectrum of **13** which shows no peaks above 15 ppm, with the majority of the sample displaying LS behaviour at this temperature. From this it can be expected that the ST of **12** will occur at a lower  $T_{1/2}$  than **13** in the solution state. It is also clear that by comparison of the paramagnetic  $^1\text{H}$  NMR spectra of the possible homoleptic iron-PyBOX and iron-thioPyBOX counterparts (Sections 3.1.4.3 and 3.2.1.7) that neither spectrum shows significant contamination from these homoleptic counterparts. Since the paramagnetic  $^1\text{H}$  NMR spectrum of  $[\text{Fe}(\text{bzimpy})_2]^{2+}$  has not been previously published in the literature,  $[\text{Fe}(\text{bzimpy})_2][\text{ClO}_4]_2$  was synthesised and the paramagnetic  $^1\text{H}$  NMR was recorded of dissolved crystals of this complex (Figure 4.35). Distinctive peaks from this spectrum such as  $\delta$  39.1, 37.5, 20.4 and 17.7 ppm which are not observed in the spectra of **12** or **13** (Figure 4.34) confirm this homoleptic species does not form from these heteroleptic complexes in solution.

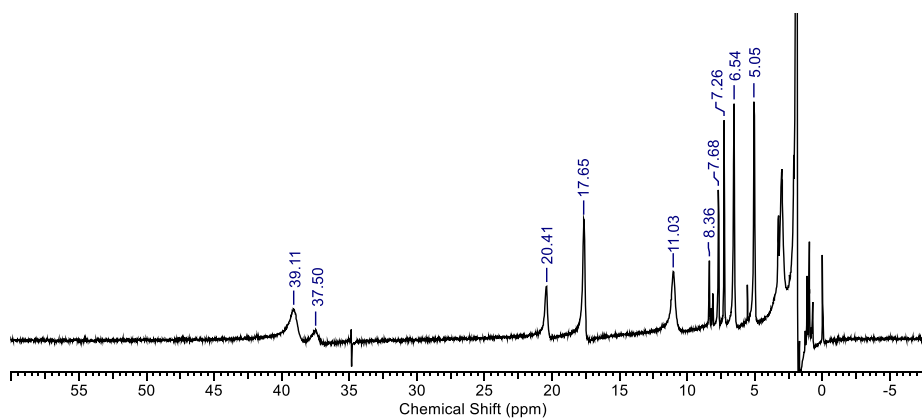


**Figure 4.35. Paramagnetic  $^1\text{H}$  NMR spectrum of  $[\text{Fe}(\text{bzimpy})_2]^{2+}$ . [ $\text{CD}_3\text{CN}$ , 300 MHz].**

The samples are both pure upon crystallisation which is confirmed by the pXRD analysis obtained (Figure 4.36).

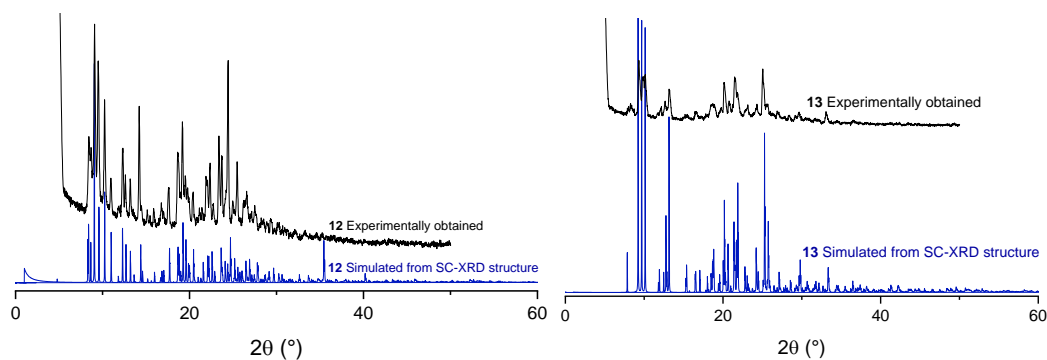


**Figure 4.36. pXRD pattern of 12 (left) and 13 (right). Experimentally obtained patterns are in black and simulated pXRD from the single crystal XRD solutions are in blue.**

#### 4.2.4.1.2 SCO studies of complexes 12 and 13

These pure samples were then subjected to variable temperature magnetic susceptibility studies in the solid and solution states. The SQUID data obtained for **12** and **13** is shown in Figure 4.37.

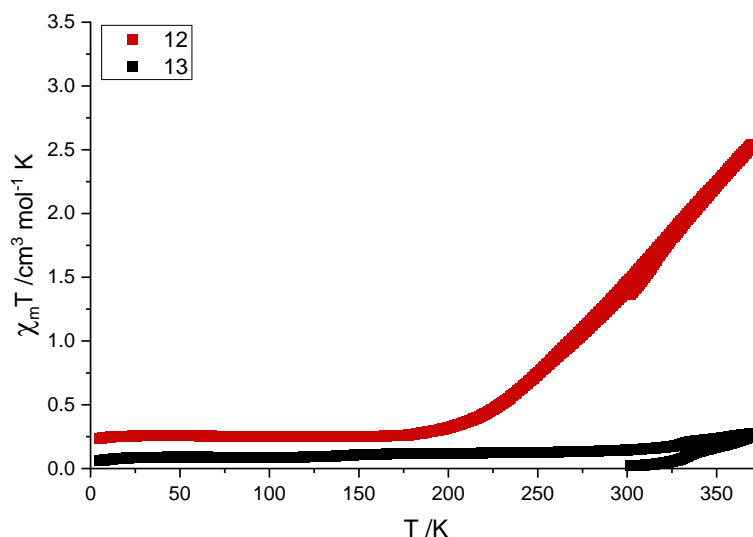


**Figure 4.37. Variable temperature solid state magnetic susceptibility of **12** (red) and **13** (black) using the SQUID magnetometer. N.B. 300→370K is the first heating cycle, upon which initial solvent is lost.**

The SQUID data for **12** and **13** shows very distinct SCO behaviour between these isostructures. The PyBOX<sup>Ph</sup> analogue **12** shows a clear ST occurring from > 200 K which does not reach completion at 370 K with just over 70% of the sample in the HS state. The  $T_{1/2}$  for this ST is 322 K (calculated from  $X_m T = 1.75 \text{ cm}^3 \text{ mol}^{-1} \text{ K}$ ). The curve for **13** however shows a completely LS sample with a small fraction of the sample undergoing the start of a ST around 350 K. This SCO behaviour for **13** is akin to that observed for **RS-9** and **RS-5**. This SQUID data reaffirms how changing the PyBOX<sup>Ph</sup> ligand for thioPyBOX<sup>Ph</sup> can significantly affect the SCO behaviour, demonstrating the power of ligand design.

The solution state data obtained for **12** and **13** using VT Evans method mirrors the data observed in the solid state (Figure 4.38).

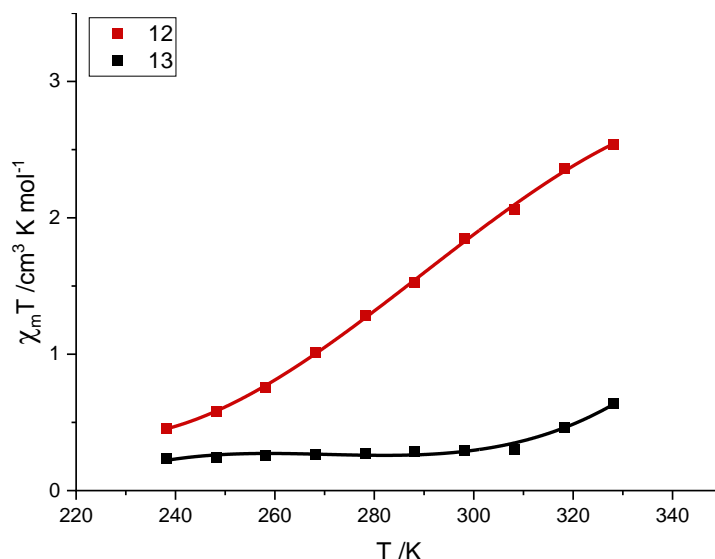


**Figure 4.38. Variable temperature solution state magnetic susceptibility of 12 (red) and 13 (black) using the Evan's  $^1\text{H}$  NMR method.**

In the solution state a clear ST is observed for **12**, which has 10-15% of the sample in the HS state at the lower temperatures, as was observed in in the SQUID. Complex **13** has half the fraction of samples in the HS state at 240 K than **12** had, which was also the case in the solid state measurements. This difference in the fractions of sample in the HS state at low T between **12** and **13** is indicative of the more LS-like nature of **13** compared to **12**. The pure homoleptic  $[\text{Fe}(\text{bzimpy})_2]^{2+}$  complex has been reported to observe a small ST in the solution state from  $X_m T = 0.37 \text{ cm}^3 \text{ mol}^{-1} \text{ K}$  at 230 K to  $1.88 \text{ cm}^3 \text{ mol}^{-1} \text{ K}$  at 330 K.<sup>355</sup> While the presence of this complex has not been identified in the paramagnetic  $^1\text{H}$  NMR spectra, it does support the observed STs of **12** and **13**.

The curves in Figure 4.38 shows a clear ST for **12** whilst **13** is mostly LS with the onset of a ST above 310 K. The  $T_{1/2}$  values and thermodynamic parameters are tabulated below (Table 4.7). N.B the  $T_{1/2}$  for **13** is a prediction based on the extrapolation of the curve in the Figure.

Complex	$T_{1/2} / \text{K}$	$\Delta H / \text{kJ mol}^{-1}$	$\Delta S / \text{J K}^{-1} \text{mol}^{-1}$
<b>12</b>	294	21.2	72
<b>13</b>	382*	-	-

**Table 4.7.  $T_{1/2}$  and thermodynamic parameters obtained for 12. \*The  $T_{1/2}$  for 13 was calculated based on the extrapolation of its solution state magnetic susceptibility data.**



The  $T_{1/2}$  for **12** is lower in solution than was observed in the solid state (322 K), and is very close to the ideal ambient temperature. The study does however highlight the impact that changing oxygen for sulfur can have on the SCO behaviour.

#### 4.2.4.2 Iron(II) (thio)PyBOX<sup>iPr</sup> complexes with bzimpy

##### 4.2.4.2.1 Structural characterisation of [Fe(PyBOX<sup>iPr</sup>)(bzimpy)][ClO<sub>4</sub>]<sub>2</sub> and its thioPyBOX<sup>iPr</sup> analogue

The *isopropyl* congeners of **12** and **13** were also investigated, giving the complexes [Fe(bzimpy)((*S*)-PyBOX<sup>iPr</sup>)] [ClO<sub>4</sub>]<sub>2</sub>, **14** and [Fe(bzimpy)((*S*)-thioPyBOX<sup>iPr</sup>)] [ClO<sub>4</sub>]<sub>2</sub>, **15**. Their XRD structures are shown in Figure 4.39 and selected data is tabulated Table 4.8.

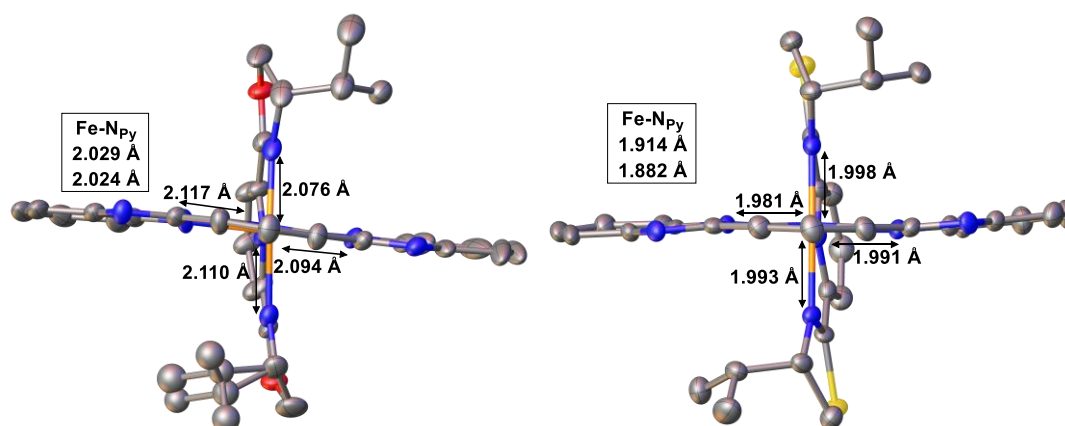


Figure 4.39. XRD structures of **14** (left) and **15** (right). Counter-ions, hydrogen atoms and solvents are omitted for clarity. Thermal ellipsoids are at the 50% probability level.

Complex	<b>14</b>	<b>15</b>
<b>Fe-N<sub>Py</sub> (Å)</b>	2.024(5) 2.029(5)	1.914(5) 1.882(6)
<b>Fe-N<sub>ox/thiox.</sub> (Å)</b>	2.076(7) 2.110(6)	1.998(6) 1.993(6)
<b>Fe-N<sub>bzimpy</sub> (Å)</b>	2.094(6) 2.117(6)	1.991(6) 1.981(5)
$\theta$ (°)	97.208	86.410
$\phi$ (°)	176.1(2)	175.1(2)
$\varphi_{ox/thiox.}$ (°)	153.5(2)	160.0(2)
$\varphi_{bzimpy}$ (°)	152.7(2)	160.2(2)

Table 4.8. Selected bond lengths and angles from the XRD structure solutions of **14** and **15**.

The XRD structure solution of **14** shows bond lengths very close to the LS-HS border of 2.0 Å, indicative of SCO occurring. The bond lengths in **14** are slightly longer than observed in the XRD data of **15** which is more indicative of the LS state.

Angular geometric distortions are apparent in both structures but in different places; complex **14** shows a clear slanting of the bzimpy ligand, which is more discrete in the thioPyBOX<sup>iPr</sup> analogue **15**. In contrast, **15** shows a higher degree of twisting of the thioPyBOX ligand out of the plane of the thioPyBOX ligand compared to the PyBOX isostructure. This is only a 1 ° difference in terms of the *trans* N<sub>Py</sub>-Fe-N<sub>Py</sub> angle, φ, which shows clear deviation from 180 ° in both complexes. What is notably distinct between the XRD data obtained for **14** and **15**, is the clamp angle, φ, which is significantly smaller in **14** than in **15**. This can be compared to the plot of the clamp angle against the average Fe-N bond length studied by Kershaw Cook *et al.* in the series of [Fe(1-bpp)<sub>2</sub>]<sup>2+</sup> complexes (Figure 4.40).<sup>329</sup>

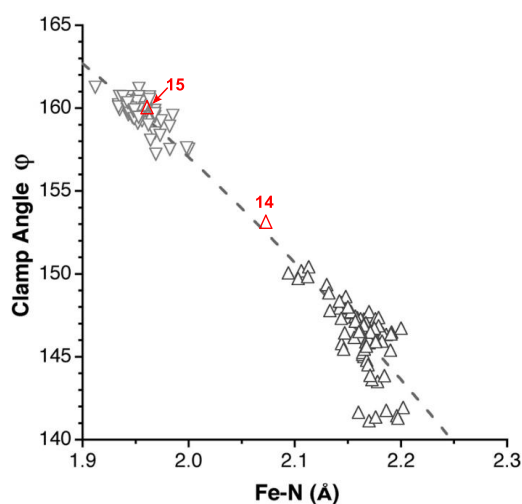


**Figure 4.40.** The clamp angle, φ compared to the average Fe-N bond distance in [Fe(1-bpp)<sub>2</sub>]<sup>2+</sup> complexes reported by Kershaw Cook *et al.*<sup>329</sup> Upwards triangles are HS complexes and downwards triangles are LS. Red triangles are approximately where complexes **14** and **15** (labelled) fit on the graph. Figure adapted from publication.

Considering where complexes **14** and **15** fall in the trend observed for the [Fe(1-bpp)<sub>2</sub>]<sup>2+</sup> series, it is clear there is quite a distinction between these isostructures. Whilst **15** perfectly fits the data observed for LS complexes, **14** fits neither the HS or LS ‘groups’ but rather falls in-between the two. This suggests that **14** will most likely display some ST between the two spin states, which agrees with the observed XRD structure which shows an intermediate structure solution. The pXRD analysis of complexes **14** and **15** are shown below in Figure 4.41.

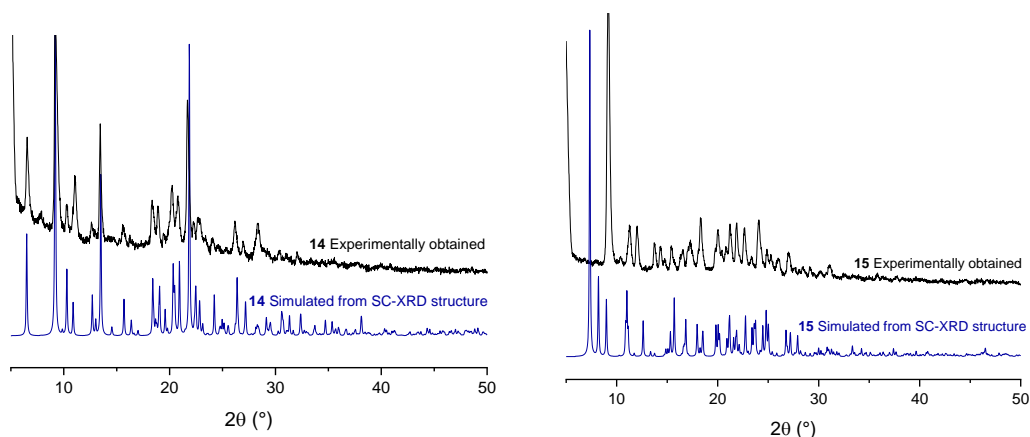


**Figure 4.41. pXRD analysis of complex 14 (left) and 15 (right). Experimentally obtained is in black and pXRD pattern simulated from the single crystal XRD structure is in blue.**

The pXRD patterns obtained shows the bulk sample of **14** to be phase pure and the **15** is very close to that simulated by the XRD structure. The few peaks differences in the latter case could be due to the solvation of the crystal structure.

The paramagnetic  $^1\text{H}$  NMR spectra of **14** and **15** are shown in Figure 4.42.

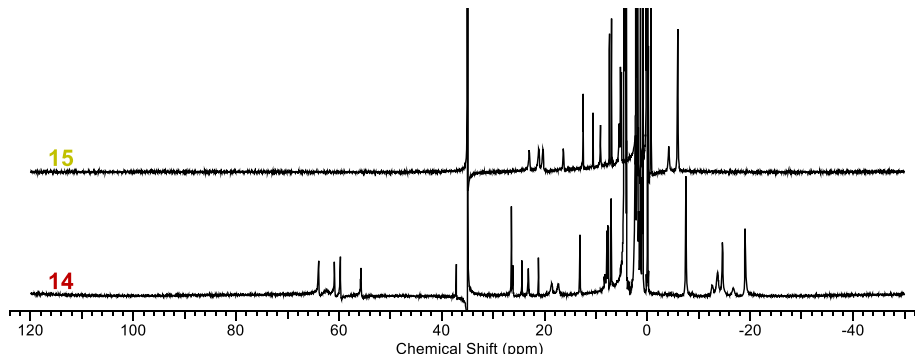


**Figure 4.42. Paramagnetic  $^1\text{H}$  NMR spectra of 14 (bottom) and 15 (top).  $[\text{CD}_3\text{CN}, 300 \text{ MHz}]$ .**

The NMR spectrum for **15** shows no contamination from any homoleptic species with 15 peaks corresponding to the different proton environments of thioPyBOX<sup>iPr</sup> and bzimpy. This spectrum shows an almost diamagnetic sample. On the other hand, the spectrum for **14** shows peaks corresponding to the heteroleptic complex in addition to the homoleptic complex  $[\text{Fe}(\text{PyBOX}^{\text{iPr}})_2]^{2+}$  (**S-2**) which is highlighted in Figure 4.43.

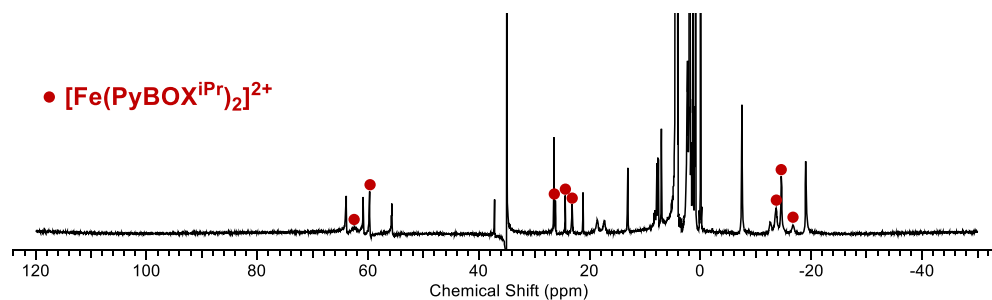


**Figure 4.43. Paramagnetic  $^1\text{H}$  NMR spectrum of **14** with red dots highlighting the peaks corresponding to  $[\text{Fe}(\text{PyBOX}^{\text{iPr}})_2]^{2+}$ . [ $\text{CD}_3\text{CN}$ , 300 MHz].**

Analysis of the peaks corresponding to **S-2** shows an approximately 1:1 ratio of this species to complex **14**. This redistribution of the  $\text{PyBOX}^{\text{iPr}}$  ligand to form its homoleptic-homochiral iron(II) complex, was first evidenced in the racemisation of the heterochiral analogue **RS-2**<sup>210</sup> and has been observed throughout the studies of heteroleptic complexes containing this ligand since. This suggests a thermodynamic preference and stability for heteroleptic solutions containing the ligand to equilibrate back to this species.

#### 4.2.4.2.2 SCO studies of complexes **14** and **15**

The solid and solution state SCO studies of **14** and **15** are shown below in Figure 4.44 and Figure 4.45 respectively.

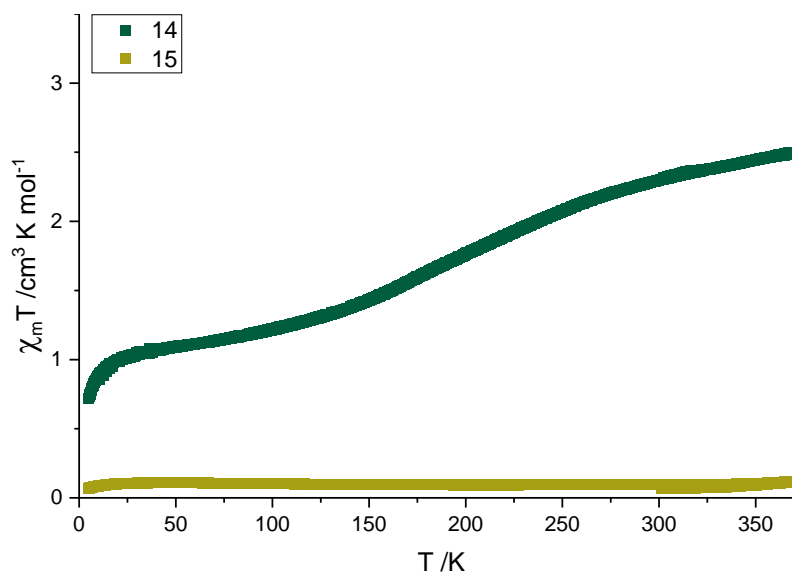


**Figure 4.44. Variable temperature solid state magnetic susceptibility of **14** (green) and **15** (gold) using the SQUID magnetometer.**

The variable temperature SQUID measurements for **14** and **15** show distinct spin state behaviours. Complex **15** is fully low spin at all temperatures from 5 – 300 K which is fitting with the XRD bond lengths and angles observed. However **14** shows that from 5- 120 K around 30% of the sample is already in the HS state. This is followed by a very gradual ST centred around 175 K (which is where  $X_mT = 1.75 \text{ cm}^3 \text{ k mol}^{-1}$ ), before reaching 300 K where approximately 70% of the sample is then in the HS state with the ST being incomplete. Considering the XRD structure of **14** was collected at 120 K this agrees well with the mixed LS-HS nature of the structure solution.

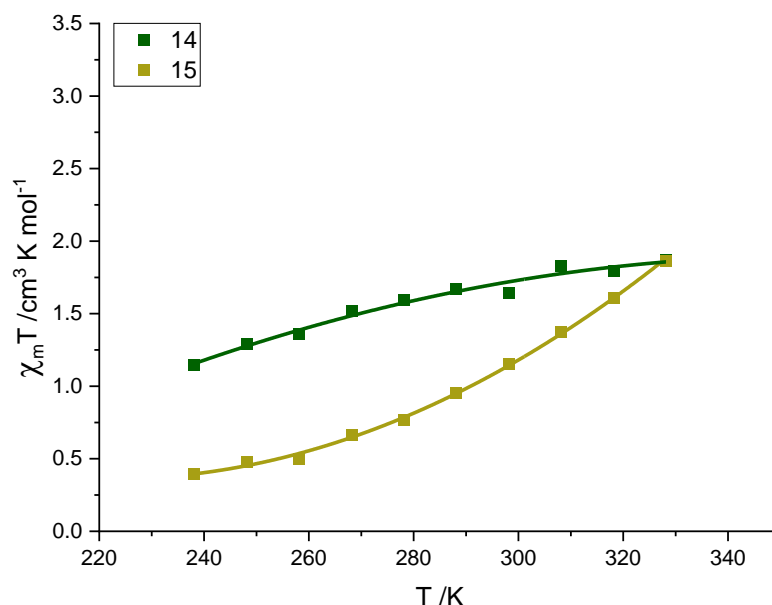


**Figure 4.45. Variable temperature solution phase magnetic susceptibility of 14 (green) and 15 (gold) using the Evan's  $^1\text{H}$  NMR method.**

As the paramagnetic  $^1\text{H}$  NMR of **14** showed, this sample equilibrates in solution to give the homoleptic complex, **S-2** which is HS across all temperatures (Section 3.1.4.2). The mixture potentially also gives  $[\text{Fe}(\text{bzimpy})_2]^{2+}$  which has been reported to undergo a thermally-induced ST with a  $T_{1/2} = 330 \text{ K}$ .<sup>355, 356</sup> These contributions to the observed solution-state SCO behaviour convolutes the SCO activity of the pure heteroleptic complex, **14**. The reduced gradient of the curve for **14** in Figure 4.45 is due to the superimposed fraction of **S-2** in the sample. Complex **15** now shows a ST occurring in Figure 4.45 which is unlike the solid state observation which showed the sample to be LS independent of temperature. The ST for **15** is more abrupt relative to the curve observed for the mixed sample of **14** in the solution phase. **15** displays just over 40% of the sample undergoing a LS→HS conversion by 328 K. The  $T_{1/2}$  values calculated and thermodynamic parameters are outlined in Table 4.9.

Complex	$T_{1/2} / \text{K}$	$\Delta H / \text{kJ mol}^{-1}$	$\Delta S / \text{J K}^{-1} \text{mol}^{-1}$
14	305	6.0	20
15	331	15.9	48

**Table 4.9.**  $T_{1/2}$  values and thermodynamic parameters calculated for 14 and 15.

As per previous heteroleptic samples that were observed to form their homoleptic counterparts in solution, the calculated  $T_{1/2}$  value and thermodynamic parameters are not accurate representations of the pure complex 14. Complex 15 shows reasonable parameters in Table 4.9, which is representative of the pure heteroleptic complex, evidenced by the stability of the complex in solution (Figure 4.42).

#### 4.2.5 Iron(II) (thio)PyBOX complexes incorporating 2,6-bis(pyrazol-1-yl)pyridine (1-bpp)

A series of heteroleptic iron(II) PyBOX<sup>R</sup> and thioPyBOX<sup>R</sup> complexes incorporating the bpp ligand are discussed below. Four complexes synthesised herein; [Fe((*R*)-PyBOX<sup>Ph</sup>)(1-bpp)][ClO<sub>4</sub>]<sub>2</sub>, **16** and its thioPyBOX analogue, [Fe((*R*)-thioPyBOX<sup>Ph</sup>)(1-bpp)][ClO<sub>4</sub>]<sub>2</sub>, **17**. Additionally, the *isopropyl*- derivatives [Fe((*S*)-PyBOX<sup>iPr</sup>)(1-bpp)][ClO<sub>4</sub>]<sub>2</sub>, **18** and [Fe((*S*)-thioPyBOX<sup>iPr</sup>)(1-bpp)][ClO<sub>4</sub>]<sub>2</sub>, **19** were also studied (Figure 4.46).

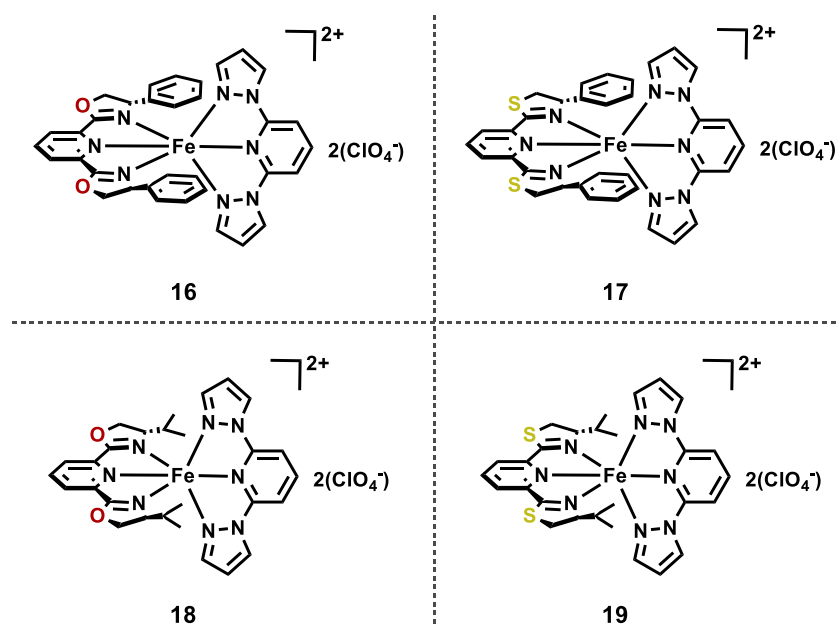


**Figure 4.46.** Structures of complexes 16-19.

#### 4.2.5.1 Structural characterisation

While there is much more scope in the research of heteroleptic iron complexes for SCO studies containing the PyBOX<sup>R</sup> and thioPyBOX<sup>R</sup> ligands than has been demonstrated thus far, a small amount of preliminary work was carried out on complexes **16-19**. An XRD structure solution of complex **17** has been obtained (Figure 4.47 and Table 4.10), whereas, single crystals for the rest of the complexes in this series (**16**, **18** and **19**) are pending to confirm their structures. It should be noted that XRD data was obtained of complex **16** which confirms the structure, however due to poor data, this dataset is pending recollection on new crystals. Elemental analysis of **16** also confirms the purity of the bulk sample (Section 4.4).

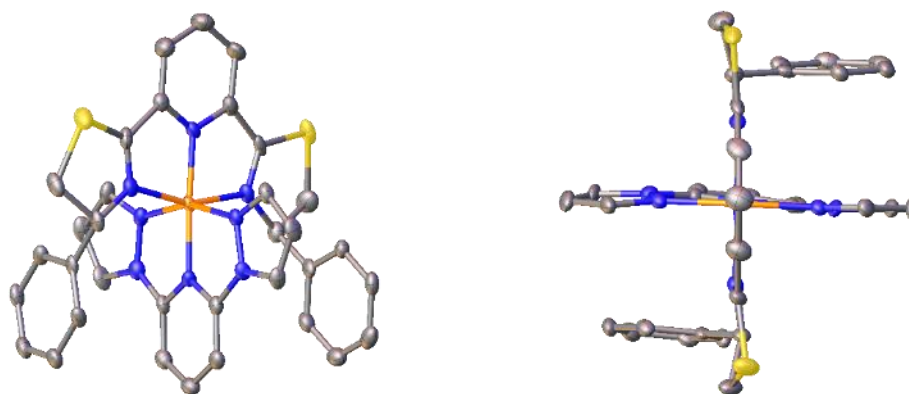


**Figure 4.47.** XRD structure of [Fe(1-bpp)((*R*)-thioPyBOX<sup>Ph</sup>)] [ClO<sub>4</sub>]<sub>2</sub>, **17**. Hydrogen atoms, counter-ions and solvents are omitted for clarity. Thermal ellipsoids are at the 50% probability level.

Complex	<b>17</b>
Fe-N <sub>Py</sub> (Å)	1.878(4), 1.904(4)
Fe-N <sub>thiox.</sub> (Å)	1.995(4), 1.975(4)
Fe-N <sub>bpp</sub> (Å)	1.956(4), 1.958(4)
$\theta$ (°)	86.683
$\phi$ (°)	176.77(18)
$\varphi$ <sub>thio.</sub> (°)	160.01(18)
$\varphi$ <sub>bpp</sub> (°)	159.78(17)

**Table 4.10.** Selected bond lengths and angles of the XRD structure of **17**.

In the XRD structure of **17**, a slight bending is visible in the 1-bpp ligand, whereas the thioPyBOX<sup>Ph</sup> does not show any significant distortion. As with the bzimpy

analogue, **13**, the phenyl rings do not experience a steric clash within its quadrant. Furthermore, the bond lengths and angles show a dominantly LS structure at the XRD temperature of 130 K, however these values indicate a likeliness to undergo a ST at higher temperatures.

The solution state purity however was able to be studied using paramagnetic  $^1\text{H}$  NMR. The spectra of **16** and **17** are shown in Figure 4.48 and the spectra of **18** and **19** are shown in Figure 4.49.

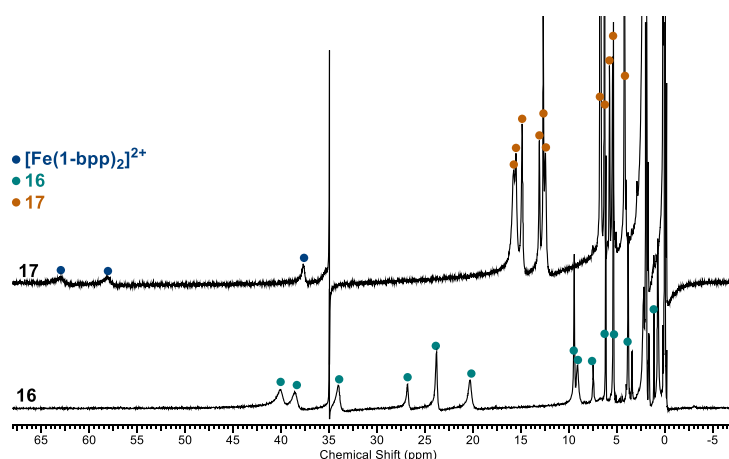


**Figure 4.48. Paramagnetic  $^1\text{H}$  NMRs of **16** (bottom) and **17** (top) with peaks identified as green circles (**16**), orange circles (**17**) and blue circles ( $[\text{Fe}(\text{1-bpp})_2]^{2+}$ ). [300 MHz,  $\text{CD}_3\text{CN}$ ].**

The paramagnetic  $^1\text{H}$  NMR spectrum of complex **16** shows 13 distinct peaks. Of these peaks, there are 6 peaks in the region  $\delta$  40.07-20.29 ppm which are clearly paramagnetically shifted, this can be attributed to a coordinated 1-bpp ligand. A further 7 potential peaks are evident more upfield in the range of  $\delta$  9.45-0.71 ppm which are somewhat broad and show no splitting patterns, indicative of also being coordinated to a paramagnetic centre. This is most likely the PyBOX<sup>Ph</sup> ligand. The 1:1 ratio of these two ligands also suggests a heteroleptic complex. Close analysis of the chemical shifts of individual peaks confirms there are no homoleptic complexes in this solution.

The spectrum of complex **17** is much less paramagnetically shifted than **16** which is indicative of an overall more LS sample. As with **16**, there are also two distinct groups of peaks, pertaining to each ligand in a heteroleptic complex. This is confirmed by the 1:1 integrations. A very small fraction of the homoleptic complex  $[\text{Fe}(\text{1-bpp})_2]^{2+}$  (~10%) is now evident in this sample (highlighted in the figure). Interestingly, the structure of complex **17** and its purity is supported by the HRMS data which shows a dicationic peak at  $m/z = 334$  (Section 4.4), this fits exactly with the heteroleptic



complex **17**. This also shows the high stability of **17**, which agrees with its LS behaviour (*vide infra*).

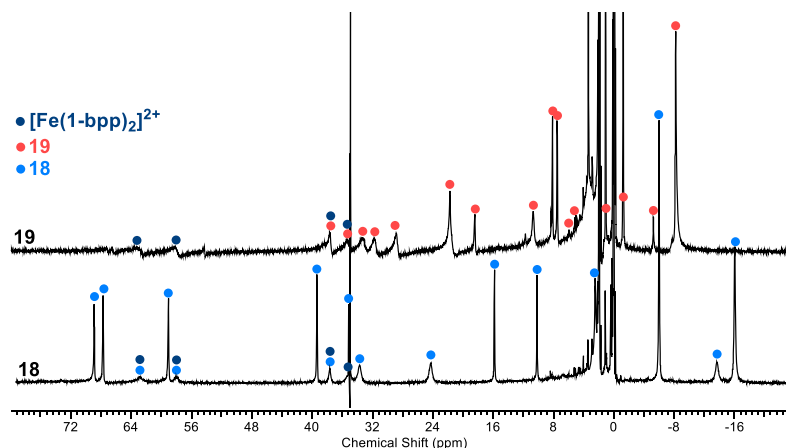


**Figure 4.49. Paramagnetic  $^1\text{H}$  NMRs of **18** (bottom) and **19** (top) with peaks identified as **18** (blue circles), **19** (red circles) or possibly  $[\text{Fe}(1\text{-bpp})_2]^{2+}$  (navy circles). [300 MHz,  $\text{CD}_3\text{CN}$ ].**

Considering now the paramagnetic  $^1\text{H}$  NMR spectra of the isopropyl- analogues, **18** and **19** in Figure 4.49 above, complex **18** shows 16 distinct proton environments which are significantly more paramagnetically shifted compared to the phenyl complexes. There are 10 very sharp peaks and 6 less intense but broader peaks, while the broader peaks at  $\delta$  62.8, 58.0, 37.6 and 35.1 ppm could evidence the homoleptic 1-bpp complex in solution, however it is possible that these peaks may not appear distinctly different from the coordinated bpp ligand in complex **18**. Furthermore, none of the peaks in the spectrum corresponds to that of the homoleptic complex **S-2**. The total integration of the sharp peaks is fitting with one PyBOX<sup>iPr</sup> ligand (23H), while the totally integration of the shorter and broader peaks agrees with a bpp ligand (9H). This suggests the heteroleptic complex **18** could be stable in solution.

The paramagnetic  $^1\text{H}$  NMR spectrum of thioPyBOX<sup>iPr</sup> analogue, **19** also shows 16 distinct peaks, none of which fit with the homoleptic complex **S-6**. As observed with complex **18**, the same peaks which could potentially correspond to  $[\text{Fe}(1\text{-bpp})_2]^{2+}$  are visible as a small group of peaks, downfield at  $\delta$  67.4, 63.2, 58.2 and 54.4 ppm. These peaks have integrations corresponding to a third of that obtained for the peaks at 38.1, 35.5, 33.4, 31.8 and 28.9 ppm, which suggests confirms an additional homoleptic complex in the solution. The majority of the peaks in the spectrum of **19** are more diamagnetically shifted compared to **18** which is as expected for thioPyBOX analogues.

#### 4.2.5.2 SCO studies

The spin state behaviour was studied in the solid and solution states which is shown below in Figure 4.50 and Figure 4.51 respectively.

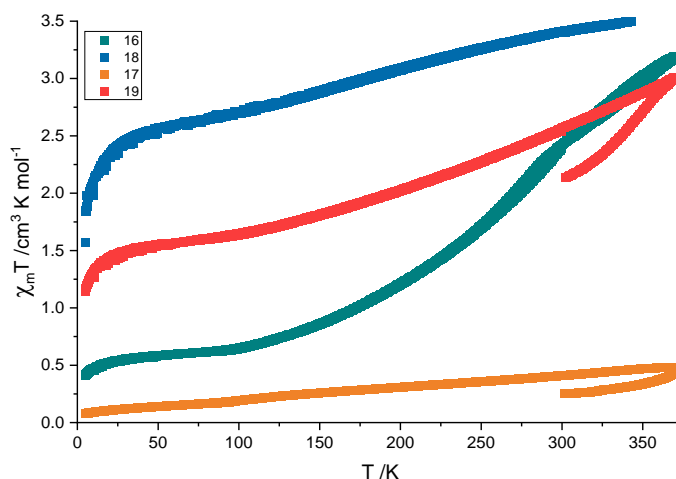


**Figure 4.50. Magnetic susceptibility data in the solid state at various temperatures, obtained using the SQUID magnetometer of 16 (green), 17 (orange), 18 (blue) and 19 (red). N.B. 300→370K is the first heating cycle, upon which initial solvent is lost.**

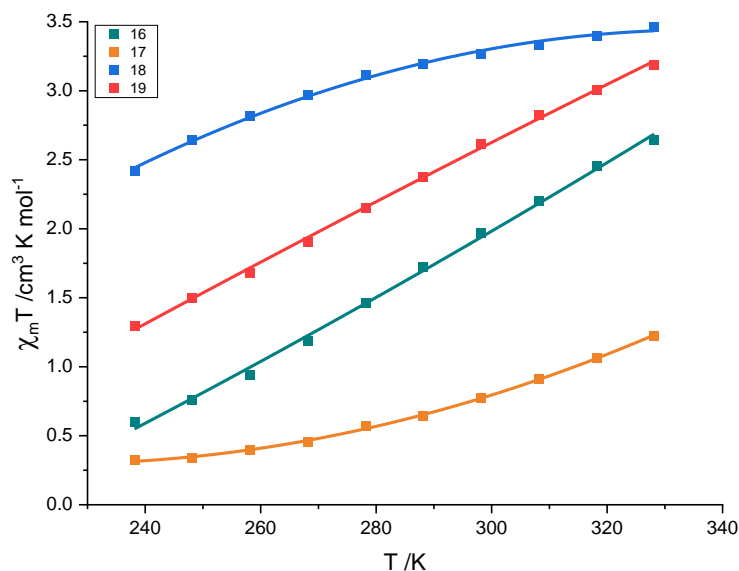


**Figure 4.51. Magnetic susceptibility data in the solution state at various temperatures, obtained using the Evan's <sup>1</sup>H NMR method of 16 (green), 17 (orange), 18 (blue) and 19 (red).**

The magnetic susceptibilities in both the solid and solution states resemble one another. In the solution state data, all four data sets of complexes **16-19** show mostly

a straight-line type spin transitions which is indicative of multiple species in solution. A pure sample undergoing a ST would show an 's'-type curve, which is not evident in any of the complexes in the solution state data. The SQUID data shows mostly straight lines with some gradient in the cases of **17**, **18** and **19**, whereas complex **16** shows a ST occurring from  $0.5 \text{ cm}^3 \text{ mol}^{-1} \text{ K}$  at 5 K to  $3.2 \text{ cm}^3 \text{ mol}^{-1} \text{ K}$  at 370 K, giving a  $T_{1/2}$  around 250 K. Since the  $^1\text{H}$  NMR spectrum of **16** showed a pure sample, this ST can be attributed to solely the heteroleptic complex **16**. The solution state measurements for **16** displays a  $X_m T \approx 0.6 \text{ cm}^3 \text{ mol}^{-1} \text{ K}$  at 240 and  $X_m T \approx 2.6 \text{ cm}^3 \text{ mol}^{-1} \text{ K}$  at 330 K, which gives a  $T_{1/2}$  of 290 K.

Accounting for the ~10%  $[\text{Fe}(1\text{-bpp})_2]^{2+}$  evident in the  $^1\text{H}$  NMR spectrum of **17**, the  $X_m T$  of pure **17** is still  $0.32 \text{ cm}^3 \text{ mol}^{-1} \text{ K}$  at 240 K and reaches  $1.22 \text{ cm}^3 \text{ mol}^{-1} \text{ K}$  at 330 K. In the solid state **17** is also mostly LS with a very small fraction of HS present, which agrees well with the  $^1\text{H}$  NMR spectrum and solution state data. Extrapolation of the ST curve observed for **17** in the solution state gives an estimated  $T_{1/2}$  to occur just above 350 K.

Complexes **18** and **19** show a higher fraction of sample in the HS state in both the SQUID and Evan's data, even in the lower temperature regions, which is consistent with the data observed for the homoleptic (thio-)PyBOX<sup>IPr</sup> complexes in Sections 3.1.4 and 3.2.1. The complex  $[\text{Fe}(1\text{-bpp})_2][\text{ClO}_4]_2$  has been shown to remain HS at all temperatures <sup>79</sup> thus the data observed here is the combined effect of the homoleptic 1-bpp complex with the magnetic susceptibility behaviour of the homoleptic PyBOX<sup>R</sup> or thioPyBOX<sup>R</sup> complexes.

Complex **18** can be considered as fully HS across the temperature range shown, which agrees with the HS behaviour observed in **S-2** and  $[\text{Fe}(1\text{-bpp})_2]^{2+}$ . While complex **19** has a significant proportion of sample is already HS at 50 K in the SQUID (~40-45%), this increases to 85-90% of the sample in the HS state at 370 K, suggesting around 40% of the sample undergoes a ST. In the solution state, 35-40% of **19** is HS at 240 K and the rest of the sample undergoes spin conversion to the HS state by 330 K, where 90 % of the sample is HS. The fraction of sample in the HS state agrees well with the potential 30-35% of  $[\text{Fe}(1\text{-bpp})_2]^{2+}$  sample evident in the  $^1\text{H}$  NMR spectrum. This data for **18** and **19** in particular is still inconclusive without further analysis of the complexes.

A brief comparison of the solution state magnetic susceptibility data for complexes **16** and **17** with their bzimpy counterparts, **12** and **13** respectively shows very similar curves for their spin transitions. This suggests a very similar extent of cooperativity between the samples. Complexes **18** and **19**, however, show a much greater percentage of HS character in the sample compared to their bzimpy analogues, **14** and **15**, which actually shows solution state curves that resembles that observed for

**12** and **13**. The greater HS contributions of **18** and **19** could be due to a greater degree of JT-type geometric distortion of the heteroleptic complexes, which would be evident by XRD analysis. Alternatively, the greater HS character could be from the averaged VT data of  $[\text{Fe}(\text{1-bbp})_2]^{2+}$  and **S-2** or **S-6** if the solutions of **18** and **19** contain a mixture of these complexes.

The overall data here from the complexes **16-19** agrees well with all conclusions reached thus far. That is, complexes containing the *isopropyl*-substituted PyBOX or thioPyBOX ligand exhibit a higher proportion of sample 'trapped' in the HS state compared to their phenyl- counterparts. The thioPyBOX isostructures of the PyBOX-containing complexes observe more overall LS activity due to the reduced electron-withdrawing effect from the ligand corroborating previous findings.<sup>216, 357</sup>

#### 4.2.6 Iron(II) (thio)PyBOX complexes incorporating 2,2':6',2''-terpyridine (terpy)

Preliminary work was carried out on heteroleptic iron(II) complexes of the  $\text{PyBOX}^{\text{R}}$  ligand coupled with the terpy ligand. Two complexes were synthesised in a 1:1:1 ratio of  $\text{PyBOX}^{\text{R}}:\text{terpy}:\text{Fe}(\text{ClO}_4)_2$  in acetonitrile to give  $[\text{Fe}((R)\text{-PyBOX}^{\text{Ph}})(\text{terpy})][\text{ClO}_4]_2$ , **20** when  $R = \text{Ph}$  and  $[\text{Fe}((S)\text{-PyBOX}^{\text{iPr}})(\text{terpy})][\text{ClO}_4]_2$ , **21** when  $R = \text{iPr}$  (Figure 4.52).

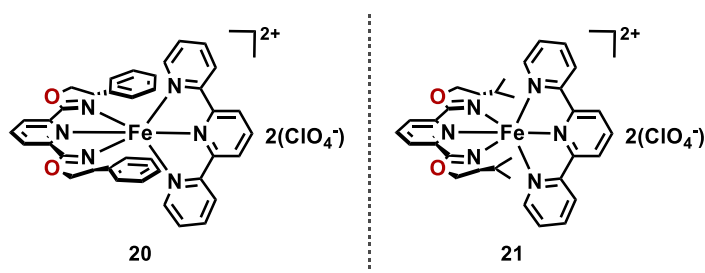
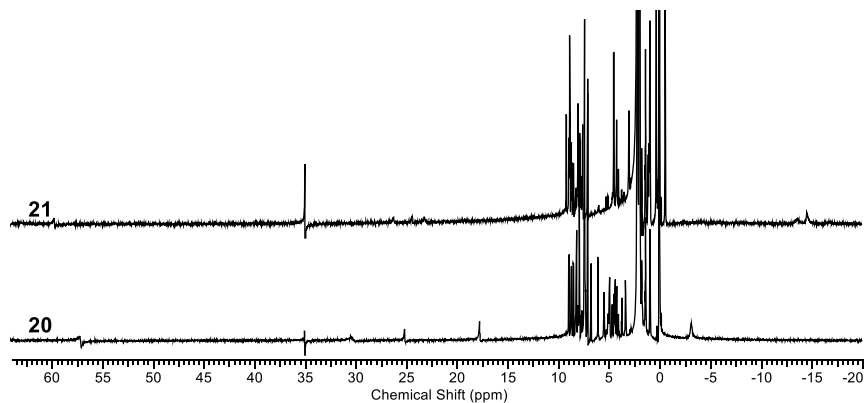


Figure 4.52. Structures of **20** (left) and **21** (right).

Single crystals suitable for single crystal XRD analysis were grown from concentrates of the heteroleptic reaction mixtures, however, both these attempts gave crystals of  $[\text{Fe}(\text{terpy})_2][\text{ClO}_4]_2$  instead which was identified by XRD.

The paramagnetic  $^1\text{H}$  NMR spectra of complexes **20** and **21** which are shown in Figure 4.53 shows dominantly of LS complexes in both cases, as the majority of the peaks fall in the diamagnetic  $^1\text{H}$  NMR region. There a multiple peaks in both spectra

indicative of multiple species in solution. From this it is clear that it is not solely the heteroleptic complexes in the solution samples of **20** and **21**.



**Figure 4.53. Paramagnetic  $^1\text{H}$  NMR spectra of  $[\text{Fe}((R)\text{-PyBOX}^{\text{Ph}})(\text{terpy})]^{2+}$ , **20** (bottom) and  $[\text{Fe}((S)\text{-PyBOX}^{\text{iPr}})(\text{terpy})]^{2+}$ , **21** (top). [300 MHz,  $\text{CD}_3\text{CN}$ ].**

A closer look at the spectrum of complex **20** (Figure 4.54) shows the presence of  $[\text{Fe}(\text{terpy})_2]^{2+}$ , **R-1** and free ligand of both  $\text{PyBOX}^{\text{Ph}}$  and  $\text{terpy}$ .<sup>358</sup> The remainder of the peaks have been assigned as the heteroleptic complex.

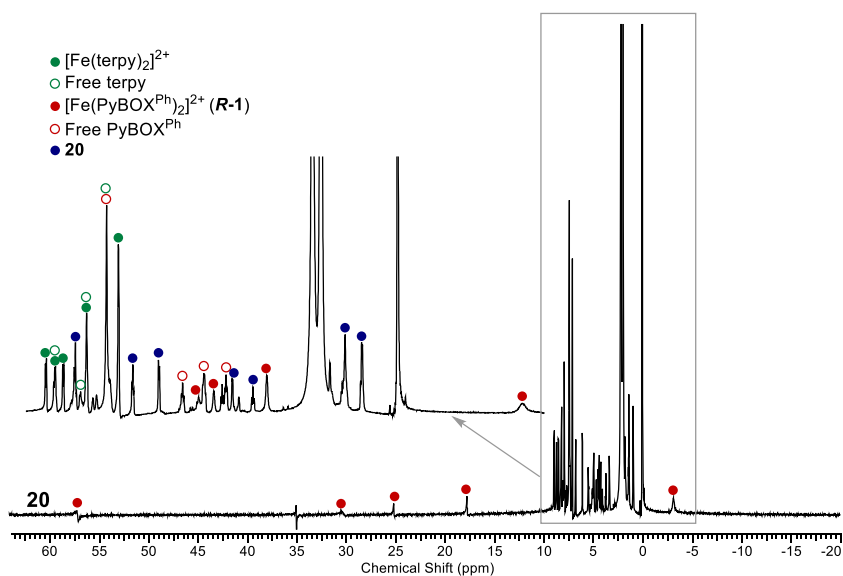


**Figure 4.54. Paramagnetic  $^1\text{H}$  NMR spectrum of complex **20** with expansion of the diamagnetic region. [300 MHz,  $\text{CD}_3\text{CN}$ ].**

This same trend of peaks can be assumed for complex **21** which shows a similar spectrum. In these NMR spectra, a small fraction of the homoleptic complexes  $[\text{Fe}((R)\text{-PyBOX}^{\text{Ph}})_2]^{2+}$  (**R-1**) and  $[\text{Fe}((S)\text{-PyBOX}^{\text{iPr}})_2]^{2+}$  (**S-2**) are evident in the spectra of **20** and **21** respectively. This is consistent with all the heteroleptic complexes discussed thus far containing these ligands in solution. In the the NMR spectrum of **20** there is an approximately 10-15% percentage of **R-1** present, whereas in the spectrum of **21**, the percentage of **S-2** present is around half of this (5-7%). This is understandable from the lower stability of **S-2** compared **R-1** in solution.

The experimentally obtained elemental analysis of these complexes agrees well with the calculated elemental analysis for the solvated complex **20**•H<sub>2</sub>O and unsolvated **21** (Section 4.4). This leaves two possibilities for the bulk sample in the solid state; they either contain mixtures of the homoleptic and heteroleptic complexes or they are the pure heteroleptic complex with negligible contamination from homoleptic counterparts. To understand this better, pXRD analysis was obtained of the bulk sample Figure 4.55.

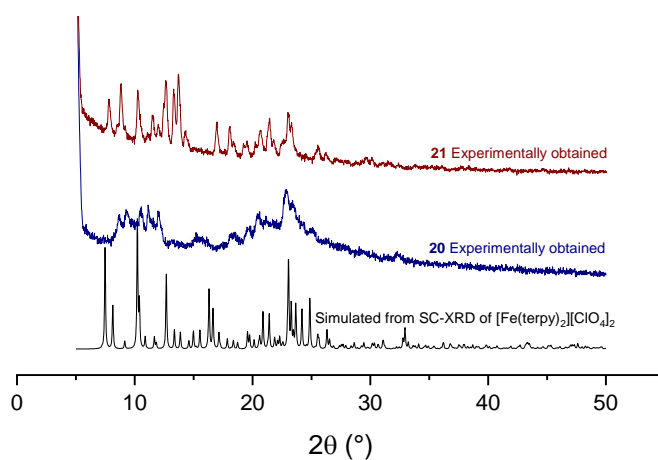


**Figure 4.55. Experimentally obtained pXRD analysis of 20 (navy blue, middle) and 21 (top, dark red), shown with the pXRD pattern simulated from the single crystal XRD structure of  $[\text{Fe}(\text{terpy})_2][\text{ClO}_4]_2$  (bottom, black).**

The pXRD patterns of **20** and **21** shows distinct peaks, which is indicative of phase pure samples, with **21** showing more defined peaks, suggesting the sample is more pure than **20**. Comparing these patterns to that simulated by the single crystal of  $[\text{Fe}(\text{terpy})_2][\text{ClO}_4]_2$  (also shown in Figure 4.55), shows that while some peaks match between the bis-terpy complex, **20** and **21**, the full pXRD pattern does not match it.

This suggests that the bulk samples of complexes **20** and **21** does not contain a significant fraction of  $[\text{Fe}(\text{terpy})_2][\text{ClO}_4]_2$  such that it would influence the pXRD pattern. The bulk sample consisting of the heteroleptic complexes is still plausible from this data.

The variable temperature spin state behaviour of complexes **20** and **21** were studied in both the solid and solution states using the SQUID magnetometer and the Evan's  $^1\text{H}$  method respectively (Figure 4.56).

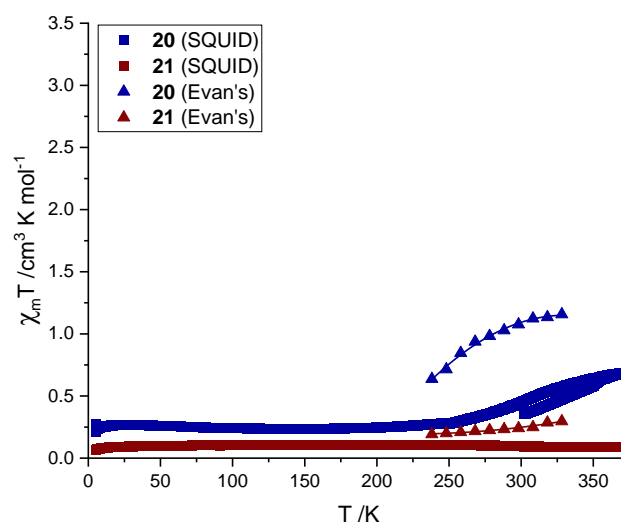


**Figure 4.56. Magnetic susceptibility data of complexes 20 (blue) and 21 (red) in the solid state (squares) and solution state (triangles) at varying temperatures using the SQUID magnetometer at 0.5T for the solid state and using the Evans  $^1\text{H}$  NMR method in (500 MHz,  $\text{CD}_3\text{CN}$ ) for the solution state.**

The magnetic susceptibility data across varying temperatures for complexes **20** and **21**, shown in Figure 4.56, are consistent between the solid and solution states. While complex **20** is LS at all temperatures in the solid state, the solution state data shows a small onset of a ST above 300 K. Considering that **S-2** is high spin independent of temperature and of phase and  $[\text{Fe}(\text{terpy})_2]^{2+}$  complexes are low spin, the Evan's data for **21** should show a curve that is a combination of these two behaviours, i.e. a curve centred around  $1.75 \text{ cm}^3 \text{ mol}^{-1} \text{ K}$ . Since this is not observed it is possible that the complex **21** is purely the heteroleptic complex which is stable, observing mostly LS behaviour. Or a mixture of the two heteroleptic complexes are present but the LS effect of the terpy complex dominates the data obtained.

Complex **20** displays LS magnetic susceptibility in the SQUID up to 250 K and then clearly shows the onset of a ST occurring above this temperature. This is consistent with the ST observed in **R-1** which undergoes a ST centred at 244 K (Section 3.1.4.2) combined with the LS behaviour of  $[\text{Fe}(\text{terpy})_2]^{2+}$ . The transition is more pronounced in the solution state. Since only a small fraction of **R-1** is evident in the paramagnetic  $^1\text{H}$  NMR spectrum of **21**, this data suggests the observed spin state behaviour is a combined effect from the mixed ligand system.

While it would be interesting to study what occurs in the case of a 1:1:1 mixture of thioPyBOX<sup>R</sup> : terpy :  $\text{Fe}(\text{ClO}_4)_2$ , due to time constraints, no further work could be carried out on this series of complexes.

### 4.3 Conclusion

The results from chapter 3 have been further explored herein with a series of heteroleptic complexes. Five new potential complexes, **S-9**, **RS-9**, **S-10**, **RS-10** and **S-11** were discussed, which are mixed iron(II) systems with PyBOX<sup>R</sup> and thioPyBOX<sup>R</sup> ligands, in both their homochiral and heterochiral diastereomers where possible. All the complexes seemed to show a structure 'in between' their homoleptic congeners. A further ten potential complexes have also been discussed of heteroleptic iron(II) complexes containing either the PyBOX<sup>R</sup> or thioPyBOX<sup>R</sup> ligand ( $R = \text{Ph}, \text{iPr}$ ) with other N,N'N''- tridentate pincer ligands including bzimpy (complexes **12**, **13**, **14** and **15**), 1-bpp (complexes **16**, **17**, **18** and **19**) and terpy (complexes **20** and **21**).

Interestingly, the complexes form in a 1:1:1 ratio in the case of the heterochiral complexes but form mixtures with their homoleptic counterparts in the cases of the homochiral complexes **S-9** and **S-11**, which is also potentially the case with **S-10**. The paramagnetic  $^1\text{H}$  NMR spectra of these homochiral complexes also contain peaks corresponding to their homoleptic counterparts.

**S-9** and **RS-9** show distinct spin state behaviours with **RS-9** almost fully LS in the solid state and **S-9** displaying a ST centred at 300 K which is lower than observed in **S-1** and **S-5**. When the crystal packing effects are removed from **RS-9**, leaving the cationic complex in solution, a ST is observed with  $T_{1/2} = 331$  K.

Both **S-10** and **RS-10** show STs in the solid and solution states. From the SQUID data both of these transitions were observed to be quite gradual, with a significant proportion of the sample already in the HS state at low T in **S-10**. **RS-10** shows an incomplete ST, with an initially lower proportion of sample in the HS state. The ST of **RS-10** becomes much more abrupt in the solution state while **S-10** is more gradual.



Both the heterochiral complexes **RS-9** and **RS-10** show structures that are 'in-between' their homoleptic counterparts, which is as anticipated for these series. The low stability of the complexes **S-9**, **S-10** and **S-11** is demonstrated through their thermodynamic preference for their homoleptic analogues, however there is not enough data in this study to confirm or explain this observation.

The XRD structure solutions of **12** compared to **13** showed some clear distinctions with a greater slanting of the bzimpy ligand in **13** compared to **12**, which could be due to the added steric bulk of the sulfur atoms in the thiazoline rings. The SCO studies showed **13** to be almost completely LS in the solid state, with a small onset of a ST above 330K, whilst its PyBOX counterpart **12** displays a clear ST from 200 K, with a  $T_{1/2} = 322$  K. The solid state observations were reinforced by the solution state studies which mirrored these findings. In the solution state the  $T_{1/2}$  of **12** was lowered to 294 K. These results highlight a significant distinction between employing the PyBOX ligand compared to the thioPyBOX ligand.

Geometric differences were also observed between the *isopropyl* complexes **14** and **15**, in which **14** displayed a slanting of the bzimpy ligand but **15** showed a slightly greater degree of bending of the thioPyBOX ligand out of the plane. The variable temperature magnetic susceptibility studies of **14** and **15** showed distinct behaviours, where **14** displayed a ST in the solid state with a  $T_{1/2} = 175$  K whilst **15** was purely LS. However in the solution state, **15** showed SCO activity with  $T_{1/2} = 331$  K, and **14** showed a ST centred at 305 K, giving  $\Delta T = 26$  K.

In the 1-bpp series, XRD structures are yet to be obtained of the complexes **16-19**. From analysis of the paramagnetic  $^1\text{H}$  NMR spectra of these complexes, there does not seem to be a significant degree of contamination of the homoleptic complexes in solution as was observed with the mixed PyBOX<sup>R</sup> and thioPyBOX<sup>R</sup> complexes. Complex **17** showed a ~10% contamination of  $[\text{Fe}(1\text{-bpp})_2]^{2+}$ , while such contamination, if present, is less obvious in **16**, **18** and **19**. In the magnetic susceptibility data, complexes **16** and **19** show some ST, but not with the typical 's'-shaped curve. **17** is mostly LS and **18** is mostly HS across the studied temperature range. The results found in the solution state agrees with that found in the solid state.

The terpy derivatives containing PyBOX<sup>R</sup> ligands, **20** and **21** were both found to give single crystals of the very stable, LS complex  $[\text{Fe}(\text{terpy})_2][\text{ClO}_4]_2$ , which is well-known in the literature.<sup>358</sup> The spin state behaviour in the solid state of **20** and **21** is mostly LS, with complex **20** showing a slight onset of a ST above 250 K, suggesting **20** is less stable than **21** (if pure). These results were overall supported by the solution state magnetic susceptibility data, but the ST towards the higher temperatures in **20** is more pronounced due to loss of crystal packing effects.

These studies have further highlighted the significant differences between the PyBOX and thioPyBOX ligand families, reaffirming the reduced electron-withdrawing nature of thiazoline compared to oxazoline corroborated in previous studies.<sup>216, 357</sup>

#### 4.4 Experimental

The instrument methods and techniques followed are as those outlined in Sections 2.4 and 3.4.

**S-9 [Fe((S)-PyBOX<sup>Ph</sup>)((S)-thioPyBOX<sup>Ph</sup>)] [ClO<sub>4</sub>]<sub>2</sub>.** Addition of solid Fe[ClO<sub>4</sub>]<sub>2</sub>·6H<sub>2</sub>O (82.5 mg, 0.23 mmol, 1 eq.) to a solution of (S)-thioPyBOX<sup>Ph</sup>, **L2** (89.5 mg, 0.22 mmol, 1 eq.) and commercially available (S)-PyBOX<sup>Ph</sup>, (82.0 mg, 0.22 mmol, 1 eq.) in acetonitrile (20 mL) afforded a plum-coloured solution, which was stirred at room temperature until all the solid had dissolved (1hr, 20 °C). The solution was concentrated, and slow diffusion of diethyl ether vapour into the concentrate produced dark purple crystals of the complex suitable for X-ray diffraction. Yield= 167.4 mg (74%). **Paramagnetic <sup>1</sup>H NMR (300 MHz, CD<sub>3</sub>CN).** **Underlined peaks are identified as S-9.** δ 56.99 (4H), 32.67 (2H), 31.36 (2H), 30.31 (2H), 27.40 (1H), 25.06 (2H), 19.37 (1H), 17.70 (4H), 16.44 (2H), 15.49 (2H), 14.07 (2H), 13.93 (2H), 12.03 (1H), 10.70 (4H), 9.33 (2H), 7.88 (4H), 7.72 (4H), 6.67 (3H), 6.31-6.12 (9H), 5.12 (4H), 4.93 (4H), 4.75 (4H), 4.65 (4H), 4.29 (4H), 3.15 (4H). **HRMS [ES]<sup>+</sup> [L+H]<sup>+</sup>** Predicted: 370.1511 Found: 370.1566 **[M-2(ClO<sub>4</sub>)]<sup>2+</sup>** Predicted: 429.0695 Found: 429.0706. **Elemental analysis calculated of S-9·0.5MeCN (%)** C 53.96, H 3.81, N 8.70; found C 53.67, H 3.69, N 9.01.

**RS-9 [Fe((S)-PyBOX<sup>Ph</sup>)((R)-thioPyBOX<sup>Ph</sup>)] [ClO<sub>4</sub>]<sub>2</sub>.** Addition of solid Fe[ClO<sub>4</sub>]<sub>2</sub>·6H<sub>2</sub>O (85.3 mg, 0.24 mmol, 1.1 eq.) to a solution of (R)-thioPyBOX<sup>Ph</sup>, **L1** (83.8 mg, 0.21 mmol, 1 eq.) and commercially available (S)-PyBOX<sup>Ph</sup>, (83.3 mg, 0.23 mmol, 1.1 eq.) in acetonitrile (15 mL) afforded a violet solution, which was stirred at room temperature until all the solid had dissolved (1hr, 20 °C). The solution was concentrated, and slow diffusion of diethyl ether vapour into the concentrate produced violet crystals of the complex suitable for X-ray diffraction. Yield= 171.0 mg (79%). **Paramagnetic <sup>1</sup>H NMR (300 MHz, CD<sub>3</sub>CN)** 15.27 (2H), 14.93 (2H), 11.54 (2H), 10.11 (2H), 7.38 (4H), 7.29 (4H), 7.02 (4H), 6.44 (4H), 6.01 (2H), 5.60 (2H), 5.48 (2H), 5.18 (2H), 5.07 (2H), 4.70 (2H), 4.28 (4H), 3.82 (2H), 3.60 (2H), 3.34 (2H), 1.10 (2H). **HRMS [ES]<sup>+</sup> [M-2(ClO<sub>4</sub>)]<sup>2+</sup>** Predicted: 413.0924 Found: 413.0939. **Elemental analysis calculated (%)** C 53.87, H 3.73, N 8.19; found C 51.76, H 3.69, N 8.42.

**S-10**  $[\text{Fe}((\text{S})\text{-PyBOX}^{\text{iPr}})((\text{S})\text{-thioPyBOX}^{\text{iPr}})][\text{ClO}_4]_2$ . Addition of solid  $\text{Fe}[\text{ClO}_4]_2 \cdot 6\text{H}_2\text{O}$  (21.5 mg, 0.06 mmol, 1 eq.) to a solution of (S)-thioPyBOX<sup>iPr</sup>, **L4** (21.5 mg, 0.06 mmol, 1 eq.) and commercially available (S)-PyBOX<sup>iPr</sup>, (19.4 mg, 0.06 mmol, 1 eq.) in acetonitrile (15 mL) afforded a bright red solution which darkened over time. This was stirred at room temperature until all the solid had dissolved (2hrs, 20 °C). The solution was concentrated, and slow diffusion of diethyl ether vapour into the concentrate produced dark red-pink crystals of the complex suitable for X-ray diffraction. Yield= 37.0 mg (69%). **Paramagnetic <sup>1</sup>H NMR (300 MHz, CD<sub>3</sub>CN). Underlined peaks are identified as S-10.**  $\delta$  75.33 (4H), 62.39 (4H), 59.55 (8H), 57.95 (4H), 49.84 (2H), 41.77 (4H), 28.74 (8H), 28.18 (4H), 27.14 (8H), 26.24 (4H), 24.45 (8H), 23.15 (4H), 20.71 (4H), 16.68 (2H), 16.08 (2H), -2.29 (12H), -4.98 (12H), -10.41 (12H), -13.64 (12H), -14.54 (12H), -15.88 (12H), -17.67 (12H), -27.90 (12H). **HRMS [ES]<sup>+</sup> [L+H]<sup>+</sup>** Predicted: 302.1824 Found: 302.1865. **Elemental analysis calculated (%)** C 45.90, H 5.21, N 9.45; found C 45.55, H 5.12, N 9.08.

**RS-10**  $[\text{Fe}((\text{R})\text{-PyBOX}^{\text{iPr}})((\text{S})\text{-thioPyBOX}^{\text{iPr}})][\text{ClO}_4]_2$ . Addition of solid  $\text{Fe}[\text{ClO}_4]_2 \cdot 6\text{H}_2\text{O}$  (22 mg, 0.06 mmol, 1.5 eq.) to a solution of (S)-thioPyBOX<sup>iPr</sup>, **L4** (15.7 mg, 0.04 mmol, 1 eq.) and (R)-PyBOX<sup>iPr\*</sup>, (18.2 mg, 0.06 mmol, 1.5 eq.) in acetonitrile (20 mL) afforded a dark red solution. This was stirred at room temperature until all the solid had dissolved (1hr, 20 °C). The solution was concentrated, and slow diffusion of diethyl ether vapour into the concentrate produced dark red-pink crystals of the complex suitable for X-ray diffraction. Yield= 25.0 mg (70%). **Paramagnetic <sup>1</sup>H NMR (300 MHz, CD<sub>3</sub>CN)**  $\delta$  61.00 (4H), 26.98 (1H), 20.77 (1H), 16.56 (4H), 15.61 (4H), 14.44 (4H), 9.23 (2H), 6.02 (2H), -1.58 (6H), -1.88 (6H), -4.82 (6H), -10.00 (6H). **HRMS [ES]<sup>+</sup> [L+H]<sup>+</sup>** Predicted: 302.1824 Found: 302.1864. **Elemental analysis calculated (%)** C 45.90, H 5.21, N 9.45; found C 45.68, H 5.01, N 9.09.

**S-11**  $[\text{Fe}((\text{S})\text{-PyBOX}^{\text{tBu}})((\text{S})\text{-thioPyBOX}^{\text{tBu}})][\text{ClO}_4]_2$ . Addition of solid  $\text{Fe}[\text{ClO}_4]_2 \cdot 6\text{H}_2\text{O}$  (23.9 mg, 0.07 mmol, 1 eq.) to a solution of (S)-thioPyBOX<sup>tBu</sup>, **L6** (23.7 mg, 0.07 mmol, 1 eq.) and commercially available (S)-PyBOX<sup>tBu</sup>, (21.8 mg, 0.07 mmol, 1 eq.) in acetonitrile (10 mL) afforded a bright orange solution which reddened over time. This was stirred at room temperature until all the solid had dissolved (1hr, 20 °C). The solvent was removed and the remaining solid was dissolved in acetone (2-3 mL), and slow diffusion of diethyl ether vapour into the concentrate produced dark red crystals of the complex suitable for X-ray diffraction. Yield= 17.0 mg (26%). **Paramagnetic <sup>1</sup>H NMR (300 MHz, CD<sub>3</sub>CN). Underlined peaks are identified as S-8.**  $\delta$  79.41 (2H), 57.45 (4H), 38.34 (4H), 28.48 (4H), 23.25 (2H), 8.16 (2H), -8.86 (12H), -16.63 (36H), -21.86 (6H). **HRMS [ES]<sup>+</sup> [L+H]<sup>+</sup>** Predicted: 330.2137 Found: 330.2192. **[L'+H]<sup>+</sup>** Predicted: 362.1680 Found: 362.1736. **Elemental analysis calculated (%)** C 48.26, H 5.76, N 8.89; found C 49.4, H 6.22, N 8.44.

**12 [Fe((*R*)-PyBOX<sup>Ph</sup>)(bzimpy)][ClO<sub>4</sub>]<sub>2</sub>.** Addition of solid Fe[ClO<sub>4</sub>]<sub>2</sub>·6H<sub>2</sub>O (110.1 mg, 0.30 mmol, 1.1 eq.) to a solution of commercially available (*R*)-PyBOX<sup>Ph</sup>, 102.8 mg, 0.28 mmol, 1 eq.) and 2,6-bis(benzimidazolyl)pyridine (bzimpy) (84.3 mg, 0.27 mmol, 1 eq.) in acetonitrile (20 mL) afforded a dark pink-red solution. This was stirred at room temperature overnight until all the solid had dissolved (20hrs, 20 °C). The solvent was reduced and slow diffusion of diethyl ether vapour into the concentrate produced dark purple crystals of the complex suitable for X-ray diffraction. Yield= 227.8 mg (90%). **Paramagnetic <sup>1</sup>H NMR (300 MHz, CD<sub>3</sub>CN)** δ 36.27 (2H), 33.96 (2H), 33.05 (1H), 27.84 (1H), 16.59 (2H), 12.11 (2H), 11.76 (1H), 6.85 (2H), 6.46 (2H), 6.00 (2H), 5.91 (2H), 5.53 (4H), 4.19 (1H), 4.08 (2H), 3.75 (2H), 1.33 (2H), 0.90 (2H). **HRMS [ES]<sup>+</sup> [L+H]<sup>+</sup>** Predicted: 312.1205 Found: 312.1245. **Elemental analysis calculated of 12·MeCN (%)** C 54.12, H 3.61, N 12.91; found C 53.92, H 3.54, N 12.78.

**13 [Fe((*R*)-thioPyBOX<sup>Ph</sup>)(bzimpy)][ClO<sub>4</sub>]<sub>2</sub>.** Addition of solid Fe[ClO<sub>4</sub>]<sub>2</sub>·6H<sub>2</sub>O (101.6 mg, 0.28 mmol, 1 eq.) to a solution of (*R*)-thioPyBOX<sup>Ph</sup>, **L1**, 111.5 mg, 0.28 mmol, 1 eq.) and commercially available 2,6-bis(benzimidazolyl)pyridine (bzimpy) (86.6 mg, 0.28 mmol, 1 eq.) in acetonitrile (20 mL) afforded a dark purple solution. This was stirred at room temperature overnight until all the solid had dissolved (20hrs, 20 °C). The solvent was reduced and slow diffusion of diethyl ether vapour into the concentrate produced violet crystals of the complex suitable for X-ray diffraction. Yield= 125.9 mg (46%). **Paramagnetic <sup>1</sup>H NMR (300 MHz, CD<sub>3</sub>CN). Underlined peaks are identified as 13.** δ 13.79 (2H), 10.79 (1H), 10.60 (2H), 10.24 (2H), 8.45 (2H), 8.25 (1H), 7.66 (2H), 7.36 (2H), 7.19 (2H), 7.03 (2H), 6.47 (5H), 5.26 (4H), 4.19 (4H), 3.90 (2H), 2.91 (2H), 1.33 (2H), 0.90 (2H). **HRMS [ES]<sup>+</sup> [L+H]<sup>+</sup>** Predicted: 312.1205 Found: 312.1245. **Elemental analysis calculated of 13·H<sub>2</sub>O (%)** C 51.18, H 3.48, N 11.37; found C 50.92, H 3.21, N 11.14.

**14 [Fe((*S*)-PyBOX<sup>iPr</sup>)(bzimpy)][ClO<sub>4</sub>]<sub>2</sub>.** Addition of solid Fe[ClO<sub>4</sub>]<sub>2</sub>·6H<sub>2</sub>O (104.7 mg, 0.29 mmol, 1 eq.) to a solution of commercially available (*S*)-PyBOX<sup>iPr</sup>, 83.2 mg, 0.28 mmol, 1 eq.) and 2,6-bis(benzimidazolyl)pyridine (bzimpy) (86.9 mg, 0.28 mmol, 1 eq.) in acetonitrile (20 mL) afforded a dark red-pink solution. This was stirred at room temperature overnight until all the solid had dissolved (20hrs, 20 °C). The solvent was removed and the solid was dissolved in nitromethane (2-3 mL) before slow diffusion of diethyl ether vapour into the concentrate was attempted. This did not produce crystals suitable for XRD, therefore the solvent was removed a two new crystallisations were set up. A concentrate of the sample in acetonitrile with slow diffusion of diethyl ether afforded a dark pink powder (70.9 mg, 29%) and slow diffusion of diethyl ether into a concentrate of the sample in acetone afforded dark pink crystals of the complex suitable for X-ray diffraction (59.4 mg, 24%).

**Paramagnetic  $^1\text{H}$  NMR (300 MHz,  $\text{CD}_3\text{CN}$ ).** Underlined peaks are identified as **14**.  $\delta$  63.96 (8H), 62.41 (4H), 60.86 (4H), 59.73 (4H), 55.70 (4H), 37.18 (2H), 26.44 (2H), 26.19 (2H), 24.43 (2H), 23.16 (4H), 21.20 (2H), 13.11 (6H), -7.47 (12H), -13.60 (9H), -14.59 (12H), -16.73 (3H), -19.03 (12H). **HRMS [ES]<sup>+</sup> [L+H]<sup>+</sup>** Predicted: 312.1205 Found: 312.1251. **Elemental analysis calculated of 14•0.25MeCN (%)** C 49.95, H 4.22, N 13.17; found C 49.64, H 3.86, N 13.45.

**15 [Fe((S)-thioPyBOX<sup>iPr</sup>)(bzimpy)][ClO<sub>4</sub>]<sub>2</sub>.** Addition of solid Fe[ClO<sub>4</sub>]<sub>2</sub>•6H<sub>2</sub>O (55.3 mg, 0.1 mmol, 1 eq.) to a solution of (S)-thioPyBOX<sup>iPr</sup>, **L4**, 53.0 mg, 0.16 mmol, 1 eq.) and 2,6-bis(benzimidazolyl)pyridine (bzimpy) (46.8 mg, 0.15 mmol, 1 eq.) in acetonitrile (20 mL) afforded a dark pink-purple solution. This was stirred at room temperature until all the solid had dissolved (1hr, 20 °C). The solvent was reduced and slow diffusion of diethyl ether into the concentrate afforded dark purple crystals of the complex suitable for X-ray diffraction (53.9 mg, 40%). **Paramagnetic  $^1\text{H}$  NMR (300 MHz,  $\text{CD}_3\text{CN}$ )**  $\delta$  22.93 (2H), 21.11 (2H), 20.28 (2H), 16.29 (1H), 12.46 (2H), 10.49 (1H), 9.08 (2H), 7.34 (2H), 6.96 (2H), 5.43 (2H), 5.19 (2H), 5.05 (2H), -0.73 (6H), -4.18 (2H), -5.90 (6H). **HRMS [ES]<sup>+</sup> [L+H]<sup>+</sup>** Predicted: 334.1367 Found: 334.1427. **Elemental analysis calculated (%)** C 48.07, H 4.03, N 12.46; found C 47.72, H 3.87, N 12.17.

**16 [Fe((R)-PyBOX<sup>Ph</sup>)(1-bpp)][ClO<sub>4</sub>]<sub>2</sub>.** Addition of solid Fe[ClO<sub>4</sub>]<sub>2</sub>•6H<sub>2</sub>O (86.2 mg, 0.24 mmol, 1 eq.) to a solution of (R)-PyBOX<sup>Ph</sup>, 87.5 mg, 0.24 mmol, 1 eq.) and 2,6-bis(pyrazol-1-yl)pyridine (1-bpp) (52.1 mg, 0.25 mmol, 1 eq.) in acetonitrile (20 mL) afforded a dark brown solution. This was stirred at room temperature (2hrs, 20 °C). The solvent was reduced and slow diffusion of diethyl ether into the concentrate afforded a dark brown residue, which when dried in air gave a dark red-brown powder of the complex suitable for X-ray diffraction (116 mg, 59%). **Paramagnetic  $^1\text{H}$  NMR (300 MHz,  $\text{CD}_3\text{CN}$ )**  $\delta$  40.07 (2H), 38.53 (2H), 34.05 (2H), 26.81 (1H), 23.80 (2H), 20.29 (2H), 9.45 (3H), 9.10 (2H), 7.48 (2H), 6.15 (3H), 5.36 (7H), 3.83 (3H), 1.65 (1H), 0.71 (4H). **HRMS [ES]<sup>+</sup> [L+H]<sup>+</sup>** Predicted: 370.1511 Found: 370.1568. **Elemental analysis calculated (%)** C 48.88, H 3.38, N 13.41; found C 48.60, H 3.38, N 13.01.

**17 [Fe((R)-thioPyBOX<sup>Ph</sup>)(1-bpp)][ClO<sub>4</sub>]<sub>2</sub>.** Addition of solid Fe[ClO<sub>4</sub>]<sub>2</sub>•6H<sub>2</sub>O (86.7 mg, 0.24 mmol, 1 eq.) to a solution of (R)-thioPyBOX<sup>Ph</sup>, **L1**, 95.8 mg, 0.24 mmol, 1 eq.) and 2,6-bis(pyrazol-1-yl)pyridine (1-bpp) (52.1 mg, 0.25 mmol, 1 eq.) in acetonitrile (20 mL) afforded a dark brown solution. This was stirred at room temperature (2hr, 20 °C). The solvent was reduced and slow diffusion of diethyl ether into the concentrate afforded dark brown crystals among which a few yellow crystals of the HS [Fe(1-bpp)<sub>2</sub>][ClO<sub>4</sub>]<sub>2</sub> were also observed. (185 mg, 89%). **Paramagnetic  $^1\text{H}$  NMR (300 MHz,  $\text{CD}_3\text{CN}$ )**  $\delta$  62.99 (0.2H), 58.16 (0.2H), 37.69 (0.5H), 35.34 (0.3H), 15.66 (4H), 14.87 (2H), 13.07 (1H), 12.65 (1H), 12.43 (1H), 6.70 (4H), 6.27 (4H), 5.76 (1H), 5.41 (1H), 4.18 (4H). **HRMS [ES]<sup>+</sup> [M-2(ClO<sub>4</sub>)]<sup>2+</sup>** Predicted: 334.0614 Found:

334.0615, [L+H]<sup>+</sup> Predicted: 402.1054 Found: 402.1113. **Elemental analysis (%)** pending.

**18 [Fe((S)-PyBOX<sup>iPr</sup>)(1-bpp)][ClO<sub>4</sub>]<sub>2</sub>.** Addition of solid Fe[ClO<sub>4</sub>]<sub>2</sub>·6H<sub>2</sub>O (88.8 mg, 0.24 mmol, 1 eq.) to a solution of (S)-PyBOX<sup>iPr</sup>, 68.7 mg, 0.23 mmol, 1 eq.) and 2,6-bis(pyrazol-1-yl)pyridine (1-bpp) (49.0 mg, 0.23 mmol, 1 eq.) in acetonitrile (20 mL) afforded a bright red solution. This was stirred at room temperature (2hr, 20 °C). The solvent was reduced and slow diffusion of diethyl ether into the concentrate afforded dark red crystals among which a few yellow crystals of the HS [Fe(1-bpp)<sub>2</sub>][ClO<sub>4</sub>]<sub>2</sub> were also observed. (66 mg, 37%). **Paramagnetic <sup>1</sup>H NMR (300 MHz, CD<sub>3</sub>CN)** δ 68.91 (2H), 67.71 (2H), 62.85 (1H), 59.04 (2H), 58.00 (1H), 39.36 (2H), 37.69 (1H), 35.13 (1H), 33.72 (2H), 24.27 (2H), 15.81 (2H), 10.17 (2H), 2.45 (4H), 1.12 (1H), -6.00 (6H), -13.66 (2H), -16.06 (6H). **HRMS [ES]<sup>+</sup> [L+H]<sup>+</sup>** Predicted: 302.1824 Found: 302.1881. **Elemental analysis (%)** pending.

**19 [Fe((S)-thioPyBOX<sup>iPr</sup>)(1-bpp)][ClO<sub>4</sub>]<sub>2</sub>.** Addition of solid Fe[ClO<sub>4</sub>]<sub>2</sub>·6H<sub>2</sub>O (44.3 mg, 0.12 mmol, 1 eq.) to a solution of (S)-thioPyBOX<sup>iPr</sup>, **L4**, 38.6 mg, 0.12 mmol, 1 eq.) and 2,6-bis(pyrazol-1-yl)pyridine (1-bpp) (24.7 mg, 0.12 mmol, 1 eq.) in acetonitrile (15 mL) afforded a dark brown-red solution. This was stirred at room temperature (3hr, 20 °C). The solvent was reduced and slow diffusion of diethyl ether into the concentrate afforded a dark brown residue which when dried in air gave a brown powder which a few yellow crystals of the HS [Fe(1-bpp)<sub>2</sub>][ClO<sub>4</sub>]<sub>2</sub> were also visible. (53.3 mg, 56%). **Paramagnetic <sup>1</sup>H NMR (300 MHz, CD<sub>3</sub>CN)** δ 67.15 (0.14H), 63.20 (0.3H), 58.2 (0.3H), 54.39 (0.07H), 38.20 (1H), 35.42 (1H), 33.41 (1H), 31.81 (1H), 28.92 (1H), 21.79 (2H), 18.49 (1H), 11.76 (0.4H), 10.73 (2H), 8.17 (3H), 7.56 (2H), 3.40 (4H), 2.90 (2H), 1.12 (3H), -5.21 (1H), -8.18 (6H). **HRMS [ES]<sup>+</sup> [L+Na]<sup>+</sup>** Predicted: 234.0756 Found: 234.0745, **[L'+H]<sup>+</sup>** Predicted: 334.1367 Found: 334.1418. **Elemental analysis (%)** pending.

**20 [Fe((R)-PyBOX<sup>Ph</sup>)(terpy)][ClO<sub>4</sub>]<sub>2</sub>.** Addition of solid Fe[ClO<sub>4</sub>]<sub>2</sub>·6H<sub>2</sub>O (102.0 mg, 0.28 mmol, 1 eq.) to a solution of (R)-PyBOX<sup>Ph</sup>, (102.0 mg, 0.28 mmol, 1 eq.) and 2,2':6',2''-terpyridine (terpy) (65.8 mg, 0.28 mmol, 1 eq.) in acetonitrile (20 mL) afforded a dark purple solution. This was left to stir at room temperature overnight (20hrs, 20 °C). The solvent was reduced and slow diffusion of diethyl ether into the concentrate afforded violet crystals. (173.9 mg, 72%). **Paramagnetic <sup>1</sup>H NMR (300 MHz, CD<sub>3</sub>CN)** δ 57.20 (0.3H), 30.40 (0.3H), 25.13 (0.3H), 17.74 (0.7H), 8.91 (d, 1H), 8.67 (d, 1H), 8.45 (d, 1H), 8.16 (q, 1H), 7.87 (1H), 7.36 (5H), 7.06 (2H), 6.70 (t, 1H), 6.03 (d, 1H), 5.44 (t, 1H), 4.90 (q, 1H), 4.65 (0.6H), 4.44-4.34 (dt, 1H), 4.18 (d, 0.6H), 3.66 (t, 0.6H), 3.31 (1H), 1.33 (2H), 0.90 (d, 2H), -3.15 (1H). **HRMS [ES]<sup>+</sup> [M]<sup>2+</sup>** Predicted: 329.0890 Found 329.0891, **[L+H]<sup>+</sup>** Predicted: 370.1511 Found: 370.1554. **Elemental analysis (%)** pending.

**21 [Fe((S)-PyBOX<sup>iPr</sup>)(terpy)][ClO<sub>4</sub>]<sub>2</sub>.** Addition of solid Fe[ClO<sub>4</sub>]<sub>2</sub>·6H<sub>2</sub>O (98.4 mg, 0.27 mmol, 1 eq.) to a solution of (S)-PyBOX<sup>iPr</sup>, (86.5 mg, 0.29 mmol, 1.1 eq.) and 2,2':6',2''-terpyridine (terpy) (64.7 mg, 0.28 mmol, 1 eq.) in acetonitrile (20 mL) afforded a dark purple solution. This was left to stir at room temperature overnight (20hrs, 20 °C). The solvent was reduced and slow diffusion of diethyl ether into the concentrate afforded violet crystals. (128.5 mg, 60%). **Paramagnetic <sup>1</sup>H NMR (300 MHz, CD<sub>3</sub>CN)** δ 59.72 (0.14H), 26.22 (0.3H), 24.41 (0.3H), 23.16 (0.3H), 9.16 (d, 2H), 8.90 (d, 1H), 8.82 (t, 3H), 8.69 (d, 1H), 8.60 (t, 1H), 8.46 (d, 1H), 8.22 (d, 0.6H), 8.00 (t, 2H), 7.83 (2H), 7.70 (0.6H), 7.62 (0.6H), 7.54 (t, 1H), 7.06 (1H), 5.96 (0.6H), 5.22 (d, 0.6H), 5.06 (d, 0.6H), 4.46 (4H), 4.18 (d, 2H), 4.01 (1H), 3.85 (0.6H), 3.70 (0.6H), 3.64 (0.6H), 3.47 (0.6H) 3.00 (t, 2H), 1.71 (0.6H), 1.33 (2H), 1.08 (0.7H), 1.01 (1.3H), 0.91 (t, 4H), 0.28 (6H), -0.60 (3H). **HRMS [ES]<sup>+</sup> [L+H]<sup>+</sup>** Predicted: 302.1824 Found: 302.1871 **Elemental analysis (%)** pending.

\*(*R,R*)-PyBOX<sup>iPr</sup> was synthesised in-house using the following method taken from the MChem project report of Sarah McGrath.

Part I. 2,6-Pyridine dicyanitrile (2.26 g, 17.5 mmols) was flushed under nitrogen with solid sodium in paraffin (0.4 g, 17.4 mmols) for 1 hour before dry methanol was added (55 mL). This produced a pale yellow solution which deepened in colour over time. The reaction was left to stir overnight (24hrs, 20 °C, N<sub>2</sub>) before acetic acid (0.15 mL, 2.6 mmols) was added which immediately turned the reaction mixture orange. This was left to stir for a further 2 hours. The solvent was then removed affording a yellow solid, which was washed with diethyl ether and filtered by vacuum filtration. The yellow-coloured filtrate was collected and the solvent was removed affording an off-white solid which is 2,6-pyridine dicarboximidate (3.0 g, 89%). **<sup>1</sup>H NMR (400 MHz, CD<sub>3</sub>Cl)** δ 7.92 (s, 3H), 4.03 (s, 6H). **HRMS [ES]<sup>+</sup> [L+H]<sup>+</sup>** Predicted: 194.1011 Found: 194.0929.

Part II. 2,6-Pyridine dicarboximidate (0.75 g, 3.88 mmols, 1 eq.) was flushed under nitrogen with *D*-valinol (1.15 mL, 10.39 mmols, 2.7 eq.) for 1 hour before dry chloroform was added (50 mL). This was left to reflux overnight (48hrs, 75 °C). The resulting pale yellow solution was cooled to room temperature and the solvent was removed. The crude yellow solid was washed with diethyl ether and filtered by vacuum filtration. The filtrate was collected and the solvent was removed to give a clean white solid of (*R,R*)-PyBOX<sup>iPr</sup>. Yield = (1.06 g, 91%). **<sup>1</sup>H NMR (400 MHz, CD<sub>3</sub>Cl)** δ 8.19 (d, 2H, J = 7.8 Hz), 7.87 (t, 1H, J = 7.9 Hz), 4.54 (dd, 2H, J = 1.3, 8.2 Hz), 4.24 (t, 2H, J = 8.2 Hz), 4.17 (td, 2H, J = 2, 6.5 Hz), 1.89 (sept, 2H, J = 6.5 Hz), 1.06 (d, 6H, J = 6.5 Hz), 0.95 (d, 6H, J = 6.5 Hz). **HRMS [ES]<sup>+</sup> [L+H]<sup>+</sup>** Predicted: 302.1824 Found: 302.1881

## Chapter 5

### Copper (thio/)PyBOX Complexes for Catalysis

#### 5.1 Introduction

The platinum-group metals (PGMs) such as ruthenium, rhodium, palladium and iridium have been fundamental to the successes of catalysis over the last 50 years. These precious metals are particularly well-known for their catalytic ability in reactions that require cleaving the strong H-H bond ( $436 \text{ kJ mol}^{-1}$ ) and forming C-C ( $377 \text{ kJ mol}^{-1}$ ) and C-H ( $411 \text{ kJ mol}^{-1}$ ) bonds.<sup>359, 360</sup> A number of Nobel Prizes have been awarded to the developments of these PGMs for the catalysis of key organic reactions crucial to the pharmaceutical, automotive and molecular electronics industries.

Wilkinson developed the rhodium-based catalyst,  $[\text{RhCl}(\text{PPh}_3)_3]$ , named 'Wilkinson's catalyst', for the hydrogenation of olefins.<sup>361</sup> Noyori *et al.* developed rhodium and ruthenium catalysts for the asymmetric hydrogenation of alkenes,<sup>362</sup> resulting in the commercial production of the enantiopure anti-inflammatory drug (*S*)-naproxen.<sup>363</sup> Noyori's work extended to the asymmetric hydrogenation of ketones to produce levofloxacin, which is an antibacterial agent, as well as the isomerisation of allylic amines to mass produce menthol. Noyori's contribution to asymmetric catalysis and 'green chemistry' resulted in his award of the Nobel Prize in 2001 along with Knowles and Sharpless.<sup>364</sup> In 2005, Grubbs was awarded the Nobel Prize for his development of ruthenium catalysts for olefin-metathesis, along with Schrock for molybdenum catalysts<sup>365</sup> while Heck, Negishi and Suzuki revolutionised C-C cross-coupling reactions in organic synthesis with the development of palladium catalysts, gaining the Nobel Prize in 2010 (Figure 5.1).<sup>366, 367</sup> Since this work, these PGMs have become an important class of metals in organic chemistry for research and industry.

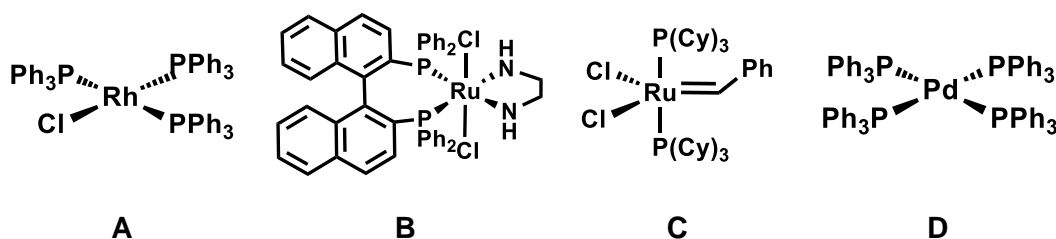


**Figure 5.1. A. Wilkinson's catalyst, B. an example of Noyori's catalysts, C. the first generation Grubbs' catalyst and D. an example of the Pd<sup>0</sup> catalyst employed by Heck, Negishi and Suzuki.**



Key issues with the PGMs includes their scarcity, cost and toxicity, which means that more sustainable and environmentally friendly alternatives are sought after that are also cheaper and more abundant in the earth.<sup>368</sup> A key goal in the search for alternatives is the ability to catalyse to at least the same standard, or surpass, the efficiency and selectivity of the PGMs.<sup>369</sup>

### 5.1.1 Base Metal Catalysis

The base metals which form the 3d row of the periodic table are much more abundant in the earth's crust, with iron being the most abundant of the base metals (5.6% in the continental crust) and the second most abundant metal altogether in the earth after aluminium (8.2%).<sup>370</sup> Additionally, the base metals are significantly cheaper than the PGMs, for example, Ni(OAc)<sub>2</sub> is only ~13% of the cost of Pd(OAc)<sub>2</sub>.<sup>369</sup> While the base metals such as iron, cobalt, copper and nickel, seem like good candidates for the replacement of the finite PGMs, the major differences in their chemistry need to be addressed. For example, the base metals most readily undergo one-electron changes to their oxidation state whereas PGMs most commonly undergo two-electron transfer processes.

A key step that enables the catalysis of organic reactions is the cleavage of a metal-carbon  $\sigma$ -bond in the organometallic catalyst.<sup>371</sup> Since catalysis with PGMs involves two-electron processes rather than one-electron, this is more consistent with the two-electron chemistry behind the formation and breakage of bonds in organic molecules. This two-electron redox of PGMs generally occurs between two diamagnetic oxidation states, whereas the 3d<sup>n</sup>-3d<sup>n</sup> elements are predisposed to undergo spin state conversions which can accompany their one-electron transfer.<sup>372-374</sup> Other issues with the base metals includes their greater affinity towards reactions with molecular oxygen<sup>375</sup> and ligand redistribution. To overcome these issues with the base metals, careful design of the ligands and/or reaction conditions is needed.<sup>376-379</sup>

#### 5.1.1.1 Copper

While other base metals such as chromium, manganese, cobalt and nickel have also proven potential in the replacement of PGMs as catalysts in key organic reactions,<sup>380-386</sup> herein the focus is on copper catalysts. Despite the one-electron redox nature of copper, two-electron processes can still be achieved with specifically selected organic ligands coordinated to copper.<sup>368</sup>

Copper is of particular interest as it has been shown to catalyse several important reactions, such as the Sonogashira C-C cross-coupling reaction,<sup>387</sup> the azide-alkyne

cycloaddition (click chemistry)<sup>388, 389</sup> and arylation reactions.<sup>390, 391</sup> Wider applications of copper catalysts have involved redox chemistry in the Water Gas Shift reaction and in the production of methanol.<sup>392-394</sup> An advantage of employing copper catalysts is the simplicity of the catalyst, as these copper catalysts are often highly efficient with simple ligands and even in the absence of a ligand (as a copper salt).<sup>393</sup>

Cross-coupling reactions catalysed by copper have been developed as an inexpensive alternative to PGMs with milder reacting conditions. An example of this is reported by Phipps and Gaunt who observed *meta*-selective C-H bond arylation using the Cu(II) salt, Cu(OTf)<sub>2</sub>, as a catalyst.<sup>395</sup> This reaction otherwise produces the *ortho*-selective product when employing the Pd(II) catalyst Pd(OAc)<sub>2</sub> (Figure 5.2).<sup>396</sup> The importance of copper was reaffirmed by the lack of catalytic activity observed in the absence of any copper species.<sup>395</sup>

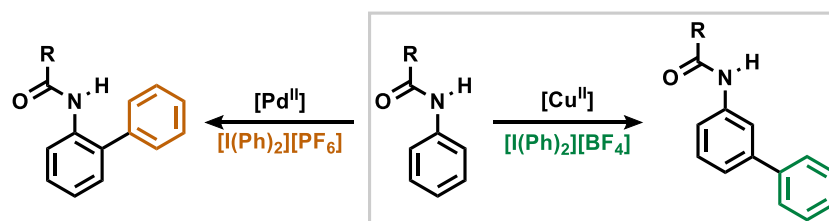


**Figure 5.2. Cu(II)-catalysed *meta*-arylation of acetanilide reported by Phipps and Gaunt and the complementary Pd(II)-catalysed *ortho*-selective reaction also shown. Figure adapted from publication.<sup>395</sup>**

The copper catalysed *N*-arylation of heterocycles and *N*-amidation of aryl halides has been presented by Klapars *et al.* who set out to enhance the Goldberg reaction (Figure 5.3).<sup>390, 397</sup> They reported highly efficient catalytic activity with a 0.2-10 mol% of copper(I)iodide with 5-20 mol% of N,N'-dimethylethylenediamine or *trans*-1,2-dimethylcyclohexanediamine in the presence of a base. These ligands were the most effective amongst their library of other, more cheaper, effective ligands.<sup>390, 391</sup> Not only did their results complement those found for Pd(II) analogues,<sup>398</sup> but they also achieved the Goldberg reaction under milder reaction conditions (at room temperature) and were able to catalyse the amination of certain functional groups that had not yet been achieved *via* Pd catalysis.<sup>391</sup>

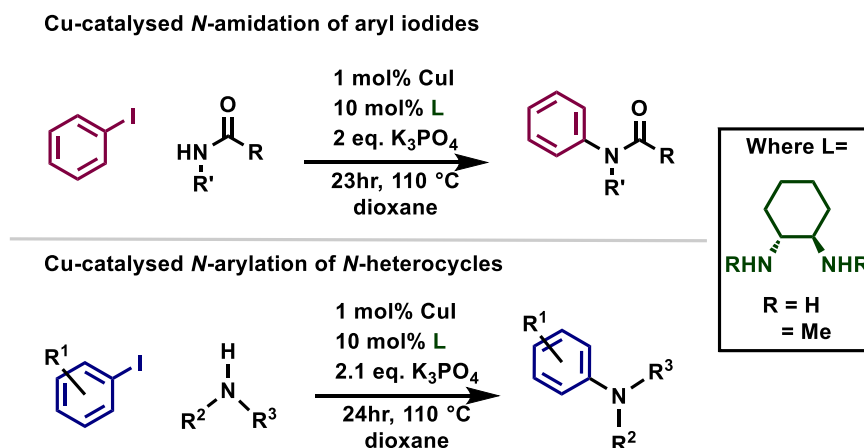


**Figure 5.3.** Reaction schemes for the Cu-catalysed *N*-amidation of aryl iodides (top) and *N*-arylation of heterocycles (bottom) studied by Klapars *et al.* Figure reproduced from publication.<sup>390</sup>

#### 5.1.1.1.1 The Ullman coupling

The copper-catalysed Ullman coupling involves the formation of biaryl units, which has been demonstrated by Ullman either through C-C bond formation between aryl halides, *N*-arylation of aniline derivatives<sup>399</sup> and in the synthesis of aryl ethers *via* phenols (Figure 5.4).<sup>400</sup> While generally speaking, the catalytic mechanism of copper species are not entirely known, Ullman coupling has been shown to work well with either Cu(0), Cu(I)- or Cu(II)-salts, Cu(I)- or Cu(II)- oxides<sup>401</sup> and even Cu(III) as the (pre)catalyst.<sup>402, 403</sup> Studies have most commonly shown the active catalyst is a Cu(I) species.<sup>404, 405</sup>

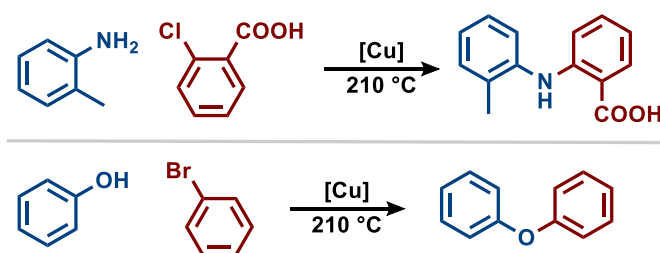


**Figure 5.4.** Ullman coupling of an aniline with an aryl halide (top reaction) and of phenol with an aryl halide (bottom reaction).<sup>399, 400</sup> Figure adapted from Sambiasi *et al.*<sup>393</sup>

A number of different mechanisms for Ullman coupling have been proposed for example using organocopper(II) intermediates, *via*  $\sigma$ -bond metathesis, *via*  $\pi$ -complexation, *via* single electron transfer (SET) and *via* different intermediates dependent on the functional group of the biaryl product.<sup>393, 406</sup> A general mechanism

is shown below which follows a similar catalytic cycle as the palladium-catalysed Buchwald-Hartwig amination reaction (Figure 5.5).

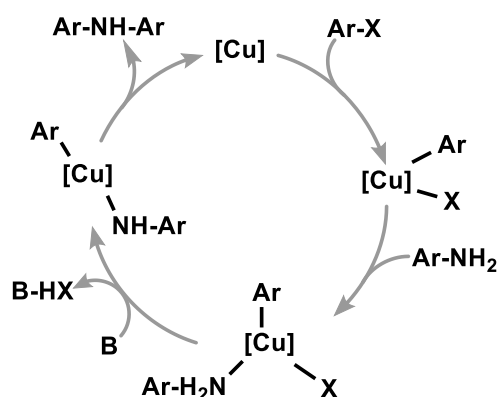


**Figure 5.5.** Reaction cycle for the copper catalysed Ullman coupling of an aryl halide with an aryl amine.

In efforts to achieve Ullman-type reactions but in milder conditions such as lower temperatures and smaller quantities of copper source, ligands were introduced to the catalytic system.<sup>393</sup> This was initially to aid the solubility of the copper(I) species or prevent disproportionation to Cu(0).<sup>407</sup> However, structure-activity relationships studied by Ouali *et al.*, suggested an electronic influence from the ligands on the Cu atom.<sup>408</sup> It was found that when imino-pyridine ligands were bound such as those shown in Figure 5.6, the reaction yield was enhanced. This was ascribed to the electron-rich nature of pyridyl donors which facilitates the oxidative addition step of the catalytic cycle, while the less electron-rich imine functional group facilitates the reductive elimination step.<sup>408</sup> The high catalytic yields of 95%, low-costs, and simple synthesis from inexpensive starting materials highlights how advantageous the iminopyridine ligands are in the copper-catalysed Ullman coupling.

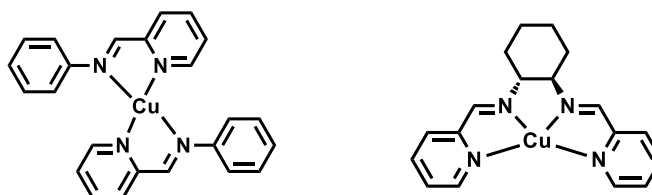


**Figure 5.6.** The two most active copper(II) iminopyridine catalysts reported by Ouali *et al.*<sup>408</sup>

### 5.1.1.1.2 The Azide-Alkyne cycloaddition (Click reaction)

The copper catalysed azide-alkyne cycloaddition (CuAAC) was independently discovered by Meldal <sup>409</sup> and Sharpless <sup>389</sup> in 2002 as an enhanced version of the 1,3-dipolar cycloaddition by Huisgen <sup>410, 411</sup>. The addition of a copper source to the uncatalysed dipolar cycloaddition was found to significantly enhance the reaction performance and selectively gave the 1,4-disubstituted regioisomer of 1,2,3-triazole (Figure 5.7). <sup>412</sup>

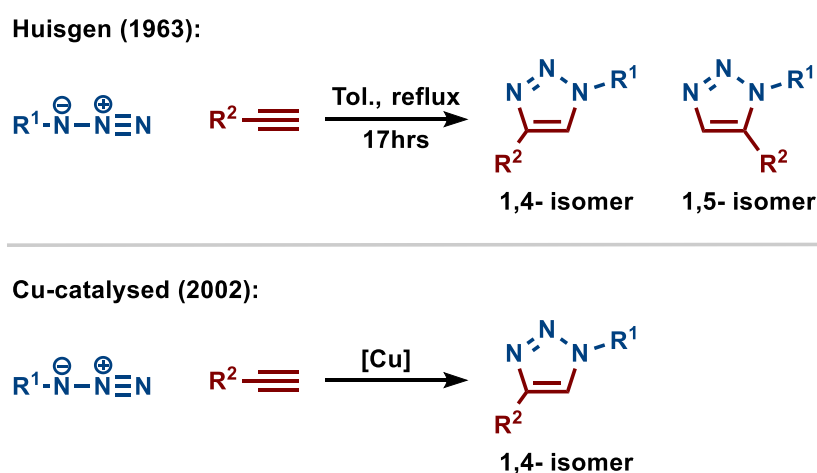


**Figure 5.7. Reaction scheme of the 1,3-dipolar cycloaddition reported by Huisgen <sup>410, 411</sup> (top) and the copper-catalysed version reported by Meldal <sup>409</sup> and Sharpless <sup>389</sup> (bottom). Figure adapted from publication. <sup>412, 413</sup>**

Since 1,2,3-triazoles are not naturally found, the CuAAC is useful for their synthesis and has been applied in their synthesis most commonly to achieve triazoles as an amide mimetic, in research areas including drug discovery, <sup>388</sup> DNA research in biochemistry <sup>414</sup> and polymer chemistry. <sup>415</sup> Additionally, the triazole functional group serves as a stable linker that can undergo hydrogen bonding and dipole-dipole interactions with biological targets. <sup>388</sup>

While the catalytically active species is known to be Cu(I), other copper sources, such as copper(II) salts, copper wire or copper nanoclusters, <sup>416, 417</sup> can also be used in the CuAAC as precatalysts, making the reaction particularly versatile. <sup>418, 419</sup> There have been recent advances in understanding the reaction mechanism of CuAAC. An initial mechanism was proposed by Sharpless and Fokin (Figure 5.8, left) which Fokin later adapted to propose another mechanism which introduces a second copper species to the reaction (Figure 5.8, right).

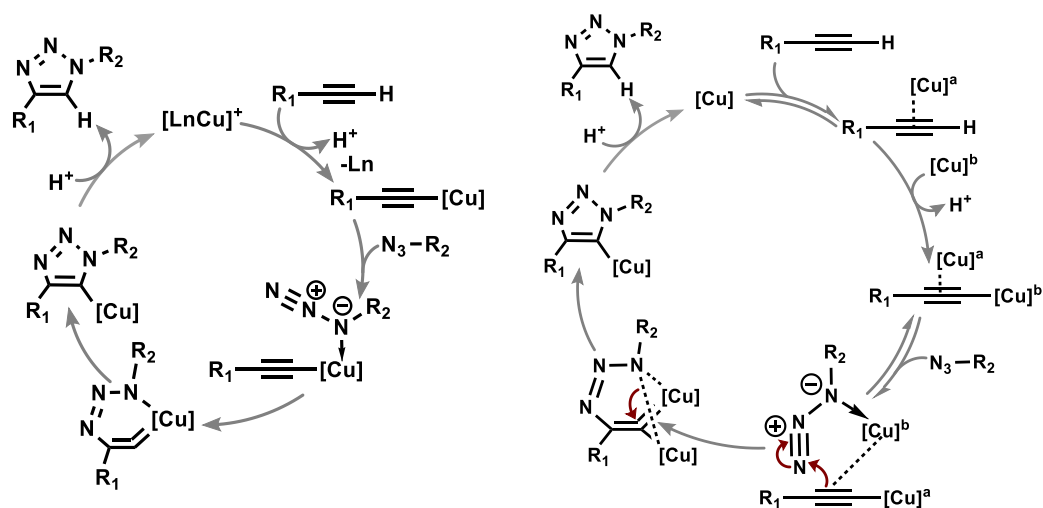


Figure 5.8. Initial catalytic cycle of the CuAAC proposed by Sharpless and Fokin (left) and more recent mechanism of the CuAAC proposed by Fokin (right). Figure adapted from El Ayouchia *et al.*<sup>420</sup>

### 5.1.2 Copper-PyBOX Catalysts

Research for more reactive catalysts has led to the success of copper-based Lewis acid catalysts for the enantioselective Diels-Alder reaction. The catalyst  $[\text{Cu}((S)\text{-BOX}^{\text{tBu}})]_2[\text{SbF}_6]_2$  showed excellent catalytic activity in the Diels-Alder reaction between cyclopentadiene and acrylimide analogues, producing the bicyclic adduct in at least 94% enantiomeric excess (ee) at ambient temperatures (Figure 5.9).<sup>421, 422</sup>

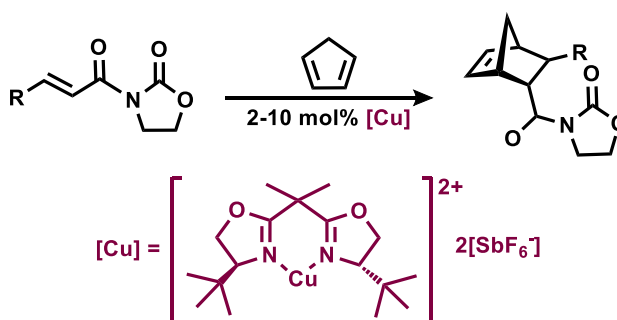
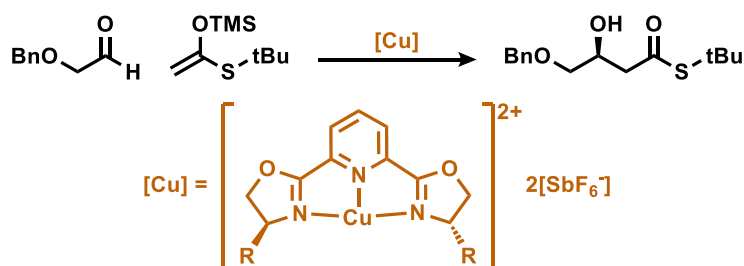


Figure 5.9. Diels-Alder reaction of cyclopentadiene with acrylimide derivatives catalysed by  $[\text{Cu}((S)\text{-BOX}^{\text{tBu}})]_2[\text{SbF}_6]_2$  reported by Evans *et al.*<sup>421, 422</sup>

Evans *et al.* also reported that using the cationic derivative of the  $[\text{Cu}((S)\text{-BOX}^{\text{tBu}})]_2[\text{SbF}_6]_2$  catalyst, in which the BOX ligand is replaced with the more electron-rich PyBOX ligand to give  $[\text{Cu}((S)\text{-PyBOX}^{\text{tBu}})]_2[\text{SbF}_6]_2$ , has proven to be an effective

catalyst for the Diels-Alder reaction and the Mukaiyama aldol reaction.<sup>423</sup> The PyBOX-based catalyst was still found to enantioselectively afford the (*S*)-cycloadduct in the Diels-Alder reaction of acrylamides, as was observed with the Cu-BOX catalyst. However, studies found that the PyBOX analogues, [Cu((*S*)-PyBOX<sup>R</sup>)] [SbF<sub>6</sub>]<sub>2</sub> (R = Ph, iPr, Bn, tBu) were better suited to catalysing the aldol reaction between benzyloxyacetaldehyde with enolsilanes (Figure 5.10). Their findings showed that the most selective catalyst of these was [Cu((*S*)-PyBOX<sup>Ph</sup>)] [SbF<sub>6</sub>]<sub>2</sub> which produced the product in a 99% ee within 15 minutes at -78 °C. The triflate salt analogues also proved highly effective, achieving 96% ee but with slower kinetics.<sup>322</sup>



**Figure 5.10. The Mukaiyama aldol reaction of benzyloxyacetaldehyde with a tBu-thioacetate silyl ketene acetal, catalysed by [Cu((*S*)-PyBOX<sup>R</sup>)] [SbF<sub>6</sub>]<sub>2</sub> where R = Ph, iPr, Bn, tBu), reported by Evans *et al.*<sup>423</sup>**

Wei and Li studied the copper(I)-catalysed *in situ* alkyne-imine addition to produce propargylic amines, using chiral ligands from the BOX and PyBOX families. In the reaction of phenylacetylene with *N*-benzylideneaniline in water, they found that employing the PyBOX ligands with copper(I) bromide gave enhanced enantioselectivity over the BOX analogues. Furthermore, they showed that while using the chiral catalyst PyBOX<sup>Ph</sup>-CuBr the product conversion was good (90%) but the enantioselectivity was poor (28%). These results were drastically improved by changing copper(I) bromide for copper(I) triflate, giving 90% conversion and 83% ee (Figure 5.11).<sup>424, 425</sup>

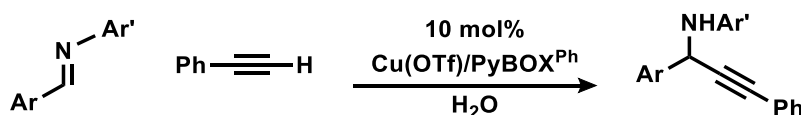


**Figure 5.11. The reaction scheme of phenylacetylene with *N*-benzylideneaniline catalysed by PyBOX<sup>Ph</sup>-CuOTf, reported by Wei and Li.<sup>424, 425</sup>**

Copper(I) PyBOX catalysts have also been demonstrated in the addition of alkynes to imines by Bisai and Singh <sup>426</sup> and Dodda and Cong-Gui, <sup>427</sup> achieving similarly good yields and ee percentages as found by Wei and Li. Other reactions that have employed Cu-PyBOX catalysts includes allylic oxidation, <sup>428</sup> cyclopropanation (using Cu(II)PyBOX catalysts) <sup>429</sup> and the azide-alkyne cycloaddition (CuAAC). <sup>430</sup>

In the azide-alkyne cycloaddition catalysed by copper(I) PyBOX complexes reported by Meng *et al.*, <sup>430</sup> ten derivatives of PyBOX ligands were screened with CuOTf, which gave conversion percentages of product no higher than 38%. Kinetic resolutions found for each ligand system in this screening showed greater enantiomer selectivity factors (~3) with the PyBOX derivative shown in Figure 5.12. This reaffirms the influence of the ligand in the catalytic process. A study of one of the PyBOX ligands with six different copper(I) salts showed similar catalytic activities between CuX salts (X = Cl, Br, I) but overall the highest conversion was observed with the triflate salt.

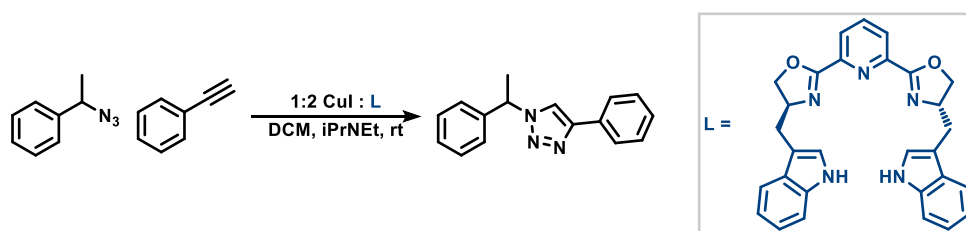


**Figure 5.12. The CuAAC reaction of phenethyl azide with phenyl acetylene catalysed by copper(I) iodide with PyBOX derivative, L studied by Meng *et al.* <sup>430</sup>**

#### 5.1.2.1 Self-assembled copper(I) PyBOX helicates

The self-assembly of transition metal-based supramolecular architectures have been well-studied in the literature, <sup>431, 432</sup> with a versatility of applications including molecular recognition, catalysis, substrate transport, synthesis of non-covalent units and DNA intercalator research. <sup>432-436</sup> Of interest herein are copper-helicate architectures featuring the PyBOX ligand for catalysis.

While the PyBOX ligand has thus far been presented in its classical tridentate coordination mode, there are publications that have demonstrated this ligand and analogous ligand systems in a bidentate coordination mode with a fluxional nature. <sup>437, 438</sup> A monodentate binding mode has also been reported in the complex [Rh((S)-PyBOX<sup>iPr</sup>)(CO)(L)<sub>2</sub>][PF<sub>6</sub>] where L = PMe<sub>2</sub>Ph, PMePh<sub>2</sub> and PPh<sub>2</sub>(C<sub>3</sub>H<sub>5</sub>). <sup>439</sup> The proven ability of the PyBOX ligand to be hemilabile has allowed access to multinuclear copper(I) PyBOX complexes.



An example of this was demonstrated by Gelalcha *et al.* who first reported the interestingly double helical structure of the dinuclear complex  $[\text{Cu}((S)\text{-PyBOX}^{\text{iPr}})_2][\text{OTf}]_2$ .<sup>435</sup> Using this catalyst *in situ*, the enantioselective allylic peroxidation of prochiral cyclic olefins was found to be particularly successful, achieving the chiral products with up to 84% ee,<sup>440</sup> building on from previous work by Gokhale *et al.* with an *in situ*-generated catalyst from bisoxazolines and  $\text{CuOTf}$ .<sup>441</sup> The work by Gelalcha *et al.* demonstrates the promising potential of such helical chiral copper(I) complexes.

Panera *et al.* had later reported the synthesis of a library of mono- di- and tetra-nuclear copper(I) PyBOX complexes using various copper(I) salts.<sup>442, 443</sup> The complexes they reported are the mononuclear structures  $[\text{Cu}(\text{PyBOX}^{\text{R}})_2][\text{PF}_6]$  where  $\text{R} = S\text{-iPr}$ ,  $R\text{-Ph}$  (Figure 5.13), the dinuclear complexes  $[\text{Cu}_2(\text{PyBOX}^{\text{R}})_2][\text{PF}_6]_2$  with  $\text{R} = R\text{-Ph}$ ,  $S\text{-iPr}$  and  $S\text{-iPr} + \text{diPh}$  and two chloro-bridged analogues of the dinuclear complexes,  $[\text{Cu}_2(\mu\text{-Cl})(\text{PyBOX}^{\text{R}})_2][\text{CuCl}_2]$  ( $\text{R} = S\text{-iPr}$ ,  $R\text{-Ph}$ ) (Figure 5.14). The tetranuclear complexes they reported are of the structure  $[\text{Cu}_4\text{X}_4(\text{PyBOX}^{\text{R}})_2]$  with combinations of  $\text{R} = R\text{-Ph}$ ,  $S\text{-iPr}$  and  $S\text{-iPr} + \text{diPh}$  and  $\text{X} = \text{Cl}$ ,  $\text{Br}$ ,  $\text{I}$  (Figure 5.15).

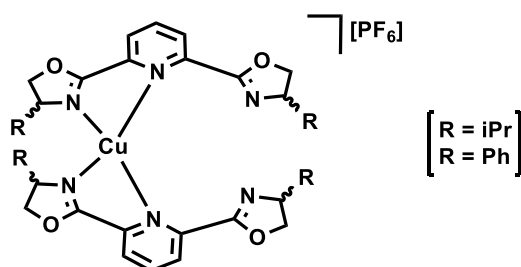


**Figure 5.13.** The structure of the mononuclear copper(I)  $\text{PyBOX}^{\text{R}}$  complexes reported by Panera *et al.*<sup>442, 443</sup>

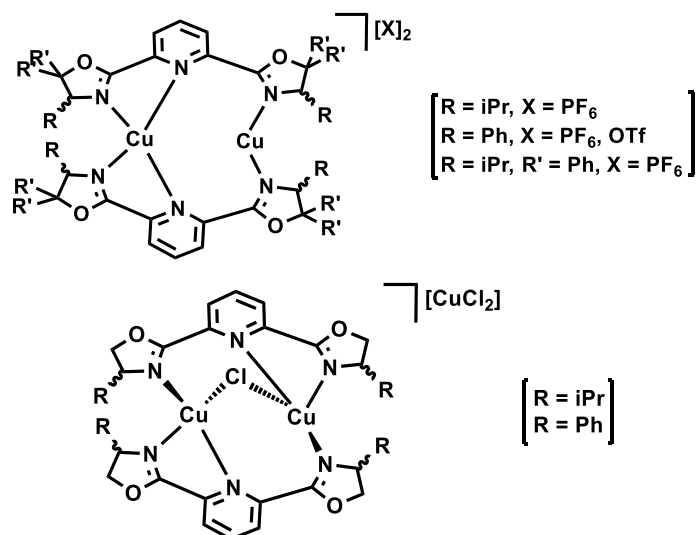


**Figure 5.14.** The structures of the dinuclear copper(I) PyBOX<sup>R</sup> complexes reported by Panera *et al.*<sup>442, 443</sup> Bottom structure is the  $\mu$ -chloro bridged analogue.

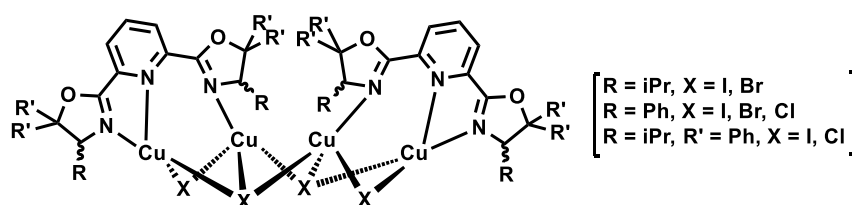


**Figure 5.15.** The structure of the tetranuclear copper(I) PyBOX<sup>R</sup> complexes reported by Panera *et al.*<sup>442, 443</sup>

The catalytic activity of the mono- di- and tetra- nuclear copper-PyBOX<sup>Ph</sup> complexes and the dinuclear PyBOX<sup>iPr</sup> analogues were studied in the enantioselective synthesis of (1,3-diphenyl-2-propynyl)aniline *via* the addition of phenyl acetylene to benzylideneaniline with a 5 mol% stoichiometry of the copper complex. It was found that the dinuclear complexes  $[Cu_2((R)\text{-PyBOX}^{Ph})_2][X_2]$  with  $X = OTf, PF_6$ , were the most efficient catalysts for this reaction with up to 88% yield and in 89% *ee*. While the NMR analysis confirmed the stability of the dinuclear cationic species, it was concluded that this may not be the active species in the catalytic mechanism, but rather the dissociated mononuclear form is the catalytically active species.<sup>442</sup>

## 5.2 Results & Discussion

### 5.2.1 Copper complexes synthesised herein

Herein a series of copper(II) PyBOX and thioPyBOX complexes have been synthesised in a 1:1 metal : ligand ratio, with a view to achieving an effective catalyst for the Ullman coupling reaction. Three copper(II) complexes of this nature have been synthesised and are discussed below; [Cu((S)-PyBOX<sup>Ph</sup>)(OTf)<sub>2</sub>], **22**, the thioPyBOX analogue [Cu((S)-thioPyBOX<sup>Ph</sup>)(OTf)][OTf], **23** and a *tert*-butyl congener, [Cu((S)-PyBOX<sup>tBu</sup>)(OTf)<sub>2</sub>], **24**. In an attempt to synthesise the thioPyBOX analogue of **24**, the bis- complex [Cu((S)-thioPyBOX<sup>tBu</sup>)<sub>2</sub>][OTf]<sub>2</sub>, **25** was isolated instead. Owing to time constraints no catalysis studies were carried out on these copper(II) complexes.

Two of the copper(I) PyBOX complexes previously reported by Panera *et al.* have been synthesised and isolated herein for catalysis studies on an azide-alkyne cycloaddition reaction. These two complexes include the tetranuclear copper(I) complex [Cu<sub>4</sub>I<sub>4</sub>((R)-PyBOX<sup>iPr</sup>)<sub>2</sub>], **26**, and the dinuclear helicate, [Cu<sub>2</sub>((S)-PyBOX<sup>iPr</sup>)<sub>2</sub>][PF<sub>6</sub>]<sub>2</sub>, **27**.<sup>442, 443</sup> Additionally, a *tert*-butyl analogue of **27** was isolated as the tetrafluoroborate salt, [Cu<sub>2</sub>((S)-PyBOX<sup>tBu</sup>)<sub>2</sub>][PF<sub>6</sub>]<sub>2</sub>, **28**, which has not yet been reported in the literature. In an attempt to synthesise the phenyl- derivative of the dinuclear helical complexes, this bis-homoleptic PyBOX<sup>Ph</sup> complex, [Cu((R)-PyBOX<sup>Ph</sup>)<sub>2</sub>][PF<sub>6</sub>], **29**, was formed. In another attempt, an unprecedented trinuclear complex [FCu<sub>3</sub>((R)-PyBOX<sup>Ph</sup>)<sub>3</sub>][BF<sub>4</sub>], **30**, was identified by XRD analysis. Preliminary catalysis studies were obtained for the click reaction of benzyl azide with phenyl acetylene, catalysed by complexes **26**, **27** and **28**, which are also discussed below.

#### 5.2.1.1 Copper(II) complexes

The mono- (thio-)PyBOX complexes **22** and **23** were synthesised by a 1:1 addition of copper(II) triflate to the dissolved ligand in solution, following the preparation reported by Evans *et al.*<sup>322</sup> (details are outlined in Section 5.4). Single crystals suitable for XRD analysis were grown by slow diffusion of diethyl ether into a concentrate of the complex in acetonitrile. The XRD structure solutions obtained for **22** and **23** are shown in Figure 5.16 and key bond lengths and angles are tabulated in Table 5.1.



**Figure 5.16.** XRD structures obtained of complex **22** (left) and **23** (right). Ball and stick models are shown for clarity. Hydrogen atoms omitted for clarity.

	<b>22</b>	<b>23</b>
<b>Cu-N<sub>Py</sub> (Å)</b>	1.970(7)	1.949(3)
<b>Cu-N<sub>ox.thiox.</sub> (Å)</b>	2.040(6), 2.040(6)	2.076(3), 2.076(3)
<b>Cu-N<sub>MeCN</sub> (Å)</b>	1.967(7)	1.940(3)
<b>Cu-O (Å)</b>	2.425(6), 2.425(6)	2.371(3)
<b>N<sub>Py</sub>-Cu-N<sub>MeCN</sub> (°)</b>	180.0(0)	179.28(14)
<b>N<sub>Py</sub>-Cu-O (°)</b>	93.84(18), 93.85(18)	90.16(12)
<b>Cu-N<sub>MeCN</sub>-C (°)</b>	180.0(0)	169.5(3)

**Table 5.1.** Selected XRD bond lengths and angles for **22** and **23**.

The syntheses of **22** and **24** (*vide infra*) are a repeat of two structures reported in the literature by Evans *et al.*<sup>322</sup> While Evans *et al.* proposed the triflate groups are simply counter-ions to the copper(II) complex, the XRD structures herein show these triflate groups coordinate to the copper(II) centre in the solid state. The solution state species are unconfirmed but is most likely the dicationic complex suggested by Evans *et al.*<sup>322</sup>

Considering that complex **23** is simply the oxygen-replaced sulfur analogue of **22**, the XRD structure solutions obtained show significant differences between the two complexes. An immediately obvious difference is the different coordination numbers owing to the nature of the triflate anion in the two complexes. Whilst both triflates symmetrically coordinate *trans* to each other in the axial direction in **22**, giving the Cu atom a coordination number of 6, only one triflate is coordinated in **23**. In the latter complex, the other triflate anion takes the role of a counter-ion owing to the cationic nature of the 5-coordinate copper complex formed.

This reflects the more electron-donating nature of the thioPyBOX ligand family compared to PyBOX family. This difference results in a greater stabilisation of the metal atom(s) when thioPyBOX is coordinated in place of PyBOX, as was demonstrated in chapter 3. The increased electron 'pull' from the PyBOX ligand in **22** is evident from the overall slightly longer bond lengths between copper and coordinating N or O atoms (Table 5.1) (with the exception of Cu-N<sub>ox</sub>, which is shorter in **22** than Cu-N<sub>thiox</sub> in **23**, due to the smaller and less sterically-bulky oxazoline ring). This renders the Cu atom of complex **22** more electron deficient than complex **23**, making it more susceptible to further coordination from the anionic triflate as is observed.

Whilst a molecule of acetonitrile from the crystallisation solvent is coordinated in both complexes and at the same equatorial position, the acetonitrile molecule is clearly bent in **23** with a Cu-N<sub>MeCN</sub>-C bond angle of 169.5(3) °. The equivalent bond angle is perfectly linear in **22** with an angle of 180.0(0) °. This can be understood from the crystal packing structures (Figure 5.17) which shows the triflate anion forming an extensive network of intermolecular contacts in **23**, including O...H contacts with the methyl substituent of acetonitrile (F<sub>3</sub>CSO<sub>3</sub><sup>-</sup>...HCH<sub>2</sub>-), resulting in the non-linearity observed. Since there is no equivalent uncoordinated triflate anion in **22**, there is nothing to dictate a bent geometry of acetonitrile.

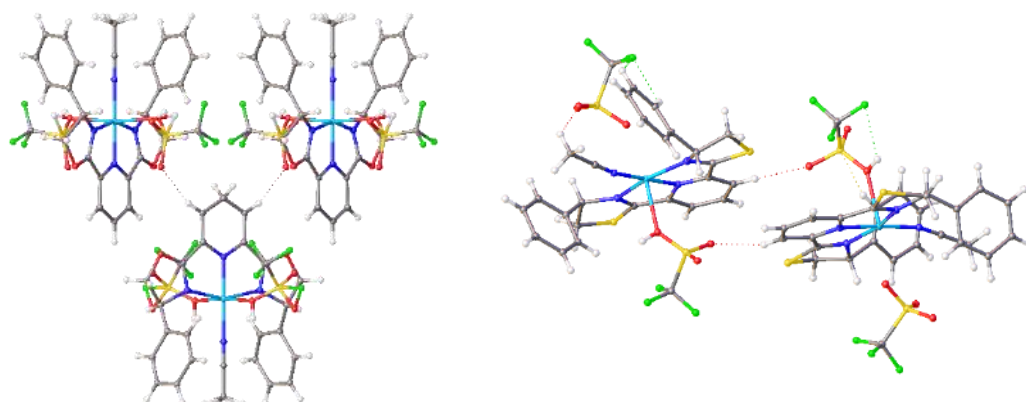


**Figure 5.17. Simplified packing structures of **22** (left) and **23** (right) with hydrogen contacts displayed.**

Another intermolecular interaction evident in Figure 5.17 which is common to both complexes, is the F<sub>3</sub>CSO<sub>3</sub><sup>-</sup>...H-C<sub>Py</sub> contacts between the coordinated triflate moiety and the *ortho* hydrogen atoms on the pyridine ring, which is 2.6 Å in **22** and 2.4 Å in **23**, suggesting a weak hydrogen contact in the latter. Furthermore, **22** shows

additional hydrogen bonding between Ph-C-H...O<sub>3</sub>SCF<sub>3</sub> which is not evident in **23**, as the oxygen atom of the oxazoline ring polarises the ring significantly more.

The *tert*-butyl analogue of **22**, complex **24**, was synthesised following the same procedure as was used to obtain **22** and **23**. The XRD structure of **24** is shown below in Figure 5.18 and selected bond lengths and angles are tabulated in Table 5.2.

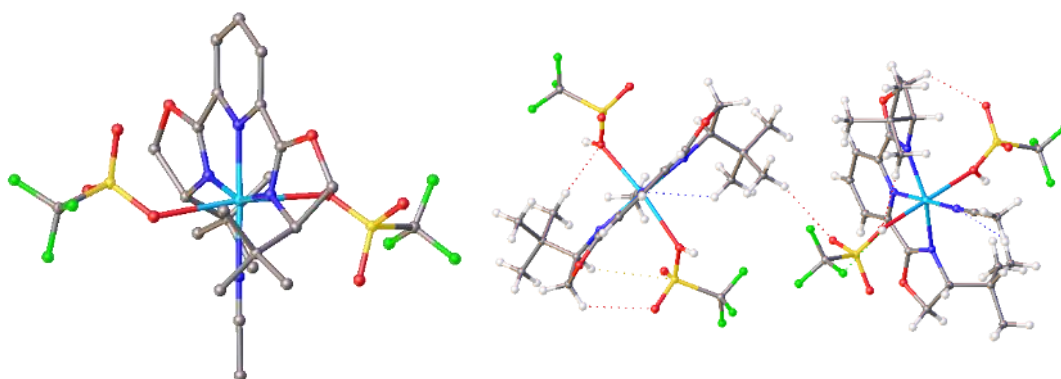


**Figure 5.18.** XRD structure solution obtained of complex **24** (left). Intermolecular interactions are also shown in a simplified packing diagram (right). Structure is shown as a ball and stick model for clarity. Hydrogen atoms omitted in the left image for clarity.

	<b>24</b>
<b>Cu-N<sub>Py</sub></b> (Å)	1.953(8)
<b>Cu-N<sub>ox.</sub></b> (Å)	2.083(8), 2.075(7)
<b>Cu-N<sub>MeCN</sub></b> (Å)	1.963(9)
<b>Cu-O</b> (Å)	2.388(6), 2.377(7)
<b>N<sub>Py</sub>-Cu-N<sub>MeCN</sub></b> (°)	178.1(3)
<b>N<sub>Py</sub>-Cu-O</b> (°)	89.3(3), 96.9(3)
<b>Cu-N<sub>MeCN</sub>-C</b> (°)	177.8(8)

**Table 5.2.** Selected XRD bond lengths and angles for complex **24**.

Similar to its phenyl- substituted equivalent, complex **24** also shows a structure with both triflate anions coordinated to the Cu atom, *trans* to each other. This agrees well with the electronic influence of the PyBOX ligand compared to the thioPyBOX ligand that was demonstrated in complex **22**, resulting in this 6-coordinate structure with both triflate anions. The structure overall shows similar bond lengths and angles compared to complex **22**, particularly the linearity of the acetonitrile molecule, which is distinctly bent in **23**. While both triflate ligands in complex **22** are oriented with their

trifluoromethyl groups facing upwards, away from the phenyl substituents of the PyBOX ligand, this is not the case for **24**.

Complexes **22**, **23** and **24** may exist in their lower-coordinate dicationic forms in donating solvents,  $[\text{Cu}(\text{L})]^{2+}$  which would make these complexes particularly good catalysts as there are vacant sites available for substrate coordination to the copper atom. The electron-withdrawing nature of the PyBOX ligand may render **22** a better catalyst compared to **23**. However it would still be interesting to study the catalytic activity of **23** and any other thioPyBOX derivatives. Considering the good catalytic activity and high enantioselectivity achieved with the complex  $[\text{Cu}((\text{S})\text{-BOX}^{\text{tBu}})]^{2+}$  in the aldol reaction,<sup>322</sup> this provides a basis for studying these complexes further, particularly the PyBOX analogue (**24**), as catalysts for other copper-catalysed reactions.

An attempt was made to synthesise the thioPyBOX analogue of **24** following the same experimental procedure. However the bis- thioPyBOX<sup>tBu</sup> copper(II) complex formed instead. Single crystals of  $[\text{Cu}((\text{S})\text{-thioPyBOX}^{\text{tBu}})_2][\text{OTf}]_2$ , complex **25**, suitable for XRD analysis were grown by diffusion of diethyl ether into a concentrate of the sample in acetonitrile as per the previous structure. The crystals were green in colour which is indicative of a copper(II) species. The XRD structure solution obtained is shown in Figure 5.19 and selected data are tabulated in Table 5.3.

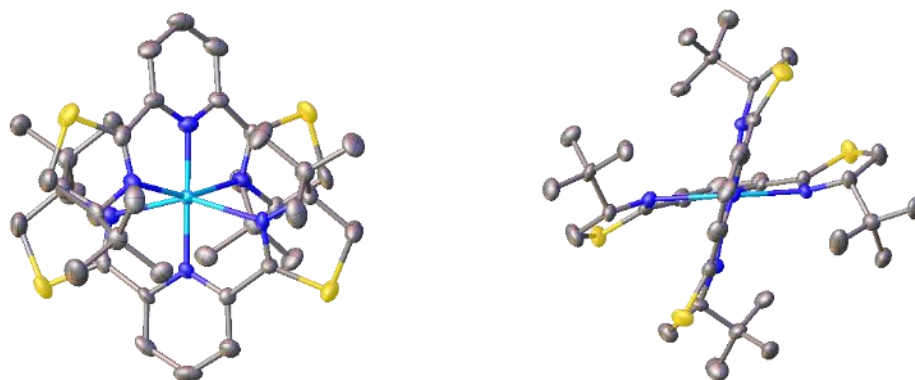


**Figure 5.19.** XRD structure solution obtained of  $[\text{Cu}((\text{S})\text{-thioPyBOX}^{\text{tBu}})_2][\text{OTf}]_2$ , complex **25**. Hydrogen atoms, counter-ions and solvents are omitted for clarity. Thermal ellipsoids are at the 50% probability level.

	<b>25</b>
<b>Cu-N<sub>Py</sub> (Å)</b>	1.971(8), 1.920(9)
<b>Cu-N<sub>thiox.</sub> (Å)</b>	2.343(8), 2.436(9), 2.156(8), 2.177(7)
<b>N<sub>Py</sub>-Cu-N<sub>Py</sub>, <math>\phi</math> (°)</b>	177.2(4)
<b>Dihedral, <math>\theta</math> (°)</b>	57.342
<b>N<sub>thiox.</sub>-Cu- N<sub>thiox.</sub>, <math>\varphi</math> (°)</b>	157.8(3), 153.0(3)

**Table 5.3. Selected XRD bond lengths and angles for complex 25.**

The XRD structure solution obtained of complex **25** is isostructural to the iron analogue **S-7** (Section 3.2.1.3.3), and shows a similar degree of distortion from the ideal octahedral geometry. While the iron centre in **S-7** is in the HS state owing to this distortion, copper(II) complexes do not exhibit such spin state dichotomy. The origins of the distortions in both **S-7** and **25** are from the bulky *tert*-butyl substituents of the thioPyBOX<sup>tBu</sup> ligand. While octahedral copper(II) complexes are well known to exhibit Jahn-Teller distortions (Section 1.3),<sup>444</sup> the strong angular distortions observed in the XRD structure of complex **25** is not attributed this JT effect.<sup>445</sup>

The pattern of the bond lengths observed in **25** are comparable to those found in the complex [Cu(bpp)<sub>2</sub>][BF<sub>4</sub>]<sub>2</sub> (Figure 5.20), which can be grouped into three distinct categories; the short z-axis, medium y-axis and long x-axis.<sup>446, 447</sup> The Cu-N bond lengths in **25** along these three axis respectively are; 1.971(8)-1.920(9), 2.156(8)-2.177(7) and 2.343(8)-2.436(9). The Cu-N<sub>thiox.</sub> bond lengths are significantly longer than their equivalent bonds observed in the [Cu(bpp)<sub>2</sub>][BF<sub>4</sub>]<sub>2</sub> complex due to the bulkier nature of the thioPyBOX<sup>tBu</sup> ligand. While the *trans* N<sub>Py</sub>-Cu-N<sub>Py</sub> angle,  $\phi$ , is similar to that of the bpp complex, the inter-ligand dihedral angle,  $\theta$ , is significantly more distorted (57.3 ° compared to 88.4 °).



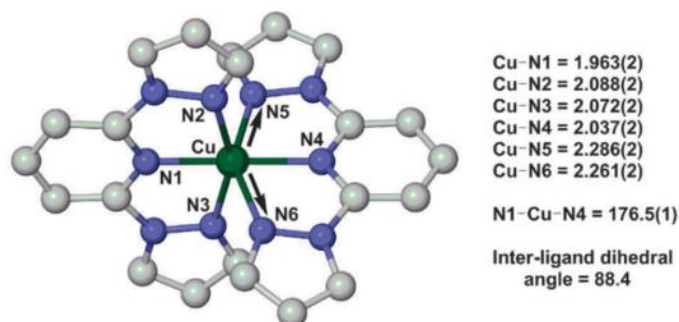


Figure 5.20. XRD structure and relevant data of the dicationic  $[\text{Cu}(\text{bpp})_2][\text{BF}_4]_2$  complex reported by Solanki *et al.*<sup>446, 447</sup> Figure taken from publication.<sup>445</sup>

### 5.2.1.2 Copper(I) complexes

Intrigued by the multinuclear copper(I) complexes reported by Panera *et al.*, two of these complexes were synthesised again following the same procedure that they employed.<sup>442, 443</sup> From this the complex  $[\text{Cu}_4\text{I}_4((R)\text{-PyBOX}^{\text{iPr}})_2]$ , **26**, was isolated and the XRD structure was obtained (Figure 5.21). Selected bond lengths and angles are tabulated in Table 5.4.

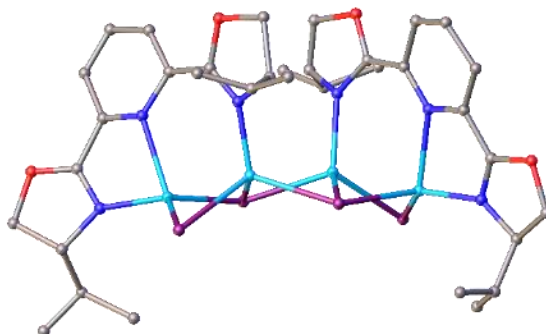
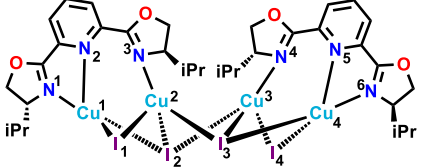


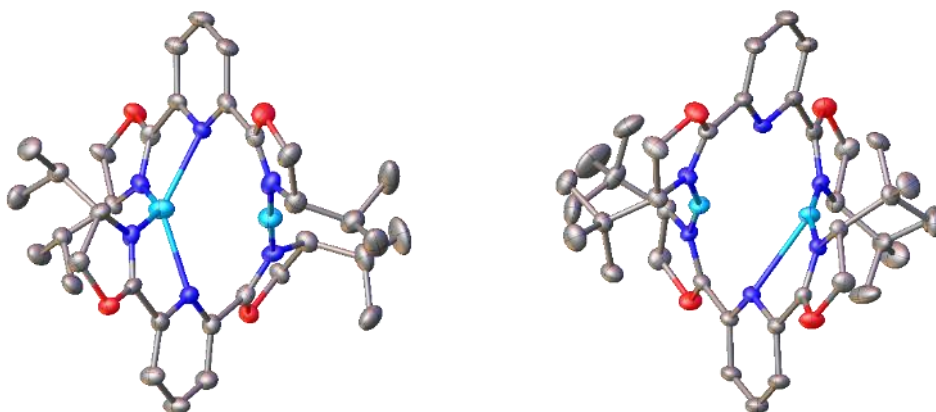
Figure 5.21. XRD structure solution obtained for  $[\text{Cu}_4\text{I}_4((R)\text{-PyBOX}^{\text{iPr}})_2]$ , **26**. Hydrogen atoms are omitted for clarity. Ball and stick model shown for clarity.

	<b>26</b>	
<b>Cu1-N2 (Å)</b>	2.28(4)	
<b>Cu4-N5 (Å)</b>	2.30(3)	
<b>Cu1-N1 (Å)</b>	1.99(4)	
<b>Cu2-N3 (Å)</b>	2.00(5)	
<b>Cu3-N4 (Å)</b>	2.11(4)	
<b>Cu4-N6 (Å)</b>	2.05(4)	
<b>Cu1-I1-Cu2-I3 (°)</b>	-150.308	
<b>Cu4-I4-Cu3-I2 (°)</b>	-154.274	

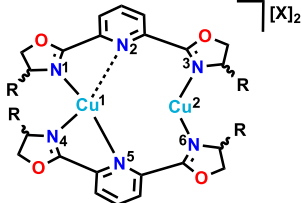
**Table 5.4. Selected bond lengths and angles from the XRD structure of 26.**

The Cu-N bond lengths and the torsion angles obtained are similar to the XRD data obtained for the same structure by Panera *et al.*<sup>442</sup>

The XRD structure solution was obtained from the repeated synthesis of one of the dinuclear copper(I) complexes reported by Panera *et al.*,  $[\text{Cu}_2((S)\text{-PyBOX}^{\text{iPr}})_2][\text{PF}_6]_2$ , **27** (Figure 5.22, left). Building on this library, the *tert*butyl analogue,  $[\text{Cu}_2((S)\text{-PyBOX}^{\text{tBu}})_2][\text{BF}_4]_2$ , **28**, was also synthesised and the XRD structure obtained (Figure 5.22, right), which has not yet been reported by Panera *et al.*<sup>442, 443</sup> Selected bond lengths and angles are tabulated in Table 5.5.



**Figure 5.22. XRD structure solutions of  $[\text{Cu}_2((S)\text{-PyBOX}^{\text{iPr}})_2][\text{PF}_6]_2$ , **27** (left) and  $[\text{Cu}_2((S)\text{-PyBOX}^{\text{tBu}})_2][\text{BF}_4]_2$ , **28** (right). Hydrogen atoms, solvent and counter-ions are omitted for clarity. Thermal ellipsoids are at the 50% probability level.**

	<b>27</b>	<b>28</b>	
<b>Cu1-N2 (Å)</b>	2.271(7)	-	
<b>Cu1-N5 (Å)</b>	2.278(6)	2.447(3)	
<b>Cu1-N1 (Å)</b>	1.956(6)	1.920(3)	
<b>Cu1-N4 (Å)</b>	1.973(6)	1.927(3)	
<b>Cu2-N3 (Å)</b>	1.887(6)	1.908(3)	
<b>Cu2-N6 (Å)</b>	1.888(7)	1.907(3)	
<b>N2-Cu1-N5 (°)</b>	134.9(2)	-	
<b>N1-Cu1-N4 (°)</b>	141.2(2)	165.12(14)	
<b>N1-Cu1-N5 (°)</b>	119.2(2)	113.12(13)	
<b>N2-Cu1-N4 (°)</b>	112.8(3)	-	
<b>N3-Cu2-N6 (°)</b>	177.2(3)	163.52(15)	
<b>Dihedral, <math>\theta</math> (°)</b>	70.9	67.0	

**Table 5.5. Selected bond lengths and angles from the XRD structure of **27** and **28**.**

While the XRD structure of complex **27** has already been reported (complex **1** in publication <sup>442</sup>), the noteworthy features of this structure are the two distinct copper coordination modes. While one copper exhibits a distorted tetrahedral geometry, the other is linear with an N-Cu-N bond angle of 177.2(3) ° which is identical to that reported in the literature (176.6(2) ° <sup>442</sup>). Interestingly, complex **28** also exhibits two copper ions of different coordination environments, however this is now a distorted 3-coordinate geometry along with the other pseudo-linear 2-coordinate copper ion. The bulkier *tert*butyl substituents on the PyBOX ligand in **28** compared to the *isopropyl* substituent in **27**, force a greater degree of distortion about the Cu atom in order to accommodate the ligand (Figure 5.23). This in turn has influenced the different coordination geometries adopted by Cu1 in both complexes. The multiple geometries that copper(I) can access is well known for  $d^{10}$  electronic configurations, which can adopt a range of 4-, 3- and 2-coordinate geometries.

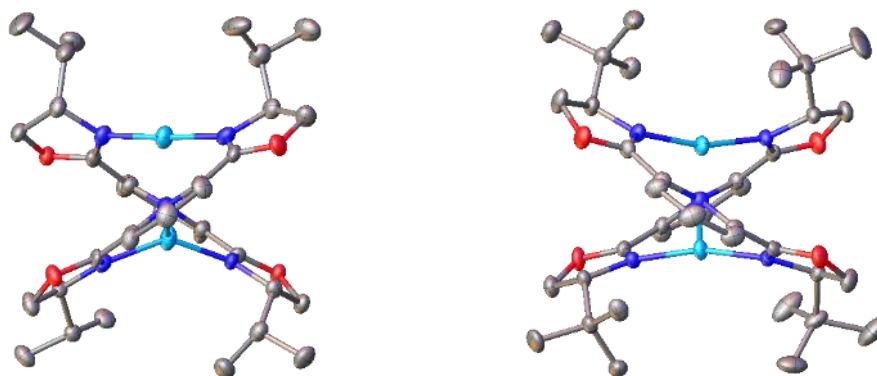


**Figure 5.23.** XRD structures of **27** (left) and **28** (right) looking down the central pyridine ring. Hydrogen atoms, counter-ions and solvent are omitted for clarity. Thermal ellipsoids are at the 50% probability level.

The Cu-Cu distances in **27** and **28** are 2.741(18) Å and 2.755(8) Å respectively, which are both significantly longer than Cu-Cu distances reported elsewhere that conclude the lack of a bond between the two copper ions.<sup>448, 449</sup> The N3-Cu2-N6 bond angle is significantly more bent in **28** than in **27**, in order to accommodate the bulky *tert*butyl groups. This is supported by the slightly more narrow dihedral angle between the two ligand planes in **28** (67.0 °) than in **27** (70.9 °). At the other copper centre, the N<sub>ox</sub>-Cu-N<sub>ox</sub> bite angle (N1-Cu1-N5) is now more obtuse in **28** (165.12(14) °) than in **27** (141.2(2) °) due to the lower coordination number of Cu1 in **28**.

The twisted conformations of the coordinated PyBOX ligands are particularly unique, as this ligand system typically exhibits minimal deviations from planarity, even in its coordination complexes. In **27**, one of the oxazoline rings from the same ligand is oriented almost perpendicularly relative to the other oxazoline ring, whereas in **28** this twisting does not occur to the same extent. This twisted geometry of PyBOX in both complexes is what enables the overall helical structure of the bimetallic species.

In attempts to synthesise the phenyl- substituted analogue of **27** and **28**, [Cu<sub>2</sub>((*R*)-PyBOX<sup>Ph</sup>)<sub>2</sub>][PF<sub>6</sub>]<sub>2</sub>, which was also reported by Panera *et al.*<sup>442</sup>, the mononuclear bis-PyBOX<sup>Ph</sup> complex was obtained, [Cu((*R*)-PyBOX<sup>Ph</sup>)<sub>2</sub>][PF<sub>6</sub>]<sub>2</sub>, **29**, (Figure 5.24, Table 5.6). A similarly-structured copper(II) analogue of this complex, [Cu((*S*)-PyBOX<sup>Ph</sup>)<sub>2</sub>][SbF<sub>6</sub>]<sub>2</sub> was reported by Evans *et al.*,<sup>421</sup> however the hexafluorophosphate salt, **29** has not been previously reported in the literature according to the Cambridge Crystallographic Structural Database (CCSD). A structure of the same formula was however reported, but in a hemilabile form where each PyBOX is coordinated to the copper atom in a bidentate manner giving the Cu atom a distorted tetrahedral geometry (Figure 5.13), though an XRD structure was not obtained to confirm this.<sup>442</sup>

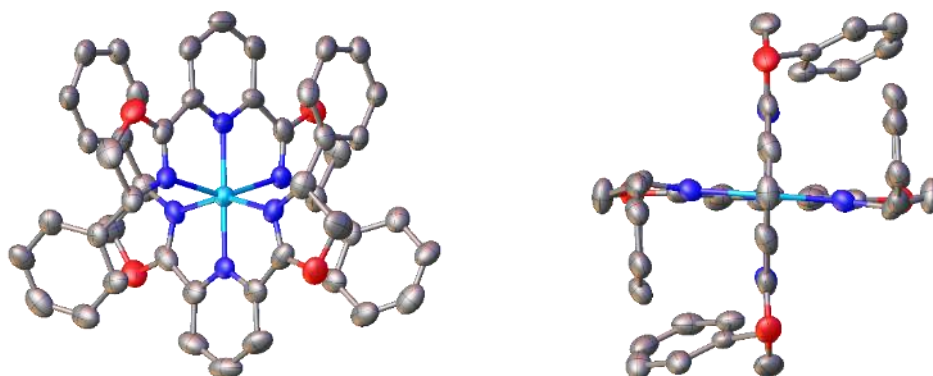
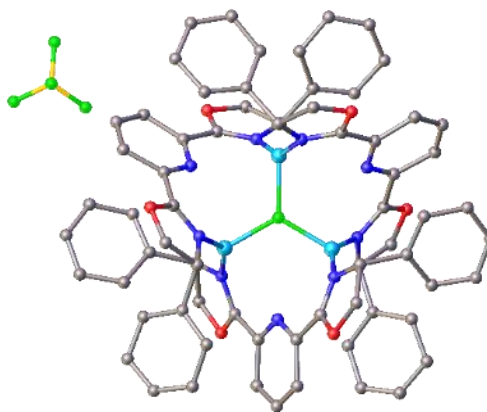


Figure 5.24. XRD structure of  $[\text{Cu}((R)\text{-PyBOX}^{\text{Ph}})_2][\text{PF}_6]$ , **29**. Hydrogen atoms, solvents and counter-ions are omitted for clarity. Thermal ellipsoids are at the 50% probability level.

	<b>29</b>
<b>Cu-N<sub>Py</sub> (Å)</b>	1.961(6), 1.995(6)
<b>Cu-N<sub>Ox</sub>. (Å)</b>	2.067(5)* - 2.282(5)*
<b>N<sub>Py</sub>-Cu-N<sub>Py</sub>, <math>\phi</math> (°)</b>	180.0(0)
<b>Dihedral angle, <math>\theta</math> (°)</b>	87.7
<b>N<sub>Ox</sub>-Cu-N<sub>Ox</sub>, <math>\varphi</math> (°)</b>	156.9(3), 154.1(3)

Table 5.6. Selected XRD bond lengths and angles of complex **29**. \*Both Cu-N<sub>ox</sub> bond lengths displayed are identical to the two not displayed.

In another attempt to synthesise the dinuclear PyBOX<sup>Ph</sup> complex  $[\text{Cu}_2((R)\text{-PyBOX}^{\text{Ph}})_2][\text{PF}_6]_2$  but using the tetrakisacetonitrile copper(I) tetrafluoroborate salt, a few crystals of the complex  $[\text{FCu}_3(\text{PyBOX}^{\text{Ph}})_3][\text{BF}_4]_2$ , **30** were isolated. The XRD structure solution obtained is shown in Figure 5.25 and selected bond lengths and angles are highlighted in Table 5.7.



**Figure 5.25.** XRD structure of  $[\text{FCu}_3((R)\text{-PyBOX}^{\text{Ph}})_3][\text{BF}_4]_2$ , complex **30**. Hydrogen atoms and solvent are omitted for clarity. Ball and stick model shown for clarity.

	<b>30</b>
<b>Cu-N (Å)</b>	1.957(7)
<b>Cu-F (Å)</b>	1.944(12)
<b>N-Cu-N (°)</b>	150.8(6)
<b>N-Cu-F (°)</b>	104.6(3)

**Table 5.7.** Selected bond lengths and angles from the XRD structure of **30**.

The formation of this trimetallic triple-stranded helicate structure was unprecedented particularly due to the nature of the central atom. While the identity of this central atom is uncertain, the most likely candidate is fluorine. Each copper centre appears planar with regards to the two nitrogen atoms and the fluorine atom it is coordinated to, which is similar to trigonal planar geometry observed other triple-helicate copper(I) coordination complexes.<sup>450</sup> It is speculated that the  $\text{F}^-$  is sourced from the  $\text{BF}_4^-$  ion which  $\text{Cu}^+$  abstracts, as has been previously demonstrated in copper(I) scorpionate complexes.<sup>451</sup> The  $\text{F}(\text{Cu})_3$  centre has been reported in a crystal structure on one other occasion by Straub *et al.* in the complex  $[\text{Cu}_3(\mu^3\text{-F})(\mu\text{-dtbpm})_3][\text{PF}_6]_2$  (where dtbpm = bis(di-tert-butylphosphino)-methane).<sup>452</sup> The Cu-F bond length in this complex (2.22 Å) is somewhat longer than the observed Cu-F length in **30** (1.94 Å), which contributes to the uncertainty of the identity of this central atom in this complex. The Cu-N bond lengths are on average 1.957(7) Å, the N-Cu-N bond angles are 150.8(6) ° and the F-Cu-N angles are 104.6(3) °. The long interatomic distance between the copper atom and the nitrogen atom of the nearest pyridine ring of

2.790 Å confirms there is no bond between these atoms. The packing structure of **30** is shown in Figure 5.26.

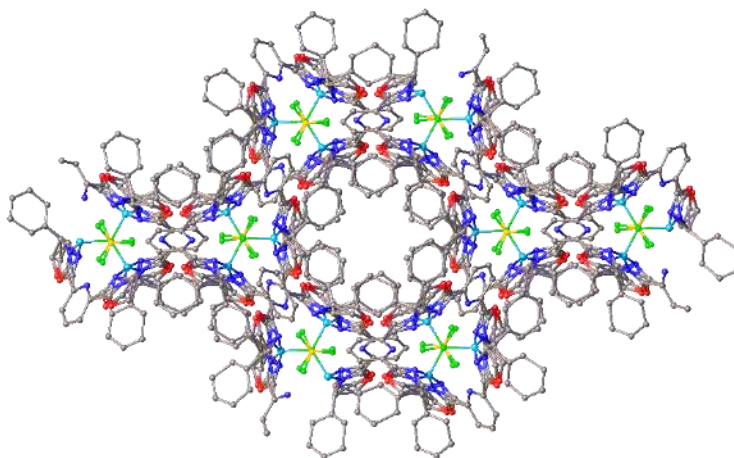


**Figure 5.26. XRD packing structure of **30** shown along the *c*-axis. Hydrogen atoms are omitted for clarity. Ball and stick model shown for clarity.**

The packing structure of **30** shows a highly symmetrical system. The tetrafluoroborate anion interacts with the C-H bonds on the oxazoline ring, with a  $\text{BF}_3\text{-F}\dots\text{H-CH-}$  distance of 2.5 Å.

### 5.2.2 Preliminary catalysis studies

Whilst copper(I) complexes have been demonstrated as effective catalysts in the copper(I) catalysed azide-alkyne cycloaddition reaction (CuAAC), the use of copper(I) helicates for such catalysis is less known. The helicate system in general has good catalytic prospects, demonstrated by Panera *et al.* who reported good catalytic activity from the dinuclear copper(I) PyBOX<sup>Ph</sup> helicates in the enantioselective synthesis of propargylamines.<sup>442</sup> Perhaps this is owing to the hemilabile nature of the ligand, which can facilitate ligand association and dissociation steps in the catalytic mechanism.

The dative-coordinate hemilabile binding of the PyBOX ligand in these dinuclear and tetranuclear complexes stabilises low-coordinate and highly reactive catalysts during the reaction pathway. Furthermore, this hemilability provides easy access to the reaction site.<sup>453</sup> The incorporation of a hemilabile ligand to a low-coordinate metal centre has resulted in enhanced catalytic activity in the palladium-catalysed Suzuki-Miyaura coupling, for example.<sup>454, 455</sup> This effect however is notably much less explored with base metal catalysts.<sup>456</sup>

### 5.2.2.1 Catalysis method

The experimental method adapted herein synthesised the 1,4-disubstituted 1,2,3-triazole from a one-pot reaction of benzyl bromide, sodium azide and phenyl acetylene with the copper catalyst, generating the benzyl azide reagent *in situ*.<sup>457, 458</sup> The benzyl azide reagent is synthesised and isolated first (Figure 5.27), then the azide-alkyne reaction was performed using this azide reagent and phenyl acetylene with the copper catalyst (Figure 5.28).

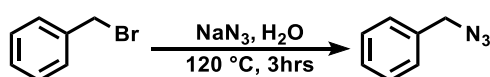


**Figure 5.27.** Reaction scheme for the synthesis of benzyl azide from benzyl bromide.

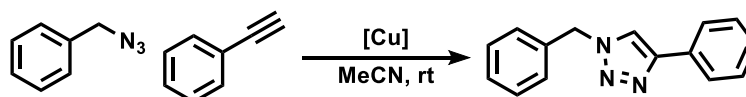


**Figure 5.28.** Reaction scheme for the click reaction employed herein to study the copper catalysts.

The copper(I) catalysts studied in this reaction are complexes **26**, **27** and **28**, the structures of which are reproduced below in Figure 5.29.

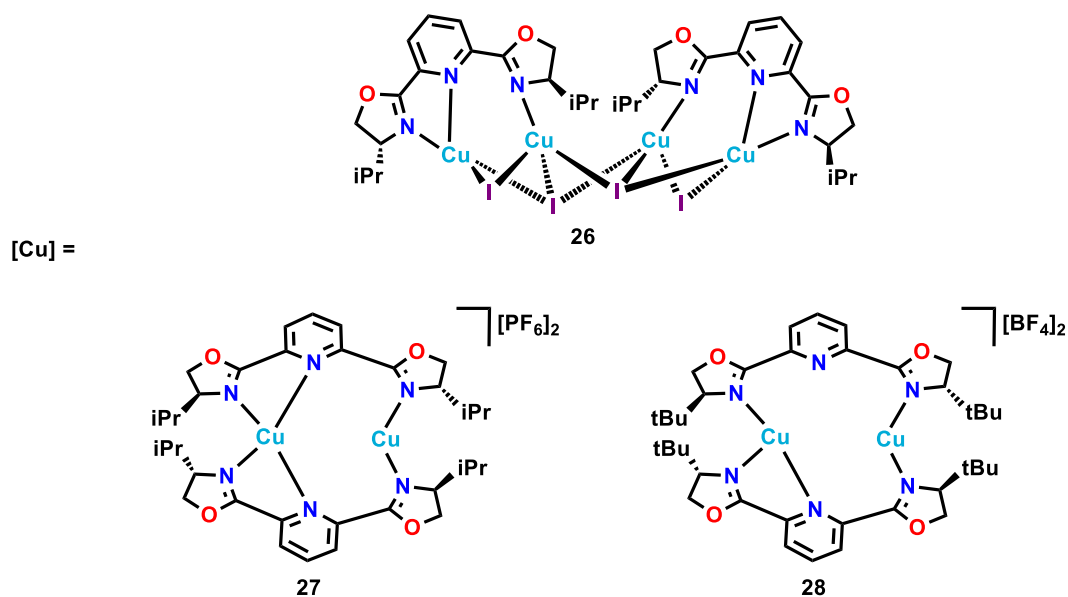


**Figure 5.29.** Copper catalysts, **26**, **27** and **28** tested herein on the CuAAC reaction in Figure 5.28.



Crucial to achieving reliable data from monitoring the reaction progression are a robust experimental method that can easily be reproduced with minimal error, and a simple method of analysis from an easy-access and reliable instrument. To determine the experimental procedure for this preliminary catalysis study, a test reaction was carried out of benzyl azide with phenyl acetylene using copper(I) oxide as the catalyst.  $\text{Cu}_2\text{O}$  was used as the model catalyst as it has been reported that this Cu source exhibits the highest catalytic activity compared to other copper(I) salts, such as copper(I) halides, for CuAAC reactions.<sup>459</sup>

Through analysis of the  $^1\text{H}$  NMR spectra of the benzyl azide, phenyl acetylene and the 1,2,3-triazole formed from this reaction, key proton peaks were identified that are easily distinguishable between these three species. The  $\text{CH}_2$  peak of benzyl azide appears at  $\delta$  4.2 ppm, the  $\text{CH}$  peak of phenyl acetylene appears at  $\delta$  3.1 ppm and the  $\text{CH}_2$  group of the triazole product, 1-benzyl-4-phenyl-1,2,3-triazole, appears at  $\delta$  5.5 ppm (Figure 5.30). An internal standard, 1,3,5-trimethoxybenzene (TMB) was used in this catalysis study to ensure reliability of the results. The TMB peak appears around  $\delta$  3.8 ppm which is distinct from the reagent and product peaks. These distinct peaks which do not overlap with common proton environments, such as aromatic protons at 7-8 ppm or alkyl protons at 1-2 ppm, along with the TMB internal standard which does not interfere with the reaction, resulted in  $^1\text{H}$  NMR being the chosen as the diagnostic tool for monitoring the reaction progression.

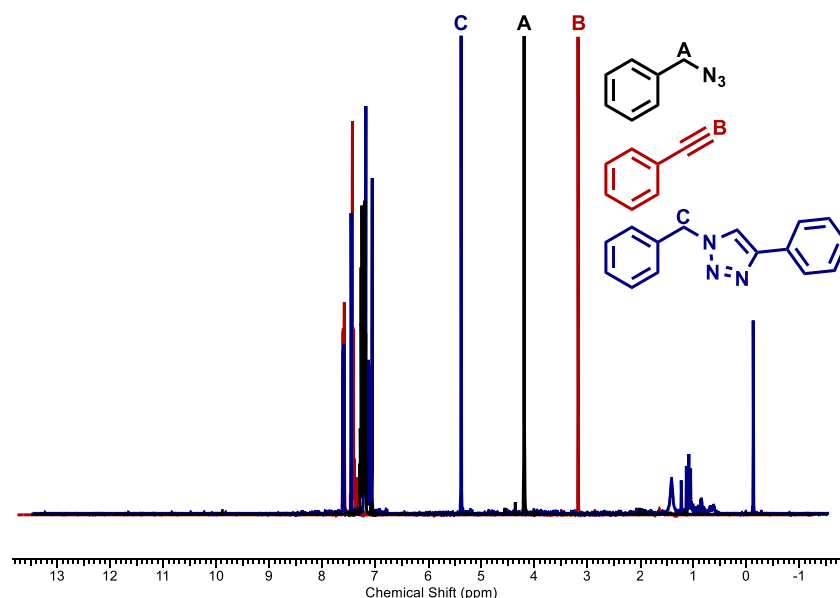


**Figure 5.30. Overlaid  $^1\text{H}$  NMR spectra of benzyl azide (black), phenyl acetylene (red) and 1-benzyl-4-phenyl-1,2,3-triazole (blue).  $\text{CD}_3\text{Cl}$ , 400 MHz.**

To assess the reaction progression, the growth of the  $^1\text{H}$  NMR peak C in Figure 5.30 was measured. The diminishing of peaks A and/or B could have also easily been used.

#### 5.2.2.2 Test reaction

Using  $\text{Cu}_2\text{O}$  as the catalyst, a test reaction was carried out to determine the duration of the reaction until completion and the frequency of reaction sampling sufficient for conclusive analysis of reaction progress.

The test reaction was initially carried out under neat conditions at room temperature using 1 mol% of the copper catalyst. The high concentration of the reagents resulted in the reaction proceeding very quickly, evident from the precipitation of the triazole product in the reaction flask after approximately 1 hour. The cream precipitate was purified and isolated to give a yield of 46% in just this short amount of time. While this shows an effective reaction, it is not sustainable for the monitoring the reaction. Another test reaction was carried out using complex **27** as the copper catalyst to determine if this reaction proceeded just as quickly. This was also performed neat with 1 mol% of **27** and it was observed that the product also precipitated out of this reaction mixture relatively quickly, achieving 56% yield with a reaction time of just under 3 hours.

To slow this down, a small volume of solvent was introduced in order to dilute the reaction mixture. A repeat of the initially neat test reactions were carried out in 2 mL of acetonitrile, which showed the same precipitation of the triazole product occurring now after ~ 28 hours with the copper oxide catalyst and after ~16 hours with **27**. This was deemed much more appropriate for monitoring the reaction and so this solvent and quantity was used in the catalytic testing

Following this, catalysts **26** and **28** were also tested in separate batch reactions to screen these complexes for catalytic activity. As with complex **27**, these also showed catalytic potential with only a ~1 mol% loading of the catalyst. The compiled results from these separate batch reactions are shown in the graph in Figure 5.31.

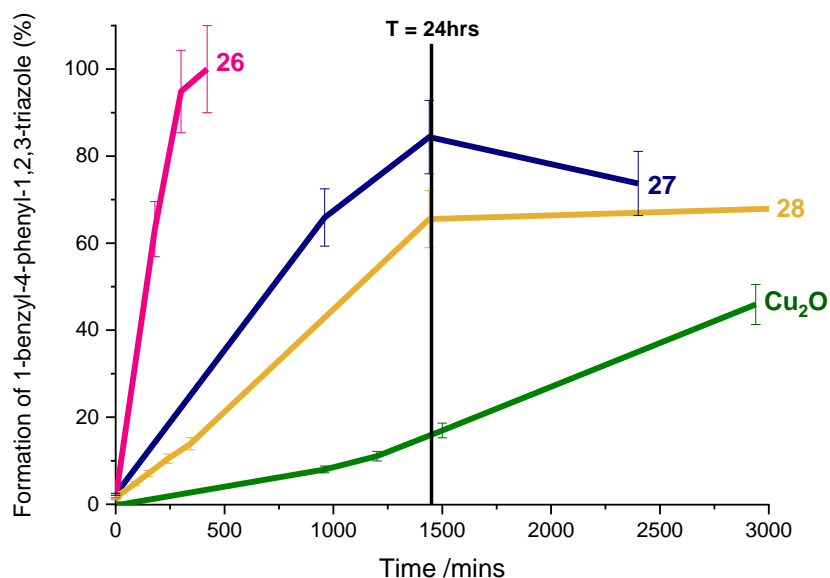


**Figure 5.31. The test reaction progression of the synthesis of 1-benzyl-4-phenyl-1,2,3-triazole, monitored by the growth of the <sup>1</sup>H NMR peak corresponding to the CH<sub>2</sub> group in the triazole, with catalysts 26 (pink), 27 (blue), 28 (orange) and Cu<sub>2</sub>O (green). The black line at 1440 mins corresponds to T = 24 hrs.**

From these test reactions, a clear catalytic effect is evident in the reactions catalysed by **26**, **27** and **28**. Overall these copper(I) PyBOX helicates appear more effective than the copper oxide standard, which was also studied for comparison. This corroborates the finding that having a ligand coordinated to copper enhances its catalytic activity and therefore it crucial to catalyst design.

### 5.2.2.3 Preliminary Click Catalysis study

After the test click reactions with these catalysts, a more accurate and robust method of catalysis was employed on a repeat of these reactions. A Radley Carousel was used which allows for multiple reactions to be run simultaneously under the same conditions. 5 reaction tubes were used for the same reaction but changing the catalysts as follows; 1. Uncatalysed, 2. Cu<sub>2</sub>O, 3. Catalyst **27**, 4. Catalyst **28** and 5. Catalyst **26**. For this study, a stock solution was made of the reagents in the solvent and with the internal standard, this stock solution was then evenly distributed to each carousel tube using a Gilson pipette to ensure accuracy. The catalysts (or no catalyst) were then introduced to the reaction tubes at T=0, which is when the reaction started. This carousel set-up ensured robustness in the experimental method and reduced error in the results, ensuring the only differences in reaction progression were due to

the different catalysts employed. The two carousel studies are shown as graphs in Figure 5.32.

While complexes **27** and **28** were used in a 1 mol% quantity in these catalysis studies, it should be noted that complex **26** was also used in a 1 mol% quantity despite having 4 copper atoms in its structure. This can be considered as equivalent to being used in a 2 mol% quantity. This should therefore be considered in the analysis of the results presented. The clearly faster kinetics of complex **26** can be rationalised by the added copper to the reaction mixture. The actual kinetics of complex **26** therefore cannot be assumed from these results. Owing to time constraints the study could not be repeated with a 0.5 mol% loading of **26**.

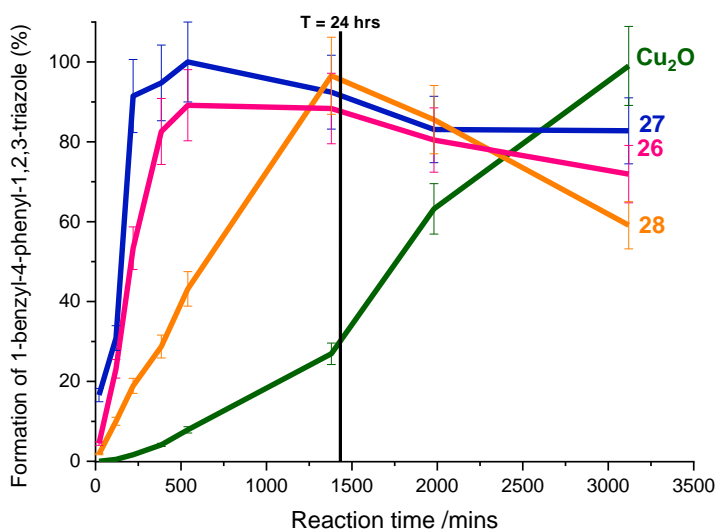
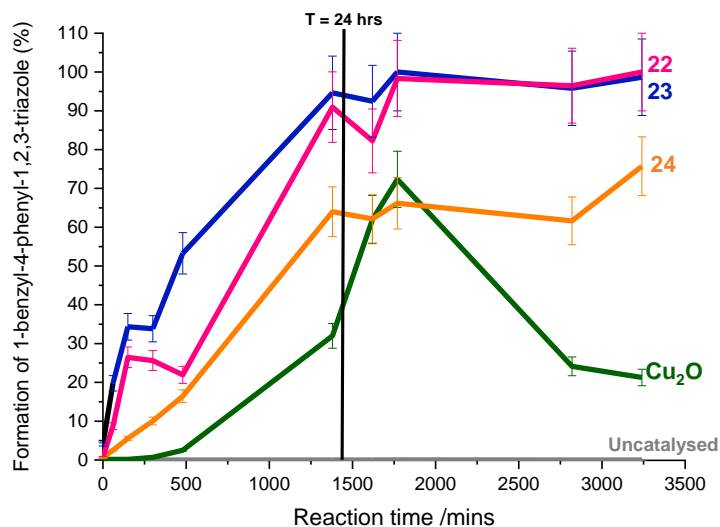


**Figure 5.32. Carousel round 1 (top) and round 2 (bottom). The reaction progression of the synthesis of 1-benzyl-4-phenyl-1,2,3-triazole, monitored by the growth of the <sup>1</sup>H NMR peak corresponding to the CH<sub>2</sub> group in the triazole, with catalysts 26 (pink), 27 (blue), 28 (orange), Cu<sub>2</sub>O (green) and an uncatalysed reaction (grey). The black line at 1440 mins corresponds to T = 24 hrs.**

There are some blips in the graphs in Figure 5.32, which are consistent between the catalysts **26**, **27** and **28** and most likely due to error in analysing the <sup>1</sup>H NMR spectra. None-the-less, the graphs of these three catalysts show an overall enhanced catalytic effect compared to Cu<sub>2</sub>O. The role of the copper source in catalysing the reaction is supported by the nil product formation in the uncatalysed reaction studied simultaneously in the first study.

In all cases, the peak catalytic activity is reached within 28 hours for **26**, **27** and **28**, whereas the slower activity of Cu<sub>2</sub>O results in its maximum catalytic potential around 30 hours. From these graphs, it is noted that the copper(I) oxide species undergoes an initiation period, whilst the other catalysts do not. Catalysts **26** and **27** interestingly show very similar catalytic behaviour in both carousel rounds (Figure 5.32) despite the doubled copper loading in **26**. Common to these two copper complexes are the *isopropyl* substituents on the PyBOX ligands, and considering the possibility that the tetranuclear complex, **26** may dissociate in solution to give an active catalyst similar to that given by complex **27**, this may explain their similarities in the catalytic behaviour.

Catalyst **28** does show a reaction progression curve most similar in shape to that observed from complexes **26** and **27**. However, **28** is less catalytically active in both rounds, with a significantly lower product formation after the same amount of time as **26** and **27**, but still more efficient than Cu<sub>2</sub>O. The lower activity of **28** could be rationalised by the bulkier *tert*butyl substituents which hinders any species accessing the catalytic copper centre. However as is the case with complexes **27** and **28**, it is not certain whether the active species is the dinuclear helicate itself or a dissociated mononuclear analogue of this. The different counter-ions are irrelevant in solution as such complexes would exist as cationic species in solution.

The catalytic activity of all three catalysts plateaus after 30 hours and for copper(I) oxide due to catalyst decay, which is commonly observed in catalytic reactions,<sup>460</sup> is observed from this point. While the kinetics of catalyst **28** are slower, evident from the less steep gradient in the first 28 hours, the overall product conversion rate is also lower than observed with **26** and **27**. This shows a more limited efficacy of this catalyst. Between catalysts **26** and **27**, **26** has slightly slower kinetics in the first 28 hours, this can be understood by the potential extra dissociation step required in order to achieve the active catalyst. However, **26** and **27** do overall reach the same product conversion as each other after 48 hours. In light of the greater copper ratio of **26**, this shows that complex **27** exceeds the catalytic capabilities of all three complexes studied herein, which agrees well with that reported by Panera *et al.* in their catalysis studies on propargylamines.<sup>442</sup>

The repeated experiment in the carousel confirms the observed catalytic activities of catalysts **26** and **27** from the first round. The copper(I) oxide shows similar results to the first carousel study, in which some product conversion occurs but at a significantly slower rate than the other catalysts. The overall catalyst kinetic activities follow the order of Cu<sub>2</sub>O < **28** < **26** < **27** in both studies, consistent with initial studies.

An obvious conflict between the two sets of data obtained using the carousel is the final catalytic performance of catalyst **28**, which is shown to succeed over **26** and **27**

in the product conversion achieved after 27 hours. Even though the first carousel round agrees well with that observed from the test reaction of catalyst **28**, a repeat study of this catalyst would need to be done in order to clarify this result. The second carousel round shows a loss of catalytic activity of **26**, **27** and **28** after 28 hours, which could be due to decay in the catalyst.<sup>460</sup> Further investigation on the kinetics would prove beneficial to understand the relative stabilities of the complexes and intermediates involved and therefore their reaction pathways.

Furthermore, all these catalysts were crystallised from acetonitrile and the catalytic reactions were performed in acetonitrile, which is also a coordinating solvent. Catalysts **27** and **28** were actually synthesised from their respective tetrakisacetonitrile copper(I) salt and so it is possible that some fraction of these complexes may even equilibrate back to this species in solution. To eliminate the possibility of this affecting the catalytic behaviour, it would be sensible to study the catalytic activity in a different non-coordinating solvent of similar polarity, such as nitromethane. It should also be noted that this reaction originally was performed neat and therefore a study in a non-coordinating solvent would confirm the catalytic activity being independent of the solvent.

In the case of **26**, whilst the precise catalytic activity is uncertain due to the incorrect mol% ratio used in the studies, it can be expected that the catalytic activity may be poor compared to the dinuclear complexes. This is due to the possibility of copper iodides reforming in solution which may impede catalytic activity, which was reported by Panera *et al.* who observed a decreased catalytic efficiency in the presence of halides.<sup>442</sup>

From these studies it is clear that the reaction progression is enhanced when the catalyst features the PyBOX ligand, as the copper(I) oxide – catalysed reactions show much lower product conversion. The electron-withdrawing effect of the PyBOX ligand perhaps contributes to a lower stability and therefore increased reactivity of the copper centre. Considering the results found by Panera *et al.*, a copper(I) helicate featuring the phenyl- substituted PyBOX ligand may be more catalytically active than the *isopropyl*- substituted complexes, which would be worth studying in future. It is also worth noting that screening of the copper(II)-PyBOX complexes **22-24** on the azide-alkyne click reaction, showed no catalytic activity.

The tetrahedral coordination of one of the copper sites in complex **27** is particularly stable as this is coordinatively saturated. Therefore if this is the catalytic site, this tetrahedral site can only be observed in the pre-catalyst and the active catalyst must be of a lower coordination number. The other copper centre with a linear geometry (coordination number = 2) is most likely an active catalytic site in this case as it has a vacant site for reagents to bind. While complex **28** contains a tricoordinate and

bicoordinate copper centre, which are coordinatively unsaturated, the added bulkiness of the *tert*butyl ligands may hinder their catalytic activity. Panera *et al.* proposed both the copper(I) centres in a tricoordinate geometry as their active species, though this was a tentative speculation as they concluded the active catalyst structure to be unknown.<sup>442, 461</sup>

The two carousel rounds show a product conversion achieved with Cu<sub>2</sub>O as the catalyst that is conflicting between the two studies. Therefore, it is imperative to repeat these studies, with the necessary aforementioned adjustments, before any further conclusions can be drawn.

### 5.3 Conclusion

A series of copper(II) PyBOX and thioPyBOX complexes have been synthesised with a view to achieving an efficient catalyst for copper(II) catalysed reactions such as an Ullman coupling reaction. These are [Cu((S)-PyBOX<sup>Ph</sup>)(OTf)<sub>2</sub>], **22**, [Cu((S)-thioPyBOX<sup>Ph</sup>)(OTf)][OTf], **23** and [Cu((S)-PyBOX<sup>tBu</sup>)(OTf)<sub>2</sub>], **24**. The bis- complex [Cu((S)-thioPyBOX<sup>tBu</sup>)<sub>2</sub>][OTf]<sub>2</sub>, **25** was also isolated in one of the reaction attempts.

The copper(II)-PyBOX<sup>R</sup> complexes (**22** and **24**) both show two coordinated triflates species, whilst the thioPyBOX complex **23** shows only one coordinated triflate, whilst the other behaves as a counter-ion. While the greater electron-withdrawing nature of the PyBOX ligands over the thioPyBOX ligand may destabilise the copper centre, making it more reactive and potentially more catalytically active, the lower coordination number of the thioPyBOX complex and cationic nature of the complex may render this complex a particularly effective catalyst. For these reasons, catalytic studies of these complexes would be particularly interesting. Owing to time constraints no catalysis studies of the Ullman coupling was carried out on these copper(II) complexes. However, it is worth noting that screening of the copper(II) complexes **22-24** in the azide-alkyne click reaction showed no catalytic activity.

A series of copper(I) PyBOX complexes were also synthesised; [Cu<sub>4</sub>I<sub>4</sub>((R)-PyBOX<sup>iPr</sup>)<sub>2</sub>], **26** and [Cu<sub>2</sub>((S)-PyBOX<sup>iPr</sup>)<sub>2</sub>][PF<sub>6</sub>]<sub>2</sub>, **27**, which have both been previously reported.<sup>442, 443</sup> Additionally, [Cu<sub>2</sub>((S)-PyBOX<sup>tBu</sup>)<sub>2</sub>][BF<sub>4</sub>]<sub>2</sub>, **28** was synthesised which has not been reported in the literature. The research by Panera *et al.* did not include any PyBOX<sup>tBu</sup> complexes.<sup>442, 443</sup> In reaction attempts, two other complexes were isolated, [Cu((R)-PyBOX<sup>Ph</sup>)<sub>2</sub>][PF<sub>6</sub>]<sub>2</sub>, **29** and [FCu<sub>3</sub>((R)-PyBOX<sup>Ph</sup>)<sub>3</sub>][BF<sub>4</sub>]<sub>2</sub>, **30**.

Preliminary catalysis studies were obtained for the click reaction of benzyl azide with phenyl acetylene, catalysed by complexes **26**, **27** and **28**. Overall the catalytic activity of **27** is the best, which agrees well with the findings by Panera *et al.*<sup>442</sup> The *tert*butyl



analogue, **28** showed less efficient catalytic activity in comparison despite the lower coordination number at one of the copper sites, most likely due to the increased steric bulk around the active centre. Complex **26** shows catalytic activity comparable to **27** however the mol% was mistakenly doubled of this complex in the carousel reactions so a conclusion cannot be accurately drawn about the behaviour of this complex. As these complexes are di- and tetra- nuclear species, it is unknown whether the active species is a dissociated form of these complexes. Evidence of some catalytic behaviour occurring provides the basis for exploring this work further with *in situ* analysis of the catalysts in real-time of the reaction progression. This would provide an understanding of the active species involved and the reaction mechanism.

## 5.4 Experimental

The instrument methods and techniques followed are as those outlined in Sections 2.4 and 3.4. Complexes **22-24** were synthesised according to the method reported by Evans *et al.*<sup>322</sup> and complexes **26-28** were synthesised according to the method reported by Panera *et al.*<sup>442, 443</sup>

**22. [Cu((S)-PyBOX<sup>Ph</sup>)(OTf)<sub>2</sub>].** (S)-PyBOX<sup>Ph</sup> (50.5 mg, 0.14 mmols, 1 eq.) was dissolved in DCM (20 mL) before Cu(OTf)<sub>2</sub> (49.5 mg, 0.14 mmols, 1 eq.) was added. The light blue solution was stirred for 2 hours at room temperature (20 °C). The solvent was then removed to give a light blue powder. A few drops of acetonitrile (~ 2-3 mL) was added to the powder until fully dissolved, and slow diffusion of diethyl ether into this concentrate afforded blue crystals of complex **22** (76.5 mg, 77%). **HRMS [ES]<sup>+</sup> [L+H]<sup>+</sup>** Predicted: 370.1511, Found: 370.1438. **[M+L]<sup>2+</sup>** Predicted: 432.0773, Found: 432.0637.

**23. [Cu((S)-thioPyBOX<sup>Ph</sup>)(OTf)][OTf]. L2** (99.3 mg, 0.29 mmols, 1 eq.) was dissolved in DCM (29 mL) before Cu(OTf)<sub>2</sub> (90.1 mg, 0.29 mmols, 1 eq.) was added. The cloudy green solution and was left to stir overnight (16hrs, 20 °C) after which the solution darkened in colour and became clear. The solvent was removed affording a green powder. A few drops of acetonitrile (~ 2-3 mL) was added to the powder until fully dissolved, and slow diffusion of diethyl ether into this concentrate afforded dark green needles of complex **23** (129 mg, 62%). **HRMS [ES]<sup>+</sup> [M+L]<sup>2+</sup>** Predicted: 464.0316, Found: 464.0305. **[M+2L]<sup>+</sup>** Predicted: 865.1337, Found: 865.1339. **Elemental analysis calculated (%)** C 40.32, H 2.76, N 6.97; found C 40.31, H 2.63, N 6.15.

**24. [Cu((S)-PyBOX<sup>tBu</sup>)(OTf)<sub>2</sub>].** (S)-PyBOX<sup>tBu</sup> (99.8 mg, 0.30 mmols, 1 eq.) was dissolved in DCM (29 mL) before Cu(OTf)<sub>2</sub> (109.7 mg, 0.30 mmols, 1 eq.) was added. The solution immediately turned clear blue and was left to stir overnight (16hrs, 20

°C). The solvent was removed affording a blue powder. A few drops of acetonitrile (~ 2-3 mL) was added to the powder until fully dissolved, and slow diffusion of diethyl ether into this concentrate afforded blue crystals of complex **24** (159.6 mg, 73%). **HRMS [ES]<sup>+</sup> [L+H]<sup>+</sup>** Predicted: 330.2537, Found: 330.2610. **Elemental analysis calculated (%)** C 37.73, H 4.13, N 7.65; found C 37.75, H 3.85, N 7.32.

**25. [Cu((S)-thioPyBOX<sup>tBu</sup>)<sub>2</sub>][OTf]<sub>2</sub>. L6** (70.1 mg, 0.19 mmols, 1 eq.) was dissolved in DCM (15 mL) before Cu(OTf)<sub>2</sub> (72.1 mg, 0.20 mmols, 1.05 eq.) was added. The solution immediately turned yellow then olive green, which darkened over time. The solution was left to stir overnight for a few hours (3 hrs, 20 °C). The solvent was removed affording a green powder. A few drops of nitromethane (~ 2-3 mL) was added to the powder until fully dissolved, and slow diffusion of diethyl ether into this concentrate afforded green crystals of complex **25** (27.4 mg, 11%). Insufficient quantity of sample for analysis.

**26. [Cu<sub>4</sub>((S)-PyBOX<sup>iPr</sup>)<sub>2</sub>].** CuI (134 mg, 0.70 mmols, 1 eq.) was dissolved in MeCN (29 mL) before (S)-PyBOX<sup>iPr</sup> (258 mg, 0.72 mmols, 1 eq.) was added. The solution immediately turned deep orange-red in colour and was left to stir overnight (24 hrs, 20°C). The solvent was removed and a few drops of nitromethane (~ 2-3 mL) was added to the powder until fully dissolved. Slow diffusion of diethyl ether into this concentrate afforded brown crystals of complex **26** (189.1 mg, 20%). **<sup>1</sup>H NMR (400 MHz, CD<sub>3</sub>CN)** δ 8.28 (6H), 4.81 (4H), 4.59 (8H), 4.32 (MeNO<sub>2</sub>)<sup>\*</sup>, 2.25 (4H), 2.05 (MeNO<sub>2</sub>)<sup>\*</sup>, 1.05 (12H), 0.97 (12H). **HRMS [ES]<sup>+</sup> [L+H]<sup>+</sup>** Predicted: 302.1828, Found: 302.1878. **Elemental analysis calculated of 26•Et<sub>2</sub>O (%)** C 31.72, H 3.92, N 5.84; found C 31.81, H 3.56, N 5.90.

**27. [Cu<sub>2</sub>((S)-PyBOX<sup>iPr</sup>)<sub>2</sub>][PF<sub>6</sub>]<sub>2</sub>.** [Cu(MeCN)<sub>4</sub>][PF<sub>6</sub>] (126.8 mg, 0.33 mmols, 1 eq.) was dissolved in DCM (20 mL) before (S)-PyBOX<sup>iPr</sup> (100.7 mg, 0.33 mmols, 1 eq.) was added. The solution immediately turned dark red and was left to stir overnight (18 hrs, 20 °C). The solvent was reduced and an excess of diethyl ether was added affording a dark red-brown powder (136.3 mg, 40%). Single crystals suitable for XRD analysis were obtained from nitromethane/diethyl ether by the vapour diffusion method. **<sup>1</sup>H NMR (400 MHz, CD<sub>3</sub>CN)** δ 8.49 (2H), 8.35 (4H), 5.05 (4H), 4.69 (4H), 4.17 (4H), 1.80 (4H), 0.69 (28H). **HRMS [ES]<sup>+</sup> [L+H]<sup>+</sup>** Predicted: 302.1828, Found: 302.1878. **Elemental analysis calculated (%)** C 40.04, H 4.55, N 8.28; found C 40.29, H 4.57, N 8.19.

**28. [Cu<sub>2</sub>((S)-PyBOX<sup>tBu</sup>)<sub>2</sub>][BF<sub>4</sub>]<sub>2</sub>.** [Cu(MeCN)<sub>4</sub>][BF<sub>4</sub>] (101.6 mg, 0.32 mmols, 1 eq.) was dissolved in DCM (20 mL) before (S)-PyBOX<sup>tBu</sup> (103.7 mg, 0.31 mmols, 1 eq.) was added. The solution immediately turned dark brown and was left to stir over the weekend (48 hrs, 20 °C). The solvent was removed and a few drops of nitromethane (~ 2-3 mL) was added to the powder until fully dissolved. Slow diffusion of diisopropyl

ether into this concentrate afforded red crystals of complex **28** (137.2 mg, 46%). **<sup>1</sup>H NMR (400 MHz, CD<sub>3</sub>CN)** δ 8.17 (6H), 4.57 (4H), 4.31 (MeNO<sub>2</sub>)\*, 4.07 (4H), 2.11 (MeNO<sub>2</sub>)\*, 0.89 (36H). **HRMS [ES]<sup>+</sup> [L+H]<sup>+</sup>** Predicted: 330.2537, Found: 330.2595. **[M+L]<sup>+</sup>** Predicted: 392.1399, Found: 392.1403. **Elemental analysis calculated of 28•MeNO<sub>2</sub> (%)** C 46.70, H 5.65, N 9.20; found C 46.45, H 5.61, N 8.87.

**29. [Cu((R)-PyBOX<sup>Ph</sup>)<sub>2</sub>][PF<sub>6</sub>]<sub>2</sub>.** [Cu(MeCN)<sub>4</sub>][PF<sub>6</sub>] (102.6 mg, 0.28 mmols, 1 eq.) was dissolved in DCM (20 mL) before (R)-PyBOX<sup>Ph</sup> (102.5 mg, 0.28 mmols, 1 eq.) was added. The solution immediately turned dark brown and was left to stir overnight (16 hrs, 20 °C). The solvent was removed and a few drops of nitromethane (~ 2-3 mL) was added to the powder until fully dissolved. Slow diffusion of diisopropyl ether into this concentrate afforded few dark crystals of complex **29**. Yield unobtainable. Insufficient quantity of sample for analysis.

**30. [FCu<sub>3</sub>((R)-PyBOX<sup>Ph</sup>)<sub>3</sub>][BF<sub>4</sub>]<sub>2</sub>.** [Cu(MeCN)<sub>4</sub>][BF<sub>4</sub>] (44.1 mg, 0.14 mmols, 1 eq.) was dissolved in DCM (15 mL) before (R)-PyBOX<sup>Ph</sup> (51.2 mg, 0.14 mmols, 1 eq.) was added. The solution immediately turned dark brown and was left to stir overnight (28 hrs, 24 °C). The solvent was removed and a few drops of acetonitrile (~ 2-3 mL) was added to the powder until fully dissolved. Slow diffusion of diethyl ether into this concentrate afforded few red-orange crystals of complex **30**. Yield unobtainable. Insufficient quantity of sample for analysis.

Analysis of complexes **25**, **29** and **30** were unable to be obtained.

\*Solvent peaks are identified as reported by Gottlieb *et al.*<sup>462</sup>

## Chapter 6

# Ruthenium PyBOX and thioPyBOX Complexes for Asymmetric Catalysis and Biological Activity

### 6.1 Introduction

#### 6.1.1 Asymmetric Catalysis

A variety of chiral ligands have been employed over the last two decades for asymmetric catalysis. These have included Schiff-base/salen motifs, which have been widely employed in the design of chiral metal complexes featuring an N,N'- bidentate bis- or N,N,O,O- tetradentate pincer framework.<sup>253, 463, 464</sup> Other ligand examples have included binaphthols,<sup>465, 466</sup> tartrate derivatives<sup>467</sup> and oxazoline variants such as phosphinooxazolines and bisoxalines.<sup>223, 468, 469</sup>

Ligands with the N,N',N''- pincer motif have been widely demonstrated in catalytic complexes in the literature, and display excellent catalytic activity in a multitude of crucial reactions. Some examples of these have included  $\beta$ -alkylation of alcohols, N-alkylation reactions,  $\alpha$ -methylation of ketones, transfer hydrogenation reactions, C-H amination reactions, epoxidation of olefins and cyclopropanation reactions.<sup>213, 220, 223, 470-475</sup>

Asymmetric catalysis allows for reactions to use achiral starting materials and produce chiral products with enantioselectivity. These reactions are fundamental to the preparation of optically active compounds.<sup>476</sup> Such catalysis has great demand, particularly in industry for ensuring drug molecules for pharmaceutical use are produced purely as the desired enantiomer, or where certain flavours and smells are solely associated with a single enantiomeric form.<sup>250</sup> Chiral metal complexes that serve as asymmetric catalysts, under the right reaction conditions, allow us to achieve this desirable enantiomeric purity.

Though there have been vast developments over the past years in the field of asymmetric catalysis, to date, one of the most challenging aspects of such highly enantioselective reactions, is the asymmetric C-C bond formation - even under catalysed conditions.<sup>477</sup> There has also been a steered interest towards achieving enantioselectivity through asymmetric catalysis in milder conditions such as in water or neat.<sup>424</sup>

In order to fine-tune the catalytic activity, the steric and electronics of the system can be varied to optimise the enantioselectivity, enantiopurity and yields, as small changes in ligand design are sensitive to the catalytic ability of resulting metal complexes. Such

complexes need to be carefully designed. Homogeneous catalysts, enable this greater selectivity desired for application in asymmetric catalysis.<sup>478</sup>

### 6.1.2 Pyridine bis(oxazoline) in Catalysis

The C<sub>2</sub>-symmetric bis(oxazoline) ligand has received a lot of attention for their applications in catalysis. Its inception in the field came from its facile route to synthesis, availability of both diastereomers and ability to further functionalise and fine-tune the ligand.<sup>469</sup> Nishiyama's success in the rhodium(III) trichloride PyBOX catalyst for the hydrosilylation of ketones<sup>197</sup> introduced the PyBOX ligand in the field of asymmetric catalysis. It was following this work that metal-PyBOX complexes became widely employed as chiral metal catalysts.<sup>196</sup>

As demonstrated in Chapter 5, the PyBOX ligand serves as a versatile building block for designing catalytic complexes, as it can coordinate to a wide range of metals and in a different coordination modes, as well as being able to vary the substituents on the ligand to optimise catalytic activity. Examples that have been reported include copper-, nickel-, iron-, lanthanum-, zinc-, titanium-, ruthenium-, rhodium- and palladium- PyBOX complexes.<sup>196, 469, 479</sup>

### 6.1.3 Ruthenium-PyBOX Catalysts

Nishiyama's ruthenium-PyBOX catalyst [Ru(PyBOX<sup>R</sup>)(PyDIC)] (where R = iPr, Ph and PyDIC = pyridine-2,6-dicarboxylate) was demonstrated in the asymmetric epoxidation of *trans*-stilbene.<sup>480</sup> The terpyridine equivalent [Ru(terpy)(PyDIC)] was also studied as a non-chiral model catalyst (Figure 6.1).

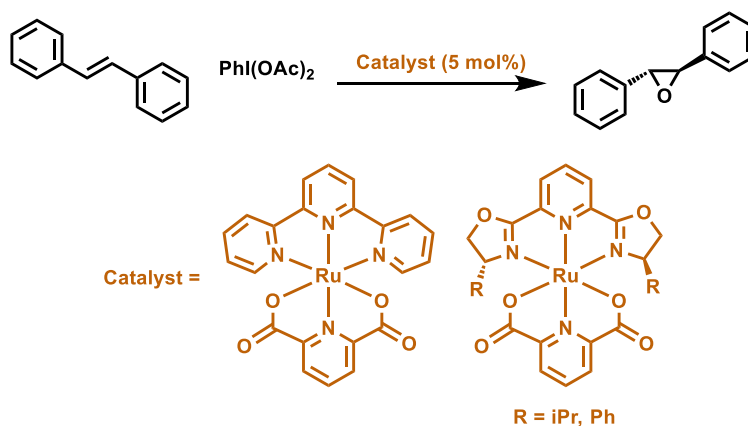
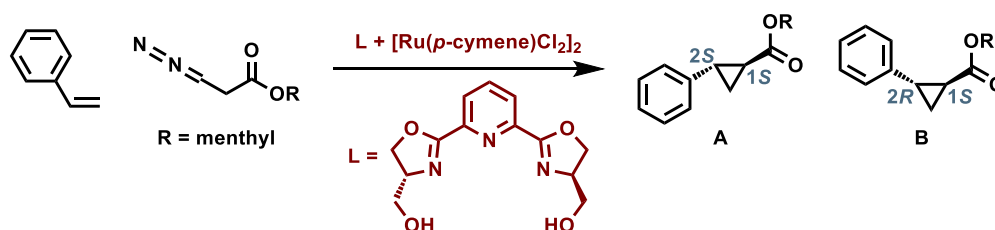


Figure 6.1. Epoxidation of *trans*-stilbene studied by Nishiyama *et al.* catalysed by ruthenium(II) PyBOX complexes; [Ru(PyBOX<sup>R</sup>)(PyDIC)] and [Ru(terpy)(PyDIC)], to give the *trans*-epoxide product.<sup>480</sup>

Their results showed that the catalyst  $[\text{Ru}(\text{PyBOX}^{\text{iPr}})(\text{PyDIC})]$  was particularly efficient at asymmetric induction in the epoxidation of *trans*-stilbene, giving the product in a 74% ee. While the  $\text{PyBOX}^{\text{Ph}}$  analogue formed the epoxide in good yield (84%) under the same conditions, the enantioselectivity was lower (58% ee) than that of the *isopropyl*- complex. Screening of the terpy complex was found to produce the product in a good yield of 92%.<sup>480</sup> Since this work, further improvements have been made to the ruthenium-PyBOX epoxidation reactions.<sup>223, 472, 481</sup>

The ruthenium(II)-PyBOX complex  $[\text{Ru}(\text{hm-PyBOX})(\text{Cl})_2]$  where *hm* = hydroxymethyl which is substituted at the 4-positions of the oxazoline rings, was reported by Iwasa *et al.*<sup>472</sup> This pre-catalyst was found to show increased enantioselectivity and yields in the catalytic cyclopropanation of styrene and methyl diazoacetate (Figure 6.2) in a biphasic solvent system containing water compared to the monophasic organic solvents. This observation was attributed to the high solubility of the ligand in water. The Ru-PyBOX catalyst they employed achieved stereoselectivity of the *trans* product (A) : *cis* product (B) in a ratio of 97 : 3.<sup>472</sup>



**Figure 6.2. The cyclopropanation of styrene with menthyl diazoacetate catalysed by  $[\text{Ru}(\text{hm-PyBOX})\text{Cl}_2]$  studied by Iwasa *et al.*<sup>472</sup>**

Milczek *et al.* employed ruthenium(II) PyBOX catalysts for the enantioselective C-H bond insertion of a sulfamate ester (Figure 6.3) as a follow-on study from initial catalytic findings demonstrated with rhodium-catalysed C-H aminations of sulfamates reported by Fiori and Du Bois.<sup>482</sup> The Ru-PyBOX pre-catalysts studied by Milczek *et al.* were those previously reported by Nishiyama *et al.* for the cyclopropanation of olefins and diazoacetates.<sup>483</sup> Improved catalytic activity and higher ee % was observed when silver(I) triflate was added to the reaction, which was proposed to abstract a halide from the Ru-PyBOX complex generating the active catalyst. It was also found that using the indenyl-PyBOX derivative also significantly improved the reaction conversion and product selectivity. Furthermore, in a comparison of the catalytic behaviour between the catalyst  $[\text{Ru}(\text{X})_2\text{L}(\text{PyBOX})]$  where X = Br or Cl, it was found that the bromide analogue gave overall better yields and ee % than the chloride, further demonstrating how such catalysts can be fine-tuned for optimum catalytic activity.

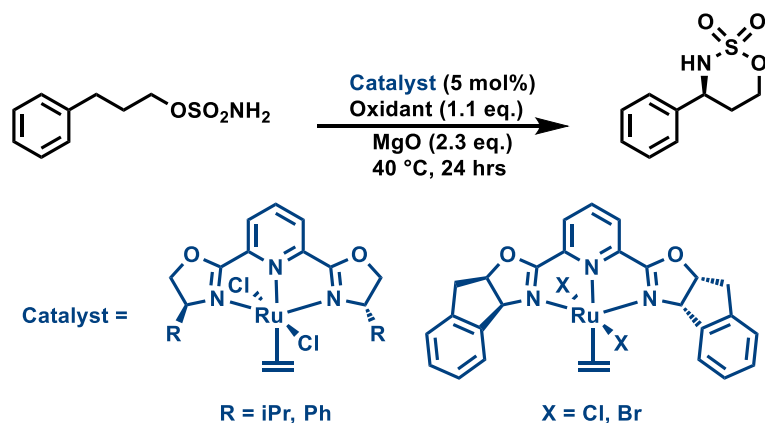


**Figure 6.3. C-H amination reaction studied by Milczek *et al.* using ruthenium(II) PyBOX catalysts.**<sup>474</sup>

### 6.1.4 Transfer Hydrogenation

Industrially, the reduction of C=O and C=N bonds dominantly uses metal hydrides, which results in metallic residues in the product, in addition to the low-atom economy of the process.<sup>364</sup> Therefore alternative metal-based catalysts have been sought out in an effort to achieve efficiently catalysed transfer hydrogenation reactions (Figure 6.4). An added complexity arises from the asymmetric transfer hydrogenation, whereby the hydrogen transfer to the ketone or imine induces a stereocentre in the corresponding alcohol or amine product.<sup>484</sup>



**Figure 6.4. The transfer hydrogenation reaction of a ketone to a secondary alcohol.**<sup>484</sup>

Noyori and Hashiguchi developed ruthenium(II) catalysts featuring C<sub>2</sub>-chiral ligands such as a tetradentate disphosphine-diamine ligand (Figure 6.5), which they studied in the transfer hydrogenation of acetophenone.<sup>470</sup> Cuervo *et al.* later studied C<sub>2</sub>-symmetric rhodium and ruthenium catalysts that incorporate the PyBOX ligand, for transfer hydrogenation reactions.<sup>439, 475, 485</sup>

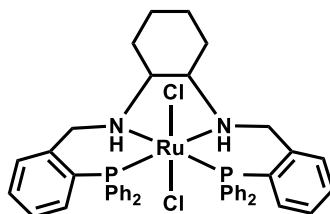


Figure 6.5. One of the  $C_2$ -symmetric ruthenium(II) catalysts studied by Noyori and Hashiguchi.<sup>470</sup>

#### 6.1.4.1 Ruthenium-PyBOX catalysts for Transfer Hydrogenation

The work by Cuervo *et al.* involved studying the catalytic activity of the transfer hydrogenation of acetophenone of the aforementioned ruthenium-PyBOX catalyst  $[Ru(PyBOX^R)CL2(C_2H_4)]$  (Figure 6.3). While Milczek *et al.* focussed on the ethylene complex in their catalytic C-H insertion research,<sup>474</sup> Cuervo *et al.* also investigated changing this L group to various phosphine and phosphite derivatives.<sup>475</sup> Their studies highlighted the importance of the diastereomeric  $PyBOX^{Ph}$  ligand in their ruthenium catalysts, for achieving high catalytic efficiency and enantioselectivity in transfer hydrogenation reactions. The high chiral induction is understood to arise from the position of the ketone when bound to the catalyst in the transition state, and then position of the alcohol due to the chirality of the PyBOX ligand, once it is formed (Figure 6.6).

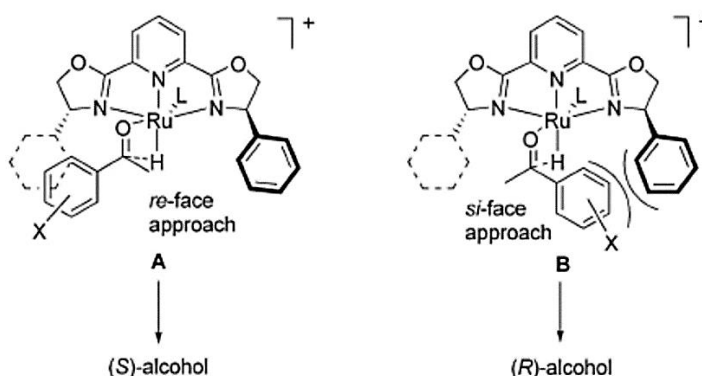


Figure 6.6. Schematic diagram of how the Ru-PyBOX catalyst behaves enantioselectively in the asymmetric transfer hydrogenation reaction of an aromatic ketone. Figure taken from publication.<sup>475</sup>

#### 6.1.5 Ruthenium-PyBOX in Anti-cancer Studies

As ruthenium is the 5<sup>th</sup> row counterpart (2<sup>nd</sup> row of transition metals) of iron, which is omnipresent in the biological world, there is a growing interest in ruthenium-based antitumour drugs that can mimic the biological binding of iron.<sup>486</sup>



Menéndez-Pedregal and Díez added to their studies of ruthenium-PyBOX catalysts with studies of these complexes on the cytotoxic activity against the (human) cervical cancer cell line, HeLa. This research was the first to demonstrate a distinction in the different behaviour of ruthenium enantiomers on the HeLa tumour cell cycle.<sup>487</sup> The cytotoxic activity of *trans*-chloro- ruthenium complexes bearing the *isopropyl*-PyBOX ligand and 1,3,5-triaza-7-phosphaadamantane (PTA) was found to be rather poor and inefficient due to the requirement of high concentrations and long incubation time before DNA degradation was observed. However, the different activity of the ruthenium enantiomers observed in the cell cycle has provided a basis for studying the cytotoxic activity of these PyBOX complexes further. This work corroborates the diversity of applications of chiral ruthenium-PyBOX complexes.

## 6.2 Results & Discussion

### 6.2.1 Ruthenium-N,N',N''- Complexes Synthesised

The research carried out in this section endeavoured to build on the existing library of Ruthenium-PyBOX complexes for catalytic applications, particularly transfer hydrogenation reactions. Owing to time constraints, some initial synthesis work on such complexes is presented, along with a preliminary test round of catalysis on the transfer hydrogenation of acetophenone. Additionally, the cell line testing of two of these complexes is also presented herein.

#### 6.2.1.1 Ruthenium-terpyridine complexes

In efforts to achieve the optimal synthetic route to ruthenium-PyBOX complexes, terpyridine (terpy) was used as a model N,N',N''-tridentate ligand. The terpy ligand was used as it is a well-known and readily available N,N',N''- ligand that is thermally and oxidatively stable.<sup>488</sup> In these attempts, two ruthenium-terpy complexes were isolated; a mono- terpy complex,  $[\text{Ru}(\text{terpy})(\text{MeCN})_2\text{Cl}][\text{PF}_6]$ , **31** and a dicationic bis-terpy complex  $[\text{Ru}(\text{terpy})_2][(\text{PF}_6)_2]$ , **32** (Figure 6.7).

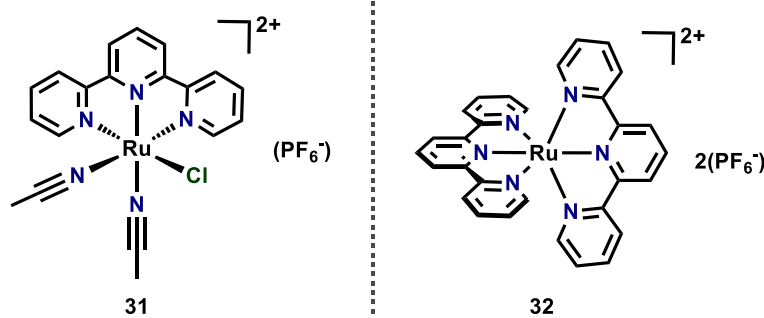


**Figure 6.7. Structures of [Ru(terpy)(MeCN)<sub>2</sub>Cl][PF<sub>6</sub>]<sub>2</sub>, **31** (left) and [Ru(terpy)<sub>2</sub>][(PF<sub>6</sub>)<sub>2</sub>], **32** (right).**

Complexes **31** and **32** were both synthesised from the dichloro ruthenium(II) dimer, [Ru(*p*-cymene)CL<sub>2</sub>]<sub>2</sub> by addition of the terpyridine ligand and ammonium hexafluorophosphate. The synthesis of **31** was carried out in acetonitrile following an adaptation of a previously reported preparation of cationic ruthenium half-sandwich complexes with a 2-substituted-1,8-naphthyridine ligand.<sup>489</sup> The synthesis of complex **32** was intended to also achieve a mono-terpy complex without the acetonitrile ligands bound. In order to achieve this, the reaction was carried out in methanol following reported experiments with the bidentate analogue, bipyridine (bpy).<sup>490</sup> This reaction however formed the bis-terpy complex instead.

The complexes were isolated by the growth of single crystals by diffusion of pentane into a concentrate of the samples in dichloromethane. While this was unsuccessful across the whole batch, some crystals which were grown gave the structures of **31** and **32** by XRD analysis (Figure 6.8). The Ru-N<sub>terpy</sub> and Ru-N<sub>MeCN</sub> bond lengths obtained from these structures (where relevant) are tabulated in Table 6.1 along with the clamp angle,  $\varphi$ , of the meridional terpy ligand (N-Ru-N), the dihedral angle,  $\theta$ , between the two terpy ligands, in the case of **32**. The *trans*-N<sub>terpy</sub>-Ru-N<sub>MeCN/terpy</sub> angle across the axial position,  $\phi$ , is also tabulated.

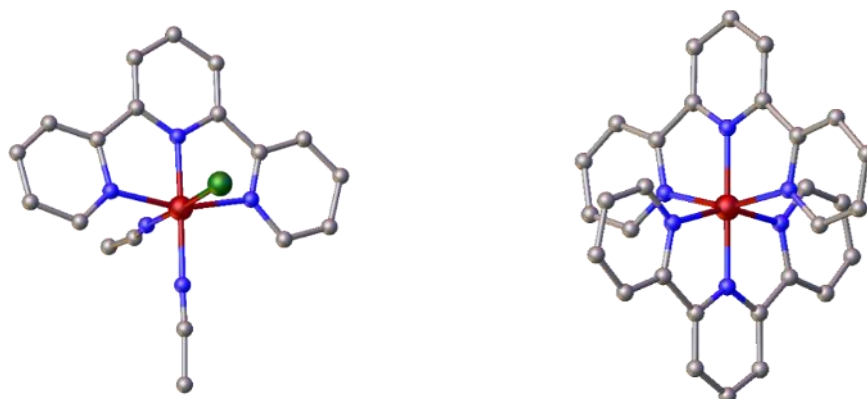


**Figure 6.8. XRD structures obtained of **31** (left) and **32** (right). Hydrogen atoms, counter-ions and solvents are omitted for clarity. Structures are shown as a ball and stick model for clarity.**

	<b>31</b>	<b>32</b>
<b>Ru-N<sub>(terpy)</sub> (Å)</b>	2.04(3) - 2.12 (3)	1.974(6) - 2.076(6),
<b>Ru-N<sub>(MeCN)</sub> (Å)</b>	1.98(4), 1.95(4)	-
<b>N-Ru-N, <math>\varphi</math> (°)<sub>terpy</sub></b>	157.4(11)	158.3(2), 158.0(3)
<b><math>\theta</math> (°)</b>	-	88.332
<b>N-Ru-N, <math>\phi</math> (°)<sub>axial</sub></b>	176.7(14)	178.8(2)

**Table 6.1. Selected bond lengths and angles from the XRD structure solutions of 31 and 32.**

The XRD structures of **31** and **32** show very similar bond lengths and angles to each other. The dihedral angle between the two planes of the terpyridine ligands in **32** shows minimal deviation from a typical octahedral geometry ( $\theta = 90^\circ$ ) as is the case with the *trans* axial N-Ru-N angles of **31** and **32** which are very close to the ideal  $\phi = 180^\circ$ . The clamp angle,  $\varphi$  (also referred to as the bite angle), of the terpy ligand (N-Ru-N) is relatively small which is known in such octahedral complexes.<sup>491</sup>

Though other mono-terpy complexes of ruthenium(II) have been discussed in the literature,<sup>488, 492, 493</sup> complex **31** has not yet been reported, which has been confirmed against the CCSD. The complex [Ru(terpy)(PPh<sub>3</sub>)Cl<sub>2</sub>], which is similar to **31**, was studied in the cross-coupling of an alcohol by Gnanamgari *et al.*<sup>488</sup> This complex gave much more efficient catalytic behaviour compared to other ruthenium(II) standards such as the dichloro ruthenium *p*-cymene dimer, [Ru(*p*-cymene)Cl<sub>2</sub>]<sub>2</sub>. The trichloro analogue of their catalyst, [Ru(terpy)Cl<sub>3</sub>] also gave relatively good conversion of product, suggesting these results are due to the terpy ligand.

The bis-terpy ruthenium(II) complex **32**, has however been previously reported in the literature, as an acetone solvate,<sup>494</sup> and a dimethylformamide (DMF) solvate,<sup>495</sup> of the hexafluorophosphate salt. **32** is however a DCM solvate of the complex which has not previously been reported. Crystallographic structures of other salts of [Ru(terpy)<sub>2</sub>]<sup>2+</sup> such as the perchlorate salt,<sup>496</sup> the tetrafluoroborate salt,<sup>497</sup> have also been previously reported.

## 6.2.2 Ruthenium-PyBOX complexes

Following on from these model complexes, ruthenium(II)-PyBOX complexes were then explored, using a similar protocol to that with the terpy complexes. Again, the dichloro *p*-cymene ruthenium dimer was used as a source of ruthenium(II), similarly to how Noyori and Hashiguchi used [RuCl<sub>2</sub>( $\eta^6$ -hexamethylbenzene)]<sub>2</sub> and [RuCl<sub>2</sub>( $\eta^6$ -benzene)]<sub>2</sub> dimers to synthesise their ruthenium(II) complexes.<sup>470</sup> Herein, a mono-PyBOX<sup>Ph</sup> ruthenium

complex,  $[\text{Ru}((R)\text{-PyBOX}^{\text{Ph}})\text{Cl}_2\text{MeCN}]$ , **33** and a bis-PyBOX<sup>Ph</sup> ruthenium complex,  $[\text{Ru}((R)\text{-PyBOX}^{\text{Ph}})]_2[\text{BF}_4]_2$ , **34**, were synthesised. These complexes were synthesised in a similar protocol to their terpy analogues, but using silver(I) tetrafluoroborate in place of ammonium hexafluorophosphate in the synthesis of **34**. Complex **33** was synthesised using acetonitrile as the solvent, whereas switching the solvent to a less-coordinating solvent (acetone in the case of **34**) formed the bis-complex, as was observed with the terpy model complexes.

The XRD structures obtained of **33** and **34** are shown below in Figure 6.9 and selected XRD data are tabulated in Table 6.2.

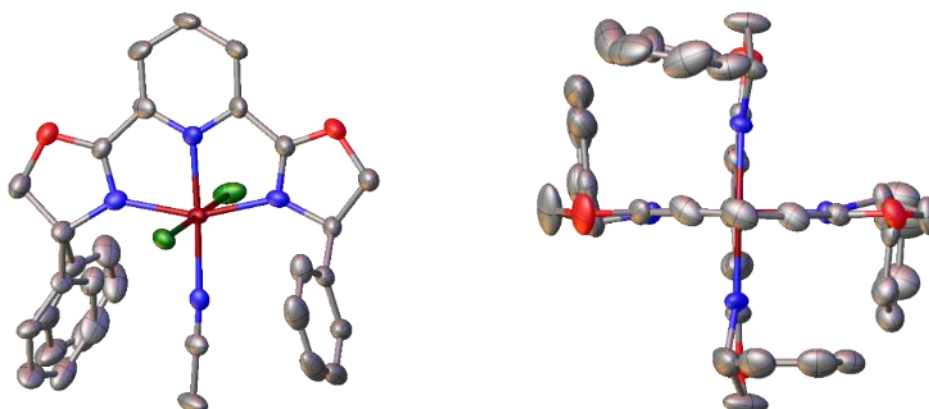


Figure 6.9. XRD structures of  $[\text{Ru}((R)\text{-PyBOX}^{\text{Ph}})\text{Cl}_2\text{MeCN}]$ , **33** (left) and  $[\text{Ru}((R)\text{-PyBOX}^{\text{Ph}})]_2[\text{BF}_4]_2$ , **34** (right). Hydrogen atoms, solvents and counter-ions are omitted for clarity. Thermal ellipsoids are at the 50% probability level.

	<b>33</b>	<b>34</b>
<b>Ru-N<sub>(terpy)</sub></b> (Å)	2.078(6) – 1.946(5)	1.994(5)-2.071(4)
<b>Ru-N<sub>(MeCN)</sub></b> (Å)	2.050(5)	-
<b>Ru-Cl</b> (Å)	2.403(16), 2.388(14)	-
<b>N-Ru-N, <math>\varphi</math> (°)<sub>terpy</sub></b>	157.2(2)	155.1(2), 155.5(2)
<b><math>\theta</math> (°)</b>	-	87.999
<b>N-Ru-N, <math>\phi</math> (°)<sub>axial</sub></b>	176.2(2)	179.3(2)
<b>Cl-Ru-Cl (°)</b>	178.59(7)	-

Table 6.2. Selected bond lengths and angles from the XRD structure solutions of **33** and **34**.

A comparison of complexes **33** against **31** show similar geometric features such as the Ru-N<sub>terpy</sub> bond lengths which are not too dissimilar from each other and a coordinated acetonitrile moiety *trans* to the central pyridine ring in both complexes. Complex **33** was crystallised from the less polar solvent, dichloromethane, whereas **31** was crystallised

from the more polar dimethylformamide. This difference in crystallisation solvents could reason the formation of a neutral complex in the case of **33** but an ionic complex in the case of **31**. The large chloride ions coordinate *trans* to each other to accommodate for their larger atom size.

Complex **34** also has a very similar geometry to its terpy analogue **32** despite the different counter-ions. The Ru-N<sub>terpy</sub> bond lengths are almost within error of each other, and the dihedral angle,  $\theta$ , and the *trans* N<sub>Py</sub>-Ru-N<sub>Py</sub> angle,  $\phi$ , are the same between the complexes. The clamp angle,  $\varphi$ , is slightly smaller in **34** than in **32** (155 ° compared to 158 °) due to the smaller size of the PyBOX ligand. The CCSD confirms that neither of the crystal structures of **33** or **34** have previously been reported.

### 6.2.2.1 Ruthenium-PyBOX *trans*-iodide complexes

With a view to achieving an effective catalyst, the synthesis of mono-PyBOX ruthenium(II) complexes was pursued, knowing this can successfully be achieved when acetonitrile is involved in their synthesis. Furthermore, the effect of swapping chloride ions for iodide was explored in the synthesis of the catalyst. The study by Milczek *et al.* which found that substituting chloride with bromide in their complexes achieved better catalytic activity,<sup>474</sup> inspired this investigation.

Two complexes, [Ru((*S*)-PyBOX<sup>Ph</sup>)<sub>2</sub>MeCN], **35** and an *isopropyl* analogue, [Ru((*R*)-PyBOX<sup>iPr</sup>)<sub>2</sub>MeCN], **36** have been synthesised. The source of the iodide ions in these reactions came from using the iodo- analogue of the ruthenium(II) dichloro *p*-cymene dimer, which is [Ru(*p*-cymene)I<sub>2</sub>]<sub>2</sub>. **35** was synthesised following the experimental procedure used for the synthesis of **33**, while complex **36** was synthesised in DCM. However, with this reaction, the DCM solvent was completely removed before the complex was set up to crystallise from acetonitrile/diethyl ether, providing the source of acetonitrile to coordinate forming the same complex.

The XRD structures obtained of **35** and **36** are shown in Figure 6.10 and selected bond lengths and angles are in Table 6.3.

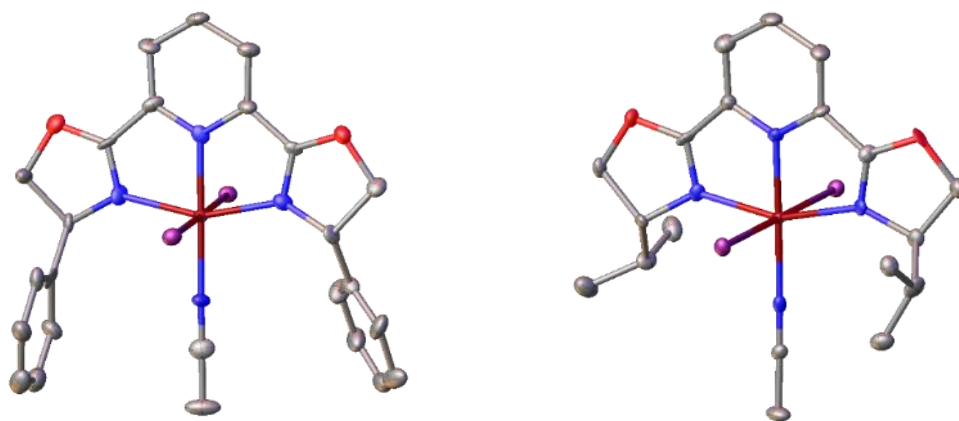


Figure 6.10. XRD structures of [Ru((*S*)-PyBOX<sup>Ph</sup>)I<sub>2</sub>MeCN], **35** (left) and [Ru((*R*)-PyBOX<sup>iPr</sup>)I<sub>2</sub>MeCN], **36** (right). Hydrogen atoms, solvents and counter-ions are omitted for clarity. Thermal ellipsoids are at the 50% probability level.

	<b>35</b>	<b>36</b>
Ru-N <sub>(PyBOX)</sub> (Å)	1.950(11) - 2.063(10)	1.964(6) – 2.121(6)
Ru-N <sub>(MeCN)</sub> (Å)	2.029(11)	2.052(7)
Ru-I (Å)	2.718(10), 2.711(10)	2.704(4), 2.699(7)
N-Ru-N, $\varphi$ (°) <sub>PyBOX</sub>	156.4(5)	156.4(3)
N <sub>Py</sub> -Ru-N <sub>MeCN</sub> , $\phi$ (°)	178.6(4)	178.6(3)
I-Ru-I (°)	178.98(4)	179.15(3)

Table 6.3. Selected bond lengths and angles from the XRD structure solutions of **35** and **36**.

The data obtained from the XRD structures of **35** and **36** are very similar to each other with regards to all bond lengths and angles, which is as expected for this pair of complexes. The iodide ions sit almost perfectly *trans* to each other across the ruthenium in both complexes with angles  $\sim 179^\circ$ . Catalysis using these complexes may be particularly interesting. The CCSD confirms that these structures have not been previously reported, nor are there any similar complexes featuring iodide ions.

Considering the literature discussed regarding PyBOX complexes in catalysis, the overarching theme is that *isopropyl*-PyBOX complexes are particularly good catalysts. From this, it is plausible that complex **36** has potentially good catalytic activity.

### 6.2.3 An unprecedented hemilabile Ru-thioPyBOX complex

A continuous narrative of this thesis has been the effect of swapping of the PyBOX ligand for thioPyBOX. In keeping with this theme, the synthesis of complex **35** was repeated but with the thioPyBOX<sup>Ph</sup> ligand. This gave the complex [Ru((*R*)-thioPyBOX<sup>Ph</sup>)<sub>2</sub>][I<sub>3</sub>], **37**. While the bulk sample was not purified, some single crystals of this complex were obtained by slow diffusion of diethyl ether into a concentrate of the sample in N,N'-dimethylformamide. The XRD structure obtained of **37** is shown below in Figure 6.11 and relevant bond lengths and angles are tabulated in Table 6.4.

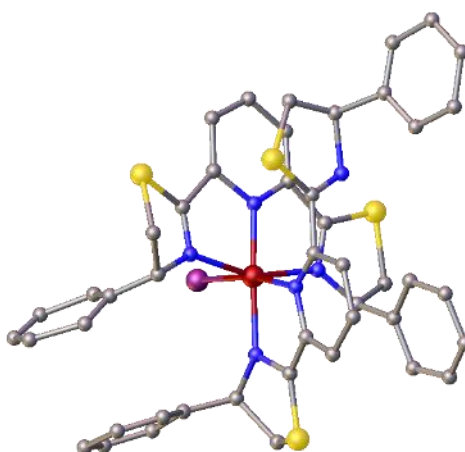


**Figure 6.11.** XRD structure solution of [Ru((*R*)-thioPyBOX<sup>Ph</sup>)<sub>2</sub>][I<sub>3</sub>], **37** (left). Hydrogen atoms and counter-ions are omitted for clarity. Ball and Stick model is shown for clarity.

	<b>37</b>
<b>Ru-N<sub>(PyBOX)</sub> (Å)</b>	1.94(3) - 2.16(3)
<b>Ru-I (Å)</b>	2.708(4)
<b>N-Ru-N, <math>\varphi</math> (°)<sub>PyBOX</sub></b>	155.4(14)
<b><math>\theta^*</math> (°)</b>	79.321
<b>N<sub>Py</sub>-Ru-N<sub>MeCN</sub>, <math>\phi</math> (°)</b>	173.8(14)
<b>N<sub>Py</sub>-Ru-I (°)</b>	170.9(9)

**Table 6.4.** Selected bond lengths and angles from the XRD structure solutions of **37**. \* The dihedral angle,  $\theta$ , was measured between the planes of only the coordinated parts of the thioPyBOX ligands.

Most interesting about this structure is the partial coordination of one of the thioPyBOX ligands which coordinates in a bidentate manner, whereas the other ligand is coordinated in its typical tridentate mode. The uncoordinated thiazoline ring is no longer in the plane of the pyridine ring and other thiazoline, but is now rotated by 78 ° out of the

plane of the rest of the ligand. This is to accommodate for the ring and the phenyl substituent, as to minimise steric clash. To satisfy the 18-electron rule, the ruthenium atom bonds with an iodine ion in place of this thiazoline ring. This preferential bonding can be rationalised by the more ionic nature of the Ru-I bond compared to the dative-covalent Ru-N bond (X vs. L – type ligand).

The Ru-N bond lengths and the clamp angle,  $\varphi$ , are reasonable as these values agree with those observed in the ruthenium-PyBOX complexes **33-36**. The dihedral angle,  $\theta$ , however, is significantly deviated ( $79^\circ$ ) from the ideal  $90^\circ$ . This is due to the partially coordinated thioPyBOX ligand, in which the coordinated thiazoline ring is quasi-planar. Of the tridentately-coordinated thioPyBOX ligand, one of these thiazoline rings is also quasi-planar. Inspection of the structure from the angle shown in Figure 6.12 shows that these thiazoline conformations are due to the phenyl substituents that are clashing with each other, causing the phenyl groups to cant, and the thiazoline rings bend to accommodate this.

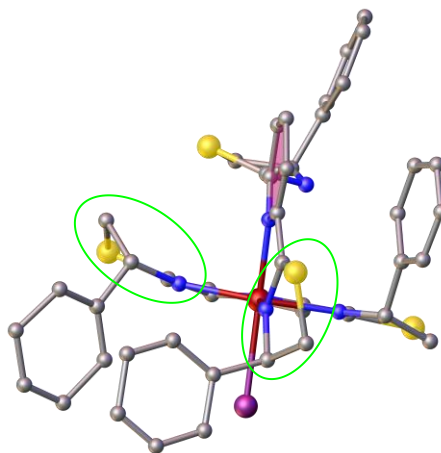


**Figure 6.12. XRD structure 37 highlighting the bent conformation of two of the thiazoline rings.**

There is an offset  $\pi$ - $\pi$  stacking motif with these phenyl substituents, which is supported by the centroid-centroid distance of  $3.8 \text{ \AA}$  between the two rings. This is close to the typical value of  $3.5 \text{ \AA}$  of  $\pi$ - $\pi$  stacking distances.<sup>498</sup> Furthermore, there is also an offset  $\pi$ - $\pi$  interaction between the pyridine ring and the uncoordinated thiazoline ring, of  $3.4 \text{ \AA}$ , which further rationalises the rotated configuration of this ring.

This partial binding of one of the thioPyBOX ligands could be a subtle blend of sterics and electronics. The added steric bulk from the sulfur atom of the thiazolines may hinder full coordination compared to oxazolines. It's also plausible that the stronger electron-donating character of thioPyBOX compared to PyBOX results in further displacement of an iodide from the ruthenium, whereas the less electron-donating PyBOX ligand simply forms the mono-ligand, diiodo complex (**35**). That highlights how significantly a complex



formation can be impacted by changing oxygen for sulfur in a ligand. This hemilability could have good potential prospects in catalysis studies and it would be particularly interesting to identify what the active catalyst would be from this precatalyst i.e. whether the Ru-I bond cleaves or whether the hemilabile thioPyBOX ligand shifts to create a vacant site.

#### 6.2.4 Preliminary catalysis work

Preliminary catalysis work was carried out on complexes **35** and **36** on the transfer hydrogenation as has been previously demonstrated.<sup>470, 475</sup> The reaction studied was the reduction of acetophenone to 1-phenylethanol (Figure 6.13) following the preparation employed by Holmes *et al.*<sup>499</sup> The internal standard used was 1,3,5-trimethoxybenzene (TMB) and the reaction progression was monitored by <sup>1</sup>H NMR. The quantity of 1-phenylethanol was measured by the integration of the methyl group which splits into a doublet at  $\delta$  1.4 ppm due to the Ph-CH<sub>2</sub>-Me proton. This proton is not in the starting material and the methyl group of acetophenone appears as a singlet at  $\delta$  2.52 ppm, which is distinct from the product.

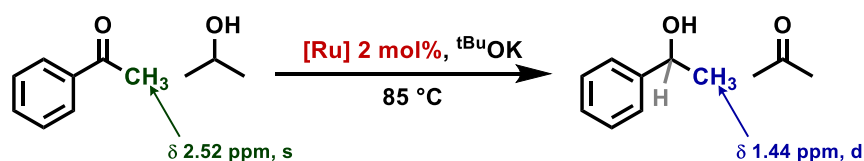


**Figure 6.13.** The transfer hydrogenation of acetophenone.  $[Ru]$  is the ruthenium(II) catalyst employed,  $tBuOK$  is the base, potassium tertbutoxide. The reaction was carried out in isopropanol.

These results from this initial catalysis study are shown in the graph in Figure 6.14, for comparison, an uncatalysed reaction was ran in parallel, as were the ruthenium(II) *p*-cymene dichloro and diiodo dimers. The catalyst loading was 2 mol% for both the dimers, **35** and **36**. Owing to time constraints a repeat was not carried out, however if it was carried out, the catalyst loading would have been changed as to use 4 mol% for the dimers (2 mol% per Ru).

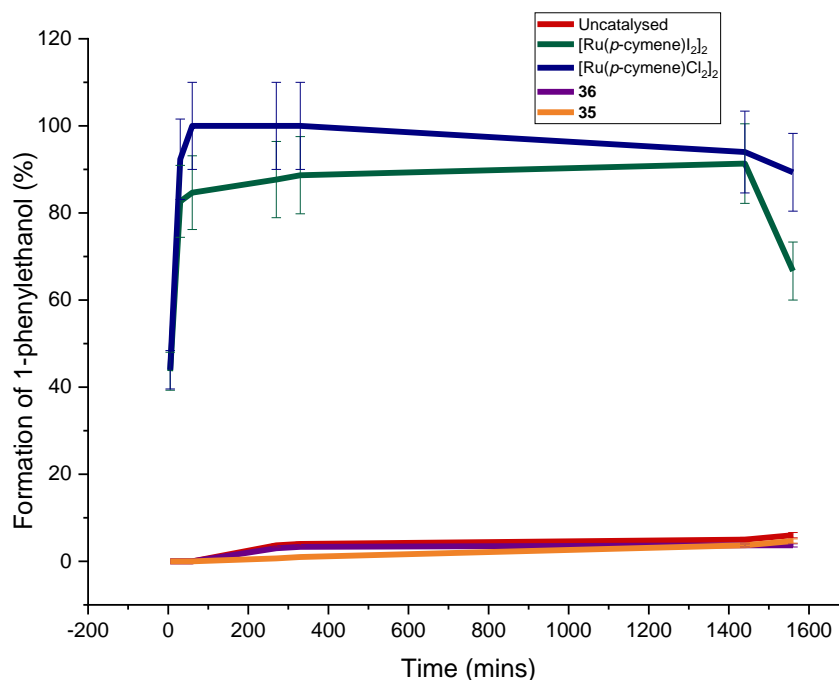


**Figure 6.14. Preliminary catalysis examination of complexes 35 and 36. An uncatalysed reaction and two standard reactions catalysed by [Ru(*p*-cymene)Cl<sub>2</sub>]<sub>2</sub> and [Ru(*p*-cymene)I<sub>2</sub>]<sub>2</sub> were simultaneously performed for comparison.**

The robustness of this catalysis study is demonstrated in the results obtained with both the ruthenium(II) *p*-cymene dimers, which despite their lower catalyst loading, still reach very high product conversion by  $T = 1$  hour. The dichloro dimer does slightly outperform the diiodo analogue, reaching 100% conversion when the diiodo dimer reaches just over 80% product conversion.

Unfortunately this data shows **35** and **36** to be completely ineffective, giving product conversion data analogous to the uncatalysed reaction. This suggests the precatalysts may be too stable in the solution, and therefore do not form an active species with a vacant site, do not partake in catalysis but rather act as a spectator. Or, it is possible that the catalysts are too unstable in solution and so immediately decompose, resulting in no active catalyst for the reaction. Cardierno *et al.* reported the high stability of the complex *trans*-[RuCl<sub>2</sub>(PPh<sub>2</sub>)(PyBOX<sup>H</sup>)] which was observed in a solution study which heated the complex in methanol for hours and found the complex to remain unaffected.<sup>475, 500</sup>

Considering that both **35** and **36** have null catalytic results, it can be concluded that ineffective product conversion is not due to the different substituents (phenyl versus *isopropyl*) of the catalysts, but rather is most likely due to a feature of the complex that is mutual to both these complexes such as the iodide ions, the neutrality of the ruthenium atom or the PyBOX ligand system.

Further studies are required to investigate this further. Such research should include studying the catalytic activity of the chloride analogue (**33**) to determine the effect of the halide, stability studies of the catalysts in solution, primarily isopropanol, studying the terpy complex or other mono-N,N',N'' – tridentate ruthenium(II) complexes and researching analogous complexes that are cationic.

## 6.2.5 Biological Investigation

Inspired by Menéndez-Pedregal and Díez on their ruthenium-PyBOX complexes that were studied for cytotoxic activity,<sup>487</sup> two complexes herein, **35** and **36** were screened against the pancreatic cancerous cell line, MIA PaCa-2 and the human bone osteosarcoma cell line, 143B for cytotoxic activity. Of the ruthenium complexes discussed thus far, **35** and **36** were pursued in these biological studies as previous studies within the McGowan group have reported an increased cytotoxicity and selectivity towards cancerous cell lines when rhodium(III) *trans*-dichloro picolinamide complexes were replaced with their diiodo counterparts.<sup>501</sup> While the ruthenium analogues showed equitoxicity between these halides, the *trans*-iodide motif in **35** and **36** are particularly intriguing.

### 6.2.5.1 Cell-line testing

Cell-line testing was performed by Dr. Rianne Lord at the University of East Anglia. Cell viability assays were conducted using human cell lines: bone osteosarcoma (143B) and pancreatic carcinoma (MIA PaCa-2). Both cell lines were routinely maintained as monolayer cultures (T25 or T75 flasks) in DMEM medium (contains sodium pyruvate (1 mM) and L-glutamine (2 mM)) supplemented with 10% foetal calf serum. Prior to chemosensitivity studies, cell monolayers were passaged using 0.25% trypsin-EDTA and diluted to a concentration of  $1 \times 10^4$  cells/mL. All assays were conducted using 96-well plates, in which 100  $\mu$ L of the cell suspension was added to each well (column 1 – medium only to serve as a blank) and incubated for 24 h (96 h assay) or 48 h (48 h assay) at 37 °C and 5% CO<sub>2</sub> to ensure sufficient adhesion to the plates. All complex stock solutions, 100 mM in dimethyl sulfoxide (DMSO), were freshly prepared on the day of incubation. After 24 h or 48 h (assay dependent), 100  $\mu$ L of drug dilutions in DMEM medium, were added to the plates in (columns 3-12 - column 1 contains medium only and column 2 contains 100% cells to serve as a control), and incubated for a further 48 or 96 h (assay dependent) at 37°C and 5% CO<sub>2</sub>. After the correct incubation time, cell viability was measured using the MTT assay. 3-(4,5-dimethylthiazol-2-yl)-2,5-diphenyltetrazolium bromide (20  $\mu$ L, 5 mg/mL in d.H<sub>2</sub>O) was added to each well and

incubated for 3 h at 37°C and 5% CO<sub>2</sub>. All solutions were then removed via pipette and 150 µL of DMSO added to each well and mixed thoroughly. The absorbance of the plates was measured at 540 nm using a CLARIO star LABTECH spectrophotometer microplate reader, and results were plotted on a logarithmic scale. The half maximal inhibitory concentration (IC<sub>50</sub>) was determined from duplicate of triplicate repeats and reported as an IC<sub>50</sub> ± Standard Deviation (SD).

The results found from this biological investigation are shown below in Figure 6.15.

### 6.2.5.2 Results

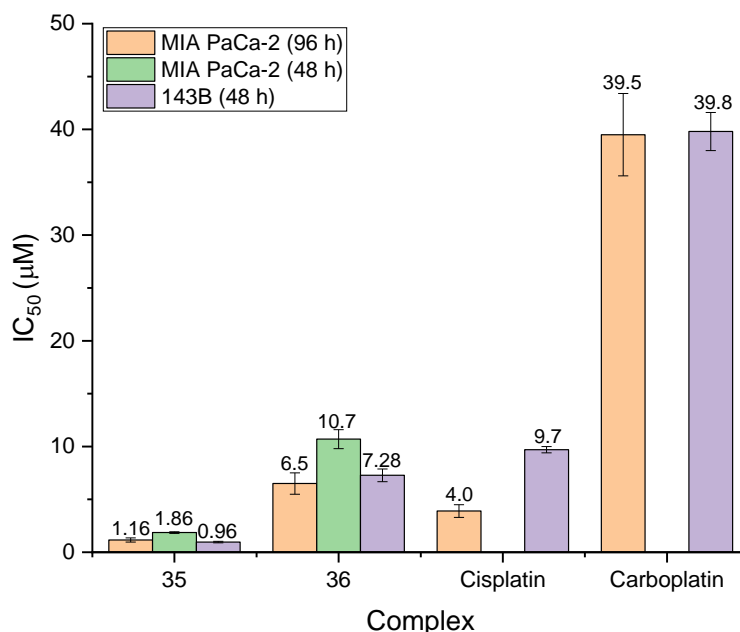


**Figure 6.15. The IC<sub>50</sub> values obtained of complexes 35, 36 cisplatin (CDDP) and carboplatin (CARB) against the pancreatic cancer cell line (MIA PaCa-2) (48 h – green\*, 96 h - orange) and the osteosarcoma cell line (143B) (48 h – purple). \*IC<sub>50</sub> values for cisplatin and carboplatin are pending. Results are obtained from duplicate of triplicate repeats.**

The IC<sub>50</sub> values of complexes **35** and **36** (Figure 6.15) both show strong cytotoxic activity, comparable to CDDP and CARB, against the two cell lines tested. Complex **35** is particularly potent against these cancerous cell lines, with the 48 hour incubation against the 143B cells giving the best result. This result has a nanomolar potency (IC<sub>50</sub> = 0.96 µM) which is more than ten times more active than cisplatin (IC<sub>50</sub> = 9.70 µM), and more than forty times more active than carboplatin (IC<sub>50</sub> = 39.80 µM). Complex **36** against 143B is also more active than cisplatin and carboplatin, but to a much lesser extent as these results give fairly similar values. Against the pancreatic cell line, MIA PaCa-2, **35** again shows significantly stronger activity than cisplatin. These results are particularly promising for these ruthenium-PyBOX complexes.

Considering studies that have shown enantiomers of chiral, octahedral ruthenium(II) complexes with different cellular uptake behaviour<sup>502</sup> and different interaction modes with DNA,<sup>487, 503</sup> it would be particularly interesting to study the chirality aspect of the PyBOX ligand in these complexes. This would involve investigating the cytotoxic activity of the isomers of **35** and **36** to determine if the chirality of the ligand affects the observed anticancer behaviour.

### 6.3 Conclusion

Seven ruthenium-based complexes have been synthesised herein, six of which have not been previously reported in the literature; [Ru(terpy)(MeCN)<sub>2</sub>Cl][PF<sub>6</sub>], **31**, [Ru((*R*)-PyBOX<sup>Ph</sup>)Cl<sub>2</sub>MeCN], **33**, [Ru((*R*)-PyBOX<sup>Ph</sup>)] [BF<sub>4</sub>]<sub>2</sub>, **34**, [Ru((*S*)-PyBOX<sup>Ph</sup>)I<sub>2</sub>MeCN], **35**, [Ru((*R*)-PyBOX<sup>iPr</sup>)I<sub>2</sub>MeCN], **36** and a ruthenium-thioPyBOX complex, [Ru((*R*)-thioPyBOX<sup>Ph</sup>)<sub>2</sub>I][I<sub>3</sub>], **37**.

The synthesis of complexes **31** and **32**, and **33** and **34**, have demonstrated how control over the formation of mono- and bis- N,N',N''-tridentate metal complexes can be achieved, through using different solvents of different coordinating abilities. Carrying out the same reaction in acetonitrile achieves the mono- N,N',N'' complex, while the same reaction in methanol (in the case of **32**) or acetone (in the case of **34**) achieved the bis-complexes.

Complexes **35** and **36** feature a *trans* iodide motif along with one PyBOX<sup>R</sup> ligand. These complexes were screened for catalytic activity in a preliminary study of the transfer hydrogenation of acetophenone, however neither showed any catalytic activity. A significant more amount of work is required to investigate this further. It is possible that the bis-N,N',N'' –tridentate complexes, **32** and **34**, may still have catalytic potential, as Nishiyama demonstrated studied with similarly 'dual closed meridonal stereotopes'.<sup>480</sup> So these complexes may also be worth screening for catalytic activity, along with the chloro- analogue of **35**, **33**.

However, the biological investigations of **35** and **36** do appear promising. Cytotoxic activity is observed by **35**, which is more potent than cisplatin and carboplatin against pancreatic cancer cells and most notably, human bone cancer cells.

## 6.4 Experimental

The instrument methods and techniques followed are as those outlined in Sections 2.4 and 3.4.

**31. [Ru(terpy)(MeCN)<sub>2</sub>Cl][PF<sub>6</sub>].** [Ru(*p*-cymene)Cl<sub>2</sub>]<sub>2</sub>\* (103.2 mg, 0.17 mmols, 1 eq.) was dissolved in acetonitrile (20 mL). Ammonium hexafluorophosphate (67.3 mg, 0.41 mmols, 2.4 eq.) was added followed by commercially available 2,2':6',2''-terpyridine (76.7 mg, 0.33 mmols, 1.9 eq.). The solution was left to stir for 5 hours. The solution was filtered to remove the ammonium chloride salt and the filtrate was collected and concentrate to a third of the solvent. The concentrate was cooled to 0 °C in an ice bath. To aid precipitation, diethyl ether was added to the concentrate (1-2 mL) and the solution was left in the freezer overnight (18 hrs, 18 °C). The dark brown precipitate was then collected by filtration. Single crystals suitable for XRD analysis were obtained by diffusion of diethyl ether into a concentrate of the sample in DMF (17.2 mg, 36%). **<sup>1</sup>H NMR (400 MHz, CD<sub>3</sub>Cl)** δ 9.00 (d, 2H, J = 5 Hz), 8.03 (dd, 4H, J = 5, 8 Hz), 7.85 (dt, 3H, J = 2, 8 Hz), 7.57 (t, 2H, J = 2, 6 Hz), 2.78 (s, 3H), 1.99 (s, 3H). **HRMS [ES]<sup>+</sup> [M-2MeCN+MeOH]<sup>+</sup>** Predicted: 401.9942, Found: 401.9578. **Elemental analysis calculated (%)** C 38.23, H 2.87, N 11.73; found C 38.08, H 3.00, N 11.57.

**32. [Ru(terpy)<sub>2</sub>][(PF<sub>6</sub>)<sub>2</sub>].** [Ru(*p*-cymene)Cl<sub>2</sub>]<sub>2</sub>\* (100.6 mg, 0.16 mmols, 1 eq.) was in methanol (10 mL). Commercially available 2,2':6',2''-terpyridine (89.7 mg, 0.38 mmols, 2.3 eq.) was then added and the reaction mixture was left to stir for 1 hour before ammonium hexafluorophosphate (86.9 mg, 0.53 mmols, 3.3 eq.) was added. The reaction was stirred for a further hour. The solvent was then removed and the black precipitate was washed with diethyl ether and left in the freezer over the weekend (48 hrs, -18°C). The sample was then filtered by vacuum filtration to give a black powder (107 mg, 38%). Growth of single crystals was attempted by diffusion of pentane into a concentrate of the sample in DCM, however this afforded a powder. Bright red single crystals suitable for XRD analysis were then successfully grown by diffusion of diethyl ether into a concentrate of the sample in DMF. **<sup>1</sup>H NMR (400 MHz, CD<sub>3</sub>CN)** δ 8.74 (d, 4H, J = 7 Hz), 8.48 (d, 4H, J = 8 Hz), 8.40 (t, 4H, J = 8 Hz), 7.90 (dt, 3H, J = 2, 8 Hz), 7.33 (d, 4H, J = 6 Hz), 7.15 (dt, 3H, J = 2, 6 Hz). **HRMS [ES]<sup>+</sup> [ML<sub>2</sub>]<sup>2+</sup>** Predicted: 284.0475, Found: 284.0472. **Elemental analysis calculated of 32•0.5DCM (%)** C 40.70, H 2.58, N 9.34; found C 40.96, H 2.79, N 9.53.

**33. [Ru((*R*)-PyBOX<sup>Ph</sup>)Cl<sub>2</sub>MeCN][BF<sub>4</sub>]<sub>2</sub>.** [Ru(*p*-cymene)Cl<sub>2</sub>]<sub>2</sub>\* (104 mg, 0.17 mmols, 1 eq.) was dissolved in acetonitrile (5 mL). Ammonium hexafluorophosphate (67.5 mg, 0.41 mmols, 2.4 eq.) was added and stirring was continued for a few minutes before commercially available (*R*)-PyBOX<sup>Ph</sup> (79.6 mg, 0.22 mmols, 1.3 eq.) was added. The solution darkened from red to brown and a further 5 mL of acetonitrile was added. The reaction mixture was left to stir overnight (16 hrs, 20 °C). The solution was then left at -

18 °C for a few hours before a liquid-liquid extraction (DCM/H<sub>2</sub>O) was carried out to remove the ammonium chloride salt. The DCM layer was combined with the MeCN layer, dried (MgSO<sub>4</sub>), filtered and the solvent was removed. Single crystals suitable for XRD analysis were obtained by diffusion of pentane into a concentrate of the sample in chloroform (106.3 mg, 83%). **<sup>1</sup>H NMR (400 MHz, CD<sub>3</sub>Cl)** δ 7.91 (d, 3H, J = 8 Hz), 7.57 (d, 1H, J = 7 Hz), 7.35 (m, br, 7H), 7.12 (t, br, 2H), 5.45 (t, br, 2H), 5.32 (d, 1H, J = 10 Hz), 5.23 (t, 1H, J = 10 Hz), 4.99 (t, 1H, J = 9 Hz), 4.57 (t, br, 1H), 2.02 (d, 3H, J = 6 Hz). **HRMS [ES]<sup>+</sup> [M-Cl-MeCN]<sup>+</sup>** Predicted: 506.0209, Found: 506.0201, **[M+Cl-MeCN]<sup>+</sup>** Predicted: 575.9586, Found: 575.0530.

**34. [Ru((*R*)-PyBOX<sup>Ph</sup>)<sub>2</sub>][BF<sub>4</sub>]<sub>2</sub>.** [Ru(*p*-cymene)Cl<sub>2</sub>]<sub>2</sub><sup>\*</sup> (103 mg, 0.17 mmols, 1 eq.) was dissolved in acetone (10 mL). Silver(I) tetrafluoroborate (61.5 mg, 0.32 mmols, 1.9 eq.) was added and stirring was continued for a few minutes before commercially available (*R*)-PyBOX<sup>Ph</sup> (124.7 mg, 0.34 mmols, 2 eq.) was added. The dark brown-black solution was left to stir overnight (20 hrs, 25 °C). The solvent was removed, leaving a black solid. Ethanol (10 mL) was added to the black solid giving a dark brown-red solution which was decanted from the residual black precipitate. The solution was evaporated to dryness giving a dark brown powder which was dried under nitrogen overnight (50 mg, 58%). A single crystal suitable for XRD analysis was obtained from this by slow diffusion of the sample concentrated in DCM. No analysis was obtained for this complex.

**35. [Ru((*S*)-PyBOX<sup>Ph</sup>)<sub>2</sub>MeCN].** [Ru(*p*-cymene)I<sub>2</sub>]<sub>2</sub><sup>\*</sup> (48.8 mg, 0.05 mmols, 1 eq.) was dissolved in acetonitrile (15 mL) giving a deep red solution. After half an hour, commercially available (*S*)-PyBOX<sup>Ph</sup> (35.6 mg, 0.10 mmols, 2 eq.) was added. The reaction mixture was left to stir overnight (22 hrs, 20 °C). The solvent was then reduced and diffusion of diethyl ether into the concentrate afforded dark red-black crystals suitable for XRD analysis (63.2 mg, 86%). **<sup>1</sup>H NMR (400 MHz, CD<sub>3</sub>Cl)** δ 7.97-7.92 (m, 2H), 7.82 (d, 1H, J = 8 Hz), 7.74 (d, 1H, J = 7.8 Hz), 7.65 (t, 1H, J = 7.7 Hz), 7.60 (d, 3H, J = 7.6 Hz), 7.41-7.31 (m, 10H), 7.13 (d, 1H, J = 2 Hz), 5.43 (dd, 1H, J = 2, 10 Hz), 5.31 (dd, 1H, J = 3.5, 8 Hz), 5.25 (t, 2H, J = 8 Hz), 4.65 (dd, 2H, J = 3.5, 9 Hz), 2.33 (s, 3H). **HRMS [ES]<sup>+</sup> [L+H]<sup>+</sup>** Predicted: 370.1511, Found: 370.1582, **[M-I-MeCN]<sup>+</sup>** Predicted: 597.9565, Found: 597.9567.

**36. [Ru((*R*)-PyBOX<sup>iPr</sup>)<sub>2</sub>MeCN].** [Ru(*p*-cymene)I<sub>2</sub>]<sub>2</sub><sup>\*</sup> (45.8 mg, 0.05 mmols, 1 eq.) was dissolved in DCM (15 mL) giving a deep red solution. After an hour, commercially available (*R*)-PyBOX<sup>iPr</sup> (30.7 mg, 0.10 mmols, 2 eq.) was added. The reaction mixture was left to stir overnight (22 hrs, 20 °C). The solvent was then removed and acetonitrile (2-3 mL) was added to the solid. Diffusion of diethyl ether into this concentrate afforded dark red-black crystals suitable for XRD analysis (38.4 mg, 54%). **<sup>1</sup>H NMR (400 MHz, CD<sub>3</sub>Cl)** δ 7.71 (d, 2H, J = 8 Hz), 7.62 (dd, 1H, J = 1.8, 8 Hz), 4.86-4.78 (m, 4H, J = 2, 8.3 Hz), 4.36 (dd+t, 2H, J = 3, 7 Hz), 2.78 (s, 3H), 2.51 (dsept, 2H, J = 3, 7 Hz), 1.09 (d, 6H, J = 7 Hz), 1.04 (d, 6H, J = 7 Hz). **HRMS [ES]<sup>+</sup> [M]<sup>+</sup>** Predicted: 697.9189, Found:

697.9185. **Elemental analysis calculated (%)** C 32.73, H 3.76, N 8.03; found C 32.68, H 3.83, N 7.90.

**37. [Ru((*R*)-thioPyBOX<sup>Ph</sup>)<sub>2</sub>][I<sub>3</sub>].** [Ru(*p*-cymene)I<sub>2</sub>]<sub>2</sub>\* 58.9 mg, 0.06 mmols, 1 eq.) was dissolved in DCM (15 mL) giving a deep red solution. After an hour, (*R*)-thioPyBOX<sup>Ph</sup>, **L1**, (77 mg, 0.19 mmols, 3.2 eq.) was added. The reaction mixture was left to stir overnight (16 hrs, 20 °C). The solvent was then removed and acetonitrile (2-3 mL) was added to the solid. Diffusion of diethyl ether into this concentrate afforded a black powder of **37** (40.5mg, 26%). Some crystals suitable for XRD analysis were obtained by a DMF/Et<sub>2</sub>O crystallisation system. **<sup>1</sup>H NMR (400 MHz, CD<sub>3</sub>CN)** δ NMR too dilute to read and insufficient quantity of sample to repeat NMR. **HRMS [ES]<sup>+</sup> [L+Na]<sup>+</sup>** Predicted: 424.0918, Found: 424.0906. **[M-L+I+MeCN]<sup>+</sup>** Predicted: 797.8419, Found: 797.8411. **Elemental analysis calculated of 31•2.75DMF (%)** C 33.65, H 2.36, N 4.83; found C 33.52, H 2.52, N 5.10 .

\*[Ru(*p*-cymene)I<sub>2</sub>]<sub>2</sub> was commercially supplied from Sigma Aldrich and [Ru(*p*-cymene)Cl<sub>2</sub>]<sub>2</sub> was synthesised in-house (3.51 g, 66%) using a method reported in the literature.<sup>504</sup>



## Future Work Prospects

The heteroleptic complexes demonstrated in chapter 4 were particularly interesting and are worth pursuing. Owing to time constraints, the studies on complexes **12-19** were essentially incomplete and whilst the iron(II) PyBOX<sup>Ph</sup>/1-bpp complex, **18**, showed SCO activity, it would be interesting to study the thioPyBOX analogue of this complex through crystallographic means, but also heteroleptic iron(II) 1-bpp/PyBOX<sup>R</sup> complexes with different R- substituents. Solid and solution state studies of these complexes with phase pure samples would be a useful study.

The copper and ruthenium PyBOX and thioPyBOX complexes should also be explored further, as these projects were discontinued. For the catalytically competent copper(I) PyBOX<sup>R</sup> complexes, **26-28**, further studies on their catalytic activity, synthetic reproducibility, phase purity and reaction specificity are crucial. Full characterisation of all the complexes is also essential. It would be crucial to investigate whether the same catalytic activity is observed in a solvent medium other than acetonitrile as the crystals were grown from acetonitrile. Synthesis of the thioPyBOX analogues of complexes **26-28** would also be worth investigating to determine whether these are also catalytically active.

The ruthenium(II)PyBOX complexes need to be synthesised again to determine the robustness of the synthesis of these complexes, but also to complete the characterisation of the novel ruthenium PyBOX and thioPyBOX complexes reported herein. Further catalysis studies on different reactions and on the same transfer hydrogenation reaction but under different reaction conditions, to understand if there is any catalytic potential in these complexes.

Cell line testing of the *R*- enantiomer of the ruthenium(II) PyBOX complex, **35**, would be an interesting study to determine whether the anticancer potency discovered is limited to an enantiomer. Further synthetic attempts to achieve the thioPyBOX analogue of complex **35** and **36** would be interesting to understand if the effect of swapping oxygen for sulfur impacts the cytotoxicity of the complex. Furthermore, it would be worth investigating the cytotoxicity of the thioPyBOX complex **37**.

## Overall Conclusions

Six variations of the ligand, 2,6-bis(thiazolanyl)pyridine (thioPyBOX), **L1-L6**, have been presented herein, with the substituents phenyl, *isopropyl* and *tertbutyl*, in both the (R,R)- and (S,S)- diastereomeric forms. These ligands were fully characterised including XRD structures obtained for the *isopropyl* and *tertbutyl* ligands. The synthetic strategies employed, reaction optimisation and purification work was discussed in detail, contributing to the eight existing pieces of literature that discuss the synthesis of thioPyBOX. A macrocyclic product formed in attempted thioPyBOX synthesis was also presented, which has previously been synthesised, however an XRD structure had not been obtained.

A series of homochiral and heterochiral iron(II) thioPyBOX<sup>R</sup> complexes (**R/S-5**, **RS-5**, **R/S-6**, **RS-6**, **S-7**, **S-7i** and **S-8**) were synthesised and their spin state behaviour was studied in the solid and solution states. The concept of chiral discrimination of spin states was corroborated with the pair of enantiomers, **RS-6** and **S-6**, displaying a high spin-low spin dichotomy at ambient conditions. The homochiral complex **R-5** showed crystallographic distortion at 100 K akin to that observed in the previously reported PyBOX analogue, **R-1**, but still underwent an abrupt spin transition in the solid state at 330 K. This is attributed to the steric clash of the phenyl rings occupying the same molecular quadrant. The *tertbutyl* complexes, **S-7** and **S-8** remained HS independent of temperature and in both the solid and solution states. This is owing to the bulky *tertbutyl* substituents which 'locks' the distorted structure in the HS state as the LS-HS transition would be accompanied by a structural rearrangement with a too large energy cost, which therefore does not occur.

Heteroleptic iron(II) (thio)PyBOX complexes (**R-9**, **RS-9**, **S-10**, **RS-10** and **S-11**) were synthesised and their SCO behaviours studied. Interestingly, the homochiral heteroleptic complexes did not form in a pure 1:1:1 iron:PyBOX:thioPyBOX ratio unlike the heteroleptic homochiral complexes. Other heteroleptic combinations have also been presented with N,N',N''-tridentate pincer ligands (**12-21**), which was found to support the overall findings observed with the iron(II) thioPyBOX series. The overall findings demonstrated an increased stability of metal-thioPyBOX complexes compared to their PyBOX counterparts, attributed to the reduced electron-withdrawing nature of thiazoline compared to oxazoline donor groups.

This can be rationalised as follows. Thiazoline is less electron-withdrawing than oxazoline due to its sulfur atom being less electronegative than oxygen. This results in a reduced electron-withdrawing effect in the six dative coordinate Fe-N bonds of the complex. This in turn, increases the ligand field experienced by the Fe<sup>2+</sup> centre, which results in a greater crystal field splitting energy,  $\Delta_{\text{oct}}$ . Therefore, more 'low-spin like'

behaviour of iron(II)thioPyBOX complexes is observed compared to their PyBOX counterpart.

A series of copper(II) PyBOX and thioPyBOX complexes are presented (**22-25**), with an aim to achieve an effective catalyst for reactions such as the Ullman Coupling. Copper(I) PyBOX complexes have also been synthesised in this chapter (**26-30**); these form dinuclear and tetranuclear helicate structures. An unprecedented trinuclear copper(I)-PyBOX cyclic helicate has also been synthesised. An initial catalysis study of the copper(I) helicates was presented on an azide-alkyne cycloaddition reaction, which interestingly shows catalytic competency, however further work is required to investigate the mechanism by which this occurs and the active species involved.

Mono- and bis- coordinated ruthenium-terpy and ruthenium-PyBOX complexes (**31-37**) have also been presented, which demonstrated how different coordination modes can be achieved through experimental design. An attempt at incorporating the thioPyBOX ligand resulted in a bis-thioPyBOX ruthenium complex with a hemilabile coordination of one of the ligands. Finally, biological investigation on the cytotoxic activity of two of these complexes, **35** and **36**, against pancreatic cancer cells, MIA-PaCa-2 and human bone cancer cells, 143B, was presented with greater anticancer activity than *cisplatin*.

## Appendix

### X-ray Diffraction Crystallographic Data

Suitable single crystals of each complex were immersed in Fomblin, mounted on the goniometer head of an Agilent SuperNova, Dual, Atlas diffractometer at home (Mo-K $\alpha$ , ( $\lambda = 0.71073 \text{ \AA}$ ) or Cu-K $\alpha$ , ( $\lambda = 1.54184 \text{ \AA}$ )), or using Synchrotron radiation ( $\lambda = 0.6889 \text{ \AA}$ ) at Diamond Light Source, Beamline I19. The crystals were cooled using an Oxford Cryostream low temperature device, and were kept at the specified temperature during data collection. Using Olex2,<sup>505</sup> the structure was solved with the olex2.solve or SHELXT structure solution program<sup>506-508</sup> using either Charge Flipping or Intrinsic Phasing and refined with the SHELXL<sup>509</sup> refinement package using Least Squares minimisation. All structures were collected by the author, with the exceptions of **M1**, **S-9**, **15**, **17**, **34** which were collected by Dr. Christopher Pask and **14** which was collected by Dr. Kay Burrows.

#### Chapter 2 XRD data

##### **L4 C<sub>17</sub>H<sub>23</sub>N<sub>3</sub>S<sub>2</sub> (M =333.50 g mol<sup>-1</sup>)**

Monoclinic, space group  $P2_1$  (no. 4),  $a = 9.3863(12) \text{ \AA}$ ,  $b = 12.4194(11) \text{ \AA}$ ,  $c = 15.6458(14) \text{ \AA}$ ,  $\beta = 100.184(10)^\circ$ ,  $V = 1795.1(3) \text{ \AA}^3$ ,  $Z = 4$ ,  $T = 119.96(18) \text{ K}$ ,  $\mu(\text{Cu K}\alpha) = 2.674 \text{ mm}^{-1}$ ,  $D_{\text{calc}} = 1.234 \text{ g/cm}^3$ , 6756 reflections measured ( $9.148^\circ \leq 2\theta \leq 148.15^\circ$ ), 6756 unique ( $R_{\text{int}} = 0.145$ ,  $R_\sigma = 0.0737$ ) which were used in all calculations. The final  $R_1$  was 0.0681 ( $I > 2\sigma(I)$ ) and  $wR_2$  was 0.1655 (all data).

##### **L6 C<sub>19</sub>H<sub>27</sub>N<sub>3</sub>S<sub>2</sub> (M =361.55 g mol<sup>-1</sup>)**

Orthorhombic, space group  $P2_12_12_1$  (no. 19),  $a = 5.94714(18) \text{ \AA}$ ,  $b = 17.5480(4) \text{ \AA}$ ,  $c = 18.4646(5) \text{ \AA}$ ,  $V = 1926.97(9) \text{ \AA}^3$ ,  $Z = 4$ ,  $T = 119.99(12) \text{ K}$ ,  $\mu(\text{Cu K}\alpha) = 2.529 \text{ mm}^{-1}$ ,  $D_{\text{calc}} = 1.246 \text{ g/cm}^3$ , 7857 reflections measured ( $6.95^\circ \leq 2\theta \leq 147.312^\circ$ ), 3704 unique ( $R_{\text{int}} = 0.0329$ ,  $R_\sigma = 0.0459$ ) which were used in all calculations. The final  $R_1$  was 0.0374 ( $I > 2\sigma(I)$ ) and  $wR_2$  was 0.0862 (all data).

##### **L5•L6 C<sub>19</sub>H<sub>27</sub>N<sub>3</sub>S<sub>2</sub> (M =361.55 g mol<sup>-1</sup>):**

Triclinic, space group  $P-1$  (no. 2),  $a = 11.8205(5) \text{ \AA}$ ,  $b = 12.6843(5) \text{ \AA}$ ,  $c = 13.5361(6) \text{ \AA}$ ,  $\alpha = 96.660(3)^\circ$ ,  $\beta = 101.084(3)^\circ$ ,  $\gamma = 90.294(3)^\circ$ ,  $V = 1977.47(14) \text{ \AA}^3$ ,  $Z = 4$ ,  $T = 120.00(10) \text{ K}$ ,  $\mu(\text{Cu K}\alpha) = 2.465 \text{ mm}^{-1}$ ,  $D_{\text{calc}} = 1.214 \text{ g/cm}^3$ , 15971 reflections measured ( $6.702^\circ \leq 2\theta \leq 144.97^\circ$ ), 7333 unique ( $R_{\text{int}} = 0.0295$ ,  $R_\sigma = 0.0352$ ) which were used in all calculations. The final  $R_1$  was 0.0357 ( $I > 2\sigma(I)$ ) and  $wR_2$  was 0.0966 (all data).

##### **M1•H<sub>2</sub>O C<sub>24</sub>H<sub>30</sub>N<sub>4</sub>O<sub>7</sub> (M =486.528 g mol<sup>-1</sup>):**

Triclinic, space group  $P1$  (no. 1),  $a = 10.0197(9) \text{ \AA}$ ,  $b = 10.6119(8) \text{ \AA}$ ,  $c = 12.1050(11) \text{ \AA}$ ,  $\alpha = 96.673(7)^\circ$ ,  $\beta = 96.059(7)^\circ$ ,  $\gamma = 103.556(7)^\circ$ ,  $V = 1230.96(19) \text{ \AA}^3$ ,  $Z = 2$ ,  $T = 119.98(13) \text{ K}$ .

K,  $\mu(\text{Cu K}\alpha) = 0.812 \text{ mm}^{-1}$ ,  $D_{\text{calc}} = 1.313 \text{ g/cm}^3$ , 9126 reflections measured ( $7.42^\circ \leq 2\theta \leq 147.6^\circ$ ), 5819 unique ( $R_{\text{int}} = 0.0559$ ,  $R_\sigma = 0.0735$ ) which were used in all calculations. The final  $R_1$  was 0.0765 ( $I \geq 2\sigma(I)$ ) and  $wR_2$  was 0.1993 (all data).

### Chapter 3 XRD data

#### **S-5 (BF<sub>4</sub>)•MeCN C<sub>48</sub>H<sub>38</sub>B<sub>2</sub>F<sub>8</sub>FeN<sub>7</sub>S<sub>4</sub> (M =1070.56 g mol<sup>-1</sup>):**

Orthorhombic, space group  $P2_12_12_1$  (no. 19),  $a = 14.238 \text{ \AA}$ ,  $b = 15.35650(10) \text{ \AA}$ ,  $c = 21.21520(10) \text{ \AA}$ ,  $V = 4638.55(4) \text{ \AA}^3$ ,  $Z = 4$ ,  $T = 100(2) \text{ K}$ ,  $\mu(\lambda = 0.69 \text{ \AA}) = 0.538 \text{ mm}^{-1}$ ,  $D_{\text{calc}} = 1.533 \text{ g/cm}^3$ , 82664 reflections measured ( $3.174^\circ \leq 2\theta \leq 72.002^\circ$ ), 22586 unique ( $R_{\text{int}} = 0.1231$ ,  $R_\sigma = 0.1210$ ) which were used in all calculations. The final  $R_1$  was 0.0416 ( $I > 2\sigma(I)$ ) and  $wR_2$  was 0.1252 (all data).

#### **RS-5 (BF<sub>4</sub>)•1.5MeCN C<sub>49</sub>H<sub>42.5</sub>B<sub>2</sub>F<sub>8</sub>FeN<sub>7.5</sub>S<sub>4</sub> (M =1094.11 g mol<sup>-1</sup>)**

Triclinic, space group  $P-1$  (no. 2),  $a = 13.92540(10) \text{ \AA}$ ,  $b = 18.22600(10) \text{ \AA}$ ,  $c = 20.58250(10) \text{ \AA}$ ,  $\alpha = 102.4270(10)^\circ$ ,  $\beta = 108.11^\circ$ ,  $\gamma = 90.9780(10)^\circ$ ,  $V = 4828.82(5) \text{ \AA}^3$ ,  $Z = 4$ ,  $T = 100(2) \text{ K}$ ,  $\mu(\lambda = 0.69 \text{ \AA}) = 0.519 \text{ mm}^{-1}$ ,  $D_{\text{calc}} = 1.505 \text{ g/cm}^3$ , 107008 reflections measured ( $2.074^\circ \leq 2\theta \leq 72.092^\circ$ ), 44075 unique ( $R_{\text{int}} = 0.0749$ ,  $R_\sigma = 0.0952$ ) which were used in all calculations. The final  $R_1$  was 0.0792 ( $I > 2\sigma(I)$ ) and  $wR_2$  was 0.2501 (all data).

#### **R-5 (ClO<sub>4</sub>)•MeCN C<sub>48</sub>H<sub>41</sub>CL2FeN<sub>7</sub>O<sub>8</sub>S<sub>4</sub> (M =1098.87 g mol<sup>-1</sup>):**

Orthorhombic, space group  $P2_12_12_1$  (no. 19),  $a = 14.23080(10) \text{ \AA}$ ,  $b = 15.53680(10) \text{ \AA}$ ,  $c = 21.23850(10) \text{ \AA}$ ,  $V = 4695.86(5) \text{ \AA}^3$ ,  $Z = 4$ ,  $T = 100(2) \text{ K}$ ,  $\mu(\lambda = 0.69 \text{ \AA}) = 0.625 \text{ mm}^{-1}$ ,  $D_{\text{calc}} = 1.554 \text{ g/cm}^3$ , 102764 reflections measured ( $3.148^\circ \leq 2\theta \leq 72.002^\circ$ ), 22810 unique ( $R_{\text{int}} = 0.0592$ ,  $R_\sigma = 0.0593$ ) which were used in all calculations. The final  $R_1$  was 0.0376 ( $I > 2\sigma(I)$ ) and  $wR_2$  was 0.0862 (all data).

#### **R-5•S-5 (ClO<sub>4</sub>)•3MeCN C<sub>91.5</sub>H<sub>77</sub>CL4Fe<sub>2</sub>N<sub>18.5</sub>O<sub>16</sub>S<sub>8</sub> (M =2201.69 g mol<sup>-1</sup>)**

Tetragonal, space group  $I-4$  (no. 82),  $a = 41.9835(3) \text{ \AA}$ ,  $c = 10.54690(10) \text{ \AA}$ ,  $V = 18590.1(3) \text{ \AA}^3$ ,  $Z = 8$ ,  $T = 125.00(10) \text{ K}$ ,  $\mu(\text{Cu K}\alpha) = 5.898 \text{ mm}^{-1}$ ,  $D_{\text{calc}} = 1.573 \text{ g/cm}^3$ , 33032 reflections measured ( $6.658^\circ \leq 2\theta \leq 147.112^\circ$ ), 16328 unique ( $R_{\text{int}} = 0.0485$ ,  $R_\sigma = 0.0755$ ) which were used in all calculations. The final  $R_1$  was 0.0539 ( $I > 2\sigma(I)$ ) and  $wR_2$  was 0.1473 (all data).

#### **RS-6•2MeCN C<sub>38</sub>H<sub>52</sub>CL2FeN<sub>8</sub>O<sub>7.835</sub>S<sub>4</sub> (M =979.86 g mol<sup>-1</sup>):**

Triclinic, space group  $P-1$  (no. 2),  $a = 13.0451(6) \text{ \AA}$ ,  $b = 13.0605(6) \text{ \AA}$ ,  $c = 15.4003(4) \text{ \AA}$ ,  $\alpha = 75.102(3)^\circ$ ,  $\beta = 75.131(3)^\circ$ ,  $\gamma = 67.058(4)^\circ$ ,  $V = 2298.73(18) \text{ \AA}^3$ ,  $Z = 2$ ,  $T = 125.00(10) \text{ K}$ ,  $\mu(\text{Cu K}\alpha) = 5.844 \text{ mm}^{-1}$ ,  $D_{\text{calc}} = 1.416 \text{ g/cm}^3$ , 21427 reflections measured ( $7.468^\circ \leq 2\theta \leq 147.296^\circ$ ), 8168 unique ( $R_{\text{int}} = 0.0241$ ,  $R_\sigma = 0.0274$ ) which

were used in all calculations. The final  $R_1$  was 0.0692 ( $I > 2\sigma(I)$ ) and  $wR_2$  was 0.2177 (all data).

**S-7•(Me)<sub>2</sub>CO C<sub>41</sub>H<sub>55</sub>CL<sub>2</sub>FeN<sub>6</sub>O<sub>9.25</sub>S<sub>4</sub> (M = 1034.90 g/mol):**

Orthorhombic, space group  $P2_12_12_1$  (no. 19),  $a = 11.0539(3)$  Å,  $b = 19.4678(4)$  Å,  $c = 22.2456(3)$  Å,  $V = 4787.15(18)$  Å<sup>3</sup>,  $Z = 4$ ,  $T = 100(2)$  K,  $\mu(\lambda = 0.69 \text{ Å}) = 0.609$  mm<sup>-1</sup>,  $D_{\text{calc}} = 1.436$  g/cm<sup>3</sup>, 19237 reflections measured ( $3.55^\circ \leq 2\theta \leq 49.442^\circ$ ), 6988 unique ( $R_{\text{int}} = 0.0689$ ,  $R\sigma = 0.1607$ ) which were used in all calculations. The final  $R_1$  was 0.0487 ( $I > 2\sigma(I)$ ) and  $wR_2$  was 0.1088 (all data).

**S-7(i)•Et<sub>2</sub>O•MeCN C<sub>24.5</sub>H<sub>40.25</sub>N<sub>5.25</sub>O<sub>10.25</sub>CL<sub>2</sub>S<sub>2</sub>Fe (M = 763.24 g mol<sup>-1</sup>):**

Triclinic, space group  $P-1$  (no. 2),  $a = 11.5525(2)$  Å,  $b = 13.2711(3)$  Å,  $c = 13.9044(3)$  Å,  $\alpha = 73.869(2)^\circ$ ,  $\beta = 70.5578(19)^\circ$ ,  $\gamma = 65.262(2)^\circ$ ,  $V = 1801.68(8)$  Å<sup>3</sup>,  $Z = 2$ ,  $T = 120.15$  K,  $\mu(\text{Cu } K\alpha) = 6.291$  mm<sup>-1</sup>,  $D_{\text{calc}} = 1.407$  g/cm<sup>3</sup>, 32272 reflections measured ( $6.832^\circ \leq 2\theta \leq 144.948^\circ$ ), 6749 unique ( $R_{\text{int}} = 0.0473$ ,  $R\sigma = 0.0263$ ) which were used in all calculations. The final  $R_1$  was 0.0496 ( $I > 2\sigma(I)$ ) and  $wR_2$  was 0.1344 (all data).

**S-8•(Me)<sub>2</sub>CO C<sub>41</sub>H<sub>60</sub>CL<sub>2</sub>FeN<sub>6</sub>O<sub>13</sub> (M = 971.70 g mol<sup>-1</sup>)**

Orthorhombic, space group  $P2_12_12_1$  (no. 19),  $a = 10.9135(3)$  Å,  $b = 19.6044(5)$  Å,  $c = 21.5429(5)$  Å,  $V = 4609.2(2)$  Å<sup>3</sup>,  $Z = 4$ ,  $T = 130.00(10)$  K,  $\mu(\text{Cu } K\alpha) = 4.269$  mm<sup>-1</sup>,  $D_{\text{calc}} = 1.400$  g/cm<sup>3</sup>, 17220 reflections measured ( $8.208^\circ \leq 2\theta \leq 144.924^\circ$ ), 8819 unique ( $R_{\text{int}} = 0.0471$ ,  $R\sigma = 0.0659$ ) which were used in all calculations. The final  $R_1$  was 0.0553 ( $I > 2\sigma(I)$ ) and  $wR_2$  was 0.1553 (all data).

## Chapter 4 XRD data

**S-9•MeCN C<sub>48</sub>H<sub>39</sub>CL<sub>2</sub>FeN<sub>7</sub>O<sub>10.76</sub>S<sub>1.24</sub> (M = 1052.52 g mol<sup>-1</sup>):**

Orthorhombic, space group  $P2_12_12_1$  (no. 19),  $a = 13.8331(4)$  Å,  $b = 15.4253(4)$  Å,  $c = 21.8069(8)$  Å,  $V = 4653.1(2)$  Å<sup>3</sup>,  $Z = 4$ ,  $T = 130.00(10)$  K,  $\mu(\text{Cu } K\alpha) = 4.768$  mm<sup>-1</sup>,  $D_{\text{calc}} = 1.502$  g/cm<sup>3</sup>, 16620 reflections measured ( $7.02^\circ \leq 2\theta \leq 144.512^\circ$ ), 8945 unique ( $R_{\text{int}} = 0.0374$ ,  $R\sigma = 0.0531$ ) which were used in all calculations. The final  $R_1$  was 0.0476 ( $I > 2\sigma(I)$ ) and  $wR_2$  was 0.1251 (all data).

**RS-9•MeCN C<sub>47</sub>H<sub>41</sub>CL<sub>2</sub>FeN<sub>7</sub>O<sub>12</sub>S<sub>2</sub> (M = 1052.52 g mol<sup>-1</sup>):**

Monoclinic, space group  $P2_1$  (no. 4),  $a = 11.9686(2)$  Å,  $b = 12.00810(10)$  Å,  $c = 16.2301(2)$  Å,  $\beta = 94.7810(10)^\circ$ ,  $V = 2324.48(5)$  Å<sup>3</sup>,  $Z = 2$ ,  $T = 125.00(10)$  K,  $\mu(\text{Cu } K\alpha) = 2.052$  mm<sup>-1</sup>,  $D_{\text{calc}} = 1.293$  g/cm<sup>3</sup>, 20843 reflections measured ( $7.412^\circ \leq 2\theta \leq 144.79^\circ$ ), 8622 unique ( $R_{\text{int}} = 0.0369$ ,  $R\sigma = 0.0423$ ) which were used in all calculations. The final  $R_1$  was 0.0343 ( $I > 2\sigma(I)$ ) and  $wR_2$  was 0.0878 (all data).

**RS-10•MeCN C<sub>36</sub>H<sub>49</sub>CL<sub>2</sub>FeN<sub>7</sub>O<sub>9.875</sub>S<sub>2</sub> (M = 928.69 g mol<sup>-1</sup>):**

Monoclinic, space group  $P2_1$  (no. 4),  $a = 11.35150(10)$  Å,  $b = 18.6328(3)$  Å,  $c = 20.5925(3)$  Å,  $\beta = 102.2460(10)^\circ$ ,  $V = 4256.42(10)$  Å<sup>3</sup>,  $Z = 4$ ,  $T = 130.01(10)$  K,  $\mu(\text{Cu K}\alpha) = 5.441$  mm<sup>-1</sup>,  $D_{\text{calc}} = 1.449$  g/cm<sup>3</sup>, 37789 reflections measured ( $7.97^\circ \leq 2\theta \leq 144.922^\circ$ ), 15763 unique ( $R_{\text{int}} = 0.0358$ ,  $R_{\text{sigma}} = 0.0391$ ) which were used in all calculations. The final  $R_1$  was 0.0516 ( $I > 2\sigma(I)$ ) and  $wR_2$  was 0.1540 (all data).

**S-11•(Me)<sub>2</sub>CO C<sub>41.01</sub>H<sub>56.02</sub>CL<sub>2</sub>FeN<sub>6</sub>O<sub>11.92</sub>S<sub>1.08</sub> (M = 985.15 g mol<sup>-1</sup>):**

Orthorhombic, space group  $P2_12_12_1$  (no. 19),  $a = 10.9215(3)$  Å,  $b = 19.4687(6)$  Å,  $c = 21.8393(8)$  Å,  $V = 4643.6(3)$  Å<sup>3</sup>,  $Z = 4$ ,  $T = 119.97(16)$  K,  $\mu(\text{Cu K}\alpha) = 4.672$  mm<sup>-1</sup>,  $D_{\text{calc}} = 1.409$  g/cm<sup>3</sup>, 14455 reflections measured ( $9.054^\circ \leq 2\theta \leq 145.002^\circ$ ), 8551 unique ( $R_{\text{int}} = 0.0583$ ,  $R_{\text{sigma}} = 0.0693$ ) which were used in all calculations. The final  $R_1$  was 0.0630 ( $I > 2\sigma(I)$ ) and  $wR_2$  was 0.1725 (all data).

**12•MeCN C<sub>44</sub>H<sub>35</sub>CL<sub>2</sub>FeN<sub>9</sub>O<sub>10</sub> (M = 976.56 g mol<sup>-1</sup>):**

Tetragonal, space group  $P4_1$  (no. 76),  $a = 10.63790(10)$  Å,  $c = 73.8154(8)$  Å,  $V = 8353.31(18)$  Å<sup>3</sup>,  $Z = 8$ ,  $T = 130.00(10)$  K,  $\mu(\text{Cu K}\alpha) = 4.698$  mm<sup>-1</sup>,  $D_{\text{calc}} = 1.553$  g/cm<sup>3</sup>, 32224 reflections measured ( $8.312^\circ \leq 2\theta \leq 144.944^\circ$ ), 16046 unique ( $R_{\text{int}} = 0.0532$ ,  $R_{\text{sigma}} = 0.0797$ ) which were used in all calculations. The final  $R_1$  was 0.0726 ( $I > 2\sigma(I)$ ) and  $wR_2$  was 0.2055 (all data).

**13 C<sub>42</sub>H<sub>32</sub>CL<sub>2</sub>FeN<sub>8</sub>O<sub>8</sub>S<sub>2</sub> (M = 967.62 g mol<sup>-1</sup>):**

Monoclinic, space group  $P2_1$  (no. 4),  $a = 9.956$  Å,  $b = 18.27020(10)$  Å,  $c = 11.260$  Å,  $\beta = 89.40^\circ$ ,  $V = 2048.018(11)$  Å<sup>3</sup>,  $Z = 2$ ,  $T = 100(2)$  K,  $\mu(\lambda = 0.69 \text{ Å}) = 0.616$  mm<sup>-1</sup>,  $D_{\text{calc}} = 1.569$  g/cm<sup>3</sup>, 44770 reflections measured ( $3.506^\circ \leq 2\theta \leq 71.804^\circ$ ), 19025 unique ( $R_{\text{int}} = 0.0287$ ,  $R_{\text{sigma}} = 0.0300$ ) which were used in all calculations. The final  $R_1$  was 0.0322 ( $I > 2\sigma(I)$ ) and  $wR_2$  was 0.1024 (all data).

**14 C<sub>36</sub>H<sub>35</sub>CL<sub>2</sub>FeN<sub>8</sub>O<sub>10</sub> (M = 867.48 g mol<sup>-1</sup>):**

Orthorhombic, space group  $P2_12_12_1$  (no. 19),  $a = 10.1310(5)$  Å,  $b = 19.1776(10)$  Å,  $c = 19.2647(10)$  Å,  $V = 3742.9(3)$  Å<sup>3</sup>,  $Z = 4$ ,  $T = 120.15$  K,  $\mu(\text{Cu K}\alpha) = 5.147$  mm<sup>-1</sup>,  $D_{\text{calc}} = 1.539$  g/cm<sup>3</sup>, 9691 reflections measured ( $6.5^\circ \leq 2\theta \leq 147.44^\circ$ ), 6463 unique ( $R_{\text{int}} = 0.0368$ ,  $R_{\text{sigma}} = 0.0535$ ) which were used in all calculations. The final  $R_1$  was 0.0533 ( $>2\sigma(I)$ ) and  $wR_2$  was 0.1426 (all data).

**15•MeCN•Et<sub>2</sub>O C<sub>42</sub>H<sub>49</sub>CL<sub>2</sub>FeN<sub>9</sub>O<sub>9</sub>S<sub>2</sub> (M = 1014.77 g mol<sup>-1</sup>):**

Monoclinic, space group  $P2_1$  (no. 4),  $a = 9.0025(3)$  Å,  $b = 24.0613(9)$  Å,  $c = 11.2550(5)$  Å,  $\beta = 106.649(4)^\circ$ ,  $V = 2335.75(16)$  Å<sup>3</sup>,  $Z = 2$ ,  $T = 130.00(10)$  K,  $\mu(\text{Cu K}\alpha) = 5.011$  mm<sup>-1</sup>,  $D_{\text{calc}} = 1.443$  g/cm<sup>3</sup>, 21424 reflections measured ( $7.348^\circ \leq 2\theta \leq 143.956^\circ$ ), 8331 unique ( $R_{\text{int}} = 0.0763$ ,  $R_{\text{sigma}} = 0.0905$ ) which were used in all calculations. The final  $R_1$  was 0.0522 ( $I > 2\sigma(I)$ ) and  $wR_2$  was 0.1326 (all data).

**17•2MeCN C<sub>38</sub>H<sub>34</sub>CL<sub>2</sub>FeN<sub>10</sub>O<sub>8</sub>S<sub>2</sub> (M =949.62 g mol<sup>-1</sup>):**

Orthorhombic, space group  $P2_12_12_1$  (no. 19),  $a = 8.8458(2) \text{ \AA}$ ,  $b = 20.3299(3) \text{ \AA}$ ,  $c = 22.9259(4) \text{ \AA}$ ,  $V = 4122.86(13) \text{ \AA}^3$ ,  $Z = 4$ ,  $T = 130.00(10) \text{ K}$ ,  $\mu(\text{Cu K}\alpha) = 5.629 \text{ mm}^{-1}$ ,  $D_{\text{calc}} = 1.530 \text{ g/cm}^3$ , 15672 reflections measured ( $7.712^\circ \leq 2\theta \leq 144.944^\circ$ ), 7951 unique ( $R_{\text{int}} = 0.0467$ ,  $R_{\text{sigma}} = 0.0661$ ) which were used in all calculations. The final  $R_1$  was 0.0432 ( $I > 2\sigma(I)$ ) and  $wR_2$  was 0.0951 (all data).

**Chapter 5 XRD data**

**22 C<sub>26.55</sub>H<sub>21.5</sub>CuF<sub>6</sub>N<sub>4</sub>O<sub>8</sub>S<sub>2</sub> (M =383.12 g mol<sup>-1</sup>):**

Orthorhombic, space group  $P2_12_12$  (no. 18),  $a = 10.19910(10) \text{ \AA}$ ,  $b = 10.4556(2) \text{ \AA}$ ,  $c = 31.4537(5) \text{ \AA}$ ,  $V = 3354.15(9) \text{ \AA}^3$ ,  $Z = 4$ ,  $T = 100(2) \text{ K}$ ,  $\mu(\lambda = 0.69 \text{ \AA}) = 0.793 \text{ mm}^{-1}$ ,  $D_{\text{calc}} = 1.517 \text{ g/cm}^3$ , 73333 reflections measured ( $1.254^\circ \leq 2\theta \leq 72.02^\circ$ ), 16377 unique ( $R_{\text{int}} = 0.0753$ ,  $R_{\text{sigma}} = 0.0929$ ) which were used in all calculations. The final  $R_1$  was 0.0882 ( $I > 2\sigma(I)$ ) and  $wR_2$  was 0.3048 (all data).

**23 C<sub>27</sub>H<sub>23</sub>CuF<sub>6</sub>N<sub>4</sub>O<sub>6</sub>S<sub>4</sub> (M =805.27 g mol<sup>-1</sup>):**

Orthorhombic, space group  $P2_12_12_1$  (no. 19),  $a = 10.09060(10) \text{ \AA}$ ,  $b = 11.00630(10) \text{ \AA}$ ,  $c = 59.5737(3) \text{ \AA}$ ,  $V = 6616.27(9) \text{ \AA}^3$ ,  $Z = 8$ ,  $T = 100(2) \text{ K}$ ,  $\mu(\lambda = 0.69 \text{ \AA}) = 0.916 \text{ mm}^{-1}$ ,  $D_{\text{calc}} = 1.617 \text{ g/cm}^3$ , 146685 reflections measured ( $1.326^\circ \leq 2\theta \leq 72.07^\circ$ ), 32156 unique ( $R_{\text{int}} = 0.0615$ ,  $R_{\text{sigma}} = 0.0580$ ) which were used in all calculations. The final  $R_1$  was 0.0445 ( $I > 2\sigma(I)$ ) and  $wR_2$  was 0.1162 (all data).

**24 C<sub>23</sub>H<sub>30</sub>CuF<sub>6</sub>N<sub>4</sub>O<sub>8</sub>S<sub>2</sub> (M =732.17 g mol<sup>-1</sup>):**

Monoclinic, space group  $P2_1$  (no. 4),  $a = 10.78050(10) \text{ \AA}$ ,  $b = 14.3636(2) \text{ \AA}$ ,  $c = 20.1711(2) \text{ \AA}$ ,  $\beta = 103.9400(10)^\circ$ ,  $V = 3031.44(6) \text{ \AA}^3$ ,  $Z = 4$ ,  $T = 100(2) \text{ K}$ ,  $\mu(\lambda = 0.69 \text{ \AA}) = 0.873 \text{ mm}^{-1}$ ,  $D_{\text{calc}} = 1.604 \text{ g/cm}^3$ , 12476 reflections measured ( $3.774^\circ \leq 2\theta \leq 49.78^\circ$ ), 7755 unique ( $R_{\text{int}} = 0.0394$ ,  $R_{\text{sigma}} = 0.0649$ ) which were used in all calculations. The final  $R_1$  was 0.0356 ( $I > 2\sigma(I)$ ) and  $wR_2$  was 0.1076 (all data).

**25•MeNO<sub>2</sub> C<sub>41</sub>H<sub>57</sub>CuF<sub>6</sub>N<sub>7</sub>O<sub>8</sub>S<sub>6</sub> (M =1145.83 g mol<sup>-1</sup>):**

Triclinic, space group  $P1$  (no. 1),  $a = 12.0720(4) \text{ \AA}$ ,  $b = 14.5569(5) \text{ \AA}$ ,  $c = 15.3776(4) \text{ \AA}$ ,  $\alpha = 88.748(2)^\circ$ ,  $\beta = 89.684(2)^\circ$ ,  $\gamma = 75.015(3)^\circ$ ,  $V = 2609.80(15) \text{ \AA}^3$ ,  $Z = 2$ ,  $T = 120.00(10) \text{ K}$ ,  $\mu(\text{Cu K}\alpha) = 3.498 \text{ mm}^{-1}$ ,  $D_{\text{calc}} = 1.458 \text{ g/cm}^3$ , 22368 reflections measured ( $7.58^\circ \leq 2\theta \leq 144.964^\circ$ ), 12556 unique ( $R_{\text{int}} = 0.0406$ ,  $R_{\text{sigma}} = 0.0523$ ) which were used in all calculations. The final  $R_1$  was 0.0679 ( $I > 2\sigma(I)$ ) and  $wR_2$  was 0.1915 (all data).

**26 C<sub>34</sub>H<sub>47</sub>Cu<sub>4</sub>I<sub>4</sub>N<sub>6</sub>O<sub>4</sub> (M =1397.06 g mol<sup>-1</sup>):**

Orthorhombic, space group  $P2_12_12_1$  (no. 19),  $a = 9.787 \text{ \AA}$ ,  $b = 29.32010(10) \text{ \AA}$ ,  $c = 34.54920(10) \text{ \AA}$ ,  $V = 9914.50(4) \text{ \AA}^3$ ,  $Z = 8$ ,  $T = 100(2) \text{ K}$ ,  $\mu(\lambda = 0.69 \text{ \AA}) = 3.905 \text{ mm}^{-1}$ ,



$D_{\text{calc}} = 1.872 \text{ g/cm}^3$ , 221638 reflections measured ( $1.766^\circ \leq 2\Theta \leq 72.344^\circ$ ), 48803 unique ( $R_{\text{int}} = 0.0789$ ,  $R_{\text{sigma}} = 0.0657$ ) which were used in all calculations. The final  $R_1$  was 0.0407 ( $I > 2\sigma(I)$ ) and  $wR_2$  was 0.1066 (all data).

**27 C<sub>34</sub>H<sub>46</sub>Cu<sub>2</sub>F<sub>12</sub>N<sub>6</sub>O<sub>4</sub>P<sub>2</sub> ( $M = 1019.79 \text{ g mol}^{-1}$ ):**

Monoclinic, space group  $P2_1$  (no. 4),  $a = 10.1349(2) \text{ \AA}$ ,  $b = 12.9665(4) \text{ \AA}$ ,  $c = 16.5459(4) \text{ \AA}$ ,  $\beta = 91.630(2)^\circ$ ,  $V = 2173.49(10) \text{ \AA}^3$ ,  $Z = 2$ ,  $T = 120.01(10) \text{ K}$ ,  $\mu(\text{Cu K}\alpha) = 2.762 \text{ mm}^{-1}$ ,  $D_{\text{calc}} = 1.558 \text{ g/cm}^3$ , 10455 reflections measured ( $8.666^\circ \leq 2\Theta \leq 145.296^\circ$ ), 6216 unique ( $R_{\text{int}} = 0.0356$ ,  $R_{\text{sigma}} = 0.0520$ ) which were used in all calculations. The final  $R_1$  was 0.0575 ( $I > 2\sigma(I)$ ) and  $wR_2$  was 0.1624 (all data).

**28•2MeNO<sub>2</sub> C<sub>40</sub>H<sub>60</sub>B<sub>2</sub>Cu<sub>2</sub>F<sub>8</sub>N<sub>8</sub>O<sub>8</sub> ( $M = 1021.43 \text{ g mol}^{-1}$ ):**

Orthorhombic, space group  $P2_12_12_1$  (no. 19),  $a = 11.091 \text{ \AA}$ ,  $b = 12.09340(10) \text{ \AA}$ ,  $c = 36.9440(2) \text{ \AA}$ ,  $V = 4955.27(5) \text{ \AA}^3$ ,  $Z = 4$ ,  $T = 100(2) \text{ K}$ ,  $\mu(\lambda = 0.69 \text{ \AA}) = 0.868 \text{ mm}^{-1}$ ,  $D_{\text{calc}} = 1.369 \text{ g/cm}^3$ , 109365 reflections measured ( $2.136^\circ \leq 2\Theta \leq 71.988^\circ$ ), 23935 unique ( $R_{\text{int}} = 0.0868$ ,  $R_{\text{sigma}} = 0.0699$ ) which were used in all calculations. The final  $R_1$  was 0.0739 ( $I > 2\sigma(I)$ ) and  $wR_2$  was 0.2169 (all data).

**29•MeNO<sub>2</sub> C<sub>47</sub>H<sub>41</sub>CuF<sub>12</sub>N<sub>7</sub>O<sub>6</sub>P<sub>2</sub> ( $M = 1153.35 \text{ g mol}^{-1}$ ):**

Orthorhombic, space group  $C222_1$  (no. 20),  $a = 13.84840(10) \text{ \AA}$ ,  $b = 15.47320(10) \text{ \AA}$ ,  $c = 22.19690(10) \text{ \AA}$ ,  $V = 4756.33(5) \text{ \AA}^3$ ,  $Z = 4$ ,  $T = 100(2) \text{ K}$ ,  $\mu(\lambda = 0.69 \text{ \AA}) = 0.584 \text{ mm}^{-1}$ ,  $D_{\text{calc}} = 1.611 \text{ g/cm}^3$ , 51130 reflections measured ( $3.826^\circ \leq 2\Theta \leq 71.784^\circ$ ), 11556 unique ( $R_{\text{int}} = 0.0544$ ,  $R_{\text{sigma}} = 0.0661$ ) which were used in all calculations. The final  $R_1$  was 0.0785 ( $I > 2\sigma(I)$ ) and  $wR_2$  was 0.2409 (all data).

**30 B<sub>2</sub>C<sub>69</sub>Cu<sub>3</sub>F<sub>9</sub>N<sub>9</sub>O<sub>6</sub> ( $M = 1434.02 \text{ g mol}^{-1}$ ):**

Hexagonal, space group  $P6_322$  (no. 182),  $a = 14.3592(2) \text{ \AA}$ ,  $c = 19.0494(3) \text{ \AA}$ ,  $V = 3401.51(11) \text{ \AA}^3$ ,  $Z = 2$ ,  $T = 100 \text{ K}$ ,  $\mu(\lambda = 0.69 \text{ \AA}) = 0.932 \text{ mm}^{-1}$ ,  $D_{\text{calc}} = 1.400 \text{ g/cm}^3$ , 74238 reflections measured ( $3.174^\circ \leq 2\Theta \leq 72.366^\circ$ ), 5803 unique ( $R_{\text{int}} = 0.0584$ ,  $R_{\text{sigma}} = 0.0708$ ) which were used in all calculations. The final  $R_1$  was 0.1179 ( $I > 2\sigma(I)$ ) and  $wR_2$  was 0.3368 (all data).

## Chapter 6 XRD data

**31 C<sub>18.25</sub>H<sub>16.25</sub>CIF<sub>7.625</sub>N<sub>5.5</sub>PRu ( $M = 213.52 \text{ g mol}^{-1}$ )**

Monoclinic, space group  $P2_1$  (no. 4),  $a = 8.2945(6) \text{ \AA}$ ,  $b = 10.2721(10) \text{ \AA}$ ,  $c = 27.947(2) \text{ \AA}$ ,  $\beta = 94.812(7)^\circ$ ,  $V = 2372.7(3) \text{ \AA}^3$ ,  $Z = 4$ ,  $T = 120.00(13) \text{ K}$ ,  $\mu(\text{Cu K}\alpha) = 1.702 \text{ mm}^{-1}$ ,  $D_{\text{calc}} = 0.149 \text{ g/cm}^3$ , 5012 reflections measured ( $9.176^\circ \leq 2\Theta \leq 152.348^\circ$ ), 5012 unique ( $R_{\text{int}} = 0.263$ ,  $R_{\text{sigma}} = 0.0997$ ) which were used in all calculations. The final  $R_1$  was 0.1271 ( $I > 2\sigma(I)$ ) and  $wR_2$  was 0.3977 (all data).

**32 C<sub>31</sub>H<sub>24</sub>CL<sub>2</sub>F<sub>12</sub>N<sub>6</sub>P<sub>2</sub>Ru (M =942.47 g mol<sup>-1</sup>)**

Orthorhombic, space group  $P2_12_12_1$  (no. 19),  $a = 8.8286(2) \text{ \AA}$ ,  $b = 9.0499(2) \text{ \AA}$ ,  $c = 43.8630(9) \text{ \AA}$ ,  $V = 3504.56(13) \text{ \AA}^3$ ,  $Z = 4$ ,  $T = 120.01(11) \text{ K}$ ,  $\mu(\text{Cu K}\alpha) = 6.798 \text{ mm}^{-1}$ ,  $D_{\text{calc}} = 1.786 \text{ g/cm}^3$ , 8920 reflections measured ( $8.062^\circ \leq 2\Theta \leq 146.9^\circ$ ), 6040 unique ( $R_{\text{int}} = 0.0408$ ,  $R_{\text{sigma}} = 0.0713$ ) which were used in all calculations. The final  $R_1$  was 0.0408 ( $I > 2\sigma(I)$ ) and  $wR_2$  was 0.0864 (all data).

**33 C<sub>25</sub>H<sub>22</sub>CL<sub>2</sub>N<sub>4</sub>O<sub>2</sub>Ru (M =582.43 g mol<sup>-1</sup>)**

Monoclinic, space group  $P2_1$  (no. 4),  $a = 8.8529(3) \text{ \AA}$ ,  $b = 15.0644(4) \text{ \AA}$ ,  $c = 10.2273(4) \text{ \AA}$ ,  $\beta = 113.289(4)^\circ$ ,  $V = 1252.82(8) \text{ \AA}^3$ ,  $Z = 2$ ,  $T = 119.96(14) \text{ K}$ ,  $\mu(\text{Cu K}\alpha) = 7.270 \text{ mm}^{-1}$ ,  $D_{\text{calc}} = 1.544 \text{ g/cm}^3$ , 4969 reflections measured ( $9.414^\circ \leq 2\Theta \leq 147.646^\circ$ ), 3490 unique ( $R_{\text{int}} = 0.0325$ ,  $R_{\text{sigma}} = 0.0469$ ) which were used in all calculations. The final  $R_1$  was 0.0345 ( $I > 2\sigma(I)$ ) and  $wR_2$  was 0.0893 (all data).

**34 C<sub>46.75</sub>H<sub>42.2</sub>B<sub>2</sub>F<sub>8</sub>N<sub>6</sub>O<sub>5.35</sub>Ru (M =1048.394 g mol<sup>-1</sup>)**

Monoclinic, space group  $P2_1$  (no. 4),  $a = 11.6573(17) \text{ \AA}$ ,  $b = 17.2845(17) \text{ \AA}$ ,  $c = 12.4581(17) \text{ \AA}$ ,  $\beta = 115.291(17)^\circ$ ,  $V = 2269.6(6) \text{ \AA}^3$ ,  $Z = 2$ ,  $T = 119.99(11) \text{ K}$ ,  $\mu(\text{Mo K}\alpha) = 0.434 \text{ mm}^{-1}$ ,  $D_{\text{calc}} = 1.534 \text{ g/cm}^3$ , 16968 reflections measured ( $6.18^\circ \leq 2\Theta \leq 62.3^\circ$ ), 11131 unique ( $R_{\text{int}} = 0.0397$ ,  $R_{\text{sigma}} = 0.0841$ ) which were used in all calculations. The final  $R_1$  was 0.0845 ( $I \geq 2u(I)$ ) and  $wR_2$  was 0.2456 (all data).

**35 C<sub>25</sub>I<sub>2</sub>N<sub>4</sub>O<sub>2</sub>Ru (M =743.16 g mol<sup>-1</sup>)**

Orthorhombic, space group  $P2_12_12_1$  (no. 19),  $a = 8.444 \text{ \AA}$ ,  $b = 15.44960(10) \text{ \AA}$ ,  $c = 20.17970(10) \text{ \AA}$ ,  $V = 2632.60(2) \text{ \AA}^3$ ,  $Z = 4$ ,  $T = 100(2) \text{ K}$ ,  $\mu(\lambda = 0.69 \text{ \AA}) = 0.749 \text{ mm}^{-1}$ ,  $D_{\text{calc}} = 1.875 \text{ g/cm}^3$ , 57659 reflections measured ( $3.218^\circ \leq 2\Theta \leq 72.03^\circ$ ), 12807 unique ( $R_{\text{int}} = 0.0444$ ,  $R_{\text{sigma}} = 0.0399$ ) which were used in all calculations. The final  $R_1$  was 0.0285 ( $I > 2\sigma(I)$ ) and  $wR_2$  was 0.0777 (all data).

**36 C<sub>19</sub>H<sub>26</sub>I<sub>2</sub>N<sub>4</sub>O<sub>2</sub>Ru (M =697.31 g mol<sup>-1</sup>)**

Orthorhombic, space group  $P2_12_12_1$  (no. 19),  $a = 8.6533(2) \text{ \AA}$ ,  $b = 14.9849(4) \text{ \AA}$ ,  $c = 17.9665(5) \text{ \AA}$ ,  $V = 2329.70(10) \text{ \AA}^3$ ,  $Z = 4$ ,  $T = 125.00(10) \text{ K}$ ,  $\mu(\text{Cu K}\alpha) = 26.428 \text{ mm}^{-1}$ ,  $D_{\text{calc}} = 1.988 \text{ g/cm}^3$ , 8745 reflections measured ( $7.682^\circ \leq 2\Theta \leq 147.428^\circ$ ), 4591 unique ( $R_{\text{int}} = 0.0349$ ,  $R_{\text{sigma}} = 0.0419$ ) which were used in all calculations. The final  $R_1$  was 0.0338 ( $I > 2\sigma(I)$ ) and  $wR_2$  was 0.0904 (all data).

**37 C<sub>43</sub>H<sub>37</sub>I<sub>4</sub>N<sub>6</sub>RuS<sub>4</sub> (M =1374.69 g mol<sup>-1</sup>)**

Monoclinic, space group  $P2_1$  (no. 4),  $a = 15.4934(4) \text{ \AA}$ ,  $b = 10.6946(3) \text{ \AA}$ ,  $c = 29.0204(10) \text{ \AA}$ ,  $\beta = 90.093(3)^\circ$ ,  $V = 4808.5(2) \text{ \AA}^3$ ,  $Z = 4$ ,  $T = 100.01(10) \text{ K}$ ,  $\mu(\text{Cu K}\alpha) = 24.715 \text{ mm}^{-1}$ ,  $D_{\text{calc}} = 1.899 \text{ g/cm}^3$ , 22472 reflections measured ( $8.356^\circ \leq 2\Theta \leq 147.946^\circ$ ), 22472 unique ( $R_{\text{int}} = 0.091$ ,  $R_{\text{sigma}} = 0.1029$ ) which were used in all calculations. The final  $R_1$  was 0.1193 ( $I > 2\sigma(I)$ ) and  $wR_2$  was 0.3557 (all data).

## List of References

1. P. Pfeiffer, *Journal of Chemical Education*, 1928, **5**, 1090.
2. Z. G. Du, *Fundamentals of structural chemistry*, World Scientific, 1993.
3. G. N. Lewis, *Valence and the Structure of Atoms and Molecules*, Chemical Catalog Company, Incorporated, 1923.
4. H. Eyring, J. Walter and G. E. Kimball, *Journal of Chemical Education*, 1944, **21**, 415.
5. C. E. S. Housecroft, A. G., *Inorganic Chemistry*, Pearson Education Limited, 4th edn., 2012.
6. H. Bethe, *Annalen der Physik*, 1929, **395**, 133-208.
7. J. Van Vleck, *Physical Review*, 1932, **41**, 208.
8. J. S. Griffith and L. E. Orgel, *Quarterly Reviews, Chemical Society*, 1957, **11**, 381-393.
9. R. G. Pearson, *Journal of Chemical Education*, 1961, **38**, 164-173.
10. L. E. Sutton, *Journal of Chemical Education*, 1960, **37**, 498.
11. W. Pauli, *Zeitschrift für Physik*, 1925, **31**, 765-783.
12. W. Pauli, *Zeitschrift für Physik*, 1925, **31**, 373-385.
13. E. Scerri, *Education in Chemistry*, 2013, **50**, 24-26.
14. S. A. Goudsmit and P. I. Richards, *Proceedings of the National Academy of Sciences*, 1964, **51**, 664-671.
15. R. D. Harcourt and A. Harcourt, *Chemical Physics*, 1973, **1**, 238-243.
16. J. Katriel and R. Pauncz, *Advances in quantum chemistry*, 1977, **10**, 143-185.
17. Y. Jean, *Molecular orbitals of transition metal complexes*, OUP Oxford, 2005.
18. T. Leyssens, D. Peeters, A. G. Orpen and J. N. Harvey, *Organometallics*, 2007, **26**, 2637-2645.
19. Y. Shimura, *Bulletin of the Chemical Society of Japan*, 1988, **61**, 693-698.
20. R. Tsuchida, *Bulletin of the Chemical Society of Japan*, 1938, **13**, 388-400.
21. K. Lonsdale, *Reports on Progress in Physics*, 1937, **4**, 368-389.
22. J. N. Lalena, D. A. Cleary and O. B. H. Duparc, *Principles of inorganic materials design*, John Wiley & Sons, Inc, 2010.
23. F. Parodi, in *Comprehensive Polymer Science and Supplements*, eds. G. Allen and J. C. Bevington, Pergamon, Amsterdam, 1989, vol. 1989, pp. 669-728.
24. R. G. Pearson, *Proceedings of the National Academy of Sciences*, 1975, **72**, 2104-2106.
25. K. I. Kugel and D. I. Khomskii, *Soviet Physics Uspekhi*, 1982, **25**, 231-256.
26. P. Gütllich, Y. Garcia and H. A. Goodwin, *Chemical Society Reviews*, 2000, **29**, 419-427.
27. P. Adler, H. Spiering and P. Gütllich, *Journal of Physics and Chemistry of Solids*, 1989, **50**, 587-597.
28. J. A. Real, A. B. Gaspar and M. C. Muñoz, *Dalton Transactions*, 2005, **2005**, 2062-2079.
29. P. Gütllich and H. A. Goodwin, in *Spin Crossover in Transition Metal Compounds I*, eds. P. Gütllich and H. A. Goodwin, Springer Berlin Heidelberg, Berlin, Heidelberg, 2004, pp. 1-47.
30. K. Takahashi, *Inorganics*, 2018, **6**, 32.
31. M. Koden, in *OLED Displays and Lighting*, 2016, vol. 2016, pp. 12-16.
32. J.-F. Létard, P. Guionneau, O. Nguyen, J. S. Costa, S. Marcén, G. Chastanet, M. Marchivie and L. Goux-Capes, *Chemistry – A European Journal*, 2005, **11**, 4582-4589.

33. C. Joachim, J. K. Gimzewski and A. Aviram, *Nature*, 2000, **408**, 541-548.
34. A. Bousseksou, G. Molnar, L. Salmon and W. Nicolazzi, *Chemical Society Reviews*, 2011, **40**, 3313-3335.
35. L. Pauling and C. D. Coryell, *Proceedings of the National Academy of Sciences*, 1936, **22**, 210-216.
36. L. Cambi and L. Szegö, *Berichte der deutschen chemischen Gesellschaft (A and B Series)*, 1931, **64**, 2591-2598.
37. L. S. Cambi, L.; Cagnasso, A., *Atti della Accademia Nazionale dei Lincei*, 1932, **15**, 266.
38. L. Cambi and L. Szegö, *Berichte der deutschen chemischen Gesellschaft (A and B Series)*, 1933, **66**, 656-661.
39. M. A. Halcrow, *Spin-crossover materials: properties and applications*, John Wiley & Sons, 2013.
40. K. Madeja and E. König, *Journal of Inorganic and Nuclear Chemistry*, 1963, **25**, 377-385.
41. A. A. Schilt, *Journal of the American Chemical Society*, 1960, **82**, 3000-3005.
42. F. Basolo and F. P. Dwyer, *Journal of the American Chemical Society*, 1954, **76**, 1454-1455.
43. W. Baker Jr and H. Bobonich, *Inorganic Chemistry*, 1963, **2**, 1071-1072.
44. W. Baker Jr and H. Bobonich, *Inorganic Chemistry*, 1964, **3**, 1184-1188.
45. J. S. Judge and W. A. Baker, *Inorganica Chimica Acta*, 1967, **1**, 68-72.
46. C. Harris, T. Lockyer, R. Martin, H. Patil and E. Sinn, *Australian Journal of Chemistry*, 1969, **22**, 2105-2116.
47. H. A. Goodwin, in *Spin Crossover in Transition Metal Compounds II*, Springer, 2004, pp. 23-47.
48. J. Zarembowitch and O. Kahn, *Inorganic Chemistry*, 1984, **23**, 589-593.
49. N. Abdullah, N. L. M. Noor, A. R. Nordin, M. A. Halcrow, D. R. MacFarlane, M. A. Lazar, J. M. Pringle, D. W. Bruce, B. Donnio and B. Heinrich, *Journal of Materials Chemistry C*, 2015, **3**, 2491-2499.
50. Y. Maeda, H. Ohshio and Y. Takashima, *Bulletin of the Chemical Society of Japan*, 1982, **55**, 3500-3505.
51. J. S. Griffith and L. E. Orgel, *Transactions of the Faraday Society*, 1957, **53**, 601-606.
52. F. A. Cotton, G. Wilkinson, C. A. Murillo, M. Bochmann and R. Grimes, *Advanced inorganic chemistry*, Wiley New York, 1988.
53. P. G. Sim and E. Sinn, *Journal of the American Chemical Society*, 1981, **103**, 241-243.
54. G. G. Morgan, K. D. Murnaghan, H. Müller-Bunz, V. McKee and C. J. Harding, *Angewandte Chemie International Edition*, 2006, **45**, 7192-7195.
55. C. Gandolfi, T. Cotting, P. N. Martinho, O. Sereda, A. Neels, G. G. Morgan and M. Albrecht, *Dalton Transactions*, 2011, **40**, 1855-1865.
56. P. N. Martinho, B. Gildea, M. M. Harris, T. Lemma, A. D. Naik, H. Müller-Bunz, T. E. Keyes, Y. Garcia and G. G. Morgan, *Angewandte Chemie*, 2012, **124**, 12765-12769.
57. I. D. Chawla and M. J. Frank, *Journal of Inorganic and Nuclear Chemistry*, 1970, **32**, 555-563.
58. M. B. Duriska, S. M. Neville, B. Moubaraki, J. D. Cashion, G. J. Halder, K. W. Chapman, C. Balde, J.-F. Létard, K. S. Murray, C. J. Kepert and S. R. Batten, *Angewandte Chemie International Edition*, 2009, **48**, 2549-2552.

59. T. M. Ross, B. Moubaraki, D. R. Turner, G. J. Halder, G. Chastanet, S. M. Neville, J. D. Cashion, J.-F. Létard, S. R. Batten and K. S. Murray, *European Journal of Inorganic Chemistry*, 2011, **2011**, 1395-1417.
60. R. W. Hogue, S. Singh and S. Brooker, *Chemical Society Reviews*, 2018, **47**, 7303-7338.
61. I. Galadzhun, I. Capel Berdiell, N. Shahid and M. A. Halcrow, *CrystEngComm*, 2019, **21**, 6330-6334.
62. R. J. Archer, H. S. Scott, M. I. J. Polson, B. E. Williamson, C. Mathonière, M. Rouzières, R. Clérac and P. E. Kruger, *Dalton Transactions*, 2018, **47**, 7965-7974.
63. A. J. McConnell, *Supramolecular Chemistry*, 2018, **30**, 858-868.
64. M. Darawsheh, L. A. Barrios, O. Roubeau, S. J. Teat and G. Aromí, *Chemistry – A European Journal*, 2016, **22**, 8635-8645.
65. P. Gütllich, in *Mössbauer Spectroscopy and Its Chemical Applications*, Journal of the American Chemical Society, 1981, vol. 194, ch. 19, pp. 405-452.
66. S. Brooker, *Chemical Society Reviews*, 2015, **44**, 2880-2892.
67. E. König, in *Progress in Inorganic Chemistry*, 1987, vol. 35, pp. 527-622.
68. M. A. Halcrow, *Chemical Society Reviews*, 2011, **40**, 4119-4142.
69. R. J. Lancashire, *Interpretation*, **30**, 13.
70. Y. Tanabe and S. Sugano, *Journal of the Physical Society of Japan*, 1954, **9**, 753-766.
71. Y. Tanabe and S. Sugano, *Journal of the Physical Society of Japan*, 1954, **9**, 766-779.
72. Y. Tanabe and S. Sugano, *Journal of the Physical Society of Japan*, 1956, **11**, 864-877.
73. A. L. Hormann and C. F. Shaw, *Journal of Chemical Education*, 1987, **64**, 918.
74. P. Gütllich, in *Chemical Mössbauer Spectroscopy*, Springer, 1984, pp. 27-64.
75. A. Hauser, *Coordination Chemistry Reviews*, 1991, **111**, 275-290.
76. P. Guionneau, M. Marchivie, G. Bravic, J.-F. Létard and D. Chasseau, in *Spin Crossover in Transition Metal Compounds II*, Springer Berlin Heidelberg, Berlin, Heidelberg, 2004, pp. 97-128.
77. M. A. Halcrow, *Coordination Chemistry Reviews*, 2009, **253**, 2493-2514.
78. J. M. Holland, J. A. McAllister, C. A. Kilner, M. Thornton-Pett, A. J. Bridgeman and M. A. Halcrow, *Journal of the Chemical Society, Dalton Transactions*, 2002, **2002**, 548-554.
79. J. Elhaik, D. J. Evans, C. A. Kilner and M. A. Halcrow, *Dalton Transactions*, 2005, **2005**, 1693-1700.
80. E. C. Constable, G. Baum, E. Bill, R. Dyson, R. van Eldik, D. Fenske, S. Kaderli, D. Morris, A. Neubrand, M. Neuburger, D. R. Smith, K. Wieghardt, M. Zehnder and A. D. Zuberbühler, *Chemistry – A European Journal*, 1999, **5**, 498-508.
81. D. L. Reger, J. R. Gardinier, J. D. Elgin, M. D. Smith, D. Hautot, G. J. Long and F. Grandjean, *Inorganic Chemistry*, 2006, **45**, 8862-8875.
82. L. J. Kershaw Cook, F. L. Thorp-Greenwood, T. P. Comyn, O. Cespedes, G. Chastanet and M. A. Halcrow, *Inorganic Chemistry*, 2015, **54**, 6319-6330.
83. C. A. Kilner and M. A. Halcrow, *Polyhedron*, 2006, **25**, 235-240.
84. H. Paulsen, L. Duelund, H. Winkler, H. Toftlund and A. X. Trautwein, *Inorganic Chemistry*, 2001, **40**, 2201-2203.
85. O. Kahn, *Chemistry in Britain*, 1999, **35**, 24-27.

86. A. H. M. Ewald, R. L.; Ross, I. G.; White, A. H.; Nyholm, R. S., *Proceedings of the Royal Society of London. Series A. Mathematical and Physical Sciences*, 1964, **280**, 235-257.
87. D. M. Halepoto, D. G. L. Holt, L. F. Larkworthy, G. J. Leigh, D. C. Povey and G. W. Smith, *Journal of the Chemical Society, Chemical Communications*, 1989, **1989**, 1322-1323.
88. G. S. Girolami, G. Wilkinson, A. M. R. Galas, M. Thornton-Pett and M. B. Hursthouse, *Journal of the Chemical Society, Dalton Transactions*, 1985, **1985**, 1339-1348.
89. T.-I. Li, G. Stucky and G. McPherson, *Acta Crystallographica Section B: Structural Crystallography and Crystal Chemistry*, 1973, **29**, 1330-1335.
90. J. W. Tracy, N. Gregory, J. Stewart and E. Lingafelter, *Acta Crystallographica*, 1962, **15**, 460-463.
91. A. H. Ewald, R. L. Martin, E. Sinn and A. H. White, *Inorganic Chemistry*, 1969, **8**, 1837-1846.
92. P. Gütllich, V. Ksenofontov and A. B. Gaspar, *Coordination Chemistry Reviews*, 2005, **249**, 1811-1829.
93. P. Gütllich, A. B. Gaspar, V. Ksenofontov and Y. Garcia, *Journal of Physics: Condensed Matter*, 2004, **16**, S1087-S1108.
94. J.-F. Létard, *Journal of Materials Chemistry*, 2006, **16**, 2550-2559.
95. A. Hauser, P. Guetlich and H. Spiering, *Inorganic Chemistry*, 1986, **25**, 4245-4248.
96. F. Varret, K. Boukheddaden, G. Chastanet, N. Paradis and J.-F. Létard, *European Journal of Inorganic Chemistry*, 2013, **2013**, 763-769.
97. S. Decurtins, P. Gütllich, C. P. Köhler and H. Spiering, *Journal of the Chemical Society, Chemical Communications*, 1985, **1985**, 430-432.
98. J. J. L. McGarvey, Ian, *Journal of the Chemical Society, Chemical Communications*, 1982, **1982**, 906-907.
99. J. J. McGarvey, I. Lawthers, K. Heremans and H. Toftlund, *Journal of the Chemical Society, Chemical Communications*, 1984, **1984**, 1575-1576.
100. I. Lawthers and J. J. McGarvey, *Journal of the American Chemical Society*, 1984, **106**, 4280-4282.
101. S. Decurtins, P. Gütllich, C. P. Köhler, H. Spiering and A. Hauser, *Chemical Physics Letters*, 1984, **105**, 1-4.
102. E. W. Mueller, J. Ensling, H. Spiering and P. Guetlich, *Inorganic Chemistry*, 1983, **22**, 2074-2078.
103. S. Decurtins, P. Gutlich, K. M. Hasselbach, A. Hauser and H. Spiering, *Inorganic Chemistry*, 1985, **24**, 2174-2178.
104. N. Negre, M. Goiran, A. Bousseksou, J. Haasnoot, K. Boukheddaden, S. Askenazy and F. Varret, *Synthetic Metals*, 2000, **115**, 289-292.
105. P. O. Ribeiro, B. P. Alho, R. M. Ribas, E. P. Nóbrega, V. S. R. de Sousa and P. J. von Ranke, *Journal of Magnetism and Magnetic Materials*, 2019, **489**, 165340.
106. P. D. Southon, L. Liu, E. A. Fellows, D. J. Price, G. J. Halder, K. W. Chapman, B. Moubaraki, K. S. Murray, J.-F. Létard and C. J. Kepert, *Journal of the American Chemical Society*, 2009, **131**, 10998-11009.
107. M. Nihei, T. Shiga, Y. Maeda and H. Oshio, *Coordination Chemistry Reviews*, 2007, **251**, 2606-2621.
108. M. Hostettler, K. W. Törnroos, D. Chernyshov, B. Vangdal and H.-B. Bürgi, *Angewandte Chemie International Edition*, 2004, **43**, 4589-4594.

109. M. d. C. Giménez-López, M. Clemente-León and C. Giménez-Saiz, *Dalton Transactions*, 2018, **47**, 10453-10462.
110. M. Clemente-León, E. Coronado, M. C. Giménez-López and F. M. Romero, *Inorganic Chemistry*, 2007, **46**, 11266-11276.
111. R.-J. Wei, J. Tao, R.-B. Huang and L.-S. Zheng, *Inorganic Chemistry*, 2011, **50**, 8553-8564.
112. P. Gütlich, *European Journal of Inorganic Chemistry*, 2013, **2013**, 581-591.
113. L. Gouy, *Comptes Rendus des Séances de l'Académie des Sciences. Paris.*, 1889, **109**, 935-937.
114. A. Saunderson, *Physics Education*, 1968, **3**, 272-273.
115. A. Earnshaw, *Introduction to magnetochemistry*, Elsevier, 2013.
116. P. W. Selwood, *Magnetochemistry*, Read Books Ltd, 2013.
117. R. Jaklevic, J. Lambe, A. Silver and J. Mercereau, *Physical Review Letters*, 1964, **12**, 159.
118. R. L. Fagaly, *Review of Scientific Instruments*, 2006, **77**, 101101.
119. M. I. Faley, U. Poppe, R. E. Dunin-Borkowski, M. Schiek, F. Boers, H. Chocholacs, J. Dammers, E. Eich, N. J. Shah, A. B. Ermakov, V. Y. Slobodchikov, Y. V. Maslennikov and V. P. Koshelets, *IEEE Transactions on Applied Superconductivity*, 2013, **23**, 1600705-1600705.
120. I. Capel Berdiell, R. Kulmaczewski and M. A. Halcrow, *Inorganic Chemistry*, 2017, **56**, 8817-8828.
121. D. F. Evans, *Journal of the Chemical Society (Resumed)*, 1959, **1959**, 2003-2005.
122. G. A. Bain and J. F. Berry, *Journal of Chemical Education*, 2008, **85**, 532.
123. D. H. Live and S. I. Chan, *Analytical Chemistry*, 1970, **42**, 791-792.
124. D. Ostfeld and I. A. Cohen, *Journal of Chemical Education*, 1972, **49**, 829.
125. C. Piguet, *Journal of Chemical Education*, 1997, **74**, 815.
126. E. M. Schubert, *Journal of Chemical Education*, 1992, **69**, 62.
127. L. A. Yatsunyk and F. A. Walker, *Inorganic Chemistry*, 2004, **43**, 757-777.
128. B. Weber and F. A. Walker, *Inorganic Chemistry*, 2007, **46**, 6794-6803.
129. E. Schrödinger, *Physical Review*, 1926, **28**, 1049.
130. M. Born and R. Oppenheimer, *Annalen der Physik*, 1927, **389**, 457-484.
131. D. R. Hartree, *Mathematical Proceedings of the Cambridge Philosophical Society*, 1928, **24**, 89-110.
132. D. R. Hartree, *Mathematical Proceedings of the Cambridge Philosophical Society*, 1928, **24**, 111-132.
133. D. R. Hartree, *Mathematical Proceedings of the Cambridge Philosophical Society*, 1928, **24**, 426-437.
134. J. C. Slater, *Physical Review*, 1928, **32**, 339.
135. J. C. Slater, *Physical Review*, 1929, **34**, 1293.
136. E. Condon, *Physical Review*, 1930, **36**, 1121.
137. C. Møller and M. S. Plesset, *Physical Review*, 1934, **46**, 618.
138. T. Tsuneda, *Density functional theory in quantum chemistry*, Springer, 2014.
139. L. H. Thomas, *Mathematical Proceedings of the Cambridge Philosophical Society*, 1927, **23**, 542-548.
140. P. A. Dirac, *Mathematical Proceedings of the Cambridge Philosophical Society*, 1930, **26**, 376-385.
141. J. S. Plaskett, *Proceedings of the Physical Society. Section A*, 1953, **66**, 178-190.
142. P. Hohenberg and W. Kohn, *Physical Review*, 1964, **136**, B864.

143. W. Kohn and L. J. Sham, *Physical Review*, 1965, **140**, A1133.
144. H. T. Paulsen, Alfred X., in *Spin Crossover in Transition Metal Compounds III*, Springer Berlin Heidelberg, Berlin, Heidelberg, 2004, vol. 2004, pp. 197-219.
145. C. Lee, W. Yang and R. Parr, *Physical Review B*, 1988, **37**, 785-789.
146. A. D. Becke, *The Journal of Chemical Physics*, 1993, **98**, 5648-5652.
147. K. Burke, *The Journal of Chemical Physics*, 2012, **136**, 150901.
148. K. L. Haas and K. J. Franz, *Chemical Reviews*, 2009, **109**, 4921-4960.
149. L. Mazaud, M. Tricoire, S. Bourcier, M. Cordier, V. Gandon and A. Auffrant, *Organometallics*, 2020, **39**, 719-728.
150. H. Schiff, *Justus Liebigs Annalen der Chemie*, 1864, **131**, 118-119.
151. H. Schiff, *Ann Chem*, 1866, **140**, 92-137.
152. T. T. Tidwell, *Angewandte Chemie International Edition*, 2008, **47**, 1016-1020.
153. L. H. Abdel-Rahman, R. M. El-Khatib, L. A. E. Nassr, A. M. Abu-Dief and F. E.-D. Lashin, *Spectrochimica Acta Part A: Molecular and Biomolecular Spectroscopy*, 2013, **111**, 266-276.
154. Â. de Fátima, C. d. P. Pereira, C. R. S. D. G. Olímpio, B. G. de Freitas Oliveira, L. L. Franco and P. H. C. da Silva, *Journal of Advanced Research*, 2018, **13**, 113-126.
155. A. M. Abu-Dief and I. M. A. Mohamed, *Beni-Suef University Journal of Basic and Applied Sciences*, 2015, **4**, 119-133.
156. A. Xavier and N. Srividhya, *IOSR Journal of Applied Chemistry*, 2014, **7**, 06-15.
157. Z. Cimerman, N. Galic and B. Bosner, *Analytica Chimica Acta*, 1997, **343**, 145-153.
158. J. Lewiński and D. Prochowicz, in *Comprehensive Supramolecular Chemistry II*, ed. J. L. Atwood, Elsevier, Oxford, 2017, pp. 279-304.
159. H. Nozaki, H. Takaya, S. Moriuti and R. Noyori, *Tetrahedron*, 1968, **24**, 3655-3669.
160. R. C. Stoufer and D. H. Busch, *Journal of the American Chemical Society*, 1956, **78**, 6016-6019.
161. J. Pernak and J. Rogoza, *ARKIVOC*, 2000, **6**, 889-904.
162. G. G. Mohamed, *Spectrochimica Acta Part A: Molecular and Biomolecular Spectroscopy*, 2006, **64**, 188-195.
163. M. A. W. Lawrence, K.-A. Green, P. N. Nelson and S. C. Lorraine, *Polyhedron*, 2018, **143**, 11-27.
164. A. Mohamadou and A. Haudrechy, *Journal of Chemical Education*, 2008, **85**, 436.
165. S. Trofimenko, *Journal of the American Chemical Society*, 1966, **88**, 1842-1844.
166. S. Trofimenko, *Journal of the American Chemical Society*, 1967, **89**, 3170-3177.
167. S. Trofimenko, J. R. Long, T. Nappier and S. G. Shore, in *Inorganic Syntheses*, 1970, vol. 12, pp. 99-109.
168. H. Vahrenkamp, *Accounts of Chemical Research*, 1999, **32**, 589-596.
169. T. Ando, M. Kamigaito and M. Sawamoto, *Macromolecules*, 2000, **33**, 5825-5829.
170. C. Slugovc, R. Schmid and K. Kirchner, *Coordination Chemistry Reviews*, 1999, **185-186**, 109-126.
171. S. Trofimenko, *Chemical Reviews*, 1993, **93**, 943-980.
172. C. A. Dodds, A. R. Kennedy, J. Reglinski and M. D. Spicer, *Inorganic Chemistry*, 2004, **43**, 394-395.
173. A. L. Rheingold, R. L. Ostrander, B. S. Haggerty and S. Trofimenko, *Inorganic Chemistry*, 1994, **33**, 3666-3676.
174. E. Peris and R. H. Crabtree, *Chemical Society Reviews*, 2018, **47**, 1959-1968.



175. C. Wei, Y. He, X. Shi and Z. Song, *Coordination Chemistry Reviews*, 2019, **385**, 1-19.
176. A. Winter and U. S. Schubert, *ChemCatChem*, **12**, 2890-2941.
177. Z. Lin, N. C. Thacker, T. Sawano, T. Drake, P. Ji, G. Lan, L. Cao, S. Liu, C. Wang and W. Lin, *Chemical Science*, 2018, **9**, 143-151.
178. H. Alemu, B. Hundhammer and T. Solomon, *Journal of Electroanalytical Chemistry and Interfacial Electrochemistry*, 1990, **294**, 165-177.
179. J. P. Sauvage, J. P. Collin, J. C. Chambron, S. Guillerez, C. Coudret, V. Balzani, F. Barigelletti, L. De Cola and L. Flamigni, *Chemical Reviews*, 1994, **94**, 993-1019.
180. T. Suzuka, M. Adachi and K. Ogihara, *Transactions of the Materials Research Society of Japan*, 2015, **40**, 103-106.
181. J. T. Ciszewski, D. Y. Mikhaylov, K. V. Holin, M. K. Kadirov, Y. H. Budnikova, O. Sinyashin and D. A. Vivic, *Inorganic Chemistry*, 2011, **50**, 8630-8635.
182. P. R. Andres and U. S. Schubert, *Advanced Materials*, 2004, **16**, 1043-1068.
183. C. J. Aspley and J. A. Gareth Williams, *New Journal of Chemistry*, 2001, **25**, 1136-1147.
184. R. V. Jagadeesh, T. Kiran, P. R. Bhagat, S. S. Kumar, P. Nithya, F. N. Khan and A. Sivakumar, *Journal of Molecular Catalysis A: Chemical*, 2011, **338**, 92-104.
185. J. Limburg, J. S. Vrettos, H. Chen, J. C. de Paula, R. H. Crabtree and G. W. Brudvig, *Journal of the American Chemical Society*, 2001, **123**, 423-430.
186. M. A. Halcrow, *Coordination Chemistry Reviews*, 2005, **249**, 2880-2908.
187. M. Marchivie, P. Guionneau, J. A. K. Howard, G. Chastanet, J.-F. Létard, A. E. Goeta and D. Chasseau, *Journal of the American Chemical Society*, 2002, **124**, 194-195.
188. T. Kitazawa, *Crystals*, 2019, **9**, 382-385.
189. S. Hayami, S. M. Holmes and M. A. Halcrow, *Journal of Materials Chemistry C*, 2015, **3**, 7775-7778.
190. I. Capel Berdiell, S. L. Warriner and M. A. Halcrow, *Dalton Transactions*, 2018, **47**, 5269-5278.
191. L. J. Kershaw Cook, R. Kulmaczewski, R. Mohammed, S. Dudley, S. A. Barrett, M. A. Little, R. J. Deeth and M. A. Halcrow, *Angewandte Chemie International Edition*, 2016, **55**, 4327-4331.
192. M. A. Halcrow, *New Journal of Chemistry*, 2014, **38**, 1868-1882.
193. G. Chastanet, C. A. Tovee, G. Hyett, M. A. Halcrow and J.-F. Létard, *Dalton Transactions*, 2012, **41**, 4896-4902.
194. H. Witte and W. Seeliger, *Angewandte Chemie International Edition in English*, 1972, **11**, 287-288.
195. J.E. Huheey, E.A. Keiter and R. L. Keiter, in *Inorganic Chemistry: Principles of Structures*, HarperCollins, 4th edn., 1993, p. 547.
196. S. A. Babu, K. K. Krishnan, S. M. Ujwaldev and G. Anilkumar, *Asian Journal of Organic Chemistry*, 2018, **7**, 1033-1053.
197. H. Nishiyama, H. Sakaguchi, T. Nakamura, M. Horihata, M. Kondo and K. Itoh, *Organometallics*, 1989, **8**, 846-848.
198. G. Balavoine, J. C. Clinet and I. Lellouche, *Tetrahedron Letters*, 1989, **30**, 5141-5144.
199. Y. Imai, W. Zhang, T. Kida, Y. Nakatsuji and I. Ikeda, *Tetrahedron: Asymmetry*, 1996, **7**, 2453-2462.
200. A. Cornejo, J. Fraile, J. García, M. Gil, V. Martínez-Merino, J. Mayoral, E. Pires and I. Villalba, *Synlett*, 2005, **2005**, 2321-2324.

201. H. Nishiyama, S. Yamaguchi, M. Kondo and K. Itoh, *The Journal of Organic Chemistry*, 1992, **57**, 4306-4309.
202. G. Desimoni, G. Faita, S. Filippone, M. Mella, M. G. Zampori and M. Zema, *Tetrahedron*, 2001, **57**, 10203-10212.
203. G. Desimoni, G. Faita, M. Guala and C. Pratelli, *Tetrahedron*, 2002, **58**, 2929-2935.
204. A. Cornejo, J. M. Fraile, J. I. García, E. García-Verdugo, M. J. Gil, G. Legarreta, S. V. Luis, V. Martínez-Merino and J. A. Mayoral, *Organic Letters*, 2002, **4**, 3927-3930.
205. M. Tilliet, S. Lundgren, C. Moberg and V. Levacher, *Advanced Synthesis & Catalysis*, 2007, **349**, 2079-2084.
206. M. I. Burguete, J. M. Fraile, E. García-Verdugo, S. V. Luis, V. Martínez-Merino and J. A. Mayoral, *Industrial & Engineering Chemistry Research*, 2005, **44**, 8580-8587.
207. R.-G. Wang, Y.-S. Meng, F.-F. Gao, W.-Q. Gao, C.-H. Liu, A. Li, T. Liu and Y.-Y. Zhu, *Dalton Transactions*, 2021, **50**, 3369-3378.
208. X. Yu, T. Yang, S. Wang, H. Xu and H. Gong, *Organic Letters*, 2011, **13**, 2138-2141.
209. S. Bhor, G. Anilkumar, M. K. Tse, M. Klawonn, C. Döbler, B. Bitterlich, A. Grotevendt and M. Beller, *Organic Letters*, 2005, **7**, 3393-3396.
210. K. E. Burrows, S. E. McGrath, R. Kulmaczewski, O. Cespedes, S. A. Barrett and M. A. Halcrow, *Chemistry – A European Journal*, 2017, **23**, 9067-9075.
211. I. Abrunhosa, M. Gulea, J. Levillain and S. Masson, *Tetrahedron: Asymmetry*, 2001, **12**, 2851-2859.
212. I. Abrunhosa, L. Delain-Bioton, A.-C. Gaumont, M. Gulea and S. Masson, *Tetrahedron*, 2004, **60**, 9263-9272.
213. P. Le Maux, I. Abrunhosa, M. Berchel, G. Simonneaux, M. Gulea and S. Masson, *Tetrahedron: Asymmetry*, 2004, **15**, 2569-2573.
214. J. D. Nobbs, A. K. Tomov, R. Cariou, V. C. Gibson, A. J. P. White and G. J. P. Britovsek, *Dalton Transactions*, 2012, **41**, 5949-5964.
215. J. Guo, B. Wang, J. Bi, C. Zhang, H. Zhang, C. Bai, Y. Hu and X. Zhang, *Polymer*, 2015, **59**, 124-132.
216. Y. Pan, Y.-S. Meng, Q. Liu, W.-Q. Gao, C.-H. Liu, T. Liu and Y.-Y. Zhu, *Inorganic Chemistry*, 2020, **59**, 7398-7407.
217. T. Nishio, Y. Kodama and Y. Tsurumi, *Phosphorus, Sulfur, and Silicon and the Related Elements*, 2005, **180**, 1449-1450.
218. L. J. Ackerman, G. M. Diamond, K. A. Hall, J. M. Longmire and M. L. Micklatcher, *Journal*, 2008.
219. G. Helmchen, A. Krotz, K.-T. Ganz and D. Hansen, *Synlett*, 1991, **1991**, 257-259.
220. N. Hisao, I. Yoshiki, S. Yuji, M. Hideki, A. Katsuyuki and I. Kenji, *Bulletin of the Chemical Society of Japan*, 1995, **68**, 1247-1262.
221. S.-F. Lu, D.-M. Du, S.-W. Zhang and J. Xu, *Tetrahedron: Asymmetry*, 2004, **15**, 3433-3441.
222. T. Nishio, *The Journal of Organic Chemistry*, 1997, **62**, 1106-1111.
223. M. K. Tse, S. Bhor, M. Klawonn, G. Anilkumar, H. Jiao, C. Döbler, A. Spannenberg, W. Mägerlein, H. Hugl and M. Beller, *Chemistry – A European Journal*, 2006, **12**, 1855-1874.
224. M. D. Towers, P. D. Woodgate and M. A. Brimble, *Arkivoc*, 2003, **1**, 43-55.
225. C. Bengtsson, H. Nelander and F. Almqvist, *Chemistry – A European Journal*, 2013, **19**, 9916-9922.

226. R. Alan Aitken, D. P. Armstrong, R. H. B. Galt and S. T. E. Mesher, *Journal of the Chemical Society, Perkin Transactions 1*, 1997, 935-944.
227. T. Ozturk, E. Ertas and O. Mert, *Chemical Reviews*, 2007, **107**, 5210-5278.
228. T. Nishio, *Tetrahedron Letters*, 1995, **36**, 6113-6116.
229. M. Z. Gao, J. H. Reibenspies, R. A. Zingaro, B. Wang and Z. L. Xu, *Journal of Heterocyclic Chemistry*, 2004, **41**, 899-908.
230. M. Jesberger, T. P. Davis and L. Barner, *Synthesis*, 2003, **2003**, 1929-1958.
231. J. T. Muckerman, J. H. Skone, M. Ning and Y. Wasada-Tsutsui, *Biochimica et Biophysica Acta (BBA) - Bioenergetics*, 2013, **1827**, 882-891.
232. K. A. Byriel, V. Gasperov, K. Gloe, C. H. L. Kennard, A. J. Leong, L. F. Lindoy, M. S. Mahinay, H. T. Pham, P. A. Tasker, D. Thorp and P. Turner, *Dalton Transactions*, 2003, DOI: 10.1039/B303825D, 3034-3040.
233. S. Takahashi and H. Togo, *Synthesis*, 2009, **2009**, 2329-2332.
234. W. E. Palke and B. Kirtman, *Journal of the American Chemical Society*, 1978, **100**, 5717-5721.
235. P. Hermange, A. T. Lindhardt, R. H. Taaning, K. Bjerglund, D. Lupp and T. Skrydstrup, *Journal of the American Chemical Society*, 2011, **133**, 6061-6071.
236. K.-H. Ernst, F. R. W. P. Wild, O. Blacque and H. Berke, *Angewandte Chemie International Edition*, 2011, **50**, 10780-10787.
237. G. B. Kauffman, *Journal of Chemical Education*, 1959, **36**, 521.
238. A. Werner, *Berichte der deutschen chemischen Gesellschaft*, 1907, **40**, 4817-4825.
239. A. Werner, *Justus Liebigs Annalen der Chemie*, 1912, **386**, 1-272.
240. A. Werner, *Berichte der deutschen chemischen Gesellschaft*, 1911, **44**, 3279-3284.
241. J. W. Canary, C. S. Allen, J. M. Castagnetto and Y. Wang, *Journal of the American Chemical Society*, 1995, **117**, 8484-8485.
242. N. Ousaka, Y. Takeyama, H. Iida and E. Yashima, *Nature Chemistry*, 2011, **3**, 856-861.
243. T. Liu, Y. Liu, W. Xuan and Y. Cui, *Angewandte Chemie International Edition*, 2010, **49**, 4121-4124.
244. E. B. Bauer, *Chemical Society Reviews*, 2012, **41**, 3153-3167.
245. D. H. Busch, *Journal of Chemical Education*, 1964, **41**, 77.
246. Z.-H. Yan, D. Li and X.-B. Yin, *Science Bulletin*, 2017, **62**, 1344-1354.
247. L. Gong, L.-A. Chen and E. Meggers, *Angewandte Chemie International Edition*, 2014, **53**, 10868-10874.
248. B. M. Zeglis, V. C. Pierre and J. K. Barton, *Chemical Communications*, 2007, 4565-4579.
249. M. Dörr and E. Meggers, *Current Opinion in Chemical Biology*, 2014, **19**, 76-81.
250. X. Zhang, *New Voices in Chemistry*, 2001, 142.
251. C. A. Busacca, D. R. Fandrick, J. J. Song and C. H. Senanayake, *Advanced Synthesis & Catalysis*, 2011, **353**, 1825-1864.
252. E. A. Hillard and G. Jaouen, *Organometallics*, 2011, **30**, 20-27.
253. L. Canali and D. C. Sherrington, *Chemical Society Reviews*, 1999, **28**, 85-93.
254. J. K. Whitesell, *Chemical Reviews*, 1989, **89**, 1581-1590.
255. G. L. Hamilton, E. J. Kang, M. Mba and F. D. Toste, *Science*, 2007, **317**, 496.
256. V. B. Jakobsen, L. O'Brien, G. Novitchi, H. Müller-Bunz, A.-L. Barra and G. G. Morgan, *European Journal of Inorganic Chemistry*, 2019, **2019**, 4405-4411.
257. E. Meggers, *Chemistry – A European Journal*, 2010, **16**, 752-758.

258. L. Gong, M. Wenzel and E. Meggers, *Accounts of Chemical Research*, 2013, **46**, 2635-2644.
259. R. Noyori, *Science*, 1990, **248**, 1194.
260. H. Nozaki, S. Moriuti, H. Takaya and R. Noyori, *Tetrahedron Letters*, 1966, **7**, 5239-5244.
261. S. Hayami, K. Danjobara, K. Inoue, Y. Ogawa, N. Matsumoto and Y. Maeda, *Advanced Materials*, 2004, **16**, 869-872.
262. S. Hayami, N. Motokawa, A. Shuto, N. Masuhara, T. Someya, Y. Ogawa, K. Inoue and Y. Maeda, *Inorganic Chemistry*, 2007, **46**, 1789-1794.
263. S. Hayami, R. Moriyama, A. Shuto, Y. Maeda, K. Ohta and K. Inoue, *Inorganic Chemistry*, 2007, **46**, 7692-7694.
264. C. Faulmann, S. Dorbes, B. Garreau de Bonneval, G. Molnár, A. Bousseksou, C. J. Gomez-Garcia, E. Coronado and L. Valade, *European Journal of Inorganic Chemistry*, 2005, **2005**, 3261-3270.
265. M. Nihei, Y. Sekine, N. Suganami, K. Nakazawa, A. Nakao, H. Nakao, Y. Murakami and H. Oshio, *Journal of the American Chemical Society*, 2011, **133**, 3592-3600.
266. L. Salmon, G. Molnár, D. Zitouni, C. Quintero, C. Bergaud, J.-C. Micheau and A. Bousseksou, *Journal of Materials Chemistry*, 2010, **20**, 5499-5503.
267. J. Ru, F. Yu, P.-P. Shi, C.-Q. Jiao, C.-H. Li, R.-G. Xiong, T. Liu, M. Kurmoo and J.-L. Zuo, *European Journal of Inorganic Chemistry*, 2017, **2017**, 3144-3149.
268. D.-W. Fu, W. Zhang, H.-L. Cai, Y. Zhang, J.-Z. Ge, R.-G. Xiong, S. D. Huang and T. Nakamura, *Angewandte Chemie International Edition*, 2011, **50**, 11947-11951.
269. Q. Kong, R. Qin, D. Li, H. Zhao, Y. Ren, L. Long and L. Zheng, *RSC Advances*, 2019, **9**, 41832-41836.
270. W. Liu, X. Bao, L.-L. Mao, J. Tucek, R. Zboril, J.-L. Liu, F.-S. Guo, Z.-P. Ni and M.-L. Tong, *Chemical Communications*, 2014, **50**, 4059-4061.
271. D.-H. Ren, D. Qiu, C.-Y. Pang, Z. Li and Z.-G. Gu, *Chemical Communications*, 2015, **51**, 788-791.
272. F. Arago, *Œuvres complètes de François Arago*, 1811.
273. F. Leclercq, *Revue d'histoire des sciences*, 2013, **66**, 395-416.
274. M. Faraday, *Philosophical Transactions of the Royal Society of London*, 1846, **136**, 1-20.
275. J. M. Thomas, *Journal of the Chemical Society, Faraday Transactions*, 1991, **87**, 2865-2870.
276. L. Pasteur, *Annales de Chimie et de Physique*, 1848, **24**, 442-459.
277. L. Pasteur, *Comptes Rendus Hebdomadaires des Séances de l'Académie des Sciences*, 1848, **26**, 535-538.
278. M. Atzori, G. L. J. A. Rikken and C. Train, *Chemistry – A European Journal*, 2020, **26**, 9784-9791.
279. S.-i. Ohkoshi, S. Takano, K. Imoto, M. Yoshikiyo, A. Namai and H. Tokoro, *Nature Photonics*, 2014, **8**, 65-71.
280. Y. Sunatsuki, Y. Ikuta, N. Matsumoto, H. Ohta, M. Kojima, S. Iijima, S. Hayami, Y. Maeda, S. Kaizaki, F. Dahan and J.-P. Tuchagues, *Angewandte Chemie International Edition*, 2003, **42**, 1614-1618.
281. K. Senthil Kumar and M. Ruben, *Coordination Chemistry Reviews*, 2017, **346**, 176-205.
282. P. G. Lacroix, I. Malfant, J.-A. Real and V. Rodriguez, *European Journal of Inorganic Chemistry*, 2013, **2013**, 615-627.

283. Y. Sekimoto, M. R. Karim, N. Saigo, R. Ohtani, M. Nakamura and S. Hayami, *European Journal of Inorganic Chemistry*, 2017, **2017**, 1049-1053.
284. G. L. J. A. Rikken and E. Raupach, *Nature*, 1997, **390**, 493-494.
285. T. Romero-Morcillo, F. J. Valverde-Muñoz, M. C. Muñoz, J. M. Herrera, E. Colacio and J. A. Real, *RSC Advances*, 2015, **5**, 69782-69789.
286. N. Hoshino, F. Iijima, G. N. Newton, N. Yoshida, T. Shiga, H. Nojiri, A. Nakao, R. Kumai, Y. Murakami and H. Oshio, *Nature Chemistry*, 2012, **4**, 921-926.
287. Y. Sunatsuki, S. Miyahara, Y. Sasaki, T. Suzuki, M. Kojima and N. Matsumoto, *CrystEngComm*, 2012, **14**, 6377-6380.
288. I. Katsuki, Y. Motoda, Y. Sunatsuki, N. Matsumoto, T. Nakashima and M. Kojima, *Journal of the American Chemical Society*, 2002, **124**, 629-640.
289. H. Nakamura, Y. Sunatsuki, M. Kojima and N. Matsumoto, *Inorganic Chemistry*, 2007, **46**, 8170-8181.
290. H. Nakamura, M. Fujii, Y. Sunatsuki, M. Kojima and N. Matsumoto, *European Journal of Inorganic Chemistry*, 2008, **2008**, 1258-1267.
291. T. Hashibe, T. Fujinami, D. Furusho, N. Matsumoto and Y. Sunatsuki, *Inorganica Chimica Acta*, 2011, **375**, 338-342.
292. M. Clemente-León, E. Coronado, C. Martí-Gastaldo and F. M. Romero, *Chemical Society Reviews*, 2011, **40**, 473-497.
293. C. Bartual-Murgui, L. Piñeiro-López, F. J. Valverde-Muñoz, M. C. Muñoz, M. Seredyuk and J. A. Real, *Inorganic Chemistry*, 2017, **56**, 13535-13546.
294. A. Ozarowski, B. R. McGarvey, A. B. Sarkar and J. E. Drake, *Inorganic Chemistry*, 1988, **27**, 628-635.
295. E. Koenig, K. Madeja and K. J. Watson, *Journal of the American Chemical Society*, 1968, **90**, 1146-1153.
296. J.-F. Létard, P. Guionneau, L. Rabardel, J. A. K. Howard, A. E. Goeta, D. Chasseau and O. Kahn, *Inorganic Chemistry*, 1998, **37**, 4432-4441.
297. M. Marchivie, P. Guionneau, J.-F. Létard and D. Chasseau, *Acta Crystallographica Section B: Structural Science*, 2003, **59**, 479-486.
298. N. Moliner, M. C. Muñoz, P. J. van Koningsbruggen and J. Real, *Inorganica Chimica Acta*, 1998, **274**, 1-6.
299. N. Moliner, M. C. Muñoz, S. Létard, J.-F. Létard, X. Solans, R. Burriel, M. Castro, O. Kahn and J. A. Real, *Inorganica Chimica Acta*, 1999, **291**, 279-288.
300. K. Michiko and M.-K. Mami, *Bulletin of the Chemical Society of Japan*, 1991, **64**, 339-345.
301. B. Gallois, J. A. Real, C. Hauw and J. Zarembowitch, *Inorganic Chemistry*, 1990, **29**, 1152-1158.
302. J. A. Real, B. Gallois, T. Granier, F. Suez-Panama and J. Zarembowitch, *Inorganic Chemistry*, 1992, **31**, 4972-4979.
303. J. A. Real, M. C. Munoz, E. Andres, T. Granier and B. Gallois, *Inorganic Chemistry*, 1994, **33**, 3587-3594.
304. S. Bonnet, M. A. Siegler, J. S. Costa, G. Molnár, A. Bousseksou, A. L. Spek, P. Gamez and J. Reedijk, *Chemical Communications*, 2008, 5619-5621.
305. Z. Arcis-Castillo, S. Zheng, M. A. Siegler, O. Roubeau, S. Bedoui and S. Bonnet, *Chemistry – A European Journal*, 2011, **17**, 14826-14836.
306. N. Bréfuel, S. Shova, J. Lipkowski and J.-P. Tuchagues, *Chemistry of Materials*, 2006, **18**, 5467-5479.
307. M. Sorai and S. Seki, *Journal of Physics and Chemistry of Solids*, 1974, **35**, 555-570.

308. J.-F. Létard, P. Guionneau, E. Codjovi, O. Lavastre, G. Bravic, D. Chasseau and O. Kahn, *Journal of the American Chemical Society*, 1997, **119**, 10861-10862.
309. C.-F. Sheu, K. Chen, S.-M. Chen, Y.-S. Wen, G.-H. Lee, J.-M. Chen, J.-F. Lee, B.-M. Cheng, H.-S. Sheu, N. Yasuda, Y. Ozawa, K. Toriumi and Y. Wang, *Chemistry – A European Journal*, 2009, **15**, 2384-2393.
310. K. Barbalace, Periodic Table of Elements - EnvironmentalChemistry.com).
311. C. F. Herold, L. M. Carrella and E. Rentschler, *European Journal of Inorganic Chemistry*, 2015, **2015**, 3632-3636.
312. C. F. Herold, S. I. Shylin and E. Rentschler, *Inorganic Chemistry*, 2016, **55**, 6414-6419.
313. S. Singh and S. Brooker, *Inorganic Chemistry*, 2020, **59**, 1265-1273.
314. A. F. Orchard, *Magnetochemistry*, Oxford University Press, 2003.
315. A. A. Pavlov, D. Y. Aleshin, I. A. Nikovskiy, A. V. Polezhaev, N. N. Efimov, A. A. Korlyukov, V. V. Novikov and Y. V. Nelyubina, *European Journal of Inorganic Chemistry*, 2019, **2019**, 2819-2829.
316. Y. Pankratova, D. Aleshin, I. Nikovskiy, V. Novikov and Y. Nelyubina, *Inorganic Chemistry*, 2020, **59**, 7700-7709.
317. A. Kimura and T. Ishida, *Inorganics*, 2017, **5**, 52.
318. M. Kruck, D. C. Sauer, M. Enders, H. Wadepohl and L. H. Gade, *Dalton Transactions*, 2011, **40**, 10406-10415.
319. K. E. Burrows, R. Kulmaczewski, O. Cespedes, S. A. Barrett and M. A. Halcrow, *Polyhedron*, 2018, **149**, 134-141.
320. K. E. Burrows, Ph.D., University of Leeds, 2019.
321. S. Hirofumi, S. Yoshitomo, T. Yoshio, K. Hideya, A. Ryuichi and S. Motohiro, *Chemistry Letters*, 2010, **39**, 564-566.
322. D. A. Evans, M. C. Kozlowski, J. A. Murry, C. S. Burgey, K. R. Campos, B. T. Connell and R. J. Staples, *Journal of the American Chemical Society*, 1999, **121**, 669-685.
323. S. Saaby, K. Nakama, M. Alstrup Lie, R. G. Hazell and K. Anker Jørgensen, *Chemistry – A European Journal*, 2003, **9**, 6145-6154.
324. C. Provent, G. Bernardinelli, Alan F. Williams and N. Vulliermet, *European Journal of Inorganic Chemistry*, 2001, **2001**, 1963-1967.
325. C. E. Housecroft and A. G. Sharpe, *Inorganic Chemistry*, Pearson Education Limited, 4th edn., 2012.
326. W.-Q. Gao, Y.-S. Meng, C.-H. Liu, Y. Pan, T. Liu and Y.-Y. Zhu, *Dalton Transactions*, 2019, **48**, 6323-6327.
327. Y.-Y. Zhu, C.-W. Liu, J. Yin, Z.-S. Meng, Q. Yang, J. Wang, T. Liu and S. Gao, *Dalton Transactions*, 2015, **44**, 20906-20912.
328. Y.-Q. Wang, Y. Pan, W.-Q. Gao, Y. Wu, C.-H. Liu and Y.-Y. Zhu, *Tetrahedron*, 2019, **75**, 3809-3814.
329. L. J. Kershaw Cook, R. Mohammed, G. Sherborne, T. D. Roberts, S. Alvarez and M. A. Halcrow, *Coordination Chemistry Reviews*, 2015, **289-290**, 2-12.
330. M. A. Halcrow, *Dalton Transactions*, 2020, **49**, 15560-15567.
331. S. Vela, J. J. Novoa and J. Ribas-Arino, *Physical Chemistry Chemical Physics*, 2014, **16**, 27012-27024.
332. P. Atkins and J. De Paula, *Elements of Physical Chemistry*, Oxford University Press, USA, 2013.
333. M. Sorai, in *Spin Crossover in Transition Metal Compounds III*, Springer Berlin Heidelberg, Berlin, Heidelberg, 2004, vol. 235, pp. 153-170.

334. C. F. Macrae, I. J. Bruno, J. A. Chisholm, P. R. Edgington, P. McCabe, E. Pidcock, L. Rodriguez-Monge, R. Taylor, J. v. d. Streek and P. A. Wood, *Journal of Applied Crystallography*, 2008, **41**, 466-470.
335. C. F. Macrae, P. R. Edgington, P. McCabe, E. Pidcock, G. P. Shields, R. Taylor, M. Towler and J. v. d. Streek, *Journal of Applied Crystallography*, 2006, **39**, 453-457.
336. I. Nikovskiy, A. Polezhaev, V. Novikov, D. Aleshin, A. Pavlov, E. Saffiulina, R. Aysin, P. Dorovatovskii, L. Nodaraki, F. Tuna and Y. Nelyubina, 2020, **26**, 5629-5638.
337. J. S. Costa, S. Rodríguez-Jiménez, G. A. Craig, B. Barth, C. M. Beavers, S. J. Teat and G. Aromí, *Journal of the American Chemical Society*, 2014, **136**, 3869-3874.
338. V. García-López, M. Palacios-Corella, V. Gironés-Pérez, C. Bartual-Murgui, J. A. Real, E. Pellegrin, J. Herrero-Martín, G. Aromí, M. Clemente-León and E. Coronado, *Inorganic Chemistry*, 2019, **58**, 12199-12208.
339. G. Aromí, C. M. Beavers, J. Sánchez Costa, G. A. Craig, G. Mínguez Espallargas, A. Orera and O. Roubeau, *Chemical Science*, 2016, **7**, 2907-2915.
340. L. A. Barrios, C. Bartual-Murgui, E. Peyrecave-Lleixà, B. Le Guennic, S. J. Teat, O. Roubeau and G. Aromí, *Inorganic Chemistry*, 2016, **55**, 4110-4116.
341. A. Abhervé, M. Clemente-León, E. Coronado, C. J. Gómez-García and M. López-Jordà, *Dalton Transactions*, 2014, **43**, 9406-9409.
342. V. García-López, M. Palacios-Corella, A. Abhervé, I. Pellicer-Carreño, C. Desplanches, M. Clemente-León and E. Coronado, *Dalton Transactions*, 2018, **47**, 16958-16968.
343. B. Vosough Razavi, A. Badiei, N. Lashgari and G. Mohammadi Ziarani, *Journal of Fluorescence*, 2016, **26**, 1723-1728.
344. B. Chetia and P. K. Iyer, *Tetrahedron Letters*, 2008, **49**, 94-97.
345. B. Chetia and P. K. Iyer, *Tetrahedron Letters*, 2006, **47**, 8115-8117.
346. H. Wu, X. Huang, J. Yuan, F. Kou, F. Jia, B. Liu and K. Wang, *European Journal of Medicinal Chemistry*, 2010, **45**, 5324-5330.
347. H.-L. Wu, J.-K. Yuan, X.-C. Huang, F. Kou, B. Liu, F. Jia, K.-T. Wang and Y. Bai, *Inorganica Chimica Acta*, 2012, **390**, 12-21.
348. R. Esteghamat-Panah, H. Hadadzadeh, H. Farrokhpour, J. Simpson, A. Abdolmaleki and F. Abyar, *European Journal of Medicinal Chemistry*, 2017, **127**, 958-971.
349. C. Rajnák, J. Titiš, O. Fuhr, M. Ruben and R. Boča, *Polyhedron*, 2017, **123**, 122-131.
350. R. Boča, P. Baran, L. u. Dlháň, H. Fuess, W. Haase, F. Renz, W. Linert, I. Svoboda and R. Werner, *Inorganica Chimica Acta*, 1997, **260**, 129-136.
351. R. Boc̣a, P. Baran, M. Boc̣a, L. u. Dlháň, H. Fuess, W. Haase, W. Linert, B. e. Papańkova´ and R. d. Werner, *Inorganica Chimica Acta*, 1998, **278**, 190-196.
352. R. Boča, M. Boča, L. Dlháň, K. Falk, H. Fuess, W. Haase, R. Jarošciak, B. Papánková, F. Renz, M. Vrbová and R. Werner, *Inorganic Chemistry*, 2001, **40**, 3025-3033.
353. K. Molčanov and B. Kojić-Prodić, *International Union of Crystallography Journal*, 2019, **6**, 156-166.
354. E. Arunan, G. R. Desiraju, R. A. Klein, J. Sadlej, S. Scheiner, I. Alkorta, D. C. Clary, R. H. Crabtree, J. J. Dannenberg, P. Hobza, H. G. Kjaergaard, A. C. Legon, B. Mennucci and D. J. Nesbitt, *Journal of Pure and Applied Chemistry*, 2011, **83**, 1637-1641.

355. W. Linert, M. Konecny and F. Renz, *Journal of the Chemical Society, Dalton Transactions*, 1994, 1523-1531.
356. A. D. Ivanova, E. V. Korotaev, V. Y. Komarov, L. A. Sheludyakova, V. A. Varnek and L. G. Lavrenova, *New Journal of Chemistry*, 2020, **44**, 5834-5840.
357. A. W. Addison, S. Burman, C. G. Wahlgren, O. A. Rajan, T. M. Rowe and E. Sinn, *Journal of the Chemical Society, Dalton Transactions*, 1987, 2621-2630.
358. L. Pazderski, T. Pawlak, J. Sitkowski, L. Kozerski and E. Szlyk, *Magnetic Resonance in Chemistry*, 2011, **49**, 237-241.
359. R. M. Bullock, *Catalysis without precious metals*, John Wiley & Sons, 2011.
360. Y.-R. Luo and J. Kerr, *CRC Handbook of Chemistry*, 2012, **89**, 89.
361. J. A. Osborn, G. Wilkinson and J. J. Mrowca, in *Inorganic Syntheses*, ed. E. L. Muetterties, 1967, pp. 67-71.
362. R. Noyori, M. Kitamura and T. Ohkuma, *Proceedings of the National Academy of Sciences of the United States of America*, 2004, **101**, 5356-5362.
363. A. Ault, *Journal of Chemical Education*, 2002, **79**, 572.
364. R. Noyori, *Chemical Communications*, 2005, **14**, 1807-1811.
365. R. H. Grubbs, *Angewandte Chemie International Edition*, 2006, **45**, 3760-3765.
366. A. M. Echavarren, *ChemCatChem*, 2010, **2**, 1331-1332.
367. NobelPrize.org, The Nobel Prize in Chemistry 2010).
368. P. J. Chirik and K. Wieghardt, *Science*, 2010, **327**, 794-795.
369. P. Chirik and R. Morris, *Accounts of Chemical Research*, 2015, **48**, 2495-2495.
370. S. R. Taylor, *Geochimica et Cosmochimica Acta*, 1964, **28**, 1273-1285.
371. B. Manna, A. V. Desai and S. K. Ghosh, *Dalton Transactions*, 2016, **45**, 4060-4072.
372. R. B. Bedford, *Accounts of Chemical Research*, 2015, **48**, 1485-1493.
373. P. L. Holland, *Accounts of Chemical Research*, 2015, **48**, 1696-1702.
374. J. P. Lomont, S. C. Nguyen and C. B. Harris, *Accounts of Chemical Research*, 2014, **47**, 1634-1642.
375. S. D. McCann and S. S. Stahl, *Accounts of Chemical Research*, 2015, **48**, 1756-1766.
376. M. Tobisu and N. Chatani, *Accounts of Chemical Research*, 2015, **48**, 1717-1726.
377. D. J. Weix, *Accounts of Chemical Research*, 2015, **48**, 1767-1775.
378. D. A. Everson, R. Shrestha and D. J. Weix, *Journal of the American Chemical Society*, 2010, **132**, 920-921.
379. B. Su, Z.-C. Cao and Z.-J. Shi, *Accounts of Chemical Research*, 2015, **48**, 886-896.
380. K. L. Peretti, H. Ajiro, C. T. Cohen, E. B. Lobkovsky and G. W. Coates, *Journal of the American Chemical Society*, 2005, **127**, 11566-11567.
381. T. J. Korstanje, J. Ivar van der Vlugt, Elsevier, C. J. and B. de Bruin, *Science*, 2015, **350**, 298-302.
382. M. B. Widegren, G. J. Harkness, A. M. Z. Slawin, D. B. Cordes and M. L. Clarke, *Angewandte Chemie International Edition*, 2017, **56**, 5825-5828.
383. S. M. Paradine, J. R. Griffin, J. Zhao, A. L. Petronico, S. M. Miller and M. Christina White, *Nature Chemistry*, 2015, **7**, 987-994.
384. L. A. MacAdams, G. P. Buffone, C. D. Incarvito, A. L. Rheingold and K. H. Theopold, *Journal of the American Chemical Society*, 2005, **127**, 1082-1083.
385. H. Hachiya, K. Hirano, T. Satoh and M. Miura, *Organic Letters*, 2009, **11**, 1737-1740.



386. M. P. McDaniel, in *Advances in Catalysis*, eds. B. C. Gates and H. Knözinger, Academic Press, 2010, vol. 53, pp. 123-606.
387. K. Sonogashira, *Journal of Organometallic Chemistry*, 2002, **653**, 46-49.
388. H. C. Kolb and K. B. Sharpless, *Drug Discovery Today*, 2003, **8**, 1128-1137.
389. V. V. Rostovtsev, L. G. Green, V. V. Fokin and K. B. Sharpless, *Angewandte Chemie International Edition*, 2002, **41**, 2596-2599.
390. A. Klapars, J. C. Antilla, X. Huang and S. L. Buchwald, *Journal of the American Chemical Society*, 2001, **123**, 7727-7729.
391. A. Klapars, X. Huang and S. L. Buchwald, *Journal of the American Chemical Society*, 2002, **124**, 7421-7428.
392. G. C. Chinen, M. S. Spencer, K. C. Waugh and D. A. Whan, *Journal of the Chemical Society, Faraday Transactions 1: Physical Chemistry in Condensed Phases*, 1987, **83**, 2193-2212.
393. C. Sambigiio, S. P. Marsden, A. J. Blacker and P. C. McGowan, *Chemical Society Reviews*, 2014, **43**, 3525-3550.
394. E. M. Alayon, M. Nachtegaal, M. Ranocchiari and J. A. van Bokhoven, *Chemical Communications*, 2012, **48**, 404-406.
395. R. J. Phipps and M. J. Gaunt, *Science*, 2009, **323**, 1593-1597.
396. O. Daugulis and V. G. Zaitsev, *Angewandte Chemie International Edition*, 2005, **44**, 4046-4048.
397. I. Goldberg, *Berichte der Deutschen Chemischen Gesellschaft*, 1906, **39**, 1691-1692.
398. I. P. Beletskaya, A. G. Bessmertnykh and R. Guilard, *Tetrahedron Letters*, 1997, **38**, 2287-2290.
399. F. Ullmann, *Berichte der Deutschen Chemischen Gesellschaft*, 1903, **36**, 2382-2384.
400. F. Ullmann and P. Sponagel, *Berichte der Deutschen Chemischen Gesellschaft*, 1905, **38**, 2211-2212.
401. J. Lindley, *Tetrahedron*, 1984, **40**, 1433-1456.
402. X. Ribas and I. Güell, *Journal of Pure and Applied Chemistry*, 2014, **86**, 345-360.
403. A. Casitas, A. E. King, T. Parella, M. Costas, S. S. Stahl and X. Ribas, *Chemical Science*, 2010, **1**, 326-330.
404. H. Weingarten, *The Journal of Organic Chemistry*, 1964, **29**, 3624-3626.
405. A. J. Paine, *Journal of the American Chemical Society*, 1987, **109**, 1496-1502.
406. E. Sperotto, G. P. M. van Klink, G. van Koten and J. G. de Vries, *Dalton Transactions*, 2010, **39**, 10338-10351.
407. A. Kiyomori, J.-F. Marcoux and S. L. Buchwald, *Tetrahedron Letters*, 1999, **40**, 2657-2660.
408. A. Ouali, J.-F. Spindler, A. Jutand and M. Taillefer, *Advanced Synthesis & Catalysis*, 2007, **349**, 1906-1916.
409. C. W. Tornøe, C. Christensen and M. Meldal, *The Journal of Organic Chemistry*, 2002, **67**, 3057-3064.
410. R. Huisgen, *Angewandte Chemie International Edition*, 1963, **2**, 565-598.
411. R. Huisgen, *Angewandte Chemie International Edition*, 1963, **2**, 633-645.
412. E. Haldón, M. C. Nicasio and P. J. Pérez, *Organic & Biomolecular Chemistry*, 2015, **13**, 9528-9550.
413. R. Berg and B. F. Straub, *Beilstein Journal of Organic Chemistry*, 2013, **9**, 2715-2750.
414. P. M. E. Gramlich, C. T. Wirges, A. Manetto and T. Carell, *Angewandte Chemie International Edition*, 2008, **47**, 8350-8358.

415. J. A. Johnson, M. G. Finn, J. T. Koberstein and N. J. Turro, *Macromolecular Rapid Communications* 2008, **29**, 1052-1072.
416. F. Alonso, Y. Moglie, G. Radivoy and M. Yus, *Tetrahedron Letters*, 2009, **50**, 2358-2362.
417. G. Molteni, C. L. Bianchi, G. Marinoni, N. Santo and A. Ponti, *New Journal of Chemistry*, 2006, **30**, 1137-1139.
418. V. Aragão-Leoneti, V. L. Campo, A. S. Gomes, R. A. Field and I. Carvalho, *Tetrahedron*, 2010, **66**, 9475-9492.
419. L. Liang and D. Astruc, *Coordination Chemistry Reviews*, 2011, **255**, 2933-2945.
420. H. Ben El Ayouchia, L. Bahsis, H. Anane, L. R. Domingo and S.-E. Stiriba, *RSC Advances*, 2018, **8**, 7670-7678.
421. D. A. Evans, D. M. Barnes, J. S. Johnson, T. Lectka, P. von Matt, S. J. Miller, J. A. Murry, R. D. Norcross, E. A. Shaughnessy and K. R. Campos, *Journal of the American Chemical Society*, 1999, **121**, 7582-7594.
422. D. A. Evans, S. J. Miller and T. Lectka, *Journal of the American Chemical Society*, 1993, **115**, 6460-6461.
423. D. A. Evans, M. C. Kozlowski and J. S. Tedrow, *Tetrahedron Letters*, 1996, **37**, 7481-7484.
424. C. Wei and C.-J. Li, *Journal of the American Chemical Society*, 2002, **124**, 5638-5639.
425. C. Wei, J. T. Mague and C.-J. Li, *Proceedings of the National Academy of Sciences of the United States of America*, 2004, **101**, 5749-5754.
426. A. Bisai and V. K. Singh, *Organic Letters*, 2006, **8**, 2405-2408.
427. R. Dodda and C.-G. Zhao, *Tetrahedron Letters*, 2007, **48**, 4339-4342.
428. S. K. Ginotra and V. K. Singh, *Organic & Biomolecular Chemistry*, 2006, **4**, 4370-4374.
429. A. D. Gupta, D. Bhuniya and V. K. Singh, *Tetrahedron*, 1994, **50**, 13725-13730.
430. J.-c. Meng, V. V. Fokin and M. G. Finn, *Tetrahedron Letters*, 2005, **46**, 4543-4546.
431. R. Saalfrank, B. Demleitner and J. Sauvage, *Transition Metals in Supramolecular Chemistry*, Wiley-VHC, Weinheim, 1999.
432. J.-M. Lehn, *Science*, 2002, **295**, 2400-2403.
433. O. Mamula, A. von Zelewsky, T. Bark and G. Bernardinelli, *Angewandte Chemie International Edition*, 1999, **38**, 2945-2948.
434. J.-M. Lehn and J. Sanders, *Angewandte Chemie - English Edition*, 1995, **34**, 2563.
435. F. Gadissa Gelalcha, M. Schulz, R. Kluge and J. Sieler, *Journal of the Chemical Society, Dalton Transactions*, 2002, 2517-2521.
436. J. F. Stoddart, *Accounts of Chemical Research*, 2001, **34**, 410-411.
437. P. J. Heard and C. Jones, *Journal of the Chemical Society, Dalton Transactions*, 1997, 1083-1092.
438. P. J. Heard and D. A. Tocher, *Journal of the Chemical Society, Dalton Transactions*, 1998, 2169-2176.
439. D. Cuervo, J. Díez, M. P. Gamasa, S. García-Granda and J. Gimeno, *Inorganic Chemistry*, 2002, **41**, 4999-5001.
440. M. Schulz, R. Kluge and F. Gadissa Gelalcha, *Tetrahedron: Asymmetry*, 1998, **9**, 4341-4360.
441. A. S. Gokhale, A. B. E. Minidis and A. Pfaltz, *Tetrahedron Letters*, 1995, **36**, 1831-1834.

442. M. Panera, J. Díez, I. Merino, E. Rubio and M. P. Gamasa, *Inorganic Chemistry*, 2009, **48**, 11147-11160.
443. J. Díez, M. P. Gamasa and M. Panera, *Inorganic Chemistry*, 2006, **45**, 10043-10045.
444. M. Veidis, G. Schreiber, T. Gough and G. J. Palenik, *Journal of the American Chemical Society*, 1969, **91**, 1859-1860.
445. M. A. Halcrow, *Chemical Society Reviews*, 2013, **42**, 1784-1795.
446. N. K. Solanki, E. J. L. McInnes, F. E. Mabbs, S. Radojevic, M. McPartlin, N. Feeder, J. E. Davies and M. A. Halcrow, *Angewandte Chemie International Edition*, 1998, **37**, 2221-2223.
447. M. A. Leech, J. A. K. Howard, S. Dahaoui, N. K. Solanki and M. A. Halcrow, *Chemical Communications*, 1999, 2245-2246.
448. C. Piguet, G. Bernardinelli and A. F. Williams, *Inorganic Chemistry*, 1989, **28**, 2920-2925.
449. F. A. Cotton, X. Feng and D. J. Timmons, *Inorganic Chemistry*, 1998, **37**, 4066-4069.
450. K. T. Potts, C. P. Horwitz, A. Fessak, M. Keshavarz-K, K. E. Nash and P. J. Toscano, *Journal of the American Chemical Society*, 1993, **115**, 10444-10445.
451. J. S. Thompson, R. L. Harlow and J. F. Whitney, *Journal of the American Chemical Society*, 1983, **105**, 3522-3527.
452. B. F. Straub, F. Rominger and P. Hofmann, *Inorganic Chemistry*, 2000, **39**, 2113-2119.
453. H.-J. Lin, S. Lutz, C. O'Kane, M. Zeller, C.-H. Chen, T. Al Assil and W.-T. Lee, *Dalton Transactions*, 2018, **47**, 3243-3247.
454. H. Weissman, L. J. W. Shimon and D. Milstein, *Organometallics*, 2004, **23**, 3931-3940.
455. Z. Weng, S. Teo and T. S. A. Hor, *Accounts of Chemical Research*, 2007, **40**, 676-684.
456. J. Vela, S. Vaddadi, S. Kingsley, C. J. Flaschenriem, R. J. Lachicotte, T. R. Cundari and P. L. Holland, *Angewandte Chemie International Edition*, 2006, **45**, 1607-1611.
457. P. Appukkuttan, W. Dehaen, V. V. Fokin and E. Van der Eycken, *Organic Letters*, 2004, **6**, 4223-4225.
458. A. K. Feldman, B. Colasson and V. V. Fokin, *Organic Letters*, 2004, **6**, 3897-3899.
459. F. Alonso, Y. Moglie, G. Radivoy and M. Yus, *Synlett*, 2012, **23**, 2179-2182.
460. H. S. Fogler, in *Elements of Chemical Reaction Engineering*, Pearson Education Inc., 4th edn., 2006, ch. 10.
461. L. Zhu, J. Li, J. Yang and H. Y. Au-Yeung, *Chemical Science*, 2020, **11**, 13008-13014.
462. H. E. Gottlieb, V. Kotlyar and A. Nudelman, *Journal of Organic Chemistry*, 1997, **62**, 7512-7515.
463. S. Shaw and J. D. White, *Chemical Reviews*, 2019, **119**, 9381-9426.
464. T. Katsuki, *Chemical Society Reviews*, 2004, **33**, 437-444.
465. A. Miyashita, A. Yasuda, H. Takaya, K. Toriumi, T. Ito, T. Souchi and R. Noyori, *Journal of the American Chemical Society*, 1980, **102**, 7932-7934.
466. A. Miyashita, H. Takaya, T. Souchi and R. Noyori, *Tetrahedron*, 1984, **40**, 1245-1253.
467. H. Shi and J. He, *Journal of Catalysis*, 2011, **279**, 155-162.
468. H. A. McManus and P. J. Guiry, *Chemical Reviews*, 2004, **104**, 4151-4202.

469. A. K. Ghosh, P. Mathivanan and J. Cappiello, *Tetrahedron Asymmetry*, 1998, **9**, 1-45.
470. R. Noyori and S. Hashiguchi, *Accounts of Chemical Research*, 1997, **30**, 97-102.
471. M. Maji, K. Chakrabarti, B. Paul, B. C. Roy and S. Kundu, *Advanced Synthesis & Catalysis*, 2018, **360**, 722-729.
472. S. Iwasa, F. Takezawa, Y. Tuchiya and H. Nishiyama, *Chemical Communications*, 2001, 59-60.
473. Z. Cao, H. Qiao and F. Zeng, *Organometallics*, 2019, **38**, 797-804.
474. E. Milczek, N. Boudet and S. Blakey, *Angewandte Chemie International Edition*, 2008, **47**, 6825-6828.
475. D. Cuervo, M. P. Gamasa and J. Gimeno, *Chemistry – A European Journal*, 2004, **10**, 425-432.
476. E. Carreira, E. Jacobsen, A. Pfaltz and H. Yamamoto, *Comprehensive Asymmetric Catalysis*, Springer, Berlin, 1999.
477. B. Trost, C. Lee and I. Ojima, Wiley-VCH, New York, 2nd edn., 2000, pp. 503-650.
478. W. Dumont, J. C. Poulin, D. T. Phat and H. B. Kagan, *Journal of the American Chemical Society*, 1973, **95**, 8295-8299.
479. S. Saaby, K. Nakama, M. A. Lie, R. G. Hazell and K. A. Jørgensen, *Chemistry – A European Journal*, 2003, **9**, 6145-6154.
480. H. Nishiyama and Y. Motoyama, *Chemical Communications*, 1997, 1863-1864.
481. M. K. Tse, S. Bhor, M. Klawonn, C. Döbler and M. Beller, *Tetrahedron Letters*, 2003, **44**, 7479-7483.
482. K. W. Fiori and J. Du Bois, *Journal of the American Chemical Society*, 2007, **129**, 562-568.
483. H. Nishiyama, Y. Itoh, H. Matsumoto, S.-B. Park and K. Itoh, *Journal of the American Chemical Society*, 1994, **116**, 2223-2224.
484. S. Gladiali and E. Alberico, *Chemical Society Reviews*, 2006, **35**, 226-236.
485. D. Cuervo, E. Menéndez-Pedregal, J. Díez and M. P. Gamasa, *Journal of Organometallic Chemistry*, 2011, **696**, 1861-1867.
486. I. Dragutan, V. Dragutan and A. Demonceau, *Molecules*, 2015, **20**, 17244-17274.
487. E. Menéndez-Pedregal, J. Díez, A. Manteca, J. Sanchez, A. C. Bento, R. Garcia-Navas, F. Mollinedo, M. P. Gamasa and E. Lastra, *Dalton Transactions*, 2013, **42**, 13955-13967.
488. D. Gnanamgari, C. H. Leung, N. D. Schley, S. T. Hilton and R. H. Crabtree, *Organic & Biomolecular Chemistry*, 2008, **6**, 4442-4445.
489. K. T. Prasad, B. Therrien and K. M. Rao, *Journal of Organometallic Chemistry*, 2008, **693**, 3049-3056.
490. L. Colina-Vegas, W. Villarreal, M. Navarro, C. R. de Oliveira, A. E. Graminha, P. I. d. S. Maia, V. M. Deflon, A. G. Ferreira, M. R. Cominetti and A. A. Batista, *Journal of Inorganic Biochemistry*, 2015, **153**, 150-161.
491. C. Garino, R. Gobetto, C. Nervi, L. Salassa, E. Rosenberg, J. B. A. Ross, X. Chu, K. I. Hardcastle and C. Sabatini, *Inorganic Chemistry*, 2007, **46**, 8752-8762.
492. A.-C. Laemmel, J.-P. Collin and J.-P. Sauvage, *Comptes Rendus de l'Académie des Sciences - Series IIC - Chemistry*, 2000, **3**, 43-49.
493. B. J. Coe, D. W. Thompson, C. T. Culbertson, J. R. Schoonover and T. J. Meyer, *Inorganic Chemistry*, 1995, **34**, 3385-3395.
494. S. Pyo, E. Pérez-Cordero, S. G. Bott and L. Echegoyen, *Inorganic Chemistry*, 1999, **38**, 3337-3343.

495. S. Mallakpour, M. Dinari, H. Hadadzadeh, M. Daryanavard and F. Roudi, *Journal of Fluorescence*, 2014, **24**, 1841-1848.
496. Mariana Kozłowska, Pawel Rodziewicz, Diana Malgorzata Brus, J. Breczko and K. Brzezinski, *Acta Crystallographica*, 2012, **E68**, m1414-m1415.
497. C. A. Tovee, C. A. Kilner, J. A. Thomas and M. A. Halcrow, *CrystEngComm*, 2009, **11**, 2069-2077.
498. E. G. Hohenstein and C. D. Sherrill, *The Journal of Physical Chemistry A*, 2009, **113**, 878-886.
499. J. Holmes, C. M. Pask and C. E. Willans, *Dalton Transactions*, 2016, **45**, 15818-15827.
500. V. Cadierno, M. P. Gamasa, J. Gimeno, L. Iglesias and S. García-Granda, *Inorg Chem*, 1999, **38**, 2874-2879.
501. R. M. Lord, M. Zegke, A. M. Basri, C. M. Pask and P. C. McGowan, *Inorganic Chemistry*, 2021, **60**, 2076-2086.
502. C. A. Puckett and J. K. Barton, *Biochemistry*, 2008, **47**, 11711-11716.
503. J. K. Barton, A. Danishefsky and J. Goldberg, *Journal of the American Chemical Society*, 1984, **106**, 2172-2176.
504. L. Biancalana, G. Pampaloni, S. Zacchini and F. Marchetti, *Journal of Organometallic Chemistry*, 2018, **869**, 201-211.
505. O. V. Dolomanov, L. J. Bourhis, R. J. Gildea, J. A. K. Howard and H. Puschmann, *Journal of Applied Crystallography*, 2009, **42**, 339-341.
506. L. J. Bourhis, O. V. Dolomanov, R. J. Gildea, J. A. K. Howard and H. Puschmann, *Acta Crystallographica*, 2015, **A71**, 59-75.
507. G. M. Sheldrick, *Acta Crystallographica*, 2015, **A71**, 3-8.
508. G. Sheldrick, *Acta Crystallographica Section A*, 2008, **64**, 112-122.
509. G. M. Sheldrick, *Acta Crystallographica*, 2015, **C71**, 3-8.